HAL
open science

Experiment and theory of plasmon coupling physics, wave effects and their study by electron spectroscopies

Hugo Lourenço-Martins

To cite this version:

Hugo Lourenço-Martins. Experiment and theory of plasmon coupling physics, wave effects and their study by electron spectroscopies. Condensed Matter [cond-mat]. Université Paris Saclay (COmUE), 2018. English. NNT : 2018SACLS284 . tel-01924457

HAL Id: tel-01924457

https://theses.hal.science/tel-01924457v1

Submitted on 16 Nov 2018

HAL is a multi-disciplinary open access archive for the deposit and dissemination of scientific research documents, whether they are published or not. The documents may come from teaching and research institutions in France or abroad, or from public or private research centers.

L'archive ouverte pluridisciplinaire **HAL**, est destinée au dépôt et à la diffusion de documents scientifiques de niveau recherche, publiés ou non, émanant des établissements d'enseignement et de recherche français ou étrangers, des laboratoires publics ou privés.

université PARIS-SACLAY

UNIVERSITÉ PARIS SUD
Comprendre le monde, construire l'avenir

NNT : 2018SACLS284

Experiment and theory of plasmon coupling physics, wave effects and their study by electron spectroscopies

Thèse de doctorat de l'Université Paris-Saclay
préparée à Université Paris-Sud

Ecole doctorale n°572 Ondes et Matière (EDOM)
Spécialité de doctorat : Nanophysique

Thèse présentée et soutenue à Orsay, le 28 septembre 2018, par

HUGO LOURENÇO-MARTINS

Composition du Jury :

M. Jean-Jacques Greffet Professeur, Institut d'Optique Graduate School	Président
M. Nicolas Bonod Directeur de recherche, Institut Fresnel	Rapporteur
Mme Cécile Hébert Professeur, École polytechnique fédérale de Lausanne	Rapporteur
M. Rafal Dunin-Borkowski Professeur, Ernst Ruska-Centre	Examinateur
Mme Lucia Reining Directrice de recherche, École polytechnique	Examinateur
M. Stefan Rotter Professeur, Vienna University of Technology	Examinateur
M. Mathieu Kociak Directeur de recherche, Laboratoire de Physique des Solides	Directeur de thèse
M. Luiz Henrique Galvão-Tizei Chargé de recherche, Laboratoire de Physique des Solides	Co-encadrant

Thèse de doctorat

Résumé de la thèse

Les plasmons de surface (SP) sont des ondes électromagnétiques se propageant à l'interface entre deux milieux, typiquement un métal et un diélectrique. Les plasmons de surface ont la capacité de confiner le champ électromagnétique dans de très petite région de l'espace, typiquement quelques nanomètres, c'est à dire bien en dessous de la limite de diffraction de la lumière. Le prix à payer pour obtenir un tel confinement est que les plasmons subissent d'énormes pertes ohmiques dans le métal, ce qui conduit à des temps de vie très courts (typiquement quelques femtosecondes). La présence de cette forte dissipation complique considérablement la description théorique des plasmons de surface. Une autre conséquence du confinement sub-longueur d'onde de la lumière associé aux plasmons est que leur observation nécessite une résolution spatiale nanométrique - ce qui exclut l'utilisation de techniques optiques standard. Néanmoins, le microscope électronique en transmission à balayage (STEM) est un outil particulièrement adapté à l'étude des plasmons de surface car il emploie des électrons rapides ayant une longueur d'onde typique comprise entre 1 et 10 picomètres. Ainsi, durant la dernière décennie, les spectroscopies électroniques appliquées à la nano-optique se sont fortement développées, parmi elle comptent : la spectroscopie de perte d'énergie électronique (EELS), la spectroscopie cathodoluminescence (CL) ou l'interférométrie de Hanbury Brown et Twiss (HBT) appliquée à la CL. Dans cette thèse, j'ai exploré différents problèmes ouverts de la plasmonique et de la nano-optique dans le cadre particulier de la microscopie électronique. Dans le chapitre 1, je présente un formalisme prenant en compte à la fois la nature quantique et relativiste des expériences d'EELS en faisant appel notamment à des éléments de théorie quantique des champs. De récents travaux ont démontré l'incroyable possibilité de modifier arbitrairement la phase d'un faisceau électronique dans un STEM. Dans le chapitre 2, nous démontrons que la réalisation d'une expérience d'EELS avec de tels faisceaux permet de mesurer des propriétés jusqu'alors inatteignable à l'échelle du nanomètre telle que la phase des plasmons, leurs chiralité optique voire même leur longueur de cohérence. Dans le chapitre 3, je présente plusieurs résultats théoriques et expérimentaux concernant des expériences de couplage. En effet, le couplage des plasmons de surface (entre eux ou avec d'autre type d'excitations) est un champ de recherche très actif car il présente d'importantes applications potentielles par exemple en l'information quantique. En premier lieu, j'étudie le couplage électromagnétique dans un dimère de nano-croix et démontre que la réponse optique de ce système peut être façonnée dans une large gamme spectrale - ce qui constitue une source potentielle d'applications en ingénierie photonique. Ensuite, je me concentre sur un second type de couplage, que l'on appelle l'auto-hybridation, et qui correspond au couplage entre différents modes propres plasmonique au sein d'une même nanoparticule. Je démontre que cet effet, a priori contre-intuitif, est une conséquence de la nature non-hermitienne du problème aux valeurs propres associé aux résonances de plasmon et établit une analogie avec les systèmes quantiques ouverts. Dans une dernière partie, je considère le couplage entre LSPs et émetteurs quantiques (dans le régime de couplage faible) et démontre expérimentalement la présence d'un effet Purcell en utilisant une approche statistique de l'interférométrie HBT. Enfin, au chapitre 4, je discute des récentes mesures de phonon réalisées dans un STEM grâce au développement de monochromateur électroniques. Sur la base des travaux précurseurs de Fuchs et Kliewer, je démontre que tout le formalisme développé jusqu'ici pour les SP peut être appliqué pour décrire l'EELS vibrationnel moyennant l'introduction du concept de phonon à surface localisé.

Remerciements

Il est temps pour moi de me lancer dans l'écriture de la partie sans doute la plus complexe mais certainement celle qui me tient le plus à cœur: les remerciements. Malgré mon immense propension à me plaindre, il ne fait aucun doute que ces trois dernières années furent heureuses, épanouissantes, parfois décadentes[1] et riches tant en rencontres qu'en science. Tout cela, je le dois à de nombreuses personnes que je tiens à chaleureusement remercier dans la grande concision et solennité qui me caractérisent. Même s'il n'y a clairement pas assez de mots pour leur exprimer toute ma gratitude et mon admiration, je vais essayer de leur rendre hommage de la meilleure des manières. Donc bon courage, comme le reste de cette thèse, ça va être long.

Je tiens à remercier Cécile Hébert et Nicolas Bonod pour avoir accepté de rapporter sur ma thèse et pour avoir relu mon manuscrit avec soin et attention. I would also like to sincerely thank Jean-Jacques Greffet, Rafal Dunin-Borkowski, Lucia Reining and Stefan Rotter for having accepted to be part of my jury and for their interest in my work. Generally, I would like to express my gratitude to all the members of the jury for their questions, inputs and the passionating discussions we had: I greatly benefited from your views.

Je tiens à remercier Sylvain Ravy, directeur du LPS, de m'avoir accueilli dans ce laboratoire où j'ai pris plaisir à venir travailler. Mes remerciements vont ensuite à Odile pour m'avoir fait l'honneur de m'accueillir dans son groupe de recherche. Je voudrais aussi et surtout la remercier pour l'aide, le soutien, la patience et la gentillesse qu'elle m'a témoignés durant ces trois dernière années. Je m'estime extrêmement chanceux d'avoir pu réaliser cette thèse avec une chef de groupe aussi bienveillante et disponible. Et enfin, je lui adresse un immense merci pour m'avoir permis d'assister à toutes ces conférences et de voyager aux quatre coins de la planète !

J'adresse un monumental merci à Mathieu qui m'a (en)cadré durant ces années de thèse. Il m'est absolument impossible de quantifier tout ce qu'il m'a appris, tant sur le plan scientifique que sur le plan humain. Comme tous ses thésards avant moi, je suis obligé de rendre hommage à son extraordinaire culture scientifique et à sa patience hors norme mais aussi à sa déconcertante humilité et à l'amitié qu'il m'a témoignée tout au long de ces trois années. Lorsque j'ai rencontré Mathieu en stage de master, j'étais évidemment extrêmement intimidé et admiratif du scientifique qu'il est. On pourrait penser que travailler quelques temps à ses côtés m'aurait rendu un peu moins complexé mais il n'en est rien. Au contraire, mon respect et mon admiration n'ont cessé de croitre et je me rend compte aujourd'hui, de l'immense chance que j'ai eu de faire cette thèse avec lui. Nul doute que Mathieu est et restera un modèle pour moi et j'espère un jour devenir le centième du scientifique qu'il est; ce serait déjà, à mon sens, un bel accomplissement. Je tiens aussi à m'excuser pour avoir tant critiqué ses blagues (ses calembours pour être précis); rétrospectivement, je pense que c'était essentiellement de la jalousie[2]. Enfin, et c'est important, je le remercie d'avoir su comprendre mon amour coupable pour les politiciens véreux et d'avoir toléré mon addiction aux boissons anisées.

[1] j'y reviendrai peut-être plus loin si ma pudeur m'y autorise.
[2] sauf peut-être une fois ou deux où là, franchement, c'était mérité.

Pour cette thèse, j'ai aussi eu le plaisir d'être co-encadré par Luiz, même si le terme "co-encadrant" ne rend pas hommage à sa large contribution à ce travail et surtout, à tout ce qu'il m'a apporté humainement ces trois dernières années. Je pense que Luiz est une des personnes les plus brillantes que j'ai rencontré. Ceux qui ont travaillé un jour avec lui savent qu'il est, sans nul doute, un expérimentateur prodige et plus généralement un excellent scientifique. Mais je suis, avant tout, bluffé par son intelligence et la rapidité déconcertante avec laquelle il a su comprendre absolument tout ce que j'ai confusément déblatéré[3] pendant nos réunions de travail. Comme si ce n'était pas suffisant, Luiz est aussi chaleureux, toujours de bonne humeur et incroyablement humble. La seule fois où Luiz m'a déçu, c'est lorsque qu'il a refusé de me suivre au Monkey Bar à Tokyo; il le sait, les saïmiris le savent, et j'espère qu'il se rattrapera. Néanmoins, je tiens à le remercier pour tout ce qu'il m'a appris, pour toutes les discussions passionnantes que nous avons eu et bien sûr, pour son amitié précieuse.

Je voudrais maintenant remercier Pabitra, sans qui cette thèse aurait été bien différente et sans nul doute bien moins riche. Je ne peux compter les longues heures que nous passées ensemble à batailler sur des calculs, à dépouiller un nombre interminable de données, à lithographier je ne sais combien d'échantillons, à enchainer des spims comme des bières ou à s'énerver à la préfecture. Même s'il est bien trop humble pour le reconnaitre, il est évidemment un remarquable scientifique et je resterai admiratif de son sens physique et de sa patience à tout épreuve. Au delà de la science, Pabitra est réellement quelqu'un de passionnant, avisé, extrêmement cultivé et j'ai énormément appris de nos longues discussions autour d'un café ou d'un pastis (on y revient). Il m'a dit qu'il écrirait un jour un livre avec son père, il me tarde déjà de le lire !

Je voudrais également remercier Sophie qui, lorsqu'elle terminait sa thèse, m'a encadré en tant que stagiaire. Je lui dois beaucoup car, sans sa patience et sa passion, je n'aurais probablement pas compris la beauté de la microscopie électronique et aurais commencé une thèse dans un tout autre domaine (donc forcément moins bien). Je la remercie également pour tous les précieux conseils qu'elle m'a distillé (jeu de mot fortuit) et que j'ai religieusement écoutés.

Il est temps maintenant de remercier tout le groupe STEM qui m'a si bien accueilli et au sein duquel je me suis épanoui durant cette thèse. Il y a tellement de monde, par où commencer?
Allez, je démarre donc en remerciant Christian, pour sa bienveillance et pour tout les conseils qu'il m'a prodigué. Merci beaucoup à la paimpolaise du groupe, Laura, pour avoir supporté mes blagues bien lourdes sur les bretons[4], pour sa gentillesse, sa bienveillance et tout ses conseils qui m'ont toujours été précieux. Un grand merci à Marcel qui m'a toujours impressionné par son savoir scientifique, sa culture, sa finesse d'esprit, sa classe (eh ouai, on peut être scientifique, porter une chemise et avoir une classe de bonhomme - j'ai plus d'excuse) et à qui je voue une admiration sans borne. Un grand merci à Mike qui, bien qu'il n'ait jamais compris un mot de ce que je raconte[5], a toujours été un sérieux et fidèle compagnon de boisson. Un autre grand merci à Marta pour toutes nos discussions passionnantes, notamment sur la politique et l'anarchisme, qui me manqueront à coup sûr ! Je voudrais ensuite remercier chaleureusement Nathalie pour sa gentillesse et son aide toujours précieuse. Merci beaucoup à Alex pour tout les potins qu'il a partagé, aussi croustillants les uns que les autres, et pour toutes les vannes caustiques que j'ai tant savourées. Un grand big-up à Jean-Denis, qui m'a accueilli dans son bureau et qui a supporté m'entendre menacer mon ordinateur de mort pendant 3 ans. Je ne te remercie en revanche pas pour toutes les fois où tu as pourri mon bureau[6]. Un grand merci à la nouvelle super ingénieure Xiaoyan pour son aide précieuse durant ces trois années. Enfin, merci beaucoup à Alberto et Michele qui m'ont fait découvrir les joies de l'enseignement (franchement c'est pas si terrible, j'ai déjà arrêté de pleurer).

Et les thésards dans tout ça? Un grand merci à Alfredo qui, à l'heure où j'écris ces lignes, doit

[3] dans un anglais approximatif, peu articulé et parlé beaucoup trop vite.

[4] Je n'aurais jamais imaginé prononcer autant de fois les mots "bigoudène" et "coco de Paimpol" durant ma thèse.

[5] promis je vais essayer de parler moins vite !

[6] D'ailleurs j'espère que tu as trouvé les surprises que je t'ai cachées en partant. Ne tarde pas trop avant qu'elles ne mutent...

être en train de préparer sa soutenance (ou boire une bière, franchement je ne jugerai pas). Je suis sûr que tout se passera bien le 31 et je te souhaite plein de bonheur et de réussite pour ton poste de professeur qui t'attend au Panama. J'adresse également un grand merci à mon tic, Adrien, avec qui j'ai adoré partager deux années de ma thèse (notamment ces deux semaines d'anthologie à QEM que je ne détaillerai pas ici). Je le remercie pour son amitié, ses anecdotes improbables et son soutien sans faille. Je lui souhaite le meilleur pour sa dernière année de thèse, il le mérite. Un grand merci à mon gars sûr, Clément, qui a été stagiaire deux fois dans le groupe et qui attaque sa thèse au CEMES pour laquelle je lui souhaite la plus grande réussite. Merci pour toutes les longues discussions philosophiques, les séances de déclamation de citations de Kaamelott, les pauses café beaucoup trop longues et les soirées au rhum qui s'enveniment. Enfin un grand merci à Noémie pour tous ces apéros mémorables et pour toujours avoir répondu présente aux PubSTEMs. Noémie commence sa thèse avec Luiz et Mathieu et je suis sûr qu'elle s'épanouira autant que moi à faire de la physique avec eux. Je lui souhaite plein de réussite pour ces trois années et surtout qu'elle en profite le plus possible ! Enfin, je remercie tous les autres chercheurs, thésards et stagiaires que j'ai eu l'immense plaisir de côtoyer ou de simplement rencontrer: Vincent[7], Steffi, Anna, Eric, Thomas[8], Arthur, Federico, Jérôme, Katia, Xuan, Kawasaki-san, Aya, Henrikas, Nicolas, Emerys, Jules, Costantino, Ibrahim, Zackaria, Romain, Victor (de Seauve), Alicia, Henrik.

Un grand merci à Raphaël pour son aide précieuse sur la nano-fabrication et à André pour avoir accepté de parrainer ma thèse. Je souhaite également remercier les personnes avec qui j'ai eu le plaisir et l'honneur de collaborer durant ces trois années: Giulio Guzzinati, Jo Verbeeck, Axel Lubk, Florent Houdellier, Xing Yi Ling, Yih Hong Lee et Hikaru Saito. Mes sincères remerciements vont également à Codruta Marinica et Andrey Borissov qui, à l'occasion de mon stage de licence, m'ont donné le goût de la recherche académique et m'ont fait découvrir le monde merveilleux de la nano-optique; je pense que c'est en très grande partie grâce à eux que j'ai décidé de poursuivre mes études jusqu'au doctorat et je leur en suis profondément reconnaissant.

Mes remerciements vont maintenant à mes compagnons de toujours, mes quatre souillon(e)s, les quatre cavaliers de l'apocalypse. Je commence par remercier Benoît, mon compagnon de galère avec qui j'ai partagé quasi-quotidiennement ces trois années de thèse et aussi plein d'expériences incroyables comme: dormir sous une tente pendant une tempête dans la vallée de la mort[9], cultiver notre goût pour l'Asahi et les ours à Tokyo, tenter péniblement de nous mettre à l'escalade, cuisiner des plats fins et délicats à base de bacon ou déguster des digestifs auvergnats devant Koh-Lanta[10]. Ensuite, je remercie Lauriane pour tous ses plats incroyables qui nous réconcilient avec la vie, pour ses dérapages "lampe frontale", pour avoir supporté tous les cadeaux immondes qu'on lui a offert, pour toutes ces soirées incroyables à Massy où elle nous a empêché de mettre le feu au canapi et surtout, pour ses conseils avisés qui m'ont toujours guidés. Je remercie également Mallory avec qui j'ai partagé des débats sans fin beaucoup trop arrosés, de la musique pas toujours très maligne[11], des films qui ne nous auront jamais mis d'accord et des soirées armageddon lors de ses retours d'Écosse qui m'ont laissées plus pauvre de quelques neurones. Enfin, je remercie Matthieu, le poto de Mont-de-Marsan, avec qui je sillonne les férias depuis l'époque du lycée. Je ne peux pas compter le nombre d'heures qu'on a perdu devant Malcolm, One Piece, Mario Kart (la carapace bleue c'est définitivement un truc de fragile), au rugby, au cinéma ou au ski mais je recommencerai avec plaisir. Merci à vous quatre pour ces années incroyables, pour votre soutien, votre aide, vos conseils et votre amitié inestimable: je vous dois énormément.
J'en profite pour remercier toutes les autres personnes qui auront marqué ces longues années d'étude. Je remercie Victor (Castaing) que je connais depuis 23 années maintenant et avec qui j'ai eu le plaisir de randonner jusqu'à Ásbyrgi. Je souhaite également remercier Robin, qui doit être quelques part entre la Thaïlande et Singapour à l'heure ou j'écris; j'espère que ton tour du monde t'apportera les réponses que tu cherche. Un grand merci à Marino et Sylvie qui ont toujours eu une pensée pour moi lors de chaques étapes difficiles (et qui m'ont envoyé de quoi fêter la Madeleine

[7] Vibi pour les intimes, qui, avec JD, m'accompagna dans l'écriture des cahiers du cinema du groupe STEM et qui réalisa une critique au vitriol de *Sharktopus vs. Pteracuda*.

[8] qui est un supporter du stade toulousain donc nécessairement un mec bien comme dirait mon grand-père.

[9] Je ne parlerai pas de Vegas...

[10] Sans cet euphémisme, ça sonne encore plus triste.

[11] Merci de m'avoir fait découvrir le hardcore, sans lequel j'aurais certainement cassé quelques portes.

au fin fond de l'Islande).

Pour terminer, je remercie du fond du cœur mes parents, Manuel et Sylvie, à qui je dois tant et à qui je ne pourrai jamais rendre hommage comme ils le méritent. Je remercie aussi mon frère, Valentin, qui est sans nul doute ma plus grande fierté. Aucun texte ne pourrait résumer convenablement ma gratitude et mon admiration envers vous trois.
Je remercie mon cousin Romain pour tous ces moments géniaux passés ensembles, mon oncle Pierre pour son soutien indéfectible et ma grand-mère Simone pour tout ce qu'elle m'a apporté. J'ai enfin une pensée pour mes autres grand-parents Robert, Maria et Francisco avec qui j'aurais tant aimé partagé ce moment important de ma vie.

Mes remerciements ne vont en revanche pas à Reed Hastings, qui m'a fait perdre beaucoup trop de temps.

À mes parents,
À mon frère

Contents

1 Introduction **1**

2 Theoretical, Experimental and numerical tools **5**
2.1 Introduction . . . 6
2.2 Elements of nano-optics and plasmonics . . . 6
2.2.1 Classical electrodynamics . . . 6
2.2.2 Basic principles of plasmonics . . . 8
2.2.3 Luminescence in semi-conductors . . . 17
2.2.4 Coupling surface plasmon and quantum emitters . . . 20
2.2.5 Green function formalism for electromagnetism: density of states and coherence . . . 21
2.3 Electron microscopy and spectroscopies . . . 24
2.3.1 Interaction between fast electron and matter . . . 24
2.3.2 Experimental setup . . . 32
2.3.3 Wave effect in electron energy loss spectroscopy . . . 39
2.4 Light interferometry in cathodoluminescence . . . 40
2.4.1 The second order correlation function $g^{(2)}(\tau)$ . . . 40
2.4.2 The Hanbury Brown and Twiss interferometry and its application in cathodoluminescence . . . 41
2.4.3 Photon bunching in cathodoluminescence, application in lifetime measurement 42
2.5 Numerical methods for nano-optics . . . 44
2.6 Sample preparation: the electron beam lithography . . . 45

3 A photonic approach to inelastic electron holography **47**
3.1 Presentation of the problem . . . 48
3.1.1 Introduction . . . 48
3.1.2 Difficulties: retardation effects, quantum description of the target . . . 49
3.1.3 State of the art . . . 50
3.1.4 Purpose of this chapter, methodology . . . 52
3.2 Preliminary remarks: conventions, Green functions, gauge fixing . . . 52
3.2.1 Conventions and notations . . . 52
3.2.2 Correlators and Green functions . . . 53
3.2.3 Lagrangian form of the Maxwell equations . . . 54
3.2.4 Gauge fixing and vacuum photon propagator . . . 54
3.3 Propagators for the electromagnetic field in presence of a polarizable medium . . . 55
3.3.1 Quasistatic approach: modification of the Coulomb propagator, electron density correlation function . . . 56
3.3.2 Retarded approach: Photon propagator and electron four-current correlation function . . . 59
3.3.3 Concluding remarks . . . 64
3.4 Kinetic equation for the electron density matrix . . . 64

3.4.1 Schrödinger equation for the electron propagator . . . 64
3.4.2 Dyson equation for the single electron propagator . . . 65
3.4.3 Bi-linear propagator for the single electron density matrix . . . 68
3.4.4 The kinetic equation for the single electron density matrix . . . 70
3.5 Single scattering approximation: application to electron energy loss experiments . 73
3.5.1 Electron energy loss probability . . . 73
3.5.2 Application to the measurement of the coherence of optical fields . . . 74
3.5.3 The self-energy formalism . . . 76
3.5.4 Relativistic anisotropy in inelastic scattering . . . 77
3.6 Summary and perspectives . . . 78

4 Measuring surface plasmons with phase-shaped electron beams 81
4.1 Introduction . . . 82
4.1.1 Missing information in conventional electron-energy loss spectroscopy . . . 82
4.1.2 Phase manipulation in the electron microscope . . . 84
4.1.3 Structure of the chapter . . . 88
4.2 Semi-classical and quasi-static transition probability: analogy with atomic physics 88
4.2.1 Derivation of the loss probability . . . 88
4.2.2 Selection rules and peculiarity of PSEELS . . . 90
4.2.3 Polarizer effect using a Hermite-Gaussian beam . . . 92
4.3 First experimental demonstration . . . 94
4.4 Application of phase-shaped EELS to actual problems in plasmonics . . . 95
4.4.1 Resolution of the problems highlighted in the introduction . . . 95
4.4.2 Selective detection of symmetries . . . 96
4.4.3 Measurement of the potential derivative and perspective in plasmon phase retrieval . . . 98
4.4.4 Measurement of the azimuthal symmetry with vortex beams . . . 100
4.4.5 Dichroic EELS mapping with point vortex probes . . . 102
4.5 Post-selection of the final state . . . 106
4.5.1 Influence of the collection angle . . . 106
4.5.2 Selection of the final state: basis change . . . 109
4.5.3 Example: measurement of the OAM carried by a vortex plasmon . . . 109
4.6 Measurement of the coherence at the nanometer scale . . . 111
4.6.1 Electron bi-prism . . . 111
4.6.2 Split-beam electron energy loss probability . . . 112
4.6.3 Coherence measurement . . . 113
4.6.4 Double bi-prism experiment . . . 114
4.7 Summary and perspectives . . . 114

5 Exploring nano-optical excitations coupling with fast electrons techniques 117
5.1 Introduction . . . 118
5.2 Nanocross: A Highly Tunable Plasmonic System . . . 119
5.2.1 Motivation: generation of low-energy high order plasmon modes . . . 119
5.2.2 Probing the morphing from nanorod to nanocross by EELS . . . 120
5.2.3 Geometrical tuning: perturbation and symmetry arguments . . . 122
5.2.4 Dimer coupling of nanocrosses . . . 124
5.2.5 Summary of the different spectral tuning processes . . . 127
5.3 Self-hybridization within non-Hermitian localized plasmonic systems . . . 128
5.3.1 Motivation of the work . . . 128
5.3.2 Algebraic analysis of the plasmon eigenproblem . . . 130
5.3.3 LSP vs. electromagnetic wave in open systems . . . 133
5.3.4 Self-hybridization within a dagger resonator . . . 135
5.3.5 Experimental demonstration of self-hybridization . . . 138
5.3.6 Physical origin of plasmonic bi-orthogonality . . . 140
5.3.7 Analogy with open quantum systems . . . 141
5.4 Substrate effect on plasmon resonances in nano-cube . . . 141

5.4.1 Classification of the nanocube's plasmon modes . . . 142
5.4.2 Substrate-induced mode splitting . . . 144
5.4.3 Experimental and simulated EELS on cube monomer . . . 144
5.4.4 Distal-proximal formation mechanism . . . 147
5.4.5 CL experiment on cube monomer . . . 148
5.4.6 Dimer coupling of silver nano-cubes . . . 149
5.4.7 Difficulties and perspectives . . . 149
5.5 Probing plasmon-NV^0 coupling at the nanometer scale with photons and fast electrons . . . 151
5.5.1 Strategy to measure the Purcell effect at the nanoscale . . . 151
5.5.2 Choice of the SP-QE system . . . 152
5.5.3 Variability of NV^0 center excited state lifetime . . . 153
5.5.4 Statistical approach to STEM-HBT . . . 154
5.5.5 Numerical verification . . . 155
5.5.6 Conclusion and perspectives . . . 156
5.6 Summary and perspectives . . . 157

6 Vibrational surface EELS probes confined phonon modes 159
6.1 Introduction . . . 159
6.2 Recent advances in vibrational EELS . . . 160
6.3 History of the local continuum dielectric model . . . 160
6.4 Definition of the confined surface phonons . . . 162
6.4.1 Quasistatic modal decomposition . . . 162
6.4.2 Pedagogical example: the nanorod . . . 163
6.4.3 Analogy between localized SP and cSPh modes . . . 164
6.5 Connection with optical quantities . . . 164
6.5.1 Validity of the quasistatic approximation . . . 164
6.5.2 Comparison with optical experiments, EMLDOS . . . 165
6.6 General properties of confined surface phonon modes . . . 166
6.7 Review and interpretation of the experimental results found in the literature . . . 167
6.7.1 Fuchs-Kliewer modes of thin material slabs . . . 167
6.7.2 Confined phonon modes of MgO nanocube . . . 168
6.8 Substrate effect . . . 169
6.9 Summary and perspectives . . . 170

7 Perspectives and ongoing works 173
7.1 Studying the degeneracy points of the plasmon eigenproblem . . . 173
7.1.1 Merging a sphere dimer . . . 174
7.1.2 Proposed experiment . . . 175
7.2 Fabrication of a tunable phase-plate on a microelectromechanical system (MEMS) 176
7.3 Realization of the plasmon coherence measurement with an electron bi-prism . . . 177

A Remarks on quantum nano-plasmonics 179

B Illumination system of the STEM, spherical lens aberrations 181

C The Boundary Element Method and its application in plasmonics 186
C.1 From Maxwell equations to boundary integral equations . . . 186
C.1.1 Quasi-static approach . . . 186
C.1.2 Retarded approach . . . 188
C.2 The boundary element methods and its implementation in the `MNPBEM` toolbox . . . 189
C.2.1 Discretization procedure . . . 189
C.2.2 The `MNPBEM` simulation scheme . . . 190
C.2.3 Performances and validity domain of the method . . . 191

D Additional calculations for chapter 3 **193**
D.1 Spectral representation of the electrostatic susceptibility 193
D.2 Reciprocity theorem and symmetry properties of the Green dyadic 194
D.3 Quasi-static density matrix for plasmonic excitation 196

E Optical chirality and its connection with the helicity of the electromagnetic field **197**
E.1 Dual electromagnetism and electric-magnetic symmetry 198
E.2 Noether theorem, conservation law for the optical helicity 198

F Cathodoluminescence experiments with phase-shaped beams **200**

G Supporting information for chapter 5 **204**
G.1 De-noising procedure, adaptative median filtering 204
G.2 Correction of the CL system transmission 204

List of publications and contributions to conferences

Publications related to this thesis

1. **Probing the symmetry of the potential of localized surface plasmon resonances with phase-shaped electron beams**, Giulio Guzzinati, Armand Béché, Hugo Lourenço -Martins, Jérôme Martin, Mathieu Kociak and Jo Verbeeck, *Nature Communication* **8**, 14999, 2017
2. **Vibrational Surface Electron-Energy-Loss Spectroscopy Probes Confined Surface-Phonon Modes**, Hugo Lourenço-Martins and Mathieu Kociak, *Physical Review X* **7** (4), 041059, 2017
3. **Probing plasmon-NV^0 coupling at the nanometer scale with fast electrons and photons**, Hugo Lourenço-Martins, Mathieu Kociak, Sophie Meuret, François Treussart, Yih Hong Lee, Xing Yi Ling, Huan-Cheng Chang and Luiz Henrique Galvão Tizei, *ACS Photonics*, **5** (2), 324–328, 2018
4. **Nanocross: A Highly Tunable Plasmonic System**, Pabitra Das, Hugo Lourenço-Martins, Luiz Henrique Galvão Tizei, Raphaël Weil and Mathieu Kociak, *The Journal of Physical Chemistry C*, **121** (30), 2017
5. **Self-hybridization within non-Hermitian plasmonic systems**, Hugo Lourenço-Martins, Pabitra Das, Luiz Henrique Galvão Tizei, Raphaël Weil and Mathieu Kociak, *Nature Physics*, **89**, 2018
6. *h*–**BN monolayer as a substrate for plasmonics on metallic nanoparticles**, Luiz Tizei, Hugo Lourenço-Martins, Pabitra Das, Leonardo Scarabelli, Christoph Hanske, Luis Liz-Marzán and Mathieu Kociak, *submitted*
7. **Probing surface plasmons with phase-shaped electrons**, Hugo Lourenço-Martins and Mathieu Kociak, *in preparation*
8. **A photonic approach to electron holography**, Hugo Lourenço-Martins, Axel Lubk and Mathieu Kociak, *in preparation*

Publications unrelated to this thesis

1. **Plexciton quenching by resonant electron transfer from quantum emitter to metallic nanoantenna**, Dana Codruta Marinica, Hugo Lourenço-Martins, Javier Aizpurua and Andreï Borisov, *Nano Letters* **13** (12), 5972-5978, 2013
2. **InGaN nanowires with high InN molar fraction: growth, structural and optical properties**, Xin Zhang, Hugo Lourenço-Martins, Sophie Meuret, Mathieu Kociak, Benedikt Haas, Jean-Luc Rouvière, Pierre-Henri Jouneau, Catherine Bougerol, Thomas Auzelle, D Jalabert, Xavier Biquard, Bruno Gayral and Bruno Daudin, *Nanotechnology* **27** (19), 195704, 2016
3. **Extinction and Scattering Properties of High-Order Surface Plasmon Modes in Silver Nanoparticles Probed by Combined Spatially Resolved Electron Energy Loss Spectroscopy and Cathodoluminescence**, Naohiko Kawasaki, Sophie Meuret, Raphaël Weil, Hugo Lourenço-Martins, Odile Stéphan and Mathieu Kociak, *ACS Photonics* **3** (9), 1654-1661, 2016

Oral contributions to conferences

1. *Combined EELS and CL STEM analysis of plasmonic coupling between chemically grown silver nanocubes*, Hugo Lourenço-Martins, Yih Hong Lee, Yejing Liu, Hiang Kwee Lee, Mathieu Kociak, Odile Steéphan and Xing Yi Ling, **10th edition of JEELS (Journées de l'EELS) conference**, June 28-30, 2016, Tarragone, Spain.
2. *Theoretical and numerical investigation of the interaction between phase-shaped electron probes and plasmonic modes*, Hugo Lourenço-Martins, Giulio Guzzinati, Jo Verbeeck and Mathieu Kociak, **16th European Microscopy Congress**, August 28-September 2, 2016, Lyon, France.
3. *Bi-orthogonality allows observation of self-hybridization in plasmonic system*, Hugo Lourenço-Martins, Pabitra Das, Luiz Henrique Galvão Tizei, Raphaël Weil and Mathieu Kociak, **CLEO/Europe-EQEC conference**, June 25-29, 2017, Munich, Germany.
4. *Probing plasmon-NV^0 coupling at the nanometer scale with fast electrons and photons*, Hugo Lourenço-Martins, Mathieu Kociak, Sophie Meuret, François Treussart, Yih Hong Lee, Xing Yi Ling, Huan-Cheng Chang and Luiz Henrique Galvão Tizei, **2nd international workshop on Electron Beam Spectroscopy for Nanophotonics**, October 25-27, 2017, Barcelona, Spain.
5. *Self-hybridization within non-Hermitian plasmonic systems*, Hugo Lourenço-Martins, Pabitra Das, Luiz Henrique Galvão Tizei, Raphaël Weil and Mathieu Kociak, **American Physical Society March Meeting 2018**, March 5-9, 2018, Los Angeles, USA.

6. *Theoretical and numerical investigation of the interaction between phase-shaped electron probes and plasmonic modes*, Hugo Lourenço-Martins, Giulio Guzzinati, Jo Verbeeck and Mathieu Kociak, **Q-sort international conference on electron beam shaping in space and time**, May 28-30, 2018, Jülich, Germany.
7. *Theoretical and numerical investigation of the interaction between phase-shaped electron probes and plasmonic modes*, Hugo Lourenço-Martins, Giulio Guzzinati, Jo Verbeeck and Mathieu Kociak, **15$^{\mathbf{th}}$ international conference of Near-field Optics and Nanophotonics**, August 26-31, 2018, Troyes, France.
8. *Self-hybridization within non-Hermitian plasmonic systems*, Hugo Lourenço-Martins, Pabitra Das, Luiz Henrique Galvão Tizei, Raphaël Weil and Mathieu Kociak, **19$^{\mathbf{th}}$ International Microscopy Congress**, September 9-14, 2018, Sidney, Australia.
9. *Theoretical and numerical investigation of the interaction between phase-shaped electron probes and plasmonic modes*, Hugo Lourenço-Martins, Giulio Guzzinati, Jo Verbeeck and Mathieu Kociak, **19$^{\mathbf{th}}$ International Microscopy Congress**, September 9-14, 2018, Sidney, Australia.

Posters presented in conferences

1. *Nano-pptics in a Scanning Transmission Microscope, features and applications*, Hugo Lourenço-Martins, Sophie Meuret, Luiz Tizei, Romain Bourellier, Thomas Auzelle, François Treussart, Alberto Zobelli, Bruno Gayral and Mathieu Kociak, **14$^{\mathbf{th}}$ symposium of the French society of Microscopy**, June 29-30, 2015 Nice, France.
2. *Combined EELS and CL STEM analysis of plasmonic coupling between chemically grown silver nanocubes*, Hugo Lourenço-Martins, Yih Hong Lee, Yejing Liu, Hiang Kwee Lee, Mathieu Kociak, Odile Steéphan and Xing Yi Ling, **16$^{\mathbf{th}}$ European Microscopy Congress**, August 28-September 2, 2016, Lyon, France.
3. *Theoretical and numerical investigation of the interaction between phase-shaped electron probes and plasmonic modes*, Hugo Lourenço-Martins, Giulio Guzzinati, Jo Verbeeck and Mathieu Kociak, **8$^{\mathbf{th}}$ edition of Enhanced Data Generated by Electrons conference**, May 14-19, 2017, Okinawa, Japan.
4. *Bi-orthogonality allows observation of self-hybridization in plasmonic system*, Hugo Lourenço-Martins, Pabitra Das, Luiz Henrique Galvão Tizei, Raphaël Weil and Mathieu Kociak, **8$^{\mathbf{th}}$ edition of Enhanced Data Generated by Electrons conference**, May 14-19, 2017, Okinawa, Japan.
5. *Vibrational EELS probes confined Fuchs-Kliewer modes*, Hugo Lourenço-Martins and Mathieu Kociak, **8$^{\mathbf{th}}$ edition of Enhanced Data Generated by Electrons conference**, May 14-19, 2017, Okinawa, Japan.
6. *Probing plasmon-NV^0 coupling at the nanometer scale with fast electrons and photons*, Hugo Lourenço-Martins, Mathieu Kociak, Sophie Meuret, François Treussart, Yih Hong Lee, Xing Yi Ling, Huan-Cheng Chang and Luiz Henrique Galvão Tizei, **American Physical Society March Meeting 2018**, March 5-9, 2018, Los Angeles, USA.
7. *Theoretical and numerical investigation of the interaction between phase-shaped electron probes and plasmonic modes*, Hugo Lourenço-Martins, Giulio Guzzinati, Jo Verbeeck and Mathieu Kociak, **American Physical Society March Meeting 2018**, March 5-9, 2018, Los Angeles, USA.
8. *Self-hybridization within non-Hermitian plasmonic systems*, Hugo Lourenço-Martins, Pabitra Das, Luiz Henrique Galvão Tizei, Raphaël Weil and Mathieu Kociak, **26$^{\mathbf{ème}}$ Colloque Alain Bouyssy Colloque Jeunes Chercheurs en Physique**, March 15, 2018, Orsay, France.
9. *Self-hybridization within non-Hermitian plasmonic systems*, Hugo Lourenço-Martins, Pabitra Das, Luiz Henrique Galvão Tizei, Raphaël Weil and Mathieu Kociak, **15$^{\mathbf{th}}$ international conference of Near-field Optics and Nanophotonics**, August 26-31, 2018, Troyes, France.
10. *Vibrational Surface Electron-Energy-Loss Spectroscopy Probes Confined Surface-Phonon Modes*, Hugo Lourenço-Martins and Mathieu Kociak, **19$^{\mathbf{th}}$ International Microscopy Congress**, September 9-14, 2018, Sidney, Australia.

Chapter 1

Introduction

In its beautiful review [1], Atwater gaves a very pictural definition of surface plasmons: "surface plasmons are density waves of electrons that propagate along the interface like the ripples that spread across the surface of a pond after you throw a stone into the water". More prosaically, surface plasmons (SP) are electromagnetic waves propagating at the interface between two media [2] typically a metal and a dielectric. Depending on their wavelength, a SP can resemble light propagating at the interface (surface-plasmon polariton or SPP) or form a charge density stationary wave localized at the nanometer scale (localized surface plasmons - LSP). This ambiguous character between optical and electronic excitation confers to SPs their amazing properties but also makes their theoretical and experimental study rather intricate.

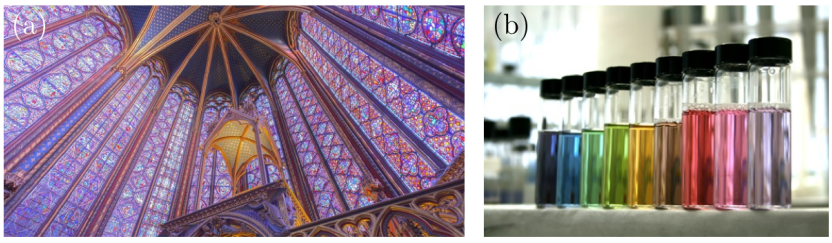

Figure 1.1: *(a) Stained-glass windows of the Sainte-Chapelle in Paris. (b) Solution of nano-particles of different sizes and shapes. Reproduced from the Sönnichsen group webpage.*

Localized surface plasmons dominate the optical properties of small metallic nanoparticles (tens of nanometer) in the near infrared to visible range. Thus, in this region and for a given metal, their optical properties will simply depend on their size and shape which is marvelously illustrated by the rich colour palette of stained-glass windows or colloïdal solutions of nanoparticles (see figure 1.1). In addition to their tunable optical response, plasmons can confine electromagnetic fields in very short volumes (typically few nanometers), well below the light diffraction limit. These combined properties have a tremendous number of possible applications in quantum optics [3], cancer therapy [4], bio-sensors [5], photovoltaics [1], metamaterials [6], spasers [7], ultrafast computer devices [8] to name a few. The recent success of plasmonics is first and foremost due to its exciting promises for the future [8].

However, the richness of plasmonics conceals a complex physical behavior and the underlying mechanisms at the nanoscale still challenge our understanding. Depending on the situation, surface plasmons must be regarded as many-body electron states or as electromagnetic waves, thus requiring either a quantum or a classical treatment with the possible inclusion of relativistic effects. This variety is a major obstacle to the establishment of a general theoretical treatment. Even more crucially, SPs suffer from huge ohmic losses in the metal which lead to very short lifetimes

(typically few femtoseconds). Theoretically, this presence of dissipation dramatically hardens the theoretical description of SPs. For example, although a modal decomposition exists in the non-quantal quasistatic regime [9, 10] ($c \to \infty$), it fails when retardation or quantum effects are taken into account and to date, a comprehensive quantification of SPs is not established.

Another consequence of the sub-wavelength confinement of light associated with SPs is that their observation requires a nanometric resolution - which excludes the use of standard optical techniques for sub-wavelength studies. Yet, the scanning transmission electron microscope (STEM) is a particularly suitable tool to study SPs as it employs fast electrons with typical wavelength ranging from 1 to 10 picometers. Thus, the last decade has seen the tremendous development of electron-based spectroscopies applied to nano-optics such as electron energy loss spectroscopy (EELS) [11], cathodoluminescence spectroscopy (CL) [12], STEM- Hanbury Brown and Twiss interferometry (HBT) [13] or electron energy gain spectroscopy (EEGS) [14, 15]. EELS consists in analyzing the energy lost by the electrons interacting with the sample. CL spectroscopy consists in measuring the spectrum of the light emitted by the sample subsequently to the interaction with the electron while the HBT interferometry aims at determining the emission statistics of this light. Finally, EEGS consists in analyzing the energy lost and gained by electrons interacting with a sample illuminated with light. These different spectroscopy techniques are schematically represented on figure 1.2.

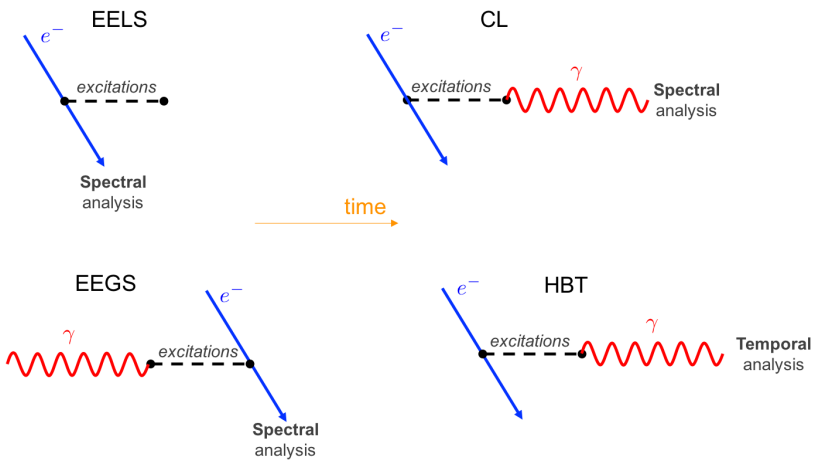

Figure 1.2: *Sketches representing the different electron-based spectroscopies involved in this manuscript. The blue lines represent the electrons, the red lines represent the photons and the dotted lines correspond to the excitations created in the sample.*

In this thesis, I explored different open problems of plasmonics and nano-optics under the scope of electron spectroscopy. The thesis is organized as follows:

- In chapter 2, I introduce the basic theoretical, experimental numerical tools used throughout this thesis. There is no original result in this chapter.
- One of the principal objectives of the present thesis is the development of EELS experiments using phase-shaped electron beams, with special emphasis on their application in plasmonics. In order to model such an experiment, a wave theory of electron energy-loss spectroscopy is naturally required. Several developments of such a theory have been proposed in the literature based on different types of formalism and assumptions. Roughly speaking, three approaches exist: **(1)** a quasi-static self-energy formalism proposed by Echenique [16], **(2)** a quasi-static density matrix approach first introduced to diffraction by Dudarev [17] and then extended to EELS by Schattschneider [18], **(3)** a retarded linear response theory proposed by García de Abajo [19]. In chapter 3, I rationalize all these different approaches and demonstrate how all these works are connected between each other. Eventually, I extend the formalism

of Echenique and Schattschneider to the retarded case, which is of fundamental interest in order to model e.g. electron holography experiments on optical systems. All this formalism has been developed in continuous discussion and with the great help of Mathieu Kociak.

- In chapter 4, I apply the latter formalism to the case of EELS measurements of SPs using electrons with shaped phase. Indeed, recent reports (e.g. [20, 21]) demonstrated the amazing possibility to modify the phase of the electron beams in a (S)TEM. I demonstrate theoretically in this thesis that performing an EELS experiment with such phase-shaped beams enables the measurement of SPs' phase and other related properties. I also contributed to the design of the first phase-shaped EELS (PSEELS) experiments realized by Guzzinati and collaborators from the Antwerp university. All these theoretical and numerical developments have been done in Orsay in a common effort with Mathieu Kociak.

- In chapter 5, I give several theoretical and experimental results on coupling experiments involving SPs. Indeed, coupling SPs is an active field of research as it would open the route toward the coherent control of light at the nano-scale with important applications e.g. in quantum information [22].
  I first focus on electromagnetic coupling on a dimer of nano-crosses and show that the optical absorption of this system can be tuned within a wide spectral range - which constitutes potential source of applications in photonic engineering. I performed all the e-beam lithography fabrication process, EELS experiments, data processing and numerical simulations in Orsay in a common effort with Pabitra Das.
  In the second section, I numerically and experimentally investigate the influence of a dielectric substrate on the plasmon resonances of a silver nano-cube, particularly the mechanism leading to the apparition of distal and proximal modes. Despite its systematic and dramatic influence in plasmonics, there is no consensus on the physical mechanism involved there and this remains an open problem in the community. The nano-cube samples have been fabricated by the team of Xing Yi Ling in NTU Singapore; all the rest of the work (EELS, data treatment, simulation) has been done in Orsay. All the developments of this section are the result of several scientific discussions with Mathieu Kociak, Yih Hong Lee and Odile Stéphan.
  Then, I focus on a second type of coupling, the so-called self-hybridization i.e. the coupling between different plasmon eigenmodes *within* a single nano-particle (NP). I demonstrate that this counter-intuitive effect is a consequence of the non-Hermitian nature of the LSP eigenproblem and draw analogy with open quantum system. I performed all the e-beam lithography fabrication process, EELS experiments, data processing, numerical simulation and theoretical developments in Orsay, in a common effort with Pabitra Das, Luiz Tizei and Mathieu Kociak.
  In the last part, I consider the coupling between LSPs and quantum emitters both in the weak coupling regime and experimentally demonstrate a Purcell effect using a statistical approach to the STEM-HBT interferometry. The samples have been prepared by our collaborators in Singapore and Taiwan. I performed all the rest of the work (HBT experiments, data treatment, simulation) in Orsay in a common effort with Luiz Tizei. I particularly benefited from his great expertise in HBT interferometry and quantum optics.

- In chapter 6, I discuss the recent result on vibrational EELS [23, 24] in monochromated STEM. Based on the seminal works of Fuchs and Kliewer [25], I demonstrate that all the formalism developed so far for SPs [10] can be applied to describe vibrational EELS leading to the concept of confined surface phonon (cSPh) mode. All these theoretical and numerical developments have been done in Orsay in a common effort with Mathieu Kociak.

- In chapter 7, I finally detail the ongoing works pursuing the different projects started during this thesis.

Globally, all these works are the results of continuous discussion and collaboration with Mathieu Kociak, Luiz Tizei and Pabitra Das, whom I would like to warmly thank.

In the rest of this thesis we will box the important equations and box in gray the important

new results. Moreover, at the end of each chapter (besides chapter 2 which does not contain any original result), a blue box summarizing the most important results will be displayed.

Chapter 2

Theoretical, Experimental and numerical tools

Contents

2.1 Introduction **6**
2.2 Elements of nano-optics and plasmonics **6**
2.2.1 Classical electrodynamics 6
2.2.1.1 Maxwell equations in real space 6
2.2.1.2 Maxwell equations in Fourier space 7
2.2.2 Basic principles of plasmonics 8
2.2.2.1 Bulk (or volume) plasmons 8
2.2.2.2 Surface plasmons(-polaritons) 11
2.2.2.3 Localized surface plasmons 12
2.2.2.4 Effect of the size of the nano-particles 14
2.2.2.5 Damping mechanisms 16
2.2.3 Luminescence in semi-conductors 17
2.2.3.1 Nano-structured materials: effect of quantum confinement . . 18
2.2.3.2 Structural point defects and molecules 18
2.2.4 Coupling surface plasmon and quantum emitters 20
2.2.5 Green function formalism for electromagnetism: density of states and coherence 21
2.2.5.1 Definition of the electric and magnetic Green dyadics 21
2.2.5.2 The electromagnetic local density of states 22
2.2.5.3 Cross-density of states and spatial coherence 23
2.3 Electron microscopy and spectroscopies **24**
2.3.1 Interaction between fast electron and matter 24
2.3.1.1 Electron energy-loss spectroscopy 26
2.3.1.2 Cathodoluminescence spectroscopy 28
2.3.1.3 Connection with optical quantities 31
2.3.2 Experimental setup 32
2.3.2.1 The scanning transmission electron microscope 33
2.3.2.2 Hyperspectral imaging 33
2.3.2.3 Image formation mechanisms 33
2.3.2.4 Electron energy loss spectrometer 36
2.3.2.5 Cathodoluminescence spectrometer 38
2.3.3 Wave effect in electron energy loss spectroscopy 39
2.4 Light interferometry in cathodoluminescence **40**

2.4.1 The second order correlation function $g^{(2)}(\tau)$ 40
2.4.2 The Hanbury Brown and Twiss interferometry and its application in cathodoluminescence 41
2.4.3 Photon bunching in cathodoluminescence, application in lifetime measurement 42
2.5 Numerical methods for nano-optics 44
2.6 Sample preparation: the electron beam lithography 45

2.1 Introduction

The central theme of this thesis is nano-optics which "is the study of optical phenoma on the nanometer scale i.e. near and beyond the diffraction limit" [26]. In this introductory chapter, we will therefore answer the following questions:

- *Which type of **phenomenon** leads to the confinement of light at the nano-scale?* This question will be addressed in section 2.2 in which we will give an overview of these phenomena as well as the theoretical tools required to their description.

- *How do we **measure** optical quantities at the nano-scale?* This question will be covered in section 2.3 where I present the key experimental tool of this work: the transmission electron microscope. I will particularly insist on the electron spectroscopies and their connection with the optical quantities presented in the latter section.

- *How do we **compute** the optical response of nano-object?* This question will be addressed in section 2.5 in which I present the boundary element method and the `MNPBEM` code which has been used throughout this thesis.

- *How do we **synthesize** such nano-objects?* Most of the samples studied in this thesis have been synthesized by electron beam lithography for which I will shortly present the synthesis protocol in section 2.6.

2.2 Elements of nano-optics and plasmonics

2.2.1 Classical electrodynamics

2.2.1.1 Maxwell equations in real space

The dynamics of the electromagnetic (EM) field is described by the Maxwell equations which read (in Gaussian units) [27]:

$$\begin{cases} \boldsymbol{\nabla}.\boldsymbol{D}(\boldsymbol{r},t) = 4\pi\rho(\boldsymbol{r},t) & (2.1a) \\ \boldsymbol{\nabla}\times\boldsymbol{H}(\boldsymbol{r},t) = \dfrac{4\pi}{c}\boldsymbol{j}(\boldsymbol{r},t) + \dfrac{1}{c}\dfrac{\partial\boldsymbol{D}(\boldsymbol{r},t)}{\partial t} & (2.1b) \\ \boldsymbol{\nabla}.\boldsymbol{B}(\boldsymbol{r},t) = 0 & (2.1c) \\ \boldsymbol{\nabla}\times\boldsymbol{E}(\boldsymbol{r},t) = -\dfrac{1}{c}\dfrac{\partial\boldsymbol{B}(\boldsymbol{r},t)}{\partial t} & (2.1d) \end{cases}$$

where $\boldsymbol{E}$ and $\boldsymbol{H}$ are respectively the electric and magnetic fields, $\boldsymbol{D}$ and $\boldsymbol{B}$ are the electric displacement and the magnetic induction, $\boldsymbol{j}$ is the local density of current and ρ is the local density of charge. Combining equations (2.1a) and (2.1b), one can show that the sources moreover satisfy the so-called continuity equation:

$$\frac{\partial\rho(\boldsymbol{r},t)}{\partial t} + \boldsymbol{\nabla}.\boldsymbol{j}(\boldsymbol{r},t) = 0 \tag{2.2}$$

At the interface between two media (labeled by indexes $i = 1, 2$), the Maxwell equations have to be completed by the following boundary conditions:

$$\begin{cases} \boldsymbol{n}_{12} \times (\boldsymbol{E}_2 - \boldsymbol{E}_1) = 0 & (2.3a) \\ \boldsymbol{n}_{12}.(\boldsymbol{D}_2 - \boldsymbol{D}_1) = 4\pi\sigma & (2.3b) \\ \boldsymbol{n}_{12} \times (\boldsymbol{H}_2 - \boldsymbol{H}_1) = \dfrac{4\pi}{c}\boldsymbol{h} & (2.3c) \\ \boldsymbol{n}_{12}.(\boldsymbol{B}_2 - \boldsymbol{B}_1) = 0 & (2.3d) \end{cases}$$

where σ and $\boldsymbol{h}$ are the surface charge and current densities and $\boldsymbol{n}_{12}$ is the normal vector at the interface directed from medium 1 to medium 2. Finally, in order to solve the Maxwell equations in any linear and non-chiral medium[1], one also need to provide the so-called constitutive equations which relate $\boldsymbol{D}$ and $\boldsymbol{B}$ to respectively $\boldsymbol{E}$ and $\boldsymbol{H}$:

$$\begin{cases} \boldsymbol{D}(\boldsymbol{r}, t) = \displaystyle\int d\boldsymbol{r} \int dt\, \overleftrightarrow{\boldsymbol{\epsilon}}(\boldsymbol{r}, \boldsymbol{r}', t, t')\boldsymbol{E}(\boldsymbol{r}', t') & (2.4a) \\ \boldsymbol{B}(\boldsymbol{r}, t) = \displaystyle\int d\boldsymbol{r} \int dt\, \overleftrightarrow{\boldsymbol{\mu}}(\boldsymbol{r}, \boldsymbol{r}', t, t')\boldsymbol{H}(\boldsymbol{r}', t') & (2.4b) \end{cases}$$

$\overleftrightarrow{\boldsymbol{\epsilon}}$ and $\overleftrightarrow{\boldsymbol{\mu}}$ are respectively the permittivity and permeability tensors. For simplicity and unless otherwise specified, we will further assume that:

- The media are non-magnetic i.e. $\overleftrightarrow{\boldsymbol{\mu}}(\boldsymbol{r}, \boldsymbol{r}') = \overleftrightarrow{\boldsymbol{I}}\delta(\boldsymbol{r} - \boldsymbol{r}')$ ($\overleftrightarrow{\boldsymbol{I}}$ being the identity tensor).
- The media are uniform and static so that they are invariant by translation both in space and time i.e. $\overleftrightarrow{\boldsymbol{\epsilon}}(\boldsymbol{r}, \boldsymbol{r}', t, t') = \overleftrightarrow{\boldsymbol{\epsilon}}(\boldsymbol{r} - \boldsymbol{r}', t - t')$.
- The media are uniform so that the permittivity tensor simply reduces to a scalar $\overleftrightarrow{\boldsymbol{\epsilon}}(\boldsymbol{r} - \boldsymbol{r}', t - t') = \epsilon(\boldsymbol{r} - \boldsymbol{r}', t - t')\overleftrightarrow{\boldsymbol{I}}\delta(\boldsymbol{r} - \boldsymbol{r}')$.

2.2.1.2 Maxwell equations in Fourier space

Because this thesis deals with electron microscopy and spectroscopies, we also need to know the spectral form of the Maxwell equations. The Fourier transforms (FT) are defined in the temporal domain as follow:

$$\begin{cases} f(\boldsymbol{r}, t) = \displaystyle\int \frac{d\omega}{2\pi} f(\boldsymbol{r}, \omega)\, e^{-i\omega t} & (2.5a) \\ f(\omega, t) = \displaystyle\int dt\, f(\boldsymbol{r}, t)\, e^{i\omega t} & (2.5b) \end{cases}$$

In the spatial domain we have:

$$\begin{cases} f(\boldsymbol{r}, t) = \displaystyle\int \frac{d\boldsymbol{k}}{(2\pi)^3} f(\boldsymbol{k}, t)\, e^{i\boldsymbol{k}.\boldsymbol{r}} & (2.6a) \\ f(\boldsymbol{k}, t) = \displaystyle\int d\boldsymbol{r}\, f(\boldsymbol{r}, t)\, e^{-i\boldsymbol{k}.\boldsymbol{r}} & (2.6b) \end{cases}$$

Applying a Fourier transform to equations (2.1), we therefore get:

$$\begin{cases} i\boldsymbol{k}.\boldsymbol{D}(\boldsymbol{k}, \omega) = 4\pi\rho(\boldsymbol{k}, \omega) & (2.7a) \\ i\boldsymbol{k} \times \boldsymbol{H}(\boldsymbol{k}, \omega) = \dfrac{4\pi}{c}\boldsymbol{j}(\boldsymbol{k}, \omega) - \dfrac{i\omega}{c}\boldsymbol{D}(\boldsymbol{k}, \omega) & (2.7b) \\ i\boldsymbol{k}.\boldsymbol{B}(\boldsymbol{k}, \omega) = 0 & (2.7c) \\ \boldsymbol{k} \times \boldsymbol{E}(\boldsymbol{k}, \omega) = \dfrac{\omega}{c}\boldsymbol{B}(\boldsymbol{k}, \omega) & (2.7d) \end{cases}$$

[1] In a chiral medium, $\boldsymbol{D}$ ($\boldsymbol{B}$) also linearly depends on $\boldsymbol{H}$ ($\boldsymbol{E}$) [28].

In real space, the Maxwell equations are non-local both in space and time while they become local in the spectral domain, which dramatically facilitates their resolution. Moreover, the constitutive equations then read:

$$\begin{cases} \boldsymbol{D}(\boldsymbol{k},\omega) = \epsilon(\boldsymbol{k},\omega)\boldsymbol{E}(\boldsymbol{k},\omega) & (2.8a) \\ \boldsymbol{B}(\boldsymbol{k},\omega) = \boldsymbol{H}(\boldsymbol{k},\omega) & (2.8b) \end{cases}$$

In absence of external source, by combining equations (2.7b) and (2.7d) and using the vector identity $\boldsymbol{\nabla} \times (\boldsymbol{\nabla} \times \boldsymbol{A}) = \boldsymbol{\nabla}(\boldsymbol{\nabla}.\boldsymbol{A}) - \boldsymbol{\nabla}^2\boldsymbol{A}$, we obtain the wave (or Helmholtz) equation:

$$\boldsymbol{k}(\boldsymbol{k}.\boldsymbol{E}) - \boldsymbol{k}^2\boldsymbol{E} = -\epsilon(\boldsymbol{k},\omega)\frac{\omega^2}{c^2}\boldsymbol{E} \tag{2.9}$$

which describes the traveling wave solutions of the Maxwell equations. The transverse waves satisfy the condition $\boldsymbol{k}.\boldsymbol{E} = 0$ which yield to the dispersion relation:

$$k^2 = \epsilon(\boldsymbol{k},\omega)\frac{\omega^2}{c^2} \tag{2.10}$$

The longitudinal waves satisfy $\boldsymbol{\nabla} \times \boldsymbol{E} = 0$ which, from equation (2.9), imposes:

$$\epsilon(\boldsymbol{k},\omega) = 0 \tag{2.11}$$

In this thesis, we will deal with metallic nano-particles with size greatly larger than the Fermi wavelength (typically 50 Å). One can therefore neglect the spatial dependence of the dielectric constant which leads to:

$$\boldsymbol{D}(\boldsymbol{k},\omega) \approx \epsilon(\omega)\boldsymbol{E}(\boldsymbol{k},\omega) \tag{2.12}$$

This is the so-called *local approximation* [29]. The validity of this approximation will be discussed in C.2.3.

2.2.2 Basic principles of plasmonics

The confinement of EM fields beyond the diffraction limit could seem surprising as the spatial spreading of light along a certain direction Δx is constrained by the relation:

$$\Delta x \geq \frac{1}{2\Delta k_x} \tag{2.13}$$

where k_x is the x component of the light wavevector. In other words, a confinement of the light in the x direction results in a spreading of the corresponding component of the wavevector. Moreover, the maximal value of k is constrained by the wavelength of the light:

$$k = \sqrt{k_x^2 + k_y^2 + k_z^2} = 2\pi/\lambda \tag{2.14}$$

The trick to overcome this apparent limit is to consider EM fields with imaginary wavevector components. Indeed, by taking e.g. $k_z \in i\mathbb{R}$, one can increase the value of k_x beyond λ and still respects (2.14). It corresponds to a so-called *evanescent* field which propagates in the (k_x, k_y) plane but confined and decaying exponentially in the z direction. Surface plasmons (SPs), which are particular solutions of the Maxwell equations in a presence of a metallic medium, constitute an important example of such evanescent fields.

2.2.2.1 Bulk (or volume) plasmons

Before looking at the optical response of a nano-structured metal, one needs to know how bulk metals react to an electromagnetic perturbation. An efficient way to picture the electronic properties of a metal is to consider its free electrons as a weakly interacting electron gas (Jellium model).

A fundamental quantity describing the electronic response of a solid to an EM perturbation is the electric susceptibility χ defined as:

$$\boldsymbol{P}(\boldsymbol{r},t) = \iint d\boldsymbol{r}'dt'\,\chi(\boldsymbol{r}',\boldsymbol{r},t,t')\boldsymbol{E}(\boldsymbol{r}',t') \tag{2.15}$$

where $\boldsymbol{P}$ is the local polarization and $\boldsymbol{E}$ is the applied electric field. Using the Kubo formula (which use will be detailed in the next chapter), one can show that for a non-interacting electron gas, the spectral electric susceptibility χ^0 reads:

$$\chi^0(\boldsymbol{q},\omega) = \frac{1}{V}\sum_{\boldsymbol{k},\sigma}\frac{n_{\mathrm{F}}(\xi_{\boldsymbol{k}}) - n_{\mathrm{F}}(\xi_{\boldsymbol{k}+\boldsymbol{q}})}{\xi_{\boldsymbol{k}} - \xi_{\boldsymbol{k}+\boldsymbol{q}} + \omega + i0^+} \tag{2.16}$$

where V is a normalization volume, n_{F} is the Fermi-Dirac distribution and $\xi_{\boldsymbol{k}} = \epsilon_{\boldsymbol{k}} - \mu$, μ is the chemical potential and $\epsilon_{\boldsymbol{k}}$ is the energy of electron of momentum $\boldsymbol{k}$. This function is called the *Lindhardt function* and is well-known is solid states physics [30]. Excitation in the gas i.e. formation of electron-hole (e-h) pairs can only happen if $\mathrm{Im}\{-\chi(\boldsymbol{q},\omega)\} \neq 0$. For simplicity, at zero temperature $T = 0$ (where the Fermi-Dirac statistic reduces to a step function), a quick analysis shows that excitations can only exists in the energy range $\omega_{\min} < \omega < \omega_{\max}$ where:

$$\begin{cases} \omega_{\min} = \dfrac{1}{2m}q^2 + v_{\mathrm{F}}q & \text{(2.17a)} \\ \omega_{\max} = \dfrac{1}{2m}q^2 - v_{\mathrm{F}}q & \text{(2.17b)} \end{cases}$$

m being the electron mass and v_{F} the Fermi velocity. We plotted these limits in blue lines on figure 2.1.

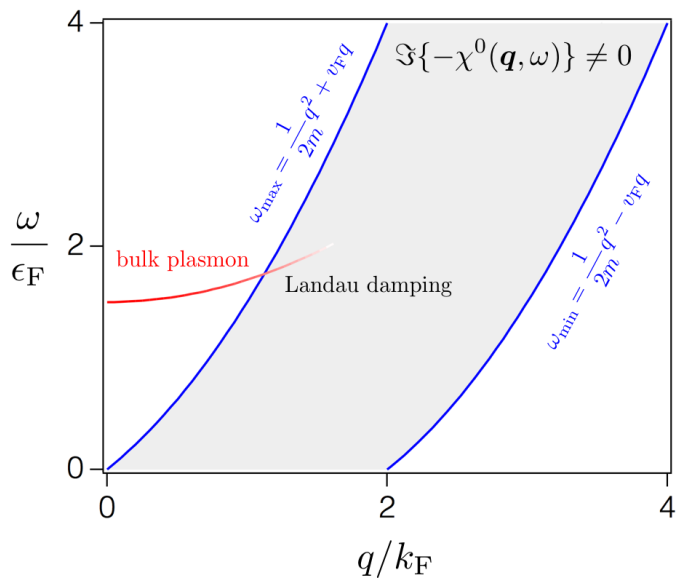

Figure 2.1: *Dispersion relation of bulk plasmon calculated within the random phase approximation (red line). The grey zone corresponds to the region where excitations can be created in the non-interacting gas (zero temperature approximation) leading to the Landau damping of the bulk plasmons.*

In order to model collective electronic modes, one needs to include the Coulomb interaction $V(\boldsymbol{q}) = e^2/q^2$ between the electrons. This is a formidable task which requires involved numerical methods such as density functional theory (DFT). However, a simplified scheme, the random

phase approximation (RPA), gives reasonable results for simple metals. Under RPA, the electric susceptibility reads:

$$\chi^{\mathrm{RPA}}(\boldsymbol{q},\omega) = \frac{\chi^0(\boldsymbol{q},\omega)}{1 - V(\boldsymbol{q})\chi^0(\boldsymbol{q},\omega)} \tag{2.18}$$

Nevertheless, the electric permittivity ϵ of the metal relates to the electric susceptibility as [30]:

$$\epsilon^{-1}(\boldsymbol{q},\omega) = 1 + V(\boldsymbol{q})\chi(\boldsymbol{q},\omega) \tag{2.19}$$

Under RPA, it leads to:

$$\epsilon^{\mathrm{RPA}}(\boldsymbol{q},\omega) = 1 - V(\boldsymbol{q})\chi^0(\boldsymbol{q},\omega) \tag{2.20}$$

We now consider the low temperature limit ($kT \ll \epsilon_{\mathrm{F}}$). We also put ourselves in the long wavelength ($q \ll k_{\mathrm{F}}$) and high frequency limits ($\omega \gg v_{\mathrm{F}}q$). Winthin these limits, using a Taylor expansion, one can show that [30]:

$$\mathrm{Re}\{\chi^0(\boldsymbol{q},\omega)\} = \frac{nq^2}{m\omega^2}\left[1 + \frac{3}{5}\left(\frac{qv_{\mathrm{F}}}{\omega}\right)\right] \tag{2.21}$$

In the high frequency limit, the imaginary part of χ^0 goes to zero which leads to:

$$\boxed{\epsilon^{\mathrm{RPA}}(\boldsymbol{q},\omega) = 1 - \frac{\omega_{\mathrm{P}}^2}{\omega^2}\left[1 + \frac{3}{5}\left(\frac{qv_{\mathrm{F}}}{\omega}\right)\right]} \tag{2.22}$$

where ω_{P} is the plasma frequency of the metal defined as:

$$\omega_{\mathrm{P}} = \sqrt{4\pi\frac{ne^2}{m}} \tag{2.23}$$

The plasma frequency is an important parameter which gives the energy scale for several processes in electron gases. Particularly, it marks the limit above which the metal essentially behaves as a dielectric and becomes transparent to the light. Below this value, the metal screens the radiation and reflects the light [30, 31]. Note that, to the zero order in q, expression (2.22) is equivalent to the classical Drude model taken at high frequency limit [2]. Indeed, at high frequency, electron-electron collisions become negligible therefore a simple independent electrons model (such as the Drude model) gives good results.

The presence of collective excitations would equivalently correspond either to a pole of χ^{RPA} or to a zero of ϵ^{RPA}. Using (2.22), we straightforwardly show that $\epsilon^{\mathrm{RPA}}(\boldsymbol{q},\omega) = 0$ gives:

$$\omega(\boldsymbol{q}) = \omega_{\mathrm{P}} + \frac{3}{10}\frac{v_{\mathrm{F}}^2}{\omega_{\mathrm{P}}}\boldsymbol{q}^2 \tag{2.24}$$

It corresponds to the dispersion of the so-called *bulk plasmons* which is plotted in red on figure 2.1. Using condition (2.11), one can see that these excitations correspond to longitudinal (compression) waves propagating in the electron gas which are basically analogous to sound waves. On can see on figure 2.1 that the bulk plasmon dispersion line crosses the blue line corresponding to ω_{max} and enter the gray zone. In this region, $\mathrm{Im}\{-\chi^0\} \neq 0$ so that the reasoning we just made is no more valid[2]. As we detailed earlier, physically it reflects the fact that the electron gas can absorb energy by generating e-h pairs. Therefore, in the gray region, bulk plasmons can dissipate energy through the creation of e-h pairs in the metal which dramatically reduces their lifetime. This mechanism is usually called *Landau damping*. Another important non-local effect appearing is this region is the *Thomas-Fermi screening* effect which corresponds to the screening of the Coulomb interaction between two electrons by the other electrons of the gas.

[2]that is why we did not plot the red curve over the whole spectral range

2.2.2.2 Surface plasmons(-polaritons)

We just saw that bulk plasmons are elementary collective excitations of the electron gas. Because of their longitudinal character, they are not optically active. However, as we will show further, they are detectable by electron spectroscopy and have some applications e.g. in temperature measurement at the nanoscale [32].
We now move to the case of nano-structured metals and place ourselves in the local approximation (2.12). The presence of an interface completely changes the picture and leads to the apparition of transverse types of plasmons.

Let's consider an interface between two semi-infinite media of respective dielectric constants ϵ_m and ϵ_d. The first medium of constant ϵ_m is assumed to be a metal while the other one is a dielectric (typically vacuum $\epsilon_d = 1$). At the interface, the EM field satisfies the continuity relations (2.3). In this configuration, the solutions of the wave equation (2.9) are the so-called *surface plasmons* (SP):

$$\boldsymbol{E}_j = \begin{pmatrix} E_{x,j} \\ 0 \\ E_{z,j} \end{pmatrix} e^{i(k_x x - \omega t)} e^{ik_{z,j} z} \tag{2.25}$$

where z is the direction perpendicular to the interface and $j = \{d, m\}$ indexes the media. The wave equation also admits transverse electric modes but one could show that they do not correspond to plasmon resonances [26, 2]. In this configuration, the dispersion relation of SPs reads:

$$k_{\mathrm{SPP}} = \frac{\omega}{c}\sqrt{\frac{\epsilon_m \epsilon_d}{\epsilon_m + \epsilon_d}} \tag{2.26}$$

and the z-component of the wavevector is:

$$k_{z,j} = \frac{\omega}{c}\sqrt{\frac{\epsilon_j^2}{\epsilon_m + \epsilon_d}} \tag{2.27}$$

Since we are seeking for propagating solutions along the surface ($\mathrm{Re}\{k_{\mathrm{SPP}}\} \neq 0$) but also evanescent along the z-direction ($\mathrm{Im}\{k_{\mathrm{z,j}}\} \neq 0$), we have the following additional requirements for the existence of SPs:

$$\begin{cases} \epsilon_m + \epsilon_d < 0 & \text{(2.28a)} \\ \epsilon_m \epsilon_d < 0 & \text{(2.28b)} \end{cases}$$

On figure 2.2, we plotted the dispersion relation (2.26) when $\epsilon_d = 1$ and ϵ_m models a lossless Drude metal:

$$\epsilon_m(\omega) = \epsilon_b - \frac{\omega_{\mathrm{P}}^2}{\omega^2} \tag{2.29}$$

where $\epsilon_b = 9.5$ and $\omega_{\mathrm{P}} = 9.096$ are taken to match the gold parameters [33].
One can see that, for small wavevectors, the dispersion relation of SPs coincides with the one of the light. Thus, in this region, SPPs essentially behave as light propagating along the surface and compressed in the orthogonal direction. Because of this light-like character, these types of surface plasmons are usually called surface plasmons-polaritons (SPPs). One remarkable consequence of this lightish character is that a complete Fourier optics can be developed for SPPs including focusing optics at the nano-scale [34], electro-optic plasmonic modulators [35], polarization-selective couplers [36] or even Fresnel-Huygens principle [37]. Moreover, SPPs can travel over tens of micrometers therefore one of their main promising applications is the sub-wavelength waveguiding of light [38].
The blue curve corresponds to Brewster modes which are not bounded to the surface therefore do not correspond to SPs. For larger wavevectors, the slope of the SPs' dispersion curve flattens and the energy asymptotically reaches a limiting value equal to $\omega_{\mathrm{S}} = \omega_{\mathrm{P}}/\sqrt{\epsilon_b + 1}$. It indicates a *localization* effect and the formation of stationary waves. It corresponds to the apparition of localized surface plasmons (LSPs) and will be detailed in section (2.2.2.3).

SPs are mixed light-matter excitations as they correspond to collective charge density waves of

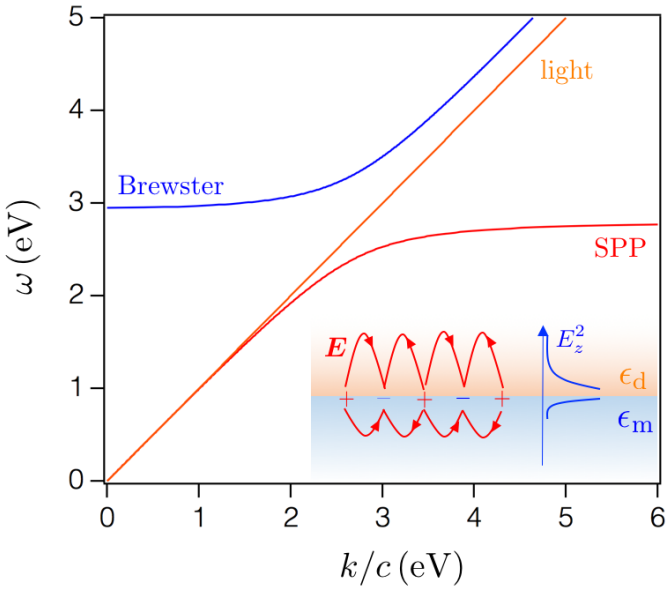

Figure 2.2: *Dispersion relations of: (red) surface plasmons for an interface between gold and vacuum, (blue) Brewster waves of the same interface and (orange) light in vacuum. The schematics in inset displays the typical shape of the EM field associated with SPs.*

electrons propagating at an interface associated to strongly confined EM fields. This mixed character constitutes the wealth of SPs' physics as it inherits both light and electronic properties. However, as we will see throughout this thesis, it also dramatically hardens their theoretical description and experimental study.

2.2.2.3 Localized surface plasmons

In the previous section, we showed that the presence of an infinite interface between a metal and a dielectric leads to the apparition of surface plasmon waves which, in the long wavelength limit, essentially behave as light. However, if we confine this wave on finite surfaces such as nano-particle, it leads to the apparition of a discrete set of modes instead of the SPPs' continuum as showed on figure 2.3. This classical quantization is analogue to a Fabry-Perot effect where SPPs reflect and interfere to form stationary standing waves which profile depends on the shape of the nano-particle. These standing waves are called *localized surface plasmons* and are the main research subject of this thesis.

Physics of LSPs becomes limpid in the *quasi-static* (QS) limit, which corresponds to $kL \ll 1$ where L is the typical nano-particle's size. In this regime, the retardation due to the finite propagation time of the EM fields can be neglected at the scale of the particle. Thus, the wave equation (2.9) reduces to the Poisson's equation:

$$\nabla^2 \phi(\boldsymbol{r}, \omega) = -4\pi\rho(\boldsymbol{r}, \omega) \tag{2.30}$$

where ϕ is the electrostatic potential. Let's now consider a nano-particle of arbitrary shape S in absence of any external EM perturbation. In this situation, one can show [9, 39, 10] that the Poisson's equation combined with the boundary relations (2.3) reduces to:

$$\boxed{\lambda\sigma(\boldsymbol{s}) = \mathcal{P} \oint_S F(\boldsymbol{s}, \boldsymbol{s}')\sigma(\boldsymbol{s}')} \tag{2.31}$$

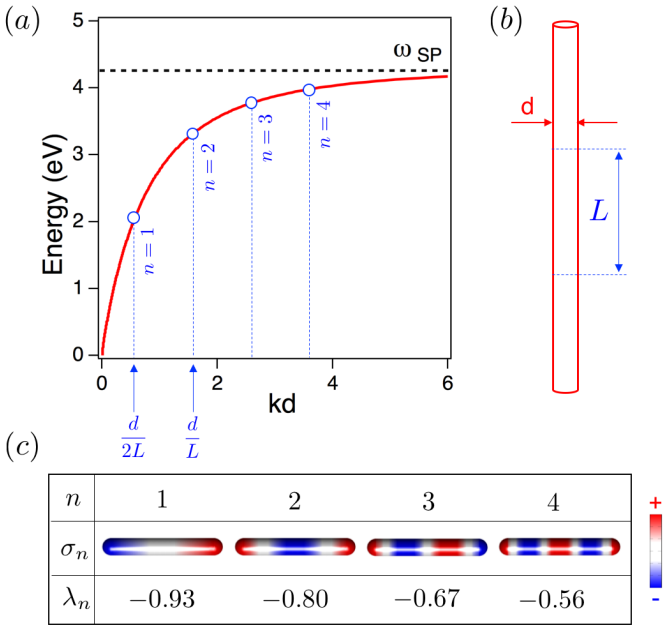

Figure 2.3: *(a) Dispersion relation of SP waves of an infinite Ag cylinder of diameter d represented in (b). When the length of the cylinder in restricted on a portion L, the wavevector of SPs is restricted to a multiple of* $1/2L$ *and a discrete set of localized modes appears (in blue). These modes are indexed by the integer n. (c) Four first LSPs of a* 30×400 *nm Ag rod calculated using equation (2.34a).*

where $\mathcal{P}$ denotes the Cauchy principal value, $\boldsymbol{s}$ is a vector pointing on the surface, $\sigma(\boldsymbol{s})$ is the surface charge density on the nano-particle and the constant λ is defined by:

$$\lambda(\omega) = 2\pi \frac{\epsilon_d(\omega) + \epsilon_m(\omega)}{\epsilon_d(\omega) - \epsilon_m(\omega)} \tag{2.32}$$

Moreover, the kernel $F(\boldsymbol{s}, \boldsymbol{s}')$ can be written:

$$F(\boldsymbol{s}, \boldsymbol{s}') = \frac{-\boldsymbol{n}(\boldsymbol{s}).(\boldsymbol{s} - \boldsymbol{s}')}{|\boldsymbol{s} - \boldsymbol{s}'|^3} \tag{2.33}$$

$\boldsymbol{n}(\boldsymbol{s})$ being the outer normal of the surface at position $\boldsymbol{s}$. Equation (2.31) is a Fredholm equation of the first kind which solutions form an infinite set $\{\lambda_n, \sigma_n\}_{n\in\mathbb{N}}$. These solutions correspond to the localized surface plasmon *modes* of the nano-particle. This boundary integral equation (BIE) has first been derived in 1989 by Ouyang and Isaacson [9] based on seminal idea of Fuchs [40]. The details on the derivation of this equation will be given in section 2.5. From (2.31), one can see that LSP modes essentially behave as electronic excitations entirely determined by their surface charge density. Let's also emphasize that the eigenvalues λ_n are dimensionless as the dielectric constants are not explicitely involved in the eigenproblem. This is remarkable because it means that LSPs are solutions of an eigenproblem, despite the fact that they are damped excitations (see section 2.2.2.5 for a discussion on the plasmon's damping).

The kernel (2.33) is generally non-Hermitian [39, 10] therefore the equation (2.34) needs to be completed by the left eigenproblem:

$$\lambda\tau(\boldsymbol{s}) = \oint_S F(\boldsymbol{s}', \boldsymbol{s})\tau(\boldsymbol{s}') \tag{2.34}$$

where $\tau_n(\boldsymbol{s})$ corresponds to a surface dipole density projected along $\boldsymbol{n}(\boldsymbol{s})$. The eigenmodes of the Ouyang and Issacson BIE are therefore given by the set $\{\lambda_n, \sigma_n, \tau_n\}_{n\in\mathbb{N}}$ i.e. requires the

knowledge of both right and left eigenvectors. This eigenbasis is bi-orthogonal because the standard orthogonality relation between right eigenvectors is relaxed and replaced by:

$$\oint \sigma_n(\boldsymbol{s})\tau_m(\boldsymbol{s})d\boldsymbol{s} = \delta_{n,m} \tag{2.35}$$

This non-Hermiticity has several physical consequences which will be studied in chapter 5.

The eigenproblem defined by equations (2.31) and (2.34) is usually refered as the *geometric eigenproblem* as it only depends on the geometry of the nano-particle. Using equation (2.32), one can now relates the λ_n factors associated to each modes to their actual energy resonances ω_n [10, 41]:

$$\mathrm{Re}\left\{\lambda(\omega_n) - \lambda_n\right\} = 0 \tag{2.36}$$

Therefore, for a given geometry of nanoparticle S, different materials will leads to different resonance energies and widths as illustrated on figure (2.4).

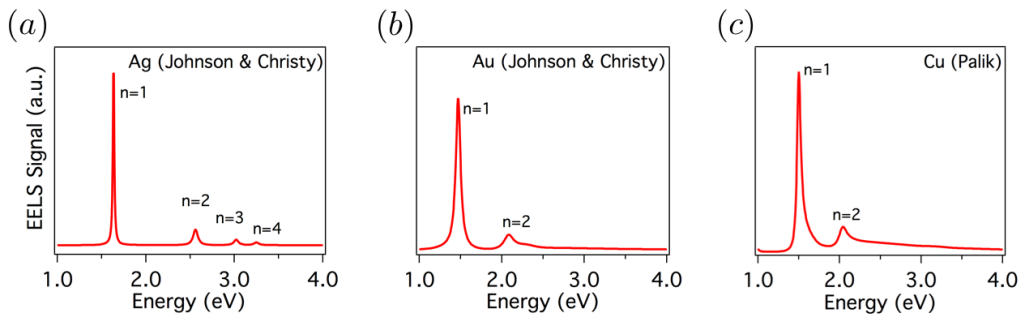

Figure 2.4: *Electron energy loss spectra calculated for the nano-rod presented in figure 2.3(c) when the constituting material of the nano-particle is: (a) silver, (b) gold or (c) copper [33, 42]. The electron beam impinges at one tip of the rod.*

From the BIEs presented here, one can immediately see that, by changing the shape and/or the material of a nano-particle, one can precisely engineer its LSPs energy resonances as well as the electric field distribution associated to each mode. This tunability is of major importance in nano-optics as it allows the shaping of EM fields at the nano-scale with several applications e.g. in medicine, quantum information, solar cells, surface enhance Raman spectroscopy, spasers (see the extended discussion in [26, 43] and references therein).
In the next sections 2.2.2.4 and 2.2.2.5, we will give some orders of magnitude of the time and length scales involved in this thesis.

2.2.2.4 Effect of the size of the nano-particles

Strictly speaking, SPs are a mixture of light and electronic surface charge density waves. As we saw so far, depending on the situation, they can be more similar to light (SPP) or to pure electronic excitation (LSP). A important parameter controlling the nature of SPs is the size of the nano-particle (NP) as illustrated on figure 2.5.
When NPs are typically 1 nm or less (region a in figure 2.5), they are called metallic clusters and are made of tens to hundreds of atoms. In this region, electronic excitations closely resemble molecular excitations and bulk plasmons do not exist.
When the particle are bigger (typically $\sim$ 10 nm, region c in figure 2.5), SP excitations can be observed and typically correspond to electrostatic LSPs. The transition region b is still under intense investigation. Particularly, the question of when quantum size effects (e.g. electron spill out, electron energy quantization) start to appear is still under debate.
On the theoretical level, in region a, the calculation of the NPs' properties requires full quantum

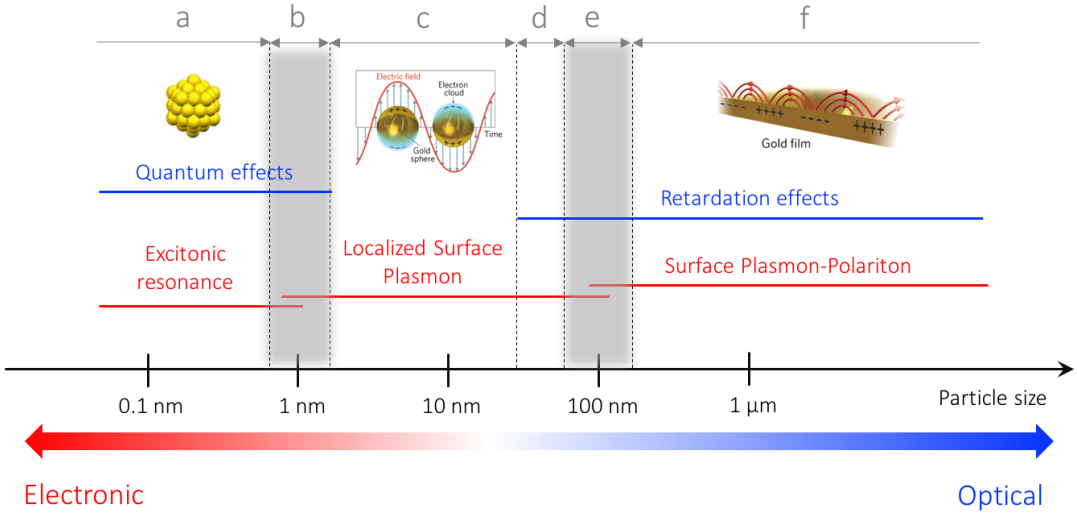

Figure 2.5: *Schematics representing the size effects in plasmonic with the typical orders of magnitude. Schematics in inset are reproduced from [44] and [45]. Grey zones represent size ranges where the nature of surface plasmon is still under debate.*

ab initio computations such as density functional theory (DFT). On the contrary, in region *c* a continuous description of matter efficiently capture the physics[3]. Problems appear in region *b*, where the number of atoms is too high to allow ab initio computations but the quantum effects are too important to allow classical methods. In this "intermediate size regime" [46], computations require statistical approach [47] or quantum corrected (i.e. semi-classical) models [48].

In region *c*, surface plasmons are essentially electrostatic resonances fully determined by their surface charge density distribution, as emphasized by Mayergoyz and collaborators [49, 39]. As we saw in section 2.2.2.3, despite the energy leaks, LSPs are exact solutions of an eigenproblem and therefore constitute, strickly speaking, real eigenmodes.
When the typical size of the NPs becomes comparable or larger than the wavelength of light, retardation effects start to appear (region *d* in figure 2.5). Thus, the Ouyang and Isaacson's BIE is no more valid and a full resolution of the Maxwell equations is required. In this region, one cannot define LSP modes anymore[4]. Nevertheless, since surface plasmons still display localized charge densities, we usually keep talking about LSP *modes* as it is a very efficient mental image to picture the mechanisms involved here.

Retardation brings new effects such as resonance energy redshift or loss of spatial coherence. Moreover, as the size of the NP increase, the radiative damping increases [51] and even the so-called *dark modes*[5] [52] emit light. Finally, when the size of the NP is sufficiently large, the classical confinement of SPs disappears and the plasmonic spectrum becomes continuous, which corresponds to SPPs (region *f* in figure 2.5). Here again, the continuous transition between SPPs and LSPs (region *e* in figure 2.5) is not comprehensively understood.

In this section we simply gave orders of magnitude of the lengths involved in plasmonics. However, dimensionality also plays an important role [53] as we will see in the case of the nano-cube in chapter 5.

[3]For example, the local approximation combined with this continuous description of matter constitute the so-called local continuum dielectric model (LCDM). This thesis is essentially based on this model.
[4]Although some tricks exist such as the definition of quasi-normal modes (QNMs), [50].
[5]i.e. modes which charge distribution displays a small dipole moment.

2.2.2.5 Damping mechanisms

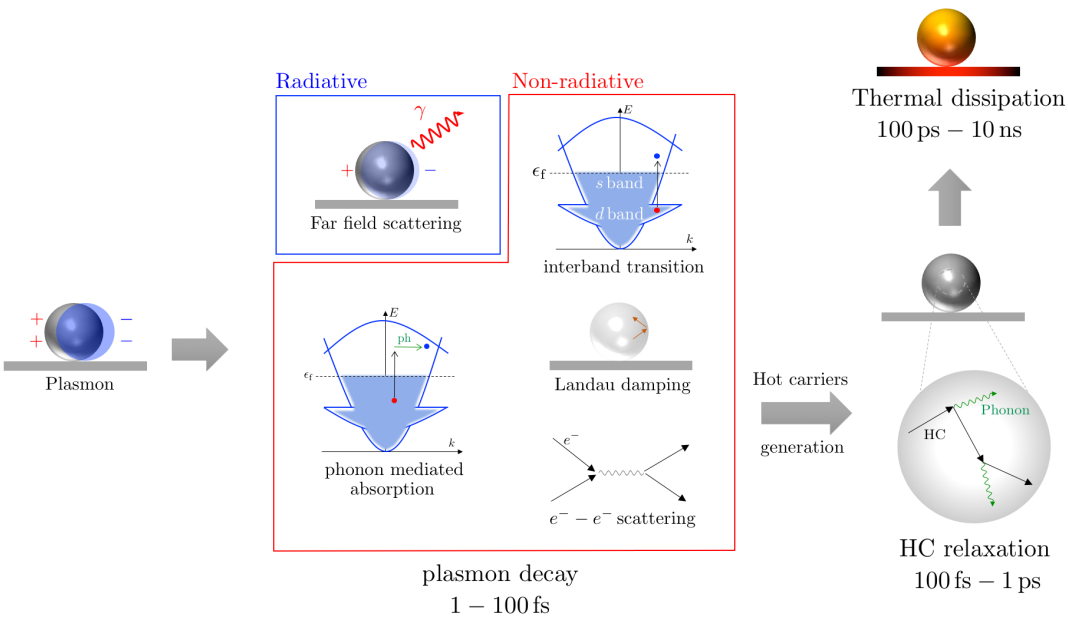

Figure 2.6: *Schematics representing the damping processes of surface plasmons with typical timescales.*

A plasmon is a collective and coherent oscillation of electrons and any scattering event (involving one or several electrons) can destroy its phase coherence. Trügler employs an efficient image: a scattering event "kicks an electron out of the lock-step march" [43]. Let's review the different decoherence phenomenon and time-scales involved in SPs' damping.

There are several possible scattering processes (e.g. with other electrons, impurities, photons, phonons) which makes the study of plasmon damping rather intricate. The decay time of plasmons is the result of the combination of these several processes and is typically of the order of *tens of femtoseconds*. An important figure of merit defining the quality of an oscillator is its quality factor Q. Using a damped oscillator model to describe LSP modes, one can show [54] that the quality factor can be defined for SPs as:

$$Q = \frac{\omega}{\Gamma} \tag{2.37}$$

where ω is the resonance energy of the plasmon and Γ its linewidth (i.e. its full width at half maximum, FWHM). Since plasmon resonances span from visible light to near infrared, the typical quality factors of LSPs are typically $Q \sim 5 - 12$ [22]. In other words, it means that LSPs are poor oscillators which relax after few cycles of oscillation which is, as we will see further, the major issue in plasmonics.
Conventionally, the decay processes are separated into a radiative and a non-radiative part. On figure 2.6, we present the typical processes leading to the damping of surface plasmons [55, 56, 57]. The radiative decay corresponds to the scattering of light into the far field, which is the quantity measured by cathodoluminescence spectroscopy (see section 2.3.2.5). The non-radiative channels are numerous and include: interband transitions, electron-electron scattering, Landau damping and phonon assisted absorption. These absorption processes in the metal lead to the generation of *hot carriers* (HC i.e. high energy electrons and holes) which relax through scattering with phonons. This generation of phonons by HCs leads to an intense heating of the NP which then dissipates its thermal energy to its environment[6].

[6]This is typically the phenomenon employed in plasmonic photo-thermal therapy [58] while the plasmon-assisted

Precise characterization of SPs' lifetime is challenging as few experimental techniques can reach simultaneously the required time-scale (fs) and length-scale (nm). Femtosecond measurements of the dynamics of electronic excitations have been achieved on bulk gold using pump-probe optical experiments [59] or on copper surface using time-resolved photoemission [60], which did not require spatial resolution. The charaterization of SPs' dynamics requires resolution both in time and length scales. Photoemission electron microscopy (PEEM) demonstrated its ability to measure femtosecond dynamics with micrometric spatial resolution [61, 62]. Moreover, using electron energy loss spectroscopy (EELS), Bosman et al. measured the lifetime of LSPs at the nanometer scale [54]. As we will see in 2.3.2.4, EELS measures the SPs in the spectral domain where the FWHM Γ of the peaks directly relate to the dephasing time of plasmons τ:

$$\tau = \frac{2\hbar}{\Gamma} \tag{2.38}$$

Nevertheless, ultrafast (down to the attosecond) electron microscopy [63, 64, 65] could soon achieve a real (spatial and temporal) space mapping of SPs with unprecedented spatial resolution.

2.2.3 Luminescence in semi-conductors

As we saw so far, surface plasmons can decay by emitting photons and therefore constitute a nano-scaled source of light. On the other hand, solids can also emit light by drastically different processes involving the radiative recombination of e-h pairs and excitons.

Electronic states of semi-conductors form band structures which last filled band is called the valence band, while the first unoccupied one is called the conduction band. The basic excitation is such a material consists in promoting a valence electron to an empty band, thus forming a so-called e-h pair. Generally, the electron and the hole are not independent and interact through the Coulomb interaction. Bounds electron and hole states can therefore be formed and constitute the so-called excitons. Existence of excitonic states highly depends on the nature of the materials (due to e.g. screening effects, the binding energy of e-h pair can be dramatically reduced).

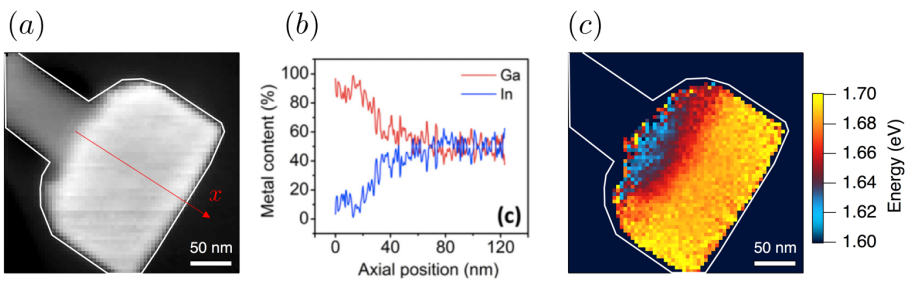

Figure 2.7: *Variation of the cathodoluminescence energy in a InGaN nanowire due to variation of the In concentration. (a) annular dark field (ADF) image of a single InGaN nanowire grown at 590 °C. (b) Concentration of In along the x direction marked in (a) measured by EDX spectroscopy. (c) Cathodoluminescence emission energy map measured on the nanowire (a). This work has been published in [66].*

Excitons and e-h pairs migrates in the materials and finally decay by exchanging energy with the phonon field or recombining through the generation of a photon. Thus, the properties of the emitted light (energy, statistics) will naturally depends on the electronic properties of the material. Any physical phenomena leading to the modification of these electronic states (stress, chemical variation, quantum confinement) will therefore impact the properties of the emitted light as shown on figure 2.7.

hot carrier generation has several applications in e.g. solar cell harvesting or catalysis [57].

2.2.3.1 Nano-structured materials: effect of quantum confinement

Nano-fabrication techniques (growth, lithography, ion milling) enable a structuration of material at the nano-scale. When the size of the nano-particle is comparable or smaller than the typical Bohr radius of the electron and hole wavefunctions, a quantum confinement leads to a discretization of the energies and dramatically modifies the electronic density of states. Depending on the dimension of the confined system, the electronic density of states takes a particular form as shown on figure 2.8.

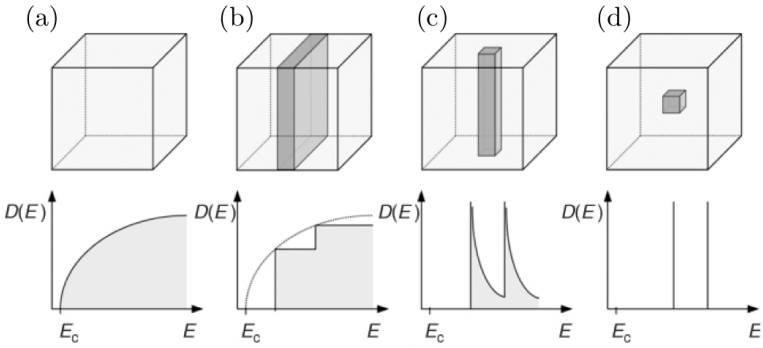

Figure 2.8: *Typical electronic density of states $D(E)$ of (a) bulk semi-conductor (b) a quantum well (c) a quantum wire and (d) a quantum dot. Reproduced from [67]*

For example, assuming a parabolic dispersion relation, when the electrons are confined along one dimension z (quantum wells, see figure 2.8(b)), the density of states becomes:

$$\rho_e^{2\mathrm{D}}(E) = \frac{m^*}{\pi\hbar^2}\sum_{n_z}\Theta(E - E_{n_z}) \tag{2.39}$$

where m^* is the effective electron mass and $n_z \in \mathbb{Z}$ indexes the energy states. The wavevectors are quantized along the z direction $k_z = 2\pi n_z/L_z$ where L_z is the quantization length. This quantization leads to well defined emission energies which values depend on the size of the wells as demonstrated in e.g. [68]. When the material is confined along its three dimensions (quantum dots, see figure 2.8(d)), the electron density of states becomes:

$$\rho_e^{0\mathrm{D}}(E) = 2\sum_{n_x,n_y,n_z}\delta(E - E_{n_x,n_y,n_z}) \tag{2.40}$$

where $n_x, n_y, n_z \in \mathbb{Z}$. From the latter, one can clearly see that a quantum dots acts as an artificial hydrogenoic system with discrete states. For this reason, transition between the closest energy states leads to light emission at a precisely defined energy [69]. Such systems emitting light in a quantized manner are generically called quantum emitters (QEs). Quantum dots are therefore promising candidate to be single photon emitters (SPEs) i.e. systems which emit only one photon at a time. SPEs have attracted tremendous interest due to their possible applications in quantum cryptography or computing [70, 71, 72]. Therefore, the design and the characterization of efficient and stable SPEs is a major field of research in nano-optics.

2.2.3.2 Structural point defects and molecules

In practice, the atomic lattice of a solid presents defects and impurities, which can have a dramatic influence on the local electronic density and therefore on the luminescence properties. These defects can be punctual (atomic vacancies or dopants), linear (dislocation), or even of higher dimension. For the sake of this thesis, we only need to consider point defects.

The presence of these point defects creates discrete states within the gap of the material. Depending on the charge state of the defect, it can be qualified as donor (brings new electrons) or acceptor (otherwise) [69]. If the energy of these states is close to the energy of the conduction or valence band, they are usually qualified as *shallow* and leads to light emission close the direct emission of the bulk material. On the contrary, the energy of these donor/acceptor states can be much different from the conduction and valence bands. If these so-called *deep* donor or acceptor states are sufficiently close, they can even form a hydrogenoic-like system embedded in the gap with possible single photon emission.

Important examples of such point-defect systems are color centers in crystals because they essentially behave as two level systems [73] which is the building block for quantum computation and cryptography. In this thesis, we will consider the nitrogen-vacancy center of diamonds which consists of a nitrogen atom and a neighboring vacancy in the carbon lattice (see figure 2.9(a)).

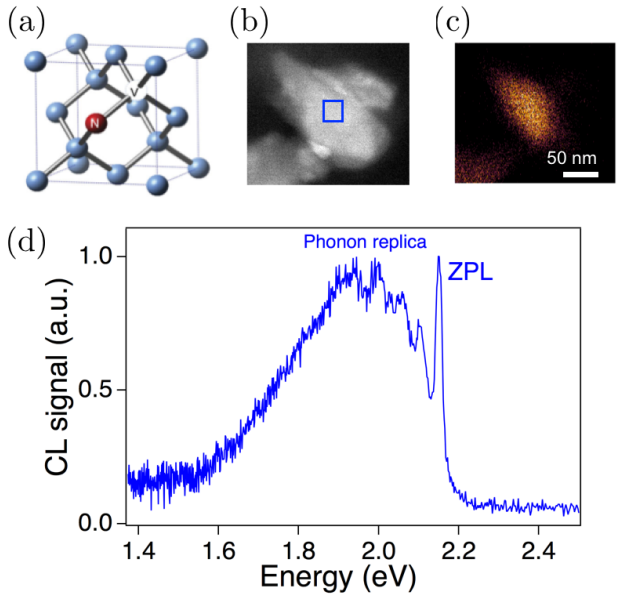

Figure 2.9: *(a) Representation of the crystalline structure of a NV center in diamond. (b) ADF image of a nano-diamond containing hundreds of NV centers. (c) CL energy filtered (between 1.5 eV and 2.2 eV) image of the nanodiamond in (b). (d) CL spectrum extracted from the blue area in (b). These data have been published in [74].*

Two forms of NV centers exist depending on their charge state: a neutral form (NV^0) and a negatively charged one (NV^-). The CL emission reported on figure 2.9(b-c) corresponds to the emission of NV^0 centers in a nano-diamond. Photons emitted by NV^- has slightly lower energy (1.9 eV) and has not been reported in CL experiment. Nevertheless, contrary to NV^0, NV^- centers carry a $S = 1$ spin and therefore are of particular interest for quantum optics experiments.
The CL spectrum of NV^0 centers (figure 2.9(c)) presents a characteristic profile with a main peak called the *zero phonon line* (ZPL) with a series of lower energy replica peaks equally spaced. The ZPL corresponds to the direct recombination of electron-hole pairs. As described by the Franck-Condon principle [75], each replica results from the recombination subsequently to the interaction with one, two or more phonons. Other types of point defects are interesting for nano-optics thanks to their temperature stability e.g. in hexagonal boron nitrite (h-BN) [76].
The last type of quantum emitters of particular importance for nano-optics are fluorescent molecules, although we do not study them in this thesis. For organic molecule, simplified models consists in considering only the *highest occupied molecular orbital* (HOMO) and the *lowest unoccupied molecular orbital* (LUMO). It defines a two level system which main radiative transition (HOMO→LUMO) is called fluorescence with typical lifetime of 1 to 10 ns [26].

2.2.4 Coupling surface plasmon and quantum emitters

In the last section, we saw that the luminescence in solids is tailored by their structural and chemical properties. In some particular situations (quantum dots, point defects), one can even design hydrogenoic-like systems with discrete emission spectra. These quantum emitters are one of the building blocks of nano-optics due to their possible application e.g. in quantum computation [70, 71, 72].

In fact, emission properties of quantum emitters are also modified by the presence of a plasmon field. Indeed, it has been shown that molecular fluorescence can be locally enhanced by the presence of SPs [77]. Even more remarkably, interaction between molecular exciton and SPs can even lead to the formation of new quantum states i.e. plexcitons [78, 79, 80]. These different experiments demonstrate that SPs are good candidates to control the luminescence of QEs [81] or to mediate interaction between them [82, 83]. With this in mind, one of the research objects of this thesis is the study of the SP-QE coupling (see chapter 5).
Interaction between confined light fields and quantum emitters is usually modeled by a toy *cavity-QE system*, see figure 2.10. Indeed, SPs are simply a particular class of optical cavities which have the property to confine light without any "real" physical cavity [84]. One can refer to the excellent review [22] for details on this physics.

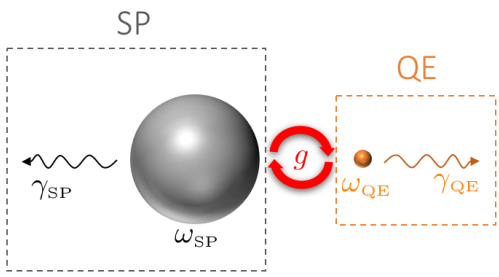

Figure 2.10: *A typical QE-SP model system. A surface plasmon resonance of energy $\hbar\omega_{SP}$ and linewidth $\hbar\gamma_{SP}$ interacts with a QE's excited state of energy $\hbar\omega_{QE}$ and linewidth $\hbar\gamma_{QE}$ with the characteristic coupling energy g.*

Let's first consider that there is only one quantum of excitation in the system. It this case, the interaction can be modeled by the phenomenological Hamiltonian:

$$H_{\rm int} = \hbar \begin{pmatrix} \omega_{\rm SP} - i\gamma_{\rm SP} & g \\ g & \omega_{\rm QE} - i\gamma_{\rm QE} \end{pmatrix} \tag{2.41}$$

which eigenvalues $E_\pm$ are:

$$\frac{E_\pm}{\hbar} = \frac{\omega_{\rm SP} + \omega_{\rm QE}}{2} - i\frac{\gamma_{\rm SP} + \gamma_{\rm QE}}{2} \pm \sqrt{g^2 + \frac{1}{4}\left(\delta - i\left(\gamma_{\rm QE} - \gamma_{\rm SP}\right)\right)^2} \tag{2.42}$$

Each of these eigenvalues corresponds to an hybridized mode (respectively bonding and anti-bonding). The conditions for the observation of a mode splitting are:

$$\begin{cases} 2g > |\gamma_{\rm QE} - \gamma_{\rm SP}| & \text{(2.43a)} \\ \Omega > \gamma_{\rm QE} + \gamma_{\rm SP} & \text{(2.43b)} \end{cases}$$

where $\Omega = \sqrt{4g^2 - (\gamma_{\rm QE} - \gamma_{\rm SP})^2}$ is the so-called Rabi splitting energy. From this criterion, the QE-SP coupling can be divided in two regimes:

1. **The strong coupling regime** in which the latter conditions are respected. In this case, the QE and the SP field coherently exchange energy over few cycles with a typical time period equal to $2\pi/\Omega$. Within the strong coupling regime, the exciton and the plasmon states do not exist anymore but rather new hybridized modes called plexcitons [85, 86, 87].

2. **The weak coupling regime** in which the linewidth of the plasmon is too large compared to the coupling energy. Roughly speaking, QE and the SP field do not have time to exchange energy before the SP excitation to be damped. In this case, the plasmonic field will rather act as a new damping channel for the QE's excited state; its lifetime will therefore be reduced although its wavefunction remains unchanged. This phenomena is known as the *Purcell effect* [88].

More precisely, the decay rate Γ of the quantum emitter is basically given by the Fermi golden rule:

$$\Gamma = \frac{2\pi}{\hbar} \sum_n |\langle g, 1_{\omega_n, \boldsymbol{k}_n} | \boldsymbol{d}.\boldsymbol{E} | e, 0 \rangle|^2 \delta(E_f - E_i) \tag{2.44}$$

where E_f, E_i are the final and initial energies of the system, $\{|g\rangle, |e\rangle\}$ denote the ground and the excited states of the QE, $n_{\omega_n, \boldsymbol{k}_n}$ is the number of photons in the state of energy $\hbar\omega_n$ and wavevector $\hbar\boldsymbol{k}_n$, $\boldsymbol{d}$ is the dipole moment operator for the QE and $\boldsymbol{E}$ is the electric field operator. As we will formally discuss in section 2.2.5.2), in presence of a plasmonic structure, the local density of photon states is increased. It results in an augmentation of the decay rate i.e. a reduction of the QE lifetime. Some simple algebra shows that the decay rate Γ is then given by:

$$\gamma = \frac{\Gamma(\boldsymbol{r})}{\Gamma_0} = \frac{\rho(\boldsymbol{r}, \omega)}{\rho_0(\omega)} \tag{2.45}$$

where Γ_0 is the QE decay rate in vacuum, $\rho_0(\omega)$ is the density of photon states in vacuum at the energy of the QE transition and $\rho(\boldsymbol{r}, \omega)$ is the local density of photon states modified by the plasmon field at the energy of the QE transition. The constant γ is usually called the Purcell factor. In chapter 5, we will demonstrate an experiment enabling the measurement of this factor in an electron microscope.

2.2.5 Green function formalism for electromagnetism: density of states and coherence

We presented so far a large variety of phenomena with very different natures (quantum, classical, electrostatic, retarded, etc) which require different theoretical tools to be properly described (e.g. Poisson, Maxwell, Schrödinger equations). An efficient way to treat all these phenomena on the same theoretical level without loss of generality is to use Green functions. In this section, we will show that these functions contain a plethora of information about the EM field and enable a stable and general definition of all the important quantities in nano-optics.

2.2.5.1 Definition of the electric and magnetic Green dyadics

Let's consider a density of electric current $j(\boldsymbol{r}', \omega)$ in a certain position $\boldsymbol{r}'$. The induced electric field $\boldsymbol{E}^{\text{ind}}(\boldsymbol{r}, \omega)$ in another position $\boldsymbol{r}$ can be written:

$$\boxed{\boldsymbol{E}^{\text{ind}}(\boldsymbol{r}, \omega) = -4\pi i\omega \int d\boldsymbol{r}' \overleftrightarrow{\boldsymbol{G}}^{\text{EE}}(\boldsymbol{r}, \boldsymbol{r}', \omega) j_e(\boldsymbol{r}', \omega)} \tag{2.46}$$

where $\overleftrightarrow{\boldsymbol{G}}^{\text{EE}}(\boldsymbol{r}, \boldsymbol{r}', \omega)$ is the so-called *electric Green dyadic*. As soon as the linear response is valid, this definition holds both in any considered regime: quantum or classical, retarded or quasi-static. This generality holds because the Green tensor "hides" all the microscopic physical details and only encodes the propagation of the field. Similarly, one can define a *magnetic Green dyadic* as:

$$\boldsymbol{H}^{\text{ind}}(\boldsymbol{r}, \omega) = \int d\boldsymbol{r}' \overleftrightarrow{\boldsymbol{G}}^{\text{HH}}(\boldsymbol{r}, \boldsymbol{r}', \omega) \epsilon(\boldsymbol{r}') \boldsymbol{m}(\boldsymbol{r}', \omega) \tag{2.47}$$

where $\boldsymbol{m}(\boldsymbol{r}', \omega)$ denotes the magnetic moment at $\boldsymbol{r}'$. These Green tensors are moreover connected through [89]:

$$\frac{\omega^2}{c^2} \overleftrightarrow{\boldsymbol{G}}^{\text{HH}}(\boldsymbol{r}, \boldsymbol{r}', \omega) = \boldsymbol{\nabla} \times \overleftrightarrow{\boldsymbol{G}}^{\text{EE}}(\boldsymbol{r}, \boldsymbol{r}', \omega).\boldsymbol{\nabla}' \times \tag{2.48}$$

2.2.5.2 The electromagnetic local density of states

We saw in section 2.2.4 that the local density of photon states determines the decay rate of a quantum emitter through the Purcell effect. The density of photon states is also involved in the Planck black-body radiation law:

$$U = \int_0^\infty \frac{\rho_0(\omega)\hbar\omega}{e^{\beta\hbar\omega} - 1} d\omega \tag{2.49}$$

where U is the spectral density of energy, $\beta = k_\mathrm{B}T$ and $\rho^0 = \dfrac{\omega^2}{\pi^2 c^3}$ is the vacuum density of photon states, which obviously does not depend on $\boldsymbol{r}$. A similar calculation in the case of two infinite conducting plates placed few nanometers apart enables the computation of the Casimir force. The description of these effects requires the help of quantum mechanics in which the concept of density of photon states is easy to interpret.

Nevertheless, in 2001, optical analogues to quantum corrals have been observed in photonic system using scanning scanning near-field optical microscopy (SNOM) [90, 91] as shown on figure 2.11.

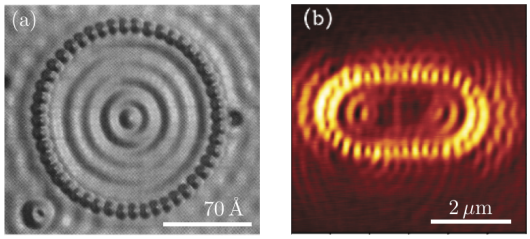

Figure 2.11: *Analogy between STM and SNOM. (a) STM image of a quantum corral in a ring of 48 Fe atoms (Cu substrate). Reproduced from [92]. (b) SNOM image of an optical corral in a stadium of gold nanoparticles (ITO substrate). Reproduced from [91].)*

The quantum corral shown in 2.11 has been observed by a scanning tunneling microscope (STM). Moreover a STM directly probes the spectral function $A(\boldsymbol{r}, \omega)$ of the surface i.e. the electronic density of states [30] which is connected to the retarded electronic Green function $\mathcal{G}$:

$$\mathcal{A}(\boldsymbol{r}, \omega) = 2\mathrm{Im}\{-\mathcal{G}(\boldsymbol{r}, \omega)\} \tag{2.50}$$

As demonstrated by Carminati [93], this apparent analogy with STM is actually formal and strongly suggests the use of density of photon states to interpret SNOM experiments. However, optical corrals are purely classical objects which raises questions about the definition of such a density of photon states in this context. This is where the concept of Green function intervenes. In the same spirit as in equation (2.50), one can define the *electromagnetic local density of states*[7] (EMLDOS) as [94, 89, 26, 84]:

$$\boxed{\rho(\boldsymbol{r}, \omega) = -\frac{2\omega}{\pi}\mathrm{Im}\left\{\mathrm{Tr}\left[\overleftrightarrow{\boldsymbol{G}}^{\mathrm{EE}}(\boldsymbol{r}, \boldsymbol{r}, \omega) + \overleftrightarrow{\boldsymbol{G}}^{\mathrm{HH}}(\boldsymbol{r}, \boldsymbol{r}, \omega)\right]\right\}} \tag{2.51}$$

where Tr denotes the trace operator. In a sense, the EMLDOS is the photonic counterpart of the electronic spectral function. Quite naturally, if one quantizes the EM field and plug the corresponding Green function into (2.51), we obtain the standard density of photon states in terms of occupation numbers. The demonstration of (2.51) is due to Agarwal [95] who understood that all the optical properties connected to the zero-point fluctuations and coherence effects (e.g. lifetime of excited states, Lamb shift, black-body radiation) can be explained only using classical electromagnetism and statistical physics. Particularly, he showed that, thanks to the fluctuation-dissipation theorem [96], all the equilibrium properties of the EM field are encoded in the fields' correlators.

[7] also called photonic density of states

The equation (2.51) defines the full EMLDOS. Actually, as we will see later, EELS does not measure this quantity but rather the partial electric[8] local density of states [100, 10]. By neglecting the excitation and detection details, the signal measured in SNOM can also be connected to the EMLDOS [101]. However, a general description required more involved developments [102]. Thus, we need to introduce the electric a-EMLDOS defined as:

$$\rho_{aa}(\boldsymbol{r},\omega) = -\frac{2\omega}{\pi}\mathrm{Im}\left\{G^{\mathrm{EE}}_{aa}(\boldsymbol{r},\boldsymbol{r},\omega)\right\} \tag{2.52}$$

where $a = \{x, y, z\}$ indexes the vector component of the electric field. Moreover, in the quasi-static limit, Boudarham and Kociak demonstrated that the electric LDOS associated with the LSP field admits a modal decomposition. Using the boundary integral equation introduced in 2.2.2.3, they showed that:

$$\rho_{aa}(\boldsymbol{r},\omega) = \frac{1}{2\pi^2\omega}\sum_n \mathrm{Im}\left\{-g_n(\omega)\right\}|\boldsymbol{E}^n_a|^2 \tag{2.53}$$

where the sum $\sum_n$ runs over the LSP modes, $\boldsymbol{E}^n$ is the electric eigenfield associated with the nth mode and $g_n(\omega)$ is the so-called spectral function defined by:

$$g_n(\omega) = \frac{2}{\epsilon_m(\omega)(1+\lambda_n) + \epsilon_d(\omega)(1-\lambda_n)} \tag{2.54}$$

ϵ_m being the dielectric function of the metal, ϵ_d the dielectric function of the embedding medium and λ_n the geometrical eigenvalue associated with the nth mode. The spectral function is basically a Lorentzian function peaked at the resonance energy of the mode and, for a lossless Drude metal embedded in vacuum, reduces to a delta function.

2.2.5.3 Cross-density of states and spatial coherence

As we described earlier, the success of Agarwal's approach lies in the fact that all the optical quantities can be related to the correlations of the EM field. Let's quickly precise this idea. The correlator C^{XY}_{ab} between two fields X_a and Y_b is defined as:

$$C^{\mathrm{XY}}_{ab}(\boldsymbol{r},\boldsymbol{r}',t,t') = \langle[X_a(\boldsymbol{r},t), Y_b(\boldsymbol{r}',t')]\rangle \tag{2.55}$$

where, here again, $\{a, b\} = x, y, z$ indexes the components of the fields and $\langle.\rangle$ denotes the canonical average on the states of the system. The fluctuation-dissipation applied to the EM field [95, 94] reads:

$$\begin{cases} C^{\mathrm{EE}}_{ab}(\boldsymbol{r},\boldsymbol{r}',\omega) = 2\hbar\coth\left(\dfrac{\hbar\omega}{2k_{\mathrm{B}}T}\right)\mathrm{Im}\{G^{\mathrm{EE}}_{a,b}(\boldsymbol{r},\boldsymbol{r}',\omega)\} & (2.56\mathrm{a}) \\ C^{\mathrm{HH}}_{ab}(\boldsymbol{r},\boldsymbol{r}',\omega) = 2\hbar\coth\left(\dfrac{\hbar\omega}{2k_{\mathrm{B}}T}\right)\mathrm{Im}\{G^{\mathrm{HH}}_{a,b}(\boldsymbol{r},\boldsymbol{r}',\omega)\} & (2.56\mathrm{b}) \end{cases}$$

It shows that there is a direct connection between the imaginary part of the Green function and the correlation functions of the EM fields. In the same spirit as in previous section, we can define the so-called *cross-density of states tensor* (CDOS tensor) [84]:

$$\overleftrightarrow{\boldsymbol{\rho}}_{ab}(\boldsymbol{r},\boldsymbol{r}',\omega) = -\frac{2\omega}{\pi}\mathrm{Im}\left\{\overleftrightarrow{\boldsymbol{G}}^{EE}_{ab}(\boldsymbol{r},\boldsymbol{r}',\omega) + \overleftrightarrow{\boldsymbol{G}}^{HH}_{ab}(\boldsymbol{r},\boldsymbol{r}',\omega)\right\} \tag{2.57}$$

The local part ($\boldsymbol{r} = \boldsymbol{r}'$ and $a = b$) of this tensor corresponds to the EMLDOS. Moreover, from (2.56), one can see that out of diagonal elements of the CDOS tensor contains all the information about the field correlations between different positions $\boldsymbol{r}$ and $\boldsymbol{r}'$ [84] but also between different directions of polarization a and b [103].

[8] The magnetic part can be measured with optical techniques [97, 98] or with EELS using exotic electron probes [99]

If the correlation between different directions of polarization are not too strong, one can rather consider the trace of the CDOS tensor:

$$\boxed{\rho(\boldsymbol{r},\boldsymbol{r}',\omega) = -\frac{2\omega}{\pi}\mathrm{Im}\left\{\mathrm{Tr}\left[\overleftrightarrow{\boldsymbol{G}}^{\mathrm{EE}}(\boldsymbol{r},\boldsymbol{r}',\omega) + \overleftrightarrow{\boldsymbol{G}}^{\mathrm{HH}}(\boldsymbol{r},\boldsymbol{r}',\omega)\right]\right\}} \tag{2.58}$$

which is usually simply called *cross-density of states* (CDOS). Cazé and collaborators [104] showed that the CDOS is the ideal tool to describe the properties of *spatial coherence of EM fields*. Particularly, they used it to analyse the Anderson localization of plasmon modes in disordered fractal metallic films. Finally, one can define the *degree of spatial coherence* as [103]:

$$\gamma(\boldsymbol{r},\boldsymbol{r}',\omega) = \frac{\rho(\boldsymbol{r},\boldsymbol{r}',\omega)}{\sqrt{\rho(\boldsymbol{r},\omega)\rho(\boldsymbol{r}',\omega)}} \tag{2.59}$$

which is simply the CDOS between $\boldsymbol{r}$ and $\boldsymbol{r}'$ normalized by their respective EMLDOS. We will come back on this quantity in chapter 4.

2.3 Electron microscopy and spectroscopies

So far, we introduced the concepts, objects and fundamental quantities of nano-optics which will be useful for the rest of this thesis. The question which need to be addressed now is: how can we measure such optical excitations at the nanoscale?

Quite naturally, the first technique which comes in mind is far-field optical techniques which consists in exciting the system with light and investigating the amount scattered or extincted in the far-field. However, this method is restricted by the light diffraction limit and therefore is unable to probe the excitations at the scale of the nano-objects. Then two routes have been considered [19]: either using near-field probes, or keep on working in the far-field but reducing the wavelength of the probe.
The first route leads to the development of scanning near-field optical microscopy (SNOM) [101]; it consists in scanning a tip onto the sample which enables us to shine light locally on the sample or, alternatively, to collect light emitted at the nano-scale. Several derived techniques have also been developed such as tip-enhanced near-field optical microscopy [105] or photon scanning tunneling microscopy [106]. SNOM has encountered great success and enabled the measurement of surface plasmon [107] or even single molecule fluorescence [108].
The other route is to reduce the wavelength of the probe. Although the use of X-ray light is technically challenging, optical microscope with spatial resolution of 15 nm has been demonstrated [109] with this source. Alternatively, one can employ electrons instead of photons, thus reducing the diffraction limit to tens of picometers and below.

In this thesis, I used a scanning transmission electron microscope (STEM) to probe optical excitations at the nano-scale. It employs fast electrons (60 keV to 200 keV) with a wavelength ranging from 1 to 10 pm. The purpose of this section is to introduce the main concepts of electron spectroscopy.

2.3.1 Interaction between fast electron and matter

The central object of this thesis is the *scanning transmission electron microscope* (STEM) which working principle will be detailed in section 2.3.2. Forgetting for the moment the experimental details, a STEM spectroscopy experiment consists in scanning a fast (typically 100 keV) and narrow (the spot size on the sample is smaller 0.5 nm) electron beam onto a sample and analyzing its interaction with the matter. Indeed, in the spectral domain, the electric field produced by a fast electron moving in an homogeneous medium of dielectric constant ϵ reads [19]:

$$\boldsymbol{E}(\boldsymbol{r},\omega) = \frac{ie}{\pi}\int d\boldsymbol{q}\,\frac{\frac{\boldsymbol{q}}{\epsilon} - \frac{k\boldsymbol{v}}{c}}{q^2 - k^2\epsilon}e^{i\boldsymbol{q}.\boldsymbol{r}}\delta(\omega - \boldsymbol{q}.\boldsymbol{v}) \tag{2.60}$$

where $k = \omega/c$ and the electron has been considered as a punctual charge moving at constant speed v along a straight line directed by unitary vector $\hat{z}$. This picture is particularly suitable for *fast* electrons. Placing ourselves in the Cartesian coordinate system $(\hat{r}_\perp, \hat{z})$ and if the electron does not exceed the speed of light in the medium[9], the calculation of the latter integral gives:

$$\boldsymbol{E}(\boldsymbol{r}, \omega) = \frac{2e\omega}{v^2\gamma\epsilon} e^{\frac{i\omega z}{v}} \left(\frac{i}{\gamma} K_0 \left(\frac{\omega R}{v\gamma} \right) \hat{z} - K_1 \left(\frac{\omega R}{v\gamma} \right) \hat{r}_\perp \right) \tag{2.61}$$

where $\gamma = (1 - \epsilon v^2/c^2)^{-1/2}$ is the Lorentz factor, K_0 and K_1 are modified Bessel functions of the second kind[10]. From equation (2.61), one can see that the electric field associated with the electron extents over a wide spectral range and is evanescent, which means that one can create an excitation lying outside the light cone (e.g. surface plasmons). For these reasons, an electron beam is usually considered as a *nanoscale source of broadband light*.

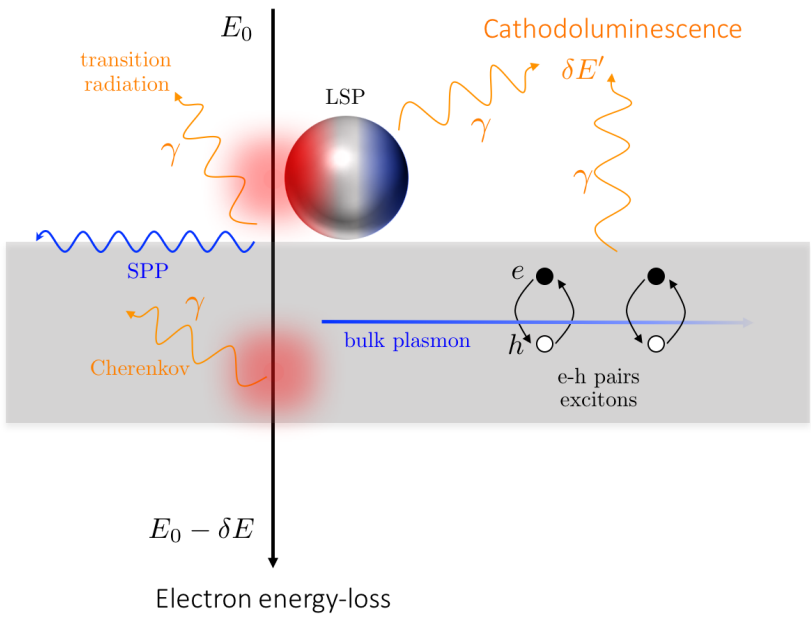

Figure 2.12: *Schematics showing a non-exhaustive list of processes happening when an electron impinges on a sample.*

When an electron hits the sample, a plethora of physical phenomena can thus happen; few of them are represented on figure 2.12. Electrons can create SPPs, LSPs, bulk plasmons, phonons, e-h pairs or even excitons (see the seminal work of [110]). By doing so, the electron gives energy to the sample and therefore is slowed down. Once excited, the dynamics of these excitations (as glimpsed in section 2.2.2.5) is dramatically complex and includes the generation of a cascade of secondary excitations (e.g. secondary electrons, Auger electrons, ...). Ultimately, and forgetting the dynamics inside the system, the sample will relax through the emission of light or secondary electrons. For the sake of this thesis, we will only consider the mechanism of light emission called *cathodoluminescence*.

Electron spectroscopy consist is getting information on these interactions through the spectral analysis of the outputs of the experiment. Two types of spectroscopies will be used in this thesis:

[9] otherwise the induced field in the medium becomes oscillatory [19] which corresponds to the presence of Cherenkov losses.

[10] Let's also highlight that the non-recoil approximation has been used. For brevity, it won't be discussed here but we will come back on this later in this manuscript.

- **The electron energy-loss spectroscopy (EELS)** which consists in analyzing the energy lost by the electrons subsequently to the interaction.
- **The cathodoluminescence spectroscopy (CL)** which consists in analyzing the energy of the photons emitted by the sample subsequently to the interaction.

2.3.1.1 Electron energy-loss spectroscopy

Due to the large energy of fast electrons, an EELS spectrum spans over a wide spectral range, typically 0-2000 eV. An example of EELS spectrum is shown on figure 2.13. Quite naturally, the physics ruling the electron interaction in such a large spectral range is quite diversified so that, traditionally, an EELS spectrum is divided in two regions: the low-loss region between (0 and 50 eV) and the core-loss region (above).

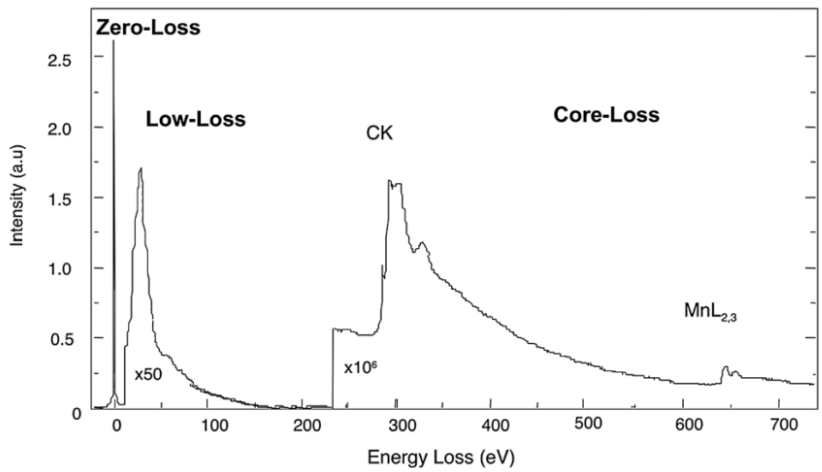

Figure 2.13: *EELS spectrum of a carbon nanotube containing manganese. Reproduced from [111].*

In the core-loss region, energy losses are due to the interaction with atomic core electrons and therefore provide information on the chemical nature or crystallographic arrangement of the sample. We will briefly come back on core-loss spectroscopy in chapter 3. Nevertheless, since I did not performed such experiments during my thesis, I will not describe it further.

This entire thesis focuses on low-loss spectroscopy. One can see on figure 2.13 that EELS spectra are dominated by the so-called *zero loss peak* (ZLP) corresponding to electrons which have not lost any energy. In practice, the ZLP has a certain energy width as the electron source is not perfectly monochromatic (see appendix B for details). Different peaks appear in a low-loss spectra corresponding to different types of excitations as we shall demonstrate hereafter.

As mentioned above, an electron moving in a homogeneous medium induces an electric field given by (2.60). As shown by Ritchie [112], in order to calculate the energy lost ΔE by an electron traveling in this medium, one simply needs to evaluate the work of the Lorentz force along its trajectory:

$$\Delta E = e \int dt \boldsymbol{v}.\boldsymbol{E}^{\text{ind}}(\boldsymbol{r}_e(t), t) \tag{2.62}$$

where $\boldsymbol{v}$ is the velocity vector of the electron and $\boldsymbol{r}_e(t)$ the position vector describing its trajectory. Naturally, the magnetic part of the Lorentz force is not involved here as the magnetic field do not work on the electron. One can now Fourier transform the electric field with respect to t in the latter expression and get:

$$\Delta E = \frac{e}{2\pi} \int_{\mathbb{R}} d\omega \int dt\, \boldsymbol{v}.\boldsymbol{E}^{\text{ind}}(\boldsymbol{r}_e(t), \omega) e^{-i\omega t} \tag{2.63}$$

Now, we separate the integral over ω into two parts (positive and negative frequencies) and get:

$$\Delta E = \frac{e}{2\pi} \int dt \left[\int_{-\infty}^{0} d\omega \, \boldsymbol{v}.\boldsymbol{E}^{\text{ind}}(\boldsymbol{r}_e(t), \omega) e^{-i\omega t} + \int_{0}^{\infty} d\omega \, \boldsymbol{v}.\boldsymbol{E}^{\text{ind}}(\boldsymbol{r}_e(t), \omega) e^{-i\omega t} \right] \tag{2.64}$$

Simple manipulations on the first integral leads to the expression:

$$\Delta E = \frac{e}{\pi} \int_{0}^{\infty} d\omega \int dt \, \text{Re} \left\{ \boldsymbol{v}.\boldsymbol{E}^{\text{ind}}(\boldsymbol{r}_e(t), \omega) e^{-i\omega t} \right\} \tag{2.65}$$

Besides, the total loss ΔE can also be written as a simple integral over the energies:

$$\Delta E = \int_{0}^{\infty} d\omega \, \hbar\omega \, \Gamma(\omega) \tag{2.66}$$

where $\Gamma(\omega)$ is the probability for the electron to lose a certain energy $\hbar\omega$. Comparing the two latter equations, we immediately get:

$$\Gamma(\omega) = \frac{e}{\pi\hbar\omega} \int dt \, \text{Re} \left\{ \boldsymbol{v}.\boldsymbol{E}^{\text{ind}}(\boldsymbol{r}_e(t), \omega) e^{-i\omega t} \right\} \tag{2.67}$$

If now we plug (2.60) in the latter equation, we obtain the so-called bulk losses probability $\Gamma^{\text{bulk}}(\omega)$ given by the equation:

$$\Gamma_{\text{bulk}}(\omega) = \frac{e^2 L}{\pi\hbar v^2} \text{Im} \left\{ \left(\frac{v^2}{c^2} - \frac{1}{\epsilon} \right) \ln \left(\frac{q_c^2 - k^2\epsilon}{\omega^2/v^2 - k^2\epsilon} \right) \right\} \tag{2.68}$$

where$L$ is the length of the electron trajectory and q_c is a cutoff wavevector which depends on the form of the detector (more details will be given later). In the quasi-static limit ($c \to 0$) equation (2.68) reduces to:

$$\boxed{\Gamma_{\text{bulk}}^{\text{QS}}(\omega) = \frac{2e^2 L}{\pi\hbar v^2} \text{Im} \left\{ -\frac{1}{\epsilon} \right\} \ln \left(\frac{q_c v}{\omega} \right)} \tag{2.69}$$

where the superscript "QS" indicates the quasi-static approximation. This formula can be used to retrieve bulk optical constants from an EELS measurement thanks to the Kramers-Kronig formula. The loss probability diverges when $\epsilon(\omega) = 0$ which corresponds to the excitation of bulk plasmons (see section for details 2.2.2.1 for details). If the electron exceeds the speed of light in the medium $v > c/\sqrt{\epsilon}$, it can couple to excitations in the medium. Then, one can show from the retarded loss probability (2.68) and for a real dielectric function that the bulk loss probability contains a so-called Cherenkov loss term:

$$\Gamma_{\text{Cherenkov}} = \frac{e^2 L}{\hbar} \left(\frac{1}{c^2} - \frac{1}{v^2 \epsilon(\omega)} \right) \tag{2.70}$$

This term corresponds to the generation of light by electrons moving faster than light in a medium i.e. the Cherenkov radiation [113].

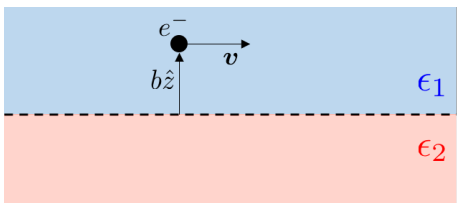

Figure 2.14: *Schematics of an electron traveling along the interface between two infinite media.*

As we saw in details in section 2.2.2, the presence of a surface dramatically modifies the electromagnetic behavior of the material and leads to the emergence of surface excitations. The simplest

system consists in an interface between two semi-infinite media of respective dielectric constants ϵ_1 and ϵ_2 (see schematics 2.14). In this case, the energy loss probability reads [19]:

$$\Gamma^{\mathrm{QS}}_{\mathrm{interface}}(\omega) = \frac{2e^2L}{\pi\hbar v^2}\left[\underbrace{\mathrm{Im}\left\{-\frac{1}{\epsilon}\right\}\ln\left(\frac{q_c v}{\omega}\right)}_{\text{bulk}} + K_0\left(\frac{2\omega b}{v}\right)\underbrace{\left(\mathrm{Im}\left\{-\frac{2}{\epsilon_1+\epsilon_2}\right\} - \mathrm{Im}\left\{-\frac{1}{\epsilon_1}\right\}\right)}_{\text{surface}}\right] \quad (2.71)$$

Naturally, we retrieve the bulk term and an additional surface term. The latter is multiplied by a Bessel function showing that it exponentially decreases away from the interface. This surface term is composed of two contributions. The first term diverges when $\epsilon_1(\omega) + \epsilon_2(\omega) = 0$ which corresponds to the excitation of surface plasmons (see section 2.2.2.2 for details). The last term is a correction to the bulk contribution which translates the fact that close to the interface, the oscillator strength is transferred from volume to surface modes. It corresponds to the so-called *begrenzungseffekt*. In the retarded case, finite size effects have also to be taken into account for the Cherenkov losses, as demonstrated in [114].

In section 2.2.2.3, we saw that the presence of a finite interface leads to the emergence of localized surface plasmon resonances. Let's consider an electron beam impinging close but outside a nano-particle as shown on figure 2.12 (a so-called aloof geometry). If we use the LSP modal decomposition introduced in section 2.2.2.3 to express the induced field in (2.67), the contribution of LSPs to the energy losses reads [9, 19, 10]:

$$\boxed{\Gamma^{\mathrm{QS}}_{\mathrm{LSP}}(\boldsymbol{R},\omega) = \frac{e^2}{\omega^2\hbar}\sum_n \mathrm{Im}\left\{-g_n(\omega)\right\}\left|E^z_n(\boldsymbol{R},q)\right|^2} \quad (2.72)$$

where z denotes the direction of propagation of the incident electron and $\boldsymbol{R} = (x, y)$ its impact point in the sample plane, $q = \omega/v$, the sum $\sum_n$ runs over all the LSP eigenmodes and E^z_n corresponds to the z component of the plasmonic electric eigenfields. Moreover, g_n is the so-called *spectral function* associated with the nth plasmon mode and reads:

$$g_n(\omega) = \frac{2}{\epsilon_m(\omega)(1+\lambda_n) + \epsilon_d(\omega)(1-\lambda_n)} \quad (2.73)$$

where ϵ_m and ϵ_d are respectively the dielectric constants of the nanoparticle and its embedding medium. As a reminder, the constants λ_n are the geometrical eigenvalues associated with each plasmon mode. Similarly to the infinite homogeneous media case, the spectral functions needs to be corrected in the case of penetrating electron trajectory in order to take the begrenzungseffekt into account.
One can see that the electric fields in (2.72) are: (i) projected along the z direction and (ii) Fourier transformed with respect to the z component. These are due to the fact that we use fast electrons propagating in straight lines along z; these specificities have dramatic consequences on the measurement of plasmon modes as we will discuss in great details in chapter 4.

The most important message for the rest of this thesis is translated into equation (2.72): the measurement of the spectrally resolved electron energy-loss probability enables us to access the plasmonic electric field at the nanoscale. It has been experimentally demonstrated for the first time in the Orsay STEM group in 2007 by Nelayah and collaborators [11]. As an example, we show on figure 2.15 an experimental spectrum and map of a silver nanocube's dipole mode. The experimental details of the acquisition of such data will be given in section 2.3.2.

2.3.1.2 Cathodoluminescence spectroscopy

As already detailed in the excellent reviews [19, 73], we usually distinguish two types of CL processes:

- **Incoherent radiation** processes occur when the electron beam creates e-h pairs (or bulk plasmons which then decay into e-h pairs) in the material which then radiativelly recombine.

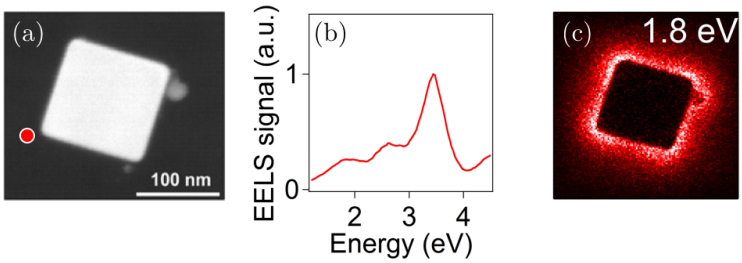

Figure 2.15: *(a) Annular dark field image of a silver nanocube. (b) EELS spectrum taken when the electron impinges at the position indicated by a red dot on image (a). (c) Spatial distribution of the EELS signal filtered at the energy of the dipole mode.*

This process is called incoherent because the e-h pairs creation processes do not have memory of the incoming electron's properties. In other words, an incoherent emission process does only depend on the sample properties and not on the excitation. We already gave examples of such processes in section 2.2.3 and we will give more details on the excitation dynamics in section 2.4. As emphasized by Kociak and Zagonel [73], roughly speaking incoherent radiations usually require the Schrodinger equation to be described.

- **Coherent radiation** processes can generally be described by Maxwell equations and are the main interest of this thesis. Naturally, these phenomena are said to be coherent because they depend on the excitation properties (impact parameter of the electron beam, phase of the incoming electron). The principal coherent emission processes are the diffraction radiation (DR), the transition radiation (TR), the generation of SPs and the Cherenkov radiation. The two latter have already been introduced earlier. The DR and TR processes are often presented together as they share several similarities [115, 116]. TR occurs when an electron crosses the interface between two media which generates surface currents and charges at the interface leading to far field radiation. A surface dipole model is usually sufficient to describe this process [19] in the case of a vacuum/metal interface. The properties of this emission (e.g. spectra, angular profile) highly depend on the incoming electron properties e.g. temporal profile [117]. On the contrary DR occurs when an electron travels close (but with a non-penetrating trajectory) to a periodic photonic material (typically a metallic grating). The evanescent field of the electron generates synchronized light emission of each element of the grating leading to far field interferences and a characteristic emission pattern. This radiation process is also referred as the Smith-Purcell effect.

For the sake of this thesis, we shall look closer to the formalism of coherent light emission. Let's go back on the situation described in figure 2.12. As we saw for EELS, an impinging electron generates an induced electric field $\boldsymbol{E}_{\text{ind}}$ which, in the far field zone (i.e. when $k_0 r \gg 1$), takes the asymptotic form:

$$\boldsymbol{E}_{\text{ind}} \xrightarrow[k_0 r \to \infty]{} \frac{e^{ik_0 r}}{r} \boldsymbol{f}_\perp(\boldsymbol{\Omega}, \omega) \tag{2.74}$$

where $\boldsymbol{k}_0 = \omega/c$ and $\Omega = (\theta, \phi)$ indicates the direction of $\boldsymbol{r}$. The function $\boldsymbol{f}_\perp$ contains all the information of the radiation and is obviously a purely transverse field. It can be calculated from the total scattered field $\boldsymbol{f}$ as $\boldsymbol{f}_\perp = \boldsymbol{f} - (\boldsymbol{f}.\hat{r})\hat{r}$. Moreover, the total field $\boldsymbol{f}$ can be computed from the boundary current $\boldsymbol{h}_2$[11] induced by the electron on the different surfaces [19]:

$$\boldsymbol{f}(\Omega, \omega) = ik_0 \oint_S d\boldsymbol{s}\, e^{-ik\hat{r}.\boldsymbol{s}} \boldsymbol{h}_2(\boldsymbol{s}, \omega) \tag{2.75}$$

where the integral is performed over the particle surface S. As we did for EELS, we can define an angle-resolved CL probability $\Gamma^{\text{CL}}(\Omega, \omega, \boldsymbol{r}_\perp)$ which is the probability of detecting a photon of

[11] The index 2 is justified in appendix C.

energy $\hbar\omega$ and in direction $\mathbf{\Omega}$ generated from an electron impinging at $\boldsymbol{r}_\perp$:

$$\Gamma^{\mathrm{CL}}(\Omega, \omega, \boldsymbol{r}_\perp) = \frac{1}{4\pi^2\hbar k_0}|\boldsymbol{f}_\perp(\mathbf{\Omega}, \omega)|^2 \tag{2.76}$$

The dependence in $\boldsymbol{r}_\perp$ is implicitly contained in $\boldsymbol{f}_\perp$. In our experimental setup, we do not have any angular resolution (contrary to e.g. [118, 116]) and rather integrate the signal coming from all the photons collected by a mirror which has a certain shape. We therefore measure:

$$\Gamma^{\mathrm{CL}}(\omega, \boldsymbol{r}_\perp) = \frac{1}{4\pi^2\hbar k_0}\int_{S_m} d\mathbf{\Omega}\, |\boldsymbol{f}_\perp(\mathbf{\Omega}, \omega)|^2 \tag{2.77}$$

where S_m represents the angular profile of the collection mirror. Finally, as we did for EELS, let's consider the particular case of localized surface plasmon resonances. Using a modal decomposition, Losquin and Kociak demonstrated that the CL loss probability for LSP reads in the quasi-static limit [119, 120]:

$$\boxed{\begin{aligned}\Gamma^{\mathrm{CL}}(\omega, \boldsymbol{r}_\perp) = {} & \frac{\omega e^2}{4\pi^2\hbar c^3}\sum_n |g_n(\omega)|^2 \int_{S_m} d\mathbf{\Omega}\, |\boldsymbol{p}_{n,\perp}(\mathbf{\Omega})|^2\, |E_{z,n}(\boldsymbol{r}_\perp, q)|^2 \\ & + \mathrm{Re}\left\{\frac{\omega e^2}{4\pi^2\hbar c^3}\sum_n\sum_{m<n} g_n(\omega)g_m^*(\omega)\int_{S_m} d\mathbf{\Omega}\, \boldsymbol{p}_{n,\perp}(\mathbf{\Omega})\boldsymbol{p}_{m,\perp}^*(\mathbf{\Omega})\, E_{z,n}^*(\boldsymbol{r}_\perp, q)E_{z,m}(\boldsymbol{r}_\perp, q)\right\}\end{aligned}} \tag{2.78}$$

where $\boldsymbol{p}_{n,\perp}$ is the transverse component of the dipole moment associated with the charge distribution of mode n. This formula is the analogue of (2.72) for EELS but technically more challenging as the presence of radiative dissipation contains the validity domain of the modal decomposition [84, 120, 119]. In details, the first term of (2.78) is the strict analogue of the eigendecomposition for the EELS probability. The second term however, which arises from interferences, is specific to the CL spectroscopy and can be misleading. Indeed, in a plasmon coupling experiment, a Fano lineshape (which is a signature of the strong coupling regime) can be confused with these far-field interferences, therefore leading to misinterpretation of experimental data.

The most important message for the rest of this thesis is translated in the first term of equation (2.78): the measurement of the spectrally resolved cathodoluminescence probability enables us to access the plasmonic electric field of *radiative modes* at the nanoscale. Indeed, contrary to EELS, plasmon modes with small dipole moment give a weak contribution to the CL probability. These modes are usually called *dark modes* even though the terminology is somehow improper [121, 52, 51].

As an example, we show on figure 2.16 the CL experimental spectrum and map of the same silver nanocube's dipole mode as in 2.15.

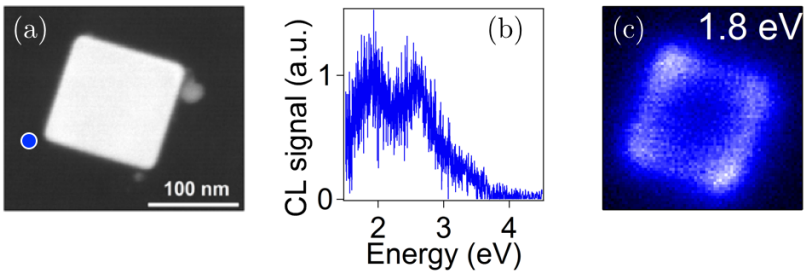

Figure 2.16: *(a) Annular dark field image of a silver nanocube. (b) CL spectrum taken when the electron impinges at the position indicated by a red dot on image (a). (c) Spatial distribution of the CL signal filtered at the energy of the dipole mode.*

As its name suggests, this dipole mode has a large dipole moment which explains the strength of the corresponding CL signal. The experimental details of the acquisition of such data will be given in section 2.3.2.

2.3.1.3 Connection with optical quantities

In the introduction of this chapter we motivated the use of electron microscopy in opposition with the diffraction limited far-field optical spectroscopy or near-field optical spectroscopies such as SNOM. It is rather crucial to understand to what extent the EELS and CL probabilities can be compared to optical quantities accessible with these techniques.

In 2015, Losquin and collaborators [119] demonstrated that while EELS is formally analogue the optical extinction spectroscopy[12], CL spectroscopy in the analogue of optical scattering spectroscopy. Particularly, the EELS probability (2.72) depends on the *imaginary part* of the response function of the system $\mathrm{Im}\{g_n(\omega)\}$ while the CL probability (2.78) depends on the *modulus* of the response function $|g_n(\omega)|^2$. Therefore, for a given plasmon mode n, the corresponding resonance in an EELS spectra is slightly energy-shifted with respect to its counterpart in a CL spectra [122].

Even more crucially, both EELS and CL probabilities can be connected to the EMLDOS defined in section 2.2.5.2. Indeed, using the definition of the electric Green dyadic (2.46), one can replace the induced electric field by the electron current in equation 2.67:

$$\Gamma^{\mathrm{EELS}}(\omega) = \frac{4e}{\hbar}\int dt\ \mathrm{Im}\left\{\int d\boldsymbol{r}'\ \boldsymbol{v}.\overleftrightarrow{\boldsymbol{G}}(\boldsymbol{r}_e(t),\boldsymbol{r}',\omega)\boldsymbol{j}(\boldsymbol{r}',\omega)e^{-i\omega t}\right\} \tag{2.79}$$

where we used the fact that for any complex number z, we have $\mathrm{Re}\{iz\} = -\mathrm{Im}\{z\}$. Beside, in the classical limit, the electron current in the spectral domain can be simply written as:

$$j(\boldsymbol{r},\omega) = -e\boldsymbol{v}\int dt' e^{i\omega t'}\delta(\boldsymbol{r}' - \boldsymbol{r}_e(t')) \tag{2.80}$$

It leads to:

$$\Gamma^{\mathrm{EELS}}(\omega) = -\frac{4e^2}{\hbar}\int dt\ \int dt'\ \mathrm{Im}\left\{\boldsymbol{v}.\overleftrightarrow{\boldsymbol{G}}(\boldsymbol{r}_e(t),\boldsymbol{r}_e(t'),\omega)\boldsymbol{v}\, e^{-i\omega(t-t')}\right\} \tag{2.81}$$

Choosing z to be the propagation axis of the electron, one can write $\boldsymbol{v} = v\hat{z}$, $\hat{z}$ being a unitary vector. We note $\boldsymbol{r}_\perp$ the position vector for the electron in the plane orthogonal to the propagation axis, this quantity does not depend on time (if we suppose the trajectory to not be modified by the interaction). We get:

$$\Gamma^{\mathrm{EELS}}(\omega) = -\frac{4e^2v^2}{\hbar}\int dt\ \int dt'\ \mathrm{Im}\left\{G_{zz}(\boldsymbol{r}_\perp,\boldsymbol{r}_\perp,z(t),z(t'),\omega)\, e^{-i\omega(t-t')}\right\} \tag{2.82}$$

The electron energy is typically 100 kV while the energy losses in the low-loss region are smaller than 50 eV. Consequently, one can assume the velocity of the electron to be constant and write $z = vt$ and $z' = vt'$. It leads to:

$$\Gamma(\omega) = -\frac{4e^2}{\hbar}\int dz\ \int dz'\ \mathrm{Im}\left\{G_{zz}(\boldsymbol{r}_\perp,\boldsymbol{r}_\perp,z,z',\omega)\, e^{-i\frac{\omega}{v}(z-z')}\right\} \tag{2.83}$$

In the latter, one can clearly identify a Fourier transform with respect to z and z'. Writing $q = \omega/v$ and using the definition of the EMLDOS (2.57), the latter equation can be re-written:

$$\boxed{\Gamma^{\mathrm{EELS}}(\omega) = \frac{2\pi e^2}{\hbar\omega}\rho_{zz}(\boldsymbol{r}_\perp,\boldsymbol{r}_\perp,q,-q,\omega)} \tag{2.84}$$

In other terms, an EELS experiment measures a projection of the EMLDOS, as first demonstrated in [100]. Let's also note that, at this point of the demonstration, we did not specify the system so

[12] Although EELS can probe dark modes while optical spectroscopy does not.

that the formula (2.84) is not restricted to plasmonics and applies to any coherent excitation. In the case of LSP, Boudarham and Kociak [10] demonstrated that the electric Green dyadic can be decomposed, in the quasistatic limit, as :

$$\overleftrightarrow{\boldsymbol{G}}(\boldsymbol{r},\boldsymbol{r}',\omega) = \frac{1}{4\pi\omega^2}\sum_n g_n(\omega)\boldsymbol{E}_n(\boldsymbol{r})\otimes\boldsymbol{E}_n^*(\boldsymbol{r}') \tag{2.85}$$

where $\otimes$ denotes the tensor product such that $(\boldsymbol{A}\otimes\boldsymbol{B})_{ij} = A_iB_j$ for any vectors $\boldsymbol{A}$ and $\boldsymbol{B}$. Plugging the latter equation into (2.84), we retrieve equation (2.72).

CL probability can also be connected to the EMLDOS [120]. However, contrary to EELS, CL spectroscopy only probes *radiative* plasmon modes and, naturally, only a sub-part of the EMLDOS is involved in this process; the latter is called radiative EMLDOS (rEMLDOS). To demonstrate it, let's first introduce an asymptotic form of the electric Green dyadic [120]:

$$\overleftrightarrow{\boldsymbol{G}}(\boldsymbol{r},\boldsymbol{r}',\omega) \xrightarrow[k_0r\to\infty]{} \frac{e^{ik_0r}}{r}\overleftrightarrow{\boldsymbol{G}}_\infty(\boldsymbol{\Omega},\boldsymbol{r}',\omega) \tag{2.86}$$

Thanks to this definition, we obtain an analogue formula of (2.46) for the far-field electric field:

$$\boldsymbol{f}_\perp(\boldsymbol{\Omega},\omega) = -4\pi i\omega\int d\boldsymbol{r}'\,\overleftrightarrow{\boldsymbol{G}}_\infty(\boldsymbol{\Omega},\boldsymbol{r}',\omega)j_e(\boldsymbol{r}',\omega) \tag{2.87}$$

Inserting this formula into (2.76) and plugging the electric current associated with the electron, we get the new formula for the Γ^{CL} [120]:

$$\boxed{\Gamma^{\mathrm{CL}}(\omega,\boldsymbol{r}_\perp) = \frac{4\omega ce^2}{\hbar}\int_{S_m} d\boldsymbol{\Omega}\;\hat{z}.\left[\overleftrightarrow{\boldsymbol{G}}_\infty^{\mathrm{T}}(\boldsymbol{\Omega},\boldsymbol{r}_\perp,q,\omega)\overleftrightarrow{\boldsymbol{G}}_\infty^{*}(\boldsymbol{\Omega},\boldsymbol{r}_\perp,q,\omega)\right].\hat{z}} \tag{2.88}$$

One can also define the rELMLDOS as :

$$\rho_{ij}^{\mathrm{rad}}(\boldsymbol{r},\omega) = \frac{2\omega^2c}{\pi}\int_{S^3} d\boldsymbol{\Omega}\left[\overleftrightarrow{\boldsymbol{G}}_\infty^{\mathrm{T}}(\boldsymbol{\Omega},\boldsymbol{r},\omega)\overleftrightarrow{\boldsymbol{G}}_\infty^{*}(\boldsymbol{\Omega},\boldsymbol{r},\omega)\right]_{ij} \tag{2.89}$$

and the integration is performed over the *full* 3-sphere S^3. This definition fully satisfies the classical interpretation [84]: it matches the definition of the power radiated to the far-field by a point-dipole oriented along a direction z and located in $\boldsymbol{r}$ when $i = j = z$. One can therefore see that *if the mirror collects all the photons* i.e. $S_m \to S^3$, the CL probability is directly proportional to the z-rEMLDOS Fourier transformed with respect to z, in strict analogy with EELS. This model for the CL spectroscopy perfectly matches the experiment as shown in [120]. Once again, this formula is valid for any coherent excitation, in the case of LSP, one can introduce a modal decomposition for the far-field Green dyadic [119]:

$$\overleftrightarrow{\boldsymbol{G}}_\infty(\boldsymbol{\Omega},\boldsymbol{r},\omega)\hat{\imath} = -\frac{1}{4\pi c^2}\sum_n g_n(\omega)E_{i,n}(\boldsymbol{r})\,\boldsymbol{p}_{n,\perp}(\boldsymbol{\Omega}) \tag{2.90}$$

where $i = x, y, z$ and $\hat{\imath}$ is the corresponding unitary vector. Once plugged in (2.88), it gives back equation (2.78).

The connection between the CL probability, the EELS probability and the EMLDOS is probably the most important point of this chapter as it demonstrates that one can perform a nano-optical experiment in an electron microscope.

2.3.2 Experimental setup

In section 2.3.1, we investigated the different processes involved in the electron-matter interaction. Particularly, we shows that EELS (resp. CL) enables us to map the EMLDOS (rEMLDOS) at the nano-scale. We will now describe in detail the experimental setup allowing the measurement of these quantities.

2.3.2.1 The scanning transmission electron microscope

On figure 2.17, we give a rough schematics of the STEM-VG HB 501 microscope principally used during this thesis. We describe hereafter its general working principle.

Electrons are generated by a cold field emission gun (cFEG) and accelerated to high energy (60 to 100 keV). A figure of merit of electron guns is their brightness (i.e. their current per unit area per solid angle) which characterizes their coherence and energy spread. The cFEGs display a brightness of typically 10^9 A.cm^{-2}.sr^{-1} [123]. It results in a smaller energy spread (typically 0.3 eV versus 1.5 to 3 eV for Schottky FEG or thermionic gun) and a better spatial coherence than other types of gun. For spectroscopic applications investigated in this thesis, cFEG are therefore the most adapted guns. Next, a set of two condenser lenses and one objective lens focus the electron beam in a small spot (typically 0.7 nm) on the sample. A so-called real objective aperture (ROA) placed in the focal plane of the objective lens enables to adjust the convergence angle of the beam thus to limit the spherical aberrations and reduce the spot size. Magnetic coils enable us to scan the beam onto the sample with adjustable speed. All these elements, from the gun to the sample, constitute the illumination system of the microscope which is described in detail in appendix B.

A mirror placed very close to the sample collects the light emitted through cathodoluminescence process. Once collected, the light is directed with an optical fiber to an optical spectrometer which enables us to measure the CL emission spectrum; greater details are given in section 2.3.2.5. Alternatively, the light can be sent to an Hanbury-Brown and Twiss (HBT) interferometer in order to measure the second order auto-correlation function $g^{(2)}(\tau)$. The entire section 2.4 is dedicated to the description of the HBT interferometry. The complete sample stage is cooled with liquid nitrogen allowing to study low-temperature luminescence phenomena.

After traversing the sample, the electrons can be elastically or inelastically scattered at different angles. A high angle annular dark field (HAADF) detector collects the electrons collected at high angle (more than 25 mrad typically) while a bright field (BF) detector collect the electrons scattered at small angle (less than 15 mrad typically). These two detectors enable the formation of images as described in detail in section 2.3.2.3.

Alternatively, the BF detector can be removed and the electron sent instead into the EELS system. It consists in a magnetic prism which disperses the electrons with respect to their kinetic energy while a combination of scintillator and CCD camera enable their detection leading to the measurement of an electron energy loss spectrum; greater details are given in section 2.3.2.4.
All these signals (CL, EELS, BF and HAADF) can be acquired simultaneously and in synchronization with the beam scan. A central concept to handle such a quantity of data is the *hyperspectral imaging* described in the following section.

2.3.2.2 Hyperspectral imaging

The system described above enables the simultaneous acquisition of a HAADF image, an EELS spectrum and a CL spectrum for a certain position of the electron beam onto the sample. By scanning the beam, one can repeat this operation for each of its positions and then obtain a so-called *spectrum-image* (SPIM) as first demonstrated in [124]. A SPIM can be visualized as a datacube in the (x, y, E)-space where (x, y) represent the impact parameter of the beam in the sample plane and E the energy loss channel. Therefore, extracting a sub-column of a SPIM gives an EELS spectra for a certain position of the beam (blue) while extracting a sub-plane gives an energy filtered EELS map (red). Beyond the practicality for data visualization, hyperspectral imaging allows an efficient numerical post-treatment of the experimental data (e.g. deconvolution, statistical analysis). The principle of hyperspectral imaging is summarized on figure 2.18.

2.3.2.3 Image formation mechanisms

The theory of image formation in a electron microscope is a rather intricate and vast topic in itself. Because this thesis mainly focuses on electron spectroscopies, we will be elusive on this topic.

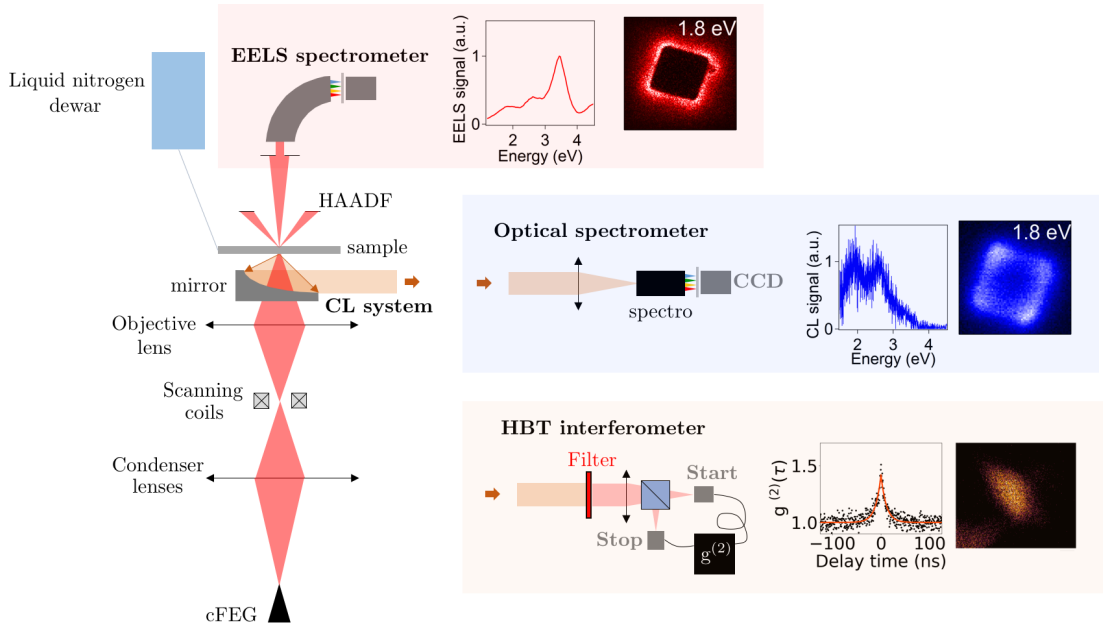

Figure 2.17: *Schematics showing the general principle of a STEM and its spectroscopies. Details are given in the text.*

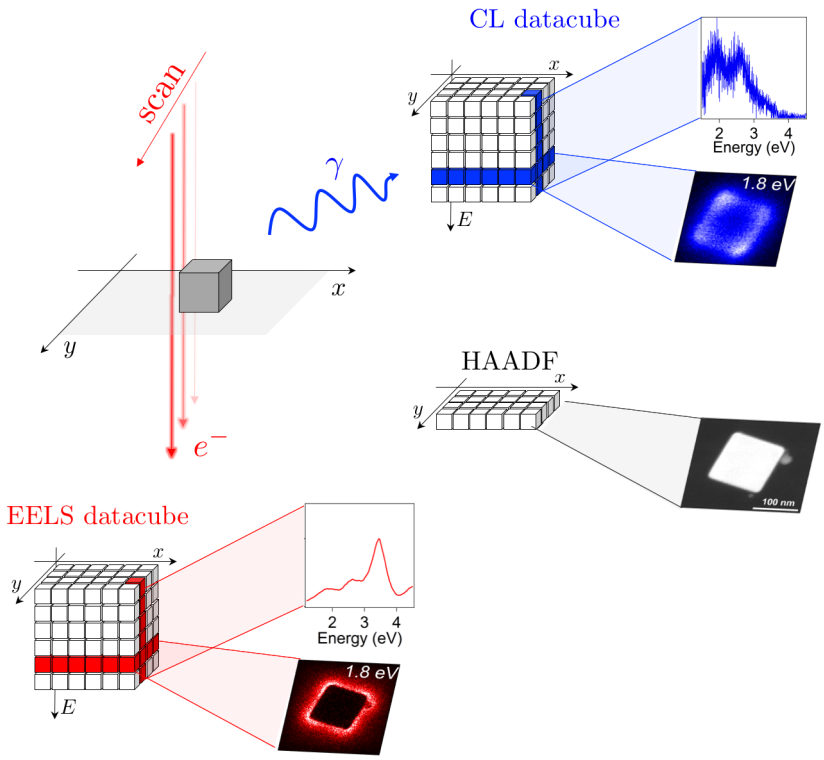

Figure 2.18: *Principle of the hyperspectral imaging.*

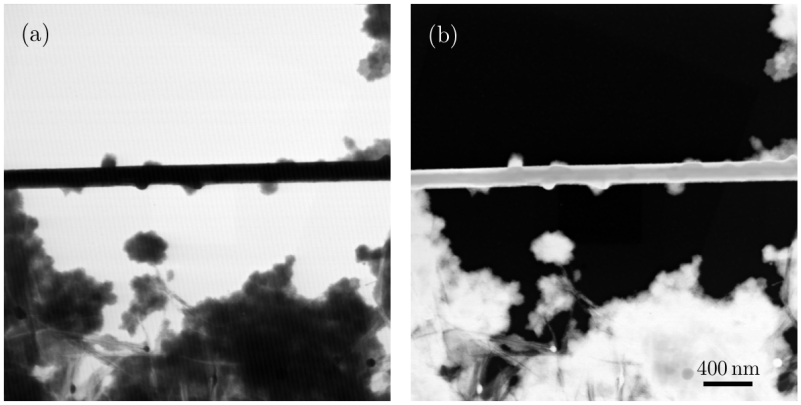

Figure 2.19: *(a) Bright field (BF) image of CdSe nano-particles deposited on a silver nano-wire acquired in our STEM-VG microscope. (b) Corresponding high angle annular dark field (HAADF) image.*

After the sample several detectors collect the scattered electrons in the far field as a function of the probe position onto the sample in order to reconstruct an image. The detectors are made of a scintillator coupled to a photomultiplier, with different sizes and geometry. Our microscope is equipped with two types of detectors: a bright field (BF) detector and a annular dark field (ADF) detector. On figure 2.19(a-b), we give examples of BF and ADF imaging of a CdSe@Ag sample. As showed on figure B.1, the BF detector collects the electrons scattered at small angles while the ADF detector has an annular shape detecting the electrons scattered at high angle. Due to the different geometry and position of the detectors, the contrast of the corresponding images will give different information [125].

To illustrate this point, let's consider an electron beam described by a wavefunction $\psi(\boldsymbol{r})$ focused on a one dimensional crystal with lattice parameter $\boldsymbol{g}$, as shown on figure 2.20(a). The crystal is defined by a transmittance function $\phi_{\mathrm{c}}(\boldsymbol{r})$. The diffraction of the electron probe by the crystal leads to the formation of diffraction spots which can overlap and interfere in the detection plane. The position of the interference fringes naturally depends on the position of the beam on the sample (but also on the aberration of the lenses). Depending on the shape and position of the detector, the recorded signal will therefore be different:

1. **The BF detector** is a small (compared to the inter-fringe) disk located on the optical axis. We illustrate it with a simple interference pattern (crystal made of only two atoms) on figure 2.20(b). In this case, one clearly sees that the signal strongly depends on the position of the detector with respect to the fringes. Under simplifying hypothesis[13], one can show that for an electron impinging at position $\boldsymbol{R}$ in the sample plane, the bright field intensity I_{BF} reads [125]:
$$I_{\mathrm{BF}} = |\psi(\boldsymbol{R}) \circledast \phi_{\mathrm{c}}(\boldsymbol{R})|^2 \tag{2.91}$$
where $\circledast$ denotes the convolution product. Thus, the BF imaging is a *coherent* imaging technique. This image formation principle is rather similar to conventional TEM (CTEM). These phase contrast images are particularly delicate to interpret as they depend on the morphology and the chemical composition of the sample. We do not tackle this problem here.

2. **The ADF detector** is an annular detector collecting the electrons scattered at high angles. Again, we illustrate it with a simple interference pattern (crystal made of only two atoms) on figure 2.20(c). In this case, one clearly see that the ADF detector sums the contribution of different fringes thus destroying the coherence effects. One can show that, for an electron

[13]Paraxial approximation, incident plane wave.

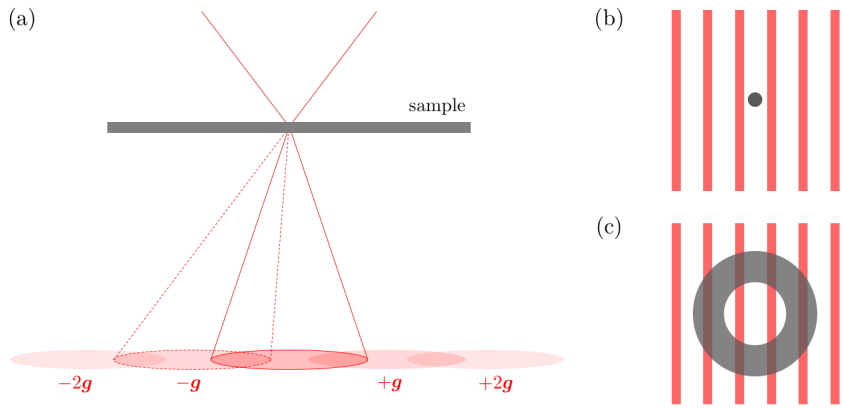

Figure 2.20: *(a) Principle of STEM image formation of a crystal. (b) BF detector (grey) geometry superimposed with the electron interference fringes (red) in the detection plane. (c) ADF detector (grey) geometry superimposed with the electron interference fringes (red) in the detection plane. Reproduced from [125]*

impinging at position $\boldsymbol{R}$, the annular dark field intensity I_{ADF} reads [125]:

$$I_{\mathrm{ADF}} = |\psi(\boldsymbol{R})|^2 \circledast O(\boldsymbol{R}) \tag{2.92}$$

where $O(\boldsymbol{R}) = |D(\boldsymbol{R}) \circledast \phi_{\mathrm{c}}(\boldsymbol{R})|^2$ and the function $D(\boldsymbol{R})$ is a transmission function describing the detector geometry[14]. For this reason, the ADF imaging is said to be an *incoherent* imaging technique. Intuitively, the number of electrons scattered at high angles increases with the thickness of the crystal; therefore, ADF images give information on the thickness of the sample.

Finally, we need to determine from which size the BF detection start to become incoherent. This value actually corresponds to the typical elastic scattering angle θ_0 given by [126]:

$$\theta_0 \approx \frac{\sqrt[3]{Z}}{k_0 a_0} \tag{2.93}$$

where Z is the atomic number of the scattering atom, $a_0 = 53 \times 10^{-12}$ m is the Bohr radius and k_0 is the wavevector of the electron. For an acceleration voltage of 100 kV and $Z = 6$, we get $\theta_0 = 20$ mrad. Other types of detection exist (e.g. annular bright field) but we do not enter these details here.

2.3.2.4 Electron energy loss spectrometer

To realize an EELS spectrum, we first remove the BF detector and collect the electrons traveling close to the optical axis. An aperture limits the collection angle to approximately 20 mrad. Then the electrons enter a curved magnetic prism which sorts them with respect to their energy (since the cyclotron radius is proportional to the speed of the electrons). Once sorted, electrons can be detected with a scintillator coupled through an optical fibers bundle to a charge-coupled device (CCD) camera. Our detection system consists in a 1340×100 pixels array which is intended to be binned along the y-direction (also called non-dispersive direction) in order to obtain an EELS spectrum consisting in 1340 pixels. Between the prism and the detection system, an ensemble of four quadrupole magnetic lenses magnifies (in order to adjust the dispersion of the EELS system) and reshapes the beam (in order to optimize the binning procedure). In our STEM-VG microscope

[14] More precisely, the detector has a ring shape in the detection plane (Fourier plane). Neglecting the outer radius, it can be considered to be a sharp high-pass filter which, in the real space, roughly means that $D(\boldsymbol{R})$ is a Bessel function [125].

an ensemble of coils (called Grigson coils, not represented on the schematics) placed before the collection aperture enables us to center the beam at the entrance of the EELS system. Finally, let's highlight that, in order to not overexpose the scintillator, an electron blanker (placed before the selected area aperture, see appendix B for details) periodically and quickly deflects the beam out of the sample. We used a Gatan spectrometer model 666 PEELS.

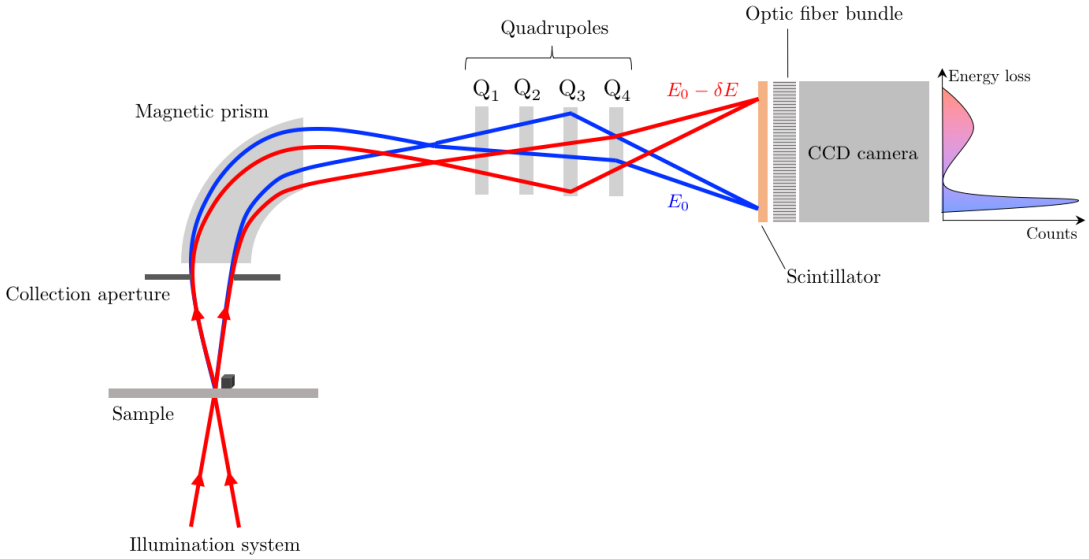

Figure 2.21: *Schematics showing the working principle of an EELS spectrometer.*

As showed in section 2.3.1, low-loss spectra are dominated by the zero-loss peak (ZLP) corresponding to the electrons which have undergone no loss. The ZLP has a characteristic asymmetric shape with a full width at half maximum (FWHM) of typically 0.2-0.3 eV and a tail extending over 4-5 eV[15] (for typical low-loss dispersions, see table 1 of [127] for details). The ZLP shape is also dictated by the aberrations in the illumination system and the intrinsic energy spread of the electron source (see appendix B for details). In the end, the presence of a broad ZLP limits the spectral resolution of the EELS system and needs to be compensated. Two methods exists:

- Using numerical post-treatment methods such as deconvolution procedure. Since the point spread function (PSF) of the microscope is known (one can measure the ZLP without any sample), an iterative method such as the Richardson-Lucy (RL) algorithm [128, 129] is particularly suitable, particularly because it is a noiseless method. It has been first implemented is 2003 for EELS [130] and since then is broadly used by the community. With such a technique, one can reduce the FWHM of the ZLP from 0.3 to 0.1 eV.

- Using an electron monochromator. Different types of monochromators exists (e.g. Wein filter, omega-shaped, alpha-shaped, see [131] for a review) but essentially rely on the same principle: a first element disperses the beam (such as an EELS spectrometer), an aperture filters the energy of electrons and a second dispersive element reassembles the beam. With a monochromator, one can obtain typically 20-100 meV ZLP energy width (depending on which type of electron gun is used) and an almost canceled tail.

In this thesis we used a non-monochromated electron beam and systematically applied a RL deconvolution to our data set. This setup is usually sufficiently resolved for the observation of SP modes. The recent acquisition of a monochromated STEM by our group (Nion U-Hermes) will enable us to study even lower energy excitations such as surface phonons (see chapter 6)

[15] i.e. the tail is greater than 10^{-4} of the full height until 4-5eV.

2.3.2.5 Cathodoluminescence spectrometer

CL spectroscopy has been first performed in a scanning electron microscope (SEM) with applications in for mineralogy [132], semi-conductors [133] or plasmonics [134]. Although extremely powerful, SEM-CL is limited by its spatial resolution (tens of nanometers). From 1980, CL spectroscopy started to be implemented in STEM [135] and applied to the study of semi-conductors' luminescence. Later, in 2001, Yamamoto, Araya and García de Abajo [12] realized the first CL maps of LSPs in a TEM with unprecedented spatial resolution. In 2010, Kociak and collaborators developed a CL system for STEM which is now patented [136] and commercialy available (Attolight system, model Mönch 4107). This CL system, which working principle is schematically represented on figure 2.22(a), allows CL spectroscopy with nanometric spatial resolution. Since then, this system demonstrated its efficiency in resolving semi-conductors' luminescence [137, 138], color centers' luminescence [139], excitons in h-BN [140], biological labels [141] and LSPs [142].

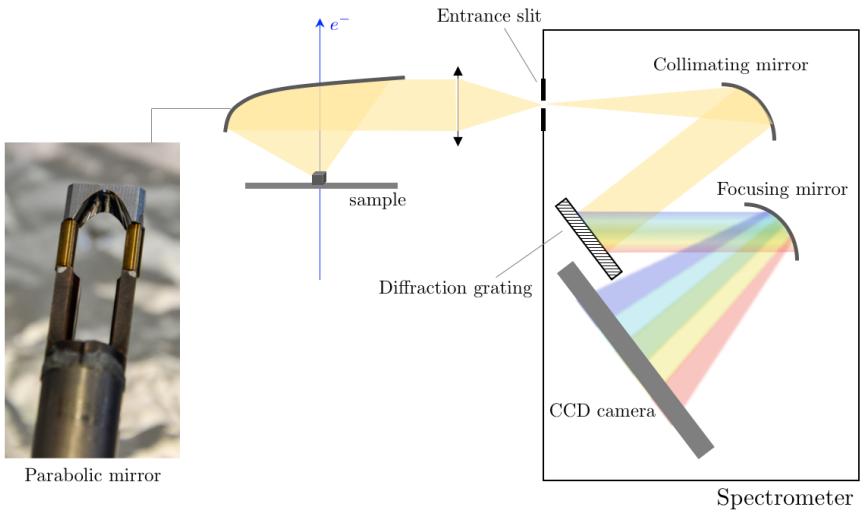

Figure 2.22: *(a) Schematics showing the working principle of a CL spectrometer. (b) Typical CL spectrum acquired on the corner of a sliver nanocube deposited on a Si3N4 membrane. (c) CL map filtered at 2.7 eV (integrated on the blue window in b) of a silver nanocube.*

The STEM-CL installed in our microscope (see figure 2.22(a)) consists in a parabolic mirror placed between the polar pieces of the objective lens. The mirror in mounted on an axis which enables its positioning by translations in the three spatial directions. The light collected on the sample is transported to an optical spectrometer by the mean of an optical fibers bundle (not represented on the schematics). A CCD camera collects the light after the spectrometer and constructs a CL spectrum as shown on figure 2.22(b). In the same way as for EELS, the acquisition of the CL system is synchronized with the scan of the STEM which enables the realization of CL hyperspectral imaging. An energy-filtered CL map of a silver nano-cube is shown on figure 2.22(c).

We use a Princeton Instruments spectrometer model Acton Advanced SP2300A equipped with a ProEM 1600^2 CCD camera. The spectrometer possesses three different gratings blazed at 300, 500 and 1000 nm and the camera has an optimal detection efficiency centered around 500 nm. The whole CL system has a specific transmission function which can be measured and corrected after acquisition of the data. This procedure is described in appendix G.

2.3.3 Wave effect in electron energy loss spectroscopy

In the section dedicated to imaging we emphasized the importance of the electronic phase in the image formation process. Then, a natural question would be: does the phase of the electrons plays a role in an EELS experiment? In other words, would a wave-like description of EELS bring new effects? The answer is naturally yes and one of the major goal of this thesis is to bring a comprehensive insight into this physics.

To the best of our knowlegde, this question has been first addressed by Ritchie and Howie in 1988 [143]. They demonstrated that, if all the inelastically scattered electrons are collected (large collection angle), a wave-like description of the electrons gives the same results as the ray optics description employed earlier. This is in fact strictly analogue to the case of imaging. Conventionally, we distinguish the coherent from the incoherent imaging. This is purely artificial since the imaging mechanism is dictated by the size of the detector and there is a continuous limit from a coherent (BF) to an incoherent (ADF) process. We can do the same type of distinction for EELS and define a "coherent" and an "incoherent" spectroscopy. To do so, let's first define the typical scattering θ_E angle for an inelastic process leading to the energy loss ΔE as [126]:

$$\theta_E = \frac{\Delta E}{2\gamma T} \tag{2.94}$$

where γ is the Lorentz factor and T is the kinetic energy of the electrons. For an acceleration voltage of 100 kV and an energy loss of $\Delta E = 2$ eV (average low-loss), we obtain $\theta_E = 13\,\mu$rad. This angle is considerably smaller than the typical elastic scattering angle for the same acceleration voltage ($\theta_0 \approx 20$ mrad, see imaging section). It means that interference effects can appear in EELS if and only if the collection angle is smaller than θ_E. In our VG microscope, the collection angle is about 20 mrad so that our EEL spectroscopy is incoherent and the classical point-like model developed earlier is fully justified. Let's also emphasize that θ_E is a considerably small angle which means that the number of collected electrons is rather small. Consequently, getting enough signal from an EELS experiment is this configuration is particularly challenging and will be discussed in great details in chapter 4. Nevertheless, in 1987, Echenique and collaborators have shown [16, 144, 19] that in the QS approximation, the low-loss formula (2.84) needs to be modified in the coherent case as:

$$\frac{d\Gamma^{\mathrm{QS}}}{dt} = \frac{2e^2}{\hbar}\sum_f \iint d\boldsymbol{r}d\boldsymbol{r'}\psi_f(\boldsymbol{r})\psi_i^*(\boldsymbol{r})\mathrm{Im}\{-W(\boldsymbol{r},\boldsymbol{r}',\omega)\}\psi_f^*(\boldsymbol{r}')\psi_i(\boldsymbol{r}')\delta(\epsilon_f - \epsilon_i + \omega) \tag{2.95}$$

where ψ_i and ψ_f the initial and final states of the electron probe with respective energy $\hbar\epsilon_i$ and $\hbar\epsilon_f$. The bounds of the sum $\sum_f$ are determined by the geometry of the detector. Moreover, W is the screened interaction defined as:

$$\phi_{\mathrm{ind}}(\boldsymbol{r},\omega) = \int d\boldsymbol{r}'\; W(\boldsymbol{r},\boldsymbol{r}',\omega)\rho_{\mathrm{ext}}(\boldsymbol{r}') \tag{2.96}$$

where ϕ_{ind} is the scalar potential induced in $\boldsymbol{r}$ by an external charge density ρ_{ext} in $\boldsymbol{r}'$. The latter propagator can be related to the electric Green dyadic through [10]:

$$\overleftrightarrow{\boldsymbol{G}}(\boldsymbol{r},\boldsymbol{r}',\omega) = \frac{1}{4\pi\omega^2}\boldsymbol{\nabla}\boldsymbol{\nabla}'W(\boldsymbol{r},\boldsymbol{r}',\omega) \tag{2.97}$$

Later, Garcia de Abajo [19] generalized the formula to include retardation effects in the medium, replacing the interaction kernel by the electric Green tensor:

$$\begin{aligned}\frac{d\Gamma^{\mathrm{R}}}{dt} = \frac{8\pi\hbar e^2}{m^2}\sum_f \iint d\boldsymbol{r}d\boldsymbol{r'}\psi_f(\boldsymbol{r})\boldsymbol{\nabla}[\psi_i^*(\boldsymbol{r})]\mathrm{Im}\{-\overleftrightarrow{\boldsymbol{G}}(\boldsymbol{r},\boldsymbol{r}',\omega)\}\\ \times\psi_f^*(\boldsymbol{r}')\boldsymbol{\nabla}'[\psi_i(\boldsymbol{r}')]\delta(\epsilon_f - \epsilon_i + \omega)\end{aligned} \tag{2.98}$$

This formalism will be re-derived and discussed in great detail in chapters 3 and 4. In the case of core-loss, the scattering angle are 10 to 100 times larger so that a coherent spectroscopy can

be achieved for reasonably large collection angle. In 2006, Schattschneider and collaborators [145] demonstrated the possibility of measuring magnetic dichroism in core-loss EELS (see section 4.1.2 for details). This technique called *electron energy-loss magnetic chiral dichroism* (EMCD) is the first example of coherent core-loss EELS [146].

2.4 Light interferometry in cathodoluminescence

In the previous section, we examined the spectra of light emitted through cathotoluminescence process. Nevertheless, other relevant information can be obtained by examining the temporal statistics of this emitted light. For example, the SPEs introduced in section 2.2.3 can be easily identified by their singular temporal profile.

2.4.1 The second order correlation function $g^{(2)}(\tau)$

A natural way to quantify the light emission statistics is to measure correlations in the number of photons in time between two positions along the beam. To do so, let's consider a light beam propagating along a certain axis and two photon detectors positioned at two different locations labeled 1 and 2 along the optical path. Measuring the correlations between the two detectors therefore corresponds to evaluate the correlation function $G^{(2)}(t_1, t_2)$ between the number of photons in 1 and the number of photons in 2:

$$G^{(2)}(t_1, t_2) = \langle n_1(t_1) n_2(t_2) \rangle = \langle a_1^\dagger(t_1) a_2^\dagger(t_2) a_1(t_1) a_2(t_2) \rangle \tag{2.99}$$

where $n_i(t) = a_i a_i^\dagger(t)$ is the photon number operator for detector i ($i = 1, 2$) and $\langle . \rangle$ is a ensemble statistical average. This is a *second order two points* correlation function as it involves four different operators and two coordinates t_1 and t_2. If we now restrict ourselves to stationary beams[16], the correlation function has to be invariant by translation in time and therefore only depends on the delay $\tau = t_1 - t_2$. Moreover, in this case, the ensemble average reduces to a time average $\langle . \rangle_t$. We then get:

$$G^{(2)}(\tau) = \langle n_1(t) n_2(t + \tau) \rangle_t \tag{2.100}$$

Moreover, we can also normalize the correlation function by dividing it by the average value of the number operators; we then obtain the normalized second order correlation function:

$$g^{(2)}(\tau) = \frac{\langle n_1(t) n_2(t + \tau) \rangle_t}{\langle n_1(t) \rangle_t \langle n_2(t) \rangle_t} \tag{2.101}$$

The latter formula is expressed in term of photon numbers and therefore is a quantum quantity. Naturally, one can also quantify the degree of coherence of a *classical* light by using the definition:

$$g^{(2)}(\tau) = \frac{\langle I_1(t) I_2(t + \tau) \rangle_t}{\langle I_1(t) \rangle_t \langle I_2(t) \rangle_t} \tag{2.102}$$

where $I_i(t)$ denotes the light intensity at position i and time t. Formula (2.101) and (2.102) are obviously equivalent since the instantaneous intensity in the beam is proportional to the number of photons.

Let's now picture the shape of $g^{(2)}$ for different simple cases:

- If the photons are randomly emitted (see figure 2.23(b)) then the events "detect a photon in 1" and "detect a photon in 2" are uncorrelated. Thus, the numerator and the denominator in (2.101) are equal and $g^{(2)}(\tau) = 1$, $\forall \tau \in \mathbb{R}$. The correlation function is therefore flat as shown in black line on figure 2.23(a). Such a source is often called *coherent* and would correspond e.g. to a perfectly monochromatic laser beam or any classical radiation with constant intensity.

[16] which is valid in practice in our experiment since we are not considering e.g. short pulse of light

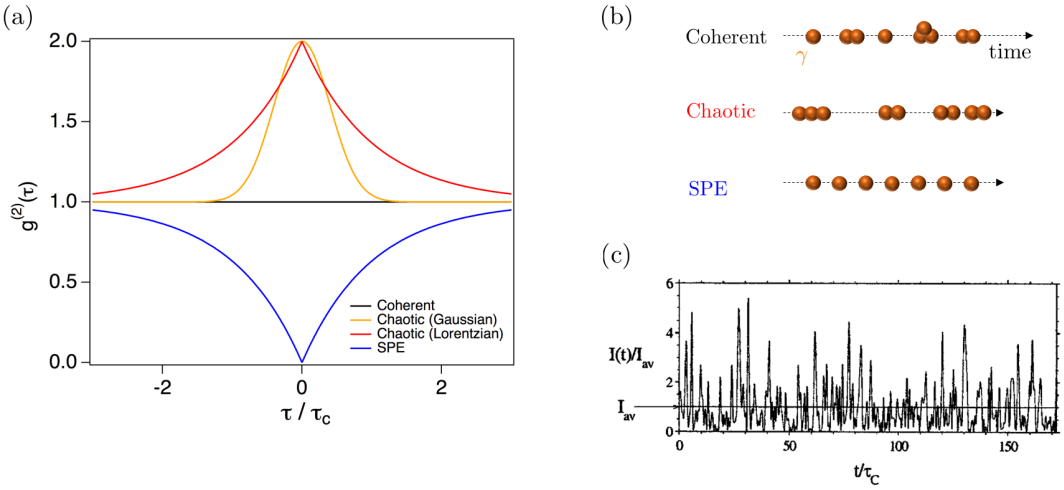

Figure 2.23: *(a) Second order correlation function of a random emission of photons (black), a bunched emission of photons with Gaussian profile (red), a bunched emission of photons with Lorentzian profile (orange) and an antibunched emission of photons corresponding to a SPE (blue). (b) Schematics showing the photons arrival time for different photon statistics. (c) Computer generated time series for the average intensity of a Gaussian source of light, reproduced from [147].*

- If the source of photon is a vapor lamp, the velocity distribution of particles in the gas will influence the photon emission statistics. Particularly, the linewidth of the emission spectra is broadened by several phenomena (e.g. collision broadening, Doppler broadening, power broadening; see [148] for details). In the time domain, this spectral broadening corresponds to the existence of a coherence time τ_c determined by the dominant broadening process (for collision broadening, it corresponds to the inverse of the collision rate $\tau_c = 1/\gamma_c$). An example is shown on figure 2.23(b c). The corresponding correlation function is shown on figure 2.23(a) for a Gaussian spectral profile (red) and a Lorentzian spectral profile (orange). The typical intensity fluctuations of a Gaussian source on figure 2.23(c) presents high intensity fluctuations which correspond to photon bunches as pictured on figure 2.23(b).

- Let's now consider the photon statistics of a SPE which is schematically represented on figure 2.23(b). In this case, the probability of detecting two photons simultaneously is zero. Thus, the correlation function presents a dip at zero delay i.e. $g^{(2)}(0) = 0$ as shown on figure 2.23(a) in blue line and first demonstrated in [149]. Contrary to the two previous cases, the antibunched emission is a purely quantum phenomena and has no classical counterpart.

2.4.2 The Hanbury Brown and Twiss interferometry and its application in cathodoluminescence

A way to measure in practice the correlation function of light is to use a so-called *Hanbury Brown and Twiss* (HBT) interferometer [148, 150], first introduced for astrophysical applications in 1956 [151]. The basic principle is to separate the beam in two outputs respectively sent onto two single photon detectors D1 and D2. When a photon is detected in D1, the detector sent a "start" command to a correlation electronics. Then, when a second photon detected in D2, a "stop" command is sent. The correlation electronics measures the delay between the "start" and the "stop" and repeat the measurement. The results are presented on a histogram $H(\tau)$ giving the number of events as a function of the time delay. For a large number of measurements, it corresponds to:

$$H(\tau) = P(2, t+\tau|1, t) \tag{2.103}$$

where $P(2, t+\tau|1, t)$ is the (conditional) probability of detecting a photon in P2 at $t+\tau$ given that

a photon has been detected in P1 at t. One can shows that, after a proper normalization [152, 13], the time delay histogram corresponds to the $g^{(2)}$ function.

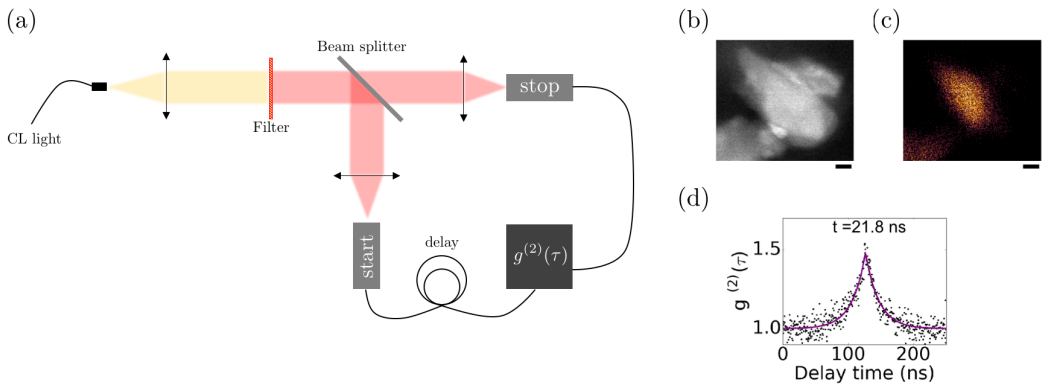

Figure 2.24: *(a) Schematics of the Hanbury Brown and Twiss interferometer used for the correlation function measurement. (b) ADF and (c) energy-filtered CL map of a nano-diamond (ND) containing hundreds of color centers. (d) Experimental second order correlation function measured on the ND shown in (e). Scale bars: 50 nm.*

In 2013, Tizei and Kociak [13] first implemented an HBT interferometer to the CL system of our VG-STEM which working principle is represented on figure 2.24(a) and described hereafter. The CL light collected by the mirror in sent onto the interferometer through an optical fiber. An optical filter is used to insulate the contribution of the considered CL emission line[17]. A 50/50 beam splitter then sent the beam onto two single photon detectors. For visible range experiments carried out in this thesis, we use Picoquant single photon avalanche diodes, τ-SPAD. The signal acquired by the detectors is sent to a time-correlated single photon counting (TCSPC) system (Picoquant Time Harp correlation electronics) which provides the time-delay histograms after a typical acquisition type of 5 min. Since the histograms are symmetric with respect to $\tau = 0$ (both detectors are equivalent) and the TCSPC system cannot measure negative delays, we introduce an artificial time delay on one detector to produce an offset of the histogram. To do so, we use a long cable (23 m) to carry the electronic signal from the detector 1 to the TCSPC which introduces a 120 ns delay offset. Moreover, in order to avoid crosstalk issues between the two SPAD [153], we used low-pass filter (not represented on the schematics). An example of time-delay histogram acquired with such a system is shown on figure 2.24(d). The signal from detector 1 is synchronized with the beam scanning system of the microscope which enables to acquire energy filtered CL map (obtained from the SPADs) together with the conventional ADF-BF images as shown on figure 2.24(b-c). We conventionally refer to this imaging mode as *pulsed imaging*. It allows a straightforward real-time identification of QEs at the nano-scale. In order to take a time-delay histogram, one need to fix the beam position onto the sample and accumulate signal for few minutes. Further details on the setup can be found in [154].

2.4.3 Photon bunching in cathodoluminescence, application in lifetime measurement

The STEM-HBT setup described earlier enables the measurement of $g^{(2)}(\tau)$ function with nanometric spatial resolution [154]. The first application of this system is the identification of SPEs at the nanoscale at it has been done for defects in hexagonal boron nitride (h-BN, [76]) or color centers in nano-diamond [13].
Nevertheless, Meuret and collaborators demonstrated that CL-HBT measurement can lead to a light bunching where a PL-HBT would not [155]. This phenomenon appears in wide band-gap

[17]Indeed, contrary to a standard HBT experiment in photoluminescence (PL), CL presents a broadband emission and therefore need to be filtered

semiconductors system containing a large number of QEs such as the nano-diamonds containing hundreds of NV^0 centers showed on figure 2.24(b-c). In this case, the correlation function measured on the particle (figure 2.24(d)) clearly display a bunching behavior. However, the NV^0 are prototypical example of two-level systems which should behave as SPEs. To understand the origin of this difference, we need to precise the electronic excitation process leading to the photon emission of the QE(s). Impinging electrons create bulk plasmons in the material which energy is much higher energy than the gap (in diamond, the bulk plasmon energy is 30 eV while the gap is 5 eV). These plasmons then decay into several e-h pairs as described in section 2.2.2.5. The different pairs then randomly migrate into the material and radiatively recombine in different defects leading to the emission of several photons [154, 155]. Therefore, through this process, a single electron can lead to the synchronized emission of different QEs inside the material i.e. a bunched emission of photons. Of course, the details of this process depend on several parameters such as e.g. the number of QEs inside the material, the electron current, the number of bulk plasmons created per incoming electron, the number of e-h pairs emitted per plasmon, the dynamics of e-h pairs inside the material, the material properties, etc. Yet, extended Monte-Carlo simulations and a comparison between different possible analytical models demonstrate that description above well reproduce the experimental results. We do not give further details on these models here and let the interested reader refers to [154, 155].

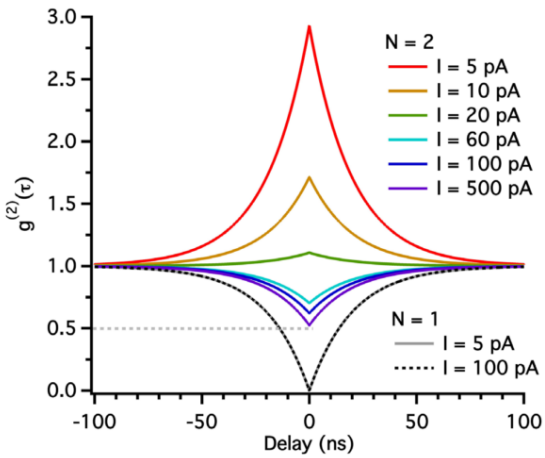

Figure 2.25: *Simulation for a nano-diamond with thickness of 30 nm and τ_e = 20 ns. Reproduced from [155].*

Nevertheless, let's emphasize that there is a competition between this bunching effect and the natural anti-bunching effect expected from the emitter dynamics. When the number N of QEs inside the material is small (N<5) and when one supposes that only one plasmon is created per incoming electron, it can be shown that the correlation function reads [155]:

$$g^{(2)}(\tau) = \frac{I_0}{I}\frac{\lambda_e}{Le^{-L/\lambda_e}}\left(1-\frac{1}{N}\right)e^{-\tau/\tau_e} + \left(1-\frac{1}{N}e^{-\tau/\tau_e}\right) \tag{2.104}$$

where L is the thickness of the sample, λ_e is the mean free path of the bulk plasmon, τ_e is the lifetime of the QEs. The normalization current $I_0 = e/\tau_e$ corresponds to one incoming electron per lifetime τ_e. Corresponding simulations for $N = 1$ and $N = 2$ are shown in figure 2.25. Equation (2.104) clearly exhibits the competition between the bunching effect due to the electron excitation (first term) and the anti-bunching effect due to the natural emission statistics of the QEs (second term). For $N = 1$, one can see that the correlation function naturally displays an anti-bunching dip which does not depend on the electron current. On the contrary, when $N = 2$, the $g^{(2)}(\tau)$ shows a bunching peak which decreases with increasing current I. For high current value, the curves invert and even reach an anti-bunching regime when $I = 500$ A. Indeed, when the current increased, photons originating from *different* incoming electrons arrive closer and closer in time to the detectors and ultimately become indistinguishable which leads to a blurring of the bunching

effect.

Let's finally note that, no matter the regime investigated (bunching or anti-bunching), the time constant of the exponential decay in the $g^{(2)}$ is systematically τ_e. Indeed:

1. The dynamics of electrons (e-h pairs, plasmons) inside the material is much faster (femtosecond to picosecond range) than the investigated decay times (nanosecond range). Therefore, their contributions to the correlation function are negligible.

2. The electrons are randomly emitted by the electron gun. Therefore, the arrival times of electrons onto the sample follow a Poisson distribution which corresponds to a flat contribution to the correlation function (black curve in figure 2.23(a)).

Thus, STEM-HBT enables the measurement of lifetime at the nano-scale in a wide range of systems and experimental conditions as demonstrated in [68]. We will use this technique in chapter 5 to probe Purcell effect in NV^0-LSP systems.

2.5 Numerical methods for nano-optics

In addition to all the theoretical and experimental elements discussed so far, the current success of nano-optics also relies on the development of efficient numerical methods. A huge variety of approaches exists which most famous representatives are:

- **The discrete-dipole approximation** (DDA, see [156]). It consists in treating a nano-particle as a discrete assembly of point dipoles which interact between each others [157]. This approach is inspired by old approach in atomic physics in which dielectric properties of a crystal were derived from the atomic polarizabilities via the Clausius-Mossotti relation. The DDA method is quite intuitive and easy to parametrize (the only stringent condition is that the dipole inter-space needs to be smaller than the typical length scales of the excitation in the material). However, DDA is particularly time consuming (typically one day of calculation for a 80 nm sphere, [158]). A free code, `DDSCAT`, is available online[18].

- **The finite difference time domain** method (FDTD, see [159]). It basically consists in solving the full Maxwell equations in the temporal domain. The space and time are discretized (following the so-called Yee cell method) but the materials are treated as continuous media described by their dielectric constants. The FDTD method computes the complete EM field in the whole space therefore enabling us to get the full optical response of the system. Although time consuming, FDTD is simple to implement and allows periodic boundary conditions, which is particularly useful in photonics. An EELS module exists for FDTD [160] but provides less accurate results than BEM. A efficient commercial implementation is the `Lumerical FTDT solutions`.

- **The boundary element method** (BEM, see [161]). It consists in taking benefit from the boundary conditions on the nano-particle in order to reformulate the Maxwell equations as a boundary integral equation (BIE) [158]; thus only the particle surface needs to be discretized. Moreover, the fields are computed in the spectral domain which is particularly convenient for applications in electron microscopy. Contrary to the previous methods, the BEM requires low computational resources and calculation time. However, the price to pay is the complex parametrization and the high sensitivity of the code to the computation parameters. The most widespread free BEM code for nano-optics is the Matlab `MNPBEM toolbox`[19] [162] which has been used thorough this thesis .

Some calculations have been performed with the FDTD method but are not presented in this manuscript. However, in this thesis, I made substantial use of the boundary elements method (version `MNPBEM 14`) which I briefly introduce in appendix C. For an extended discussion, one can refer to [161].

[18] `http://ddscat.wikidot.com`
[19] `http://physik.uni-graz.at/mnpbem/`

2.6 Sample preparation: the electron beam lithography

From the details given so far, one can see that the central object of this thesis are metallic nano-particles. In order to perform the electron microscopy experiments described earlier, one needs to synthesize these nano-structures onto microscopy grids which have stringent dimension restriction. Our nano-particles have been synthesized through two approaches: chemical growth or e-beam lithography. The chemically grown samples have been prepared by our collaborators in the form of colloidal solutions which we then drop onto our grids. On the other hand, we performed the e-beam lithography synthesis therefore we will give the details of the method in this section. We show on figure 2.26(a1-a5) some lithographed structures realized in the context of this thesis. One can see that contrary to chemical synthesis, e-beam lithography produces poly-crystalline and grained particles which can in practice reduces the quality factor of the plasmon resonances. However, lithography can produce any kind of shapes while chemistry is limited to certain geometries.

The lithography process described hereafter and shown of figure 2.26(b1-b6) has been developed in the STEM group thanks to the combined efforts of Zackaria Mahfoud and Sophie Meuret.

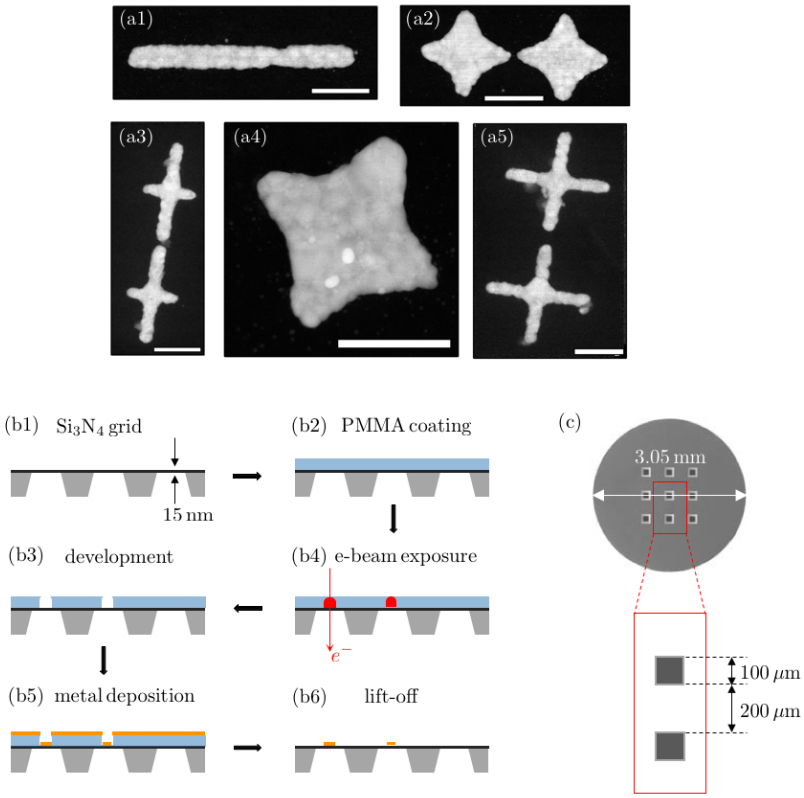

Figure 2.26: *(a1-a5) ADF images of lithographied silver and gold nano-structures. Scale bar: 200 nm. (b1-b6) Schematics showing the different steps of an e-beam lithography fabrication. (c) Schematics (reproduced from Ted Pella website) showing the geometry of the Si3N4 grids used in our experiments.*

The synthesis is done on a Si_3N_4 grid bought from Ted Pella (product number 21569-10) which geometry is shown on figure 2.26(c). It consists in a 3.05 mm Si disk pierced with nine 100x100 μm Si_3N_4 membranes. The membranes are sufficiently thin (15 nm) in order to let the electron beam pass, see figure 2.26(a1). The lithography proceeds as follow:

1. A 100 nm layer of Polymethyl-methacrylate (PMMA) is spin-coated onto the sample, see figure 2.26(a2). We use an A3 type PMMA which is the standard e-beam lithography resist.

In order to make the PMMA layer uniform the sample is heated at 180°C for 15 min prior to the deposition. The sample is baked for 15 min at the same temperature afterward in order to solidify the polymer. The spinning is done at 4000 revolutions per minute for 30 s.

2. The PMMA is then patterned by e-beam exposure, see figure 2.26(a3). We employed a Zeiss SEM-FEG Supra55vp electron microscope operated at 30 kV with a 7.5 μm objective aperture. The current in the probe is systematically measured before the lithography in order to adapt the exposition time. The typical probe current is $I \approx 15$ pA and the electron dose required to produce small structures of few hundreds of nanometers is typically 800 μC.cm^{-2}[20]. The drawing of the nano-structures is handled by the `NPGS` software which employs CAD design files.

3. We then remove the part of the PMMA which has been exposed to the beam, see figure 2.26(a4). To do so, we dip the sample in Methyl-isobutyl-ketone (MIBK) for 1 min which preferentially dissolves the polymer chains altered by the electron beam. After development, the sample is washed for 30 s with isopropanol.

4. We deposit a film of metal (gold, silver or aluminum) onto the sample by Joule evaporation method, see figure 2.26(a5). The sample is placed in a vacuum chamber (the pressure is typically set at 10^{-6} mbar). Pieces of metal are disposed on a tungsten boat which is heated by the application of high current (typically 200 A) leading to the evaporation of the targets. The deposition rate onto the sample is monitored with a piezoelectric quartz.

5. We then remove the mask of PMMA by dipping the sample in acetone, see figure 2.26(a6). Contrary to standard lift-off procedure (where the sample is heated and sonicated), we need to take precaution as the membranes are particularly fragile. The sample is therefore left in acetone for 4 hours and the metal film is plucked manually.

[20]For readers familiar with e-beam lithography, this dose is particularly high and is justified by the thinness of our grid which reduces the electron-sample interaction.

Chapter 3

A photonic approach to inelastic electron holography

Contents

3.1 Presentation of the problem . . . 48
3.1.1 Introduction . . . 48
3.1.2 Difficulties: retardation effects, quantum description of the target . . . 49
3.1.3 State of the art . . . 50
3.1.4 Purpose of this chapter, methodology . . . 52
3.2 Preliminary remarks: conventions, Green functions, gauge fixing . 52
3.2.1 Conventions and notations . . . 52
3.2.2 Correlators and Green functions . . . 53
3.2.3 Lagrangian form of the Maxwell equations . . . 54
3.2.4 Gauge fixing and vacuum photon propagator . . . 54
3.3 Propagators for the electromagnetic field in presence of a polarizable medium . . . 55
3.3.1 Quasistatic approach: modification of the Coulomb propagator, electron density correlation function . . . 56
3.3.1.1 Linear response electrostatic susceptibility . . . 56
3.3.1.2 Dyson equation for the electrostatic propagator, screened interaction . . . 57
3.3.1.3 Connection between the mixed dynamic form factor and the screened interaction . . . 58
3.3.2 Retarded approach: Photon propagator and electron four-current correlation function . . . 59
3.3.2.1 Linear response electromagnetic susceptibility . . . 60
3.3.2.2 Dyson equation for the photon propagator . . . 61
3.3.2.3 Retarded electric Green dyadic . . . 62
3.3.2.4 Reciprocity theorem and symmetry properties of the Green dyadic 63
3.3.3 Concluding remarks . . . 64
3.4 Kinetic equation for the electron density matrix . . . 64
3.4.1 Schrödinger equation for the electron propagator . . . 64
3.4.2 Dyson equation for the single electron propagator . . . 65
3.4.3 Bi-linear propagator for the single electron density matrix . . . 68
3.4.4 The kinetic equation for the single electron density matrix . . . 70
3.4.4.1 First case: Quasistatic interaction kernel . . . 71
3.4.4.2 Second case: Retarded interaction kernel . . . 72

3.5 Single scattering approximation: application to electron energy loss experiments **73**
3.5.1 Electron energy loss probability 73
3.5.2 Application to the measurement of the coherence of optical fields 74
3.5.3 The self-energy formalism 76
3.5.4 Relativistic anisotropy in inelastic scattering 77
3.6 Summary and perspectives **78**

3.1 Presentation of the problem

3.1.1 Introduction

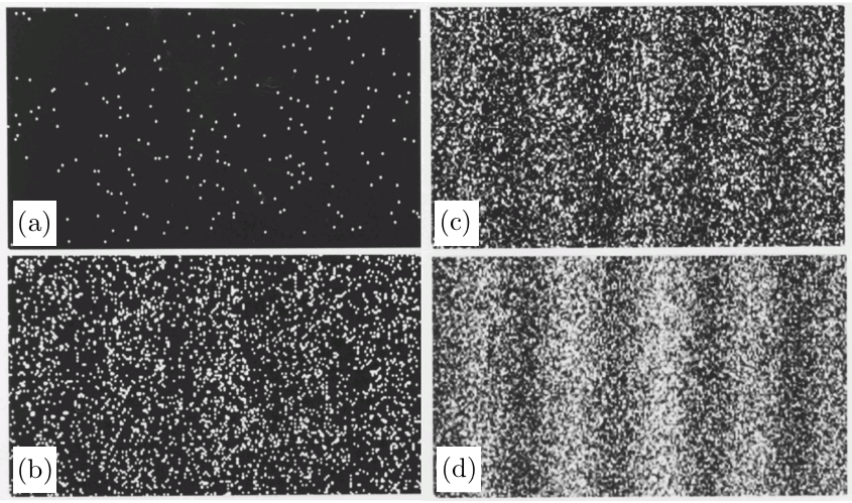

Figure 3.1: *Interference patterns of a two slits experiment realized by Tonomura et al. [163] in a TEM for: (a) 100 (b) 3000 (c) 20 000 and (d) 70 000 electrons.*

Electron microscopy is basically built upon the concept of wave-particle duality. A fascinating manifestation of this prorperty is the Young's double-slit experiment realized by Tonomura and collaborators in a TEM [163] as shown on figure 3.1. More generally, electron microscopists are constantly juggling between two points of views:

- A **ray optics** perspective, where an electron is represented by a point-like particle and its propagation is modeled by the laws of geometrical optics. As we saw in the introductory chapter, electron energy loss experiments (such as the one performed on plasmonic resonators) are efficiently described by this simple classical perspective [100]. Moreover, ray optical simulations appear to be extremely useful for microscopes alignment in exotic illumination modes [164], which proves the theoretical validity of this approach.
- A **wave optics** perspective, where an electron is represented by a wavefunction and its propagation is modeled by the Schrödinger equation. Such a representation is required as soon as an interferometric or phase-related effects need to be modeled such as holography experiments, aberration corrections or coherent image formation mechanisms.

These two perspectives are intimately connected as ray optics is a limiting theory of wave optics (through the eikonal approximation [165, 166]). This dual character is not without reminding light optics, where Fermat principle and Maxwell equations provide the same two representations [167]. In fact, there is a formal analogy between electron and light optics and several concepts of electron microscopy have been inspired from optics[1], e.g. beam shaping [169].

[1] And the opposite is also true; for example the holography is intially an electron optics concept [168].

One of the principal objectives of the present thesis is the development of EELS experiments using phase-shaped electron beams, with special emphasis on its application in plasmonics. This problem is tackled in detail in chapter 4. In order to model such an experiment, a wave theory of electron energy loss spectroscopy is naturally required. The goal of this chapter is to formulate such a theory. Before tackling this problem, let's first describe the major technical difficulties involved as well as the existing formalisms.

3.1.2 Difficulties: retardation effects, quantum description of the target

Working out such a theory is challenging because both quantum and relativistic effects need to be taken into account. An electron energy loss process can be roughly schematized by the diagram 3.2.

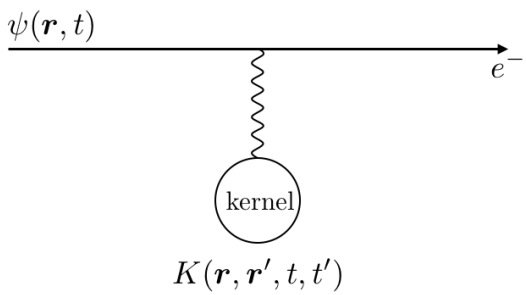

Figure 3.2: *Schematics showing a simple representation of an electron energy loss process: an electron of wavefunction $\psi(r, t)$ interacts with a system represented by a kernel $K(r, r', t, t')$ which contains all the information on the target.*

This diagram is basically made of two parts: the electron represented by the wavefunction $\psi(\boldsymbol{r}, t)$ and the target represented by the *interaction kernel* $K(\boldsymbol{r}, \boldsymbol{r}', t, t')$. Thus relativistic effects can emerge from [170]:

- **The large velocity ($c/v > 0.5$) of electrons in a TEM**. Indeed, as described in section B.0.0.1, beam acceleration voltages in TEM range from 30 to 300 kV which means that the Lorentz factor:
$$\gamma = \frac{1}{\sqrt{1 - v^2/c^2}} \tag{3.1}$$
varies from 1.059 to 1.587 [126]. Therefore, TEM electrons are relativistic which translate into a re-normalized mass, a contraction of the electron impact parameter [171] and the possible presence of Cherenkov losses.

- **The finite propagation time of the electromagnetic interaction**. Indeed, the interaction kernel essentially represents an electromagnetic interaction (providing the inclusion of e.g. screening effects, electronic polarization) which has a finite propagation speed c. When the length-scale L of the charge density fluctuations associated with an excitation of energy $\hbar\omega$ in the target become important $\omega L/c > 1$, one cannot neglect the retardation effects in the interaction anymore. As described in section 2.2.2.4, this situation typically occurs in plasmonics which leads to frequency red-shift, loss of spatial coherence or even mode splitting [172] (we will come back to this particular effect in section 5.4).

To these relativistic corrections, one needs to add a quantum description of both the electron and the target. Let's however stress two important points.

First, the quantum description of the target is strongly case-dependent. Indeed, as we saw in the introductory chapter, some phenomena (e.g. excitons) are intrinsically quantum while others

(e.g. localized surface plasmons in large nano-particles) are essentially classical. The strategy to overcome this diversity of nature is to employ Green functions which are general statistical quantities defined beyond the classical/quantum specificities, as we already emphasized in section 2.2.5.

In addition, let's stress that there are no "real" quantum effects in the conventional (S)TEM spectroscopy experiment in this work. For example, effects related to finite temporal length of electron wavepackets [15, 173, 117] or spin-related effects [174] play no role in our experiments. In other words, the wavefunctions encountered throughout this chapter do not represent quantum wavepackets but rather electron beams in a *steady-state illumination*, in a strictly anologue way to standard wave optics [167]. The quantum formalism is necessary in order to rigorously take into account the phase of the electrons and model interference effects. A corollary to the absence of spin-related effects is that a full quantum relativistic modeling of the electron beam is not required. Indeed, approaches to EELS or electron diffraction based on the Dirac equations have been developed [175, 176, 177, 178] and give results comparable to what the Schrödinger or the Klein-Gordon equations do [179, 180, 17, 181].

3.1.3 State of the art

Most of quantum relativistic theories for TEM electrons have been developed for diffraction and holography [175, 176, 177, 179, 180, 17] and only a few deal with electron energy loss spectroscopy [178, 181]. In this section, we will review the principal results and theories of the literature.

The most widespread theory of EELS for plasmon spectroscopy [100] is built upon a point-like description of electron microscopy as demonstrated in section 2.3.1.3. We recall that the most important result of this formalism is that the electron energy-loss probability Γ^{R} reads:

$$\Gamma^{\mathrm{R}}(\boldsymbol{r}_\perp,\omega) = \frac{4e^2}{\hbar}\mathrm{Im}\left\{-G_{zz}(\boldsymbol{r}_\perp,\boldsymbol{r}_\perp,q,-q,\omega)\right\} \tag{3.2}$$

where the superscript R indicates that the retardation effects are taken into account and $\overleftrightarrow{\boldsymbol{G}}$ is the electric Green dyadic[2] defined as [182, 19, 183]:

$$\boldsymbol{E}_{\mathrm{ind}}\left(\boldsymbol{r}',\omega\right) = -4\pi i\omega \int_{\mathbb{R}^3} d\boldsymbol{r}\ \overleftrightarrow{\boldsymbol{G}}\left(\boldsymbol{r}',\boldsymbol{r},\omega\right)\boldsymbol{j}_{\mathrm{ext}}\left(\boldsymbol{r},\omega\right) \tag{3.3}$$

In 1987, Echenique and collaborators proposed a quantum version of the quasistatic loss probability Γ^{QS} using a self-energy formalism [16]:

$$\frac{d\Gamma^{\mathrm{QS}}}{dt} = \frac{2e^2}{\hbar}\sum_f \iint d\boldsymbol{r}\, d\boldsymbol{r}'\psi_f(\boldsymbol{r})\psi_i^*(\boldsymbol{r})\mathrm{Im}\{-W(\boldsymbol{r},\boldsymbol{r}',\omega)\}\psi_f^*(\boldsymbol{r}')\psi_i(\boldsymbol{r}')\delta(\epsilon_f-\epsilon_i+\omega) \tag{3.4}$$

where the superscript QS indicates that the quasistatic approximation has been used, ψ_i and ψ_f are the initial and final states of the electron probe with respective energy $\hbar\epsilon_i$ and $\hbar\epsilon_f$. W is the so-called *screened interaction*[3] defined as:

$$\phi_{\mathrm{ind}}\left(\boldsymbol{r}',\omega\right) = \int_{\mathbb{R}^3} d\boldsymbol{r}\ W\left(\boldsymbol{r}',\boldsymbol{r},\omega\right)\mathfrak{n}_{\mathrm{ext}}\left(\boldsymbol{r},\omega\right) \tag{3.5}$$

where $\phi_{\mathrm{ind}}\left(\boldsymbol{r}',\omega\right)$ is the scalar potential induced at $\boldsymbol{r}'$ by a density of charges $\mathfrak{n}_{\mathrm{ext}}\left(\boldsymbol{r},\omega\right)$ located at $\boldsymbol{r}$. The quantity W contains all the quantum mechanical information about the excitations inside the target and is relevant to describe the valence as well as the core excitations. It can thus be applied both for low-loss and core-loss EELS. The formula (3.4) has been further employed to study quantal effects in valence EELS [184, 185, 144]. Later, García de Abajo re-derived it using

[2] Compared to the introductory chapter, we dropped the E superscript for brevity since there is no chance of confusion with the magnetic part.

[3] In practice, the screened interaction is the sum of two terms: the free space interaction and the term (3.5). In the rest of this thesis and following the denomination of [19], we will improperly denote the term (3.5) as the screened interaction.

a linear response theory and the Fermi golden rule [19]. However, this equation is derived in the quasi-static limit $k \to 0$, that is why the kernel corresponds to the Green function for the scalar potential W only. Still using the linear response theory, García de Abajo proposed[4] an extension of (3.4) to the retarded regime [19]:

$$\frac{d\Gamma^{\mathrm{R}}}{dt} = \frac{8\pi\hbar e^2}{m^2} \sum_f \iint d\boldsymbol{r}d\boldsymbol{r'}\psi_f(\boldsymbol{r})\boldsymbol{\nabla}[\psi_i^*(\boldsymbol{r})]\mathrm{Im}\{-\overleftrightarrow{\boldsymbol{G}}(\boldsymbol{r},\boldsymbol{r}',\omega)\}\psi_f^*(\boldsymbol{r'})\boldsymbol{\nabla}'[\psi_i(\boldsymbol{r'})]\delta(\epsilon_f-\epsilon_i+\omega) \quad (3.6)$$

This equation has been used in several works [186, 31, 187] in order to calculate the dichroism in the interaction between a vortex electron state and a (geometrically) chiral plasmonic nano-particle. Although the formula (3.6) is remarkably elegant and intuitive, it only gives the loss probability but provides no information on the propagation of the wavefunction in the microscope. However, a proper description of a phase-shaped EELS experiment requires the precise description of the illumination and detection systems. Moreover, information on the coherence of the electron beam, which plays a crucial role in holography, is not explicitly present in the latter formalism. Equation (3.6) is therefore not sufficient to model such an experiment.

In order to go further, a fundamental object to be considered is the density matrix operator which in a basis $\{|\Psi_n\rangle\}$ reads:

$$\hat{\varrho} = \sum_n p_n \left|\psi_n\right\rangle \left\langle\psi_n\right| \quad (3.7)$$

where p_n are the occupation probabilities associated to each vector n. Inserting the completeness relation $\sum_r |r\rangle\langle r| = \mathbb{1}$, we obtain the fundamental tool for the description of wave optical experiments: the (energy-dependent) density matrix. It is defined as [18, 188]:

$$\varrho(\boldsymbol{r},\boldsymbol{r'}) = \sum_n p_n\psi_n(\boldsymbol{r})\psi_n^*(\boldsymbol{r'}) \quad (3.8)$$

This quantity is particularly rich in terms of information as $I = \varrho(\boldsymbol{r},\boldsymbol{r})$ gives the intensity at position $\boldsymbol{r}$ in the image plane. Even more importantly, the out-of-diagonal elements measure the *mutual coherence* of the electron field between positions $\boldsymbol{r}$ and $\boldsymbol{r'}$ [189]. In other words, non-zero out-of-diagonal terms mean that electron interferences can be produced.
In 1993, Dudarev, Peng and Whelan [17] demonstrated[5] that, in the quasi-static limit, the inelastic scattering of high energy electrons by a polarizable material can be described by the *kinetic equation*:

$$\varrho_f(\boldsymbol{r},\boldsymbol{r'},E) = (4\pi)^2e^4 \int d\boldsymbol{r}_1d\boldsymbol{r}_1'\, U_0(\boldsymbol{r},\boldsymbol{r}_1,E)\, U_0^\dagger(\boldsymbol{r'},\boldsymbol{r}_1',E)\mathscr{F}_{\boldsymbol{k},-\boldsymbol{k'}}\left(\frac{S(\boldsymbol{k},\boldsymbol{k'},\omega)}{k^2k'^2}\right)\varrho_i(\boldsymbol{r}_1,\boldsymbol{r}_1',E+\hbar\omega) \quad (3.9)$$

where $\mathscr{F}$ denotes the Fourier transform, ϱ_i and ϱ_f are the density matrices of the electron probe before and after the interaction, U_0 is the free-space electron propagator and $S(\boldsymbol{k},\boldsymbol{k'},\omega)$ is the so-called *mixed dynamic form factor* (MDFF,[190]) defined as :

$$\boxed{S(\boldsymbol{k},\boldsymbol{k'},\omega) = \frac{1}{\hbar}\sum_n \langle 0|\mathfrak{n}(\boldsymbol{k})|n\rangle\langle n|\mathfrak{n}^\dagger(\boldsymbol{k'})|0\rangle\,\delta(\omega_0-\omega_n+\omega)} \quad (3.10)$$

where $\boldsymbol{k}$ is a wave-vector, $\mathfrak{n}$ is the electron density operator and $\{|n\rangle, \hbar\omega_n\}$ is an eigenbasis of the target electron density where 0 indexes the ground state. The MDFF contains all the information on the correlations in the electronic charge density of the scatterer [189]. Remarkably, equation (3.9) shows that these correlations are imprinted in the mutual coherence of the beam during the scattering process. It leads to a fundamental principle of electron holography: generating interferences in order to trace back to the electronic correlations in the target. It would be rather seducing to use such a formalism in the case of nano-optics and e.g. interpret EELS interference effects on

[4] To the best of our knowledge, there is no published demonstration of this formula.
[5] The different hypothesis leading to this formula will be reviewed in details in the rest of this chapter.

surface plasmons in terms of electric field correlations measurements. The MDFF is particularly adapted to model core-loss spectroscopy as the measured phenomena appear to be quasi-static. However, it gives an incomplete picture of plasmonics where *retardation effects dramatically constrain the coherence properties of the field.*

3.1.4 Purpose of this chapter, methodology

The goal of this chapter is to extend equation (3.9) to the retarded regime and therefore generalize the formula of Dudarev and collaborators. From the remarkable work of García de Abajo, it can already be inferred that the retarded counterpart of the MDFF has to be connected to the CDOS. Nevertheless, we aim at giving a comprehensive and rigorous demonstration from most basic results of nano-optics and electron spectroscopy. Finally, this chapter is also an opportunity to connect all the works quoted above together and provide an overview of these formalisms as well as the different levels of approximation they lay on.

The chapter is organized as the diagram 3.2 suggests:

- In section 3.2, we introduce the various conventions and notations used throughout this chapter. We also recall some results on free-space photon propagator and their expression in different gauges.

- In section 3.3 we focus on the interaction kernel. For completeness and pedagogy, we first re-derive the expression for the MDFF and connect it to the screened potential. This way, we draw a parallel between the formalism of nano-optics with the one of core-loss spectroscopy. We then focus on the retarded case and show that the interaction needs to be modeled in terms of EM field correlations and photons propagators rather than electronic correlations and polarizability. Using a pedestrian approach to quantum field theory (QFT), we calculate the exact photon propagator in the presence of a polarizable material. In a complete analogy to what has been done with the MDFF, we then connect this photonic kernel to the charge and current density correlation functions of the scatterer.

- In section 3.4 we then consider in details the electron probe part. For reasons exposed earlier, we model the electron propagation using the Schrödinger equation with a semirelativistic correction i.e. mass renormalization [181]. Following the seminal demonstration of Dudarev and collaborators [17], we employ a Dyson development in terms of arbitrary (but weak) interaction potential, the Wick theorem and detailed approximations in order to calculate the electron propagation equation. We then consider separately the quasi-static and the retarded interaction which respectively give the kinetic equation of Dudarev and the *retarded kinetic equation* that we aim to demonstrate.

- Section 3.5 is dedicated to the contextualization of our developments and proposal of different applications. Particularly, by taking the appropriate limits, we demonstrate that our equations encompass all the results detailed above.

3.2 Preliminary remarks: conventions, Green functions, gauge fixing

3.2.1 Conventions and notations

We employ Gaussian units throughout this thesis. The 3-vectors are labeled by roman letters and written in standard font like $\boldsymbol{x} \equiv x^a = (x^1, x^2, x^3)$. The 4-vectors are labeled by greek letters and written in roman font like $\mathrm{x}^\mu = (\mathrm{x}^0, \mathrm{x}^1, \mathrm{x}^2, \mathrm{x}^3) = (ct, \boldsymbol{x})$. The metric $\mathrm{g}_{\mu,\nu}$ for the Minkowski space

$\mathbb{M}^4$ is chosen with the signature $(+,-,-,-)$ i.e. :

$$\mathrm{g}_{\mu,\nu} = \mathrm{g}^{\mu,\nu} = \begin{pmatrix} 1 & 0 & 0 & 0 \\ 0 & -1 & 0 & 0 \\ 0 & 0 & -1 & 0 \\ 0 & 0 & 0 & -1 \end{pmatrix}$$

Under this convention, the raising or lowering of a spatial index changes the sign of a tensor; raising or lowering the temporal index leaves the sign unchanged. Unless otherwise specified, we will always use the implicit Einstein summation on repeated indices:

$$\mathrm{x}^\mu \mathrm{x}'_\mu \equiv \sum_{\mu,\nu=0}^{4} \mathrm{g}^{\mu,\nu} \mathrm{x}^\mu \mathrm{x}'_\nu = c^2 t t' - \boldsymbol{x}.\boldsymbol{x}' \tag{3.11}$$

The Fourier transform in $\mathbb{M}^4$ is defined as:

$$\begin{cases} f(\mathrm{x}) = \displaystyle\int_{\mathbb{M}^4} \frac{d^4\mathrm{k}}{(2\pi)^4} f(\mathrm{k})\, e^{i\mathrm{k}_\mu \mathrm{x}^\mu} & (3.12a) \\ f(\mathrm{k}) = \displaystyle\int_{\mathbb{M}^4} d^4\mathrm{x}\, f(\mathrm{x})\, e^{-i\mathrm{k}_\mu \mathrm{x}^\mu} & (3.12b) \end{cases}$$

where the 4-wavevector is defined as $k^\mu = (\omega/c, \boldsymbol{k})$. The latter definition is naturally in agreement with the $\mathbb{R}^3$ convention (2.6). We also define the 4-gradient as:

$$\partial_\mu = \frac{\partial}{\partial \mathrm{x}^\mu} = \left(\frac{1}{c}\frac{\partial}{\partial t}, \boldsymbol{\nabla}\right) \tag{3.13}$$

We can therefore define the 4-impulsion operator:

$$p_\mu = i\hbar\partial_\mu = \left(\frac{i\hbar}{c}\frac{\partial}{\partial t}, i\hbar\boldsymbol{\nabla}\right) \tag{3.14}$$

and in presence of an EM field, one needs to perform the minimal substitution $p_\mu \to p_\mu - qA_\mu$, q being the charge of the particle. Moreover, the 4-current associated with a wavefunction ψ reads:

$$j_\mu = i\left(\psi^*\partial_\mu\psi - \psi\partial_\mu\psi^*\right) \tag{3.15}$$

3.2.2 Correlators and Green functions

The time ordering operator $\mathcal{T}$ between two fields $A(\mathrm{x})$ and $B(\mathrm{y})$ is defined as:

$$\mathcal{T}\{A(\boldsymbol{r},t)B(\boldsymbol{r}',t')\} = \theta(t-t')A(\boldsymbol{r},t)B(\boldsymbol{r}',t') \pm \theta(t'-t)B(\boldsymbol{r}',t')A(\boldsymbol{r},t) \tag{3.16}$$

where a $+$ sign applies for bosons and a $-$ sign for fermions. For a scalar field A, one can also define three different Green functions:

- The retarded Green function:

$$G^{\mathrm{R}}(\boldsymbol{r},\boldsymbol{r}',t,t') = -\frac{i}{\hbar}\theta(t-t')\left\langle[A(\boldsymbol{r},t),A(\boldsymbol{r}',t')]_\pm\right\rangle_0 \tag{3.17}$$

- The advanced Green function:

$$G^{\mathrm{A}}(\boldsymbol{r},\boldsymbol{r}',t,t') = -\frac{i}{\hbar}\theta(t'-t)\left\langle[A(\boldsymbol{r},t),A(\boldsymbol{r}',t')]_\pm\right\rangle_0 \tag{3.18}$$

- The causal Green function:

$$G^{\mathrm{C}}(\boldsymbol{r},\boldsymbol{r}',t,t') = -\frac{i}{\hbar}\left\langle\mathcal{T}\{A(\boldsymbol{r},t)A(\boldsymbol{r}',t')\}\right\rangle_0 \tag{3.19}$$

In each case, $\langle . \rangle$ represents the statistical average value at thermal equilibrium and $[,]_\pm$ represents the fermion anti-correlator (resp. boson correlator).

3.2.3 Lagrangian form of the Maxwell equations

The four-potential defined as $\mathrm{A}^\nu = (\phi/c, \boldsymbol{A})$ and the four-current defined as $\mathrm{J}^\nu = (c\rho, \boldsymbol{j})$ are connected by the equation of motion for the EM field:

$$\partial^\nu \partial_\mu \mathrm{A}^\mu - \partial^\mu \partial_\mu \mathrm{A}^\nu = -4\pi \mathrm{J}^\nu \tag{3.20}$$

where A_μ is defined up to a scalar gauge function Λ:

$$\mathrm{A}_\mu(\mathrm{x}) \longrightarrow \mathrm{A}_\mu(\mathrm{x}) + \partial_\mu \Lambda(\mathrm{x}) \tag{3.21}$$

The anti-symmetric Faraday tensor $F^{\mu\nu}$ is defined as:

$$\mathrm{F}^{\mu\nu} = \partial^\mu \mathrm{A}^\nu + \partial^\nu \mathrm{A}^\mu \tag{3.22}$$

which explicitly reads:

$$F^{\mu\nu} = \begin{pmatrix} 0 & -E_x & -E_y & -E_z \\ E_x & 0 & -B_z & B_y \\ E_y & B_z & 0 & -B_x \\ E_z & -B_y & B_x & 0 \end{pmatrix} \tag{3.23}$$

For any anti-symmetric tensor T, we also introduce the *Hodge dual* as:

$$^\star T^{\alpha\beta} = \frac{1}{2} \epsilon^{\alpha\beta\mu\nu} T_{\mu\nu} \tag{3.24}$$

where $\epsilon^{\alpha\beta\mu\nu}$ is the Levi-Civita pseudotensor defined as:

$$\epsilon^{\alpha\beta\mu\nu} = \begin{cases} +1, & \text{if } (\alpha,\beta,\mu,\nu) \text{ is an even permutation of } (0,1,2,3) \\ -1, & \text{if } (\alpha,\beta,\mu,\nu) \text{ is an odd permutation of } (0,1,2,3) \\ 0, & \text{otherwise} \end{cases} \tag{3.25}$$

The Maxwell equations (2.1) then read:

$$\begin{cases} \partial_\mu \mathrm{F}^{\mu\nu} = \mathrm{J}^\nu & (3.26\text{a}) \\ \partial_\mu (^\star \mathrm{F}^{\mu\nu}) = 0 & (3.26\text{b}) \end{cases}$$

The last equation can be derived from the Lagrange equation applied to the *standard* EM Lagrangian density defined as $\mathcal{L}$:

$$\mathcal{L} = -\frac{1}{4} \left(\partial_\alpha \mathrm{A}_\beta - \partial_\beta \mathrm{A}_\alpha\right) \left(\partial^\alpha \mathrm{A}^\beta - \partial^\beta \mathrm{A}^\alpha\right) - \mathrm{J}_\alpha \mathrm{A}^\alpha \tag{3.27}$$

The first term concerns only the EM field while the second is the field-source interaction.

3.2.4 Gauge fixing and vacuum photon propagator

The Green function of equation (3.20) is the *vacuum photon propagator* D^μ_ν defined by:

$$\mathrm{A}^\nu(\mathrm{x}') = \int d\mathrm{x}\, \mathrm{D}^\mu_\nu(\mathrm{x}', \mathrm{x}) \mathrm{J}^\nu(\mathrm{x}) \tag{3.28}$$

In order to calculate D^μ_ν one needs to invert the Kernel in (3.20). Depending on the gauge, this task can require involved mathematical techniques due to the possible presence of singularities. In nano-optics, principally three gauges for the electromagnetic field [191] are encountered in the literature: the Coulomb gauge, the (partial) Lorenz gauge and the temporal (or Weyl) gauge - each of them having different specific interests. We will therefore give D^μ_ν in these cases [192, 193] only, but keeping in mind that this can be done in arbitrary gauges:

- **The Coulomb gauge** corresponds to the condition:

$$\partial_i \mathrm{A}^i = 0 \tag{3.29}$$

It is of particular interest in standard quantum electrodynamics as it enables a simple quantification of the potentials and leaves the Coulomb interaction in its classical non-retarded form. In the Coulomb gauge the photon propagator reads [192, 193]:

$$\boxed{\begin{cases} \mathrm{D}^{ij} = \dfrac{4\pi}{k^2 - \frac{\omega^2}{c^2}} \left(\delta^{ij} + \dfrac{k^i k^j}{k^2} \right) & (3.30a) \\ \mathrm{D}^{00} = -\dfrac{4\pi}{k^2} & (3.30b) \\ \mathrm{D}^{i0} = 0 & (3.30c) \end{cases}}$$

- **The temporal gauge** corresponds to the condition:

$$\mathrm{A}^0 = 0 \tag{3.31}$$

It is particularly interesting because it drastically facilitates the calculation of the conductivity in linear response theory. In the temporal gauge the photon propagator reads [192, 193]:

$$\boxed{\begin{cases} \mathrm{D}^{ij} = \dfrac{4\pi}{k^2 - \frac{\omega^2}{c^2}} \left(\delta^{ij} + \dfrac{k^i k^j}{\omega^2/c^2} \right) & (3.32a) \\ \mathrm{D}^{00} = 0 & (3.32b) \\ \mathrm{D}^{i0} = 0 & (3.32c) \end{cases}}$$

- **The Lorenz gauge** corresponds to the condition:

$$\partial_\mu \mathrm{A}^\mu = 0 \tag{3.33}$$

Its main interest is to decouple the motion equation for the four components of the potential. Indeed, in the Lorenz gauge, the propagator reads [193]:

$$\boxed{\mathrm{D}^{\mu\nu} = \frac{4\pi g^{\mu\nu}}{k^2 - \frac{\omega^2}{c^2}}} \tag{3.34}$$

3.3 Propagators for the electromagnetic field in presence of a polarizable medium

In this section, we focus on the propagator for the EM field in the presence of a polarizable medium e.g. a metallic nano-particle. For completeness, we first consider the quasi-static case and show that the screened interaction can be connected to the MDFF (see section 3.3.2). This way, we connect the standard formalism of EELS to optical quantities.

In section 3.3.2, using a Dyson development, we calculate the exact photon propagator in the presence of a polarizable material. In a complete analogy to what has been done with the MDFF, we then connect this photonic kernel to the charge and current density correlation functions of the scatterer.

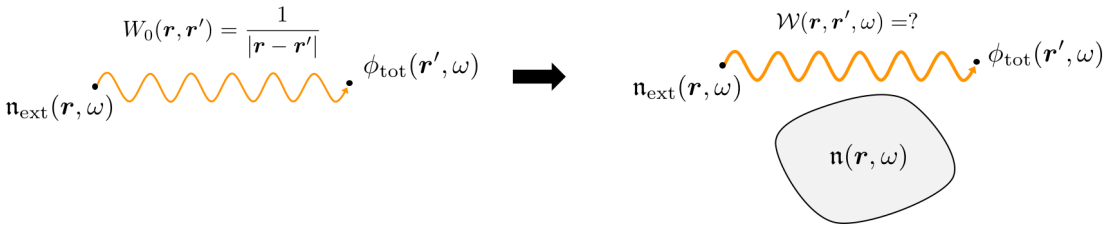

Figure 3.3: *Schematics illustrating the problem tackled in this section. The Green function for the electrostatic potential in vacuum is simply the Coulomb propagator. In the presence of a polarizable medium (e.g. a metallic nanoparticle), this Green function needs to be modified.*

3.3.1 Quasistatic approach: modification of the Coulomb propagator, electron density correlation function

We first consider the quasi-static limit $c \to \infty$. In this situation, as we already showed in section 2.5, the calculation of the EM field propagation simply reduces to the resolution of the Poisson equation. Thus, as illustrated on figure 3.3, we simply need to consider the scalar potential and the electron charge density of the nano-particle.
In vacuum the potential ϕ_{ind} induced in $\boldsymbol{r}'$ by an external charge ρ_{ext} in $\boldsymbol{r}$ is simply given by the Coulomb law. In other terms, the free-space EM propagator is simply given by $W_0(\boldsymbol{r},\boldsymbol{r}',\omega) = 1/|\boldsymbol{r}-\boldsymbol{r}'|$. This law needs to be modified is the presence of a dielectric medium in order to take into account e.g. the screening effect in the material. Particularly we expect the new propagator $\mathcal{W}$ to be energy-dependent as, contrary to the vacuum, the nano-particle can be dispersive.

In this section, we will derive the new propagator $\mathcal{W}$ and connect it to the mixed dynamic form factor.

3.3.1.1 Linear response electrostatic susceptibility

In the following, we define the electronic charge density operator $\mathfrak{n}$ for the nanoparticle as $\mathfrak{n}(\boldsymbol{r}) = e\hat{n}(\boldsymbol{r})$ where $\hat{n}$ is the particle number operator for the electrons. We first need to calculate the response of the nanoparticle of electronic density $\mathfrak{n}(\boldsymbol{r},t)$ to an external perturbation $\phi_{\text{ext}}(\boldsymbol{r},t)$. The electronic charge $\delta\langle\mathfrak{n}(\boldsymbol{r},t)\rangle \equiv \mathfrak{n}_{\text{ind}}(\boldsymbol{r},t)$ induced on the target by this electrostatic field can be calculated using the Kubo formula [96, 30]:

$$\begin{aligned}\delta\langle\mathfrak{n}(\boldsymbol{r},t)\rangle &= \langle\mathfrak{n}(\boldsymbol{r},t)\rangle - \langle\mathfrak{n}(\boldsymbol{r},t)\rangle_0 && (3.35)\\ &= -\frac{i}{\hbar}\int_{t_0}^{\infty} dt'\ \theta(t-t')\ \langle[\mathfrak{n}(\boldsymbol{r},t), H(t')]\rangle_0\ e^{-\eta(t-t')} && (3.36)\end{aligned}$$

where $\eta \to 0^+$, t_0 the starting time of the interaction and $H(t)$ is the perturbation Hamiltonian given by:

$$H(t) = \int_{\mathbb{R}^3} d\boldsymbol{r}'\ \mathfrak{n}(\boldsymbol{r}',t)\phi_{\text{ext}}(\boldsymbol{r}',t) \tag{3.37}$$

Therefore, one can write:

$$\begin{aligned}\mathfrak{n}_{\text{ind}}(\boldsymbol{r},t) &= \int_{t_0=0}^{\infty} dt'\Big\{-\frac{i}{\hbar}\theta(t-t')\,\langle[\mathfrak{n}(\boldsymbol{r},t), \int_{\mathbb{R}^3} d\boldsymbol{r}'\mathfrak{n}(\boldsymbol{r}',t')\phi_{\text{ext}}(\boldsymbol{r}',t')]\rangle_0\Big\}\ e^{-\eta(t-t')}\\ &= \int_0^{\infty} dt' \int_{\mathbb{R}^3} d\boldsymbol{r}'\Big\{-\frac{i}{\hbar}\theta(t-t')\,\langle[\mathfrak{n}(\boldsymbol{r},t), \mathfrak{n}(\boldsymbol{r}',t')]\rangle_0\Big\}\phi_{\text{ext}}(\boldsymbol{r}',t')e^{-\eta(t-t')}\end{aligned} \tag{3.38}$$

Besides, the linear-response electric susceptibility is defined as:

$$\mathfrak{n}_{\text{ind}}(\boldsymbol{r},t) = \int d\boldsymbol{r}' \int dt'\ \chi(\boldsymbol{r},\boldsymbol{r}',t,t')\phi_{\text{ext}}(\boldsymbol{r}',t') \tag{3.39}$$

Comparing equations (3.38) and (3.39), one can deduce the following expression for χ:

$$\boxed{\chi(\boldsymbol{r},\boldsymbol{r}',t,t') = -\frac{i}{\hbar}\theta(t-t')\left\langle[\mathfrak{n}(\boldsymbol{r},t),\mathfrak{n}(\boldsymbol{r}',t')]\right\rangle_0} \tag{3.40}$$

We retrieve the well-known linear response susceptibility at thermal equilibrium in the real space. In the spectral domain, the electrostatic susceptibility reads (see appendix D for the detailed derivation):

$$\mathrm{Im}\left\{\chi(\boldsymbol{r},\boldsymbol{r}',\omega)\right\} = -\frac{\pi}{Z\hbar}\sum_{n,n'}\langle n|\,\mathfrak{n}(\boldsymbol{r})\,|n'\rangle\,\langle n'|\,\mathfrak{n}(\boldsymbol{r}')\,|n\rangle\,e^{-\beta\hbar\omega_n}\left(1+e^{-\beta\hbar\omega}\right)\delta\left(\omega+\omega_n-\omega_{n'}\right) \tag{3.41}$$

The latter equation is valid for any temperature as soon as we are at thermal equilibrium. We now take the limit of the latter expression for null temperature $T=0$. This is fully justified when the energy of the electronic excitations are significantly greater than the thermal energy at room temperature $k_{\mathrm{B}}T \approx 25$ meV. This will be the case in the following developments because e.g. the energy of SPs is typically of 1 eV. In equation (D.13), we can then replace $\frac{1}{Z}\sum_n \langle n|.|n\rangle \exp(-\beta\hbar\omega_n) \to \langle 0|.|0\rangle$ and $\beta \to 0$ which gives:

$$\boxed{\mathrm{Im}\left\{-\chi(\boldsymbol{r},\boldsymbol{r}',\omega)\right\} = \frac{2\pi}{\hbar}\sum_n \langle 0|\,\mathfrak{n}(\boldsymbol{r})\,|n\rangle\,\langle n|\,\mathfrak{n}(\boldsymbol{r}')\,|0\rangle\,\delta(\omega+\omega_n-\omega_0)} \tag{3.42}$$

Therefore we see that the latter corresponds to the Fourier transform of the MDFF (3.10).

3.3.1.2 Dyson equation for the electrostatic propagator, screened interaction

Now, we are in position to calculate the exact electrostatic propagator $\mathcal{W}$ which is formally defined such that:

$$\phi_{\mathrm{tot}}(\boldsymbol{r},t) = \int d\boldsymbol{r}' \int dt'\ \mathcal{W}(\boldsymbol{r},\boldsymbol{r}',t,t')\rho_{\mathrm{ext}}(\boldsymbol{r}',t') \tag{3.43}$$

In order to solve this equation, we use a Dyson development [194]:

$$\mathcal{W}(\boldsymbol{r},\boldsymbol{r}',t,t') = W_0(\boldsymbol{r},\boldsymbol{r}',t,t') + \int d\boldsymbol{r}_1 d\boldsymbol{r}_2 \int dt_1 dt_2\ W_0(\boldsymbol{r},\boldsymbol{r}_1,t,t_1)\chi(\boldsymbol{r}_1,\boldsymbol{r}_2,t_1,t_2)\mathcal{W}(\boldsymbol{r}_2,\boldsymbol{r}',t_2,t') \tag{3.44}$$

which in compact notation (the overline indicates the integrated variable) reads:

$$\mathcal{W}(a,b) = W_0(a,b) + W_0(a,\overline{1})\chi(\overline{1},\overline{2})\mathcal{W}(\overline{2},b) \tag{3.45}$$

One can then expand the series and write:

$$\mathcal{W}(a,b) = W_0(a,b) + W_0(a,\overline{1})\chi(\overline{1},\overline{2})W_0(\overline{2},b) + W_0(a,\overline{1})\chi(\overline{1},\overline{2})W_0(\overline{2},\overline{3})\chi(\overline{3},\overline{4})W_0(\overline{4},b) + \dots \tag{3.46}$$

This development basically means that the propagation of the electrostatic potential from position a to position b can be decomposed as an infinite sum of alternating free-space and screened Coulomb propagation. The summation on all the intermediate positions indeed enables us to take into account all the propagation processes. We schematically present on figure 3.4 the first terms of the latter decomposition.
We then neglect the second order and higher terms which leads to the following expression for the electrostatic propagator:

$$\mathcal{W}(a,b) = W_0(a,b) + W_0(a,\overline{1})\chi(\overline{1},\overline{2})W_0(\overline{2},b) \tag{3.47}$$

It corresponds to the so-called *Born approximation* which is valid for weak fields. The second term is usually called the screened interaction W [19] and reads, in the spectral domain:

$$\boxed{W(\boldsymbol{r},\boldsymbol{r}',\omega) = \int d\boldsymbol{r}_1 \int d\boldsymbol{r}_2\ \frac{\chi(\boldsymbol{r}_1,\boldsymbol{r}_2,\omega)}{|\boldsymbol{r}-\boldsymbol{r}_1|\,|\boldsymbol{r}'-\boldsymbol{r}_2|}} \tag{3.48}$$

where we used the time-translation invariance of W_0 and χ to simply express the Fourier transform.

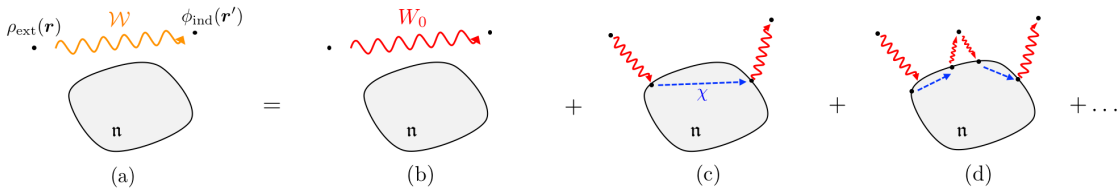

Figure 3.4: *Diagrams representing the three first terms in the decomposition of (a) the exact electrostatic propagator: (b) the free-space propagator and (c-d) the two first screened propagators. The red lines correspond to Coulomb (free-space) propagators while blue lines correspond to χ i.e. polarization in the medium.*

3.3.1.3 Connection between the mixed dynamic form factor and the screened interaction

We just saw that the screened potential corresponds to the linear response susceptibility convoluted with two Coulomb propagators, as equation (3.48) can be rewritten:

$$W(\boldsymbol{r},\boldsymbol{r}',\omega) = \frac{1}{r} * \chi(\boldsymbol{r},\boldsymbol{r}',\omega) * \frac{1}{r'} \tag{3.49}$$

where $*$ denotes the convolution product. The latter can be Fourier transformed with respect to $\boldsymbol{r}$ and $\boldsymbol{r}'$ which leads to:

$$W(\boldsymbol{k},-\boldsymbol{k}',\omega) = (4\pi)^2 \frac{\chi(\boldsymbol{k},-\boldsymbol{k}',\omega)}{k^2 k'^2} \tag{3.50}$$

We used the identity [195] $\mathscr{F}_k\left\{\frac{1}{r}\right\} = \frac{4\pi}{k^2}$ where $\mathscr{F}$ denotes the Fourier transform. Nevertheless, in the quasistatic regime, the screened potential and the electric Green dyadic are related by [10]:

$$\overleftrightarrow{\boldsymbol{G}}(\boldsymbol{r},\boldsymbol{r}',\omega) = \frac{1}{4\pi\omega^2}\boldsymbol{\nabla}\boldsymbol{\nabla}' W(\boldsymbol{r},\boldsymbol{r}',\omega) \tag{3.51}$$

Moreover, Fourier transforming the latter gives:

$$\overleftrightarrow{\boldsymbol{G}}(\boldsymbol{k},-\boldsymbol{k}',\omega) = \frac{1}{4\pi\omega^2}\boldsymbol{k}\boldsymbol{k}' W(\boldsymbol{k},-\boldsymbol{k}',\omega) \tag{3.52}$$

Therefore, using (3.50) we get:

$$\overleftrightarrow{\boldsymbol{G}}(\boldsymbol{k},-\boldsymbol{k}',\omega) = \frac{4\pi}{\omega^2}\frac{\boldsymbol{k}}{k^2}\frac{-\boldsymbol{k}'}{k'^2}\,\chi(\boldsymbol{k},-\boldsymbol{k}',\omega) \tag{3.53}$$

We also need to calculate the imaginary part of the screened interaction as it is involved in the definition of the loss probability (3.4). Therefore, taking the imaginary part of (3.48) and using equation (3.42), we get:

$$\mathrm{Im}\{-W(\boldsymbol{r},\boldsymbol{r}',\omega)\} = 2\pi \int d\boldsymbol{r}_1 \int d\boldsymbol{r}_2 \, \frac{\sum_n \langle 0|\,\rho(\boldsymbol{r}_1)\,|n\rangle\,\langle n|\,\rho(\boldsymbol{r}_2)\,|0\rangle}{|\boldsymbol{r}-\boldsymbol{r}_1|\,|\boldsymbol{r}'-\boldsymbol{r}_2|}\delta(\hbar\omega + \hbar\omega_n - \hbar\omega_0) \tag{3.54}$$

Finally using the latter equation combined together with equations (3.48) and (3.10), we get:

$$\boxed{\mathrm{Im}\{-W(\boldsymbol{r},\boldsymbol{r}',\omega)\} = \frac{2}{\pi}\mathscr{F}_{\boldsymbol{k},-\boldsymbol{k}'}\left[\frac{S(\boldsymbol{k},-\boldsymbol{k}',\omega)}{k^2 k'^2}\right]} \tag{3.55}$$

A quick look to the latter formula clearly indicates that, as expected, the kernel of equations (3.4) and (3.9) are the same. Depending on the situation investigated, each of these kernels can be interchangeably used:

- When ab initio calculations are required (typically in the case of core-loss spectroscopy), one will preferably use the MDFF as it explicitly displays the quantum mechanical charge density correlations.

- When classical photonic systems are investigated, one will preferably use the screened interaction as it can be simply calculated by e.g. boundary element method.

Finally, by using the definition of the CDOS (2.57) together with (3.53), we obtain:

$$\overleftrightarrow{\boldsymbol{\rho}}(\boldsymbol{r},\boldsymbol{r}',\omega) = \frac{4\omega}{\pi^2}\mathscr{F}_{\boldsymbol{k},-\boldsymbol{k}'}\left[\frac{\boldsymbol{k}\boldsymbol{k}'\,S(\boldsymbol{k},-\boldsymbol{k}',\omega)}{k^2k'^2}\right] \tag{3.56}$$

This equation shows that, **in the quasi-static limit, the CDOS and the EMLDOS are respectively given by the MDFF and the dynamic form factor** (DFF,[190]). **In other words, in this limit, the electric field correlations (encoded in the CDOS) simply reproduce the electronic charge correlations in the target (encoded in the MDFF).** This result is of course expected as, in the quasi-static limit, the electric field and the charge density are simply related through:

$$\boldsymbol{E}(\boldsymbol{r},t) = -\boldsymbol{\nabla}\int d\boldsymbol{r}'dt\; W_0(\boldsymbol{r},\boldsymbol{r}',t,t')\rho(\boldsymbol{r}',t') \tag{3.57}$$

Although intuitive, equations (3.55) and (3.56) have, to the best of our knowledge, never been derived. It enables to put on the same level the MDFF formalism for the electronic correlations [18, 189, 196] and the CDOS formalism for the photonic correlations [95, 197, 104].

3.3.2 Retarded approach: Photon propagator and electron four-current correlation function

We now turn to the retarded case where both the scalar ϕ and the vector potential $\boldsymbol{A}$ need to be considered. In his wonderful review [19], García de Abajo suggested to use the Kubo formalism for the current density to derive a retarded form of the latter equations. However, we could not find such a demonstration in the literature; therefore, in this section, we will follow this suggestion and derive a retarded version of the linear response formalism established in the last section.

The main difficulty in the retarded regime is the choice of the gauge. The developments found in the literature use different choices of gauge depending on the problem, so that a straightforward application is not possible. Some gauge choices are particularly convenient to calculate the EM field in vacuum e.g. the Coulomb gauge. However, these choices may, on the other hand, harden the calculation of the response function of the material. In order to avoid this difficulty while keeping a compact formalism, we will carry, when necessary, the calculation with four-vectors.

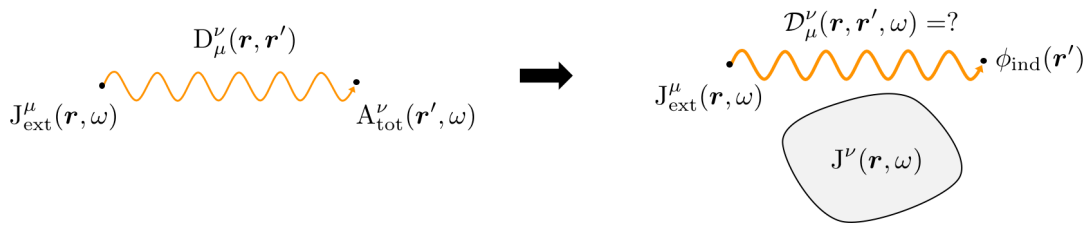

Figure 3.5: *Schematics illustrating the problem tackled in this section. The Green function for the electromagnetic field in vacuum is simply the photon propagator which expression depends on the gauge choice. In the presence of a polarizable medium (e.g. a metallic nanoparticle), this Green function needs to be modified.*

In vacuum, the 4-current J^{ν}_{ext} in x generates a 4-potential A^{μ}_{ind} in x′ which are related by the vacuum photon propagator $\mathrm{D}^{\mu}_{\nu}(\mathrm{x}',\mathrm{x})$, see equation (3.28). In the same way as in the quasi-static regime, the presence of a polarizable material will modify the EM propagator. The goal of this section is therefore to calculate the exact photon propagator $\mathcal{D}^{\nu}_{\mu}$ in the presence of the nano-particle

as illustrated on figure 3.5. However, contrary to the quasi-static case, we need to take into account both the induced *charge and current* densities in the medium which are compactly represented by the 4-current density J^μ.

3.3.2.1 Linear response electromagnetic susceptibility

The main interest of the previous quasi-static developments is that, now, the retarded case can be straightforwardly treated by analogy. Particularly, the 4-current $\delta\langle \mathrm{J}^\nu(\boldsymbol{r},t)\rangle$ induced in the medium by an external perturbation $\mathrm{A}^\nu_{\mathrm{ext}}$ is given by the Kubo formula:

$$\begin{aligned}\delta\langle \mathrm{J}^\nu(\boldsymbol{r},t)\rangle &= \langle \mathrm{J}^\nu(\boldsymbol{r},t)\rangle - \langle \mathrm{J}^\nu(\boldsymbol{r},t)\rangle_0 && (3.58)\\ &= -\frac{i}{\hbar}\int_{t_0}^{\infty} dt'\ \theta(t-t')\ \langle[\mathrm{J}^\nu(\boldsymbol{r},t), H(t')]\rangle_0\ e^{-\eta(t-t')} && (3.59)\end{aligned}$$

where the perturbation Hamiltonian is given by:

$$H(t') = \int d\boldsymbol{r}'\mathrm{J}^\mu(\boldsymbol{r}',t')\mathrm{A}_\mu(\boldsymbol{r}',t') \tag{3.60}$$

Substituting the latter in the former, we get:

$$\mathrm{J}^\nu_{\mathrm{ind}}(\boldsymbol{r},t) = -\frac{i}{\hbar}\theta(t-t')\int dt'\int d\boldsymbol{r}'\ \big\langle\big[\mathrm{J}^\nu(\boldsymbol{r},t), \mathrm{J}_\mu(\boldsymbol{r}',t')\big]\big\rangle_0 \mathrm{A}^{\mathrm{ext}}_\mu(\boldsymbol{r}',t') \tag{3.61}$$

we can then define a four-susceptibility χ^ν_μ as:

$$\mathrm{J}^\nu_{\mathrm{ind}}(\boldsymbol{r},t) = \int dt'\int d\boldsymbol{r}'\ \chi^\nu_\mu(\boldsymbol{r},\boldsymbol{r}',t,t')\mathrm{A}^{\mathrm{ext}}_\mu(\boldsymbol{r}',t') \tag{3.62}$$

from which we deduce the linear response (four-)susceptibility tensor:

$$\chi^\nu_\mu(\boldsymbol{r},\boldsymbol{r}',t,t') = -\frac{i}{\hbar}\theta(t-t')\big\langle\big[\mathrm{J}^\nu(\boldsymbol{r},t), \mathrm{J}_\mu(\boldsymbol{r}',t')\big]\big\rangle_0 \tag{3.63}$$

The structure of (3.63) being exactly analogue to (3.40), we can immediately deduce the spectral representation of the four-susceptibility at $T=0$:

$$\boxed{\chi^\nu_\mu(\boldsymbol{r},\boldsymbol{r}',\omega) = \frac{2}{\hbar}\sum_n \frac{\langle 0|\,\mathrm{J}^\nu(\boldsymbol{r})\,|n\rangle\,\langle n|\,\mathrm{J}_\mu(\boldsymbol{r}')\,|0\rangle}{\omega+\omega_n-\omega_0+i\eta}} \tag{3.64}$$

From equation (3.63), one can see that the linear-response four susceptibility has the following structure:

$$\chi^\nu_\mu = \left(\begin{array}{c|c} C_{\rho,\rho} & C_{\rho,j^b} \\ \hline C_{j_a,\rho} & C_{j_a,j^b}\end{array}\right) \tag{3.65}$$

where we recall that $C_{\hat{A},\hat{B}}$ denotes the correlator between two fields $\hat{A}$ and $\hat{B}$. The diagonal elements of this tensor are therefore the charge-charge and current-current correlators while the out of diagonal elements correspond to charge-current correlators.

Let's stress an important semantic point. Both susceptibilities (3.40) and (3.63) are called retarded as they involved retarded electronic Green functions defined as (3.17). Nevertheless, let's keep in mind that, in our case, the retardation needs to be understood in the sense of the EM field, the regime is therefore defined by the value taken for c. Therefore, to summarize:

- In the quasi-static regime ($c\to\infty$), the problem reduces to the Poisson equation and only the scalar potential and charge density play a role in the response of the system. The light-matter interaction Hamiltonian is then taken to be (3.37) and the response function of the target is determined, to the first order, by charge-charge correlations.

- In the retarded regime (finite c), both scalar and vector potentials need to be considered and the light-matter interaction Hamiltonian is then (3.60). The problem essentially reduces to a choice of gauge. If one is interested in e.g. the conduction properties of a metal, a suitable choice would be to use the temporal gauge $\phi = 0$ where the electric field is fully determined by the vector potential $\boldsymbol{E} = -i(\omega/c)\boldsymbol{A}$. In this case, the conductivity tensor defined as:

$$E^a(\boldsymbol{r}, t) = \iint d\boldsymbol{r}' dt' \; \sigma^a_b(\boldsymbol{r}, \boldsymbol{r}', t, t') j^b(\boldsymbol{r}', t') \tag{3.66}$$

  can be straightforwardly obtained by the Kubo formula and gives:

$$\mathrm{Re}\{-\sigma^a_b(\boldsymbol{r}, \boldsymbol{r}', \omega)\} = \frac{2\pi c}{\hbar\omega} \sum_n \langle 0| \, j^a(\boldsymbol{r}) \, |n\rangle \, \langle n| \, j_b(\boldsymbol{r}') \, |0\rangle \, \delta(\omega + \omega_n - \omega_0) \tag{3.67}$$

  If one chooses a gauge where both $\boldsymbol{A}$ and ϕ are non-zero, both the temporal and spatial parts of the Hamiltonian need to be considered and conductivity would include charge densities in its definition.

However, although the temporal gauge seems to simplify the situation on the electronic level, it complicates the expression of the photon propagators. In fact, in our case, where both electron and photon propagation need to be taken into account, no gauge seems to give a dramatically simpler solution.

3.3.2.2 Dyson equation for the photon propagator

We are now in position to calculate the propagator for the EM field in presence of the polarizable medium. Thus, we consider the situation described in the introduction of this section: an external source term represented by the four-current $\mathrm{J}^\mu_{\mathrm{ext}}$ is positioned at $\boldsymbol{r}$ and we want to calculate the total four-potential $\mathrm{A}^\nu_{\mathrm{tot}}$ induced at $\boldsymbol{r}'$.

To do so, we apply the Dyson equation as we did in the quasi-static case. We note $\mathcal{D}$ the exact photon propagator and D the vacuum one. We then get:

$$\mathcal{D}^\beta_\alpha(b, a) = \mathrm{D}^\beta_\alpha(b, a) + \mathrm{D}^\beta_\mu(b, \overline{2}) \, \chi^\mu_\nu(\overline{2}, \overline{1}) \, \mathcal{D}^\nu_\alpha(\overline{1}, a) \tag{3.68}$$

keeping in mind that there is an implicit summation on the repeated indexes. To help the interpretation, we can represent the latter equation in the form of a diagram as we did in figure 3.4:

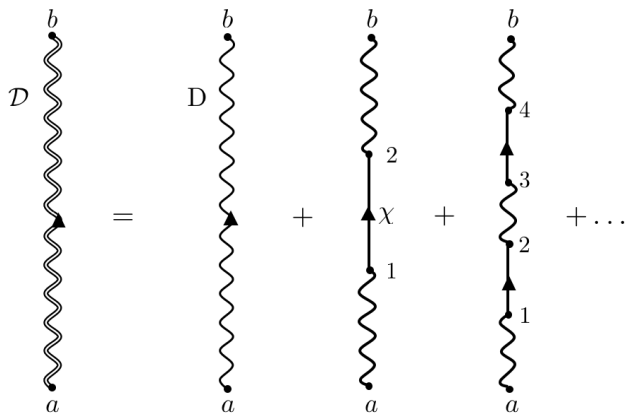

(3.69)

Like we did in the quasi-static case, we apply the Born approximation and get:

$$\boxed{\mathcal{D}^\beta_\alpha(b, a) = \mathrm{D}^\beta_\alpha(b, a) + \mathrm{D}^\beta_\mu(b, \overline{2}) \, \chi^\mu_\nu(\overline{2}, \overline{1}) \, \mathrm{D}^\nu_\alpha(\overline{1}, a)} \tag{3.70}$$

The first term is of course the vacuum photon propagator while the second term then corresponds to the *retarded screened interaction*.

3.3.2.3 Retarded electric Green dyadic

In nano-optics, we commonly work with electric and magnetic fields so that the electric Green dyadic $\overleftrightarrow{\boldsymbol{G}}$ is one of the most important and fundamental object of the theory. These objects have the advantage to be gauge-independent. However, so far we worked with the potentials $(\phi, \boldsymbol{A})$ as they have simpler transformation laws and symmetries; moreover, they strongly facilitate the connection with the many-particles Kubo formalism. Nevertheless, in this section, we will derive the electric Green dyadic using the results of the previous section in order to obtain formula adapted to discuss nano-optical experiments.

Combining the definition of the Faraday tensor (3.22) and the one of the photon propagator (3.28), we can write:

$$\mathrm{F}^{\epsilon\gamma}(\mathrm{x}') = \int d^4\mathrm{x}\big[\partial'^{\epsilon}\,\mathcal{D}^{\gamma}_{\alpha}(\mathrm{x}',\mathrm{x}) - \partial'^{\gamma}\,\mathcal{D}^{\epsilon}_{\alpha}(\mathrm{x}',\mathrm{x})\big]\mathrm{J}^{\alpha}(\mathrm{x}) \tag{3.71}$$

where the prime in ∂'^{ϵ} indicates that the derivative is taken with respect to x'. Besides, from the explicit form of the Faraday tensor (3.23), one can directly deduce that the component E^i of the electric field is given by:

$$E^i = F^{i0} = -F^{0i} = \partial^i \mathrm{A}^0 + \partial^0 \mathrm{A}^i \tag{3.72}$$

Therefore, using (3.71) we get:

$$E^i(\mathrm{x}') = \int d^4\mathrm{x}\bigg(\partial'^{i}\,\mathcal{D}^{0}_{\alpha}(\mathrm{x}',\mathrm{x}) - \partial'^{0}\,\mathcal{D}^{i}_{\alpha}(\mathrm{x}',\mathrm{x})\bigg)\mathrm{J}^{\alpha}(\mathrm{x}) \tag{3.73}$$

Now, we decompose the sums over α as:

$$\begin{cases} \mathcal{D}^{i}_{\alpha}(\mathrm{x}',\mathrm{x})\mathrm{J}^{\alpha}(\mathrm{x}) = \mathcal{D}^{i}_{0}(\mathrm{x}',\mathrm{x})\mathrm{J}^{0}(\mathrm{x}) - \mathcal{D}^{i}_{a}(\mathrm{x}',\mathrm{x})\mathrm{J}^{a}(\mathrm{x}) & (3.74\text{a}) \\ \mathcal{D}^{0}_{\alpha}(\mathrm{x}',\mathrm{x})\mathrm{J}^{\alpha}(\mathrm{x}) = \mathcal{D}^{0}_{0}(\mathrm{x}',\mathrm{x})\mathrm{J}^{0}(\mathrm{x}) - \mathcal{D}^{0}_{a}(\mathrm{x}',\mathrm{x})\mathrm{J}^{a}(\mathrm{x}) & (3.74\text{b}) \end{cases}$$

Besides, one can write the continuity equation as:

$$\partial_\mu \mathrm{J}^\mu = (\tfrac{\partial_t}{c}, -\boldsymbol{\nabla}).(c\rho, \boldsymbol{j}) = \partial_t\rho + \boldsymbol{\nabla}.\boldsymbol{j} = 0 \tag{3.75}$$

Fourier transforming the latter gives:

$$-\,i\omega\rho + ik_a J^a = 0 \tag{3.76}$$

which finally gives:

$$\mathrm{J}^0 = c\rho = \frac{ck_a}{\omega}\mathrm{J}^a \tag{3.77}$$

Fourier transforming equations (3.74) and using the latter equation, we get:

$$\begin{cases} \mathcal{D}^{i}_{\alpha}(\mathrm{k}',\mathrm{k})\mathrm{J}^{\alpha}(\mathrm{k}) = \dfrac{c}{\omega}\mathcal{D}^{i}_{0}(\mathrm{k}',\mathrm{k})k_j\mathrm{J}^{j}(\mathrm{k}) - \mathcal{D}^{i}_{a}(\mathrm{k}',\mathrm{k})\mathrm{J}^{a}(\mathrm{k}) & (3.78\text{a}) \\ \mathcal{D}^{0}_{\alpha}(\mathrm{k}',\mathrm{k})\mathrm{J}^{\alpha}(\mathrm{k}) = \dfrac{c}{\omega}\mathcal{D}^{0}_{0}(\mathrm{k}',\mathrm{k})k_j\mathrm{J}^{j}(\mathrm{k}) - \mathcal{D}^{0}_{a}(\mathrm{k}',\mathrm{k})\mathrm{J}^{a}(\mathrm{k}) & (3.78\text{b}) \end{cases}$$

We now Fourier transform (3.73) and get:

$$E^i(\mathrm{k}') = \int d^4\mathrm{k}\bigg(ik'^{i}\,\mathcal{D}^{0}_{\alpha}(\mathrm{k}',\mathrm{k}) + \frac{i\omega}{c}\,\mathcal{D}^{i}_{\alpha}(\mathrm{k}',\mathrm{k})\bigg)\mathrm{J}^{\alpha}(\mathrm{k}) \tag{3.79}$$

We can inject equations (3.78) in the latter expression and by substituting the summation index $a \to j$, we get the following equation:

$$E^i(\mathrm{k}') = \int d^3\boldsymbol{k}d\omega\bigg(\frac{i}{\omega}k'^{i}\,\mathcal{D}^{0}_{0}(\mathrm{k}',\mathrm{k})k_j - \frac{i}{c}k'^{i}\,\mathcal{D}^{0}_{j}(\mathrm{k}',\mathrm{k}) + \frac{i}{c}\mathcal{D}^{i}_{0}(\mathrm{k}',\mathrm{k})k_j - \frac{i\omega}{c^2}\,\mathcal{D}^{i}_{j}(\mathrm{k}',\mathrm{k})\bigg)\mathrm{J}^{j}(\mathrm{k}) \tag{3.80}$$

where we used $d^4\mathrm{k} = d^3\boldsymbol{k}d\omega/c$. A Fourier transform with respect to $\boldsymbol{r}$ and $\boldsymbol{r}'$ then gives:

$$E^i(\boldsymbol{r}',\omega) = \int d^3\boldsymbol{r}d\omega\Big(-\frac{i}{\omega}\nabla'^i\,\mathcal{D}_0^0(\boldsymbol{r}',\boldsymbol{r},\omega)\nabla_j - \frac{1}{c}\nabla'^i\,\mathcal{D}_j^0(\boldsymbol{r}',\boldsymbol{r},\omega) + \frac{1}{c}\mathcal{D}_0^i(\boldsymbol{r}',\boldsymbol{r},\omega)\nabla_j - \frac{i\omega}{c^2}\,\mathcal{D}_j^i(\boldsymbol{r}',\boldsymbol{r},\omega)\Big)\mathrm{J}^j(\boldsymbol{r},\omega) \tag{3.81}$$

Besides, for any fields Φ and $\boldsymbol{V}$ the integration by part in $\mathbb{R}^3$ reads:

$$\int_\Omega \Phi\boldsymbol{\nabla}.\boldsymbol{V}d\boldsymbol{r} = \int_{\partial\Omega}\Phi\,\boldsymbol{V}.d\boldsymbol{s} - \int_\Omega \boldsymbol{V}.\boldsymbol{\nabla}\Phi d\boldsymbol{r} \tag{3.82}$$

which can be applied to the latter equation in order to get:

$$E^i(\boldsymbol{r}',\omega) = \int d^3\boldsymbol{r}d\omega\Big(\frac{i}{\omega}\nabla'^i\nabla_j\,\mathcal{D}_0^0(\boldsymbol{r}',\boldsymbol{r},\omega) - \frac{1}{c}\nabla'^i\,\mathcal{D}_j^0(\boldsymbol{r}',\boldsymbol{r},\omega) - \frac{1}{c}\nabla_j\mathcal{D}_0^i(\boldsymbol{r}',\boldsymbol{r},\omega) - \frac{i\omega}{c^2}\,\mathcal{D}_j^i(\boldsymbol{r}',\boldsymbol{r},\omega)\Big)\mathrm{J}^j(\boldsymbol{r},\omega) \tag{3.83}$$

We can now use the definition (3.3) in order to identify the Green dyadic and get:

$$G_j^i(\boldsymbol{r}',\boldsymbol{r},\omega) = \frac{-1}{4\pi\omega^2}\nabla'^i\nabla_j\,\mathcal{D}_0^0(\boldsymbol{r}',\boldsymbol{r},\omega) + \frac{i}{4\pi\omega c}\big[\nabla'^i\,\mathcal{D}_j^0(\boldsymbol{r}',\boldsymbol{r},\omega) + \nabla_j\mathcal{D}_0^i(\boldsymbol{r}',\boldsymbol{r},\omega)\big] + \frac{1}{4\pi c^2}\,\mathcal{D}_j^i(\boldsymbol{r}',\boldsymbol{r},\omega) \tag{3.84}$$

To the best of our knowledge, this equation has never been derived so far. We can also Fourier transform it back with respect to $\boldsymbol{r}$ and $\boldsymbol{r}'$ and get:

$$G_j^i(\boldsymbol{k}',\boldsymbol{k},\omega) = \frac{1}{4\pi\omega^2}k'^ik_j\,\mathcal{D}_0^0(\boldsymbol{k}',\boldsymbol{k},\omega) - \frac{1}{4\pi\omega c}\big[k'^i\,\mathcal{D}_j^0(\boldsymbol{k}',\boldsymbol{k},\omega) + k_j\mathcal{D}_0^i(\boldsymbol{k}',\boldsymbol{k},\omega)\big] + \frac{1}{4\pi c^2}\,\mathcal{D}_j^i(\boldsymbol{k}',\boldsymbol{k},\omega) \tag{3.85}$$

3.3.2.4 Reciprocity theorem and symmetry properties of the Green dyadic

We now impose the following condition:

$$\mathscr{S}\left(G_j^i(\boldsymbol{r}',\boldsymbol{r},\omega)\right) = G_i^j(\boldsymbol{r},\boldsymbol{r}',\omega) = G_j^i(\boldsymbol{r}',\boldsymbol{r},\omega) \tag{3.86}$$

where we define the operator $\mathscr{S}$ exchanging the indexes $i \leftrightarrow j$ and coordinates $\boldsymbol{r} \leftrightarrow \boldsymbol{r}'$. This *reciprocity* condition [19] states that a current in $\boldsymbol{r}$ creating a EM field in $\boldsymbol{r}'$ is equivalent to a current in $\boldsymbol{r}'$ creating a EM field in $\boldsymbol{r}$. In some particular situations (e.g. chiral meta-materials, moving media or topological materials), the latter condition is no longer true [198]. In this work, we only consider metallic nano-particles so that the reciprocity condition can be applied.

Therefore, in a *reciprocal medium*, the Green dyadic reads:

$$\boxed{G_j^i(\boldsymbol{r}',\boldsymbol{r},\omega) = -\frac{1}{4\pi\omega^2}\nabla'^i\nabla_j\,\mathcal{D}_0^0(\boldsymbol{r}',\boldsymbol{r},\omega) + \frac{1}{4\pi c^2}\,\mathcal{D}_j^i(\boldsymbol{r}',\boldsymbol{r},\omega)} \tag{3.87}$$

where the first term is a charge-charge correlator while the second term is a current-current correlator. Therefore, in the Lorenz gauge, the Green dyadic can be written as:

$$G_j^i(\boldsymbol{k}',\boldsymbol{k},\omega) = \frac{4\pi}{k^2 - \frac{\omega^2}{c^2}}\Big(\frac{1}{4\pi\omega^2}k'^ik_j\,\chi_0^0(\boldsymbol{k}',\boldsymbol{k},\omega) + \frac{1}{4\pi c^2}\,\chi_j^i(\boldsymbol{k}',\boldsymbol{k},\omega)\Big)\frac{4\pi}{k'^2 - \frac{\omega^2}{c^2}} \tag{3.88}$$

This equation is probably the most important new result of the section as it generalizes the Kubo approach derived in the quasi-static case (3.53) to the retarded regime. Moreover, by taking the quasi-static limit $c \longrightarrow \infty$, we indeed obtain:

$$G_j^i(\boldsymbol{k}',\boldsymbol{k},\omega) = \frac{4\pi}{\omega^2}\frac{k_jk'^i}{k^2k'^2}\,\chi_0^0(\boldsymbol{k}',\boldsymbol{k},\omega) \tag{3.89}$$

which corresponds to the formula (3.53) that we derived in the well-known quasi-static formalism.

3.3.3 Concluding remarks

In the nano-optics community, we usually calculate the Green dyadic $\overleftrightarrow{\boldsymbol{G}}$ as this is the sole quantity required to describe the equilibrium properties of the electromagnetic field as demonstrated by Agarwal [95] and recalled in the introductory chapter. On the other hand, from a condensed matter physicist point-of-view, the relevant quantity is the mixed dynamic form factor (or the susceptibility) of the material because it encodes all the information on the space and time dependent electronic correlations as demonstrated by Van Hove [199, 200].

These two approaches are completely equivalent and based on the fluctuation-dissipation theorem which connects the response of the system (Green dyadic or susceptibility) to correlations of the underlying fields (electromagnetic or electronic correlation). The essence of section 3.3 was to explicitly show this equivalence and demonstrate that, to the first order, the two propagators χ and W (or χ_μ^ν and G_i^j) are simply connected by two vacuum photon propagators.

3.4 Kinetic equation for the electron density matrix

Following the logic of diagram (3.2), we will now focus on the electron probe. Let's consider a fast electron described by the wavefunction $\psi(\boldsymbol{r}, t)$. We can then define the *single electron density matrix* as:

$$\varrho(\boldsymbol{r}, t, \boldsymbol{r}', t') = \psi(\boldsymbol{r}, t)\psi^*(\boldsymbol{r}', t') \tag{3.90}$$

In the following, we will also consider the case of a density matrix invariant by translation in time $\rho(\boldsymbol{r}, t, \boldsymbol{r}', t') = \varrho(\boldsymbol{r}, \boldsymbol{r}', t - t')$. In this case, the corresponding Fourier transform reads:

$$\varrho(\boldsymbol{r}, \boldsymbol{r}', \omega) = \frac{1}{2\pi}\int d(t - t')\varrho(\boldsymbol{r}, \boldsymbol{r}', t - t')e^{i\omega(t-t')} \tag{3.91}$$

If the Hamiltonian is time independent then the corresponding wavefunction becomes separable $\psi(\boldsymbol{r}, t) = \psi(\boldsymbol{r})e^{i\epsilon t}$ and the density matrix can be written:

$$\varrho(\boldsymbol{r}, \boldsymbol{r}', \omega) = \psi(\boldsymbol{r})\psi(\boldsymbol{r}')\delta(\omega - \epsilon) \tag{3.92}$$

which corresponds to the *spectral one-electron density matrix*. The goal of this section is to calculate the kinetic equation for the density matrix i.e. the equation ruling the evolution of the density matrix during elastic and inelastic events. In the quasi-static limit, this equation has been derived for the first time by Dudarev, Peng and Whelan [17] and corresponds to equation (3.9). It has then been introduced to EELS by Schattschneider and collaborators [18] and later applied to various situations such as EMCD [201], core-loss spectroscopy [202] or diffraction [203]. The goal of this section is to adapt this formula to the case of a retarded interaction kernel. As a matter of fact, apart from the final step, the demonstration is essentially the same both in the quasi-static and the retarded case. Therefore, this section is organized as follows:

1. In sections 3.4.1, 3.4.2 and 3.4.3, we review the seminal demonstration of Dudarev and collaborators with special emphasis on the different approximations made. The result of the demonstration is a kinetic equation in the temporal domain valid for any weak interaction potential V.

2. In section 3.4.4, we use an explicit expression for V and derive the kinetic equation in the spectral domain in both the quasi-static and retarded interactions case. To do so, we use the result of section 3.3 and assume a steady-state of illumination for the electron beam.

3.4.1 Schrödinger equation for the electron propagator

For generality, we consider a fast electron interacting with a nano-particle. The Hamiltonian of the total system $\{\mathrm{NP} + e^-\}$ is then given by:

$$\hat{H}_{\mathrm{tot}} = \hat{H}_{\mathrm{NP}} + \hat{H}_e + \hat{H}_{\mathrm{int}} \tag{3.93}$$

where $\hat{H}_e$ describes the free propagation of the electron, $\hat{H}_{\rm NP}$ encodes the electronic properties of the NP only and $\hat{H}_{\rm int}$ gives the interaction between the excitations in the NP and the impinging electron. We now separate the interaction potential into a thermodynamically averaged and a fluctuating part:

$$\hat{H}_{\rm int} = \langle \hat{H}_{\rm int} \rangle + \hat{V} \tag{3.94}$$

The thermodynamical average is taken over the ensemble of realizations of electronic states in the nano-particle:

$$\langle \hat{H}_{\rm int} \rangle = \frac{1}{Z} \sum_n \langle n | \hat{H}_{\rm int} | n \rangle \, e^{-\beta \epsilon_n} \tag{3.95}$$

with the same notations we used in section 3.3. To simplify the notations, we suppose that $\langle \hat{H}_{\rm int} \rangle = 0$ which has no incidence on the following demonstration. A non-zero average could be included by modifying the free electron Hamiltonian as:

$$\hat{H}'_e = H_e + \langle \hat{H}_{\rm int} \rangle = -\frac{\hbar^2}{2m} \nabla^2 + \langle \hat{H}_{\rm int} \rangle \tag{3.96}$$

Besides, the time evolution operator $\hat{U}_0$ of the free electron as well as the time evolution operator for the total system $\hat{T}$ follow the Schrodïnger equation:

$$\begin{cases} i\hbar \dfrac{\partial}{\partial t} \hat{U}_0(t, t_0) = \hat{H}_e \, \hat{U}_0(t, t_0) + \delta(t - t_0) & \text{(3.97a)} \\ i\hbar \dfrac{\partial}{\partial t} \hat{T}(t, t_0) = \hat{H}_{\rm tot} \, \hat{T}(t, t_0) + \delta(t - t_0) & \text{(3.97b)} \end{cases}$$

Equation (3.97a) can be straightforwardly integrated and gives:

$$\hat{U}_0(t - t_0) = -\frac{i}{\hbar} \Theta(t - t_0) e^{-\frac{i}{\hbar} \hat{H}_e (t - t_0)} \tag{3.98}$$

However, equation (3.97b) cannot be explicitly solved. To overcome this difficulty, we first define the operator $\hat{U}$ as:

$$\hat{U}(t, t_0) = e^{\frac{i}{\hbar} \hat{H}_{\rm NP} (t - t_0)} \hat{T}(t, t_0) \tag{3.99}$$

which corresponds to the evolution operator for the *interacting* electron. Moreover, we define the Heisenberg representation of the fluctuating part of the interaction $\hat{V}$ as:

$$\hat{V}(t - t_0) = e^{\frac{i}{\hbar} \hat{H}_{\rm NP} (t - t_0)} \hat{V} e^{-\frac{i}{\hbar} \hat{H}_{\rm NP} (t - t_0)} \tag{3.100}$$

Combining equations (3.97b), (3.99) and (3.100), we get the Schrödinger equation for the time evolution operator of the interacting electron:

$$i\hbar \frac{\partial \hat{U}(t, t_0)}{\partial t} = \left(\hat{H}_e + \hat{V}(t - t_0) \right) \hat{U}(t, t_0) + \delta(t - t_0) \tag{3.101}$$

In the next section, we will use a perturbation approach in order to calculate a good approximation of this evolution operator.

3.4.2 Dyson equation for the single electron propagator

We first integrate equation (3.101) in order to obtain the following integral representation:

$$\hat{U}(t, t_0) = \hat{U}_0(t, t_0) + \frac{1}{i\hbar} \int_{t_0}^{t} dt_1 \hat{U}_0(t, t_1) \hat{V}(t_1) \hat{U}(t_1, t_0) \tag{3.102}$$

The latter equation can be solved iteratively by writing:

$$\begin{aligned} \hat{U}(t, t_0) = \hat{U}_0(t, t_0) &+ \frac{1}{i\hbar} \int_{t_0}^{t} dt_1 \hat{U}_0(t, t_1) \hat{V}(t_1) \hat{U}_0(t_1, t_0) \\ &+ \frac{1}{i^2 \hbar^2} \int_{t_0}^{t} dt_1 \hat{U}_0(t, t_1) \hat{V}(t_1) \int_{t_0}^{t_1} dt_2 \hat{U}_0(t_1, t_2) \hat{V}(t_2) \hat{U}_0(t_2, t_0) + \dots \end{aligned} \tag{3.103}$$

The latter equation can be diagrammatically represented as:

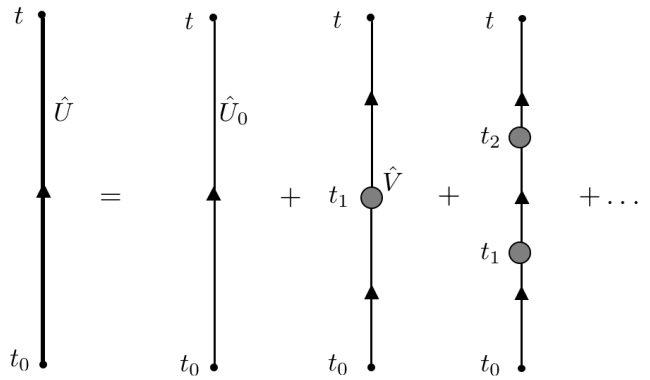

(3.104)

Let's now re-arrange the previous integrals by looking at the second term in (3.103) and exceptionally taking $\hat{U}_0 = \mathrm{Id}$ for the sake of the demonstration. Separating the integral in two parts and changing the integration variable leads to:

$$\int_{t_0}^{t} dt_1 \hat{V}(t_1) \int_{t_0}^{t_1} dt_2 \hat{V}(t_2) = \frac{1}{2} \int_{t_0}^{t} dt_1 \hat{V}(t_1) \int_{t_0}^{t_1} dt_2 \hat{V}(t_2) + \frac{1}{2} \int_{t_0}^{t} dt_2 \hat{V}(t_2) \int_{t_0}^{t_2} dt_1 \hat{V}(t_1) \tag{3.105}$$

The integration limit of the integrals can then be all set to t_0 and t if one introduce the proper Heaviside functions:

$$\begin{aligned}\int_{t_0}^{t} dt_1 \hat{V}(t_1) \int_{t_0}^{t_1} dt_2 \hat{V}(t_2) = \frac{1}{2} \int_{t_0}^{t} dt_1 \int_{t_0}^{t} dt_2\, \hat{V}(t_1)\hat{V}(t_2)\theta(t_1 - t_2) \\ + \frac{1}{2} \int_{t_0}^{t} dt_2 \int_{t_0}^{t} dt_1\, \hat{V}(t_2)\hat{V}(t_1)\theta(t_2 - t_1)\end{aligned} \tag{3.106}$$

And using the definition of the time ordering operator (3.16), we finally obtain:

$$\int_{t_0}^{t} dt_1 \hat{V}(t_1) \int_{t_0}^{t_1} dt_2 \hat{V}(t_2) = \frac{1}{2} \int_{t_0}^{t} dt_1 \int_{t_0}^{t} dt_2\, \mathcal{T}\{\hat{V}(t_1)\hat{V}(t_2)\} \tag{3.107}$$

The same trick can be applied to all orders but keeping in mind that, the prefactor for the nth order term is $(1/n!)$. It enables to re-write equation (3.103) as:

$$\hat{U}(t, t_0) = \sum_{n=0}^{\infty} \frac{(-i)^n}{\hbar^n n!} \int_{t_0}^{t} dt_1 \ldots \int_{t_0}^{t} dt_n \mathcal{T}\{\hat{U}_0(t, t_1)\hat{V}(t_1)\hat{U}_0(t_1, t_2) \ldots \hat{V}(t_n)\hat{U}_0(t_n, t_0)\} \tag{3.108}$$

In order to use the linear response theory derived in section (3.3), we now calculate the average value of the exact electron propagator $\langle \hat{U}(t, t_0) \rangle \equiv \hat{\mathcal{U}}(t, t_0)$:

$$\hat{\mathcal{U}}(t, t_0) = \sum_{n=0}^{\infty} \frac{(-i)^n}{\hbar^n n!} \int_{t_0}^{t} dt_1 \ldots \int_{t_0}^{t} dt_n \Big\langle \mathcal{T}\{\hat{U}_0(t, t_1)\hat{V}(t_1)\hat{U}_0(t_1, t_2) \ldots \hat{V}(t_n)\hat{U}_0(t_n, t_0)\} \Big\rangle \tag{3.109}$$

We now use the Isserlis-Wick theorem which states that for a set of Gaussian random variable $\{X_1, \ldots, X_n\}$, any monomial of these variables satisfies:

$$\langle X_1 X_2 \ldots X_{2m+1} \rangle = 0 \tag{3.110a}$$

$$\langle X_1 X_2 \ldots X_{2m} \rangle = \sum_{\substack{\text{All possible} \\ \text{grouping}}} \prod_{i,j} \mathrm{Cov}[X_i X_j] \tag{3.110b}$$

(3.110c)

where Cov denotes the covariance. And since by construction the mean value of $\hat{V}$ is zero, we have $\mathrm{Cov}[V(t_i)V(t_j)] = \langle V(t_i)V(t_j)\rangle - \langle V(t_i)\rangle \langle V(t_j)\rangle = \langle V(t_i)V(t_j)\rangle$. Equation (3.109) then becomes:

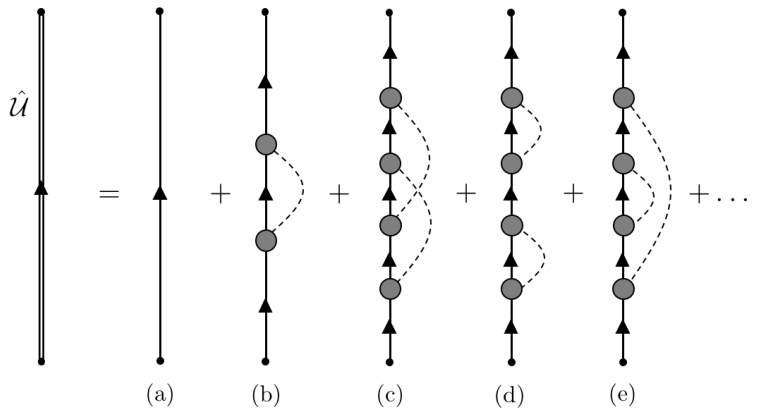

(3.111)

where each dotted line represents a covariance product $\langle V(t_i)V(t_j)\rangle$. We now turn to the main approximation of this development [204, 205, 206]: *we only keep diagrams involving correlations between neighboring vertexes*. For example, we neglect terms (c) and (e) in equation (3.111). This approximation can be interpreted in two equivalent ways:

- First, as pointed out in [17], this approximation consists in treating all the successive scatterings as single independent scatterings which corresponds to the Born approximation. Following [207, 17], in order to determine its condition of validity, we introduce the typical correlation length r_c of the excitations in the particle, v the speed of the traveling electron and $|\hat{V}|$ the order of magnitude of the interaction. Then the Born approximation holds if:

$$\frac{\hbar v}{r_c} \gg |\hat{V}| \tag{3.112}$$

  In other terms, the correlation length should be short enough, or the interaction weak enough, for no dynamical effect to appear. Nevertheless, this Born approximation applies to the fluctuating part of the interaction only while the static part is included a priori. Thus, this approximation is rather a distorted-wave Born approximation [17].

- One can also interpret this approximation in a quantum field theory fashion [208] as the dotted lines can be regarded as a particle exchange. In this case, the approximation above consists in forbidding two excitations to be in the scatterer at a same time τ which is valid in the weak interaction limit. We exemplify it on diagram (e):

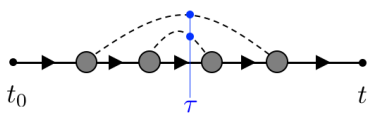

(3.113)

Thanks to the approximation made, equation (3.111) is dramatically simplified and can be factor-

ized as follow:

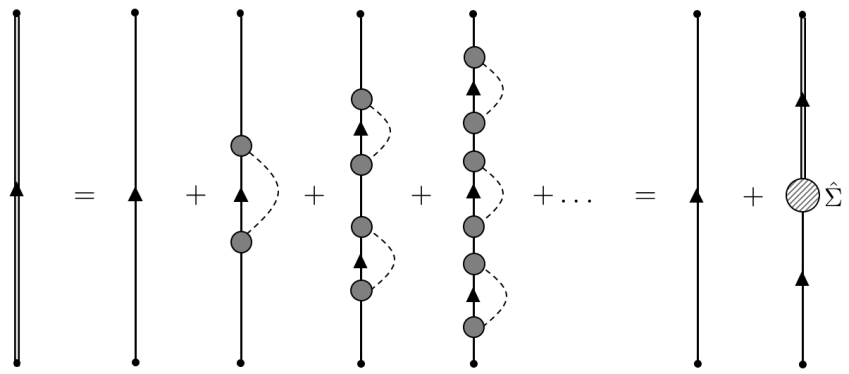

(3.114)

where $\hat{\Sigma}$ is the *self-energy* of the probe electrons [209] and reads, in a synthetic form:

$$\hat{\Sigma} = \hat{U}_0^{-1} - \hat{\mathcal{U}}^{-1} = \langle \mathcal{T}\{\hat{V}\hat{U}_0\hat{V}\}\rangle \tag{3.115}$$

Equation (3.115) is the starting point of Echenique's et al. formalism [16] that we will review at the end of this chapter. The Dyson equation (3.114) can be re-written in its explicit form, in the time domain, as:

$$\hat{\mathcal{U}}(t,t_0) = \hat{U}_0(t,t_0) - \frac{1}{\hbar^2}\int_{t_0}^{t} dt_1 \int_{t_0}^{t} dt_2\, \hat{U}_0(t,t_1)\big\langle \mathcal{T}\{\hat{V}(t_1)U_0(t_1,t_2)\hat{V}(t_2)\}\big\rangle \hat{\mathcal{U}}(t_2,t_0) \tag{3.116}$$

3.4.3 Bi-linear propagator for the single electron density matrix

We will now construct the propagator of the single-electron density matrix. To do so, we will use (3.116) to construct an average propagator $\hat{\mathcal{K}}$ of the exact density-matrix propagator $\hat{K}$. Starting from the exact electron propagator $\hat{U}$, one can construct $\hat{K}$ as a tensor product:

$$\hat{K} = \hat{U} \otimes \hat{U}^\dagger \tag{3.117}$$

Injecting the development (3.108) in the latter development, we obtain:

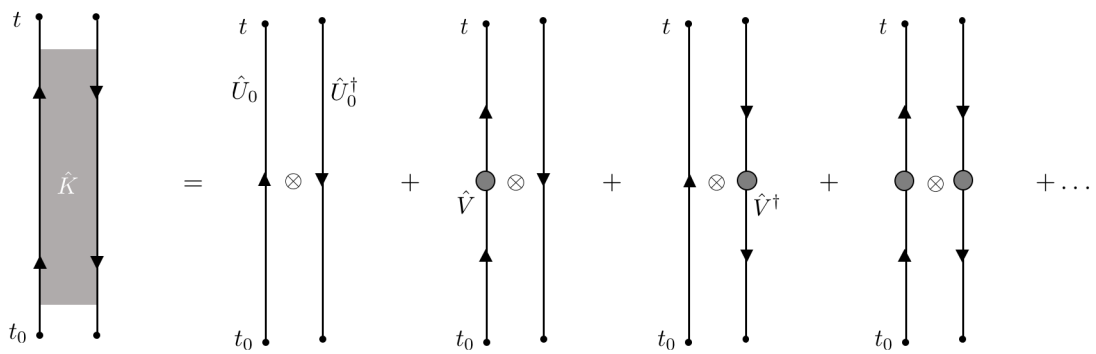

(3.118)

In the following, for brevity reasons, we will omit the $\otimes$ symbol in the diagrams. As we did for the electron propagator, we now take the average value of $\hat{K}$. Using the Isserlis-Wick theorem, we obtain the following expression for $\hat{\mathcal{K}}$:

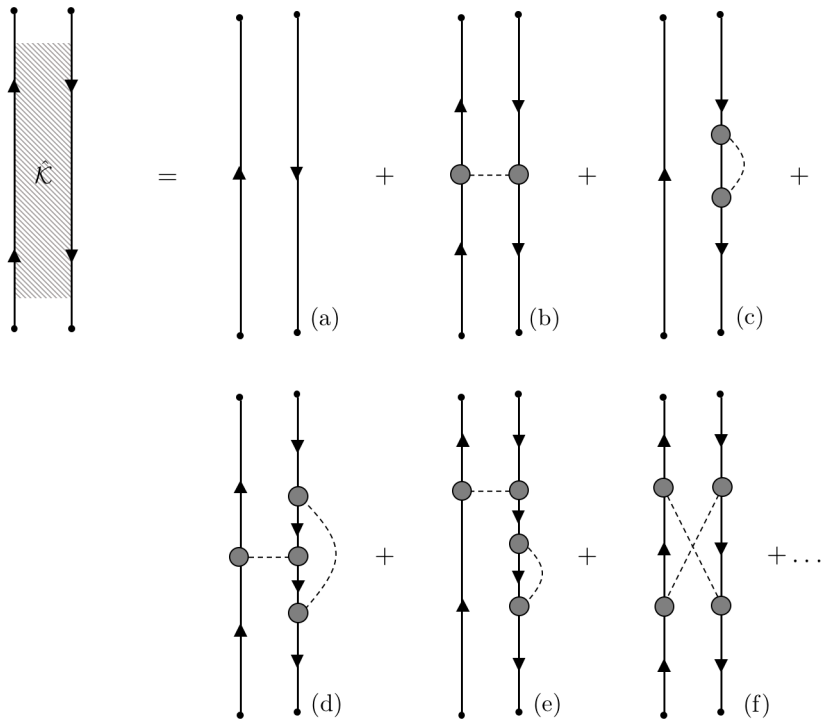

(3.119)

At this point, we will make the same approximation as in the last section and neglect all the diagrams with several simultaneous excitations e.g. diagram (d) in (3.119). Diagrams like (f) correspond to coherent back-scattering events which appears to be sufficiently small to be neglected [17]. This approximation is the so-called forward scattering approximation and is standard in electron microscopy.

Within these approximations, the expansion contains only two building blocks: electron self-energy term (c) and mutual correlations (b). We can of course encounter sequences of these blocks like diagram (e). We can then partially re-sum the self-energy terms which leads to:

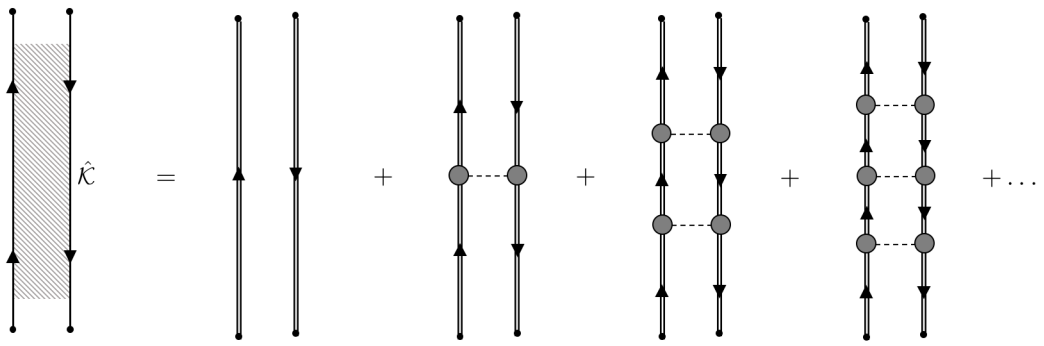

(3.120)

The latter equation formally corresponds to a Bethe-Salpeter equation in the very specific case where the two bound states correspond to ψ and $\psi^\dagger$ and within the so-called *ladder approximation*.

This equation can be re-summed and reads:

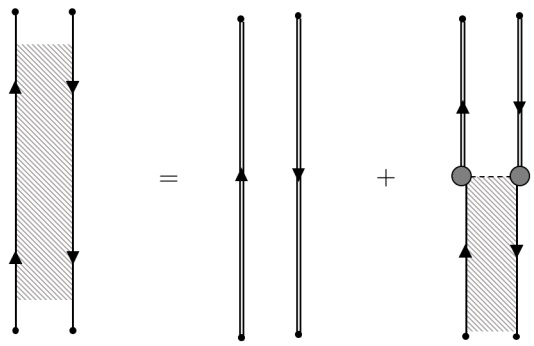

(3.121)

Or alternatively in its explicit form:

$$\hat{\mathcal{K}}(\boldsymbol{r},t;\boldsymbol{r}_0,t_0|\boldsymbol{r}',t';\boldsymbol{r}_0',t_0') = \hat{\mathcal{U}}(\boldsymbol{r},t;\boldsymbol{r}_0,t_0)\,\hat{\mathcal{U}}^\dagger(\boldsymbol{r}',t';\boldsymbol{r}_0',t_0') + \int_{t_0}^{t} dt_1 dt_1' \int_{t_0}^{t} d\boldsymbol{r}_1 d\boldsymbol{r}_1'\,\hat{\mathcal{U}}(\boldsymbol{r},t;\boldsymbol{r}_1,t_1) \times \hat{\mathcal{U}}^\dagger(\boldsymbol{r}',t';\boldsymbol{r}_1',t_1')\,\left\langle \mathcal{T}\{\hat{V}(\boldsymbol{r}_1,t_1)\hat{V}^\dagger(\boldsymbol{r}_1',t_1')\}\right\rangle \hat{\mathcal{K}}(\boldsymbol{r}_1,t_1;\boldsymbol{r}_0,t_0|\boldsymbol{r}_1',t_1';\boldsymbol{r}_0',t_0') \tag{3.122}$$

3.4.4 The kinetic equation for the single electron density matrix

We are now in position to derive the master equation describing the propagation of the single electron density matrix i.e. the so-called *kinetic equation*. Thus let's consider an incident density matrix $\varrho_i(\boldsymbol{r}_0,t_0;\boldsymbol{r}_0',t_0')$ and propagate it to the point $(\boldsymbol{r},t;\boldsymbol{r}',t')$. Taking into account the interaction with the nano-particle and within the approximations detailed earlier, the final density matrix $\varrho_f(\boldsymbol{r},t;\boldsymbol{r}',t')$ satisfies:

$$\varrho_f(\boldsymbol{r},t;\boldsymbol{r}',t') = \int dt_0 \int dt_0' \int d\boldsymbol{r}_0 \int d\boldsymbol{r}_0'\,\hat{\mathcal{K}}(\boldsymbol{r},t;\boldsymbol{r}_0,t_0|\boldsymbol{r}',t';\boldsymbol{r}_0',t_0')\,\varrho_i(\boldsymbol{r}_0,t_0;\boldsymbol{r}_0',t_0') \tag{3.123}$$

plugging (3.122) in the latter, we finally get:

$$\varrho_f(\boldsymbol{r},t;\boldsymbol{r}',t') = \varrho_0(\boldsymbol{r},t;\boldsymbol{r}',t') + \int dt_1 dt_1' \int d\boldsymbol{r}_1 d\boldsymbol{r}_1'\,\mathcal{U}(\boldsymbol{r},t;\boldsymbol{r}_1,t_1)\,\mathcal{U}^\dagger(\boldsymbol{r}',t';\boldsymbol{r}_1',t_1') \times \hat{C}(\boldsymbol{r}_1,t_1,\boldsymbol{r}_1',t_1')\,\varrho_i(\boldsymbol{r}_1,t_1;\boldsymbol{r}_1',t_1') \tag{3.124}$$

where the correlation function reads $C(\boldsymbol{r}_1,t_1,\boldsymbol{r}_1',t_1') = \left\langle \mathcal{T}\{\hat{V}(\boldsymbol{r}_1,t_1)\hat{V}^\dagger(\boldsymbol{r}_1',t_1')\}\right\rangle$. Equation (3.124) is the kinetic equation in the temporal domain where the interaction Hamiltonian is not yet specified. Let's highlight that at this point, the latter equation is very general and can be applied e.g. to model time-resolved spectroscopy experiments.

We now suppose that the electron beam is in a *steady-state of illumination* which is valid for standard EELS experiments we are describing in this thesis. In this case, the density matrix only depends on the time difference. We now Fourier transform equation (3.124) with respect to t and t' therefore taking the limits of the integrals over t_1 and t_1' to be $\pm\infty$. We therefore obtain:

$$\varrho_f(\boldsymbol{r},E,\boldsymbol{r}',E') = \varrho_0(\boldsymbol{r},E,\boldsymbol{r}',E') + \int dt e^{-iEt/\hbar} dt' e^{iE't'/\hbar} \int dt_1 dt_1' \int d\boldsymbol{r}_1 d\boldsymbol{r}_1'\,\mathcal{U}(\boldsymbol{r},\boldsymbol{r}_1,t-t_1) \times \mathcal{U}^\dagger(\boldsymbol{r}'\boldsymbol{r}_1',t'-t_1')\hat{C}(\boldsymbol{r}_1,\boldsymbol{r}_1',t_1-t_1')\,\varrho_i(\boldsymbol{r}_1,\boldsymbol{r}_1',t_1-t_1') \tag{3.125}$$

Changing the integration variables leads to:

$$\varrho_f(\boldsymbol{r},E,\boldsymbol{r}',E') = \varrho_0(\boldsymbol{r},E,\boldsymbol{r}',E') + \int dt_1 dt_1' \int d\boldsymbol{r}_1 d\boldsymbol{r}_1' \hat{C}(\boldsymbol{r}_1,\boldsymbol{r}_1',t_1-t_1')\,\varrho_i(\boldsymbol{r}_1,\boldsymbol{r}_1',t_1-t_1') \times \int dt e^{-iE(t+t_1)/\hbar} dt' e^{iE'(t'+t_1')/\hbar}\,\mathcal{U}(\boldsymbol{r},\boldsymbol{r}_1,t)\,\mathcal{U}^\dagger(\boldsymbol{r}'\boldsymbol{r}_1',t') \tag{3.126}$$

which can be re-written as:

$$\varrho_f(\boldsymbol{r}, E, \boldsymbol{r}', E') = \varrho_0(\boldsymbol{r}, E, \boldsymbol{r}', E') + \int d\boldsymbol{r}_1 d\boldsymbol{r}_1' \mathcal{U}(\boldsymbol{r}, \boldsymbol{r}_1, E)\mathcal{U}^\dagger(\boldsymbol{r}'\boldsymbol{r}_1', E') \\ \times \int dt_1 dt_1' \hat{C}(\boldsymbol{r}_1, \boldsymbol{r}_1', t_1 - t_1')\ \varrho_i(\boldsymbol{r}_1, \boldsymbol{r}_1', t_1 - t_1') e^{-iEt_1/\hbar} e^{iE't_1'/\hbar} \tag{3.127}$$

And we recognize a convolution product with respect to $t_1 - t_1'$. Noting $-\hbar\omega$ the convolution variable, we finally get:

$$\varrho_f(\boldsymbol{r}, \boldsymbol{r}', E) = \varrho_0(\boldsymbol{r}, \boldsymbol{r}', E) + \int d\boldsymbol{r}_1 d\boldsymbol{r}_1'\ \mathcal{U}(\boldsymbol{r}, \boldsymbol{r}_1, E)\mathcal{U}^\dagger(\boldsymbol{r}'\boldsymbol{r}_1', E) \int d\omega\, \hat{C}(\boldsymbol{r}_1, \boldsymbol{r}_1', -\omega)\ \varrho_i(\boldsymbol{r}_1, \boldsymbol{r}_1', E + \hbar\omega) \tag{3.128}$$

We now need to calculate the Fourier transform of the correlation function. We will distinguish the quasi-static from the retarded case and note $\hat{C}^{\mathrm{QS}}$ and $\hat{C}^{\mathrm{R}}$ the corresponding correlation functions.

3.4.4.1 First case: Quasistatic interaction kernel

The quasi-static interaction $\hat{V}^{\mathrm{QS}}$ between the electron and the particle is given by the Coulomb interaction:

$$\langle\psi_f|\, \hat{V}^{\mathrm{QS}}(\boldsymbol{r}, t)\, |\psi_i\rangle = \langle\psi_f| \int d\boldsymbol{r}' \frac{\hat{\mathfrak{n}}(\boldsymbol{r}', t)}{|\boldsymbol{r} - \boldsymbol{r}'|} |\psi_i\rangle \tag{3.129}$$

where $\hat{\rho}$ is the charge density operator for the particle. Therefore, C^{QS} reads:

$$\hat{C}^{\mathrm{QS}}(\boldsymbol{r}_1, t_1, \boldsymbol{r}_1', t_1') = \int d\boldsymbol{r}_2 \int d\boldsymbol{r}_2' \frac{\langle 0|\, \mathcal{T}\{\hat{\mathfrak{n}}(\boldsymbol{r}_2, t_1)\hat{\mathfrak{n}}^\dagger(\boldsymbol{r}_2', t_1')\}\, |0\rangle}{|\boldsymbol{r}_1 - \boldsymbol{r}_2|\, |\boldsymbol{r}_1' - \boldsymbol{r}_2'|} \tag{3.130}$$

Writing explicitly the time ordering operator, we get:

$$\hat{C}^{\mathrm{QS}}(\boldsymbol{r}_1, \boldsymbol{r}_1', t_1 - t_1') = \left(\int d\boldsymbol{r}_2 \int d\boldsymbol{r}_2' \frac{\sum_n \langle 0|\, \hat{\mathfrak{n}}(\boldsymbol{r}_2)\, |n\rangle \langle n|\, \hat{\mathfrak{n}}^\dagger(\boldsymbol{r}_2')\, |0\rangle}{|\boldsymbol{r}_1 - \boldsymbol{r}_2|\, |\boldsymbol{r}_1' - \boldsymbol{r}_2'|} e^{-i(\omega_0 - \omega_n)(t_1 - t_1')} \theta(t_1 - t_1') \right) \\ + \left(t_1 \leftrightarrow t_1' \right) \tag{3.131}$$

Noting $\tau = t_1 - t_1'$, the Fourier transform reads:

$$\int e^{-i\omega\tau} \hat{C}^{\mathrm{QS}}(\boldsymbol{r}_1, \boldsymbol{r}_1', \tau) d\tau = \left(\int d\boldsymbol{r}_2 \int d\boldsymbol{r}_2' \frac{\sum_n \langle 0|\, \hat{\mathfrak{n}}(\boldsymbol{r}_2)\, |n\rangle \langle n|\, \hat{\mathfrak{n}}^\dagger(\boldsymbol{r}_2')\, |0\rangle}{|\boldsymbol{r}_1 - \boldsymbol{r}_2|\, |\boldsymbol{r}_1' - \boldsymbol{r}_2'|} \int d\tau\, e^{-i(\omega + \omega_0 - \omega_n)\tau} \theta(\tau) \right) \\ + \int e^{-i\omega\tau} \left(\tau \leftrightarrow -\tau \right) d\tau \tag{3.132}$$

which gives:

$$\hat{C}^{\mathrm{QS}}(\boldsymbol{r}_1, \boldsymbol{r}_1', \omega) = \left(\int d\boldsymbol{r}_2 \int d\boldsymbol{r}_2' \frac{\sum_n \langle 0|\, \hat{\mathfrak{n}}(\boldsymbol{r}_2)\, |n\rangle \langle n|\, \hat{\mathfrak{n}}^\dagger(\boldsymbol{r}_2')\, |0\rangle}{|\boldsymbol{r}_1 - \boldsymbol{r}_2|\, |\boldsymbol{r}_1' - \boldsymbol{r}_2'|} \right) \left[\mathcal{P} \left(\pi\delta(\omega + \omega_0 - \omega_n) - i \frac{1}{\omega + \omega_0 - \omega_n} \right) \right] \\ + \left(\mathscr{F} \right)^* \tag{3.133}$$

and using the fact that for any complex number $z \in \mathbb{C}$ we have $z + z^* = 2\mathrm{Re}(z)$, we finally get:

$$\hat{C}^{\mathrm{QS}}(\boldsymbol{r}_1, \boldsymbol{r}_1', \omega) = 2\pi \int d\boldsymbol{r}_2 \int d\boldsymbol{r}_2' \frac{\sum_n \langle 0|\, \hat{\mathfrak{n}}(\boldsymbol{r}_2)\, |n\rangle \langle n|\, \hat{\mathfrak{n}}^\dagger(\boldsymbol{r}_2')\, |0\rangle}{|\boldsymbol{r}_1 - \boldsymbol{r}_2|\, |\boldsymbol{r}_1' - \boldsymbol{r}_2'|} \delta(\omega + \omega_0 - \omega_n) \tag{3.134}$$

From equation (3.54), one can see that $\hat{C}^{\mathrm{QS}}(\boldsymbol{r}_1, \boldsymbol{r}'_1, -\omega) = \mathrm{Im}\{-W(\boldsymbol{r}_1, \boldsymbol{r}'_1, \omega)\}$. Therefore, plugging it in (3.128), we finally obtain:

$$\boxed{\begin{aligned}\varrho_f(\boldsymbol{r}, \boldsymbol{r}', E) = \varrho_0(\boldsymbol{r}, \boldsymbol{r}', E) + \int d\boldsymbol{r}_1 d\boldsymbol{r}'_1\, \mathcal{U}(\boldsymbol{r}, \boldsymbol{r}_1, E)\mathcal{U}^\dagger(\boldsymbol{r}'\boldsymbol{r}'_1, E) \\ \times \int d\omega\, \mathrm{Im}\{-W(\boldsymbol{r}_1, \boldsymbol{r}'_1, \omega)\}\, \varrho_i(\boldsymbol{r}_1, \boldsymbol{r}'_1, E + \hbar\omega)\end{aligned}} \tag{3.135}$$

which, thanks to equation (3.55), can also be identified to the result on Dudarev's paper (3.9).

3.4.4.2 Second case: Retarded interaction kernel

The retarded interaction $\hat{V}^{\mathrm{R}}$ between the electron and the particle is given by the minimal coupling Hamiltonian:

$$\langle\psi_f|\, \hat{V}^{\mathrm{R}}(\boldsymbol{r}, t)\, |\psi_i\rangle = -\frac{e}{m}\, \langle\psi_f|\, \mathrm{A}^\mu(\boldsymbol{r}, t) p_\mu\, |\psi_i\rangle = -\frac{i\hbar e}{m}\, \langle\psi_f|\, \mathrm{A}^\mu(\boldsymbol{r}, t)\partial_\mu\, |\psi_i\rangle \tag{3.136}$$

where A^μ is the 4-potential associated with the excitations in the nano-particle and p_μ is the probe electron 4-impulsion operator. Moreover, within the linear response theory, the photon propagator can also be connected to the 4-potential correlation function which gives [193]:

$$\mathcal{D}^\nu_\mu(\boldsymbol{r}, \boldsymbol{r}', t, t') = -\frac{i}{\hbar}\theta(t - t')\, \langle 0|[\mathrm{A}_\mu(\boldsymbol{r}, t), \mathrm{A}^\nu(\boldsymbol{r}', t')]|0\rangle \tag{3.137}$$

where $\mathcal{D}$ is the exact propagator of the EM field (taking into account the polarizability of the medium) which has been calculated using a Dyson development in section 3.3.2.2. By strict analogy with formula (3.40) and (3.42), we obtain:

$$\mathrm{Im}\left\{-\mathcal{D}^\nu_\mu(\boldsymbol{r}, \boldsymbol{r}', \omega)\right\} = \frac{2\pi}{\hbar}\sum_n \langle 0|\, \mathrm{A}_\mu(\boldsymbol{r})\, |n\rangle\, \langle n|\, \mathrm{A}^\nu(\boldsymbol{r}')\, |0\rangle\, \delta(\omega + \omega_n - \omega_0) \tag{3.138}$$

The Fourier transform of C^{R} can be done in the exact same way as the quasi-static case and leads to:

$$\hat{C}^{\mathrm{R}}(\boldsymbol{r}_1, \boldsymbol{r}'_1, -\omega) = \mathrm{Im}\big\{-\mathcal{D}^\nu_\mu(\boldsymbol{r}_1, \boldsymbol{r}'_1, \omega)\big\}\partial^\mu\partial'_\nu \tag{3.139}$$

Thus, plugging it in (3.128), we finally obtain:

$$\begin{aligned}\varrho_f(\boldsymbol{r}, \boldsymbol{r}', E) = \varrho_0(\boldsymbol{r}, \boldsymbol{r}', E) + \frac{\hbar^2 e^2}{m^2}\int d\boldsymbol{r}_1 d\boldsymbol{r}'_1\, \mathcal{U}(\boldsymbol{r}, \boldsymbol{r}_1, E)\mathcal{U}^\dagger(\boldsymbol{r}'\boldsymbol{r}'_1, E) \\ \times \int d\omega\, \mathrm{Im}\big\{-\mathcal{D}^\nu_\mu(\boldsymbol{r}_1, \boldsymbol{r}'_1, \omega)\big\}\partial^\mu\partial'_\nu\, \varrho_i(\boldsymbol{r}_1, \boldsymbol{r}'_1, E + \hbar\omega)\end{aligned} \tag{3.140}$$

we can now expand the sums over μ and ν with respect to the spatial and temporal coordinates as we did in equations (3.74); we will obtain four terms respectively involving $\mathcal{D}^0_0$, $\mathcal{D}^i_0$, $\mathcal{D}^0_j$ and $\mathcal{D}^i_j$. We now move to the temporal gauge $\phi = 0$ where, as we explained in section 3.2.4 and detailed in [192], the temporal part of the vacuum photon propagator cancels $\mathrm{D}^0_0 = \mathrm{D}^0_j = \mathrm{D}^i_0 = 0$. Using the Dyson developments (3.70) and the expression of the Green dyadic (3.84), equation (3.140) can be directly reduced to:

$$\begin{aligned}\varrho_f(\boldsymbol{r}, \boldsymbol{r}', E) = \varrho_0(\boldsymbol{r}, \boldsymbol{r}', E) + \frac{\hbar^2 e^2}{m^2}\int d\boldsymbol{r}_1 d\boldsymbol{r}'_1\, \mathcal{U}(\boldsymbol{r}, \boldsymbol{r}_1, E)\mathcal{U}^\dagger(\boldsymbol{r}'\boldsymbol{r}'_1, E) \\ \times \int d\omega\, \mathrm{Im}\Big\{-\overleftrightarrow{\boldsymbol{G}}(\boldsymbol{r}_1, \boldsymbol{r}'_1, \omega)\Big\}\boldsymbol{\nabla}\boldsymbol{\nabla}'\varrho_i(\boldsymbol{r}_1, \boldsymbol{r}'_1, E + \hbar\omega)\end{aligned} \tag{3.141}$$

All the quantities involved in the latter equation being gauge-independent, expression (3.141) must be valid in the general case of arbitrary gauge. This expression could also be derived by applying the continuity equation for the probability current in equation (3.140) and by using the Green theorem (3.82).

Equations (3.135), (3.140) and (3.141) are the essential results of this section. Before concluding, we will apply them to the case of electron energy loss spectroscopy.

3.5 Single scattering approximation: application to electron energy loss experiments

We now want to apply the previous results to the specific case of electron energy loss spectroscopy. We will therefore make furthers approximations:

1. The first term of the right hand side of equation (3.128) describes the elastic part of the interaction. As we are going to discuss EELS experiment in the following, we will not consider this term.
2. As done by Schattschneider, Nelhiebel and Jouffrey [18], we will consider a monochromatic electron, of energy $\hbar\epsilon_0$ and density matrix ϱ_i, interacting a single time with the sample. It enables us to replace $\mathcal{U}$ by the free space electron Green functions U_0.
3. As we are now interested in energy-resolved quantity, we remove the integral over ω.

Under these assumptions equation (3.128) reads:

$$\varrho_f(\boldsymbol{r},\boldsymbol{r}',\epsilon_f) = \int d\boldsymbol{x}d\boldsymbol{x}'\, U_0(\boldsymbol{r},\boldsymbol{x},\epsilon_f)\, U_0^*(\boldsymbol{r}',\boldsymbol{x}',\epsilon_f)\hat{C}(\boldsymbol{x},\boldsymbol{x}',\omega)\, \varrho_i(\boldsymbol{x},\boldsymbol{x}',\epsilon_f+\hbar\omega) \tag{3.142}$$

where we intentionally do not specify the operator $\hat{C}$ in order to not lose generality as both the quasi-static and retarded interactions can be used indifferently.

3.5.1 Electron energy loss probability

From equation (3.142), one can deduce the wave-optical EELS probability (3.4) and (3.6). To do so, we first decompose the final density matrix as (3.8):

$$\varrho_f(\boldsymbol{r},\boldsymbol{r}',\epsilon_f) = \sum_n p_n\psi_n(\boldsymbol{r})\psi_n^*(\boldsymbol{r}')\delta(\epsilon_n-\epsilon_f) \tag{3.143}$$

while the initial electron can be considered as a monochromatic pure state[6] [18] i.e.:

$$\varrho_i(\boldsymbol{x},\boldsymbol{x}',\epsilon_0) = \psi_i(\boldsymbol{x})\psi_i^*(\boldsymbol{x}')\delta(\epsilon_i-\epsilon_f-\omega) \tag{3.144}$$

We multiply each side of equation (3.142) by $\psi_n^*(\boldsymbol{r})\psi_n(\boldsymbol{r}')$, which leads to:

$$\begin{aligned}\varrho_f(\boldsymbol{r},\boldsymbol{r}',\epsilon_f)\psi_n^*(\boldsymbol{r})\psi_n(\boldsymbol{r}') = \int d\boldsymbol{x}d\boldsymbol{x}'\, U_0(\boldsymbol{r},\boldsymbol{x},\epsilon_f)\, U_0^*(\boldsymbol{r}',\boldsymbol{x}',\epsilon_f)\hat{C}(\boldsymbol{x},\boldsymbol{x}',\omega)\\ \times\, \varrho_i(\boldsymbol{x},\boldsymbol{x}',\epsilon_0)\psi_n^*(\boldsymbol{r})\psi_n(\boldsymbol{r}')\delta(\epsilon_i-\epsilon_f-\omega)\end{aligned} \tag{3.145}$$

We now perform an integral over $\boldsymbol{r}$ and $\boldsymbol{r}'$ which leads to:

$$\begin{aligned}\int d\boldsymbol{r}d\boldsymbol{r}'\, \varrho(\boldsymbol{r},\boldsymbol{r}',\epsilon_f)\psi_n^*(\boldsymbol{r})\psi_n(\boldsymbol{r}') = \int d\boldsymbol{x}d\boldsymbol{x}'\, \left(\int d\boldsymbol{r}\, U_0(\boldsymbol{r},\boldsymbol{x},\epsilon_f)\psi_n^*(\boldsymbol{r})\right)\\ \times \left(\int d\boldsymbol{r}\, U_0^*(\boldsymbol{r}',\boldsymbol{x}',\epsilon_f)\psi_n(\boldsymbol{r}')\right)\hat{C}(\boldsymbol{x},\boldsymbol{x}',\omega)\psi_i(\boldsymbol{x})\psi_i^*(\boldsymbol{x}')\delta(\epsilon_i-\epsilon_f-\omega)\end{aligned} \tag{3.146}$$

Since the Green function U_0 is symmetric with respect to the positions $\boldsymbol{x}$ and $\boldsymbol{r}$, we have by definition of the electron propagator:

$$\int d\boldsymbol{r}\, U_0(\boldsymbol{r},\boldsymbol{x},\epsilon_f)\psi_n^*(\boldsymbol{r}) = \psi_n^*(\boldsymbol{x}) \tag{3.147}$$

Thus, we get:

$$\begin{aligned}\int d\boldsymbol{r}d\boldsymbol{r}'\, \varrho(\boldsymbol{r},\boldsymbol{r}',\epsilon_f)\psi_n^*(\boldsymbol{r})\psi_n(\boldsymbol{r}') =\\ \int d\boldsymbol{x}\, d\boldsymbol{x}'\, \psi_n^*(\boldsymbol{x})\psi_n(\boldsymbol{x}')\hat{C}(\boldsymbol{x},\boldsymbol{x}',\omega)\psi_i(\boldsymbol{x})\psi_i^*(\boldsymbol{x}')\delta(\epsilon_i-\epsilon_f-\omega)\end{aligned} \tag{3.148}$$

[6] But we could also take into account the energy spread of the source by taking a non pure state and thus studying its effect on the quality of the interference pattern.

Coming back to the definition of the density operator (3.7), one can write:

$$\varrho(\boldsymbol{r},\boldsymbol{r}',\epsilon_f) = \sum_m p_m \langle \boldsymbol{r}|\psi_m\rangle \langle \psi_m|\boldsymbol{r}'\rangle \delta(\epsilon_n - \epsilon_f) \tag{3.149}$$

Therefore, one can write:

$$\int d\boldsymbol{r}d\boldsymbol{r}'\, \varrho(\boldsymbol{r},\boldsymbol{r}',\epsilon_f)\psi_n^*(\boldsymbol{r})\psi_n(\boldsymbol{r}') = \int d\boldsymbol{r}d\boldsymbol{r}' \sum_m p_m \langle \boldsymbol{r}|\psi_m\rangle \langle \psi_m|\boldsymbol{r}'\rangle \langle \boldsymbol{r}'|\psi_n\rangle \langle \psi_n|\boldsymbol{r}\rangle \delta(\epsilon_n - \epsilon_f) \tag{3.150}$$

Using $\int d\boldsymbol{r}\, |\boldsymbol{r}\rangle \langle \boldsymbol{r}| = \mathrm{Id}$, we get:

$$\begin{aligned}
\int d\boldsymbol{r}d\boldsymbol{r}'\, \varrho(\boldsymbol{r},\boldsymbol{r}',\epsilon_f)\psi_n^*(\boldsymbol{r})\psi_n(\boldsymbol{r}') &= \int d\boldsymbol{r} \sum_m p_m \langle \boldsymbol{r}|\psi_m\rangle \langle \psi_m|\psi_n\rangle \langle \psi_n|\boldsymbol{r}\rangle \delta(\epsilon_n - \epsilon_f) && (3.151)\\
&= \int d\boldsymbol{r} \sum_m p_m \langle \boldsymbol{r}|\psi_m\rangle \langle \psi_n|\boldsymbol{r}\rangle \delta_{n,m}\delta(\epsilon_n - \epsilon_f) && (3.152)\\
&= \int d\boldsymbol{r}\, p_n \langle \boldsymbol{r}|\psi_n\rangle \langle \psi_n|\boldsymbol{r}\rangle \delta(\epsilon_n - \epsilon_f) && (3.153)
\end{aligned}$$

Replacing the latest equation in (3.148), we obtain:

$$\int d\boldsymbol{r}\, p_n \langle \boldsymbol{r}|\psi_n\rangle \langle \psi_n|\boldsymbol{r}\rangle \delta(\epsilon_n - \epsilon_f) = \int d\boldsymbol{x}\, d\boldsymbol{x}'\, \psi_n^*(\boldsymbol{x})\psi_n(\boldsymbol{x}')\hat{C}(\boldsymbol{x},\boldsymbol{x}',\omega)\psi_i(\boldsymbol{x})\psi_i^*(\boldsymbol{x}')\delta(\epsilon_i - \epsilon_f - \omega) \tag{3.154}$$

Summing over n we finally obtain:

$$\varrho(\boldsymbol{r},\boldsymbol{r},\epsilon_f) = \sum_n \int d\boldsymbol{x}\, d\boldsymbol{x}'\, \psi_n^*(\boldsymbol{x})\psi_n(\boldsymbol{x}')\hat{C}(\boldsymbol{x},\boldsymbol{x}',\omega)\psi_i(\boldsymbol{x})\psi_i^*(\boldsymbol{x}')\delta(\epsilon_i - \epsilon_f - \omega) \tag{3.155}$$

Finally, observing that $\varrho(\boldsymbol{r},\boldsymbol{r},\epsilon_f)$ is the probability of finding an electron at $\boldsymbol{r}$ with the energy ϵ_f, one can directly identify the integral as the total electron energy loss probability $\Gamma(\omega)$ and get:

$$\boxed{\Gamma(\omega) = \sum_n \int d\boldsymbol{x}\, d\boldsymbol{x}'\, \psi_n^*(\boldsymbol{x})\psi_n(\boldsymbol{x}')\hat{C}(\boldsymbol{x},\boldsymbol{x}',\omega)\psi_i(\boldsymbol{x})\psi_i^*(\boldsymbol{x}')\delta(\epsilon_i - \epsilon_f - \omega)} \tag{3.156}$$

Replacing $\hat{C}$ by either its quasi-static or the retarded form, one respectively obtain equations (3.4) and (3.6).

3.5.2 Application to the measurement of the coherence of optical fields

In the following, we will note $\boldsymbol{p}_f$ and $\boldsymbol{p}_i$ respectively the wave-vectors of the final and initial electrons. The subscript z will denote the component of vectors parallel to the propagation axis while the subscript $\perp$ denotes the plane perpendicular to z. The vector $\boldsymbol{k}$ correspond to the conjugate variable of $\boldsymbol{r}$ therefore indexing the reciprocal space. First of all, let's calculate the Fourier transform of equation (3.142) in the plane $\perp$:

$$\varrho_f\left(\boldsymbol{k}_\perp,\boldsymbol{k}'_\perp,\boldsymbol{r}_z,\boldsymbol{r}'_z\right) = \int d\boldsymbol{x}\, d\boldsymbol{x}' \mathscr{F}_{\boldsymbol{r}_\perp}\left\{U_0\left(\boldsymbol{r},\boldsymbol{x}\right)\right\} \mathscr{F}_{-\boldsymbol{r}'_\perp}\left\{U_0^*\left(\boldsymbol{r},\boldsymbol{x}\right)\right\} \hat{C}\left(\boldsymbol{x},\boldsymbol{x}',\omega\right) \varrho_i\left(\boldsymbol{x},\boldsymbol{x}'\right) \tag{3.157}$$

where for brevity we omitted the energy in the argument of the density matrices. The free particle Green function reads [18]:

$$U_0\left(\boldsymbol{r},\boldsymbol{x}\right) = -\frac{m}{2\pi\hbar^2}\frac{e^{ip_f|\boldsymbol{r}-\boldsymbol{x}|}}{|\boldsymbol{r}-\boldsymbol{x}|} \tag{3.158}$$

Therefore its Fourier transform is given by [17, 18]:

$$\mathscr{F}_{\boldsymbol{r}_\perp}\left\{U_0\left(\boldsymbol{r},\boldsymbol{x}\right)\right\} = \mathscr{F}^*_{-\boldsymbol{r}'_\perp}\left\{U_0^*\left(\boldsymbol{r},\boldsymbol{x}\right)\right\} = \frac{-im}{\hbar^2 p_{f,z}} e^{-i\boldsymbol{k}_\perp.\boldsymbol{x}} e^{ip_{f,z}(r_z - x_z)} \tag{3.159}$$

The latter inserted in equation (3.157) gives:

$$\varrho_f\left(\boldsymbol{k}_\perp, \boldsymbol{k}'_\perp, \boldsymbol{r}_z, \boldsymbol{r}'_z\right) = \frac{m^2}{\hbar^4 p_{f,z}^2} e^{ip_{f,z}(r_z - r'_z)} \int d\boldsymbol{x}\, d\boldsymbol{x}' e^{-ip_{f,z}(x_z - x'_z)} e^{-\boldsymbol{k}_\perp.\boldsymbol{x}} e^{\boldsymbol{k}'_\perp.\boldsymbol{x}'} \hat{C}\left(\boldsymbol{x}, \boldsymbol{x}', \omega\right) \varrho_i\left(\boldsymbol{x}, \boldsymbol{x}'\right) \tag{3.160}$$

Now the Fourier transforms with respect to r_z and r'_z become trivial and give:

$$\begin{aligned}\varrho_f\left(\boldsymbol{k}_\perp, \boldsymbol{k}'_\perp, \boldsymbol{k}_z, \boldsymbol{k}'_z\right) = \frac{4\pi^2 m^2}{\hbar^4 p_{f,z}^2} \delta(k_z - p_{f,z})\delta(k'_z - p_{f,z}) \\ \times \int d\boldsymbol{x}\, d\boldsymbol{x}' e^{-ip_{f,z}(x_z - x'_z)} e^{-\boldsymbol{k}_\perp.\boldsymbol{x}} e^{\boldsymbol{k}'_\perp.\boldsymbol{x}'} \hat{C}\left(\boldsymbol{x}, \boldsymbol{x}', \omega\right) \varrho_i\left(\boldsymbol{x}, \boldsymbol{x}'\right)\end{aligned} \tag{3.161}$$

We can integrate over the variables $\boldsymbol{k}_z$ and $\boldsymbol{k}'_z$ as they are not observed experimentally [18]:

$$\varrho_f\left(\boldsymbol{k}_\perp, \boldsymbol{k}'_\perp\right) = \frac{4\pi^2}{\hbar^2 v^2} \int d\boldsymbol{x}\, d\boldsymbol{x}' e^{-ip_{f,z}(x_z - x'_z)} e^{-\boldsymbol{k}_\perp.\boldsymbol{x}} e^{\boldsymbol{k}'_\perp.\boldsymbol{x}'} \hat{C}\left(\boldsymbol{x}, \boldsymbol{x}', \omega\right) \varrho_i\left(\boldsymbol{x}, \boldsymbol{x}'\right) \tag{3.162}$$

where we used $p_{f,z} \approx mv/\hbar$. We now consider the case of the retarded interaction and again make use of the paraxial approximation but in a slightly different formulation:

$$\varrho_i\left(\boldsymbol{x}, \boldsymbol{x}'\right) = \frac{1}{L} \rho^e_{i,\perp}\left(\boldsymbol{x}_\perp, \boldsymbol{x}'_\perp\right) e^{ip_{i,z}x_z} e^{-ip_{i,z}x'_z} \tag{3.163}$$

Moreover the incident electron kinetic energy being principally contained in its z-component, one can write [19]:

$$\boldsymbol{\nabla}\psi_i(\boldsymbol{r}) \approx \psi_i(\boldsymbol{r}) i k_i \hat{z} = \frac{imv}{\hbar}\psi_i(\boldsymbol{r})\hat{z} \tag{3.164}$$

Plugging equations (3.163), (3.164) and the retarded form of K in (3.162), one gets:

$$\begin{aligned}\varrho_f\left(\boldsymbol{k}_\perp, \boldsymbol{k}'_\perp\right) = \frac{4\pi^2 e^2}{L\hbar^2} \int d\boldsymbol{x}\, d\boldsymbol{x}' \mathrm{Im}\{-G_{zz}(\boldsymbol{x}, \boldsymbol{x}', \omega)\} \varrho_i\left(\boldsymbol{x}_\perp, \boldsymbol{x}'_\perp\right) \\ \times e^{-i(p_{f,z} - p_{i,z})x_z}\ e^{i(p_{f,z} - p_{i,z})x'_z}\ e^{-\boldsymbol{k}_\perp.\boldsymbol{x}}\ e^{\boldsymbol{k}'_\perp.\boldsymbol{x}'}\end{aligned} \tag{3.165}$$

The integration over x_z and x'_z gives:

$$\varrho_f\left(\boldsymbol{k}_\perp, \boldsymbol{k}'_\perp\right) = \frac{4\pi^2 e^2}{L\hbar^2} \int d\boldsymbol{x}\, d\boldsymbol{x}' \mathrm{Im}\{-G_{zz}(\boldsymbol{x}_\perp, \boldsymbol{x}'_\perp, \omega)\} \varrho_i\left(\boldsymbol{x}_\perp, \boldsymbol{x}'_\perp, q, -q,\right)\ e^{-\boldsymbol{k}_\perp.\boldsymbol{x}}\ e^{\boldsymbol{k}'_\perp.\boldsymbol{x}'} \tag{3.166}$$

Using the definition of the CDOS, one can then conclude that:

$$\varrho_f\left(\boldsymbol{k}_\perp, \boldsymbol{k}'_\perp\right) = \frac{2\pi^3 e^2}{L\hbar^2\omega} \int d\boldsymbol{x}\, d\boldsymbol{x}' \rho_{zz}(\boldsymbol{x}_\perp, \boldsymbol{x}'_\perp, q, -q, \omega) \varrho_i\left(\boldsymbol{x}_\perp, \boldsymbol{x}'_\perp\right)\ e^{-\boldsymbol{k}_\perp.\boldsymbol{x}}\ e^{\boldsymbol{k}'_\perp.\boldsymbol{x}'} \tag{3.167}$$

which simply reads:

$$\varrho_f\left(\boldsymbol{k}_\perp, \boldsymbol{k}'_\perp\right) = \frac{2\pi^3 e^2}{L\hbar^2\omega}\ \rho_{zz}(\boldsymbol{k}_\perp, \boldsymbol{k}'_\perp, q, -q, \omega) * \varrho_i\left(\boldsymbol{k}_\perp, \boldsymbol{k}'_\perp\right) \tag{3.168}$$

Finally, one can come back in the real space and deduce the rather elegant formula:

$$\varrho_f\left(\boldsymbol{r}_\perp, \boldsymbol{r}'_\perp\right) = \frac{2\pi^3 e^2}{L\hbar^2\omega}\ \rho_{zz}(\boldsymbol{r}_\perp, \boldsymbol{r}'_\perp, q, -q, \omega)\ \varrho_i\left(\boldsymbol{r}_\perp, \boldsymbol{r}'_\perp\right) \tag{3.169}$$

As we discussed in the introductory chapter, Agarwal demonstrated [95], using the fluctuation-dissipation theorem, that the CDOS is proportional to the electromagnetic correlation function. Thus, equation (3.169) shows that, when an electron is scattered by an optical field, *the electromagnetic correlations are imprinted in the coherence properties of the electron beam.* Producing electronic interferences thus constitutes a measurement of these correlations.

Formula (3.169) should remind a standard result of electron holography; indeed, during an inelastic interaction and for small scattering angles, the final and initial density matrices are connected by the relation [188]:

$$\varrho_f(\boldsymbol{r}_\perp, \boldsymbol{r}'_\perp, E - \hbar\omega) = T(\boldsymbol{r}_\perp, \boldsymbol{r}'_\perp, \hbar\omega)\ \varrho_i(\boldsymbol{r}_\perp, \boldsymbol{r}'_\perp, E) \tag{3.170}$$

where $T(\boldsymbol{r}_\perp, \boldsymbol{r}'_\perp, \hbar\omega)$ is the so-called *mutual object transparency* which only depends on the scatterer and the energy loss $\hbar\omega$. In the quasistatic limit, Kohl and Rose showed that the mutual object transparency corresponds to the MDFF [190]. **Equation (3.169) is basically the extension to the retarded case of their results and show that in this case, the mutual object transparency corresponds to the CDOS**.

The formalism recalled or developed here is the building block of inelastic electron holography. Such an experiment can be schematized in three steps:

1. We prepare an initial electron state which density matrix $\varrho_i(\boldsymbol{r}_\perp, \boldsymbol{r}'_\perp, E)$ corresponds to a pure state. In standard off-axis electron holography, it simply corresponds to a plane-wave but, with modern phase-shaping techniques, it could corresponds to e.g. a vortex with a pure OAM.

2. The initial electron states is scattered by the sample to a set of final states. After an energy loss $\hbar\omega$ and for small scattering angle, the final density matrix is given by $\varrho_f(E - \hbar\omega) = T(\hbar\omega)\ \varrho_i(E)$ where the mutual object transparency corresponds: (1) to electronic charge correlation in the quasi-static regime or (2) to photon correlation in the retarded regime. In other words, the scattering event imprints the signature of the correlations in the target onto the beam density matrix. The final density matrix does not correspond to a pure state anymore but rather to mixed electron states i.e. a partially coherent wave [188]. The out-of-diagonal elements of the density matrix, which modulus gives the mutual coherence of the field [189], encodes the correlations in the scatterer.

3. We produce interferences in order to retrieve these off-diagonal elements and therefore obtain information on the electronic or photonic correlations in the target.

3.5.3 The self-energy formalism

In 1987, Echenique and collaborators demonstrated (3.4) using a different approach based on the calculation of the probe electron self-energy [16]. Their formalism have the advantage to be compact and easily applicable although they did not provide details of the demonstration in their paper. Here, we briefly demonstrate that their equation can be formally derived from our latter developments. Indeed, in section (3.4.2), we calculated the self energy $\hat{\Sigma}$ of the electron and obtained:

$$\hat{\Sigma}(\boldsymbol{r}, \boldsymbol{r}', t, t') = \hat{U}_0(\boldsymbol{r}, \boldsymbol{r}', t, t')\hat{C}(\boldsymbol{r}, \boldsymbol{r}', t, t') \tag{3.171}$$

where we recall that $\hat{C}(\boldsymbol{r}, \boldsymbol{r}', t, t') = \langle \mathcal{T}\{\hat{V}(\boldsymbol{r}, t)\hat{V}(\boldsymbol{r}, t)\}\rangle$. Since all the quantities above only depend on $t - t'$, Fourier transforming the latter expression will give the following convolution product:

$$\hat{\Sigma}(\boldsymbol{r}, \boldsymbol{r}', E) = \int d\omega\ \hat{U}_0(\boldsymbol{r}, \boldsymbol{r}', E + \hbar\omega)\hat{C}(\boldsymbol{r}, \boldsymbol{r}', -\hbar\omega) \tag{3.172}$$

Moreover, the Fourier transform of the electron propagator is simply [17]:

$$\hat{U}_0(\boldsymbol{r}, \boldsymbol{r}', E + \hbar\omega) = \frac{1}{E + \hbar\omega - \hat{H}_e + i0^+} \tag{3.173}$$

Therefore, the self-energy in the spectral domain reads:

$$\boxed{\hat{\Sigma}(\boldsymbol{r}, \boldsymbol{r}', E) = \int d\omega\ \frac{\hat{C}(\boldsymbol{r}, \boldsymbol{r}', -\hbar\omega)}{E + \hbar\omega - \hat{H}_e + i0^+}} \tag{3.174}$$

The mean energy Σ_0 of an electron of wavefunction $|\psi_0\rangle$ and energy E_0 can then be written as:

$$\Sigma_0 = \langle\psi_0|\hat{\Sigma}|\psi_0\rangle \tag{3.175}$$

Inserting the completeness relation $\sum_f |\psi_f\rangle \langle\psi_f| = 1$ for a basis of final states and two others for the $\{|r\rangle\}$ and $\{|r'\rangle\}$ basis, we obtain:

$$\Sigma_0 = \sum_f \int d\boldsymbol{r}\, d\boldsymbol{r}' \, \frac{\psi_0(\boldsymbol{r})\psi_0^*(\boldsymbol{r}')\hat{C}(\boldsymbol{r},\boldsymbol{r}',-\hbar\omega)\psi_f(\boldsymbol{r}')\psi_f^*(\boldsymbol{r})}{E+\hbar\omega-E_0+i0^+} \tag{3.176}$$

Replacing $\hat{C}$ by its quasi-static form, we obtain the equation (3) of Echenique et al. [16]. Even more interestingly, if we replace $\hat{C}$ by its retarded form, we obtain the retarded form of the self-energy formalism of Echenique et al.

3.5.4 Relativistic anisotropy in inelastic scattering

In this section, we give a brief insight on how our formalism could be used in core-loss spectroscopy, although it is not the main topic of this chapter. In their remarkable paper [181], Schattschneider and collaborators have shown how relativistic corrections would modify the inelastic scattering cross section and particularly modify the value of the magic angle. Here, we connect our theory to formula (12) of their paper. Let's highlight that the following demonstration is still fledgling and further verifications are required before having a final form of the formula. We simply aim at giving an idea of the demonstration.
Equation (3.156) with the retarded kernel reads:

$$\Gamma(\omega) = \sum_f \int d\boldsymbol{x}\, d\boldsymbol{x}' \, \psi_f^*(\boldsymbol{x})\psi_f(\boldsymbol{x}')\mathrm{Im}\{-\mathcal{D}_\mu^\nu(\boldsymbol{x},\boldsymbol{x}',\omega)\}\partial^\mu\partial'_\nu \, \psi_i(\boldsymbol{x})\psi_i^*(\boldsymbol{x}')\delta(\epsilon_i-\epsilon_f-\omega) \tag{3.177}$$

Expanding the sum over μ and ν and keeping only the purely temporal and spatial terms, we get:

$$\begin{aligned}\Gamma(\omega) = &\frac{\omega^2}{c^2}\sum_f \int d\boldsymbol{x}\, d\boldsymbol{x}' \, \psi_f^*(\boldsymbol{x})\psi_f(\boldsymbol{x}')\mathrm{Im}\{-\mathcal{D}_0^0(\boldsymbol{x},\boldsymbol{x}',\omega)\} \, \psi_i(\boldsymbol{x})\psi_i^*(\boldsymbol{x}')\delta(\epsilon_i-\epsilon_f-\omega)\\ &+\frac{m^2v^2}{\hbar^2}\sum_f \int d\boldsymbol{x}\, d\boldsymbol{x}' \, \psi_f^*(\boldsymbol{x})\psi_f(\boldsymbol{x}')\mathrm{Im}\{-\mathcal{D}_{zz}(\boldsymbol{x},\boldsymbol{x}',\omega)\} \, \psi_i(\boldsymbol{x})\psi_i^*(\boldsymbol{x}')\delta(\epsilon_i-\epsilon_f-\omega)\end{aligned} \tag{3.178}$$

where we used approximation (3.164) to treat the spatial derivatives. Now, we consider that both the incident and outgoing electrons correspond to planewaves of respective wavevector $\boldsymbol{k}_i$ and $\boldsymbol{k}_f$. We then obtain:

$$\begin{aligned}\Gamma(\omega) = &\frac{\omega^2}{c^2}\sum_f \int d\boldsymbol{x}\, d\boldsymbol{x}' \, \mathrm{Im}\{-\mathcal{D}_0^0(\boldsymbol{x},\boldsymbol{x}',\omega)\} \, e^{(\boldsymbol{k}_f-\boldsymbol{k}_i)(\boldsymbol{x}-\boldsymbol{x}')}\delta(\epsilon_i-\epsilon_f-\omega)\\ &+\frac{m^2v^2}{\hbar^2}\sum_f \int d\boldsymbol{x}\, d\boldsymbol{x}' \, \mathrm{Im}\{-\mathcal{D}_{zz}(\boldsymbol{x},\boldsymbol{x}',\omega)\} \, e^{(\boldsymbol{k}_f-\boldsymbol{k}_i)(\boldsymbol{x}-\boldsymbol{x}')}\delta(\epsilon_i-\epsilon_f-\omega)\end{aligned} \tag{3.179}$$

We now note $\boldsymbol{q} = \boldsymbol{k}_f - \boldsymbol{k}_i$ and place ourselves in the Lorenz gauge. Following [173], the double differential cross section $\partial^2\sigma/\partial\omega\partial\Omega$ and the EELS probability must be related through:

$$\Gamma(\omega) = \frac{1}{\hbar}\sum_{k_f}\frac{\partial^2\sigma}{\partial\omega\partial\Omega}\delta(\epsilon_i-\epsilon_f-\omega) \tag{3.180}$$

So that:

$$\begin{aligned}\frac{\partial^2\sigma}{\partial\omega\partial\Omega} = &\frac{\omega^2}{\hbar c^2}\int d\boldsymbol{x}\, d\boldsymbol{x}' \, \mathrm{Im}\{-\mathcal{D}_0^0(\boldsymbol{x},\boldsymbol{x}',\omega)\} \, e^{\boldsymbol{q}(\boldsymbol{x}-\boldsymbol{x}')}\\ &+\frac{m^2v^2}{\hbar^3}\int d\boldsymbol{x}\, d\boldsymbol{x}' \, \mathrm{Im}\{-\mathcal{D}_3^3(\boldsymbol{x},\boldsymbol{x}',\omega)\} \, e^{\boldsymbol{q}(\boldsymbol{x}-\boldsymbol{x}')}\end{aligned} \tag{3.181}$$

and we moreover have:

$$\begin{cases}\mathcal{D}_0^0(\boldsymbol{x},\boldsymbol{x}',\omega) = \displaystyle\int d\boldsymbol{x}_1 d\boldsymbol{x}_2 \mathrm{D}_0^0(\boldsymbol{x}-\boldsymbol{x}_1,\omega)\chi_0^0(\boldsymbol{x}_1,\boldsymbol{x}_2,\omega)\mathrm{D}_0^0(\boldsymbol{x}_2-\boldsymbol{x}',\omega) & (3.182\text{a})\\ \mathcal{D}_3^3(\boldsymbol{x},\boldsymbol{x}',\omega) = \displaystyle\int d\boldsymbol{x}_1 d\boldsymbol{x}_2 \mathrm{D}_3^3(\boldsymbol{x}-\boldsymbol{x}_1,\omega)\chi_3^3(\boldsymbol{x}_1,\boldsymbol{x}_2,\omega)\mathrm{D}_3^3(\boldsymbol{x}_2-\boldsymbol{x}',\omega) & (3.182\text{b})\end{cases}$$

where the susceptibilities have been calculated in section (3.3):

$$\begin{cases} \chi_0^0(\boldsymbol{x},\boldsymbol{x}',\omega) = \dfrac{2}{\hbar}\displaystyle\sum_n \langle 0|\,\mathfrak{n}(\boldsymbol{x})\,|n\rangle\,\langle n|\,\mathfrak{n}(\boldsymbol{x}')\,|0\rangle \left(\mathcal{P}\left(\tfrac{1}{\omega+\omega_n-\omega_0}\right) - i\pi\delta(\omega+\omega_n-\omega_0)\right) & \text{(3.183a)} \\ \chi_3^3(\boldsymbol{x},\boldsymbol{x}',\omega) = \dfrac{2}{\hbar}\displaystyle\sum_n \langle 0|\,j_z(\boldsymbol{x})\,|n\rangle\,\langle n|\,j_z(\boldsymbol{x}')\,|0\rangle \left(\mathcal{P}\left(\tfrac{1}{\omega+\omega_n-\omega_0}\right) - i\pi\delta(\omega+\omega_n-\omega_0)\right) & \text{(3.183b)} \end{cases}$$

The Fourier transforms of the photon propagators will give two $1/(q^2-\omega^2/c^2)$ terms. We therefore obtain:

$$\begin{aligned} \frac{\partial^2\sigma}{\partial\omega\partial\Omega} = \frac{2\pi\omega^2}{\hbar^2c^2}\left(\frac{1}{q^2-\frac{\omega^2}{c^2}}\right)^2 \sum_n \left|\langle n|\,\mathfrak{n}(\boldsymbol{q})\,|0\rangle\right|^2 \delta(\omega+\omega_n-\omega_0) \\ + \frac{2\pi m^2v^2}{\hbar^4}\left(\frac{1}{q^2-\frac{\omega^2}{c^2}}\right)^2 \sum_n \left|\langle n|\,j_z(\boldsymbol{q})\,|0\rangle\right|^2 \delta(\omega+\omega_n-\omega_0) \end{aligned} \tag{3.184}$$

Now assuming a point target we can write $\mathfrak{n}(\boldsymbol{r}) = e\delta(\boldsymbol{r}-\boldsymbol{R})$ and $\boldsymbol{j} = e\delta(\boldsymbol{r}-\boldsymbol{R})\boldsymbol{v} = \delta(\boldsymbol{r}-\boldsymbol{R})\dfrac{\boldsymbol{p}}{m_a}$ where m_a is the mass of the target, we get:

$$\begin{aligned} \frac{\partial^2\sigma}{\partial\omega\partial\Omega} = \frac{e^2 2\pi\omega^2}{\hbar^2c^2}\left(\frac{1}{q^2-\frac{\omega^2}{c^2}}\right)^2 \sum_n \left|\langle n|\,e^{i\boldsymbol{q}.\boldsymbol{R}}\,|0\rangle\right|^2 \delta(\omega+\omega_n-\omega_0) \\ + \frac{e^2 2\pi m^2v^2}{\hbar^4}\left(\frac{1}{q^2-\frac{\omega^2}{c^2}}\right)^2 \sum_n \left|\langle n|\,\frac{p_z}{m_a}e^{i\boldsymbol{q}.\boldsymbol{R}}\,|0\rangle\right|^2 \delta(\omega+\omega_n-\omega_0) \end{aligned} \tag{3.185}$$

which closely ressemble equation (12) of [181] which reads:

$$\frac{\partial^2\sigma}{\partial\omega\partial\Omega} = \left(\frac{2\gamma me^2}{\hbar^2}\right)^2 \left(\frac{1}{q^2-\frac{\omega^2}{c^2}}\right)^2 \frac{k_f}{k_i}\sum_{i,n}\left|\langle n|\,e^{i\boldsymbol{q}.\boldsymbol{R}}\left(1-\frac{\boldsymbol{p}.\boldsymbol{v}_0}{mc^2}\right)|i\rangle\right|^2 \delta(\omega+\omega_n-\omega_i) \tag{3.186}$$

where γ is the Lorentz factor, m and $\boldsymbol{v}_0$ are the mass and the velocity (oriented along z) of the electron and they considered different possible initial states of the target $\{\omega_i, |i\rangle\}$. All the other notations matches ours. Nevertheless, further checking are required (particularly the prefactors) before having a definite form of the latter formula.

3.6 Summary and perspectives

Summary of the main results

To this date, several developments of a wave theory of EELS have been proposed in the literature based on different types of formalism and assumptions. Roughly speaking, three types of approaches exist: **(1)** a quasi-static self-energy formalism proposed by Echenique [16], **(2)** a quasi-static density matrix approach first introduced to diffraction by Dudarev [17] and then extended to EELS by Schattschneider [18], **(3)** a retarded linear response theory proposed by García de Abajo [19]. In this chapter we thus have:

1. Rationalized all these different approaches and demonstrate how all these works are connected between each other.
2. Extended the formalism of Echenique and Schattschneider to the retarded case in order to model e.g. electron holography experiments on optical systems.

First of all, in section 3.3, we have connected the propagator for the EM field to the linear response function of a polarizable material both in the quasi-static and retarded regime. We demonstrated that:

- **In the quasi-static regime**, the CDOS and the MDFF are proportional up to two Coulomb propagators, see equation (3.56). Thus, in this limit, the electric field correlations simply reproduce the electronic charge correlations in the target.
- **In the retarded regime**, the Green dyadic is the sum of two terms: (1) a charge-charge correlator multiplied by two vacuum EM propagators and (2) a current-current correlator multiplied by two vacuum EM propagators, see equation (3.87). Consequently in this limit, the electric field correlations arise from a combination of electronic charge and current correlations in the target.

In section 3.4, we have applied the latter results in order to extend the kinetic equation to the retarded case. Eventually, and following the seminal demonstration of Dudarev et al [17], we have shown that the retarded kernel is given either by the CDOS or by the imaginary part of the photon propagator, see equations (3.140) and (3.141).

Finally, in section 3.5 we applied the latter formalism to EELS as it is of main interest for the rest of this thesis. First of all, we connected our present developments to the linear-response formalism of García de Abajo [19] and to the self-energy formalism of Echenique [16]. This way, we generalized their approach to the retarded case. Finally, we show how the fundamental principles of electron holography could be extended to the retarded case as summed up on the following table:

Quantity	**Quasi-static**	**Retarded**
Correlations	Electronic	Photonic
Fluctuation-dissipation formalism	Van Hove [200]	Agarwal [95]
Linear-response function	(3.56)	(3.87)
Kinetic equation	(3.135)	(3.140), (3.141)
Mutual object transparency	MDFF, $S(\boldsymbol{k}, \boldsymbol{k}', \omega)$	CDOS, $\rho(\boldsymbol{r}, \boldsymbol{r}', \omega)$

In this chapter, we tried to rationalize, as far as possible, the different results found in the literature. We hope that this work will facilitate the comparison between the different theoretical and experimental results, particularly in the case of EELS.

Moreover, the theory of inelastic electron scattering is strongly established in the quasi-static case [196] and the essence of this chapter was to show how one could generalize it to the retarded case. Quite remarkably, this somehow more general formalism could be applied to model both valence and core-loss spectroscopy experiments. For example our formalism could be employed to:

- Interpret core-loss spectroscopy experiments in terms of photon exchange thus enabling a direct comparison with inelastic X-ray scattering. Such a comparison is exactly analogue to the standard analogy between EELS and optical extinction experiments on plasmons [119].
- Apply all the powerful tools developed for electron holography [210, 188] to the nano-photonics. Particularly, recent developments in differential phase contrast or ptychography for plasmonics should be described with this language.
- Model EELS experiments in the retarded regime with ab-initio calculations. This could be applied to calculate the response e.g. of guided modes or to investigate the quantum behavior of LSPs.

We recently started a collaboration with Axel Lubk from Dresden university in order to connect these developments to a Klein-Gordon formalism and thus justify, from the most fundamental principles, the physical origin of relativistic effects.

Chapter 4

Measuring surface plasmons with phase-shaped electron beams

Contents

4.1 Introduction **82**
4.1.1 Missing information in conventional electron-energy loss spectroscopy . 82
4.1.2 Phase manipulation in the electron microscope 84
4.1.2.1 Vortex electron states 84
4.1.2.2 Generation of vortex in a TEM, phase-shaping techniques . . 86
4.1.2.3 Other types of phase structured electron beams 87
4.1.3 Structure of the chapter 88
4.2 Semi-classical and quasi-static transition probability: analogy with atomic physics **88**
4.2.1 Derivation of the loss probability 88
4.2.2 Selection rules and peculiarity of PSEELS 90
4.2.3 Polarizer effect using a Hermite-Gaussian beam 92
4.3 First experimental demonstration **94**
4.4 Application of phase-shaped EELS to actual problems in plasmonics **95**
4.4.1 Resolution of the problems highlighted in the introduction 95
4.4.2 Selective detection of symmetries 96
4.4.3 Measurement of the potential derivative and perspective in plasmon phase retrieval 98
4.4.3.1 Measurement of the potential derivative 98
4.4.3.2 Perspective in phase reconstruction 99
4.4.4 Measurement of the azimuthal symmetry with vortex beams 100
4.4.5 Dichroic EELS mapping with point vortex probes 102
4.4.5.1 Connection between the Hermite-Gaussian and Laguerre-Gaussian beams 102
4.4.5.2 Dichroic EELS probability 103
4.4.5.3 Mapping the local chirality properties of surface plasmon fields 105
4.5 Post-selection of the final state **106**
4.5.1 Influence of the collection angle 106
4.5.2 Selection of the final state: basis change 109
4.5.3 Example: measurement of the OAM carried by a vortex plasmon 109
4.6 Measurement of the coherence at the nanometer scale **111**
4.6.1 Electron bi-prism 111
4.6.2 Split-beam electron energy loss probability 112

4.6.3 Coherence measurement 113
4.6.4 Double bi-prism experiment 114
4.7 Summary and perspectives 114

4.1 Introduction

4.1.1 Missing information in conventional electron-energy loss spectroscopy

In chapter 2, we presented the electron energy-loss spectroscopy and showed that, in the case of a quasi-static plasmon field and assuming a point-like electron probe, the measured electron energy loss probability is given by the formula:

$$\Gamma^{\mathrm{QS}}(\omega, \boldsymbol{r}_\perp) = \frac{e^2}{\omega^2 \hbar} \sum_n \mathrm{Im}\left\{-g_n(\omega)\right\} |E_n^z(\boldsymbol{r}_\perp, q_z)|^2 \tag{4.1}$$

where the superscript "QS" indicates that this equation is only valid in the quasi-static limit. Alternatively, by using the relation $E_n^z(\boldsymbol{r}_\perp, q) = -iq\phi_n(\boldsymbol{r}, q)$, this equation can also be written:

$$\Gamma^{\mathrm{QS}}(\omega, \boldsymbol{r}_\perp) = \frac{e^2}{v^2 \hbar} \sum_n \mathrm{Im}\left\{-g_n(\omega)\right\} |\phi_n(\boldsymbol{r}_\perp, q_z)|^2 \tag{4.2}$$

where, as a reminder, the sum runs over the LSP's eigenmodes, $g_n(\omega)$ is the spectral function associated with mode n and ϕ_n is the corresponding eigenpotential. The potential (or equivalently the electric field) is Fourier transformed along the z direction which corresponds to the propagation axis of the electron.

Due to the great spatial and spectral resolution of modern electron microscopes, EELS has been used to study a large variety of plasmonic systems over the last decade with an impressive success. Nevertheless, important information on plasmon resonances cannot be resolved with this standard EELS technique.

First of all, one can see from equation (4.1) that only the component of $\boldsymbol{E}$ which is aligned with the trajectory of the electrons can be measured. This is a consequence of the fact that the in-plane component of the electric force does not work on the electrons. In other words, plasmon fields which are entirely contained in the orthogonal plane are not detected by EELS.
Although it may sound anecdotal, this situation often happens in practice e.g. in dimers. On figure 4.1(a), we show differenr EELS spectra calculated for a dimer of 400×60 nm silver nanorods separated by a 5 nm gap when the electron impinges in the gap (blue line) or at one end of the dimer (red line). One can clearly see that, when the electron impinges in the gap, the dipole mode ($n = 1$) is absent from the EELS spectrum while it is detected for the other impact parameter. The same effect is present on experimental data (see figure 4.1(d) or [211]). Therefore, at first sight, one could naively conclude that this mode does not present charges in the gap. However, looking closer to the charge distributions of the modes (figure 4.1(c)), one can see that it is not the case. We recognize the dipole bonding mode ($n = 1$) and dipole anti-bonding mode ($n = 2$). In the case of mode 1, the charges on both side of the gap have opposite signs; this situation is completely analogue to a capacitor which confines the field lines in the dimer plane i.e. $E_z = 0$ in the gap. Consequently, these regions of high field enhancement and confinement are, a priori, undetectable by standard EELS.

This situation can be problematic as these so-called "gap modes" are of major interest in terms of applications. A solution, illustrated on figure 4.1(b) is to tilt the sample to break the orthogonality between the field lines and the electrons' path. This could be pushed even further by performing a tomographic reconstruction [212] but with the price of heavy computations. Moreover, not all microscopes possess the technical specificities (large pole piece) to perform such experiments.

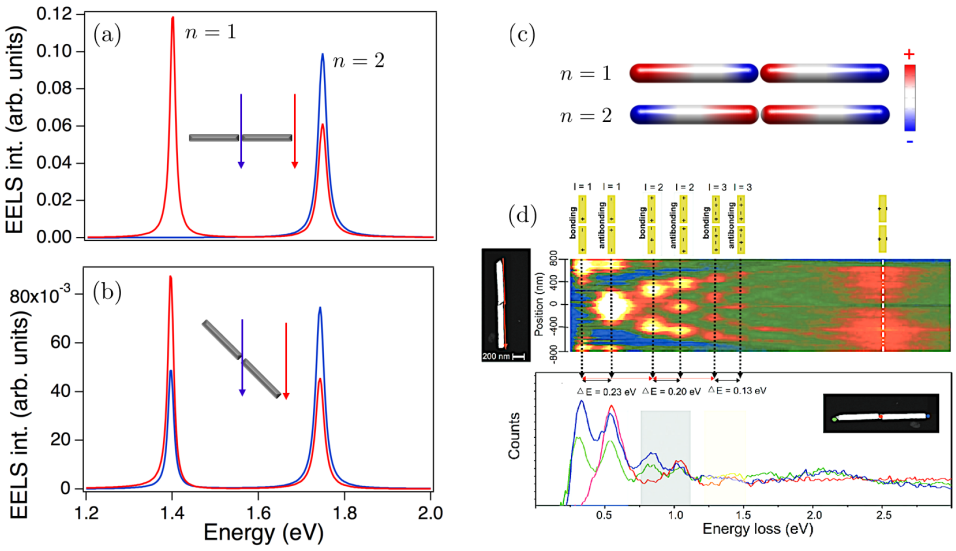

Figure 4.1: *EELS spectra calculated for a dimer of* 400×60 *nm silver nanorods separated by a 5 nm gap with: (a) the electron beam in normal incidence or (b) the electron beam impinging at 45° of the dimer axis (see insets). (c) Charge distributions associated with the two measured plasmon modes: the dipolar bonding mode* ($n = 1$) *and the the dipolar antibonding mode* ($n = 2$)*. (d) Experimental EELS spectral image and spectra acquired on a dimer of gold nanorods (reproduced from [211]).*

The second drawback of EELS is that it is insensitive to the phase of plasmon fields. Indeed, from equation (4.2), one can see that the sign of the potential is not measured which can lead to severe confusions. As an example, we plotted on figure 4.2(a-b) the charge distributions associated with the two first modes of a silver nano-square together with the corresponding simulated EELS maps on figure 4.2(c-d). One can clearly see that these modes cannot be straightforwardly distinguished from their EELS maps; this appears even more strikingly from experimental data 4.2(e-f).

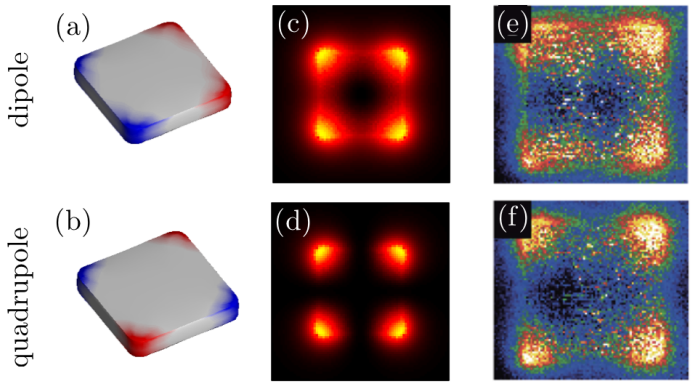

Figure 4.2: *(a-b) Surface charge densities associated with the dipole and quadrupole modes of a silver nano-square. (c-d) Simulated EELS maps corresponding respectively to the dipole and quadrupole modes. (e-f) Corresponding experimental EELS maps; reproduced from [213].*

One can argue that this ambiguity could be removed by assisting the experiment with simulations. Following this logic, in 2013, Hörl and collaborators proposed a tomographic reconstruction methods [214] based on compressed sensing reconstruction algorithm coupled with BEM calculations. In 2015, it was experimentally applied by Collins et al. to reconstruct the phase of plasmon modes

in silver bipyramids [215]. Later, Hörl and collaborators went even further by proposing [216] and experimentally demonstrating [217] a tomographic reconstruction method of the full electric Green tensor, or equivalently, of the EMLDOS.
These methods are extremely powerful as they provide *all* the information on the plasmon field in one experiment but:

- They cannot be implemented on every microscopes as tomography requires a large pole piece to allow tilting up to 45°.
- They require the acquisition of a large dataset, heavy computations and time-consuming post-treatments.

Besides, optical circular dichroism (OCD) consists in sequentially sending a left and a right-handed circularly polarized optical beam and measuring the difference between the two absorption cross sections. For plasmonics, it has been demonstrated (see e.g. [218, 219]) that the dichroic signal in OCD is connected to the (geometrical) chirality of the nano-particle. In complete analogy, it would be seducing to do the same with electron beams, thus overcoming the light diffraction limit.

In contrast with optics, conventional electron beam are unpolarized and described by a scalar field. A possibility to generate electron dichroism would be to use spin-polarized electron guns [220, 221] but this technology still requires development. In a seminal paper [186], Asenjo-Garcia and García de Abajo rather proposed to modify the *phase* of electron beams. More specifically, they numerically demonstrated that electron dichroism could be achieved by sequentially sending vortex electron beams of opposite orbital angular momentum (see next section) and measure the difference between the two EELS cross sections. Due to the fast development of phase-shaping techniques in the TEM, this experiment proposal has recently attracted tremendous interest.

In order to overcome the latter limitation of tomography, this chapter is dedicated to the development of an alternative approach based on phase-shaped electron beams enabling to recover the missing information in conventional EELS.

4.1.2 Phase manipulation in the electron microscope

In 1974, Nye and Berry demonstrated that phase singularity is a general phenomenon in wave physics [222]. Following this idea, the field of *singular optics* (i.e. the study optical beams with phase singularity) emerged in the 90s and encountered a great success [223] thanks to several possible applications e.g. topological photonics [224].

Interestingly, as shown in [222], any beam satisfying the wave equation can have phase singularity. This is the case of electron microscopy where, for reasons detailed in chapter 3, fast electron beams can be described by the Schrödinger in the paraxial approximation. It therefore enables us to transpose all the concepts of singular photon optics to electron microscopy.
This remarkable effort has been first achieved in 2010 by the teams of Tonomura [21] and Verbeeck [20] which reported the first experimental generation of a vortex beam (i.e. an electron beam with an helical phase front). Since then, the field of phase-structured electron beams has encountered an extremely fast development.

In this section, we will review the basics of electron phase-shaping with special emphasis on vortex beams.

4.1.2.1 Vortex electron states

The most famous example of phase-shaped electron beams are the free-electron vortex states generically called *vortex electrons*. Roughly speaking, a vortex beam is a wave with an helical phase front which carries a topological charge (i.e. a phase singularity). The simplest way to describe a vortex beam is the Bessel wavefunction [225] defined by:

$$\psi_l(\boldsymbol{r}) \propto J_{|l|}(\kappa r)e^{il\phi}e^{ik_z z} \tag{4.3}$$

where κ is the radial wavevector, l is the charge of the vortex and $J_{|l|}(r)$ is the Bessel function of the first kind. Indeed, when $l \neq 0$ the phase is therefore singular in $r = 0$ and therefore the radial part must satisfy $J_{|l|}(r = 0) = 0$. The states (4.3) are axially symmetric solutions of the stationary Schrödinger equation. However, these Bessel wavefunctions are not power normalizable i.e. $\int_0^\infty r dr |\psi_l|^2$ diverges [226, 225]. It means that such a state cannot be produced in practice. However, one can produce quasi-Bessel beams [227] i.e. beams satisfying (4.3) but only in a finite region of space. Formally, proper square-integrable vortex states are the so-called Laguerre-Gaussian (LG) beams [225] which are solutions of the Schrödinger equation in the paraxial equation. The Laguerre-Gaussian wavefunctions of order (n, l) (and denoted HG_{nl}) read in cylindrical coordinate [228, 225]:

$$\psi_{n,l}(r,\phi,z) = \frac{|l|}{w(z)}\sqrt{\frac{2}{\pi n!(n-|l|)!}}\left(\frac{r\sqrt{2}}{w(z)}\right)^{|l|} L_n^{(|l|)}\left(\frac{2r^2}{w^2(z)}\right)\exp(ikr^2/2R(z))\exp(-r^2/w^2) \times \exp(i(l\phi + kz))\exp(-i(2n+|l|+1)\zeta(z)) \tag{4.4}$$

where $n \in \mathbb{N}$ and $l \in \mathbb{Z}$ are respectively the radial and azimuthal quantum numbers. For any real number α, $\{L_n^{(\alpha)}\}_{n\in\mathbb{N}}$ denotes a set of generalized Laguerre polynomials. We also defined [225]:

$$\begin{cases} R(z) = (z_R^2 + z^2)/z & (4.5a) \\ w(z) = w_0\sqrt{1 + z^2/z_R^2} & (4.5b) \\ \zeta(z) = \arctan(z/z_R) & (4.5c) \\ z_R = kw_0^2/2 & (4.5d) \end{cases}$$

The quantity $R(z)$ corresponds to the radius of curvature of the wavefront, $w(z)$ is the width of the beam, z_R is the so-called Rayleigh diffraction length and w_0 is the beam waist. The normalization constants have been chosen so that $\int |\psi_{n,l}(\boldsymbol{r}_\perp)|^2 d\boldsymbol{r}_\perp = 1$. The term $(2n + |l| + 1)\zeta(z)$ corresponds to the so-called Gouy phase which leads to a $(2n + |l| + 1)\pi$ phase shift between the $z \gg z_R$ and $z \ll z_R$ regions. On figure 4.3, we plotted examples of Laguerre-Gaussian wavefunctions for $n = 0$ and $l \in \{-2, -1, 0, 1, 2\}$.

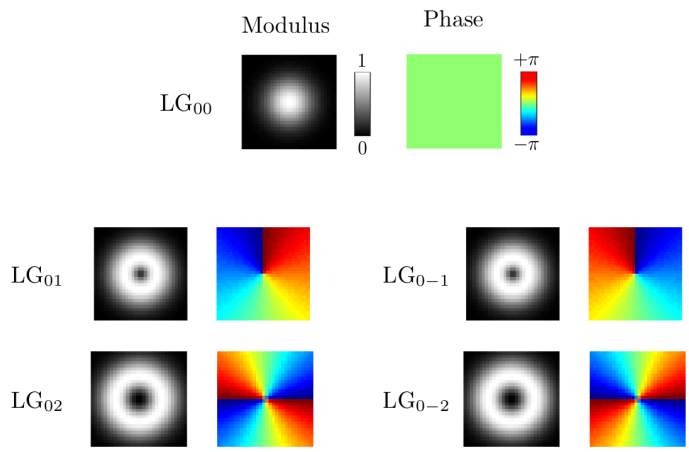

Figure 4.3: *Modulus and phase of Laguerre-Gaussian wavefunctions for $n = 0$ and $l \in \{-2, -1, 0, 1, 2\}$ at $z = 0$.*

Vortex electrons posses several interesting properties which are presented in details in [225]. Particularly, they carry an *orbital angular momentum* (OAM). The OAM operator $\hat{\boldsymbol{L}}$ is defined as:

$$\hat{\boldsymbol{L}} = \boldsymbol{r} \times \hat{\boldsymbol{p}} = -i\hbar\, \boldsymbol{r} \times \hat{\boldsymbol{\nabla}} \tag{4.6}$$

One can show that any vortex state (i.e. states satisfying $\psi(\boldsymbol{r}) \propto \exp(il\phi)$), the z-component of the OAM is given by:

$$L_z = \frac{\langle\psi|\hat{L}_z|\psi\rangle}{\langle\psi|\psi\rangle} = \hbar l \tag{4.7}$$

Therefore, the topological charge of a vortex l determines the OAM $\hbar l$ carried by the beam. Moreover, the current associated with a Bessel beam reads:

$$\boldsymbol{j}_l(r,\phi) = \frac{\hbar}{m}\mathrm{Im}\{\psi_l^* \boldsymbol{\nabla}\psi_l\} \propto \frac{\hbar}{m}\left(\frac{l}{r}\hat{\boldsymbol{\phi}} + k_z\hat{\boldsymbol{z}}\right)|J_{|l|}(\kappa r)|^2 \tag{4.8}$$

In other words, a vortex electron carries a spiraling current. A consequence of this coiling current is that vortex electrons carry a magnetic momentum [229]. There are several promising application of such beams in EELS. In the low-loss regime, using equation (2.98), García de Abajo and Asenjo-Garcia [186] and later Ugarte and Ducati [187] predicted the possibility of measuring LSPs' chirality in EELS with vortex. In the core-loss regime, Verbeeck, Tian and Schattschneider [20] suggested that vortex electrons can be used to enhance electron energy-loss magnetic chiral dichroic (EMCD) signal.

4.1.2.2 Generation of vortex in a TEM, phase-shaping techniques

The generation of electron vortex or more generally the art of electron phase-crafting in the TEM is detailed in [230]; in the following, we will simply give some insights into the different possible techniques:

- **Abberation correctors**. The first phase-shaping technique is presented in greater details in appendix B.0.0.3 and relies on the use of C_S correctors. Indeed, aberration correctors are used to flatten the electron phase and compensate the aberration in lenses. One can therefore deviate them from their original purpose and introduce aberrations in order to generate exotic beam profiles. In 2013, Clark and collaborators [231] used this method to generate a $l = 1$ vortex beam. Nevertheless, an aberration corrector can only deform the phase and cannot introduce topological charges required to generate vortices; an annular aperture has therefore been used to produce the phase singularity. Although limited for phase-shaping applications, aberration correctors have the advantage of being easily tunable.

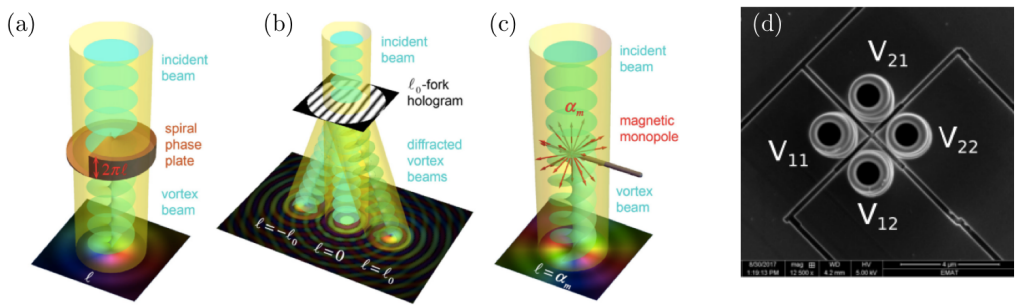

Figure 4.4: *Schematics showing the principle of vortex formation using (a) a phase-plate, (b) a diffraction grating and (c) a magnetic needle. Reproduced from [232]. (d) SEM image of a 2 by 2 programmable phase-plate. Reproduced from [233].*

- **Phase-plate**. A phase-plate consists in a material (graphite, silicon nitride) with variable thickness placed in the path of the electron beam. The differences in thickness produce variations in the electrons' optical path leading to phase modulations. Properly designed (e.g. a spiral shape leads to the formation of a vortex), it enables to deform the wavefront

of the beam into any phase profile. The working principle is shown of figure 4.4(a). This technique, inspired by optical experiments [234], has been used by Uchida and Tonomura in 2010 to generate the first electron vortex into a TEM [21]. Recently, it has been suggested that such a phase-plate can be used to correct electron aberrations in the TEM [235].

- **Holographic gratings**. An efficient method to generate vortex is to use diffraction gratings. The working principle is shown of figure 4.4(b). Indeed, it is known from optics that diffraction of a plane-wave by a fork dislocation grating produces a vortex beam in the Fourier plane [223]. This technique has been used by Verbeeck and collaborators to generate vortex beams in a TEM [20]. This method has the advantage to be able to generate any kind of beam [236, 237, 230] and simply requires one to compute the form of the required diffraction grating. Particularly, it has been used to generate vortex with huge OAM ($l \approx 1000$) [238]. The main drawbacks of this technique are: (i) the gratings are delicate to fabricate, (ii) they are not tunable i.e. one needs to produce a grating for each desired beam, (iii) all the diffraction orders are produced simultaneously, therefore one need to filter the beam after shaping, (iv) the grating stops a significant part of the electrons and therefore limits the current. Let's also emphasize that for certain application such as EMCD, one needs to be able to dynamically switch the sign of the vortex. This operation is impossible with an holographic grating.

- **Magnetic needle**. When electron trajectories enclose a magnetic flux, they acquire an additional phase shift $\Delta\phi$ due to the Aharonov-Bohm effect:

$$\Delta\phi = \frac{e}{\hbar c} \oint \boldsymbol{A}.d\boldsymbol{s} \tag{4.9}$$

  where $\boldsymbol{A}$ is the magnetic vector potential. It has been theoretically demonstrated that, if the magnetic field corresponds to a monopole, the Aharonov-Bohm phase shift applied to a plane wave leads to the formation of a vortex [239]. The working principle is shown on figure 4.4(c). Following this idea, Béché and collaborators generated a vortex beam by using a long magnetic needle, which magnetic moment locally ressembles a monopole [240]. Other types of beams, such as Hermite-Gaussian beam [241], can be generated through Aharonov-Bohm phase shift. However, it requires a precise engineering of the magnetic material which can be long and challenging.

- **Programmable phase-plate**. This technique is basically the electronic analogue of adaptive optics. It consists of an array of Einzel lenses which electric potentials are individually tuned. The phase shift acquired by the electrons traveling through a lens is proportional to this potential (and also depends on the geometry of the lens). Therefore, by creating an array with a large number of pixels, one can dynamically tune the phase of each points of the wavefront and generate any type of beam profile. A 2 by 2 programmable phase plate (see figure 4.4(d)) has been recently experimentally demonstrated [233] and used to generate a vortex beam.

4.1.2.3 Other types of phase structured electron beams

In this section, we particularly insisted on the generation of electron vortex states, as it is the most widespread phase-shaped beam. Nevertheless, let's emphasize that there are numerous different beams which can be produced using the methods described above such as:

- **Gaussian-Airy beams** which have a remarkable parabola trajectory and are therefore called *self-accelerating beams* [242, 243]. However, this apparent contradiction has been solved since it has been shown that the center of mass of the beam follow a straight trajectory in agreement with the Ehrenfest's theorem [244].

- **Bessel beams** also called diffraction-free beams, predicted by Durnin and collaborators [245] and recently demonstrated in an electron microscope [227]. These beams have the remarkable property to maintain their transverse density profile over long distances.

- **Spiraling or snaking Bessel beams** [246] which are other types of non-diffracting beams. Contrary to a vortex beam where only the phase possesses an helical structure, these Bessel beams present either spiraling or "snaking" intensity profiles.
- **Hermite-Gauss** beams which will be extensively presented within the rest of this thesis.
- **C-shape vortex beams** [247] which present a vortex-like phase structure and a C-shaped intensity profile.

4.1.3 Structure of the chapter

The goal of this chapter is to lay the foundation of a phase-shaped electron energy loss spectroscopy (PSEELS) with special emphasis on plasmon spectroscopy. Particularly, we will show that playing with the phase of the electron beam enables us to recover information unreachable with conventional EELS. The chapter is organized as follow:

- In section 4.2, we will first consider the quasi-static limit and show that the PSEEL probability takes the form of a *transition matrix* between the impinging electron state and a set of final states. It leads to the existence of selection rules from which important information on the symmetry of plasmon modes can be deduced.
- In section 4.3, we present the results of the first experimental realization of a PSEELS experiment designed in collaboration with the team of Jo Verbeeck of Antwerp university and carried out by Guzzinati and collaborators [241].
- In section 4.4, we present possible applications of PSEELS and demonstrate, through simulation, how it could solve current problems in plasmonics.
- In section 4.5, we extensively discuss the experimental constraints and feasibility of PSEELS and show that the addition of an electron sorter after the interaction could enable the increase of the signal to noise ratio in PSEELS spectra.
- In section 4.6, and in the continuity of chapter 3, we demonstrate how phase-shaping could be used to measure spatial coherence of optical fields below the diffraction limit.

4.2 Semi-classical and quasi-static transition probability: analogy with atomic physics

In this section, we will first set the basic formalism describing a phase-shape electron energy-loss spectroscopy experiment on surface plasmons in the quasi-static limit $c \to \infty$. The validity of this approximation will be discussed later and the retarded case will be extensively studied in section 4.6.

4.2.1 Derivation of the loss probability

First of all, we need to calculate the loss probability when, contrary to the classical case (4.2), the electron is treated as a wave in order to take into account the electronic phase in the interaction. The starting point of this chapter is therefore the formalism reviewed and completed in chapter 3. Particularly, as we re-demonstrated, the electrostatic interaction between an incident electron, of wavefunction ψ_i and energy $\hbar\epsilon_i$, and a coherent electronic excitation is described by the transition rate [19]:

$$\frac{d\Gamma^{\mathrm{QS}}(\omega)}{dt} = \frac{2e^2}{\hbar} \sum_f \int d\boldsymbol{r}\, d\boldsymbol{r}'\, \psi_f(\boldsymbol{r})\psi_i^*(\boldsymbol{r})\, \mathrm{Im}\{-W(\boldsymbol{r},\boldsymbol{r}',\omega)\}\, \psi_f^*(\boldsymbol{r}')\psi_i(\boldsymbol{r}')\, \delta(\epsilon_f - \epsilon_i + \omega) \quad (4.10)$$

As we already detailed in the introductory chapter, in the QS limit, an eigendecomposition of the classical SP field exists [9]. The SPs are therefore fully described by a set of modes $\{(\lambda_m, \sigma_m)\}$ indexed by $m \in \mathbb{N}$ where λ_m are dimensionless geometrical eigenvalues and σ_m are surface charge

densities. These quantities are numerically accessible through e.g. the boundary element method [248]. Moreover, Boudarham and Kociak showed [10] that this modal decomposition reflects in the expression of the screened interaction which reads:

$$W(\boldsymbol{r}, \boldsymbol{r}', \omega) = \sum_m g_m(\omega)\phi_m(\boldsymbol{r})\phi_m^*(\boldsymbol{r}') \tag{4.11}$$

where we recall that ϕ_m is the electrostatic potential associated with the charge distribution σ_m and g_m is the spectral function defined as:

$$g_m(\omega) = \frac{2}{\epsilon_{\text{in}}(\omega)(1+\lambda_m) + \epsilon_{\text{out}}(\omega)(1-\lambda_m)} \tag{4.12}$$

$\epsilon_{\text{in, out}}$ are respectively the dielectric function inside and outside the nano-particle sustaining the plasmon modes. This expression neglects the begrenzung term concerning only the bulk plasmons, which is out of the scope of the current work. The advantage of this description is that now the Green function is separable which, as we will see later, significantly simplifies the derivation of the loss probability.

As discussed in the previous chapter, in equation (4.10) the interaction is described on a complete quantum level, the term W containing all the peculiar quantum details of the SP field. We now turn to the principle approximation of our theory: now and hereafter, we will treat the SP field as a classical field i.e. we will neglect all the pathological quantum effects which could appear in plasmonics (e.g. spill out effects, quantum non-linearities). Thus, as suggested in the supplementary material of [249], we can use now expression (4.11) to simplify W and, by multiplying by the characteristic time L/v (L being the length of the electron trajectory and v its speed), one gets the following expression for the loss probability Γ^{QS} :

$$\begin{aligned}\Gamma^{\text{QS}}(\omega) = \frac{2Le^2}{v\hbar}\sum_m\sum_f \text{Im}\{-g_m(\omega)\}\int d^3\boldsymbol{r}\, d^3\boldsymbol{r}'\, \psi_f(\boldsymbol{r})\,\phi_m(\boldsymbol{r})\,\psi_i^*(\boldsymbol{r}) \\ \times\, \psi_f^*(\boldsymbol{r}')\phi_m^*(\boldsymbol{r}')\,\psi_i(\boldsymbol{r}')\delta(\epsilon_f - \epsilon_i + \omega)\end{aligned} \tag{4.13}$$

where we used the fact that ϕ_m is a real field in the quasi-static limit. The latter equation can be rewritten :

$$\boxed{\Gamma^{\text{QS}}(\omega) = \frac{2Le^2}{v\hbar}\sum_m\sum_f \text{Im}\{-g_m(\omega)\}\left|\int d^3\boldsymbol{r}\, \psi_f(\boldsymbol{r})\phi_m(\boldsymbol{r})\psi_i^*(\boldsymbol{r})\right|^2 \delta(\epsilon_f - \epsilon_i + \omega)} \tag{4.14}$$

The typical convergence angle of modern microscopes being of few milliradians, most of the electron wavevector k_i is contained in its z-component $k_{i,z}$ (corresponding to the propagation axis) i.e. $k_i \approx k_{i,z}$. One can therefore apply the paraxial equation and write [19]:

$$\begin{cases} \psi_i(\boldsymbol{r}) = \dfrac{1}{\sqrt{L}}\psi_{i,\perp}(\boldsymbol{r}_\perp)e^{ik_{i,z}z} & \text{(4.15a)} \\ \psi_f(\boldsymbol{r}) = \dfrac{1}{\sqrt{L}}\psi_{f,\perp}(\boldsymbol{r}_\perp)e^{ik_{f,z}z} & \text{(4.15b)} \end{cases}$$

where $\boldsymbol{r}_\perp$ is the vector position in the (x, y) plane. Under this assumption, we can also separate the sum over the final states as:

$$\sum_f \longrightarrow \frac{L}{2\pi}\int dk_{f,z}\sum_{f_\perp} \tag{4.16}$$

Combining equations (4.14), (4.15a), (4.15b) and (4.16), one gets:

$$\Gamma^{\mathrm{QS}}(\omega) = \frac{e^2}{\pi v \hbar} \sum_m \sum_{f_\perp} \mathrm{Im}\left\{-g_m(\omega)\right\} \left| \int d^2\boldsymbol{r}_\perp \; \psi_{f,\perp}(\boldsymbol{r}_\perp)\phi_m(\boldsymbol{r}_\perp, z)\psi^*_{i,\perp}(\boldsymbol{r}_\perp) \right|^2 \times \int dk_{f,z} e^{i(k_{z,f}-k_{z,i})(z-z')}\delta(\epsilon_f - \epsilon_i + \omega) \tag{4.17}$$

Besides, one can use the so-called non-recoil approximation which reads $\omega = q_z v$ where $q_z = k_{f,z} - k_{i,z}$. This expression is simply the energy conservation condition where we neglected the terms in q^2, which is valid for fast electrons [19]. Therefore the last integral in equation (4.17) reads:

$$\int dk_{z,f} \; e^{i(k_{z,f}-k_{z,i})(z-z')}\delta(\epsilon_f - \epsilon_i + \omega) = \frac{1}{v} e^{-iq_z(z-z')} \tag{4.18}$$

Moreover, we recognize the Fourier transform of ϕ_m in the z-direction as:

$$\phi_m(\boldsymbol{r}_\perp, q_z) = \int dz \; \phi_m(\boldsymbol{r}_\perp, z) e^{-iq_z z} \tag{4.19}$$

Putting (4.17), (4.18) and (4.19) together, one gets the final and compact formula:

$$\Gamma^{\mathrm{QS}}(\omega) = \frac{2e^2}{hv^2} \sum_m \sum_{f_\perp} \mathrm{Im}\left\{-g_m(\omega)\right\} \left| \int d^2\boldsymbol{r}_\perp \; \psi_{f,\perp}(\boldsymbol{r}_\perp)\phi_m(\boldsymbol{r}_\perp, q_z)\psi^*_{i,\perp}(\boldsymbol{r}_\perp) \right|^2 \tag{4.20}$$

Equation (4.20) is the wave-optical analogue of equation (4.2). One can see that, within the semi-classical approach, the $|\phi_m|^2$ term appearing in (4.2) is replaced by the modulus squared of a transition matrix between the impinging electron state and an ensemble of final states mediated by the plasmon potential. This new term reveals the presence of electronic interferences which are the main ingredient of this new type of spectroscopy.

4.2.2 Selection rules and peculiarity of PSEELS

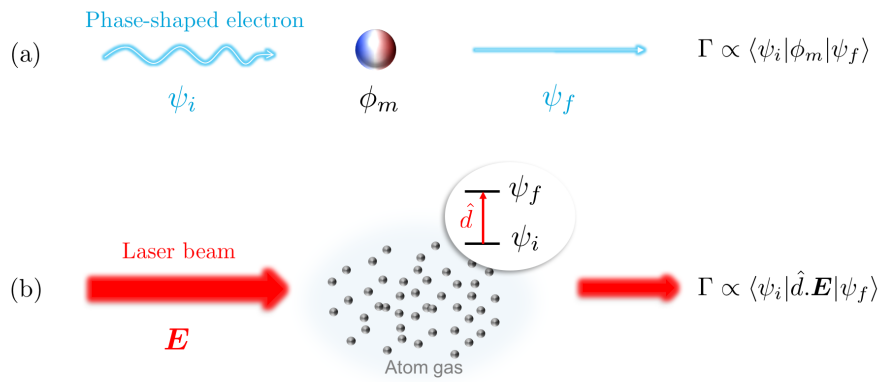

Figure 4.5: *Schematics comparing (a) the phase-shaped electron energy-loss spectroscopy and (b) atomic spectroscopy*

Such a transition matrix is formally analogue to what is encountered in atomic spectroscopy where the emission (or absorption) spectra are governed by the existence of *selection rules* as shown on figure 4.5. Indeed, for a certain polarization of the excitation laser E, transition between different orbitals can be allowed or forbidden depending on the parity of the initial and final electronic states encoded in the dipole moment $\hat{d}$ on the electronic transition. In our PSEELS experiment,

free electron wavefuntions $\psi_{i/f}$ play the role of atomic orbitals while the excitation laser is replaced by the plasmonic field ϕ_m. **Playing with the selection rules and the form of the incident wavefunction, one can therefore get information on the plasmon field's symmetry and phase**.

Conceptually, EELS and PSEELS experiments on surface plasmons are thus completely different:

- In *conventional EELS*, the initial wavefunction corresponds to a focused probe impinging at a point $\boldsymbol{R}$ in the plane of the sample. The phase of the beam is homogeneous and symmetric (besides adjustable aberrations). The collection plane of the microscope being a Fourier plane, the final states are conveniently expended on the plane-wave basis. By changing the collection angle, one can modify the maximum wavevectors collected and therefore adjust the cutoff of the sum over the final states $\sum_{f_\perp}$. The collection angle is chosen sufficiently large to increase the number of collected electrons (therefore improving the signal to noise ratio) but sufficiently small in order to reduce the aberrations. Typically the collection semiangle is $\beta \approx 10 - 80$ mrad.

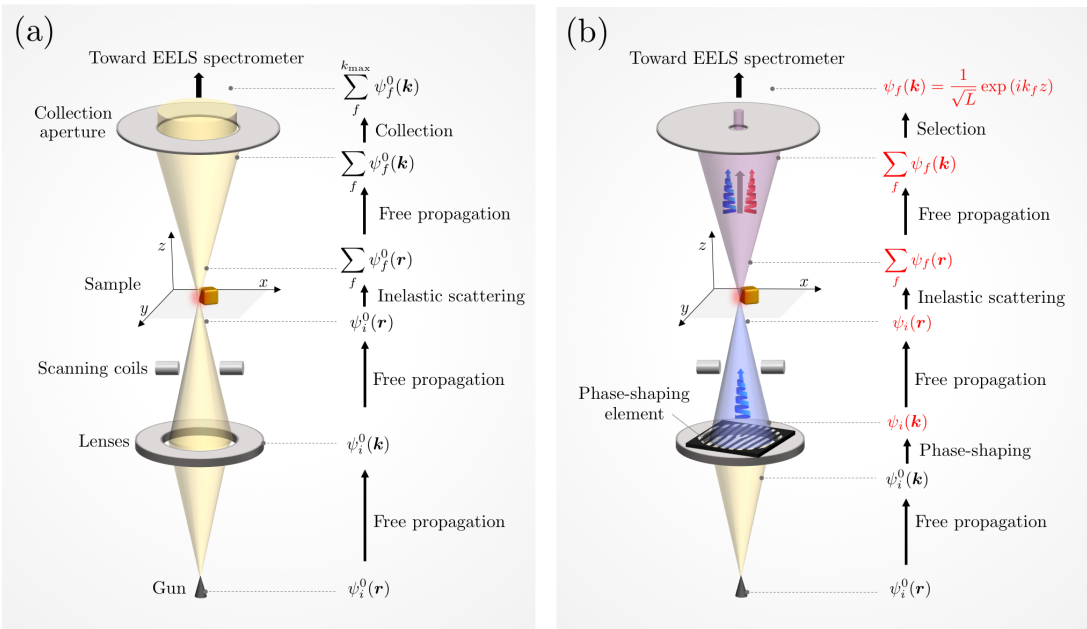

Figure 4.6: *Schematics comparing (a) the conventional electron energy loss spectroscopy with (b) the phase-shaped electron energy loss spectroscopy.*

- In *phase-shaped EELS*, the impinging electron wavefunction is intentionally structured by any phase-shaping technique demonstrated in section 4.1.2.2. The initial electron state is therefore precisely controlled. The aim of the experiment is to probe *one specific transition* therefore only one final state needs to be detected. As we saw in the introductory chapter, the typical inelastic scattering angle is given by:

$$\theta_E = \frac{\Delta E}{2\gamma T} \tag{4.21}$$

where ΔE is the energy loss, γ the Lorentz factor and T the kinetic energy of the beam. For a plasmonic excitation at 2 eV with a 100 keV acceleration voltage, we have $\theta_E \approx 13$ μrad. This quantity basically gives the angular width of a planewave. In order to select one specific transition, the collection angle therefore needs to be of the same order as (or less than) θ_E.

which drastically reduces the signal to noise ratio. As we will study in details in section 4.5, increasing the collection angle beyond θ_E leads to a blurring of the interference effects.

We summarized on figure 4.6 these two different configurations of spectroscopy. An important configuration for PSEELS is when only the in-axis electrons are collected i.e. $\psi_{f,\perp} = \text{constant}$. In this case, the loss probability simply reads:

$$\Gamma^{\text{QS}}(\omega) = \frac{2e^2}{hv^2} \sum_m \text{Im}\left\{-g_m(\omega)\right\} \left| \int d^2\boldsymbol{r}_\perp \; \phi_m(\boldsymbol{r}_\perp, q_z)\psi^*_{i,\perp}(\boldsymbol{r}_\perp) \right|^2 \tag{4.22}$$

For simplicity, we usually call this case the *coherent limit* while the configuration where all the electrons are collected is usually referred as the *incoherent limit*. This denomination is inherited from the usual distinction between coherent (bright field) and incoherent (annular dark field) imaging. Now, before going further in the details of the experiment, let's take a look to a pedagogical example.

At this point, an important point needs to be stressed. Formally, taking $\psi_{f,\perp} = \text{constant}$ corresponds to expand the loss probability on the planewave basis as [19]:

$$\Gamma^{\text{QS}}(\omega) = \int d\boldsymbol{k}_\perp \; \frac{d\Gamma^{\text{QS}}(\omega)}{d\boldsymbol{k}_\perp} \tag{4.23}$$

and keep only one component (it will be rigorously treated in section 4.5.1). Thus, (4.22) formally corresponds to an infinitesimal part of the total EELS signal.

4.2.3 Polarizer effect using a Hermite-Gaussian beam

Hermite-Gaussian beams are another widespread type of Gaussian beams in photon optics. In the paraxial approximation, the corresponding Hermite-Gaussian electronic wavefunction of order (n, m) and denoted HG_{nm} reads (in cathesian coordinate) [228]:

$$\begin{aligned}\psi_{n,m}(x,y,z) = \frac{1}{w(z)}\sqrt{\frac{2}{\pi n! m!}}2^{-(n+m)/2}\exp(-ik(x^2+y^2)/2R)\exp(-(x^2+y^2)/w^2) \\ \times \exp(-i(n+m+1)\zeta(z))\, H_n(x\sqrt{2}/w)\, H_m(y\sqrt{2}/w)\end{aligned} \tag{4.24}$$

where $\{H_n\}_{n\in\mathbb{N}}$ denotes Hermite polynomials and all the other quantities have already been defined for the Laguerre-Gaussian beams in section 4.1.2.1. On figure 4.7, we plotted few examples of Hermite-Gaussian wavefunctions for $n, m \in \{0, 1, 2\}$. Looking at the phase maps, one can see that the integers n and m respectively indexes the number of π-phase jumps in the x and y directions. Moreover, the modulus cancels at the jumps since the phase is undetermined at these positions.

The most important wavefunction for the rest of this chapter is the HG_{10} beam which corresponds to two lobes with a π phase-shift, see figure 4.7(a). For simplicity, we usually call it *pi-beam*. In fact, this beam is the electronic analogue of a linear polarization as we will exemplify hereafter.

Let's simulate a PSEELS experiment in the coherent limit (4.20) when only the in-axis electrons are detected. As shown on figure 4.8(a-c), we consider a pi-beam impinging on a silver nano-rod. As we did for the vortex, we use the following simplified representation for the pi-beam wavefunction:

$$\psi_{i,\perp}(\boldsymbol{r}_\perp) = x \exp\left(-\frac{x^2+y^2}{w^2}\right) \tag{4.25}$$

rather than the full polynomial (4.24). Since we are not interested in *quantitatively* estimating the EELS cross-section, this approximation is fully justified. The lateral extension of the beam w has been adjusted to match the size of the rod (100×15 nm). For the sake of the demonstration, we only consider the dipole mode of the rod which charge distribution is shown on figure 4.8(c). The

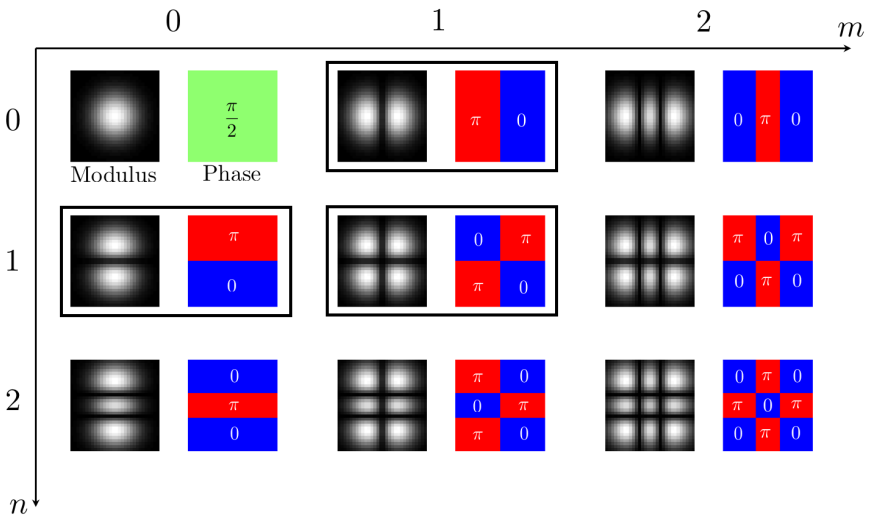

Figure 4.7: *Modulus and phase of the nine first Hermite-Gaussian wavefunctions computed at $z = 0$. We boxed in black the wavefunctions which will be important for the rest of the thesis.*

angle θ between the pi-beam and the axis of the rod is varied from 0° to 90°. We arbitrarily define x as the axis of the rod. On figure 4.8(d), we plotted the EELS spectra calculated for different values of θ. The maximum value of the EELS signal is set to 1 for $\theta = 0$; all the other spectra are normalized with this convention.

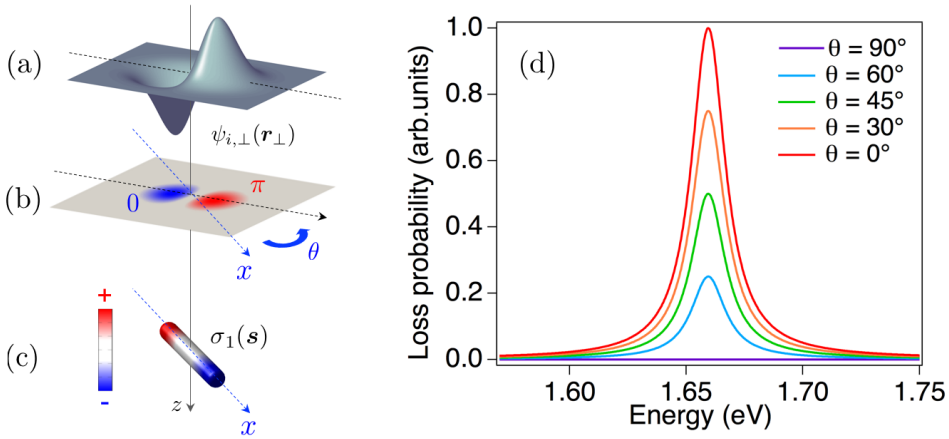

Figure 4.8: *(a-c) Schematics of the situation: a Hermite-Gaussian beam impinges onto a 100 × 15 nm silver nanorod. The size of the electron wavefunction is chosen to match the size of the rod and the angle θ between the rod and the beam axis is tuned. Plots (a) and (b) represent the same wavefunction respectively in 3D and 2D with colors. For the rest on this chapter, we will privilege the 2D representation. (d) Electron energy loss spectra calculated for different values of θ. The peak corresponds to the dipolar mode which charge density is displayed on schematics (c). The final state is chosen to be a planewave propagating along the optical axis. The maximum value of the peak is set to 1 for $\theta = 0$; all the other spectra are normalized with this convention.*

When the angle is varied from 90° to 0°, we progressively cancel the dipolar plasmon EELS peak. This can be understood with equation (4.22). When the two axis are aligned the interferences are constructive since both ϕ_m and $\psi_{i,\perp}$ are two odd functions of x. On the contrary, when $\theta = 90°$, $\psi_{i,\perp}$ becomes an even function of x and the interferences turn out to be destructive. This effect is perfectly analogue to the light intensity variations observed when the angle between a polarizer and a linearly polarized light is varied. Particularly, the EELS signal follows the Malus law i.e.

$\Gamma \propto \cos^2(\theta)$. However, a major difference with an optical experimental is that, in our case, the beam has to be centered on the rod for this effect to be observed.

4.3 First experimental demonstration

In order to validate the previous developments, in collaboration with the group of Jo Verbeeck of Antwerp university, we designed the first PSEELS experiment with a pi-beam sent on a silver nano-rod. The experiment has been fully carried out by our collaborators in EMAT, particularly Giulio Guzzinati. We will give the main results in this section. An extended presentation of the experiment can be found in [241].

In order to generate a pi-beam, one needs to produce a sharp π phase-shift. To do so, a ferromagnetic needle has been introduced in the path of the electron beam, see figure 4.9. The magnetic moment is orientated along the needle axis and produces an Aharonov-Bohm phase-shift which intensity is controlled by engineering the geometry of the needle. We present respectively on figure (b) and (c) the beam intensity profile and the electronic phase measured by holography. Due to the difficulty of the nano-fabrication, the phase jump is about 0.87π and the beam is slightly asymmetric.

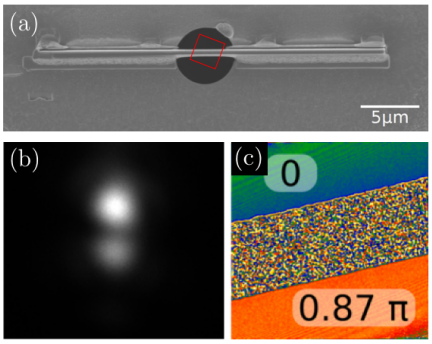

Figure 4.9: *(a) SEM image of the phase-shaping element: a ferromagnetic needle placed on a round aperture. (b) Experimental beam intensity profile. (c) Electronic phase measured by holography in the region indicated by a red square on image (a).*

The beam was then sent onto a 200 nm aluminium nano-rod. A series of nano-rods with different orientations have been produced by e-beam lithography (see figure 4.10(a)) in order to have different possible angles between the axis of the rod and the pi-beam. For this first experiment, the pi-beam is aligned with the axis of the rod.

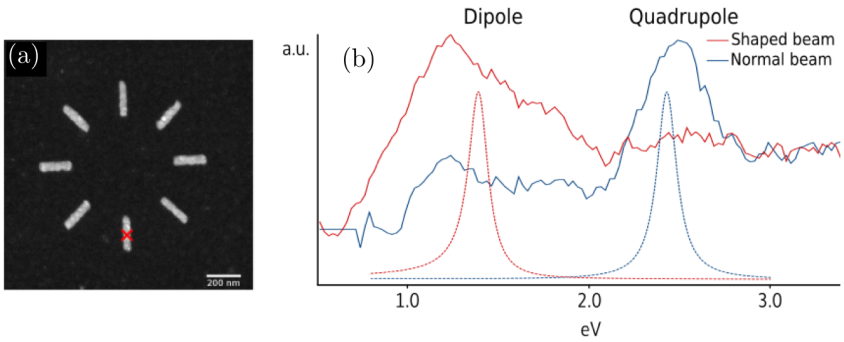

Figure 4.10: *(a) ADF image of the sample. The red cross indicates the impact parameter of the electron. (b) Experimental (plain lines) and simulated (dotted lines) EELS spectra for a pi-beam (red line) or a normal symmetric beam (blue line) impinging at the center of the nano-rod. The pi-beam is aligned with the axis of the rod and the size of the probe on the sample is about 50 nm.*

We present on figure 4.10(b) the EELS spectra for a pi-beam (red line) or a normal symmetric beam (blue line) impinging at the center of the nano-rod. One can clearly see that, with a pi-beam only the dipole mode is detected. Indeed, the quadrupole mode being an even function of x, the integral in (4.22) gives a zero contribution. On the contrary, for the same symmetry reasons, with a normal symmetric beam, only the quadrupole mode is detected.

Finally, we check the possibility of making standard STEM-EELS with a phase-shaped electron beam. Using this time a *focused* pi-beam scanned onto a 400 nm aluminium nano-rod, we recorded EELS maps filtered at the energy of the dipole mode. As shown on figure 4.11(a,d), two orientations of the probe have been investigated corresponding to $\theta = 0^o$ and $\theta = 90^o$ (keeping the conventions of figure 4.8). For these two configurations, we compare the simulated and experimental energy-filtered EELS maps on figure 4.11(b-c) and (e-f). The maps we obtain are naturally quite different from what one could get from conventional EELS. Indeed, we will see in section 4.4 that, while a normal beam probes the plasmonic potential, a pi-beam probes its derivative.

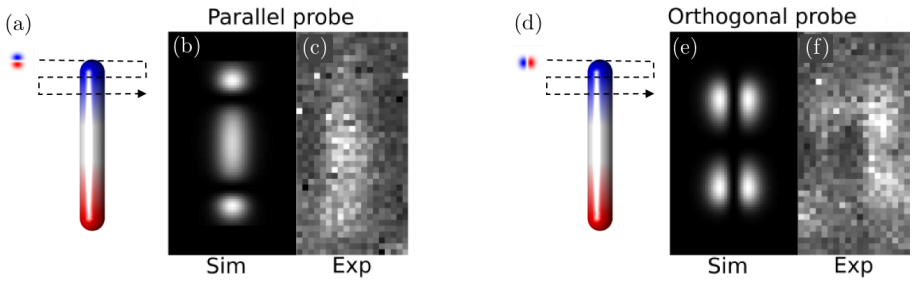

Figure 4.11: *(a) Schematics describing the experiment, a pi-beam aligned with the axis of the nano-rod is scanned and the contribution of the dipole mode to the EELS signal is recorded. Corresponding (b) simulated and (c) experimental EELS energy filtered maps. (d) Schematics describing the experiment, a pi-beam orthogonal to the axis of the nano-rod is scanned and the contribution of the dipole mode to the EELS signal is recorded. Corresponding (e) simulated and (f) experimental EELS filtered maps.*

It is important to highlight that this experiment was the first ever of its kind and several lessons have been learned from it:

- A PSEELS experiment on surface plasmon is possible and can also been performed in a STEM-EELS mode with a scanned probe.
- The main issue with this experiment is the poor signal to noise ratio (SNR). The reason is that we used a collection semi-angle of $\beta \approx 20\,\mu$rad. Indeed, as we already explained earlier, only the in-axis electrons need to be collected in order to probe one and only one electronic transition. This issue will be tackled in section 4.5.

4.4 Application of phase-shaped EELS to actual problems in plasmonics

So far, we have set the basic ideas of PSEELS and demonstrated that an actual experiment is doable. In this section, thanks to numerical simulations, we will proposed different applications of PSEELS in plasmonics.

4.4.1 Resolution of the problems highlighted in the introduction

We motivated our work by giving two examples of difficulties in conventional EELS for plasmonics (figures 4.1 and 4.2). We shall therefore start by showing how PSEELS could be a solution.

First of all, we saw that conventional EELS is insensitive to fields orthogonal to the electron path. This situation typically appears in the gap of dimers where the high field confinement

cannot be measured. Particularly, we gave the example of the dipole bonding mode of a silver nano-rod dimer. We now consider the same example but using equation (4.22) (instead of (4.2)) with a normal and a pi-beam impinging in the gap. The size of the beam matches the size of the gap as shown in the inset of figure 4.12(a). The pi-beam is aligned with the dimer axis. We clearly see from the simulations that the pi-beam only detects the bonding mode while the normal beam only detects the anti-bonding one. In other words, for symmetry reasons, pi-beams are particularly sensitive to capacitor-like charge configurations while in the same situation a symmetric beam leads to destructive interference. Thus, mapping plasmonic structures with a pi-beam enables a straightforward detection of gap modes.

Even more importantly, we showed that the phase of plasmon modes cannot be retrieved from conventional EELS. Particularly, we gave the example of a silver nano-square where dipole and quadrupole modes give similar EELS maps. We now consider a phase-shaped beam impinging on the same nano-square. The size of the beam matches the size of the particle as shown in the inset of figure 4.12(b). Using equation (4.22), we calculate the EELS probability when the impinging beam corresponds to a normal beam (black line), a pi-beam beam (red line) or a HG_{11} beam described by the simplified wavefunction:

$$\psi_{i,\perp}(x,y) = xy \exp\left(-\frac{x^2+y^2}{w^2}\right) \tag{4.26}$$

We naturally see that the normal beam detects both the dipole and quadrupole modes, in agreement with the experiment. On the contrary, for symmetry reasons, the pi-beam (resp. the HG_{11} beam) selects only the dipole mode (the quadrupole mode). Let's also emphasize that, because of the $\pi/2$-rotational invariance of the square geometry, there are two degenerate dipole modes with orthogonal orientations. Therefore, no matter the orientation of the pi-beam, the dipole mode will always be detected. Thus, by taking only two spectra with two different beams, one can already differentiate without any ambiguity the dipole from the quadrupole mode.

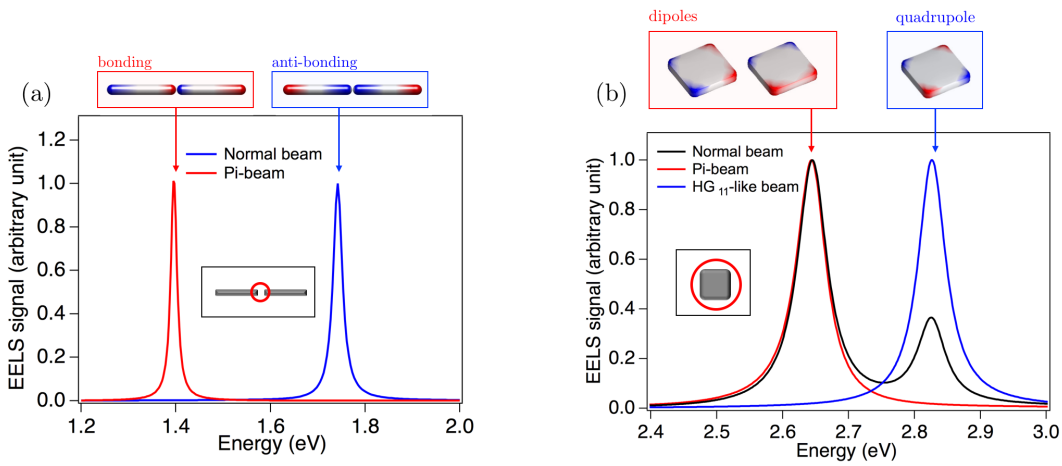

Figure 4.12: *(a) EELS spectra calculated for a normal beam and a pi-beam impinging in the gap of a silver nano-rod dimer. In the inset, we indicated with a red circle the size and position of the beam in the sample plane. In the top panel, we plotted the charge distributions associated with each plasmon peaks. (b) EELS spectra calculated for a normal beam, a pi-beam and a HG_{11} beam impinging on a silver nano-square. In the inset, we indicated with a red circle the size and position of the beam in the sample plane. In the top panel, we plotted the charge distributions associated with each plasmon peaks.*

4.4.2 Selective detection of symmetries

The basic idea behind the examples above is to *match the symmetry of the beams with the symmetry of the modes* we want to detect. This principle can be basically generalized to the detection

of any kind of symmetry as we exemplify on two structures below.

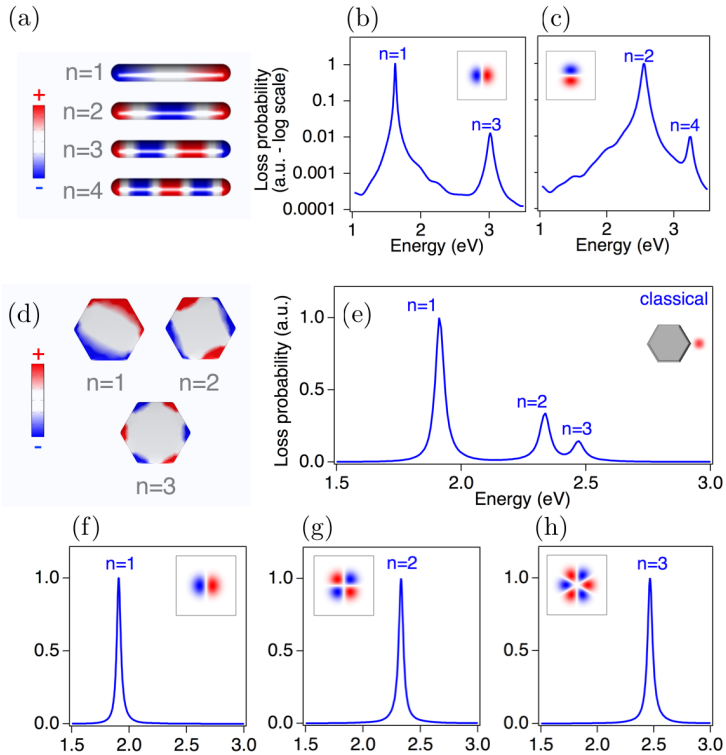

Figure 4.13: *(a) First four plasmon eigenmodes of a 100×10 nm silver rod. We calculated the loss probability for an HG-wavefunction impinging at the center of the rod (b) parallel and (c) perpendicular to it . (d) First three plasmon eigenmodes of a 100×5 nm silver hexagon. (e) Classical EELS spectrum calculated for an electron impinging at a corner of the hexagon (see inset). In the semi-classical limit, the loss probability has been calculated for an electron impinging at the center of the hexagon with a (f) a 2-lobbed wavefunction (HG), (g) a 4-lobbed wavefunction and (h) a 6 lobbed wavefunction. Each of these wavefunctions has a spatial extension comparable to the hexagon's size.*

On figure 4.13(a) we plotted the charge distributions of the four first plasmon modes of a 100×10 nm silver rod. As it is now well know [250], the odd modes ($n \in 2\mathbb{N}+1$) are anti-symmetric along the x-direction (main axis of the rod) while the even modes ($n \in 2\mathbb{N}$) are symmetric. We send at the center of this rod a Hermite-Gaussian electron beam (HG-beam) which can be experimentally generated using e.g. magnetic phase-plate technique. As one can see on inset Fig. 4.13(b), this wavefunction is antisymmetric along a certain axis x'. Therefore if the beam is sent so that x and x' are aligned (figure 4.13(b)), only the anti-symmetric (odd) modes are detected but if x and x' are orthogonal (figure 4.13(c)), only the symmetric (even) modes are. This is the phenomenon experimentally demonstrated in section 4.3.

An even more striking illustration is the case of an 100×5 nm hexagon of which three first eigen-charge distributions are given in figure 4.13(d). Let's emphasize that, for symmetry reasons, mode 1 (resp. mode 2) is degenerated with a second mode 1' (mode 2') for which the eigencharge is the same but rotated by $\pi/3$ angle. Mode 1 displays a dipolar symmetry while mode 2 and 3 have respectively a quadrupolar and a hexapolar symmetry. On figure 4.13(e), we calculated the standard EELS spectra (for an electron impinging at a corner of the hexagone) and we clearly see that all the modes are detected. Moreover, if one measures the energy-filtered EELS maps for the different modes of the hexagon (see [251]), he will find the same profile for each mode, with intensity peaked at the corners. Without assisting computation, standard EELS cannot give information on the symmetry of the modes, which can become prohibitive for the study of more complex systems.

We now calculate the PSEELS probability for three different electron wavefunctions: a 2-lobbed wavefunction (pi-beam), a 4-lobbed wavefunction (HG_{11}) and a 6-lobbed wavefunction (typically a 4f hydrogen-like orbital) given by:

$$\psi_{i,\perp}(x,y) = x(x^2 - 3y^2)\exp\left(-\frac{x^2+y^2}{w^2}\right) \tag{4.27}$$

The results are given in figure 4.13(f-h) and the wavefunctions (of extension comparable with the hexagon's size) are plotted in insets. We clearly notice that here again, for symmetry-matching reasons raised earlier, each wavefunction will detect the modes of similar symmetry.

All these examples show that, where standard EELS failed, **PSEELS enables us to access phase-symmetry of SP modes**. This fundamental idea was already present in the seminal paper of Ugarte and Ducati [187].

4.4.3 Measurement of the potential derivative and perspective in plasmon phase retrieval

4.4.3.1 Measurement of the potential derivative

So far, we saw that PSEELS was sensitive to plasmon phase and to different symmetries unreachable with standard EELS. By properly choosing the phase of the electron probes, one could retrieve information on plasmons in few spectra only, which constitutes the strength of this method. Another essential feature of modern electron spectroscopies is the spectral imaging [124, 11] and one could ask the input of our method for this particular technique.

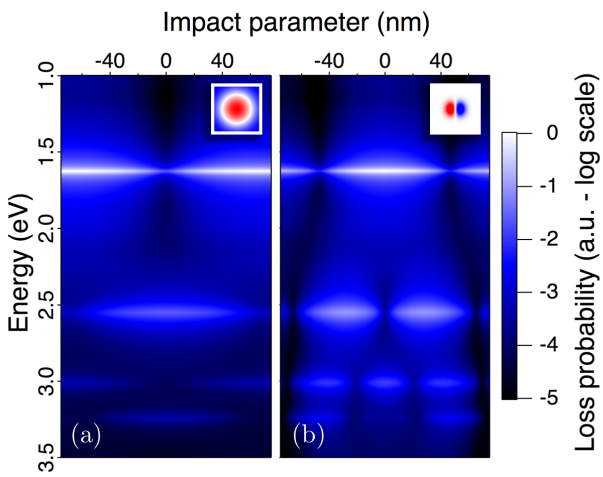

Figure 4.14: *Loss probability calculated for an (a) Sinc-wavefunction (b) HG-wavefunction interacting with the plasmon modes of a silver rod as a function of the energy and the position of the electron on the rod. The rod is 100 nm long with a 10 nm cross section while the width of the electron wavefunction is set at 30 nm. The wavefunctions are represented in the top corner of each graph.*

In figure 4.14, we calculated the line spectrum image (line SPIM) of a 100×10 nm silver nano-rod when (a) a standard symmetric beam (noted sinc-beam because it is modelled by a cardinal sine function) or (b) a HG-beam is scanned along its main axis. The typical extension of the wavefunctions is 30 nm. Signal is detected with both beams at energies corresponding to mode $n = 1...4$ of figure 4.13(a). One immediately see that the sinc-beam probes the extrema of the plasmon field while the HG-beam probes the nodes i.e. the positions where the plasmon field sign changes.

We can actually go further if the probe is supposed infinitely small compared to the size of the

nano-particle. A symmetric probe can be properly described by a Gaussian wavefunction:

$$\psi_{\perp}^{\mathrm{S}}(\boldsymbol{r}_{\perp}) = \frac{1}{2\sqrt{\pi w}} \exp\left(\frac{-(\boldsymbol{r}_{\perp} - \boldsymbol{r}_0)^2}{w}\right) \tag{4.28}$$

where $\boldsymbol{r}_0$ is the impact parameter of the beam onto the sample and the superscript S stands for "symmetric". When the width of the wavefunction goes to zero $w \to 0$, then the Gaussian function can be approximated by a Dirac distribution:

$$\psi_{\perp}^{\mathrm{S}}(\boldsymbol{r}_{\perp}) = \delta(\boldsymbol{r}_{\perp} - \boldsymbol{r}_0) \tag{4.29}$$

Plugging this approximation in (4.22), we retrieve the classical EELS probability (4.2). This fundamental limit has been first derived by Ritchie and Howie [143] in a different context. We will come back on this point in section 4.5.

If one wants to take into account the diffraction of the beam by the different circular apertures in the microscope, one can rather use a cardinal sine function which also tends to a Dirac distribution when w goes to zero. We also saw that the pi-beam is properly described by an Hermite-Gaussian wavefunction which tends to:

$$\psi_{\perp}^{\mathrm{A}}(x, y) = \delta'(x - x_0)\delta(y - y_0) \tag{4.30}$$

where we assumed the pi-beam to be aligned along the x-axis and the subscript A stands for "anti-symmetric". Plugging the latter equation in equation (4.22), we can show that the anti-symmetric point probe will give:

$$\boxed{\Gamma^{\mathrm{A}}(x_0, y_0, \omega) = \frac{2e^2}{v^2 h} \sum_n \mathrm{Im}\left\{-g_n(\omega)\right\} \left| \left[\frac{\partial}{\partial x}\phi_n(x, y, \tfrac{\omega}{v})\right]_{(x_0, y_0)} \right|^2} \tag{4.31}$$

and changing the orientation of the pi-beam will modify the direction of the derivative.

4.4.3.2 Perspective in phase reconstruction

Being able to access both the modulus of the potential and the modulus of the potential derivative present interesting perspective in phase-reconstruction. As an example, let's look at a toy model.

We consider an unidimensional plasmon potential of the form $\phi(x) = \cos(x)$ represented in figure (4.15)(a). It roughly corresponds to the potential of a quadrupole mode. We consider that x spans over a 6 nm interval with 1000 points. On graph (b) we represented what an EELS measurement with a normal beam would give i.e. $\Gamma^{\mathrm{S}}(x) = \cos^2(x)$. Similarly, on graph (c) we represented what an EELS measurement with a pi-beam would give i.e. $\Gamma^{\mathrm{A}}(x) = \sin^2(x)$.
Besides, the derivative of the potential $\phi'(x)$ reads:

$$\phi'(x) = \frac{\phi(x + h) - \phi(x)}{h} \tag{4.32}$$

where $h \ll 1$. Taking the modulus square of the latter espression and supposing that ϕ is a real field[1], we get:

$$\phi(x + h) = \frac{\phi^2(x + h) + \phi^2(x) - h^2(\phi'(x))^2}{2\phi(x)} \tag{4.33}$$

Identifying the quantities we can access experimentally in the previous expression and introducing the discrete variable $x_i = i \times h$, we obtain:

$$\phi(x_{i+1}) = \frac{\Gamma^{\mathrm{S}}(x_{i+1}) + \Gamma^{\mathrm{S}}(x_i) - h^2\Gamma^{\mathrm{A}}(x_i)}{2\phi(x_i)} \tag{4.34}$$

[1]This is of course perfectly valid here but not straightforward in a real experiment where we map the Fourier transform along z.

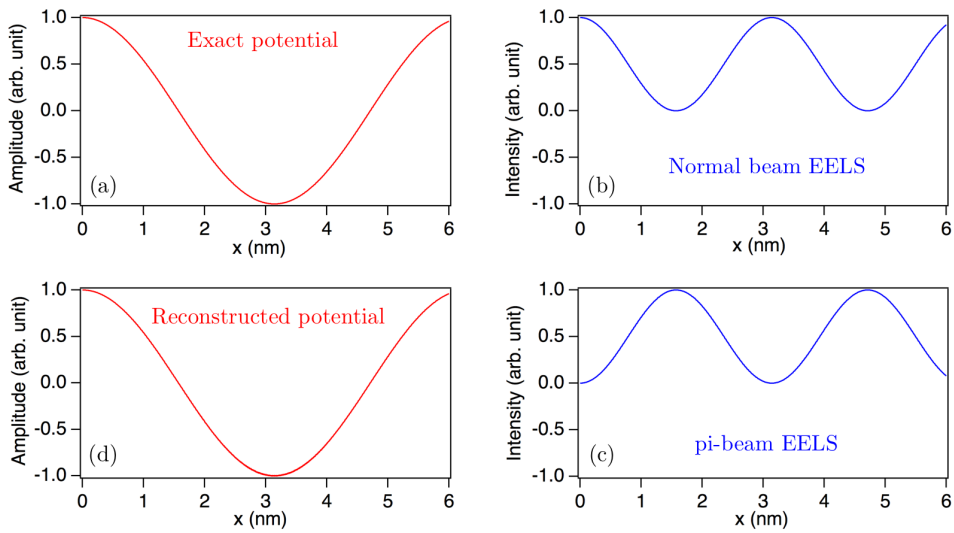

Figure 4.15: *(a) Exact potential. (b) EELS intensity using a normal beam. (c) EELS intensity using a pi-beam. (d) Potential reconstructed from the EELS data. We supposed* $\phi(0) = 1$.

In a real experiment, i basically indexes the pixels of a line SPIM. One can see that, from the latter Euler-like recursive relation, one can obtain the full potential from the two experimental spectra (b-c). We simply need to provide an initial guess for $\phi(x_0)$. We applied this algorithm to our toy model and got the experimental potential (d) which perfectly reproduced the exact potential (a). We have naturally chosen the initial value $\phi(x_0) = 1$ but we could have chosen $\phi(x_0) = -1$ and would have got the opposite result. Any result is correct since the overall sign of the plasmon field is purely conventional and only the relative variations of the phase are relevant.

The algorithm (4.34) is the most trivial procedure that one could imagine. It depends quadratically on h which means that the spatial sampling needs to be extremely fine for the algorithm to converge. However, the goal of the latter development is not to provide an efficient algorithm but rather to show that **there is enough information in a PSEELS experiment to reconstruct the total potential**. Moreover, the phase reconstruction from intensity measurement is a long standing problem in optics and a dense literature exploring different methods can be found [252, 253]. With some effort, it is a safe bet that an efficient reconstruction algorithm can be adapted to PSEELS.
Let's also emphasize that one can easily extend the latter developments to 2D EELS maps. We simply need to make a third measurement with a pi-beam oriented along the y axis. This way, we access the gradient of the potential and the same Euler method can be applied.

4.4.4 Measurement of the azimuthal symmetry with vortex beams

In 2015, Ugarte and Ducati have shown that a vortex beam can measure the azimuthal phase structure of a plasmon field [187]. In this work, they modeled the probe as an ensemble of classical trajectories of point electrons weighted by a phase factor *artificially* introduced a posteriori in order to mimic the vortex behavior. Their semi-classical equation can be straightforwardly retrieved from our formalism. We start from equation (4.22) and insert their vortex wavefuntion $\psi_{i,\perp}(\boldsymbol{r}) = D(\boldsymbol{r}_\perp)e^{il\phi}$, where l is the momentum of the vortex and D is a donut-like function. Moreover, using the BEM formalism detailed in appendix C, we write the plasmonic eigenpotentials ϕ_m in terms of eigencharges σ_m as [10]:

$$\phi_m(\boldsymbol{r}_\perp, q_z) = 2 \oint d\boldsymbol{s}\, \sigma_m(\boldsymbol{s}) e^{-i\omega/v s^\parallel} K_0\left(\frac{\omega|\boldsymbol{r}_\perp - \boldsymbol{s}^\perp|}{v}\right) \tag{4.35}$$

where the integral is performed over the surface of the nano-particle, $\boldsymbol{s}^\perp$ and $s^\parallel$ are respectively the

components of $\boldsymbol{s}$ which are orthogonal and parallel to the electron trajectory and K_0 is a modified Bessel function. Eventually, we obtain:

$$\Gamma^{\mathrm{QS}}(\omega) = \frac{8e^2}{hv^2}\sum_m \mathrm{Im}\left\{-g_m(\omega)\right\}\left|\int r_\perp dr_\perp d\phi \oint d\boldsymbol{s}\,\sigma_m(\boldsymbol{s})e^{-i\omega/vs^\parallel}\,K_0\left(\frac{\omega|\boldsymbol{r}_\perp-\boldsymbol{s}^\perp|}{v}\right)D(\boldsymbol{r}_\perp)e^{il\phi}\right|^2 \tag{4.36}$$

If, like they did, we suppose the the donut function to be a circle of radius b, we finally get:

$$\Gamma^{\mathrm{QS}}(\omega) = \frac{8e^2}{hv^2}\sum_m \mathrm{Im}\left\{-g_m(\omega)\right\}\left|\int d\phi \oint d\boldsymbol{s}\,\sigma_m(\boldsymbol{s})e^{-i\omega/vs^\parallel}\,K_0\left(\frac{\omega|\boldsymbol{R}-\boldsymbol{s}^\perp|}{v}\right)e^{il\phi}\right|^2 \tag{4.37}$$

where we defined $\boldsymbol{R} = (\boldsymbol{b}, \phi)$. We thus retrieve their semi-classical expression. In essence, this model has to work because, as we explained in the previous chapter, all the effects appearing in this experiment are classical and the only required ingredient is the electronic phase. However, all the intricate coherence effects cannot be reproduced with their model; despite this limitation, their formalism provides a remarkable and intuitive insight into the vortex-plasmon interaction.
Naturally, the same effects can be deduced from our wave-optical formalism as we will demonstrate in this section. As we saw in the introduction, within the paraxial approximation, a vortex electron state can be efficiently modeled by the transverse wavefunction:

$$\psi_{i,\perp}(\boldsymbol{r}_\perp) = e^{i\nu\theta}J_{|\nu|}\left(\kappa\, r_\perp\right) \tag{4.38}$$

where ν corresponds to the amount of OAM carried by the electron and κ its radial wavevector. We do not bother with the normalization of the wavefunction here as it has no consequence on further developments. Plugging this wavefunction in (4.22) we obtain:

$$\Gamma^{\mathrm{QS}}(\omega) = \frac{2e^2}{hv^2}\sum_m \mathrm{Im}\left\{-g_m(\omega)\right\}\left|\iint r_\perp\, dr_\perp\, d\theta\, \phi_m(\boldsymbol{r}_\perp, q_z)e^{-i\nu\theta}J_{|\nu|}\left(\kappa\, r_\perp\right)\right|^2 \tag{4.39}$$

We now consider the plasmon field to be the one of a nano-disk. The four first plasmon eigencharges of a 100×5 nm silver disk are represented on Fig. 4.16(a). As it was for the hexagon, these modes are degenerated. From these charge maps, one can infer that a reasonable hypothesis is to consider that the plasmon eigenpotentials are separable and read:

$$\phi_m(\boldsymbol{r}_\perp) = f(r_\perp)e^{im\theta} \tag{4.40}$$

where $f(r_\perp)$ is the radial component of the potential. We now note $F_\nu(\kappa)$ the ν-Hankel transform of $f(r_\perp)$ defined as:

$$F_\nu(\kappa) = \int r_\perp\, dr_\perp\, J_\nu\left(\kappa r_\perp\right)\, f(r_\perp) \tag{4.41}$$

Therefore integral (4.39) can be re-written:

$$\Gamma^{\mathrm{QS}}(\omega) = \frac{2e^2}{hv^2}\sum_m \mathrm{Im}\left\{-g_m(\omega)\right\}\left|F_{|\nu|}(\kappa)\int d\theta\, e^{i(m-\nu)\theta}\right|^2 \tag{4.42}$$

Which, providing that the complex exponentials are orthogonal when $m \neq \nu$, we finally get:

$$\boxed{\Gamma^{\mathrm{QS}}(\omega) = \frac{2e^2}{hv^2}\sum_m \mathrm{Im}\left\{-g_m(\omega)\right\}\left|F_{|\nu|}(\kappa)\right|^2\delta_{m,\nu}} \tag{4.43}$$

Thus, in agreement with [187], we see that a vortex electron will only probe plasmon states of which the angular symmetry order matches the OAM of the probe. In other words, vortex electrons probe the azimuthal symmetry of plasmons. We verify this conclusion through numerical simulations on figure 4.16 where we compared a classical EELS spectrum (b) with PSEELS spectra for vortex electrons of different OAMs (c-d-e). The expected selectivity is observed.

Finally, let's emphasize that selectivity appearing in equation (4.4.4) is perfect only if equation (4.40) is valid, which is exact only for rotational invariant objects e.g. disk, sphere or cylinder. However, for less symmetrical objects, the non-separability will introduce some deviations to this perfect selectivity but the azimuthal detection effect is still present[2].

[2]see [187] where the case of the triangle is investigated.

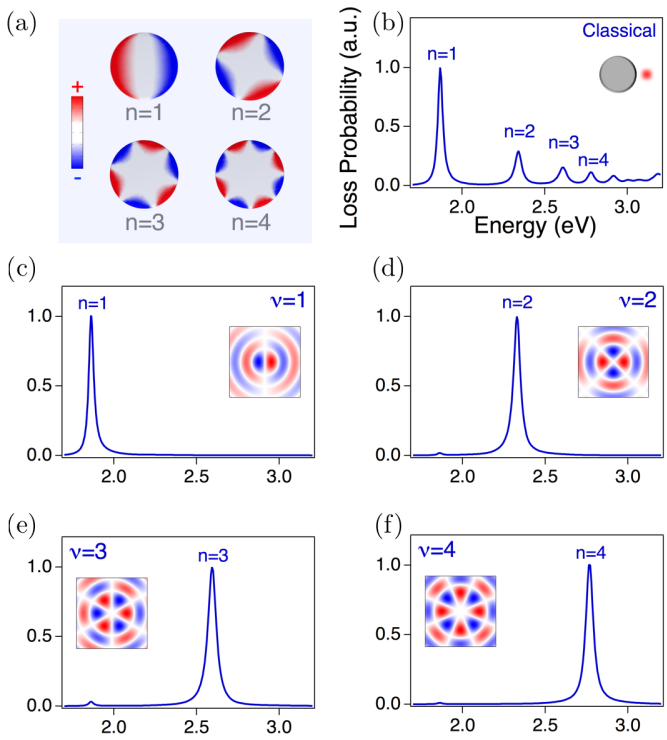

Figure 4.16: *(a) Four first plasmon eigenmodes of a 100 nm × 5 nm silver disk. (b) Classical EELS spectrum calculated for an electron impinging at the edge of the disk (see inset). In the semi-classical limit, the loss probability has been calculated for a vortex electron impinging at the center of the disk with a momentum of (c) ν=1, (d) ν=2, (e) ν=3, (f) ν=4. Each of these wavefunctions has a spatial extension of typically 10 nm and we plotted their real part in insets of (c-f).*

4.4.5 Dichroic EELS mapping with point vortex probes

In section 4.4.3, we demonstrated that a punctual pi-beam constitutes a local probe of the potential derivative with potential applications in phase reconstruction. Similarly, in this section we will try to determine what does a scanning point vortex measure. Particularly we are interested in *dichroic spectral imaging* which consists in taking sequentially two separate EELS maps with a $l = +1$ and $l = 1$ and constructing the difference of the two signals. Such an experiment has been investigated in core-loss spectroscopy and appears to measure the atomic magnetic properties [20, 254, 255]. In this section, we will determine the quantity mapped by a low loss dichroic spectral imaging. In order to answer this question, we will first take a closer look at the connections between the different sets of Gaussian beams.

4.4.5.1 Connection between the Hermite-Gaussian and Laguerre-Gaussian beams

From the development so far, we saw that a pi-beam is the electronic analogue of a linearly polarized electric field. Moreover, it appears that vortex beams (when $l = \pm 1$) can measure chirality [186] which suggests a close resemblance with circularly polarized light. In fact, these analogies can be pushed even further since vortex beams and pi-beams are linearly connected.

Propagating light is characterized by a two-components (Jones') vector $\boldsymbol{E}_\perp = (E_x, E_y)$ which represent the electric field in the plane orthogonal to the propagation axis. This vector contains all the information on the state of polarization of the light beam. Alternatively, one can also represent this vector in the circular polarization basis $\boldsymbol{E}_\perp = (E_{\circlearrowright}, E_{\circlearrowleft})$. Thus, the state of polarization of elliptic light can be visualized on the so-called Poincaré sphere (figure 4.17(a)) which is constructed by representing $E_{\circlearrowleft}/E_{\circlearrowright} = tan(\theta/2)\exp(i\Phi)$ [256].

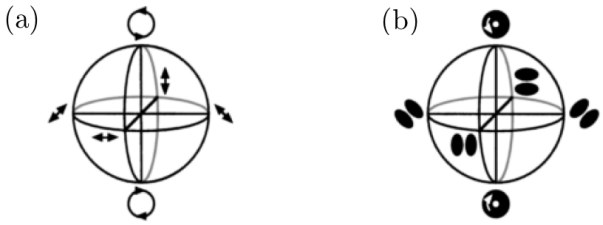

Figure 4.17: *(a) Poincaré sphere representation of the elliptic polarization of light. (b) Similar representation showing the connection between LG_{01} and HG_{01} beams. Reproduced from [257].*

On the north and south poles of the sphere are represented circularly polarized light while the equator corresponds to linearly polarized light. All the intermediate positions correspond to elliptically polarized light. This representation allows a geometrical visualization of the effects of different optical elements (e.g. waveplates) on the polarization state.

Quite remarkably, it has been shown that the same kind of relation holds between first order Gaussian beams [257] where: the role of the linear polarization is played by the HG_{01} beam (i.e. the pi-beam) while the circular polarization corresponds to the LG_{01} beam (i.e. vortex beam with $|l| = 1$). This is a consequence of the relation between the Hermite and Laguerre polynomials. They can be also positioned on a Poincaré-like sphere (figure 4.17(b)) where the intermediate positions correspond to first order generalized Hermite-Laguerre-Gaussian beams [258]. The latter states can therefore be represented as a linear combinations of HG or LG beams while these two basis are connected through:

$$\begin{pmatrix} \psi_{\circlearrowleft} \\ \psi_{\circlearrowright} \end{pmatrix} = \frac{1}{\sqrt{2}} \begin{pmatrix} 1 & -i \\ 1 & i \end{pmatrix} \begin{pmatrix} \psi_x \\ \psi_y \end{pmatrix} \tag{4.44}$$

where $\psi_{\circlearrowleft}$ and $\psi_{\circlearrowright}$ represent the LG_{01} and LG_{0-1} wavefunctions (see figure 4.3). Similarly, ψ_x and ψ_y represent the HG_{01} and HG_{10} wavefunctions (see figure 4.7). Consequently, a vortex beam can be represented as a linear combination of pi-beams:

$$\begin{cases} \psi_{\circlearrowleft} = \dfrac{1}{\sqrt{2}} \left(\psi_x + i\psi_y\right) & \text{(4.45a)} \\ \psi_{\circlearrowright} = \dfrac{1}{\sqrt{2}} \left(\psi_x + i\psi_y\right) & \text{(4.45b)} \end{cases}$$

A consequence of the latter equation is the fact that one can transform a vortex beam to a pi-beam (and conversely) by applying a $\pi/2$ phase-shift (astigmatic transform [258]). Such a transformation is called a *mode conversion* and can be deduced from the properties of Hermite and Laguerre polynomials [228]. This behavior has been experimentally demonstrated on electron beams by Schattschneider and collaborators [259] through the introduction of a strong astigmatism[3] on the vortex beam.

4.4.5.2 Dichroic EELS probability

We will now try to determine precisely which quantity is measured by a punctual vortex electron probe. To do so, we will exploit relations (4.45a) and (4.45b) which show that a vortex beam can be represented in terms of pi-beams. Indeed, we demonstrated in section 4.4.3 that a punctual pi-beam maps the derivative of the potential which will enable us to formulate the vortex loss probability in terms of derivative along the x and y axis. First of all, let's recall that, in the

[3] Let's also highlight that such a mode conversion illustrates the conservation of the topological structure of the electron beam as both first order LG and HG beams present a phase singularity.

coherent limit, the EELS probability is given by:

$$\Gamma^{\mathrm{QS}}(\omega) = \frac{2e^2}{hv^2}\sum_m \mathrm{Im}\left\{-g_m(\omega)\right\}\int d^2\boldsymbol{r}_\perp \int d^2\boldsymbol{r}'_\perp\ \phi_m(\boldsymbol{r}_\perp, q_z)\,\psi^*_{i,\perp}(\boldsymbol{r}_\perp)\,\phi^*_m(\boldsymbol{r}'_\perp, q_z)\,\psi_{i,\perp}(\boldsymbol{r}'_\perp) \quad (4.46)$$

Then, let's plug (4.45a) in the latter equation and calculate the EELS probability for a LG_{01} beam:

$$\begin{aligned}\Gamma^{\circlearrowleft}(x_0, y_0, \omega) = \frac{e^2}{v^2 h}\sum_m \mathrm{Im}\left\{-g_m(\omega)\right\}\Bigg(&\left|\left[\frac{\partial}{\partial x}\phi_m(x, y, \tfrac{\omega}{v})\right]_{(x_0,y_0)}\right|^2 + \left|\left[\frac{\partial}{\partial y}\phi_m(x, y, \tfrac{\omega}{v})\right]_{(x_0,y_0)}\right|^2 \\ &+ i\int d^2\boldsymbol{r}_\perp \int d^2\boldsymbol{r}'_\perp\ \phi_m(\boldsymbol{r}_\perp, q_z)\,\psi^*_x(\boldsymbol{r}_\perp)\,\phi^*_m(\boldsymbol{r}'_\perp, q_z)\,\psi_y(\boldsymbol{r}'_\perp) \\ &- i\int d^2\boldsymbol{r}_\perp \int d^2\boldsymbol{r}'_\perp\ \phi_m(\boldsymbol{r}_\perp, q_z)\,\psi_x(\boldsymbol{r}'_\perp)\,\phi^*_m(\boldsymbol{r}'_\perp, q_z)\,\psi^*_y(\boldsymbol{r}_\perp)\Bigg)\end{aligned} \quad (4.47)$$

where (x_0, y_0) is the impact parameter of the beam. After few simple manipulations, the latter can be re-written:

$$\Gamma^{\circlearrowleft}(x_0, y_0, \omega) = \frac{e^2}{v^2 h}\sum_m \mathrm{Im}\left\{-g_m(\omega)\right\}\Big(\left|\partial_x\phi_m\right|^2 + \left|\partial_y\phi_m\right|^2 - 2\mathrm{Im}\left\{(\partial_x\phi_m)(\partial_y\phi_m)^*\right\}\Big) \quad (4.48)$$

where we used a simplify notation:

$$\partial_x\phi_m \equiv \left[\frac{\partial}{\partial x}\phi_m(x, y, \tfrac{\omega}{v})\right]_{(x_0,y_0)} \quad (4.49)$$

Now, plugging (4.45a) in equation (4.46), we calculate the EELS probability for a LG_{0-1} beam and obtain:

$$\Gamma^{\circlearrowright}(x_0, y_0, \omega) = \frac{e^2}{v^2 h}\sum_m \mathrm{Im}\left\{-g_m(\omega)\right\}\Big(\left|\partial_x\phi_m\right|^2 + \left|\partial_y\phi_m\right|^2 + 2\mathrm{Im}\left\{(\partial_x\phi_m)(\partial_y\phi_m)^*\right\}\Big) \quad (4.50)$$

Therefore, the dichroic signal $D(x_0, y_0, \omega)$ reads:

$$D(x_0, y_0, \omega) = \Gamma^{\circlearrowleft}(x_0, y_0, \omega) - \Gamma^{\circlearrowright}(x_0, y_0, \omega) = -\frac{4e^2}{v^2 h}\sum_m \mathrm{Im}\left\{-g_m(\omega)\right\}\ \mathrm{Im}\left\{(\partial_x\phi_m)(\partial_y\phi_m)^*\right\} \quad (4.51)$$

Noticing that any complex number $z \in \mathbb{C}$ satisfies $\mathrm{Im}(2z) = \mathrm{Im}(z - z^*)$, one can re-write the latter equation as:

$$D(x_0, y_0, \omega) = -\frac{2e^2}{v^2 h}\sum_m \mathrm{Im}\left\{-g_m(\omega)\right\}\ \mathrm{Im}\left\{(\partial_x\phi_m)(\partial_y\phi_m)^* - (\partial_x\phi_m)^*(\partial_y\phi_m)\right\} \quad (4.52)$$

Let's moreover notice that:

$$\boldsymbol{\nabla}\phi_m \times \boldsymbol{\nabla}\phi^*_m = \begin{pmatrix}\partial_y\phi_m\,\partial_z\phi^*_m - \partial_y\phi^*_m\,\partial_z\phi_m \\ \partial_z\phi_m\,\partial_x\phi^*_m - \partial_z\phi^*_m\,\partial_x\phi_m \\ \partial_x\phi_m\,\partial_y\phi^*_m - \partial_x\phi^*_m\,\partial_y\phi_m\end{pmatrix} \quad (4.53)$$

Thus, we can re-write:

$$D(x_0, y_0, \omega) = -\frac{2e^2}{v^2 h}\sum_m \mathrm{Im}\left\{-g_m(\omega)\right\}\ \mathrm{Im}\left\{(\boldsymbol{\nabla}\phi_m \times \boldsymbol{\nabla}\phi^*_m)_z\right\} \quad (4.54)$$

Besides, let's consider a complex scalar field $\Psi(\boldsymbol{r}) = M(\boldsymbol{r})\exp(i\theta(\boldsymbol{r}))$ where $M(\boldsymbol{r})$ and $\theta(\boldsymbol{r})$ respectively represent the modulus and the phase. Then, the current $\boldsymbol{J}$ associated to this field reads:

$$\boldsymbol{J}(\boldsymbol{r}) = \mathrm{Im}\left\{\Psi^*(\boldsymbol{r})\boldsymbol{\nabla}\Psi(\boldsymbol{r})\right\} \tag{4.55}$$

Then the *current vorticity* $\boldsymbol{\Omega}(\boldsymbol{r})$ can be written [260]:

$$\boldsymbol{\Omega}(\boldsymbol{r}) = \boldsymbol{\nabla}\times\boldsymbol{J}(\boldsymbol{r}) = \mathrm{Im}\left\{\boldsymbol{\nabla}\Psi^*(\boldsymbol{r})\times\boldsymbol{\nabla}\Psi(\boldsymbol{r})\right\} \tag{4.56}$$

Comparing the latter equation with (4.54), we conclude that:

$$D(x_0, y_0, \omega) = \frac{2e^2}{v^2 h}\sum_m \mathrm{Im}\left\{-g_m(\omega)\right\}\,\Omega_{z,m}(x_0, y_0, q) \tag{4.57}$$

where $\Omega_{z,m}$ is the z-component of the vorticity associated with the scalar potential of mode m. Therefore, as we intuitively felt, a dichroic EELS measurement maps the vorticity of the plasmon potential.

4.4.5.3 Mapping the local chirality properties of surface plasmon fields

Another important quantity in nano-optics is the *optical chirality density* $\mathscr{C}$ which reads:

$$\mathscr{C} = \frac{c}{8\pi\omega}\left(\boldsymbol{E}.\boldsymbol{\nabla}\times\boldsymbol{E} + \boldsymbol{H}.\boldsymbol{\nabla}\times\boldsymbol{H}\right) \tag{4.58}$$

Phenomenologically, optical chirality measures the asymmetry in the rates of excitation between a small chiral molecule and its enantiomer as demonstrated by Tang and collaborators [261, 262]. Thus, this quantity plays a central role in the study of chiral light-matter interaction and in the control of light emission at the nanoscale. As we detail in appendix E, optical chirality appears to be a fundamental quantity of the electromagnetic field which satisfies the continuity equation [263]:

$$\frac{\partial\mathscr{C}}{\partial t} + \boldsymbol{\nabla}.\boldsymbol{\Phi} = 0 \tag{4.59}$$

where $\boldsymbol{\Phi}$ is the corresponding *optical chirality flow*:

$$\boldsymbol{\Phi} = \frac{c^2}{8\pi\omega}\left(\boldsymbol{E}\times(\boldsymbol{\nabla}\times\boldsymbol{H}) + \boldsymbol{H}\times(\boldsymbol{\nabla}\times\boldsymbol{E})\right) \tag{4.60}$$

Importantly, it appears that the optical chirality flow is proportional to *the spin angular momentum* of the electromagnetic field [263, 264] which enables a more concrete physical interpretation of $\boldsymbol{\Phi}$. Importantly, by time averaging, one can define the spectral version of (4.58) and (4.60) as:

$$\begin{cases} \mathscr{C}(\omega) = -\dfrac{1}{8\pi}\mathrm{Im}\left\{\boldsymbol{E}^*.\boldsymbol{H}\right\} & \text{(4.61a)} \\ \boldsymbol{\Phi} = \dfrac{c}{16\pi}\mathrm{Im}\left\{\boldsymbol{E}^*\times\boldsymbol{E} + \boldsymbol{H}^*\times\boldsymbol{H}\right\} & \text{(4.61b)} \end{cases}$$

As an illustration, we reported from [265], the spectral optical chirality and chirality flow associated with a surface plasmon-polariton resonance of a silver film on figure 4.18. Examples for other geometries can be found in [266].

Comparing equation (4.61b) with (4.54), we therefore conclude that:

$$D(x_0, y_0, \omega) = \frac{32\pi e^2}{v^2 hc}\sum_m \mathrm{Im}\left\{-g_m(\omega)\right\}\,\Phi^{\mathrm{E}}_{z,m}(x_0, y_0, q) \tag{4.62}$$

where $\boldsymbol{\Phi}^{\mathrm{E}}_m$ denotes the electric part of the chirality flow associated with the plasmon mode m. Therefore, low-loss dichroic EELS measures the local electric chirality flow of the plasmon field. Such an experiment could therefore be a important tool in the investigation of so-called *super-chiral*

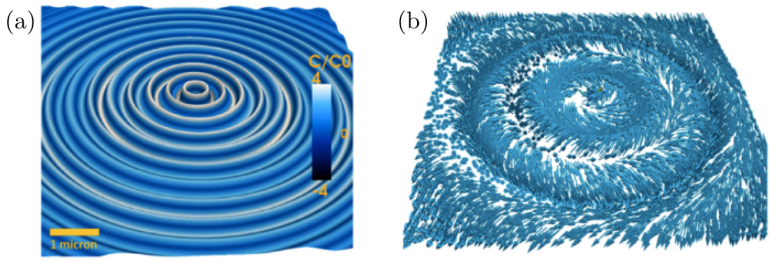

Figure 4.18: *Calculation reported from [265] showing the (a) Optical chirality distribution and (b) optical chirality flow carried by a surface plasmon polariton field of a semi-infinite silver film excited by a circularly polarized dipole $p(\hat{x} + i\hat{y})$ placed 50 nm above the surface.*

fields [267, 268, 269] which currently constitutes a hot field of research.

Interestingly, $\mathbf{\Phi}^{\mathrm{E}}$ has been connected to the optical torque $\boldsymbol{\tau}$ undergone by an electric dipole [270] so that dichroic EELS is somehow a measurement of a torque applied by the electron on the nano-particle[4]. This connects our development with the work of Asenjo-Garcia and García de Abajo [186] who already noticed that the z-component of the torque exerted by the electron on a nano-particle is proportional to the EELS probability:

$$\tau_z(\omega) = -\hbar\Delta l\,\Gamma(\omega) \tag{4.63}$$

where $\hbar\Delta l = \hbar(l_f - l_i)$ is the OAM difference between the initial and final electron state.

4.5 Post-selection of the final state

In section 4.2.2, we explained that a PSEELS experiment basically consists in probing *one* specific electronic transition mediated by a plasmon potential. Consequently, only one final state needs to be measured in order to observe an interference effect. Due to the experimental setup (the entrance of the EELS spectrometer being a Fourier plane), the selection of the final states has been done in the planewave basis. Thus, in order to satisfy the conditions above, we imposed the semi-collection angle β to be smaller than $\theta_{\mathrm{E}} \approx 20\,\mu$rad. In other words, only the electrons traveling along the optical axis are collected what consists in assuming $\psi_f(\boldsymbol{r}) \propto \exp(ikz)$. This so-called *coherent limit* enabled us to further explore the physics of phase-shaped EELS in plasmonics. However, we also saw in section 4.3 that this condition ($\beta < \theta_E$) imposes stringent restrictions on the experimental conditions and dramatically reduces the signal to noise ratio.

The purpose of this section is to extend it to other basis and understand how the signal to noise ratio could be increased without destroying the coherent effects.

4.5.1 Influence of the collection angle

First of all, let's confirm our intuition and rigorously study the effect of the collection angle on the interferences' quality. To do so, we first decompose the final electron wavefunction on the plane wave basis, separating the propagating axis and the transverse plane as:

$$\psi_f(\boldsymbol{r}) = \frac{1}{L^{3/2}} e^{ik_{f,z}z} e^{i\boldsymbol{k}_{f,\perp}\cdot\boldsymbol{r}_\perp} \tag{4.64}$$

and we still use equation (4.15a) for ψ_i. Following [19], we can decompose the QS PSEELS (4.10) probability as :

$$\Gamma^{\mathrm{QS}}(\omega) = \int d^2k_{f,\perp} \frac{d\Gamma^{\mathrm{QS}}(\omega)}{dk_{f,\perp}} \tag{4.65}$$

[4]Let's higlight the remarkable similarity between (4.62) and equation (11) of [270].

where,

$$\frac{d\Gamma^{\mathrm{QS}}(\omega)}{dk_{f,\perp}} = \frac{e^2}{4\pi^3\hbar v^2}\int d\boldsymbol{r}\int d\boldsymbol{r}'\psi^*_{i,\perp}(\boldsymbol{r}_\perp)\psi_{i,\perp}(\boldsymbol{r}'_\perp)e^{iq_z(z'-z)}e^{i\boldsymbol{k}_{f,\perp}\cdot(\boldsymbol{r}_\perp-\boldsymbol{r}'_\perp)}\mathrm{Im}(-W(\boldsymbol{r},\boldsymbol{r}',\omega)) \quad (4.66)$$

Using the eigendecomposition of the screened potential (4.11) and the non-recoil approximation, the latter equation can be re-written as:

$$\begin{aligned}\frac{d\Gamma^{\mathrm{QS}}(\omega)}{dk_{f,\perp}} = \frac{e^2}{4\pi^3\hbar v^2}\sum_m \mathrm{Im}\left\{-g_m(\omega)\right\}\int d\boldsymbol{r}_\perp\int d\boldsymbol{r}'_\perp\psi^*_{i,\perp}(\boldsymbol{r}_\perp)\psi_{i,\perp}(\boldsymbol{r}'_\perp)\, e^{i\boldsymbol{k}_{f,\perp}\cdot(\boldsymbol{r}_\perp-\boldsymbol{r}'_\perp)} \\ \times\int dz\int dz'\, e^{iq_z(z'-z)}\phi_m(\boldsymbol{r}_\perp,z)\phi^*_m(\boldsymbol{r}'_\perp,z')\end{aligned} \quad (4.67)$$

The integration over z and z' is straightforward and corresponds to a Fourier transform of the potential ϕ_m. Combining the latter expression with equation (4.65), one can write Γ^{QS} as:

$$\Gamma^{\mathrm{QS}}(\omega) = \frac{e^2}{4\pi^3\hbar v^2}\sum_m \mathrm{Im}\left\{-g_m(\omega)\right\}\iint d\boldsymbol{r}_\perp d\boldsymbol{r}'_\perp\psi^*_{i,\perp}(\boldsymbol{r}_\perp)\phi_m(\boldsymbol{r}_\perp,q_z)\, T(\boldsymbol{r}_\perp,\boldsymbol{r}'_\perp)\,\psi_{i,\perp}(\boldsymbol{r}'_\perp)\phi^*_m(\boldsymbol{r}'_\perp,q_z) \quad (4.68)$$

where we have set:

$$T(\boldsymbol{r}_\perp,\boldsymbol{r}'_\perp) = \int_D d\boldsymbol{k}_{f,\perp}\, e^{i\boldsymbol{k}_{f,\perp}\cdot(\boldsymbol{r}_\perp-\boldsymbol{r}'_\perp)} \quad (4.69)$$

The integration volume D corresponds to the surface of the collection aperture. In polar basis, the later equation reads:

$$T(\boldsymbol{r}_\perp,\boldsymbol{r}'_\perp) = \int_0^{k_{\max}} k_{f,\perp}\, dk_{f,\perp}\int_0^{2\pi} d\theta e^{ik_{f,\perp}|\boldsymbol{r}_\perp-\boldsymbol{r}'_\perp|\cos(\theta)} \quad (4.70)$$

where θ is the angle between the two vectors $\boldsymbol{k}_{f,\perp}$ and $(\boldsymbol{r}_\perp-\boldsymbol{r}'_\perp)$. Using the following expression of the n-th order Bessel function of the first kind J_n:

$$J_n(x) = \frac{1}{2\pi}\int_{-\pi}^{\pi} e^{i(nu-x\,sin(u))}du \quad (4.71)$$

and the following property of Bessel integrals [195]:

$$\int_0^a x\,J_0(bx)dx = \frac{a}{b}J_1(ab) \quad (4.72)$$

We can finally deduce:

$$T(\boldsymbol{r}_\perp,\boldsymbol{r}'_\perp) = \frac{2\pi k_{\max}}{|\boldsymbol{r}_\perp-\boldsymbol{r}'_\perp|}J_1\left(k_{\max}|\boldsymbol{r}_\perp-\boldsymbol{r}'_\perp|\right) \quad (4.73)$$

Combining equations (4.68) and (4.73) we obtain:

$$\boxed{\begin{aligned}\Gamma^{\mathrm{QS}}(\omega) = \frac{e^2k_{\max}}{2\pi^2\hbar v^2}\sum_m \mathrm{Im}\left\{-g_m(\omega)\right\}\iint d\boldsymbol{r}_\perp d\boldsymbol{r}'_\perp\psi^*_{i,\perp}(\boldsymbol{r}_\perp)\phi_m(\boldsymbol{r}_\perp,q_z) \\ \times\frac{J_1\left(k_{\max}|\boldsymbol{r}_\perp-\boldsymbol{r}'_\perp|\right)}{|\boldsymbol{r}_\perp-\boldsymbol{r}'_\perp|}\psi_{i,\perp}(\boldsymbol{r}'_\perp)\phi^*_m(\boldsymbol{r}'_\perp,q_z)\end{aligned}} \quad (4.74)$$

which constitutes the analogue of formula (4.22) when several final states are collected. We are now in position to study the influence of β on the PSEELS measurement. To do so, we re-computed the calculation of figure 4.19(b) but using equation (4.74) instead of equation (4.22), and varied β from 1 to 100 μrad. The results are plotted on figure 4.19.

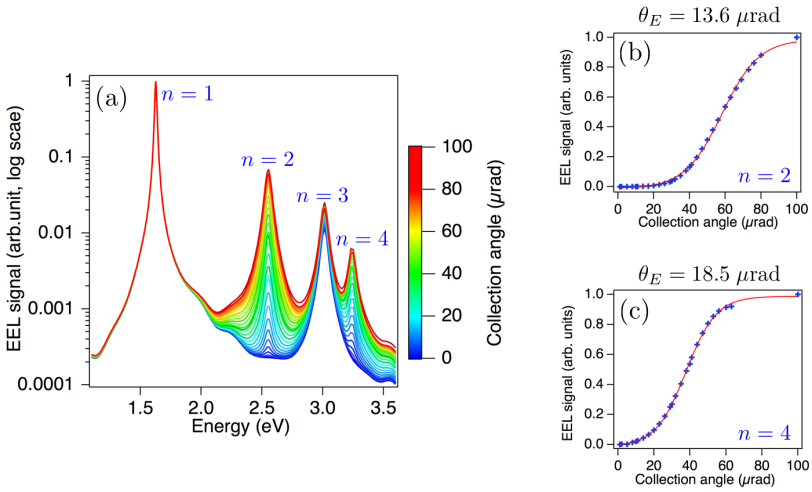

Figure 4.19: *(a) Same calculation as figure 4.13(b) but taking into account the collection angle influence. For each value of the collection angle, the EEL signal is normalized to its maximum value. (b-c) Intensity of the $n = 2$ and $n = 4$ peaks as a function of the collection angle. Both curves are normalized with respect to their value at $\beta = 100\,\mu rad$. The value of θ_E for the modes 2 and 4 are displayed on the top of graphs (b) and (c).*

We see that when the collection semi-angle is small ($\sim 5\ \mu$rad) the dichroic effect is maximal while is completely vanishes at large collection semi-angle ($\sim 100\ \mu$rad). Thus, when we open the EELS aperture, we add additional undesirable terms in equation (4.74) which ends up in a blurring of the interference patterns. To check the consistency of the previous analysis, we calculate the behavior of equation (4.74) in the limits $\beta \longrightarrow 0$ and $\beta \longrightarrow \frac{\pi}{2}$.

Reducing the size of the collection aperture corresponds to take the limit $\beta \longrightarrow 0$ in the previous expressions. In this case, $k_{\max} \longrightarrow 0$, thus following [195] we can Taylor expand J_1 to the second order which leads to:

$$T(\boldsymbol{r}_\perp, \boldsymbol{r}'_\perp) \sim \frac{\pi k_{max}^2}{\Gamma(2)} \tag{4.75}$$

As expected, we lose the dependence in $|\boldsymbol{r}_\perp - \boldsymbol{r}'_\perp|$ in T which enables us to write Γ^{QS}:

$$\Gamma^{\mathrm{QS}}(\omega) \sim \frac{e^2 k_{max}^2}{4\pi^2 \hbar v^2 \Gamma(2)} \sum_m \mathrm{Im}\left\{-g_m(\omega)\right\} \left| \int d\boldsymbol{r}_\perp \phi_m(\boldsymbol{r}_\perp, q_z) \psi^*_{i,\perp}(\boldsymbol{r}_\perp) \right|^2 \tag{4.76}$$

We retrieve our equation (4.22) what confirms our initial intuition. On the contrary, increasing the size of the collection aperture corresponds to taking the limit $\beta \longrightarrow \frac{\pi}{2}$ i.e. $k_{max} \longrightarrow +\infty$. Using properties of Bessel functions, one finds:

$$\Gamma^{\mathrm{QS}}(\omega) \sim \frac{e^2 k_{max}}{\pi^2 \hbar v^2} \sum_m \mathrm{Im}\left\{-g_m(\omega)\right\} \int d\boldsymbol{r}_\perp \left|\phi_m(\boldsymbol{r}_\perp, q_z) \psi^*_{i,\perp}(\boldsymbol{r}_\perp)\right|^2 \tag{4.77}$$

The modulus is now under the integral sign which corresponds to an incoherent sum of terms: the interference terms vanish along with the dichroïc effects. Indeed, as first demonstrated by Ritchie and Howie (see equation (11) of [143]), the latter equation can be re-written:

$$\Gamma^{\mathrm{QS}}(\omega) \sim \int d\boldsymbol{r}_\perp\, \Gamma^{\mathrm{CLA}}(\omega) \times \left|\psi^*_{i,\perp}(\boldsymbol{r}_\perp)\right|^2 \tag{4.78}$$

where Γ^{CLA} is the classical expression (4.2) obtained with the point electron model. Our numerical analysis confirms the initial guess: θ_{E} is a stringent limit to any PSEELS experiment such as we considered so far. In fact, this effect has already been studied by Ritchie and Howie [143] who tried to determine why the quantum nature of electrons play no role in a conventional EELS

experiments. The major conclusion of their work is that, when all the electrons are collected, a ray optical formulation of the problem is sufficient, which is in agreement with the present developments. However, they also concluded that "*when a small solid angle of axial collection is employed, the energy-loss spectrum will still approximate to the classical expression*". Indeed, they (naturally at the time) did not consider the possibility of shaping the phase of the electron beams and only considered symmetric probes which, indeed, basically reproduce a classical behavior.

4.5.2 Selection of the final state: basis change

The previous developments boil down to the following question: is it possible to go beyond the θ_{E} limit i.e. collect more electrons and still measure interferences? We will see in this section that the answer is positive.

In fact, the reason of the above limitation is that we are constrained by the experimental setup: we systematically choose ψ_f in the planewave basis because the collection plane is a Fourier plane. Nevertheless, *depending on the type of physics we want to probe, the relevant final state basis will differ*. For example:

- In order to probe a **momentum transfer** between the electron and the plasmon field (to reconstruct a dispersion relation), the relevant basis is, indeed, the **planewave basis**. We therefore prepare a initial planewave state $\psi_i \propto \exp(i\boldsymbol{k}_i.\boldsymbol{r})$ and select a final planewave state $\psi_f \propto \exp(i\boldsymbol{k}_f.\boldsymbol{r})$ which corresponds to a measurement of the wavevector $\boldsymbol{q} = \boldsymbol{k}_f - \boldsymbol{k}_i$ transferred to the plasmon field. This essentially corresponds to an angle-resolved electron energy loss spectroscopy experiment [271].

- In order to probe an **orbital angular momentum transfer** between the electron and the plasmon field, the relevant basis is the **vortex basis** $\{\mathrm{LG}_{0,l}\}_{l\in\mathbb{Z}}$. We therefore need to prepare a initial vortex state $\psi_i \propto \exp(il_i\phi)$ and select a final vortex state $\psi_f \propto \exp(il_f\phi)$ which corresponds to a measurement of the OAM $\Delta l = l_f - l_i$ transferred to the plasmon field.

- In order to probe the **multipolar symmetry** of a (quasi-)unidimensional plasmon field (e.g. a rod aligned along a certain x axis) the relevant basis is a **Hermite-Gaussian beam basis** $\{\mathrm{HG}_{0,n}\}_{n\in\mathbb{N}}$.

One therefore needs to make a *basis change* after the interaction in order to select the proper final state. This can be achieved by the addition of an *electron sorter* as shown on figure 4.20.
An electron sorter is an optical element which spatially decomposes an electron beam on a certain basis. For example an OAM sorter, as demonstrated by Grillo and collaborators [272], transforms any beam in an ensemble of spatially separated pure vortex beams of different OAMs. By looking at the relative intensity of the spots associated with each vortex, one can deduce the amount of OAM carried by the initial beam. In our case, by putting such a sorter after the sample one can decompose the final electron beam in the vortex basis in the collection plane. One can then use the collection aperture to select one of the spots and therefore realize an EELS measurement of a *vortex* $\rightarrow$ *plasmon* $\rightarrow$ *vortex* transition. Let's highlight that such an experiment has been first suggested by Ugarte and Ducati [187]. Nevertheless, the underlying principle is much more general and can possibly be applied to any kind on symmetry and final state basis.

4.5.3 Example: measurement of the OAM carried by a vortex plasmon

In this section, we simply aim at giving a brief example of final states' post-selection. Let's highlight that the following calculations is still fledgling and further verifications are required before having a final form of the formula. A similar and somehow more rigorous calculation will be done in section 4.6.4 in the particular case of a split-beam experiment.

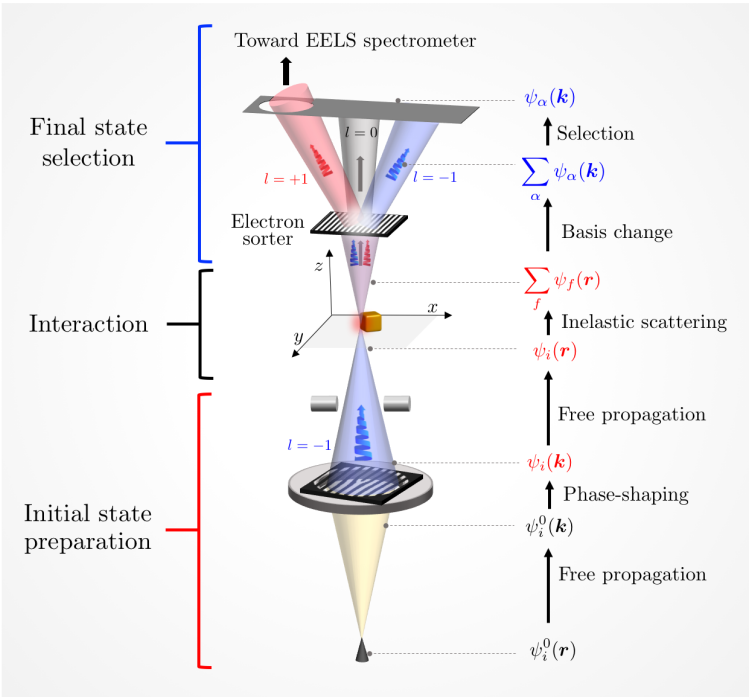

Figure 4.20: *Schematics describing a phase-shaped electron energy loss spectroscopy experiment when a post-selection of the final state is applied.*

Let's consider a vortex plasmon field [273, 274] in interaction with a vortex electron. The electric dyadic Green function of a vortex plasmonic system can be written [10]:

$$\overleftrightarrow{\boldsymbol{G}}(\boldsymbol{r}, \boldsymbol{r}', \omega) = \frac{1}{4\pi\omega^2} \sum_m g_m(m) \boldsymbol{E}_m(\boldsymbol{r}) \otimes \boldsymbol{E}_m^*(\boldsymbol{r}') \tag{4.79}$$

where the plasmon modes are indexed by $m \in \mathbb{Z}$ and the z-component of the plasmonic electric eigenfields can be written in cylindrical coordinates $(r_\perp, \theta, z)$ as [275]:

$$\boldsymbol{E}_{z,m}(r_\perp, \theta, z) = \boldsymbol{E}_0 \, \mathrm{sign}(z) \, J_m(\kappa_p r_\perp) e^{im\phi} e^{-k_p z} \tag{4.80}$$

In the latter κ_p and k_p are respectively the radial and axial wavectors. We can also consider that the incident electron kinetic energy is principally contained in its z-component, therefore [19]:

$$\boldsymbol{\nabla} \psi_i(\boldsymbol{r}) \approx \psi_i(\boldsymbol{r}) i k_i \hat{z} = \frac{imv}{\hbar} \psi_i(\boldsymbol{r}) \, \hat{z} \tag{4.81}$$

where $\hat{z}$ is the unitary vector of z-axis. Plugging the modal decomposition (4.79) and (4.81) in (3.6), we obtain:

$$\Gamma(\omega) = \frac{2e^2 v L}{\hbar \omega^2} \sum_m \sum_f \mathrm{Im}\left\{-g_m(\omega)\right\} \left| \int d\boldsymbol{r} \; \psi_f(\boldsymbol{r}) E_{z,m}(\boldsymbol{r}) \psi_i^*(\boldsymbol{r}) \right|^2 \delta(\epsilon_f - \epsilon_i + \omega) \tag{4.82}$$

Now, we suppose that the initial electron state is a vortex and we expand the final states over the vortex basis so that the corresponding wavefunctions read:

$$\psi_\alpha(\boldsymbol{r}) = e^{i\nu_\alpha \theta} J_{|\nu_\alpha|}(\kappa_\alpha r_\perp) e^{ik_\alpha z} \tag{4.83}$$

where $\alpha = i, f$ indexes the initial and final states. Then the sum over the final states reduces to a sum over the final OAMs ν_f. In this situation, since both the plasmon field and the electron probe have the same symmetry, the integral (4.82) becomes separable and can be re-written as:

$$\Gamma(\omega) = \frac{2e^2 vL}{\hbar\omega^2} \sum_m \sum_{\nu_f} \mathrm{Im}\left\{-g_m(\omega)\right\} \left| \int dr_\perp \; J_{|\nu_f|}(\kappa_f r_\perp)\, J_m(\kappa_p r_\perp)(\boldsymbol{r})\, J^*_{|\nu_i|}(\kappa_i r_\perp) \right|^2 \\ \times \left| \int dz\, \mathrm{sign}(z) \exp\left(i(k_f - k_i - k_p)z\right) \right|^2 \left| \int d\theta \exp\left(i(\nu_f - \nu_i + m)\theta\right) \right|^2 \delta(\epsilon_f - \epsilon_i + \omega) \tag{4.84}$$

The Fourier transform of the sign function is $\mathscr{F}(\mathrm{sign}(x)) = \mathcal{P}(2/ik)$ where $\mathcal{P}$ is the Cauchy principal value. Moreover the triple Bessel integral:

$$\xi(\kappa_i, \kappa_f, \kappa_p) \doteq \left| \int dr_\perp \; J_{|\nu_f|}(\kappa_f r_\perp)\, J_m(\kappa_p r_\perp)(\boldsymbol{r})\, J^*_{|\nu_i|}(\kappa_i r_\perp) \right|^2 \tag{4.85}$$

can be solved analytically [276] although it is a pretty tedious work. Finally, as we saw in section 4.4.4, the integral over θ gives a Dirac delta function. Eventually, the electron-energy loss signal reads:

$$\Gamma(\omega) = \frac{4e^2 vL}{\hbar\omega^2} \sum_m \sum_{\nu_f} \mathrm{Im}\left\{-g_m(\omega)\right\} \xi(\kappa_i, \kappa_f, \kappa_p) \mathcal{P}\left(\frac{1}{i(k_f - k_i - k_p)}\right) \\ \times \delta(\nu_f - \nu_i + m)\delta(\epsilon_f - \epsilon_i + \omega) \tag{4.86}$$

Thus, from the latter equation, one can see that the OAM m carried by the plasmon field can be deduced by working in the final vortex state basis.

4.6 Measurement of the coherence at the nanometer scale

We will now get interested in a very particular type of phase-shaped beam, the so-called split-beam, and show how they can be used to measure the spatial coherence of optical fields at the nanometer scale.

4.6.1 Electron bi-prism

Electron holography has been introduced by Gabor in 1948 [168] in order to overcome spatial resolution issues due to lenses aberration. It consists in generating an interference pattern between a wave which went through the specimen (secondary wave) and a reference wave which did not (primary wave). Several variants of this method exist such as differential phase contrast [277], in-line holography [278] or ptychography [188]. The most widespread method is the off-axis electron holography [279] of which working principle is shown on figure 4.21(a).
A central element in electron holography is the *Möllenstedt electrostatic biprism* which allows to tilt the electronic wavefront in order to form the hologram. It consists of a metallic filament (typically made of tungsten) carrying an electrostatic potential V. A planewave impinging on the biprism produces two symmetrically tilted planewaves given by the formula:

$$\psi_{\mathrm{tilt}}(x, z) = \exp i\left(k_z z - \frac{me}{\hbar^2 k_z} \int_{-\infty}^{z} V(x, z')dz'\right) \tag{4.87}$$

Propagating this wavefunction to the sample plane, it produces two focused spots (instead of one single spot for the simple planewave) impinging at positions $\boldsymbol{r}_1$ and $\boldsymbol{r}_2$ separated by a distance tunable by changing the voltage V. The corresponding wavefunction can therefore be written [19]:

$$\psi_{i,\perp}(\boldsymbol{r}_\perp) = \frac{1}{\sqrt{2}}\left(f(\boldsymbol{r}_\perp - \boldsymbol{r}_1) + f(\boldsymbol{r}_\perp - \boldsymbol{r}_2)e^{i\delta}\right) \tag{4.88}$$

where $f(\boldsymbol{r}_\perp - \boldsymbol{r}_1)$ is a function centered in $\boldsymbol{r}_1$ modeling a beam spot (typically a Lorentzian function). The latter wavefunction therefore represents two coherent beams, dephased by $\delta = mv(a)/\hbar$ where (a) is the difference between their respective optical paths.

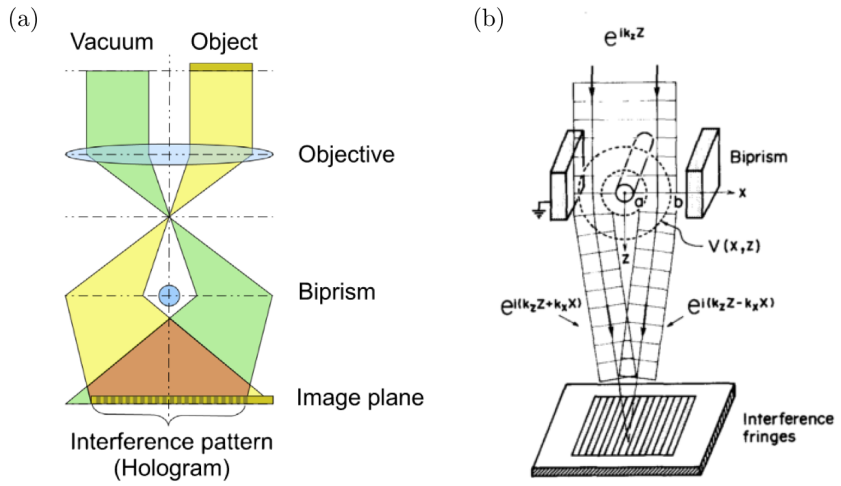

Figure 4.21: *(a) Simplified schematics showing the mechanism of hologram formation in off-axis electron holography. Reproduced from [280]. Schematics showing the working principle of a Möllenstedt electrostatic biprism. Reproduced from [163].*

4.6.2 Split-beam electron energy loss probability

In this section we will determine which quantity is measured with such a split-beam. As we demonstrated in the previous chapter, the retarded EEL probability reads:

$$\frac{d\Gamma^{\mathrm{R}}(\omega)}{dt} = \frac{8\pi\hbar e^2}{m^2}\sum_f \int d\boldsymbol{r}\, d\boldsymbol{r}'\; \psi_f^*(\boldsymbol{r})\psi_f(\boldsymbol{r}')\; [\boldsymbol{\nabla}\psi_i(\boldsymbol{r})]\,\mathrm{Im}\Big\{-\overleftrightarrow{\boldsymbol{G}}(\boldsymbol{r},\boldsymbol{r}',\omega)\Big\}\,[\boldsymbol{\nabla}\psi_i^*(\boldsymbol{r}')]\,\delta(\epsilon_f-\epsilon_i+\omega) \tag{4.89}$$

where $\overleftrightarrow{\boldsymbol{G}}$ is the Green dyadic. We can now use equations (4.15a) and (4.15b) to separate the incident and outgoing wavefunctions. For simplicity, we also consider the coherent limit where $\psi_f \propto \exp(ik_{f,z}z)$. We can again consider that the incident electron kinetic energy is principally contained in its z-component so that equation (4.81) is valid. Using equation (4.18), one can finally re-write Γ^{R} as:

$$\Gamma^{\mathrm{R}}(\omega) = \frac{4e^2}{\hbar}\int d\boldsymbol{r}_\perp\, d\boldsymbol{r}'_\perp \int dz\, dz'\; \psi_{i,\perp}^*(\boldsymbol{r}_\perp)\psi_{i,\perp}(\boldsymbol{r}'_\perp)\,\mathrm{Im}\Big\{-\hat{z}.\overleftrightarrow{G}(\boldsymbol{r}_\perp,\boldsymbol{r}'_\perp,z,z',\omega).\hat{z}\Big\}e^{-iq_z(z-z')} \tag{4.90}$$

We then note $G_{zz} = \hat{z}.\overleftrightarrow{\boldsymbol{G}}.\hat{z}$. Therefore, using the definition of the spatial Fourier transform (4.19), one gets:

$$\Gamma^{\mathrm{R}}(\omega) = \frac{4e^2}{\hbar}\int d\boldsymbol{r}_\perp\, d\boldsymbol{r}'_\perp\; \psi_{i,\perp}^*(\boldsymbol{r}_\perp)\psi_{i,\perp}(\boldsymbol{r}'_\perp)\,\mathrm{Im}\{-G_{zz}(\boldsymbol{r}_\perp,\boldsymbol{r}'_\perp,q_z,-q_z,\omega)\} \tag{4.91}$$

We recognize in the latter expression the $\hat{z}$-projection of the CDOS tensor defined as [84]:

$$\rho_{\hat{z}}(\boldsymbol{r},\boldsymbol{r}',\omega) = \frac{2\omega}{\pi}\mathrm{Im}\Big\{-\hat{z}.\overleftrightarrow{G}(\boldsymbol{r},\boldsymbol{r}',\omega).\hat{z}\Big\} \tag{4.92}$$

Using the latter definition in equation (4.91), one can thus write:

$$\Gamma^{\mathrm{R}}(\omega) = \frac{2\pi e^2}{\hbar\omega}\int d\boldsymbol{r}_\perp\, d\boldsymbol{r}'_\perp\; \psi_{i,\perp}^*(\boldsymbol{r}_\perp)\psi_{i,\perp}(\boldsymbol{r}'_\perp)\;\rho_z(\boldsymbol{r}_\perp,\boldsymbol{r}'_\perp,q_z,-q_z,\omega) \tag{4.93}$$

where ρ_z has been Fourier transformed with respect to z and z'. For brevity we will hereafter note $\tilde{\rho}_z(\boldsymbol{r}_\perp,\boldsymbol{r}'_\perp,q_z,\omega) \equiv \tilde{\rho}_z(\boldsymbol{r}_\perp,\boldsymbol{r}'_\perp,q_z,-q_z,\omega)$. We can now plug the split-beam wavefunction (4.88) and use the *reciprocity theorem* $\rho(\boldsymbol{r},\boldsymbol{r}',\omega) = \rho(\boldsymbol{r}',\boldsymbol{r},\omega)$. Putting everything together, it leads to:

$$\boxed{\Gamma^{\mathrm{R}}(\boldsymbol{r}_1,\boldsymbol{r}_2,\omega)=\frac{\pi e^2}{\hbar\omega}\left(\rho_z\left(\boldsymbol{r}_1,\boldsymbol{r}_1,q_z,\omega\right)+\rho_z\left(\boldsymbol{r}_2,\boldsymbol{r}_2,q_z,\omega\right)+2\rho_z\left(\boldsymbol{r}_1,\boldsymbol{r}_2,q_z,\omega\right)\cos\left(\delta\right)\right)} \tag{4.94}$$

One can therefore see that the electron energy loss probability for a split-beam impinging at positions $\boldsymbol{r}_1$ and $\boldsymbol{r}_2$ is the sum of:

- The photonic density of state at position $\boldsymbol{r}_1$.
- The photonic density of state at position $\boldsymbol{r}_2$.
- The cross-density of state between positions $\boldsymbol{r}_1$ and $\boldsymbol{r}_2$ which appears as an interference term.

Such an experiment has been first suggested by García de Abajo in [19] to measure non local information on the quasistatic screened interaction. Quite remarkably, and as a result of the connection between the screened interaction and the MDFF shown in chapter 3, equation (4.94) is analogue to the EMCD double differential cross section [281].

Let's investigate the physics which can be accessed with such an experiment.

4.6.3 Coherence measurement

The optical coherence measures the spatial and temporal correlations of the electromagnetic field. As pointed out by Mandel and Wolf [282]: "*The concept of optical coherence has long been associated with interference, presumably because interference is the simplest phenomenon that reveals correlation between light beams*". Indeed, light interferometry enables the measurement of optical coherence even in sub-wavelength regime [283]. Although remarkable, these optical experiments are rather challenging as one needs to find tricks to overcome the light diffraction limit. As we will see in the following, a split beam experiment (electronic interferometry) constitutes a good candidate to measure optical coherence with sub-nanometric spatial resolution.

As we explained in the previous chapter, the CDOS is connected through the fluctuation-dissipation theorem to the electric field correlation function C_{ij}^{EE} by [95, 84]:

$$\frac{\pi\hbar}{\omega}\coth\left(\frac{\hbar\omega}{2kT}\right)\rho_{ij}(\boldsymbol{r},\boldsymbol{r}',\omega)=C_{ij}^{EE}(\boldsymbol{r},\boldsymbol{r}',\omega) \tag{4.95}$$

where $i,j\in\{x,y,z\}$. From equation (4.94), one can therefore see that *a split-beam measures the correlations between the z-component of the electric field at positions $\boldsymbol{r}_1$ and $\boldsymbol{r}_2$*. Let's now suppose that we also performed standard EELS measurements at position $\boldsymbol{r}_1$ and $\boldsymbol{r}_2$ and thus obtained the loss probability $\Gamma(\boldsymbol{r}_1,\boldsymbol{r}_1,\omega)$ and $\Gamma(\boldsymbol{r}_2,\boldsymbol{r}_2,\omega)$. From the combination of these split-beam and standard measurements, we can immediately deduce:

$$\gamma_z(\boldsymbol{r}_1,\boldsymbol{r}_2,\omega)=\frac{\rho_z(\boldsymbol{r}_1,\boldsymbol{r}_2,\omega)}{\sqrt{\rho_z(\boldsymbol{r}_1,\boldsymbol{r}_1,\omega)\rho_z(\boldsymbol{r}_2,\boldsymbol{r}_2,\omega)}} \tag{4.96}$$

This quantity corresponds to the *degree of spatial coherence* [103] of the z-component of the field. Due to the Cauchy-Schwarz inequality, it satisfies $\gamma_z\leq 1$ where:

- $\gamma_z=1$ indicates a perfect coherence between the points $\boldsymbol{r}_1$ and $\boldsymbol{r}_2$.
- $0<\gamma_z<1$ indicates a partial coherence between the points $\boldsymbol{r}_1$ and $\boldsymbol{r}_2$.
- $\gamma_z=0$ indicates an absence of coherence between the points $\boldsymbol{r}_1$ and $\boldsymbol{r}_2$.

Thus, a split-beam measurement allows one to map the spatial coherence of an optical field at the nano-scale. As emphasized by Cazé and collaborators [104], mapping the spatial dependence of γ_z can enable us to measure the *coherence length* of a plasmon field down to the nanoscale which could have important applications in the study e.g. of the Anderson localization of optical modes in random media.

4.6.4 Double bi-prism experiment

The latter derivation is based on the coherent limit formula when only the in-axis electrons are detected; let's see how it impacts the detection part. To do so, we start from the equation demonstrated in the previous chapter:

$$\varrho_{f,\perp}(\boldsymbol{k}_\perp, \boldsymbol{k}'_\perp) = \rho_z(\boldsymbol{k}_\perp, \boldsymbol{k}'_\perp, \omega)\varrho_{i,\perp}(\boldsymbol{k}_\perp, \boldsymbol{k}'_\perp) \tag{4.97}$$

where ϱ_i and ϱ_f denotes the initial and final density matrices of the probe electron. We also dropped the multiplicative constants for brevity as it no consequences on our developments. The wavefunction of a split-beam can be written:

$$\psi_{i,\perp}(\boldsymbol{r}_\perp) = \delta(\boldsymbol{r}_\perp - \boldsymbol{r}_A) - \delta(\boldsymbol{r}_\perp + \boldsymbol{r}_A) \tag{4.98}$$

We also define the position of the two split-beams as $\pm\boldsymbol{r}_A$ by choosing an arbitrary spatial origin. Plugging the latter equation in (4.97), we obtain:

$$\varrho_f(\boldsymbol{k}, \boldsymbol{k}') = \rho_{++}e^{i(\boldsymbol{k}-\boldsymbol{k}').\boldsymbol{r}_A} + \rho_{--}e^{i(\boldsymbol{k}'-\boldsymbol{k}).\boldsymbol{r}_A} + \rho_{+-}e^{-i(\boldsymbol{k}'+\boldsymbol{k}).\boldsymbol{r}_A} + \rho_{-+}e^{i(\boldsymbol{k}'+\boldsymbol{k}).\boldsymbol{r}_A} \tag{4.99}$$

where we defined $\rho_{\pm,\pm} = \rho_z(\pm\boldsymbol{r}_A, \pm\boldsymbol{r}_A, a, -q, \omega)$ and we dropped the $\perp$ subscript for simplicity. Therefore the EELS intensity at point $\boldsymbol{k}$ is given by:

$$\varrho_f(\boldsymbol{k}, \boldsymbol{k}) = \rho_{++} + \rho_{--} + \rho_{+-}e^{-2i\boldsymbol{k}.\boldsymbol{r}_A} + \rho_{-+}e^{2i\boldsymbol{k}.\boldsymbol{r}_A} \tag{4.100}$$

If we integrate the signal in the k-plane as it is done in a conventional EELS experiment, the total loss probability reads:

$$\Gamma(\omega) = \int dk_x dk_y \left(\rho_{++} + \rho_{--} + \rho_{+-}e^{-2ik_x r_A} + \rho_{-+}e^{2ik_x r_A}\right) \tag{4.101}$$

where we have chosen y as the axis of the bi-prism and therefore x is the orthogonal direction. Supposing the medium reciprocal ($\rho_{+-} = \rho_{-+}$) and noting $k_{\max}$ the maximum wavevector allowed, we obtain:

$$\Gamma(\omega) = \rho_{++} + \rho_{--} + 2\mathrm{sinc}(k_{\max}\, r_A)\rho_{+-} \tag{4.102}$$

and we indeed see that the interference term vanishes when $k_{\max} \gg r_A^{-1}$ in agreement with the finding of section 4.5. Following the prescription found earlier in this chapter, we would like to add a post-selection part to increase the signal.

Let's apply a new transformation $M(\boldsymbol{k}, \boldsymbol{k}')$ to the density matrix in the Fourier plane. We assume this transformation to be also a tilt and reads:

$$M(\boldsymbol{k}, \boldsymbol{k}') = \frac{1}{2}\left(e^{i\boldsymbol{k}.\boldsymbol{r}_0} + e^{-i\boldsymbol{k}.\boldsymbol{r}_0}\right)\left(e^{-i\boldsymbol{k}'.\boldsymbol{r}_0} + e^{i\boldsymbol{k}'.\boldsymbol{r}_0}\right) \tag{4.103}$$

Inserted in (4.99) and taking $\boldsymbol{k} = \boldsymbol{k}'$, we get:

$$\begin{aligned}\varrho_f(\boldsymbol{k}, \boldsymbol{k}) = {} & \rho_{++} + \rho_{--} + \rho_{+-}\left(e^{2i\boldsymbol{k}.\boldsymbol{r}_A} + e^{-2i\boldsymbol{k}.\boldsymbol{r}_A}\right) \\ & + \frac{\rho_{++}}{2}\left(e^{2i\boldsymbol{k}.\boldsymbol{r}_0} + e^{-2i\boldsymbol{k}.\boldsymbol{r}_0}\right) + \frac{\rho_{--}}{2}\left(e^{2i\boldsymbol{k}.\boldsymbol{r}_0} + e^{-2i\boldsymbol{k}.\boldsymbol{r}_0}\right) \\ & + \frac{\rho_{+-}}{2}\left(e^{2i\boldsymbol{k}.(\boldsymbol{r}_A+\boldsymbol{r}_0)} + e^{-2i\boldsymbol{k}.(\boldsymbol{r}_A+\boldsymbol{r}_0)} + e^{2i\boldsymbol{k}.(\boldsymbol{r}_0-\boldsymbol{r}_A)} + e^{-2i\boldsymbol{k}.(\boldsymbol{r}_0-\boldsymbol{r}_A)}\right)\end{aligned} \tag{4.104}$$

If now we impose $\boldsymbol{r}_0 = \boldsymbol{r}_A$, we obtain:

$$\varrho_f(\boldsymbol{k}, \boldsymbol{k}) = \rho_{++} + \rho_{--} + 2\rho_{+-}\cos(\boldsymbol{k}.\boldsymbol{r}_A) + \rho_{++}\cos(\boldsymbol{k}.\boldsymbol{r}_A) + \rho_{--}\cos(\boldsymbol{k}.\boldsymbol{r}_A) + \rho_{+-}\left(\cos(\boldsymbol{k}.\boldsymbol{r}_A) + 1\right) \tag{4.105}$$

Integration over $\boldsymbol{k}$ in the limit of $k_{\max} \gg r_A^{-1}$ will remove the oscillating terms and gives:

$$\Gamma(\omega) = \rho_{++} + \rho_{--} + \rho_{+-} \tag{4.106}$$

which constitutes a measurement of the CDOS without destructive interferences.

4.7 Summary and perspectives

Summary of the main results

The essence of this chapter was to lay the foundations of low-loss phase-shaped electron energy loss spectroscopy with special emphasis on surface plasmon excitations. The purpose of this technique being to access quantities unreachable with a conventional EELS experiment such as the phase of plasmon fields.

In section 4.2, we have demonstrated that under reasonable assumptions (classical LSP fields, paraxial approximation, quasi-static regime), the EELS probability for a phase-shaped electron in interaction with a plasmon field takes the elegant form of a transition matrix 4.20, formally analogue to what is encountered in atomic physics:

$$\Gamma^{\mathrm{QS}}(\omega) = \frac{2e^2}{hv^2} \sum_m \mathrm{Im}\left\{-g_m(\omega)\right\} \left| \int d^2\boldsymbol{r}_\perp \, \phi_m(\boldsymbol{r}_\perp, q_z) \psi^*_{i,\perp}(\boldsymbol{r}_\perp) \right|^2 \tag{4.107}$$

This remarkable equation translates into *selection rules* depending on the symmetries of the electron wavefunction and plasmon field. Finally we identified, a so-called *coherent limit* (in complete analogy with BF/ADF imaging) where only the in-axis electrons are collected and which enables the measurement of a single electronic transition. In this limit the EELS probability is even simpler and can be written as (4.22). In section 4.3, we have presented the first experimental demonstration of PSEELS carried out by our collaborators in EMAT. This preliminary experiment is first and foremost a proof of principle although, this experiment suffers from a poor signal to noise ratio (SNR) (due to the coherent limit).

This poor SNR issue has been solved in section 4.5. Indeed, we demonstrated that a proper choice of the final electron state basis enables us to increase the number of collected electrons. This is achieved by adding an electron sorter after sample which acts as a basis changer. As a proof of principle, we theoretically apply this new configuration to the case of the interaction between a vortex electron and a vortex plasmon and show that it leads to a perfect detection of the plasmon OAM.

Finally, in sections 4.4 and 4.6, we gave several examples of potential applications of PSEELS as summarized in the table hereafter. Particularly, we demonstrated that a vortex electron is able to map, at the nano-scale, the optical chirality - a fundamental property of the EM field unreachable with other techniques. Equation (4.62) constitutes one of the major result of this chapter.

Wavefunction	**Quantity measured**
Conventional beam	potential, EMLDOS
Pi-beam	Parity, potential derivative
Vortex beam	Azimuthal symmetry, OAM, chirality flow, potential vorticity
n-lobbed beam	n-fold symmetry
Split-beam	CDOS, coherence

In this section, we laid the foundation of low-loss phase-shaped electron energy loss spectroscopy and showed the different quantities which can be accessed with this new type of spectroscopy. The next logical step is thus to prove its experimental feasibility. Toward this aim, we are currently performing split-beam experiments on plasmonic resonators in collaboration with Florent Houdellier of CNRS-CEMES laboratory, in order to realize the first coherence measurement of plasmons at the nanometer scale. Several exciting perspectives and questions still need to be addressed:

- In this thesis we essentially explored the use of Gaussian beams. As already described in section 4.1.2.3, another important class of beams are the self-accelerating Bessel beams with particularly counter-intuitive properties. We still have to explore how these beams could be applied to EELS, for example for depth sectioning applications.

- Spiraling beams such as vortex or helicon beams carry a magnetic moment. It has been recently suggested in [99] that these beams can thus be used to measure magnetic properties of optical fields and particularly the magnetic part of the Green dyadic. However, the magnetic signal is much smaller and superimposed on the electric one so that it seems to be experimentally impossible to resolve the magnetic signal. Nevertheless, it has been recently showed that vortex beams with huge OAMs can be produced [238] which could give rise to stronger magnetic signal. Therefore, PSEELS could have some applications in magnetic mapping and this possibility deserves further investigation.

- It is still to determine if analogue electronic interference could be observed in cathodoluminescence spectroscopy. We started exploring this possibility in appendix F.

Chapter 5

Exploring nano-optical excitations coupling with fast electrons techniques

Contents

5.1 Introduction **118**
5.2 Nanocross: A Highly Tunable Plasmonic System **119**
5.2.1 Motivation: generation of low-energy high order plasmon modes 119
5.2.2 Probing the morphing from nanorod to nanocross by EELS 120
5.2.2.1 Starting plasmonic structure: the nanorod 120
5.2.2.2 Experimental study of the morphing from a rod to a cross . . 120
5.2.2.3 Complementary simulations 122
5.2.3 Geometrical tuning: perturbation and symmetry arguments 122
5.2.3.1 First order perturbation theory of BEM 123
5.2.3.2 Remark on the symmetry conservation 124
5.2.4 Dimer coupling of nanocrosses 124
5.2.4.1 Hybridization model for localized surface plasmon 125
5.2.4.2 Application to the nanocrosses dimer 125
5.2.5 Summary of the different spectral tuning processes 127
5.3 Self-hybridization within non-Hermitian localized plasmonic systems **128**
5.3.1 Motivation of the work 128
5.3.1.1 Mode mixing in a single plasmon resonator 128
5.3.1.2 The growing field of non-Hermitian physics 128
5.3.2 Algebraic analysis of the plasmon eigenproblem 130
5.3.2.1 The F and S symmetries 130
5.3.2.2 The overlap matrix 132
5.3.2.3 Symmetry analysis of the overlap matrix 133
5.3.3 LSP vs. electromagnetic wave in open systems 133
5.3.3.1 Dependence in time 134
5.3.3.2 Quasinormal modes 134
5.3.4 Self-hybridization within a dagger resonator 135
5.3.4.1 Mode mixing within the BEM perturbation theory 135
5.3.4.2 Connection between the mixing term and the overlap matrix . 135
5.3.4.3 Simulation of the cross and dagger morphing 137
5.3.4.4 Phase diagram 138
5.3.5 Experimental demonstration of self-hybridization 138
5.3.6 Physical origin of plasmonic bi-orthogonality 140

5.3.7 Analogy with open quantum systems 141
5.4 Substrate effect on plasmon resonances in nano-cube 141
5.4.1 Classification of the nanocube's plasmon modes 142
5.4.2 Substrate-induced mode splitting 144
5.4.3 Experimental and simulated EELS on cube monomer 144
5.4.4 Distal-proximal formation mechanism 147
5.4.5 CL experiment on cube monomer 148
5.4.6 Dimer coupling of silver nano-cubes 149
5.4.7 Difficulties and perspectives 149
5.5 Probing plasmon-NV^0 coupling at the nanometer scale with photons and fast electrons 151
5.5.1 Strategy to measure the Purcell effect at the nanoscale 151
5.5.2 Choice of the SP-QE system 152
5.5.3 Variability of NV^0 center excited state lifetime 153
5.5.4 Statistical approach to STEM-HBT 154
5.5.5 Numerical verification 155
5.5.6 Conclusion and perspectives 156
5.6 Summary and perspectives 157

5.1 Introduction

In chapters 3 and 4 we focused on electron energy loss spectroscopy itself with special emphasis on applications in nano-optics. We demonstrated that recent advances in electron phase-shaping could bring new insights in plasmonics by enabling the measurement of the coherence, the phase or even the chirality of optical excitations down to the nanoscale.
We will now focus on the properties of surface plasmons under the scope of conventional EELS or CL. While the two first chapters were essentially theoretical, the present one has a major experimental component. The common denominator of the different works presented here is that they all deal with the physics of plasmon coupling.

Coupling is at the heart of plasmonics and its applications as it is one of the building blocks of nano-photonics engineering. Moreover, the interaction between surface plasmon resonances and quantum emitters is a key ingredient toward the coherent control of light emission at the nanoscale [22]. For these reasons, surface plasmon coupling is currently an active field of research and consequently a part of my thesis has been dedicated to its study.

In this chapter, I present four works focusing on different aspects of plasmon coupling physics:

1. In section 5.2, I first focus on the coupling between two plasmon resonators in a dimer configuration. More specifically, we investigate dimers of silver nanocrosses and show the remarkable spectral tuning of optical properties which can be achieved in these structures [250]. This section will also be the opportunity to detail the basic concepts of plasmon coupling physics.

2. An essential feature of localized surface plasmon is their tunability. Indeed, it is well known that by precisely modifying the shape of a nano-particle, one can engineer the optical properties of its plasmon modes. In section 5.3, we demonstrate that again, plasmon coupling is at the core of this physics but in an unexpected fashion. Indeed, we will deal with coupling between two plasmon modes *within* a single nano-particle. We will see that the laws ruling this particular phenomenon of *self-hydridization* can be understood in terms of non-Hermitian effects encountered in many other fields of physics.

3. In section 5.4, we will turn to a somehow more prosaic but also crucial aspect in plasmonics: the effect of a dielectric substrate on plasmon resonances. By studying the pathological case of the nano-cube where the substrate effect appears to be dramatic, we will, as far as possible, rationalize and conciliate the different approaches found in the literature.

4. Finally, in section 5.5, we will study the weak coupling between plasmon modes of a silver nano-cube and excited states of neutral nitrogen-vacancy defects (NV^0 centers) in nano-diamonds. Using a statistic approach to STEM-HBT interferometry, we will evidence the presence of a Purcell effect and give an estimation of the enhancement factor.

5.2 Nanocross: A Highly Tunable Plasmonic System

In this section we demonstrate that morphing a nanorod to a nanocross by growing another arm along the perpendicular bisector of a nanorod can lead to a spectacular evolution of modes of various orders in the EEL spectra. One can keep a mode fixed in energy while bringing the next higher order mode close to it, or even make it cross. This allows to control the relative separation of energy of the plasmon modes. Hybridization of individual nanocross plasmon modes has also been studied by bringing two nanocrosses close together along one of their arms. An analytical approach based on first order perturbation theory and symmetry arguments based on group theory aptly fits the experimental observations.

5.2.1 Motivation: generation of low-energy high order plasmon modes

The surface plasmons' resonant energy and their charge density oscillation pattern are determined by the material properties, shape and surrounding dielectric environment of the metallic nano-particles (MNP). Exploiting the sensitivity of the LSP modes over these parameters results in optical tunability of MNPs [2, 284, 285, 286].

According to classical electrodynamics, even for a MNP of fixed geometry and dielectric constant, there can be various LSP modes corresponding to different multipolar excitations. For particle sizes small enough, so that the quasistatic approximation is valid, only the dipolar LSP mode couples with light. Beyond the quasistatic approximation, the external electric field of an electromagnetic plane wave is not anymore uniform along the nanoparticle and the higher order components of the external excitation can directly couple to the corresponding higher order LSP modes [287, 122].
Apart from being fundamentally interesting, multipolar plasmons also have applied aspects. In this regard, a long-standing research goal is to achieve tunability of higher order modes. The increasing interest in this direction is mediated by several factors. Higher order LSP modes can yield a higher Q-factor [288], attain intense field confinement which have important applications in sensing [289], surface enhanced scattering [290] and solar cells [291, 292]. In the domain of surface enhanced spectroscopy, higher orders such as quadrupolar surface plasmon modes can contribute to an enhanced Raman intensity compared to a dipolar mode. This forms the basis of emerging techniques like quadrupole-enhanced Raman scattering (QERS) [293, 294, 295]. Applications like these and many others require a fine tunability of the higher order modes in the MNPs. For the last two decades, researchers have studied almost all possible geometries fabricated via top down and/or bottom up approach. Despite this huge amount of studies, higher order LSP tunability still remains one of the key problems to overcome.
An efficient tunable structure should fulfill certain conditions. The structure has to be a simple system, that can be fabricated easily by either top down and/or bottom up approach. A slight variation of the geometrical parameter(s) should lead to a definite shift of the mode energy. The structure should also be geometrically simple enough to be modeled easily with the existing computational tools. This, in turn, would facilitate to optimize the design parameters. Finally from an application point of view, large scale and reproducible fabrication is also important. Metallic nanorod is an ideal example that fulfills all the above conditions. Till date, an incredible extent of studies have been done and is still being done on nanorods and their plasmonic properties [296, 297, 298, 299, 300, 301, 302, 303, 304, 305, 306, 307, 308, 309].

In this section, we study the plasmonic property of the nanocross, which is a variation of the nanorod geometry. A cross is a geometry where another arm is grown along the perpendicular bisector of the nanorod. We demonstrate that the cross can be used as an extremely tunable plasmonic system especially for engineering the higher order LSP modes. The discussion in this paper evolves from simple to complex arrangements of nanocrosses. We started from a nanorod

and then morph it to form a nanocross by growing the second arm with the help of electron beam lithography. To follow the modal evolution during the morphing process, we have used spectrally and spatially resolved electron energy-loss spectroscopy in a scanning transmission electron microscope (STEM-EELS). Morphing a nanorod to a nanocross allows us to control the relative energy separation between two neighboring plasmon modes easily.

The experimental results are supported by BEM simulations [162], analytical calculations based on first order perturbation theory [41] and group theory. We also study the hybridization of plasmon modes when two crosses are brought in close proximity (30 nm) of one another along one of their arms. The plasmonic properties of metallic nanocross have been reported before in a few studies [310, 311, 312, 313, 314, 315, 54]. Varellen et al. [310, 311] have done extensive study on the effect of size and angle between the two arms of a cross on the observed plasmonic spectrum and showed that quadrupolar and octupolar modes can display high Q-factor. They have also demonstrated the application of a nanocross coupled to a nanorod for LSP sensing [310]. In this paper we have approached the issue of tuning modes in a different way. Instead of changing the length of both the arms of the cross together equally, we fixed one arm and change the length of the other arm. This way of morphing the individual cross and the coupling between the crosses gives us access to a wide range of plasmonic tunability opening up pathways for new types of structures e.g. cross arrays.

5.2.2 Probing the morphing from nanorod to nanocross by EELS

5.2.2.1 Starting plasmonic structure: the nanorod

The nano-rod is the starting structure of our coupling experiment. For completeness, we produce a nano-rod by e-beam lithography and measure its plasmon resonance by EELS. We have completed the experiment with BEM calculations and presented the charge maps corresponding to different modes n for a nanorod of dimension (400 nm $\times$ 40 nm $\times$ 40 nm) in figure 5.1. Because of the large size of the studied objects, all the spectra and related quantities have been processed in the retarted regime (using the Johnson and Christy experimental data for the silver dielectric permittivity [316]) one major consequence is that the surface charge densities associated to the plasmon resonances are then complex fields: two quantities have thus to be plotted to fully represent these distributions i.e. phase and modulus. For the sake of brevity, we decided to represent on one map the phase times the modulus of each charge densities. This being so, the high density areas reveal where the charges tend to accumulate while the overall sign keeps the signature of the phase and thus highlights how the charges oscillate.

Obviously, we retrieve the standard Fabry-Pérot-like modes of a nano-rod where plasmons with an odd index n present an anti-symmetric charge distribution while even ones have a symmetric charge distribution.

5.2.2.2 Experimental study of the morphing from a rod to a cross

Employing electron beam lithography, we have fabricated a silver nanorod and then slowly grown another arm of the same cross-section along the perpendicular bisector of the former one. The cross-sectional dimension of the rod is (40 nm $\times$ 40 nm) and is maintained in all the rods and crosses used in the present work. Using STEM-EELS, we have followed the evolution of the plasmon resonance as the growing arm length L increases.

In figure 5.2(a), we present the experimental EEL spectra taken near one tip of the cross (white square on the HAADF images) for different lengths of the growing arm L ranging from 100 to 400 nm varied in steps of 50 nm. Alongside the experimental results, we also present the simulated spectra which have been computed using MNPBEM Matlab toolbox (see appendix C for details) in figure 5.2(b). We denote the modes as Sn, where n represents the order of the plasmon mode and S stands for single cross. We have done all the simulations without taking into account the effect

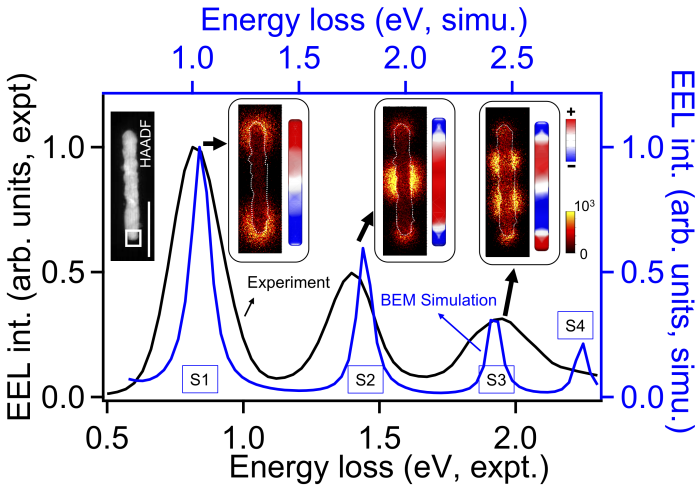

Figure 5.1: *Plasmon modes of an isolated silver nanorod probed by EELS (black curve). The BEM simulated spectrum (blue) is also overlaid for comparison. The dimension of the rod is 400 nm × 40 nm in length and width. The crosssection is a square with dimension 40 nm × 40 nm. In the simulation we did not put any substrate. In the inset, we have included the EELS maps at different resonance energies and BEM simulated charge distributions. Scale bar of the HAADF image correspond to 200 nm.*

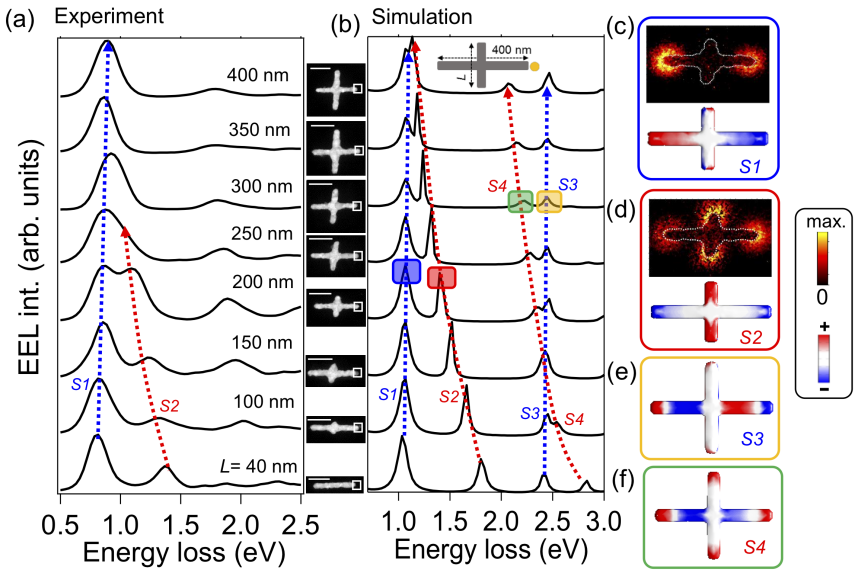

Figure 5.2: *(a) Experimental and (b) BEM simulated spectra obtained from the morphing of a silver rod into a cross using EEL spectroscopy. The growing arm length L, which plays the role of the detuning parameter of the modes, is varied from 40 nm to 400 nm (HAADF images of the lithographed structures are shown in the column between (a) and (b)). The white squares on the HAADF images and the yellow circle on the schematic of inset (b), represent the location from where the EEL spectra have been acquired. The blue (resp. red) dashed lines indicates the evolution of the antisymmetric (symmetric) modes (c, d) experimental EEL maps and simulated surface charge maps corresponding to S1 and S2 modes (blue and red box respectively) of a cross of 400 nm × 200 nm. (e,f) simulated charge maps corresponding to modes S3 and S4 for a cross of dimension 400 nm × 300 nm. The scale bar in the HAADF image corresponds to 200 nm.*

of the substrate. The structures in our work have a high aspect ratio and are thin. Consequently, only the in plane plasmon modes are significant. Hence the presence of the substrate would only bring an overall energy shift and broadening of the peaks. In our case the particle size is beyond

the quasistatic regime. So, we need to make all the calculations in the retarded regime. With the substrate, the full retarded simulation is a challenge in terms of computation time and computer memory. Nevertheless, the simulation without substrate requires less time and memory and it reproduces the main features of the phenomena, the only noticeable difference being a reproducible rigid (and small) energy shift of all modes, which has absolutely no influence on our conclusions.

From figure 5.2(a,b), we see that, when the second arm is grown along the perpendicular bisector of the rod to form a cross, the symmetric plasmon modes (even n) are strongly red-shifted while the anti-symmetric ones (odd n) remain almost at the same energy. $S2$ (quadrupolar mode) comes close to $S1$ (dipolar) in energy with the increase in arm length. Experimentally we can follow the trend well until $L = 250$ nm. Beyond this value, the peaks become very close to each other. Moreover, the presence of a substrate creates additional decay channels for plasmons causing a broadening of the LSP peaks. Thus, the EELS spectrometer resolution is not sufficient to spectrally resolve them.

5.2.2.3 Complementary simulations

Nevertheless in simulations, we can follow all the modal evolution. As is evident from figure 5.2(b), $S2$ and $S1$ come close to each other in energy as L increases and finally for a cross with equal arm length (400 nm $\times$ 400 nm), $S2$ and $S1$ are almost degenerated. In the simulation of figure 5.2(b) without taking into account the substrate, the measured energy difference between $S1$ and $S2$ is 0.06 eV for L=400 nm. In figure 5.2 (c,d) we present the simulated surface charge distribution and experimental EEL map of $S1$ and $S2$ corresponding to $L = 200$ nm. The map corresponding to $S1$ shows a charge distribution similar to the dipolar distribution of the rod (see figure 5.1) except the appearance of some mirror charges on the growing arm. The charge distribution corresponding to $S2$ for a rod has a maximum at the middle. With the growth of the second arm at this location, the charges of the same polarity become delocalized. The degree of delocalization increases with the increasing arm length L. The behavior of the two next higher order modes $S3$ and $S4$ is particularly interesting. With the gradual increase of L, the mode $S4$ comes close to $S3$ in energy and for $L > 150$ nm, it crosses $S3$. In this crossing event, the modes $S4$ and $S3$ conserve their characteristic charge distribution symmetries. This means that one can bring a mode of higher order ($S4$) at a lower energy compared to a lower order mode ($S3$). In figure 5.2(e,f), we have shown the charge distributions corresponding to $S3$ and $S4$ after they cross each other, for a value of $L = 300$ nm. Limited spectral resolution of our EELS spectrometer and damping due to substrate forbid us to follow the evolution of modes $S3$ and $S4$ experimentally.

It is also to be noted that only the modes which have a maxima of their charge distribution in the second arm growth location shift towards lower energy; the other modes, which have a node (null charge density) at the growing location ($S1, S3$), remains utterly unaffected by this morphing process from rod to cross. This way, a LSP mode of lower order can be placed at a higher energy with respect to its' next higher order mode; this phenomenon has very interesting consequences such as the possibility of generating low-energy modes with high Q-factor.

In the following section we present an analytical explanation of this interesting phenomena based on a first order perturbation and group theories.

5.2.3 Geometrical tuning: perturbation and symmetry arguments

We have seen in figure 5.2 that with the increasing arm length of the cross, the asymmetric modes (n odd, like $S1$, $S3$) almost do not change position, whereas the symmetric modes (n even, like $S2$, $S4$) shifts towards lower energy. The mode $S4$ even crosses mode $S3$. From the charge distribution corresponding to $S2$ in figure 5.2, we can say that the symmetric modes (e.g. $S2$ and $S4$) have a maximum at the growth position of the second arm. When the arm gets elongated, the charges get delocalized keeping the symmetry intact.

With the help of first order perturbation and group theories symmetry arguments, this can be

explained in a more systematic way.

5.2.3.1 First order perturbation theory of BEM

As we already presented in the introductory chapter and demonstrated in appendix C, in the quasistatic regime, the plasmon resonances of a nano-particle of shape S are solutions of the boundary integral equation (BIE):

$$\Lambda(\omega)\sigma(\boldsymbol{s},\omega) = \mathcal{P}\oint_S F(\boldsymbol{s},\boldsymbol{s}')\sigma(\boldsymbol{s}',\omega)d\boldsymbol{s}' \tag{5.1}$$

where $\sigma(\boldsymbol{s}',\omega)$ is the surface charge density at frequency ω, $\mathcal{P}$ is the Cauchy principal value, $F(\boldsymbol{s},\boldsymbol{s}')$ corresponds to the normal derivative of the Coulomb kernel which, for $\boldsymbol{s} \neq \boldsymbol{s}'$, reads:

$$F(\boldsymbol{s},\boldsymbol{s}') = -\frac{\boldsymbol{n}.(\boldsymbol{s}-\boldsymbol{s}')}{|\boldsymbol{s}-\boldsymbol{s}'|^3} \tag{5.2}$$

and Λ is a dimensionless quantity which only depends on the dielectric constants of the metallic nano-particle ϵ_1 and the embedding medium ϵ_2 as:

$$\Lambda(\omega) = 2\pi\frac{\epsilon_2(\omega)+\epsilon_1(\omega)}{\epsilon_2(\omega)-\epsilon_1(\omega)} \tag{5.3}$$

Equation (5.1) is a Fredholm equation of the first kind and corresponds to an eigenvalue equation. Since the kernel of this equation is generally not symmetric, we know from spectral theory that its solutions correspond to the set of 3-tuples $\{(\lambda_n,\sigma_n,\tau_n)\}_{n\in\mathbb{N}}$ where:

- λ_n is the so-called geometrical eigenvalue and is a dimensionless quantity which can be connected to the resonance energy $E_n = \hbar\omega_n$ [10, 41] by using (5.3):

  $$\mathrm{Re}\left\{\Lambda(\omega_n)+\lambda_n\right\} = 0 \tag{5.4}$$

  By analogy with the analytic Mie theory, one could roughly interpret λ_n as a *depolarization factor*.

- The right eigenvector σ_n corresponds to the surface charge density of mode n.

- The left eigenvector τ_n corresponds to the surface density of dipoles (orientated orthogonally to the particle surface) of mode n.

Since the kernel is not symmetric, the basis is bi-orthogonal which has crucial consequences as we will see in section 5.3. Nevertheless, we can disregard this difficulty for the present section. Although this formalism holds true for small nano-particles (for the QS approximation to be valid), it also provides plausible results for larger particles to a first approximation. This allows an intuitive interpretation of the EELS results presented in this chapter.

Analogous to quantum mechanics, Trügler et al. [317] first introduced a beautiful perturbation theory to the BEM. They consider the perturbation to be a distortion of surface from its ideal shape, leading to a change of F to $F+\delta F$. To the first order, this perturbation of the Kernel does not affect the symmetry of the charge distribution of the plasmon modes but leads to a slight correction in the eigenvalue viz. $\{\sigma_n,\lambda_n\} \longrightarrow \{\sigma_n,\lambda_n+\delta\lambda_n\}$ which is given by:

$$\boxed{\delta\lambda_n = \oint_S d\boldsymbol{s}\oint_S d\boldsymbol{s}'\,\tau_n(\boldsymbol{s})\,\delta F(\boldsymbol{s},\boldsymbol{s}')\,\sigma_n(\boldsymbol{s})} \tag{5.5}$$

This equation is analogue to the first order correction to the energy of a quantum system when it is perturbed by a weak potential δH:

$$E_n = E_n^0 + \langle\psi_n^0|\delta H|\psi_n^0\rangle \tag{5.6}$$

where E_n^0 and ψ_n^0 are the unperturbed energy and wavefunction and E_n the corrected energy. The main difference being that the "bra" vector has to be replace by the left eigenvector since the basis is bi-orthogonal (we will come back on this in the next section). If, for simplicity, we assume a Drude model for the material's electronic properties, $\epsilon(\omega)$ can be written as:

$$\epsilon(\omega) = 1 - \frac{\omega_P^2}{\omega(\omega + i\Gamma)} \tag{5.7}$$

where ω_P is the plasma frequency and Γ the spectral linewidth. Equation (5.5) can then be translated in the ω-space where the correction $\delta\omega_n$ to the energy of the nth plasmon mode is given by:

$$\delta\omega_n = -\frac{\omega_P^2}{4\omega_n} \oint_S d\boldsymbol{s} \oint_S d\boldsymbol{s}'\, \tau_n(\boldsymbol{s})\, \delta F(\boldsymbol{s}, \boldsymbol{s}')\, \sigma_n(\boldsymbol{s}') \tag{5.8}$$

Although we have used the Drude model to derive equation 5.8, one can always use other dielectric functions as well. Equations (5.5) or (5.8) are remarkable as they synthetically show how a deformation of a nano-particle shift the energy of its modes, to the first order.

In the rest of this thesis, and for the sake of simplicity, we will follow the notation [317] and employ a bra-ket notation to perform the calculations of the BEM perturbation theory.

Now, according to equation 5.8, the value of the integral is non-zero only when δF and σ_n both are non-zero. So, if we perturb the rod to form a cross by growing an arm at a node of any mode Sn, its' energy remains unchanged, (integral of equation 5.8 becomes zero). In the present experiment, we are growing an arm in the middle of the rod which corresponds to a node for all the anti-symmetric modes (n odd, e.g. $S1$, $S3$) and a maximum for all symmetric modes (n even, e.g. $S2$, $S4$). This explains our observation in figure 5.2 where $S1$, $S3$ do not change position while $S2$, $S4$ shift towards lower energy.

5.2.3.2 Remark on the symmetry conservation

A very important aspect to be noted here is that, during the morphing process, the overall symmetry of the charge distributions as well as that of the geometry of the structure retains a C_{2v} type character. Thin plate-like structures belonging to C_{2v} symmetry group are characterized by the following symmetry operations: identity (E), a vertical C_2 rotation axis (180°), two vertical mirror planes that contains the C_2 axis. For example, from figure 5.2(d) the charge distribution of the mode $S2$ has the same symmetry as that of the nanorod. Thus, the total number of LSP modes is preserved during the whole deformation and no dramatic change (e.g. mode splitting) should be expected. The conservation of the overall symmetry of the eigenvectors is essential because it fully justifies the use of the first order perturbation approach to interpret the energy shifts. So it can be concluded that, in this case, a first order correction is sufficient to reproduce the geometrical tuning (GT) effect as it simply causes a shift in the energy of the different plasmonic modes depending on the location of the arm growth. Moreover, we clearly see on figure 5.2(b) that the shifting rates of $S2$ and $S4$ with the deformation are identical i.e the red arrows indicating the shifts are parallel. In addition, starting from L=100 nm, these parallel curves are linear functions of L. It suggests that the energy shift does not depend on the form of the modes but only on the perturbation parameter L.
Hence, one can see that the symmetry conservation enables a simple and intuitive interpretation of the mode morphing. When the length reaches the value of 400nm, the symmetry of the structure changes to C_{4v} where the rotation axis becomes C_4 (rotation by 90°). All other symmetry operations remain the same as in the C_{2v} case. Therefore we have restricted our study to $0 \leq L \leq 400$ nm, where the symmetry group is conserved.

5.2.4 Dimer coupling of nanocrosses

While the single nanocross gives us access to the tunability, especially for higher order LSP modes, we also probed a more complex system built by bringing the two crosses close together separated

by a small gap along one of their arms. This so-called *dimer configuration* leads to the formation of new modes and therefore a richer and broader plasmonic spectrum.

5.2.4.1 Hybridization model for localized surface plasmon

We intuitively know that when two particles are brought together, the coupling between different plasmon modes should lead to the formation of new resonances. But how can we simply picture the modes of a dimer by the simple knowledge of the monomer's ones? Quite remarkably, the hybridization model for plasmonic dimer is formally analogy to the *linear combination of atomic orbital* (LCAO) employed in chemistry [318]. Thus, like in a H_2 molecule where the s hydrogen orbitals give rise to bonding σ and anti-bonding σ^* molecular orbitals, a bonding and an anti-bonding plasmon modes will emerge from the dipole modes coupling in a dimer of spheres (see pictured on figure 5.3). The strength of this electromagnetic coupling naturally depends on the distance between the two nano-particles. This model has been numerically and experimentally tested countless times [319] and appears to robustly picture the physics of plasmon dimer-coupling. However, we will see in section 5.4 that in some systems, like nano-cubes dimers, the scheme can be dramatically more complex.

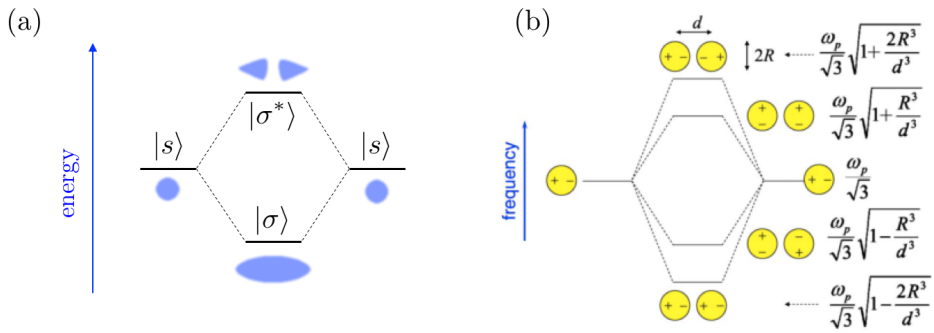

Figure 5.3: *(a) Formation of molecular $|\sigma\rangle$ and $|\sigma^*\rangle$ orbitals from the linear combination of atomic $|s\rangle$ orbitals in a H_2 molecule. (b) Plasmon hydridization between dipole modes in a spheres dimer. Reproduced from [320].*

It enable us to apply all the arguments of symmetry and algebraic tools used in quantum chemistry is the case of plasmonics. The analogy between LCAO and this plasmonic hybridization is so strong that we sometime talk about *plasmon chemistry* [320].

5.2.4.2 Application to the nanocrosses dimer

From the latter arguments, it appears that bringing two nanocrosses in close proximity would allow the rich plasmonic features of the single cross to be exploited even further, resulting in a higher tunability. For this purpose, with the help of electron beam lithography, we designed the structure shown in the inset HAADF image of figure 5.4(a). The dimensions of the individual nanocross are (400 nm $\times$ 200 nm) and the cross sectional dimension of each arm has been kept at (40 nm $\times$ 40 nm). The measured gap between them along the short arm is $\sim$ 30 nm.

In figure 5.4(a), we display experimental (solid line) and simulated (dashed line) EEL spectra from different color-coded locations on the coupled cross. Due to the limited spectral resolution of our spectrometer, the experimental spectra are broad. The BEM simulations have been performed without any substrate. In figure 5.4(b-f) we present the simulated charge maps and the corresponding experimental EEL maps (as far as it could be resolved). We now denote the modes as Dn, where D stands for dimer. The charge distributions of $D1$ and $D2$ (figure 5.4(b,c)) show that they correspond to anti-symmetric and symmetric combinations of individual cross dipole modes ($S1$), respectively, along the long arm of the individual cross. Since these two modes present very similar symmetries, they lie very closely in energy so that we could discriminate them only in our calculations. In our BEM simulations, the mode $S1$ for the individual cross of 400 X 200 nm is at

energy 1.067 eV. When the two crosses couple, the mode $D1$ is at energy 1.042 eV and mode $D2$ is at energy 1.102 eV (figure 5.4(a), green dotted curve). $D2$ is too feeble even to be well detected in simulations. In our EELS experiments on coupled crosses this is reflected in a broad envelope in the range 0.7-1 eV (figure 5.4(a), green solid curve). The simulated surface charge distributions and the experimental EEL maps are shown in figure 5.4(b,c). The charge distributions corresponding to modes $D3$ and $D4$ reveal that they correspond to the anti-symmetric and symmetric configurations of the quadrupolar[1] mode of the individual cross. In our simulations, the energy of $S2$ is 1.4 eV, while the lower energy anti-symmetric configuration of the coupled cross $D3$ is at 1.263 eV and the symmetric mode $D4$ is at 1.44 eV. So the simulated splitting between $D3$ and $D4$ is 0.177 eV compared to 0.06 eV between $D1$ and $D2$. This indicates a strong coupling between individual $S2$ modes.

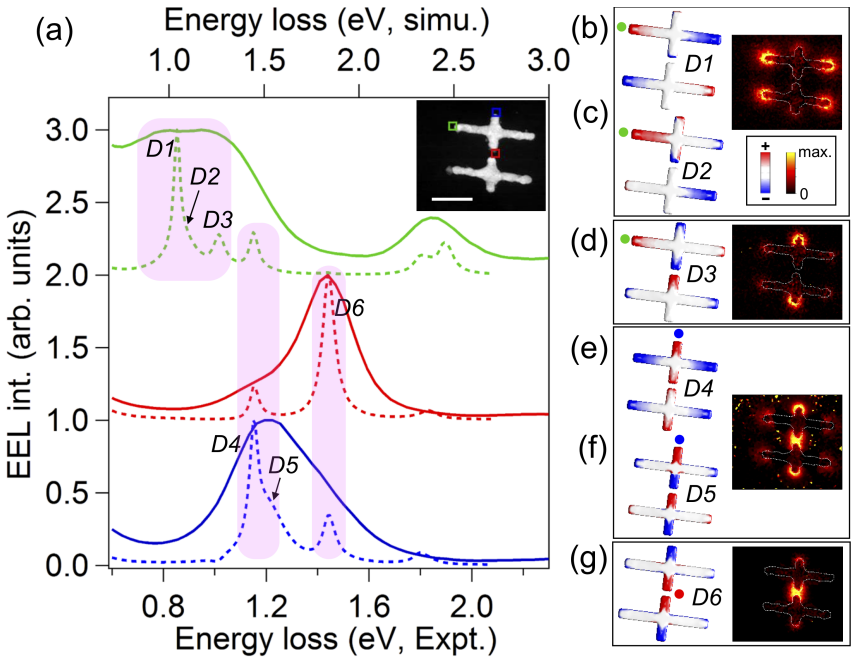

Figure 5.4: *(a) Experimental (solid line) and BEM simulated (dashed line) EEL spectra from different locations on the pair of nanocrosses shown in the inset. The two crosses are separated along the short arm by a gap of $\sim$ 30 nm. The simulations were performed without any substrate. This causes a linear energy shift between the experimental and the numerical results which is depicted in the top and the bottom energy axis. Different LSP modes in the simulated spectra have been named as $D1 - D6$. In panel (b-g), we have shown the simulated charge maps (to the left) corresponding to different plasmon modes ($D1 - D6$) together with the corresponding experimental EEL maps. The color-coded squares on the HAADF image correspond the location from which the experimental spectra have been acquired. The color of the spectrum line corresponds to the color of the box from which it has been acquired. Similarly the color-coded dots on the the simulated maps correspond to the electron beam impact positions. The scale bar in the HAADF images corresponds to 200 nm.*

Finally $D5$ and $D6$ correspond to the anti-symmetric and symmetric configurations of dipolar modes along the short arm of the individual cross. The short arm dipolar mode of a single cross, according to our simulations, lies at 1.67 eV while, when they couple, the anti-symmetric and symmetric modes lie at 1.55 eV ($D5$) and 1.836 eV ($D6$) respectively. It is to be noted that $D4$ and $D5$ are too close ($\sim$ 110 meV in simulation without substrate) to be resolved experimentally and we have presented a combined EEL map again corresponding to a broad experimental peak at 1.2 eV. Experimentally $D6$ is located at $\sim$ 1.5 eV. The simulated charge and experimental EELS map corresponding to $D6$ are shown in figure 5.4(g).
In our experiments, both with single or coupled crosses, we could not resolve the modes which are

[1] by quadrupolar here we mean n=2 mode of individual cross $S2$

very close in energy and only resolve them in the simulations. This is due to several factors. Our experimental resolution is 0.327 eV initially, which after deconvolution according to the Richardson-Lucy algorithm [130] using 20 iterations, goes to about 0.15 eV. However the substrate (Si_3N_4) and the surface roughness (as we prepared our samples by lithography) also play an important role in determining the width of the resonant peaks.

5.2.5 Summary of the different spectral tuning processes

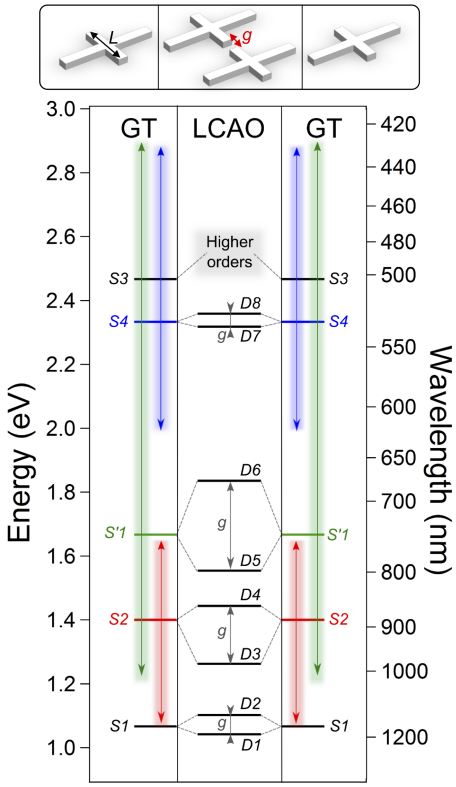

Figure 5.5: *Energy diagram representating the hybridization of cross plasmon modes in a dimer configuration. The short arm length is fixed at 200 nm. We indicated with colored shaded arrows the spectral range within which the energy of the single cross modes can be tuned using geometrical tuning (GT). When bringing two crosses together in a dimer configuration with a gap g, the resulting hybridized modes appear according to a LCAO scheme.*

We investigated two different types of energy engineering so far. First, through the *geometrical tuning* (GT) of the structure, we modified the LSP modes' energy of a single cross. This process, the strength of which relies on the conservation of the structure symmetry group, has to be interpreted with geometrical arguments only. Next, by forming a dimer of crosses, a new and rich plasmonic spectrum emerges from the hybridization of the initial modes. This scheme, which contrary to the geometrical tuning fully relies on a symmetry breaking, is perfectly suitable for a LCAO-like interpretation [41, 321]. In addition, let's point out that this separability of the problem (GT *vs.* LCAO) is a particularly interesting feature because it enables one to easily grasp the engineering in any kind of cross-based superstructure.

In figure 5.5, we sum up, on an energy diagram, the different features of the cross plasmon modes and their coupling in a dimer configuration. We draw in color the single cross modes (i.e. $S2$, $S'1$ and $S4$, $S'1$ stands for the dipole mode along the short arm of the cross) the energy of which can be tuned by modifying the short arm length (GT). The spectral range within which their energy can be varied is indicated by shades. When the two crosses are brought together, new hybridized

modes appear that can be interpreted using a LCAO scheme. Therefore, one has two different parameters i.e. the arm length of the cross L and the gap g in the dimer to tune the final dimer modes energy. As mentioned earlier, these two parameters correspond to two different physical processes (resp. GT and LCAO) but their combined effects lead to a super-tunability which enables one to engineer a plasmon resonance at any energy between 400 nm and 1200 nm. Moreover, because of the simplicity of the structure, we have a remarkable control and understanding of the charge distribution symmetry associated to each plasmon mode, both numerically and experimentally. Hence, one can possibly generate any kind of plasmon symmetry (i.e. polarization) with a precise control of energy which is a key feature in several plasmonic engineering problems. One could even go further and consider creating more complex assemblies of crosses (e.g. trimmer, arbitrary large periodic arrays) and still keep a great control of the plasmon physics. This make cross an amazingly strong and versatile building block to design dedicated optically active plasmonic systems.

5.3 Self-hybridization within non-Hermitian localized plasmonic systems

In section 5.2, we investigated two ways of engineering the optical response of a plasmonic system. The first approach is the geometrical tuning which consists in applying specific deformations to the surface of the nano-particle. The second consists in building complex oligomers in order to generate intricate collective plasmon resonances.

In this section, we will go deeper into the physics of the geometrical tuning and address a natural question arising from the previous work: **how precisely do the modes evolve when the structure is morphed?**

5.3.1 Motivation of the work

5.3.1.1 Mode mixing in a single plasmon resonator

The question raised above was remarkably tackled by Schmidt and collaborators [41] who proposed a LCAO-like scheme in order to model a morphing experiment. The principal ingredient of their theory is the *mode mixing* i.e. the fact that when the structure is morphed, the modes within the cavity, as defined before morphing, will spectrally overlap and interact. Indeed, on figure 5.6, they compared the results given by a first order perturbation theory (equation (5.5)) with (b) and without (a)taking into account the mode mixing. The former approach perfectly reproduces the results given by the exact calculation (gray lines).

Concomitantly, Collins and collaborators were interested in understanding why the energy-filtered EELS maps of a nano-rod are inhomogeneous [322]. Indeed, as shown on figure 5.6(c), the maxima of the potential present different intensity which is in conflict with a standard Fabry-Pérot model. Using an extended coupled oscillator (ECO) model, they demonstrated that these inhomogeneities could be explained by the coupling between different modes of the rod, see figure 5.6(d).
At the core of these two wonderful works is the possibility of *mixing different plasmon modes inside a single monomer*. At first glance, this could sound surprising as localized surface plasmons resonances form a basis of eigenmodes which, by construction, should be orthogonal.

In fact, localized surface plasmon resonances are *bi-orthogonal*, as the kernel of equation (5.1) is not symmetric, which allows the different plasmon modes to overlap. This point was missed in the work on Collins and just hinted in the work of Schmidt. The goal of the present study is to show the central role of the bi-orthogonality in plasmon physics and therefore justify the approach employed in [41] and [322].

5.3.1.2 The growing field of non-Hermitian physics

In any situation described by a linear equation (e.g. in mechanics, acoustics, quantum mechanics, electromagnetism...) the usual approach is to apply the concept of eigenmodes. Examples are

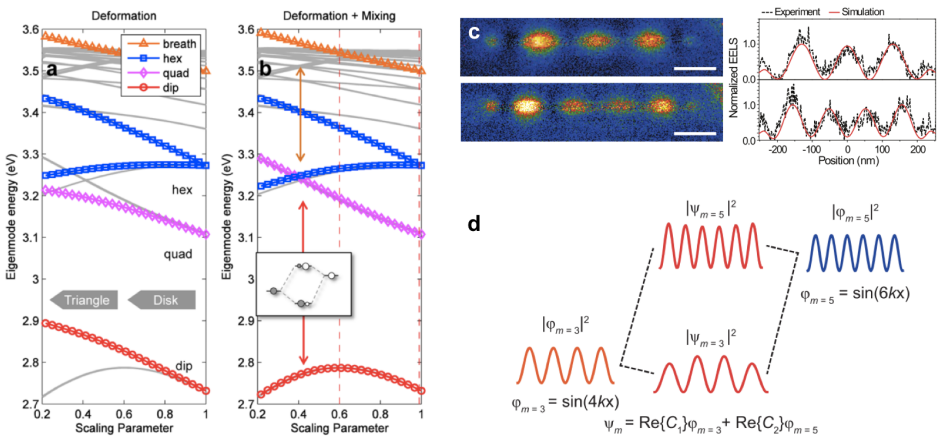

Figure 5.6: *Evolution of the eigenmodes of a triangle when it is morphed into a disk calculated by a first order perturbation theory: (a) without and (b) with taking into account the mode mixing. The grey lines represent the exact calculation. Reproduced from [41]. (c) EELS maps and profiles from surface plasmons of a silver nano-rod (scale bar is 100 nm). (d) Coupling model reproducing the asymmetry of the EELS maps by mixing different Fabry-Pérot-like modes of the rod. Reproduced from [322].*

endless: the vibrations of a guitar string are best understood as a superposition of string eigenmodes and the properties of an atom can be simply deduced from its orbitals' properties. If the kernel K of the equation is Hermitian ($K = K^\dagger$), the eigenmodes consist in pairs of eigenvalue and eigenvector, the latter forming an orthogonal basis.
Many systems of importance are however not Hermitian, but nevertheless can be advantageously described in terms of eigenmodes. In this case, the price to pay to get an eigendecomposition is that the basis becomes bi-orthogonal instead of being orthogonal. Then, eigenmodes consist in triplet of eigenvalue, left eigenvector and right eigenvector. This situation typically happens when the energy of a system is not constant and dissipated at infinity. These so-called open systems span a wide range of physical situations, from gravity waves close to black holes to lasers cavities or propagating surface plasmons [323, 324, 325, 326]. For example, a full quantum theory of bi-orthogonal modes has been developed [327, 328]. We learned from textbooks that the Hermitian prescription ensures the reality of the Hamiltonian spectrum so that non-Hermitian systems could sounds puzzling. Nevertheless, in 1998, Bender and Boettcher [329] discovered a particular class of non-Hermitian system: the so-called PT-symmetric systems. These are characterized by an Hamiltonian commuting with the parity-time operator $\hat{P}\hat{T}$. In these situations, although not Hermitian, the Hamiltonian still possesses real eigenvalues and left and right eigenvectors form a so-called quasi-normal modes (QNMs) basis. Because of this mathematical property, PT-symmetric physics became a fertile field of research [330].

Indeed, the entire field of non-Hermitian physics has grown increasing interest over the last decade. The reason is that bi-orthogonality has famous and exciting consequences, including the existence of "exceptional points" (EP) where both the eigenvalues and eigenvectors coalesce [331, 332, 333, 334] as illustrated on figure 5.7. EPs are usually associated with the apparition of non-trivial physical effects e.g. asymmetric mode switching [333]. Such effects have only very recently been studied experimentally, in the case of open systems [335, 336, 337, 338].

Nevertheless, the experimental realization and study of a non-Hermitian systems is a massive task as it requires to precisely engineer the energy dissipation [331, 340]. Particularly, the realization of a PT-symmetric system requires to exactly balance the gain and the loss. Optical systems appear to be promising canditates [330] where gain and loss can be simply tuned by playing with refractive indexes.

As emphasized in section 5.2.3.1, the localized surface plasmon eigenproblem (5.1) is non-Hermtian.

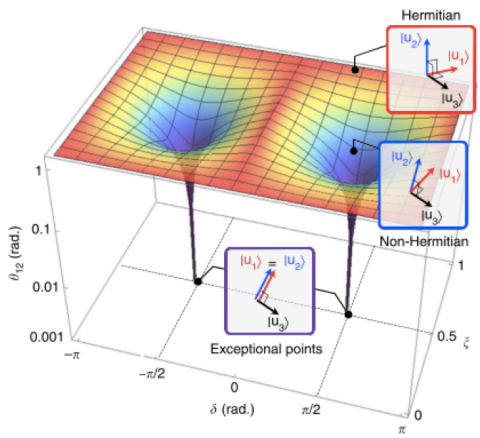

Figure 5.7: *Cosine angle* $\theta_{12} = \arccos(|\langle u_1|u_2\rangle|)$ *between two Floquet-Bloch eigenvectors* $|u_1\rangle$ *and* $|u_2\rangle$ *of an optical holographic lattice as of function of a phase difference* δ *and a balance factor* ξ*. These two parameters are defining the form of the lattice. For certain points in this parameter space, the angle goes to zero which indicates the coalescence of the two modes and therefore the presence of an EP. Reproduced from [339].*

In the original paper of Ouyang and Isaacson [9] which introduces this equation, the concept of QNM and related quantities were already present without explicitly using the modern denominations. Surprisingly, using LSPs to explore non-Hermitian physics has not been reported, although dissipation balancing is not required in this case. Indeed, the need to use bi-orthogonal modes for describing LSPs physics has mostly been seen as an extra mathematical annoyance [39] without further interpretation. Nevertheless, let's point out that non-Hermitian properties of surface plasmon-polaritons have already been studies in details e.g. by Alaeian and Dionne [341, 326]. However, the bi-orthogonality in these systems is due to energy leaks, in sharp contrast with the LSP case in which it comes from simple geometrical properties of the nano-particle.

Here, we show that the non-Hermitian physics can be investigated theoretically and experimentally with LSPs. We explore the symmetry conditions required to evidence bi-orthogonality signatures in LSP systems. We show that both the surface plasmons equation's kernel symmetry and the overall system symmetry have to be tuned towards that aim. As a counter-intuitive consequence of non-Hermiticity, we predict the possibility of observing self-hybridization within a single plasmonic particle. This coupling within a nano-particle involves two bi-orthogonal modes of different orders - a situation which cannot occur in Hermitian systems. Studying silver nano-daggers through spatially resolved electron energy-loss spectroscopy (EELS), we demonstrate that this effect is strong enough to be observed experimentally, enabling a real space visualization of self-hybridization. Defining the relevant free energy, we then draw an analogy between plasmons and other non-Hermitian systems such as open quantum cavities. Given the easily tunable parameters, we conclude that LSPs constitute an excellent platform for probing non-Hermitian physics.

5.3.2 Algebraic analysis of the plasmon eigenproblem

5.3.2.1 The F and S symmetries

The non-Hermtian Fredholm equation (5.1) can be re-written in matrix form as:

$$\begin{cases} F\ |\sigma_m\rangle = \lambda_m\,|\sigma_m\rangle\,, & (5.9a)\\ \langle\tau_m|\ F = \lambda_m\,\langle\tau_m|\,, & (5.9b)\\ F\,(\boldsymbol{r},\boldsymbol{r}') = -\dfrac{\boldsymbol{n}\,(\boldsymbol{r})\,.\,(\boldsymbol{r}-\boldsymbol{r}')}{|\boldsymbol{r}-\boldsymbol{r}'|^3} \quad \text{where} \quad \boldsymbol{r},\boldsymbol{r}'\in S & (5.9c)\end{cases}$$

Where $\boldsymbol{n}(\boldsymbol{r})$ is the outgoing normal at $\boldsymbol{r}$, F is the normal derivative of the Coulomb kernel, the right eigenvectors $\{|\sigma_m\rangle\}$ can be identified as surface charge densities, the left eigenvectors $\{\langle\tau_m|\}$ are surface dipole densities projected along $\boldsymbol{n}$ and the eigenvalues $\{\lambda_m\}$ are dimensionless quantities associated with each pair of left-right eigenvectors.

Hence, in contrast to systems recently considered [342, 343, 336, 338, 339, 344], non-Hermiticity arises from the non-symmetry of F, what is always a real matrix. As detailed is appendix C and in section 2.5, solutions of equation (5.9) can be computed with the boundary element method [345, 248, 10, 49, 39]. Moreover, let's remind that the integer m indexes the modes by increasing values of λ_m. In the following, for the sake of simplicity, we will indifferently discuss the geometrical eigenvalues $\{\lambda_m\}$ or the plasmon eigenenergies $\{\omega_m\}$ assuming a one-to-one correspondence between the two spaces $\{\lambda_m\} \leftrightarrow \{\omega_m\}$. This is exact within the Drude model approximation for the dielectric function.

Quite remarkably, it can be shown that F is a quasi-Hermitian matrix [9] and therfore that $\{|\sigma_m\rangle\}$ (resp. $\{|\tau_m\rangle\}$) form a set of QNMs. To properly introduce the concept of QNM in the LSP problem, one has to remind the definition of *quasi-Hermiticity*. A non-Hermitian matrix M is called quasi-Hermitian if it satisfies the additional condition:

$$\eta M = M^* \eta \tag{5.10}$$

where η is a positive definite self-adjoint operator and M^* is the conjugate (Hermitian or real) of M [346]. The matrix η is usually called the *metric*. The quasi-Hermiticity of the operator M ensures that its eigenvalues are real. As first demonstrated in [9], the LSP's kernel F is a quasi-Hermitian operator with respect to the metric:

$$\eta_0 : f(\boldsymbol{r}) \longrightarrow \oint_S d\boldsymbol{r}\,' \frac{f(\boldsymbol{r}\,')}{|\boldsymbol{r} - \boldsymbol{r}\,'|} \tag{5.11}$$

From this property, it follows that the right (resp. left) eigenvectors of the LSP eigenproblem are orthogonal in term of η_0:

$$\langle\sigma_m|\eta_0|\sigma_n\rangle = \delta_{m,n} \tag{5.12}$$
$$\langle\tau_m|\eta_0|\tau_n\rangle = \delta_{m,n} \tag{5.13}$$

From the latter equations, it comes out that $\{|\sigma_m\rangle\}$ (resp. $\{|\tau_m\rangle\}$) form a set of QNMs for the norm η_0. Therefore the $\{\lambda_m\}$ are real numbers [9].

Before going further, one must emphasize that there are fundamentally two types of symmetry involved in a plasmonic eigenproblem. The first one is *the kernel symmetry* which controls the structure of the vector space solution and thus the (bi-)orthogonality of the plasmon modes. The second is *the surface symmetry* (invariance of the surface charge or dipole distributions under any geometrical transformation) which may lead to additional properties of the plasmons. To avoid any confusion, in the following, we will refer to the kernel symmetry (the surface symmetry) as F-symmetry (S-symmetry). As a practical example, in figure 5.8(a), we present σ and τ corresponding to the first two eigenmodes of an F-symmetric surface (sphere) and an F-asymmetric surface (torus). As expected, for the sphere, the solutions are orthogonal and thus the left and right eigenvectors are identical while, in the case of the torus, the solutions are bi-orthogonal and the corresponding left and right eigenvectors are strikingly different.

The particularity of the LSP's bi-orthogonality is that it only depends on the geometry of the metallic nano-particle. Indeed, a set of LSPs sustained by a given surface S will be orthogonal (i.e. F-symmetric) if $F^\top = F$ which reads $\forall \boldsymbol{r}, \boldsymbol{r}' \in S,\ F(\boldsymbol{r}', \boldsymbol{r}) = F(\boldsymbol{r}, \boldsymbol{r}')$. Using expression (5.9c) for F, one can re-write the previous condition as:

$$\forall \boldsymbol{r}, \boldsymbol{r}' \in S,\ \boldsymbol{n}(\boldsymbol{r}) \,.\, (\boldsymbol{r} - \boldsymbol{r}') = \boldsymbol{n}(\boldsymbol{r}') \,.\, (\boldsymbol{r}' - \boldsymbol{r}) \tag{5.14}$$

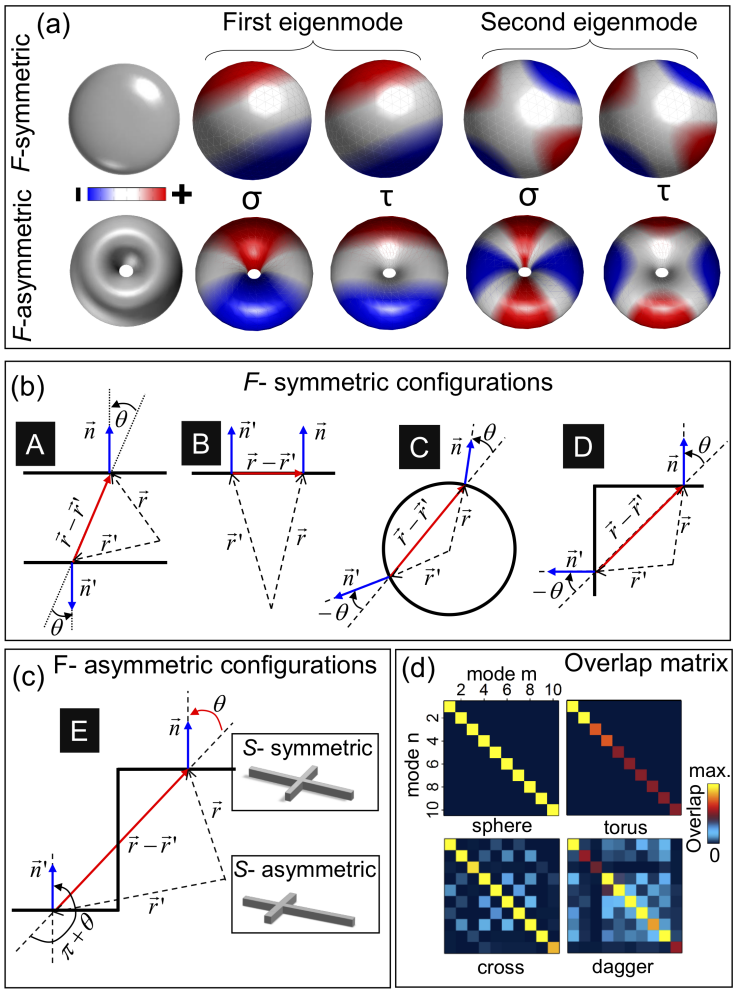

Figure 5.8: *(a) The first two left and right eigenvectors of F-symmetric (sphere) and F-asymmetric (torus) surfaces. (b) Geometrical configurations of two normal vectors located on the surface leading to a symmetric contribution to the kernel. (c) Example of an asymmetric configuration corresponding e.g. to a cross or a dagger particle. (d) Overlap matrix between the 10 first eigenmodes of a sphere, a torus, a cross and a dagger.*

which corresponds to:

$$(\boldsymbol{n}(\boldsymbol{r}) + \boldsymbol{n}(\boldsymbol{r}')).(\boldsymbol{r} - \boldsymbol{r}') = 0 \tag{5.15}$$

One can then list all the geometrical configurations satisfying this equation. These situations are called F-symmetric configurations (configurations A, B, C and D on figure 5.8). Thus, a surface displaying only F-symmetric configurations is F-symmetric. Otherwise, it is F-asymmetric. In figure 5.8(b), we show four F-symmetric configurations A-D. From these, one can immediately deduce that a sphere (configuration C), a rod (configurations A, B and C), a cuboid [347] (configurations A, B and D) or a disk (configurations C and D) are F-symmetric. Similarly, in figure 5.8(c), configuration E is obviously F-asymmetric and consequently the cross and the dagger (see inset) are F-asymmetric structures.

5.3.2.2 The overlap matrix

Moreover, when a surface is F-asymmetric, two right (or left) eigenvectors of different orders may have a non-zero spatial overlap, which may have dramatic consequences, as we demonstrate both theoretically and experimentally later. Therefore, quite counter-intuitively, two eigenmodes of the same nanoparticle and of different orders may interact, while this is obviously impossible for

orthogonal modes. In addition, we expect this interaction to be stronger as the overlap gets larger and, thus, one could formulate the following ansatz which will be justified later:

$$\Omega_{m,n} \propto T_{m,n} \tag{5.16}$$

where $\Omega_{n,m}$ is the so-called classical Rabi energy of the two interacting modes n and m and the overlap matrix is defined as:

$$T_{m,n} = \langle \tau_m | \tau_m \rangle \langle \sigma_m | \sigma_n \rangle + \langle \sigma_n | \sigma_n \rangle \langle \tau_m | \tau_n \rangle \tag{5.17}$$

This expression will be justified in section 5.3.4.1 and constitutes a fundamental quantity to consider in the study of bi-orthogonal systems.

5.3.2.3 Symmetry analysis of the overlap matrix

The fundamental quantity describing the LSP's bi-orthogonality is the *overlap matrix* given by equation (5.17). To evaluate this matrix, we first calculate the left and right eigenvectors using the `MNPBEM` toolbox and then deduce the overlap. This matrix is formally analogue to a Gram matrix, usually used to test the linear independence of a set of vectors. Therefore, by direct inspection of the form of the matrix, one can get important information on the vector space of the eigenproblem. The figure of merit of bi-orthogonality is (surprisingly) given by the diagonal elements. Indeed, when the system is bi-orthogonal, both left and right eigenvectors cannot be normalized at the same time. Thus in a bi-orthogonal system, the diagonal elements are not equal to one. The off diagonal elements give additional information on the skewness of the vector space but also depend on the S-symmetry of the surface.

We should emphasize that the hybridization mediated by the eigencharges we consider here is fundamentally different from the coupling in orthogonal systems mediated by the fields. In figure 5.8(d), we plot the absolute value[2] of the overlap matrix between the ten first eigenmodes of a sphere, a torus, a cross and a dagger. The sphere being F-symmetric, its overlap matrix obviously corresponds to the identity, as expected for orthogonal modes. As emphasized earlier, the torus is F-asymmetric but its matrix does not display any off-diagonal elements. This is a consequence of the strong S-symmetry (rotational invariance) of the torus shape which imposes $\langle \sigma_m | \sigma_n \rangle \propto \delta_{m,n}$ and $\langle \tau_m | \tau_n \rangle \propto \delta_{m,n}$. Consequently, although it is F-asymmetric, the torus behaves essentially like an orthogonal system, the only difference being the absence of normalization of the elements on the diagonal. As discussed earlier, cross and dagger are two F-asymmetric structures which display weaker S-symmetry than the torus (see inset figure 5.8(c)). The cross is still centro-symmetric which imposes a null overlap between modes of different parity i.e. $\langle \sigma_m | \sigma_m \rangle = \langle \tau_m | \tau_n \rangle = 0$ if $n+m$ is odd, resulting in the appearance of a checkerboard-like matrix. A comprehensive experimental and numerical study of the plasmonic cross system away from the hybridization point is developed in section 5.2 or in [250]. By shifting one arm of the cross, we break the centro-symmetry and the latter relation does not hold anymore. Consequently, the dagger overlap matrix has its off-diagonal elements with non-null values except for modes 4 and 10. Indeed, these two modes correspond to LSPs located on the short arm of the cross only. All the others are modes delocalized on the whole dagger. Therefore, F-asymmetry ensures that $|\sigma\rangle$ and $|\tau\rangle$ are different but does not guarantee that two different $|\sigma\rangle$ overlap. When the surface is F-asymmetric, the S-symmetry is the parameter controlling the overlap between modes of different orders.

5.3.3 LSP vs. electromagnetic wave in open systems

Now that we have set the basics of the LSP eigenproblem, an important comparison needs to be done. Indeed, the current work describing the LSP's bi-orthogonality should remind of the well-known problem in optics e.g. electromagnetic waves in open system, non-Hermiticity and

[2] Indeed, all the eigenvectors are determined up to an $e^{i\pi}$ phase. Consequently $T_{m,n}$ can indifferently take two values $\pm T_{m,n}$. To remove this uncertainty and to increase the dynamics of the colorscale, we plot the absolute value of the overlap matrix.

quasinormal modes (QNM) expansion. LSP being also solution of the Maxwell's equations, it is rather tempting to identify the two problems. However, although there is a strict analogy between the two systems, the nature of the underlying physics is rather different. To avoid any confusion, in this section, we clarify the differences and analogies between EM waves in open systems and LSPs - particularly the status of QNMs.

5.3.3.1 Dependence in time

Obviously, the first, trivial but essential, difference between LSPs and EM waves is the dependence in time. The latter are properly described by the Helmholtz equation while LSPs are pure electrostatic resonance, solution of the Ouyang and Isaacson equation. Surface plasmon-polaritons are therefore an important example of EM waves in open systems [348, 341, 326]. The main consequence is that when the kernel is complex for EM waves, it is real in the case of LSPs. A major consequence of this difference is the co-dimension of exceptional points [334].

In the case of EM waves in open systems, the non-Hermiticity in triggered by the time-reversal symmetry breaking. Thus leaks (resp. gain) play a central role in this problem. As it will be developed in section 5.3.6, the bi-orthogonality of LSPs is controlled by the minimization of a surface energy. However, it is rather non-intuitive that leaks play no role in LSP bi-orthogonality as it is well known that they are highly lossy systems. Actually, losses appear in LSP problem when considering the temporal coherence of these excitations, as detailed in [10]. In short, losses will affect the experimental observability of LSPs [10] but play no fundamental role with respect to their bi-orthogonality property.
Finally, because of it is time-independence, the LSP bi-orthogonality is a very singular system which, to the best of our knowledge, has no known analogue. However, as pointed out in [40], surface phonon excitations are also solution of Ouyang and Isaacson eigenproblem and therefore constitute a second example of static bi-orthogonal systems.

5.3.3.2 Quasinormal modes

A powerful tool to handle the non-Hermitian systems is the QNM expansion [324]. Particularly, it is well-known that, in the case of EM waves in open systems, QNMs suffer from a problem of normalization [349].

In the case of EM waves in open systems, the QNMs $\tilde{f}_\mu$ of the electric field are defined as the solution of the Helmholtz equation [349]:

$$\Delta \tilde{f}_\mu(\boldsymbol{r}\,) - \tilde{k}_\mu^2\, \epsilon(\boldsymbol{r}, \tilde{\omega}_\mu) \tilde{f}_\mu(\boldsymbol{r}\,) = 0 \tag{5.18}$$

where $\tilde{k}_\mu^2$ and $\tilde{\omega}_\mu$ are respectively the wavevector and the energy associated to mode μ. Equation (5.18) has to be completed by a proper radiation condition to take into account the leaky nature of the system (e.g. Silver-Müller condition for homogeneous dielectric [349]). The difficulty comes in the definition of the norm for the QNMs $\langle\langle \tilde{f}_\mu | \tilde{f}_\mu \rangle\rangle$ which of course depends on the radiation condition. In the case of a homogeneous dielectric, one can use, for example, the Lai norm, the Sauvan norm or the Muljarov norm [349]. However, all these norms suffer from regularization problems in different limits for fundamental reasons which will be clearer later. In section 5.3.2.1, we saw that $\{|\sigma_m\rangle\}$ (resp. $\{|\tau_m\rangle\}$) forms a set of QNMs for the norm η_0. However, in this case, thanks to the quasi-Hermiticity of F, there is no regularization problem involved in the definition or the norm. In other words, the concept of QNM is naturally and properly defined in the case of quasi-Hermitian operators which is the case for the LSP eigenproblem. Otherwise, when the construction of the QNMs is done ad-hoc (to satisfy some physical constraints), without the quasi-Hermiticity property, some normalization problems dramatically appear. Consequently, contrary to the case of the EM waves in open systems, LSPs are a rare example where the QNM concept is properly defined. Some cases of quasi-Hermiticity also exist in dynamic problem e.g. exact PT-symmetric systems [350, 351].

As emphasized in [352], a key property of quasi-Hermitian operators is the positive-definiteness

of the metric η. Indeed, it ensures the positive-definiteness of the scalar product which is a requirement to construct a proper Hilbert space. However, it is still possible to treat non-Hermitian systems without this positive-definiteness property. In this case, η is usually called a pseudo-metric [350] and the operator M is called *pseudo-Hermitian*. This property is thus weaker than the quasi-Hermiticity but still ensures that the eigenvalues of M are real. As pointed out in [352], the distinction between quasi- and pseudo-Hermitian is often omitted (see [352] and references therein). However, let's emphasize that, although pseudo-Hermitian operators have real spectra (which is a basic physical requirement), only quasi-Hermitian operators enable a stable definition of QNMs.

5.3.4 Self-hybridization within a dagger resonator

Bi-orthogonality enables eigenmodes of different orders to overlap therefore to interact. This non-intuitive phenomenon of *self-hybridization* should be accessible experimentally. More specifically, we expect the energy spectra of the LSPs to display characteristic features of coupling i.e. an eigenvalues' anti-crossing and an eigenfunctions' hybridization as a function of a certain coupling parameter. In the present work, we used STEM-EELS as it has demonstrated its efficiency in mapping plasmonic resonances spatially and spectrally with nanometric spatial resolution [11]. For the sake of the demonstration, we first consider 400 nm $\times$ L silver crosses with a 40$\times$40 nm square cross-section. The length L, which will be shown to be the relevant detuning parameter, is varied from 80 nm to 170 nm.

5.3.4.1 Mode mixing within the BEM perturbation theory

The effect of the variation of L on the eigenquantities can be modeled using a first order perturbation theory as detailed in section 5.2.3.1. The first order perturbation theory is formally derived for bi-orthogonal systems in [328] and has been first introduced for the boundary element method by Trügler et al. [317]. Within this approximation, when two modes spectrally overlap, one has to take into account the possible hybridization between them by diagonalizing the typical Rabi-like matrix [41]:

$$M = \begin{pmatrix} \lambda_m^{(0)} + \lambda_m^{(1)} & C_{m,n} \\ C_{n,m} & \lambda_n^{(0)} + \lambda_n^{(1)} \end{pmatrix} \tag{5.19}$$

Using the convention of [353, 354, 355, 322], we call the eigenvectors of the unperturbed basis $\{\sigma_m^{(0)}, \tau_m^{(0)}\}$ in which M is expressed in equation (5.19) *diabatic*, and the eigenvectors of the hybridized basis $\{\sigma_{m,n}^{\pm}, \tau_{m,n}^{\pm}\}$ in which M is diagonal *adiabatic*. At this point it is worth emphasizing, as was done in [41], that equation (5.19) is similar to matrices encountered in the LCAO theory. This analogy is valid on a mathematical level but omits an important physical aspect of the problem. Indeed, LCAO theory describes the hybridization between orbitals belonging to different systems. Therefore, it can efficiently model dimer-like coupling where the two hybridized modes belong to two different and independent surfaces i.e. two monomers [319] or two independent sub-surfaces of a large monomer [347]. On the other hand, the self-hybridization process we describe here takes place within a single surface and would be comparable, for example, to the hybridization between two notes of a single guitar string. Consequently, although mathematically analogous to LCAO, self-hybridization belongs to a specific universality class which is rather counter-intuitive.

5.3.4.2 Connection between the mixing term and the overlap matrix

We will now connect the mixing term $C_{n,m}$ to the overlap matrix $T_{n,m}$. By inserting the completeness relation $\sum_i |\tau_i^0\rangle \langle\sigma_i^0| = 1$ [328], one can rewrite the coupling constant $C_{m,n}$ as:

$$\begin{aligned} C_{n,m} &= \langle\tau_m^{(0)}|\delta F|\sigma_n^{(0)}\rangle && (5.20)\\ &= \langle\tau_m^{(0)}|\,\delta F \sum_i |\tau_i^{(0)}\rangle \langle\sigma_i^{(0)}|\sigma_n^{(0)}\rangle && (5.21)\\ &= \langle\tau_m^{(0)}|\delta F|\tau_m^{(0)}\rangle \langle\sigma_m^{(0)}|\sigma_n^{(0)}\rangle + \langle\tau_m^{(0)}|\delta F|\tau_n^{(0)}\rangle \langle\sigma_n^{(0)}|\sigma_n^{(0)}\rangle && (5.22) \end{aligned}$$

where we assumed that only modes n and m overlap. We define the matrices $s_{m,n} = \langle \sigma_m^{(0)} | \sigma_n^{(0)} \rangle$ and $t_{m,n} = \langle \tau_m^{(0)} | \tau_n^{(0)} \rangle$ which leads to:

$$C_{n,m} = \langle \tau_m^{(0)} | \delta F | \tau_m^{(0)} \rangle \, s_{m,n} + \langle \tau_m^{(0)} | \delta F | \tau_n^{(0)} \rangle \, s_{n,n} \tag{5.23}$$

From equation (52) of [328], one can write:

$$\langle \tau_m^{(1)} | \left(\lambda_m^{(0)} - F \right) + \langle \tau_m^{(0)} | \, \lambda_m^{(1)} = \langle \tau_m^{(0)} | \, \delta F \tag{5.24}$$

If we multiply the previous equation by $|\tau_n^0\rangle$, we get:

$$\begin{aligned}
\langle \tau_m^{(0)} | \delta F | \tau_n^{(0)} \rangle &= \langle \tau_m^{(1)} | \left(\lambda_m^{(0)} - F \right) | \tau_n^{(0)} \rangle + \lambda_m^{(1)} \langle \tau_m^{(0)} | \tau_n^{(0)} \rangle && (5.25)\\
&= \langle \tau_m^{(1)} | \left(\lambda_m^{(0)} - F \right) | \tau_n^{(0)} \rangle + \lambda_m^{(1)} t_{m,n} && (5.26)\\
&= \langle \tau_m^{(1)} | \sum_i | \sigma_i^{(0)} \rangle \langle \tau_i^{(0)} | \left(\lambda_m^{(0)} - F \right) | \tau_n^{(0)} \rangle + \lambda_m^{(1)} t_{m,n} && (5.27)\\
& && (5.28)
\end{aligned}$$

which gives:

$$\begin{aligned}
\langle \tau_m^{(0)} | \delta F | \tau_n^{(0)} \rangle &= \sum_i \langle \tau_m^{(1)} | \sigma_i^{(0)} \rangle \left(\lambda_m^{(0)} - \lambda_i^{(0)} \right) \langle \tau_i^{(0)} | \tau_n^{(0)} \rangle + \lambda_m^{(1)} t_{m,n} && (5.29)\\
&= \sum_i \langle \tau_m^{(1)} | \sigma_i^{(0)} \rangle \left(\lambda_m^{(0)} - \lambda_i^{(0)} \right) t_{i,n} + \lambda_m^{(1)} t_{m,n} && (5.30)
\end{aligned}$$

Assuming that only modes n and m overlap, we see that only term $i = n$ will give a non-null contribution to the sum and therefore:

$$\begin{cases}
\langle \tau_m^{(0)} | \delta F | \tau_n^{(0)} \rangle = \langle \tau_m^{(1)} | \sigma_n^{(0)} \rangle \left(\lambda_m^{(0)} - \lambda_n^{(0)} \right) t_{n,n} + \lambda_m^{(1)} t_{m,n} & (5.31a)\\
\langle \tau_m^{(0)} | \delta F | \tau_m^{(0)} \rangle = \lambda_m^{(1)} t_{m,m} & (5.31b)
\end{cases}$$

Using equations (5.31a) and (5.31b), it is then possible to re-write equation (5.23) as:

$$C_{n,m} = \lambda_m^{(1)} \left(t_{m,m} s_{m,n} + t_{m,n} s_{n,n} \right) + \langle \tau_m^{(1)} | \sigma_n^{(0)} \rangle \left(\lambda_m^{(0)} - \lambda_n^{(0)} \right) t_{n,n} s_{n,n} \tag{5.32}$$

Now, we can assume that the coupled modes are perfectly degenerated i.e. $\lambda_m^{(0)} = \lambda_n^{(0)}$, one can then write:

$$C_{n,m} = \lambda_m^{(1)} \left(t_{m,m} s_{m,n} + t_{m,n} s_{n,n} \right) \tag{5.33}$$

We can now define the **overlap matrix** $T_{m,n}$ as:

$$T_{m,n} = t_{m,m} s_{m,n} + t_{m,n} s_{n,n} \tag{5.34}$$

And finally:

$$C_{n,m} = \lambda_m^{(1)} T_{m,n} \tag{5.35}$$

Thus, **one can immediately see that self-hybridization is only possible when $T_{n,m} \neq 0$ i.e when the system is bi-orthogonal**. In other words, the surface defining the diabatic modes needs to be F-asymmetric while the F-symmetry of the perturbative kernel δF can be arbitrary. Assuming a bijection between the geometric eigenvalue space and the energy space, one can rewrite equation (5.35) using the corresponding energetic quantities $C_{m,n} \to \Omega_{m,n}$ and $\lambda_m^{(1)} \to \omega_m^{(1)}$

$$\Omega_{m,n} = \omega_m^{(1)} T_{m,n} \tag{5.36}$$

The mixing term $C_{n,m}$ can be mapped in energy space to the classical Rabi energy $\Omega_{n,m}$ which justifies the ansatz (5.16). Contrary to $C_{n,m}$, $\Omega_{n,m}$ is an observable. Therefore, by measuring the energy splitting between two coupled modes, one can directly relate it to the degree of bi-orthogonality of a system.

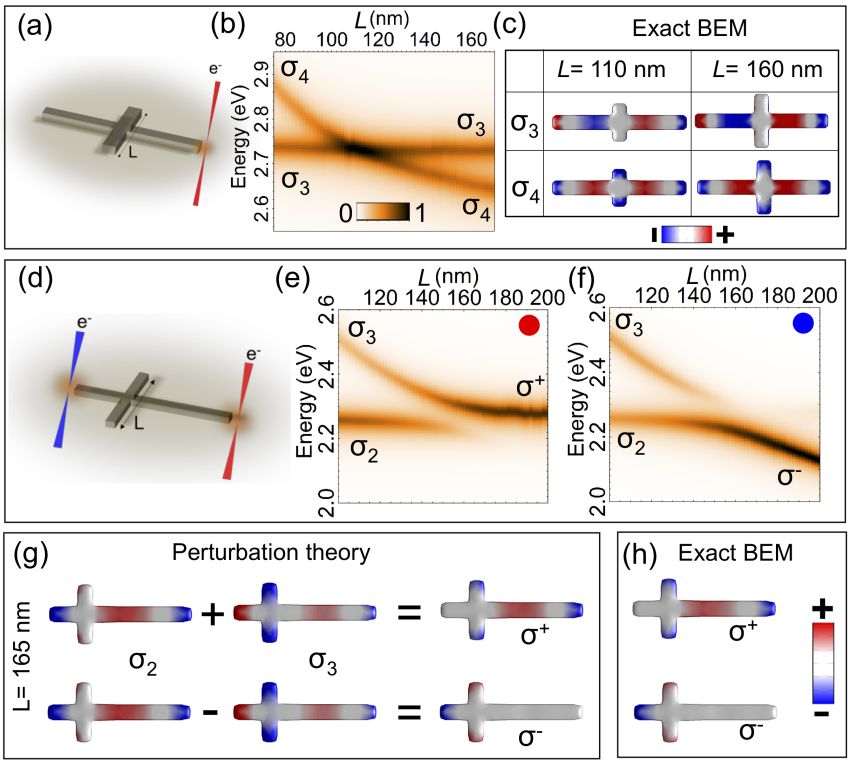

Figure 5.9: *(a) Schematic representation of an EELS experiment on a cross. (b) Simulated EEL spectra taken at the position of the electron beam indicated in (a) and as a function of L. (c) Simulated right eigenvectors corresponding to modes 3 and 4 at (L=110 nm) and after (L=160 nm) the crossing point. (d) Schematic representation of the EELS experiment on the dagger. (e) Simulated EELS spectra taken at the red position of the electron beam indicated in (d) and as a function of L. (f) Simulated EEL spectra taken at the blue position of the electron beam indicated in (d) and as a function of L. (g) Hybridized eigenvectors calculated at the anti-crossing point using first order perturbation theory. (h) Hybridized eigenvectors calculated at the anti-crossing point using the exact BEM.*

5.3.4.3 Simulation of the cross and dagger morphing

In figure 5.9(a-b), using the exact BEM, we calculate the EELS spectra of the silver cross (when the beam impinges at one end of main axis, see figure 5.9(a)) as a function of the length L. When L is small, the cross eigenmodes have the same spatial profile as the well-known rod eigenmodes [322]. The corresponding eigenvectors $|\sigma_n\rangle$ thus display periodic profiles with n nodes, see figure 5.9(c). When the length L of the arm is increased, the odd modes (odd n) which have no charge at the center remain almost unchanged while the even modes are expected to be red-shifted. Consequently, for particular values of L, modes of different parities can spectrally overlap, justifying the use of L as a detuning parameter. As shown in figure 5.9(b), when L=110 nm, modes 3 and 4 spectrally overlap. However, although the cross is F-asymmetric, no sign of self-hybridization appears as the corresponding eigenvectors keep the same spatial profile at and after the crossing point (see figure 5.9(c)). As mentioned in figure 5.8(d), this is due to the (S-)centro-symmetry of the cross which imposes a checkerboard form to the overlap matrix. In order to enable self-hybridization, one needs to break this S-symmetry. To do so, we shift the position of the orthogonal growing arm to form a dagger-like geometry, see figure 5.9(d). The position of the small arm of the dagger is chosen to correspond to a maximum of mode 3 and a node of mode 2. As for the cross, in figure 5.9(e-f), we calculate the EELS spectra as a function of L for two different positions of the beam[3]. The spectra display a strong anti-crossing behavior, which is a signature of the self-hybridization between modes 2 and 3. In order to validate our earlier interpretation, we calculate the adiabatic

[3]The dagger being not left-right S-symmetric, the spectra are different at the two positions; however, modes 2 and 3 always have a maximum at one of the two positions, making these two positions sufficient to retrieve the energy diagrams of these modes

(hybridized) modes $\sigma^{\pm}$ both using the first order perturbation theory and the exact BEM in figure 5.9(g-h). The calculations are done exactly at the crossing point (L=165 nm) where the adiabatic modes are known to be equal mixtures of diabatic modes $\sigma^{\pm} = \sigma_2 \pm \sigma_3$. The two results are in remarkably good agreement, proving that the perturbation theory gives a realistic picture of the self-hybridization physics.

One can also highlight the exotic profile of the hybrid modes. In particular, the mode σ^{-} strongly confines charges at one tip, leading to a so-called hot-spot configuration which is of particular interest in a wide range of applications. Self-hybridization thus constitutes a very attractive procedure for designing specific plasmonic states.

5.3.4.4 Phase diagram

Fundamentally, a coupling experiment (no matter if one considers a dimer-like coupling or a self-hybridization) between two modes $|\sigma_n\rangle$ and $|\sigma_m\rangle$ is controlled through two parameters i.e. the spectral detuning $\beta_{n,m}$ and the coupling constant $\Omega_{n,m}$. In other words, a coupling experiment can be represented by a certain path in the (β, Ω) phase-space (see figure 5.10). A dimer-like coupling corresponds to an iso-β transition [347] where only the coupling parameter is varied. The dagger self-hybridization scheme we described is an iso-Ω transition where only the detuning parameter L is varied and the coupling constant is fixed by the overlap between the diabatic eigenvectors. This fully justifies the efficiency of the perturbation theory. On figure 5.10, we summed up the different paths in the (Ω,β)-space that one can follow during a coupling experiment.

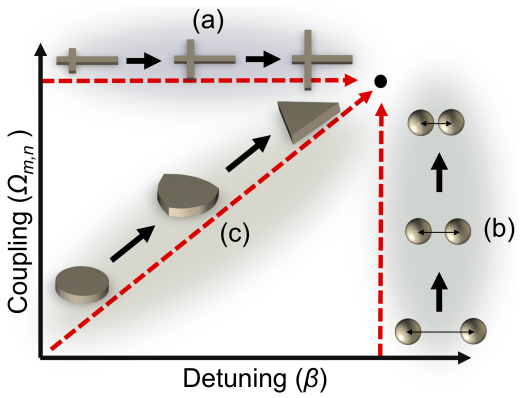

Figure 5.10: *(a) Iso-Ω transition corresponding to the dagger hybridization investigated in the present paper. (b) Iso-β transition corresponding to a dimer like coupling e.g. [347] (c) Intermediate path within the phase-space corresponding to e.g. [41].*

5.3.5 Experimental demonstration of self-hybridization

Finally, we need to verify that the bi-orthogonality is a sufficiently strong phenomenon to be measured experimentally. To do so, we reproduced experimentally the simulations described in figure 5.9(d-f) by lithographing a series of silver daggers with increasing L and measuring the energy of modes 2 and 3 using the STEM-EELS technique.

We report in figure 5.11(a) the spectra extracted from spectral-images acquired on a series of daggers with varying arm length L, at beam positions where the intensity of the modes of interest is the highest. The location of the beam has been shown in the HAADF image of (b) in color-coded boxes. In (c) and (d), the energy filtered EELS maps are presented for the two modes, and the corresponding simulated charges distributions are displayed to the right of each experimental maps.

By counting the number of maxima/minima on the charge distributions, one can clearly see the symmetry exchange expected from a coupling between modes. Since EELS does not map directly

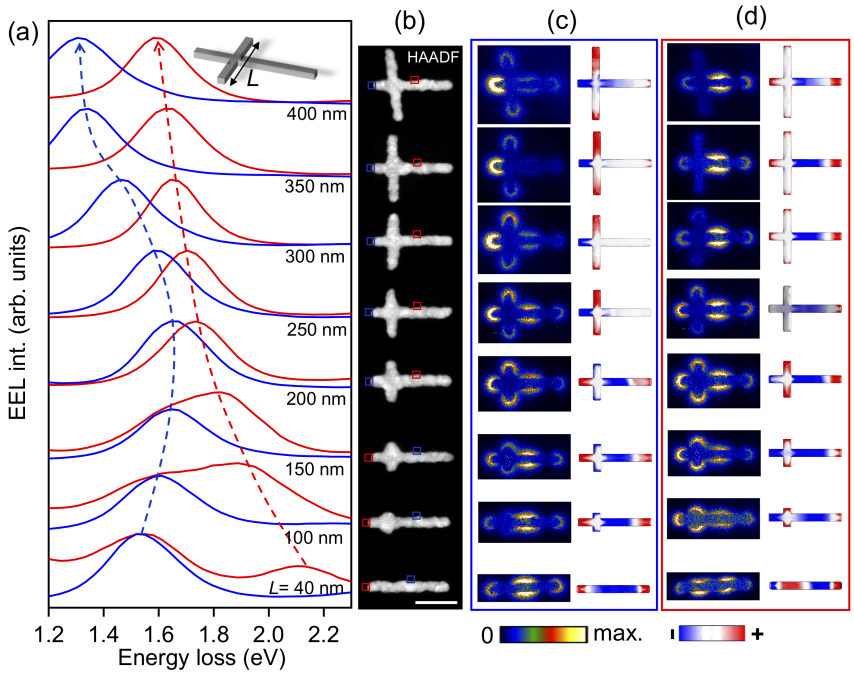

Figure 5.11: *(a) Experimental EELS spectra for different arm lengths zoomed on the mode 2 and 3 energy regions. EELS spectra have been extracted from full spectral-images, deconvoluted following prescriptions in [356, 11] and summed on the regions of interest indicated on the right high angle annular dark field (shown in column (b)) images by the corresponding colors. Scale bars in (b) are 200 nm. (c,d) Energy filtered map and corresponding BEM simulation for modes 2 and 3 respectively.*

eigencharges, but eigenfields (or eigenpotentials) [10], maxima and minima of eigencharges do not directly convert to maxima of EELS intensity. Thus, the symmetry exchange is less obvious in EELS. On the EELS maps, the mode 2 has three maxima at $L = 40$ nm, and conversely mode 3 has four maxima at $L = 400$ nm. However, mode 3 has four maxima at $L = 40$ nm (rod), but only two seem to be observed for mode 2 at $L = 400$ nm. This is due to the asymmetric intensity profiles of the eigencharge for mode 2 at $L = 400$ nm, as compared to the quite symmetric one for mode 3 at the same length, and mode 2 and 3 at $L = 40$ nm. The first charge oscillation is much stronger on the left of the $L = 400$ nm for mode 2, leading to a strongly enhanced EELS signal on the left. A closer inspection, however, permits to observe four maxima along the cross length on the $L = 400$ nm for mode 2. This symmetry exchange together with the clear anti-crossing shape of the experimental data are strong signatures of a coupling between mode 2 and 3.

In order to make the anti-crossing behavior even clearer, as shown on figure 5.12(a), we performed a systematic Gaussian fitting of the deconvoluted data in order to precisely extract the position of the plasmons resonances. Figure 5.12(b) summarizes the behavior of the energies of the *fitted* plasmon peaks maxima as a function of the arm length L. One can see that we reproduce the anti-crossing behavior calculated in figure 5.9. The small red-shift between the experiments and the simulations is due to the fact that the simulations do not take into account the presence of a substrate [250].

The lower (σ^-) and the upper (σ^+) branches of the hybridization figure 5.12(b) are separated by a coupling constant $\Omega_{exp} \approx 84$ meV which is a remarkably high value considering that the studied structures are lithographed polycrystalline nano-particles. In figure 5.12(c-f), we reported the EELS maps measured at the resonance energies for two different values of L. When $L = 100$ nm, the two modes display the spatial signature of the diabatic modes σ_2 and σ_3 showing that the two plasmons are not coupled. At L=250 nm, the coupling regime is clearly established as the two adiabatic plasmon modes display the characteristic spatial distributions expected from figure 5.9(h). Let's point out that maps 5.12(e-f) have been obtained by a Gaussian fitting of the plasmon

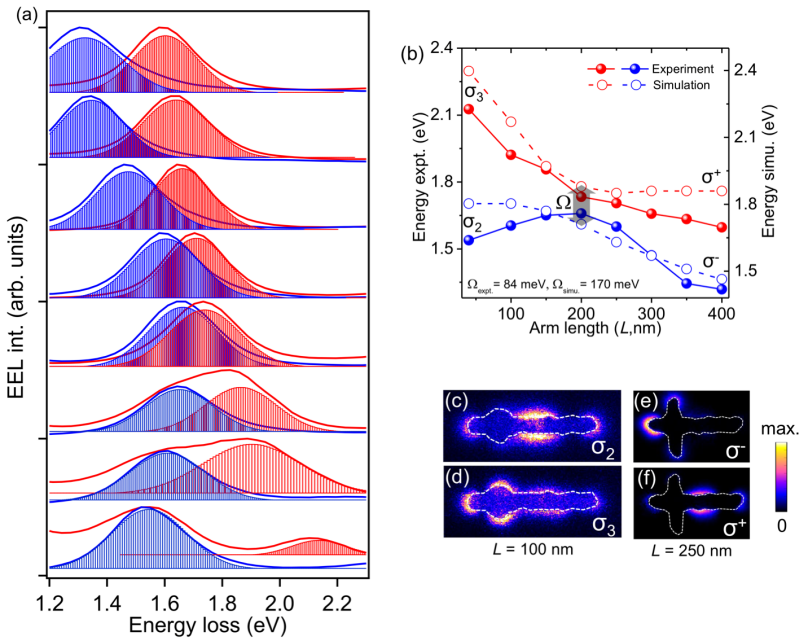

Figure 5.12: *(a) Gaussian fitting of the deconvoluted data (shown in figure 5.11) in order to extract the experimental energy positions of the plasmon resonances. (b) Experimental and simulated energies of the two plasmon modes as a function of the arm length L. Experimental energies have been deduced from the gaussian fitting in (a). Note the shift of the energy axis between experiment and theory related to the absence of substrate in the simulations. (c-d) EELS filtered maps measured at energies corresponding to an uncoupled case for L =100 nm. (e-f) EELS fitted maps for the coupled case at L =250 nm.*

peaks over the whole spectrum image.

In conclusion, self-hybridization is a strong and measurable phenomenon characteristic of the non-Hermiticity of the LSP's equation. We should point out that this strong coupling regime has been reached by maximizing the overlap between the two eigenvectors. Therefore, the key parameter triggering the self-hybridization is the overlap matrix $T_{m,n}$. This quantity thus constitutes a measurement of the degree of bi-orthogonality of the system and therefore can be seen as classical analogue of the Petermann factor for lasers [357]. Interestingly, we also note that S. Collins et al. [322] proposed phenomenologically that harmonic plasmonic modes within single nanorods could hybridize as shown on figure 5.6. The authors suggested that this could be the reason for an increase in intensity at certain nodes along the nanorod as measured by EELS. Most of the nanorods, either in the form of parallelepipeds or cut cylinders are F-symmetric or slightly F-asymmetric. Local variations (e.g. rugosities) or global ones (if for example the nanorod has an ellipsoidal shape) may increase the degree of F-asymmetry. However, the 1D confinement along the long axis of the ellipsis induces a hierarchical (harmonic) quantification of surface plasmons energies that prevents modes of different orders from having degenerate eigenvalues. Therefore, only a very weak spectral overlap between different modes is possible, which may explain why S. Collins et al. [322] could only measure a very weak influence of self-hybridization.

5.3.6 Physical origin of plasmonic bi-orthogonality

In open quantum systems, the appearance of bi-orthogonality is related to the broken time-reversal symmetry of the Hamiltonian. In complete analogy, one should identify what fundamental law controls the bi-orthogonality in classical plasmonic systems. To this aim, first let us remind that, for a dielectric material the density of electromagnetic energy is $U = \boldsymbol{D}.\boldsymbol{E}$ [27], where $\boldsymbol{D}$ and $\boldsymbol{E}$ are respectively the electric displacement and the electric field in the medium. In plasmonics,

since eigenmodes are fully determined by their surface charge (resp. dipole) densities (σ and τ), the relevant energy operator of the system must involve the sources instead of the fields. More precisely, τ being the source of $\boldsymbol{D}$ and σ the source of $\boldsymbol{E}$ [10], this energy has to be related to a charge-dipole interaction. Indeed, $F(\boldsymbol{r}, \boldsymbol{r}')$ (see equation 5.9c) gives the interaction energy between a unitary dipole $\boldsymbol{n}$ located in $\boldsymbol{r}$ and a unitary point charge $q = 1$ located in $\boldsymbol{r}'$ in an embedding medium $\epsilon = 1$. At this point, for a given surface S, one can thus define a *plasmonic energy functional* Ξ, which is the total surface charge-dipole interaction energy, as :

$$\Xi = \frac{1}{4\pi} \oint_{S\times S} \frac{F^\top + F}{2} \, d\boldsymbol{s} \, d\boldsymbol{s}' \tag{5.37}$$

where the 1/2 factor removes double counting. The minimization of Ξ should lead to appearance of new properties in the system. One can determine the surfaces that minimize Ξ by solving the variational problem: $\delta\Xi|_S = 0$. Since $\boldsymbol{n}$ and q are unitary, the equation is easily solvable and has two solutions: $F^\top = -F$ and $F^\top = F$. The first solution corresponds to a skew-symmetric matrix with pure imaginary eigenvalues and thus can be omitted (since F is quasi-Hermitian with real eigenvalues). The second solution corresponds to any surface S where the interaction energy of a dipole $\boldsymbol{n}(\boldsymbol{r})$ with a charge in $\boldsymbol{r}'$ and the interaction energy of a dipole $\boldsymbol{n}(\boldsymbol{r}')$ with a charge in $\boldsymbol{r}$ *are equal*. Therefore, a dipole $\tau_m \boldsymbol{n}$ interacting with an uniform layer of unitary charges distributed on this surface S will have the same energy as a charge $\sigma_m \delta(\boldsymbol{r})$ interacting with an uniform layer of unitary dipole (orientated by the surface normal) distributed on S. In other terms, this can be written as $\langle \tau_m | F = F | \sigma_m \rangle$, which corresponds to an orthogonal (in opposition to bi-orthogonal) basis. To sum up, the surfaces which respect $\delta\Xi|_S = 0$ are F-symmetric and thus the basis is orthogonal ($\{\sigma_n\} \propto \{\tau_n\}$). The surfaces violating this minimization principle, $\delta\Xi|_S \neq 0$, are not F-symmetric and thus the basis is bi-orthogonal ($\{\sigma_n\} \neq \{\tau_n\}$).

In conclusion, while the time-reversal symmetry controls the Hermiticity of the Hamiltonian, the physical origin of the plasmonic bi-orthogonality is the violation of a variational principle.

5.3.7 Analogy with open quantum systems

This chapter deals with the non-Hermitian properties of LSPs; we will conclude by connecting the present work to analogous effects encountered in other fields of physics. Non-Hermiticity has been observed in a wide range of systems e.g. leaky electromagnetic cavities [343], acoustic cavities [338] or electronic resonators [335], to name a few. Moreover, non-Hermitian effects have also been considered in (propagating) plasmonic systems [326, 337]. However, as emphasized in [333], in these systems the non-Hermiticity is fully driven by the energy dissipation whereas in the case of LSPs, non-Hermiticity arises from purely geometrical reasons, which means that even in an idealized lossless plasmonic resonator, non-Hermiticity could still appear. This unique property marks LSPs as a singular, previously unencountered, type of non-Hermitian system. Although singular, one can retrieve well-known features of non-Hermitian systems in LSP physics, as it is summarized in table 5.1. Indeed, as described in greater details in section 5.3.3, LSP modes constitute canonical examples of quasi-normal modes, thanks to the quasi-Hermiticity of the problem. Therefore, LSPs are analogous to PT-symmetric systems [358], which have been extensively investigated, particularly in optics [359, 351, 341]. Moreover, the skewness of the vector space in LSP problems is measured by the overlap matrix, which is similar to the Petermann factor [360] encountered in open quantum systems. The self-hybridization phenomenon investigated in this paper is a strong manifestation of the LSPs' bi-orthogonality. Several exotic effects arising in non-Hermitian systems such as power oscillations [361] or asymmetric propagation [351] of light in optical systems should therefore have a counterpart in LSPs. More generally, we expect all the features of non-Hermitian physics to appear is LSP systems, particularly the presence of EPs.

5.4 Substrate effect on plasmon resonances in nano-cube

Despite the systematic effort to characterize the widest variety of plasmonic nano-particles, some structures still remain challenging e.g. the nano-cube. In the latest case, the difficulties encountered

Physical quantities	Open quantum cavity	Plasmonics
Time dependence	Dynamic	Static
Kernel	Non-Hermitian Hamiltonian H	Non-symmetric Coulomb kernel F
Eigenvalues	Complex energies ω_m	Real geometrical eigenvalues λ_m
Broken invariance	Time-reversal symmetry of H	F and S spatial symmetry
Constant characterizing the bi-orthogonality	Petermann factor K	Overlap matrix $T_{n,m}$

Table 5.1: *Table summing up the analogous quantities encountered in an open quantum system and a plasmonic system.*

are plural. First, this structure being highly symmetric, plasmonic modes exhibit a significant number of natural degeneracies leading to superposition or hybridization of modes, which dramatically hardens their understanding. Second, cube's plasmonic modes turned out to be very sensitive to the geometry of the underlying nano-structure (e.g. edge rounding [362]) and to be strongly affected by the presence of substrate [363]. Third, particularly because of the degeneracies mentioned above, the coupling between two nanocubes brings unexpected difficulties, which are enhanced when the inter-particle gap goes below 1 nm. Although this coupling has been widely tackled recently, no definitive theory has been given and this question remains controversial [364, 365].

In 2015, we started a collaboration with the team of Xing Yi Ling in NTU Singapore who developed a technique [366, 367] to fabricate metacrystals of chemically grown silver nano-cubes with a tunable configuration (hexagonal, cubic, ...). Contrary to e-beam lithography, their method enables to generate lattices with almost no defect. Moreover, since the cubes are synthesized by chemical means, they display a purer crystaline structure than what can be achieved in lithography, and therefore display better quality factors [368]. Their technique in thus a good candidate to generate optically effective plasmonic metasurfaces.

The initial line of research was to study the cube dimer coupling as it constitutes the building block of such plasmonic metasurfaces. We thus performed series of EELS and CL experiments coupled with BEM simulations on several monomers and dimers of silver nano-cubes. However, to our surprise, we could not conciliate our observations with the results and models found in the literature. Eventually, we identified the discrepancies as being essentially due to the influence of substrate on the SPs, this effect being poorly understood and challenging to implement numerically. We have therefore changed our strategy and studied in depth the substrate influence on the nano-cube's plasmonic spectrum.

The goal of this section is to shortly present our recent efforts towards the understanding of the nano-cube's plasmonic spectrum, with particular emphasis on the substrate effect. Finally, and as a relic from our initial research line, some perspectives in the study of cube dimer coupling will also be presented in section 5.4.6.

5.4.1 Classification of the nanocube's plasmon modes

Before tackling the problem of the effect of the substrate, let's consider the plasmon resonances of a cube embedded in vacuum. The plasmon eigenmodes of such a system have been first investigated by Fuchs in 1975 [40] in the case of phononic excitations (we will come back on this in the next chapter).
Charges tend to localize on the sharpest surface, this is the so-called lightning rod effect. Therefore, on a nano-cube, charges will primarily localize on the corners, then on the edges and finally on the faces. Consequently, as shown on figure 5.13(a), the plasmonic spectrum of a cube can be divided in three families of modes of increasing energy: the corner modes, the edge modes and the face modes. A very similar classification can be found in [363, 212, 369, 24]
Within a family, the modes can be sorted thanks to their symmetry. In the case of the corner modes, three types of LSPs exists:

- The dipolar modes which present two opposite faces oscillating out of phase thus possessing a net dipole moment. Three modes exist depending on the orientation of the moment.

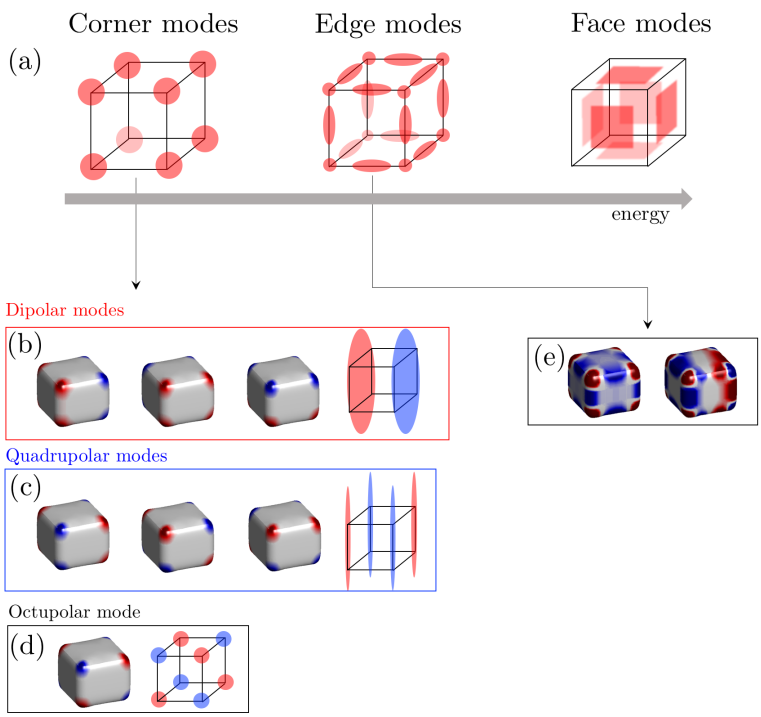

Figure 5.13: *(a) The three families of the nano-cubes plasmon eigenmodes: the corner modes, the edge modes and the face modes. The red shades indicates the localization of the charges. (b-d) Eigencharges associated with the corner modes classified by symmetry: (b) dipolar modes, (c) quadrupolar modes and (d) octupolar mode. The sketches picture the symmetry of the different modes. (e) Examples of edge modes.*

- The quadrupolar modes which present two opposite edges oscillating out of phase while the neighboring ones oscillate in phase. Three modes exist depending on the orientation of the quadrupolar moment.
- The octupolar mode which neighboring corners are oscillating out of phase.

The eigencharges associated with the corner modes are presented on figure 5.13(b-d). The same effort of classification by symmetry could be done for the edge and face modes. However, as we saw in the introductory chapter, the dispersion curve of surface plasmons flattens for large wavevectors and asymptotically converges toward the interface plasmon resonance at ω_S (we will come back on this point in the next chapter in the case of phonons). This translates in a pilling up of high energy modes close to ω_S so that they cannot even be resolved. For this reason, the symmetry of edge and face modes cannot be accessed by EELS; we rather measure a broad edge (or face) plasmon peak corresponding to the incoherent sum of a large number of modes. Since EELS measure the density of states, these peaks are usually stronger than the low energy ones. We will observe this phenomenon on experimental curves in section 5.4.3.

Thus, in vacuum, the plasmonic spectrum of the nano-cube is elegantly determined by the combination of two simple principles:

1. The lightning rod effect which dictates where the charges localize. It is thus responsible for the existence of three families of modes.
2. The symmetry group of the cube which determines the different possible phase symmetries of the modes. It is thus responsible for the fine structure of the spectrum within each family.

If one forgets the first factor and focuses on a particular family, the full spectrum can be deduced from group theory [370]. Although rather elegant, let's emphasize that this plasmonic spectrum is

rather different from what is usually encountered e.g. in triangles, squares, rods, etc. For example, in the cube, there is no such thing as breathing modes [371, 51].

Nevertheless, as we will see in the next section, this simple and elegant scheme completely breaks down in presence of a substrate.

5.4.2 Substrate-induced mode splitting

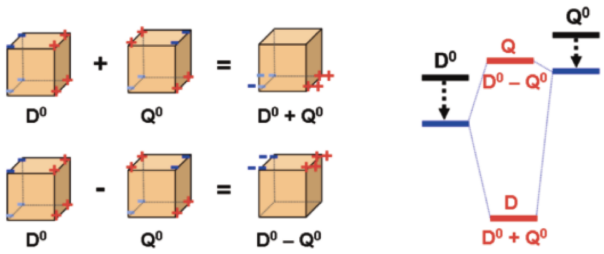

Figure 5.14: *The distal-proximal splitting splitting model of Zhang and collaborators. The distal and proximal modes emerge from the coherent coupling between the dipole and quadrupole modes. Reproduced from [372].*

Indeed, any spectroscopic technique performed in microscopes to probe plasmons requires the sample under study to be placed on some type of substrate. The presence of this substrate has dramatic consequences on the SPs (e.g. energy shifting [363]) that we have to daily deal with. Despite its systematic and dramatic influence in plasmonics, there is no consensus on the physical mechanism involved there. Moreover, the nano-cube suffers from an additional problem when put onto a substrate: its whole spectrum got split in two families of modes with distinct features. The first ones are the *distal* modes, where the charges are localized on the face opposite to the substrate. Symmetrically, the second ones are the *proximal* modes, where the charges are localized on the face onto the substrate. This so-called *distal-proximal splitting* has been widely tacked in the literature and two interpretations on the underlying mechanism emerged:

1. The substrate-Induced Fano resonance [373]. As shown on figure 5.14, it consists in the coherent hybridization of the cube modes mediated by the substrate. It has been proposed in 2011 by Zhang and collaborators in the case of small nano-cubes (< 5 nm).

2. The ultralocal modification of SP properties [363]. It consists in an incoherent and local energy shift of the SPs' energy due to the presence of an inhomogeneous dielectric environment. It has been proposed in 2012 by Mazzucco and collaborators in the case of larger nano-cubes ($\gtrsim 60$ nm) and later confirmed by Nicoletti et al. [212].

These two mechanisms seem to properly reproduce the experimental observations and yet are physically completely incompatible. While the first is a coherent process based on the modal view of SP excitations, the second is a proximity effect constructed around the confined propagating wave nature of plasmons. Moreover, the mechanism suggested Zhang and collaborators requires a strong spectral overlap between the quadrupole and dipole modes. This condition is satisfied for small cubes but it has been shown that when the size of the cube is increased, the two modes become spectrally separated [363].

5.4.3 Experimental and simulated EELS on cube monomer

In order to further disentangle this issue, we first performed systematic EELS experiments on 100 nm silver cubes (with some variations, typically $\pm$ 10 nm) deposited on 15 nm thick silicon nitride Si_3N_4 substrate (see section 2.6 for the exact geometry of the membranes). This substrate has been chosen because it is the most widely used in the literature for his interesting properties (e.g. insulator, weak dielectric constant). Samples were prepared by drop casting solutions of

Ag nanocubes on empty membranes. The experiments have been repeated on several cubes and systematically give the same results.
We present in figure 5.15 the results of our study on a particular nanocube which HAADF image is shown in (a). Due to the symmetry group of the cube, only two electron impact parameters are required to probe the entire plasmonic spectrum: one at the corner and one in the middle of an edges. In figure 5.15, we display the numerical (black line) and experimental (blue line) EELS spectra when the electron impinges (b) at the middle of an edge and (c) at a corner of the cube. In order to reproduce the experimental point spread function due to the width of the ZLP, we convoluted the numerical EELS spectra with a 300 meV Gaussian function and represented the result in red line. The experimental spectra have also been deconvolved using the Richardson-Lucy algorithm (see introductory chapter and [130]). In addition, in figure 5.15(d), we represented the experimental EELS filtered maps integrated on energy ranges indicated by gray shaded windows in figures ((b-c)). In addition, we displayed the numerical charge density maps associated with each peak of the simulations in 5.15(b-c).

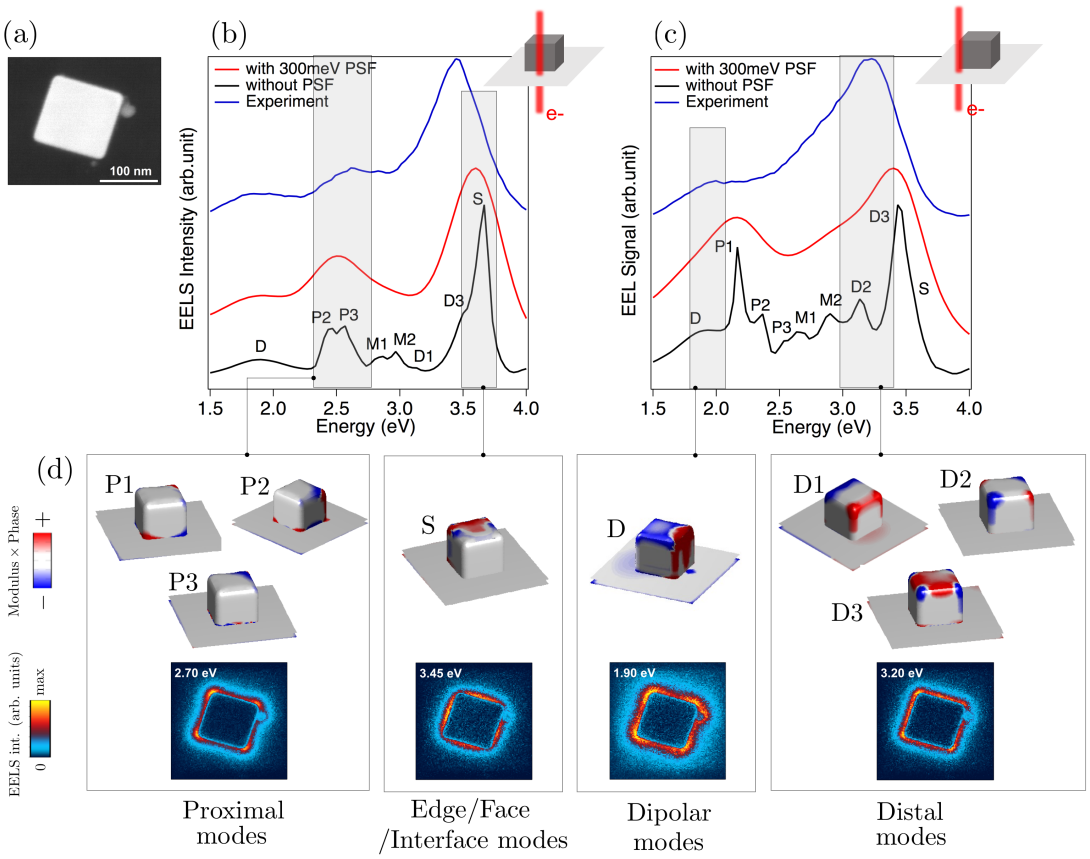

Figure 5.15: *(a) HAADF of a silver nanocube deposited on Si_3N_4 (top view). (b-c) Experimental, simulated and simulated+convoluted EELS spectra of a silver nanocube deposited on Si_3N_4. The insets indicate the impact parameter of the electron beam. (d) BEM simulations of SPs' charge distributions along with their associated experimental energy filtered EELS map. The charge maps are calculated with the impact parameter of (b-c). We indicated on figures (b-c) the energy ranges from which the EELS filtered maps have been extracted.*

First and foremost, let's highlight the remarkable agreement between the convoluted simulations and the experiments. Such a match is, in practice, very hard to obtain due to the large number of experimental and numerical parameters needing to be controlled. From the data, we observe four categories of modes (figure 5.15(b)):

- A dipolar mode D **which has no distal or proximal character**.

- A set of proximal modes $\{P1, P2, P3\}$ constituted of a quadrupolar mode ($P1$), an edge mode ($P2$) and a higher order mode ($P3$).
- A set of distal modes $\{D1, D2, , D3\}$ constituted of a dipolar mode ($D1$), a quadrupolar mode ($D2$) and an edge mode ($D3$). The mode $D1$ is very weak on the simulated EELS spectra although its charge density has a clear dipolar character.
- A certain set of face, edge or interface modes S where the charges are delocalized over the whole particle. Due to the projected view we have in STEM, it is impossible to know if the charges are localized on the edges, the faces or both. The latter situation is the most probable, as mode S must correspond to an incoherent piling-up of face and edge modes at the energy of the interface mode.

Let's emphasize that no proximal dipole mode has been detected. However, since the proximal dipole mode $D1$ is weak and hidden in the tail of the S mode, we expect this hypothetical proximal dipole to be weak and hidden in the tail of D. Interestingly, the proximal and distal modes seem to be gathered within two distinct energy bands. This feature was already observable in the simulations of [212]. However, although using a much more involved technique, they could not retrieve it experimentally. Due to the experimental energy resolution (300 meV), we cannot resolve other modes but from simulation, we know that they exist (e.g. modes $M1$ and $M2$ plus others not specified here). This already illustrates the complexity of the nano-cube plasmonic spectrum. In order to confirm the proximal or distal character of these modes, we repeated the experiment on a cube from the a side view in figure 5.16. Such a configuration has been obtained by breaking the Si_3N_4 membrane after deposition of the nano-particles solution.

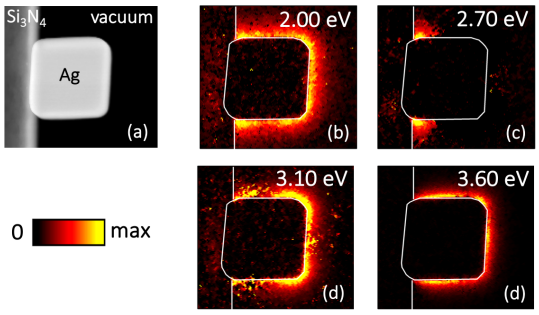

Figure 5.16: *(a) HAADF image showing a silver nano-cube laying on a broken Si_3N_4 membrane (side view). Fitted energy-filtered EELS maps corresponding to (b) mode D, (c) modes $\{P1, P2, P3\}$, (d) modes $\{D1, D2, D3\}$ and (e) mode S.*

Following the same procedure as in section 5.3, the energy-filtered EELS maps have been obtained by fitting the peaks associated with each modes by a Gaussian function. The resulting maps have been de-noised by using an adaptative median filter (see [374] for an introduction and appendix G for the comparison with the raw fitted maps). The resonance energies are slightly different from 5.15 which is not surprising since this cube is not the same as in the other experiment. Some parameters must be different (slight size variation, different substrate thickness) which result in these shifts. Nevertheless, this new experiment indeed confirms our interpretation of the experimental data shown in 5.15 particularly the symmetry of the modes measured.

The most crucial observation is the presence of the *unsplitted* dipole mode D. Interestingly, this mode is present in the literature [212, 363] but not discussed. In [212], Nicoletti and collaborators even describe this mode as "*experimentally [...] broad, spatially diffuse and at low energy*" which exactly matches our observations. Moreover, although the dipole mode D is unsplitted, the distal dipole mode $D1$ and the proximal and distal quadrupole modes $P1$ and $D2$ are detected. These observations indicate that the substrate-Induced Fano resonance mechanism cannot be responsible for the splitting because it would have lead to the disappearance of D (because mixed with the quadrupole mode). It suggests that the splitting mechanism is ultralocal and that modes $P1$,

$D1$ and $D2$ originate from the splitting of several quadrupole modes with different orientations[4]. Then, how to explain that D remains unsplitted despite the presence of substrate?

5.4.4 Distal-proximal formation mechanism

In order to conciliate these results, we propose the following interpretation:

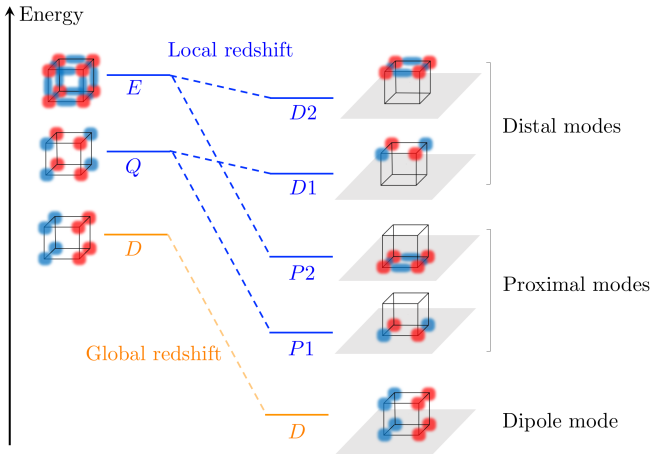

Figure 5.17: *Schematics of the splitting mechanism leading to the formation of distal and proximal modes for a 100 nm silver cube deposited on a Si_3N_4 membrane.*

The quadrupole, edge and higher order modes (Q, E and others not represented here) are splitted by an ultralocal effect. The face of the cube in contact with the substrate sees the dielectric constant of the Si_3N_4 while the upper face is embedded in vacuum. For high order modes, the two faces are uncoupled and have two separated plasmonic spectra. Obviously, the modes of the top face have energy close to the one of the nano-cube in vacuum. The bottom face displays a similar spectra but strongly red-shifted due to the different embedding dielectric constant.

However, the dipole mode is a low energy mode and therefore is coherent over a larger distance than the higher orders ones. At this frequency the two opposite faces are still coupled and the dipole mode undergoes a global red-shift without splitting. Interestingly, even if the effect is incoherent and local, this is the coherence of mode D which prevents its splitting. We are therefore somehow in between the two interpretations presented above. It suggests that when the size of the cube is increased, the coupling between each faces at different frequencies evolves from a completely coherent situation [373] for small cubes to an incoherent one [363] for larger ones. This effect is closely related to the edge mode coupling reported in [347] although in a different situation unrelated to substrate. The domain of validity of each interpretation depends on the nature of the materials involved, the size of the cube, the thickness of the substrate and probably on some minute details of the system (edge rounding, surface roughness, carbon contamination, etc).

This suggested mechanism has the advantage to conciliate the models of [373] and [363], and to explain the presence of the unsplitted dipole as well as the band-like structure of the plasmonic spectrum. Moreover, it suggests that a single parameter rules the mode-splitting mechanism i.e. the *coherence length* of the plasmon modes. We are currently performing calculations in order to corroborate this interpretation.

[4]Indeed, depending on its orientation with respect to the substrate, a splitted quadrupole mode may give rise to distal and proximal dipole or quadrupole modes.

5.4.5 CL experiment on cube monomer

We have also performed extended CL spectroscopy experiments on the same monomers as we studied in EELS. The reason is that the CL emission intensity of the plasmon modes is connected to the strength of their dipole moment, as we saw in the introductory chapter. This enables us to get additional information on the symmetry of the modes.

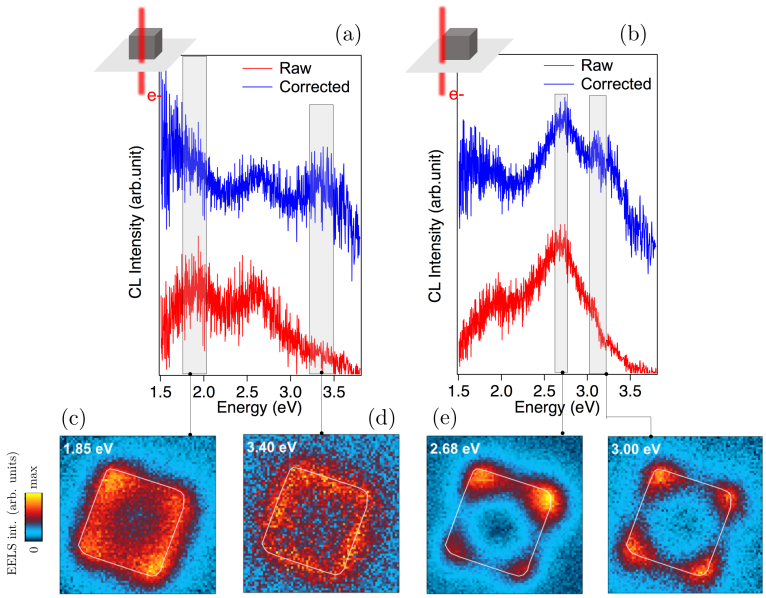

Figure 5.18: *(a-b) Raw and corrected CL spectra measured on the same nano-cube as in figure 5.15. (c-e) Energy filtered CL maps. We indicated on figures (a-b) the energy ranges from which the CL maps have been extracted.*

On figure 5.18, we present CL spectra and maps acquired on the same cube as in figure 5.15. Since we are interested in the difference in intensity between the different plasmon peaks, we need to correct the transmission function of our CL system. Indeed, the different elements of the system (optical fiber, grating, CCD,...) are not equally efficient within the whole spectral range. For the detection of plasmonic excitations, which spans over the whole visible range and beyond, this difference in efficiency can have dramatic consequences. Therefore, we have measured the transmission function of our CL system (see appendix G) using a calibrated commercial lamp and have corrected our CL spectra accordingly. On figure 5.18(a-b) we present the raw (red) and corrected (blue) CL spectra. One can see that some plasmon peaks which were barely present on the raw data, become predominant once the transmission is corrected.

Quite remarkably, the cube present different strong CL emission peaks in contrast with planar structures (triangles, disks,...) of comparable size in which the emission is dominated by a single dipolar peak. Our interpretation is that these different emission lines correspond to different dipoles modes:

- The map 5.18(c) would correspond to the unsplitted dipole D. The energy matches with what as been measured in EELS, besides a slight variation which is expected as we saw in the introductory chapter and [122].
- The map 5.18(e) would correspond to a proximal dipole mode which has not been detected in EELS due to its weak contribution. However, in CL emission, this mode must become predominant due to its large dipole moment. This hypothesis is coherent with the supposed energy of the proximal dipole mode.
- The map 5.18(f) would correspond to a distal dipole mode $D1$. Interestingly, this mode

could not have been detected without the data correction. Here again, the CL emission energy matches the distal peak measured in EELS.

In addition to the energy matching, this interpretation fully justifies why we find exactly three emission lines, one per dipole. The surface mode S is also detected (map (d)) because, as we saw earlier, it corresponds to a large pilling-up of modes contributing incoherently to the signal.

The next logical step would be to simulate the CL experiments in order to corroborate our intuition as we did for EELS. However, contrary to EELS spectroscopy, this is a massive task. Indeed, as we saw in the introductory chapter, the CL emission probability corresponds to the integral of the far-field electric field associated with each modes. To perform this integral, one need to know the shape of the collection mirror as well as the orientation of the cube with respect to it. This has been partially done in [51] but since the authors studied the CL emission from disks, which displays a rotational symmetry, the shape of the mirror had less influence on the measured signal. We have already performed several simulations of CL maps and spectra but no satisfying results came out.

5.4.6 Dimer coupling of silver nano-cubes

The understanding of the substrate-induced mode splitting mechanism enables us to simplify the study of the dimer coupling for large gap separation $g = 5$ nm. We have basically carried the exact same EELS+CL study on the cube dimer as we did with the monomer. Systematic BEM simulations have also been performed. On figure 5.19, we present the experimental and simulated (and convoluted) EELS spectra of the dimer for the different impact parameters: (b) at a middle of edge, (c) at a corner and (d) in the gap. We also present some energy filtered maps in (e).

Contrary to the case of the monomer and for the sake of brevity, we will not detail the full plasmonic spectrum. Indeed, from the simulation we identified 30 different modes and it would be quite tedious to describe them one by one. However, we identified some interesting features. Particularly, and as we saw in section 5.2.4.1, the plasmonic spectrum of this dimer can be understood by applying the LCAO to the monomer spectrum. Quite interestingly, it appears that the dimer modes principally emerge for pure dipole-dipole, distal-distal, proximal-proximal or face-face modes coupling. Mixing between the four families of modes detailed earlier is barely visible. This is consistent with our mode splitting model: for hight order modes, the top and bottom faces of the cubes are uncoupled so that proximal and distal modes are independent. The LCAO scheme can therefore be applied on the top and bottom faces independently.

The consequence is that the first peak corresponds to a dipolar bonding mode as shown on the simulation in figure 5.19(e). This mode is rather interesting as it possesses a huge dipole moment and therefore a potential strong CL emission line in the infrared. Our CL system cannot detect signal in this spectral range but some infrared detectors could be able to measure this emission. Moreover, quite remarkably, this dipole bonding mode seems to be particularly robust to deformation e.g. cube shifting. As shown on figure 5.20, we have performed EELS experiments on several dimers and, even when the cubes are not perfectly aligned, this mode seems to be always present. This property is quite remarkable and could be: (1) a consequence of the large coherence length of this low-energy mode or (2) a property of these so-called flat gap terminations [365]. In any case, this feature is particularly appealing in terms of applications because it means that even a defective metasurface could potentially display coherent collective dipolar modes.

Although the progress in the understanding of the substrate effect efficiently helped us in the study of the dimer coupling of cubes, we are far from having reached a comprehensive picture.

5.4.7 Difficulties and perspectives

Although not entirely presented in this thesis, we performed an extended numerical and experimental study of the plasmonic nanocube and its dimer coupling. It provided us a new insight into the substrate-induced mode splitting which dramatically facilitates the interpretation of the coupling

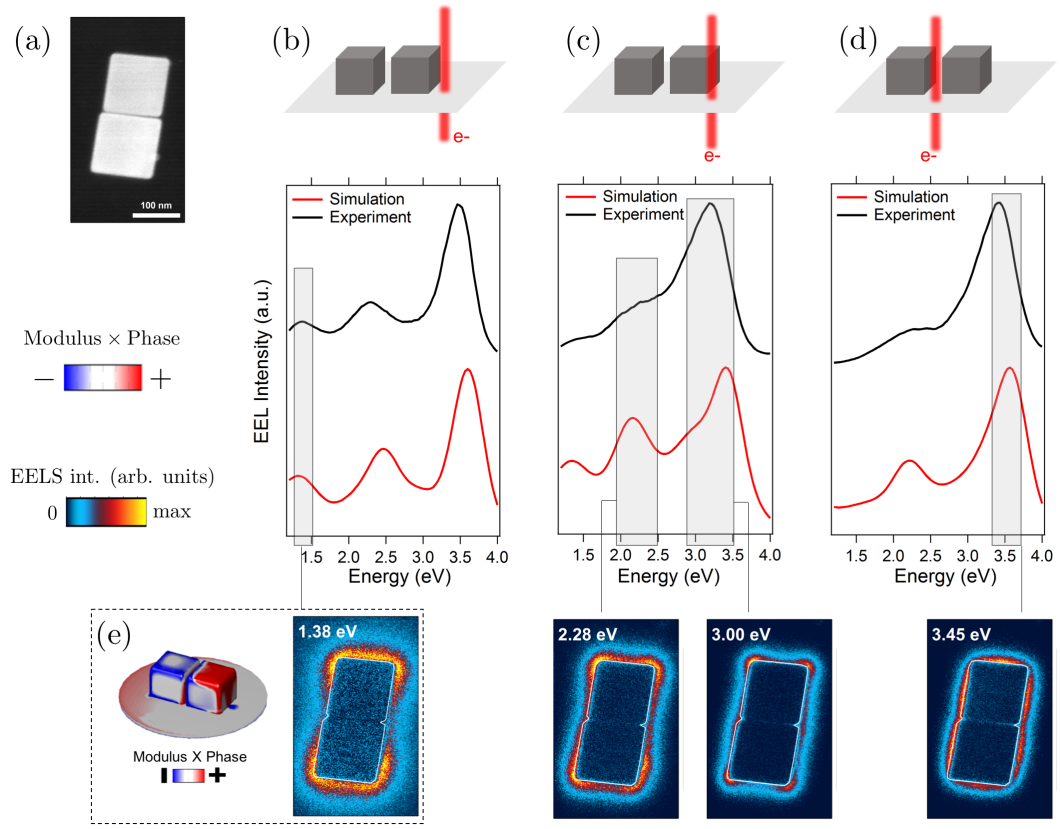

Figure 5.19: *(a) HAADF of a dimer of silver nanocubes deposited on a Si_3N_4 membrane (top view). (b-d) Experimental (black) and simulated convoluted (red) EELS spectra of a dimer of silver nanocubes lying on Si_3N_4. The insets represent the impact parameters of the electron beam. (d) Energy filtered EELS maps of the dimer extracted from regions indicated on figures (b-d). We have moreover calculated the charge distributions associated with the first peak.*

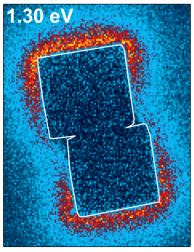

Figure 5.20: *Energy filtered map corresponding to the dipole bonding mode of a shifted dimer.*

experiments. However, and even though it may sounds surprising for such a simple geometry, the nanocube remains a challenging system to model and simulate. Nevertheless, specific issues which particularly limited us these last years may be solved in a near future:

- The lack of spectral resolution in EELS will be overcome by the recent acquisition of a monochromated STEM: the Nion U-Hermes. It will enable us to explore experimentally the fine structure of the cube's plasmonic spectrum and probably resolve the different modes withing the proximal and distal bands. Since our microscope is equipped with a large pole piece, it would even be possible to realize a tomographic reconstruction of the modes.

- The U-Hermes microscope will also be soon equipped with a CL system which will enable us to make a correlative monochromated EELS-CL experiment. In addition, we could also use an infrared CL system in order to investigate the emission of the dipole bonding mode in the dimer.
- Such a large structure as the cube dimer pushes our computational resources to their limit as it requires around 10000 polygons to be simulated. This dramatically hardens the simulations, particularly when a substrate needs to be included. Recently, Hohenester [375] introduced an extension to the `MNPBEM` code which enables us to speed up the calculation by using hierarchical matrices and iterative solvers. We did not test this new code yet but we expect a clear reduction of the computation time as well as an improvement of the number of polygons we can use in our simulations.
- In a recent work [376], we explored an alternative route: employing a mono-atomic layer of hexagonal boron nitride (h-BN) as a substrate for EELS measurement. We experimentally observed that with this h-BN substrate, the plasmonic spectra are almost identical to what they should be in vacuum. This method could enable us to get rid of the substrate problematic and study the dimer coupling of the nanocube in its purest form.

5.5 Probing plasmon-NV^0 coupling at the nanometer scale with photons and fast electrons

So far, we only considered coupling between plasmonic excitations. As detailed in the introductory chapter, another important field of research is the coupling between quantum emitters and surface plasmon as it would open the route toward the coherent control of light emission at the nanoscale [81, 82, 83]. Due to the short lifetime of surface plasmons [54] (typically few femtoseconds), this coupling is usually weak. The hallmark of this regime is the so-called *Purcell effect* corresponding to the shortening of the radiative lifetime of QEs in presence of a plasmon field. More precisely, the transition rate enhancement factor γ is given [26]:

$$\gamma = \frac{\rho(\boldsymbol{r}, \omega)}{\rho_0(\boldsymbol{r}, \omega)} \tag{5.38}$$

ρ and ρ_0 being the LDOS with and without the plasmonic structure. The goal of this section is to show that a combination of electron-based imaging, spectroscopies and photon-based correlation spectroscopy enables the measurement of the Purcell effect with nanometer and nanosecond spatio-temporal resolutions. Determining the Purcell enhancement factor may sounds anecdotal since such a measurement is somehow trivial with nano-optical techniques. However, it is far from being trivial in electron microscopy and it required the amazing efforts of former members of the team to eventually achieve such a coupling. In the perspectives of his thesis [377], Zackaria Mahfoud explored the feasibility of a plasmon-exciton coupling by probing with CL an ensemble of gold nanorods and CdSe-CdS quantum dots. However, he could not find a clear signature of coupling. Moreover, also in the perspectives of her thesis [154], Sophie Meuret presented preliminary results on a coupling experiment realized between a gold triangle and neutral nitrogen-vacancy (NV^0) centers in nanodiamonds probed by STEM-HBT. Although she could only measure one dimer, her results showed interesting features which seem to indicate a possible coupling. Although not conclusive, this experiment laid the foundations of the experiment presented here.

In this section, we probed the coupling between NV^0 centers in nanodiamonds and LSP modes of Ag nanocubes by STEM-HBT. This experiment is the first demonstration of a plasmon-exciton coupling (although weak) probed by fast electrons techniques.

5.5.1 Strategy to measure the Purcell effect at the nanoscale

If one wants to probe a Purcell enhancement, both the lifetime with and without the plasmon field needs to be measured. To date, only two strategies have been considered to measure the Purcell effect in QE-SP dimers:

- A macroscopic lifetime measurement is performed simultaneously on a large ensemble of particles [378, 379]. By comparing the average lifetime of samples containing or not plasmonic resonators, one can estimate the average Purcell factor. However, this method do not give any information of the exact configuration of the dimer in the sample.
- One can otherwize carry out the experiment on a single dimer [380, 381, 382] with a precise positioning of the QE. A remarkable fluorescence lifetime imaging microscopy experiment has been demonstrated by Beams and collaborators [383] who brought a plasmon pyramidal resonator close to a NV center with an AFM tip. As shown on figure 5.21, it enabled them to measure the Purcell enhancement in this system.

Both approaches present limitations due to the *large variability of the isolated QEs' lifetimes* [384, 385, 386, 387].

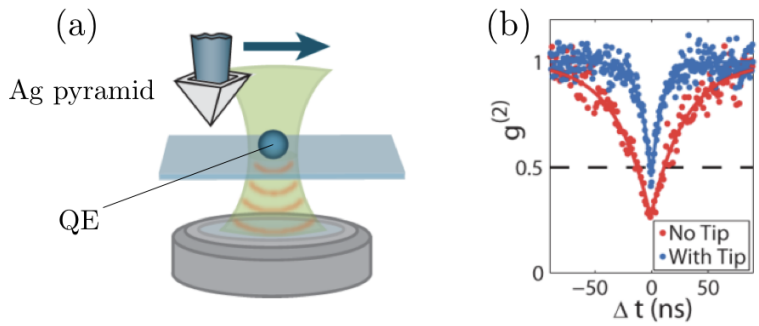

Figure 5.21: *(a) Schematics showing the principle of fluorescence lifetime imaging microscopy. An Ag pyramid is approached to a nano-diamond containing NV-centers. The fluorescence lifetime is acquired in parallel. (b) Correlation functions of the center with and without the pyramid showing a typical Purcell enhancement. Reproduced from [383].*

Here, to overcome this intrinsic variability we adopt a *statistical method* applied to individual nano-objects, where the lifetimes of large sets of isolated QEs and dimers are measured. To quantify the Purcell effect at the nanoscale we applied a combination of ADF imaging, EELS, CL spectroscopy and STEM-HBT interferometry as:

- Annular dark field images allows us to determine the position of the QE with respect to the plasmonic resonator with a nanometer resolution, giving us all the parameters necessary to estimate the expected enhancement factor.
- EELS and CL respectively enable us to determine the *absorption spectrum* of the plasmon and the *emission spectrum* of the QE. The measurement of these two quantities allows us to match of the resonances energy of the two systems [11, 137, 119, 73].
- Lifetimes can be inferred from the second order correlation function ($g^{(2)}(\tau)$) of the light emitted from the QE through a STEM-HBT measurement[5] (see section 2.4 or [155, 68, 389, 390] for the experimental details).

5.5.2 Choice of the SP-QE system

The figure 5.22(a) shows a typical EEL spectrum for an isolated Ag nanocube and a CL spectrum for an isolated nanodiamond containing NV^0 centers. The EEL spectrum presents three peaks corresponding to different plasmon modes. The peak at 1.8 eV with a 500 meV width matches the energy range of the NV^0 emission, indicating the possibility of coupling between SPs and the NV^0 centers. We note that the SPs' spatial intensity distribution is highly anisotropic, as seen in

[5]Note that lifetimes can also be measured using a pulsed electron source and a cathodoluminescence setup, but with limited spatial resolution (50 nm) up to now [388].

figure 5.22(b-c) for the mode at 1.8 eV. In principle, this could play a role on the choice of the nanodiamond's positioning. As discussed later, this does not play a major role due to the large spatial extent of SP modes.

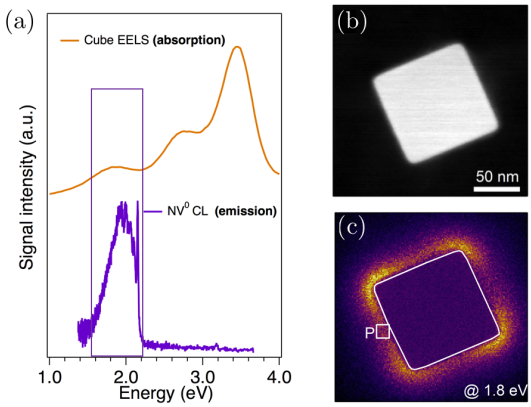

Figure 5.22: *(a) EELS spectrum (absorption) of an Ag nanocube measured in region P indicated in (c). Each peak corresponds to a plasmon resonance. The purple rectangle indicates the energy window where the optical filter is active. (b) ADF image of an Ag nanocube. (c) Energy filtered (at 1.8 eV) EELS map of the silver nanocube showed in (c). Scale bar: 50 nm.*

For these reasons, we decided to choose this system to quantify the Purcell effect. Of course, it does not correspond to an ideal system as we could have:

- Chosen a system with fewer color centers in order to isolate the contribution of a single quantum emitter.
- Engineered the geometry of the plasmon resonator to create an intense hot spot in resonance with the emission.

Nevertheless for a proof of principle of our experimental approach, it perfectly fulfills the criteria.

5.5.3 Variability of NV^0 center excited state lifetime

Samples were prepared by sequentially drop casting solutions of Ag nanocubes and nanodiamonds containing multiple NV^0 centers onto a 15 nm thick Si_3N_4 membrane. Nanodiamonds typically appear as aggregates (figure 5.22(a)). However, among these aggregates a larger and luminescent nanoparticle is always observed, which is the one considered in each measurement. Most of the nanodiamonds tend to be adsorbed on the nanocubes faces. Moreover, a distribution of sizes is observed in our nanocubes sample (100 nm average size with some variation). This influences the energy of a specific SP. But as a continuum of SP modes is observed for each given nanocube and since the NV^0 emission line is spectrally wide, a coupling is always possible. Isolated nanodiamonds and dimers were identified using ADF images that are acquired simultaneously with wavelength-filtered CL maps (first and second columns in figure 5.23). A quick access to this information allows an effortless identification. After a target isolated nanodiamond or dimer is selected, the $g^{(2)}(\tau)$ function of the emitted photons is measured using the HBT interferometer while the electron beam scans a fixed small area on the nanodiamond. The photon counting rate and the ADF image can be recorded live, allowing sample drift to be corrected by repositioning the scanning area. In total, the lifetime of 56 isolated nanodiamonds and 62 dimers were measured in the same sample in a single experimental run, ensuring identical experimental conditions.
Examples of measurements in two isolated nanodiamonds and two dimers are shown in figure 5.23(a-b) and figure 5.23(c-d), respectively. The isolated nanodiamond in figure 5.23(a) and the dimer in 5.23(d) have a lifetime of 36 ± 5 ns and $\tau = 11 \pm 1$ ns, respectively, in agreement with an enhancement effect. However, isolated nanodiamonds and dimers (figure 5.23(b-c)) with similar

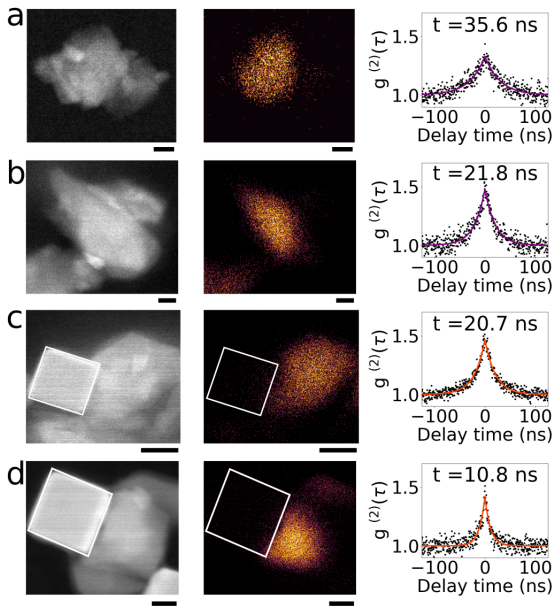

Figure 5.23: *(a-b) From left to right: ADF image, energy-filtered NV0 emission intensity image and $g^{(2)}$ correlation function of single nanodiamonds. (c-d) From left to right: ADF image, energy filtered CL maps (see figure 5.22) and $g^{(2)}$ correlation function of nanodiamonds close to a silver nanocube. Scale bars: 50 nm.*

lifetimes are also present ($\tau = 22 \pm 2$ ns and $\tau = 21 \pm 1$ ns in these examples). Such observations occur due to the large dispersion in NV^0 lifetimes in nanodiamonds, as already reported in the literature [385, 391, 392]. The lifetime for NV^0 in bulk diamond is 19 ns [393] and is distributed between 10 and 40 ns [385] in nanodiamond. A similar behavior is known for the NV$^-$ (charged NV) center, for which the lifetime changes from 13 ns in bulk [394] to larger values (17 ns and 25 ns) in nanoparticles [391, 392], with a broad distribution [395]. This excited state lifetime increase is the result of the smaller LDOS in nanoparticle than in bulk (i.e. $\gamma < 1$, as predicted in the quasistatic regime i.e. for a particle size smaller than the vacuum emission wavelength of the embedded emitter), while the lifetime dispersion is mainly due to the nanoparticle size variability [396].

5.5.4 Statistical approach to STEM-HBT

To overcome this variability, a measurement of the Purcell effect can be performed by sequentially probing the NV^0 lifetime of an isolated nanodiamond, followed by coupling the nanodiamond to a plasmonic structure (either by mechanical movement or lithography), as shown by Beams *et al* [383]. However, this approach would normally involves taking the sample out of vacuum and performing a series of processes which can modify its local environment and, hence, its lifetime. Here, we rather overcome the variability by measuring the excited state lifetime in a large ensembles of either isolated nanodiamonds or dimers.
The histograms (top) and a scattered plot (bottom) of the lifetime of isolated nanodiamonds (purple) and dimers (orange) are shown in figure 5.24. The average lifetimes of isolated nanodiamonds and dimers are 24 ± 5 ns and 18 ± 4 ns (the most probable values are 22.5 ± 2.5 ns and 12.5 ± 2.5 ns). The two distributions overlap. However, they are significantly distinct, as confirmed by the Wilcoxon-Mann-Whitney statistical u-test ($p = 1.91 \times 10^{-6}$). Therefore, the 40% reduction of lifetime can be unambiguously associated to a Purcell effect with a spontaneous decay rate enhancement factor of 1.4, indicating some coupling, although weak, between NV^0 centers in nanodiamonds and SPs in Ag nanocubes.

Lifetimes shorter than the bulk value are observed in both histograms, although with a small

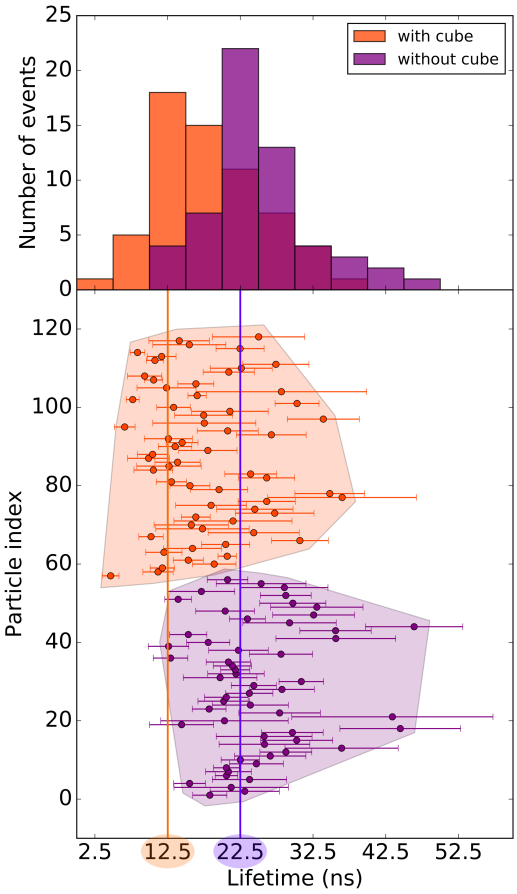

Figure 5.24: *Distribution of single nanodiamonds' lifetime (purple) and close to a silver nanocube (orange) measured on a population of 118 diamonds. The two vertical lines indicate the maxima of the nanodiamonds' lifetime distribution alone (22.5±2.5 ns in purple) and close to a silver nanocube (12.5±2.5 ns in orange).*

probability. These occur due to non-radiative decay channels involving e.g. surface defects. Overall, the coupling leads to a rigid shift of NV^0 lifetime histogram to shorter values. These features are only accessible with a statistical approach which emphasizes the strength of our experimental method.

5.5.5 Numerical verification

As recently pointed out [397], the calculation of the luminescence enhancement of defects in presence of a plasmonic field is an intricate problem. A quantitative simulation of our experiment would require the precise knowledge of a large set of parameters: the shape of the nanodiamonds, the exact number of defects, their position in the nanoparticle, their respective lifetime or the profile of the plasmonic field within the nanodiamond. Although we do not tackle this problem in the current paper, we have performed numerical calculations to verify that the order of magnitude of the expected effect matches our observations. A key point for these calculations is the presence of numerous NV^{0}s in our nanodiamonds. In principle, the NV^0 lifetime may vary with the position of the emitter within a nanoparticle for subwavelength-sized nanodiamonds (electrostatic regime) but experimentlly we have observed that it is constant throughout the nanodiamond, as pointed out by Greffet *et al*[396]. No variation within the same nanodiamond was observed, despite the nanometer spatial resolution provided by our experiments. Even if electron-hole diffusion in the

nanodiamond could decrease our expected spatial resolution (as it is known to occur [398]), variations of NV^{0}s lifetimes could be observed if they occurred in scales larger than 50 nm.

The expected radiative rate enhancement factor due to the Purcell effect was calculated by considering an isolated Ag nanocube, taken the Si_3N_4 substrate into account. Calculations performed with the `MNPBEM` toolbox [248] show a SP mode centered at 2.1 eV, in agreement with the experimental value (figure 5.22(a)). Considering that most nanodiamonds were observed on a facet of the nanocubes, we calculated the LDOS enhancement factor at 2.1 eV along a line centered on a nanocube's face and perpendicular to it, for an emitter at a distances between 10 to 100 nm from the nanocube surface (arrow on figure 5.25).

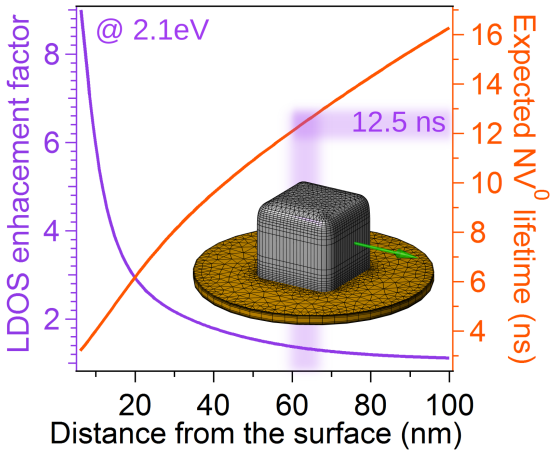

Figure 5.25: *(Purple) LDOS enhancement factor γ due to SPs sustained by an Ag cube, at 2.1 eV calculated along the green arrow represented on the inset. (Orange) Corresponding expected NV^0 lifetime. When the LDOS enhancement factor is equal to one, the lifetime is assumed to 22.5 ns (as measured in figure 5.24).*

The enhancement factor is plotted on figure 5.25 (purple). Taking into account that the most probable lifetime for NV^{0}s in isolated nanodiamonds is 22.5 ns, we plotted in orange the expected NV^0 lifetime given the calculated enhancement factor. We see that the most probable lifetime measured in presence of a nanocube (12.5 ns) corresponds to a distance of 65 nm, also associated to the enhancement factor 1.4. This value is in qualitative agreement with the possible distance of a NV^0 center to the surface of a 100-200 nm nanodiamond (these sizes are typically observed in our sample). Although this result relies on the specific positioning of the emitters in the dimer, obtaining a consistent distance value is a strong evidence to support our conclusion.

5.5.6 Conclusion and perspectives

We have used a combination of fast electron/photon techniques to quantify the Purcell effect resulting from the coupling of dipolar emitters embedded in nanoparticles to plasmonic structures. NV^0 in nanodiamond-SP coupling is evidenced by the reduction of the mean excited state lifetime of a distribution of individual isolated nanodiamonds and dimers. This effect could have been masked if we had limited our study to few objects because of the instrinsic lifetime dispersion. We have shown that a combination of fast electron/photon techniques provide the required measurement throughput, spatial and temporal resolutions to disentangle the two effects. The ensemble of techniques described here can be applied seamlessly to any emitter with excited state lifetime in the 0.5 ns - 50 ns range which emits light under electron irradiation, covering a wide range of nanoscale systems.

5.6 Summary and perspectives

Summary of the main results

In this chapter, we employed conventional EELS and CL to explore experimentally, numerically and theoretically, different aspects of the surface plasmon coupling physics.

In section 5.2, we have demonstrated that, by morphing a metallic nanorod into a nanocross (i.e. by growing a second arm along the perpendicular bisector of the first arm), one can selectively tune the resonance energy of any mode. Quite counter-intuitively, this principle has been used to bring higher order modes to lower energy than low order ones, with promising applications in the generation of high quality factor plasmonic resonators. We also showed that when a dimer of crosses is formed, the individual monomer modes hybridize and give an even much better tunability of the plasmons' resonance energies.

Ouyang and Isaacson have shown that the plasmon modes are the solutions of an eigenvalue problem [9], which kernel, depending on the geometry of the nano-particle, can be non-Hermitian; the solutions then form a bi-orthogonal basis in which left and right eigenvectors are different. In section 5.3, we demonstrated that, far from being a simple mathematical curiosity, plasmonic bi-orthognality has dramatic physical consequences. Relying on the perturbation theory introduced by Trügler et al [317, 41], we have shown that this bi-orthogonality can trigger the interaction between different plasmon modes within a single particle. Moreover, we related the splitting energy of this self-hybridization phenomenon to the overlap matrix of the system. This way, we demonstrated that the measurement of the coupling energy enables a direct measurement of the degree of bi-orthogonality of the plasmonic system. We unambiguously determined the role of the particle's symmetries in the apparition of bi-orthogonality and designed a model system (dagger) in which the non-Hermiticity is expected to strongly express. Using EELS and e-beam lithography, we numerically and experimentally realized a self-hybridization in this dagger system with a strong experimental coupling energy ($\Omega \approx$100 meV). This way, we demonstrated that LSPs could constitute an interesting and simple platform for testing non-Hermitian physics.

In section 5.4, using combined EELS and CL spectroscopies, we investigated the plasmon resonances of silver nano-cubes. Particularly, we tackled the problem of the substrate effect on the plasmon resonances, what is a long-term ongoing problem in the community. We showed that the distal-proximal splitting is mainly an ultralocal phenomenon for large cube. While all the modes display a distal-proximal character, we showed that the dipole mode is unaffected by the presence of the substrate due to its large coherence length.

Finally, in section 5.5, we have shown that the Purcell enhancement factor can be precisely measured at the nano-scale by a combination of EELS and CL-HBT measurements assisted by a statistical analysis. By investigating the lifetime of NV^0 centers excited states in nanodiamonds coupled to LSP modes of Ag nanocubes, we unambiguously demonstrated the first realization of a plasmon-exciton coupling (although weaks) probed by fast electrons.

In this chapter, we investigated different problems of the surface plasmon coupling physics. Different avenues remain to be explored:

- The work of section 5.2 could be applied to design plasmon modes with high quality factors and low energy with potential application e.g. in sensing or surface enhanced scattering.

- We are currently working on the non-Hermitian problem introduced in section 5.3. Our objective is to formally identify the presence (or the absence) of exceptional points in this localized surface plasmon eigenproblem. Greater details will be given in the perspective chapter 7.

- The work presented in section 5.4 still needs further experimental and numerical confirmations. As described in the end of this section, we have several short term plans in order to overcome the difficulties we highlighted. Particularly, the recent acquisition of a monochromated STEM together with the new features of the `MNPBEM` toolbox will undoubtedly help us to experimentally and numerically explore the fine plasmonic spectrum of the cube.
- The statistical scheme we presented in section 5.5 could perfectly be automatized. Moreover, we are currently trying to go to the strong coupling regime and maybe probe the lifetime of hybrid excitations.

Chapter 6

Vibrational surface EELS probes confined phonon modes

Contents

6.1 Introduction **159**
6.2 Recent advances in vibrational EELS **160**
6.3 History of the local continuum dielectric model **160**
6.4 Definition of the confined surface phonons **162**
6.4.1 Quasistatic modal decomposition 162
6.4.2 Pedagogical example: the nanorod 163
6.4.3 Analogy between localized SP and cSPh modes 164
6.5 Connection with optical quantities **164**
6.5.1 Validity of the quasistatic approximation 164
6.5.2 Comparison with optical experiments, EMLDOS 165
6.6 General properties of confined surface phonon modes **166**
6.7 Review and interpretation of the experimental results found in the literature **167**
6.7.1 Fuchs-Kliewer modes of thin material slabs 167
6.7.2 Confined phonon modes of MgO nanocube 168
6.8 Substrate effect **169**
6.9 Summary and perspectives **170**

6.1 Introduction

In the introductory chapter, we showed that a low-loss EELS experiment can be modeled with the so-called *local continuum dielectric model* (LCDM, [399]). The basic assumption behind this model is that the dependence in the transferred momentum $\boldsymbol{q}$ can be neglected in the dielectric function of the material i.e. $\epsilon(\omega) \equiv \epsilon(\boldsymbol{q} \to 0, \omega)$. Physically, this model consists in considering that excitations in the material are local which however does not prevent any spatial dependence. This assumption is valid in the long wavelength regime so that it can be applied to e.g. surface plasmon excitations as we did in chapters 4 and 5. As we saw in chapter 3, some situations require to include non-local terms so that the LCDM fails to properly describe the experimental results. This is typically the case for bulk excitations such as bulk phonons [24, 400, 401, 402].
In 1965, Fuchs and Kliewer first developed a dielectric theory [25], based on the LCDM, modeling the phononic excitations in an ionic crystal slab. Later, Ibach was able to experimentally probe the surface phonon modes of a Zn0 crystal using HREELS, which, roughly speaking, corresponds to EELS without spatial resolution and with slow electrons. He found a good agreement between

its experimental value of the phonon resonance energy and what was foreseen by the LCDM. Besides, the development of transmission electron microscopes and electron-energy loss spectrometers enabled the measurement of excitations in materials with nanometric resolution. Due to the lack of spectral resolution of TEM at the time, low energy excitations such as phonons (tens of meV) could not be measured at the nanoscale. Instead, the field of plasmonics, which energy range (few eV) was experimentally accessible, encountered a great success and contributed to the further developments of LCDM-based dielectric theories.

Almost fifty years after the seminal publication of Fuchs and Kliewer, thanks to development of electron monochromators, we are now able to probe phononic excitations at the nanoscale, leading to the emergence of a new and quickly growing field of research: the *vibrational EELS*. Surprisingly enough, the early developments of Fuchs and Kliewer have somehow fallen into disuse and recent publications or conference presentations seem to be vitiated by a manifest confusion concerning the nature of the phononic excitations.

In this chapter and in [403], we decided to fill the gap in the literature and rationalize all the experimental results to the light of the plasmonic formalism. Thanks to numerical calculations, we demonstrate that all these experiments can be understood on a common ground to the price of introducing the concept of confined surface phonon modes (cSPh), the phononic counterpart of LSP modes.

6.2 Recent advances in vibrational EELS

Recently, two reports [23, 24] have demonstrated the amazing possibility to probe vibrational excitations from nanoparticles with a spatial resolution much smaller than the corresponding free-space phonon wavelength using electron energy loss spectroscopy. Krivanek et al. [23] probed the phonon excitations of thin films made of various materials (such as h-BN or SiC) and observed no spatial modulation of the EELS signal. In 2017, Lagos and collaborators mapped the phononic excitations in a MgO nanocube [24] thus reproducing the experiment theoretically explored by Fuchs in 1975 [40].
As foreseen by Fuchs, Lagos et al. observed a strong spatial and spectral modulation of the EELS signal over the nanocube, see figure 6.1. The energy-filtered maps 6.1(b-c) strongly resemble the plasmon modes of a nano-cube [212] which already suggest a formal proximity between the two systems. In section 6.7, we will show that one can easily identify these modes by using a phononic form of the Ouyang and Isaacson formalism [9].

6.3 History of the local continuum dielectric model

In a pioneering work, Ibach [404] used HREELS to analyse the vibrational excitations of a ZnO surface. He could retrieve the measured value of the surface phonons energy ω_s within what was later called the local continuum dielectric model (LCDM) [399]. This simple and powerful model relies on the assumption that the local dielectric constant $\epsilon(\omega) = \epsilon(\omega, q = 0)$ (where ω is the energy and $\epsilon(\omega)$ is equal to its value at zero transferred momentum q) is sufficient to describe electromagnetic excitations in a finite system. In Ibach's simple geometry, ω_s was such that $\epsilon(\omega_s) = -1$. Fuchs and Kliewer demonstrated the amazing efficiency of the LCDM to describe more complicated geometries, such as slabs [25] and infinite cylinders [405]. Already in these simple systems, the electromagnetic coupling between surfaces induces surface phonons splitting in so-called Fuchs-Kliewer (FK) modes with different charge distribution symmetries (figure 6.2(a)). Most materials' dielectric constants can be described in the optical phononic range with a Drude-Lorentz model, thus requiring the sole knowledge of the longitudinal and transverse optical phonon energies (ω_{LO} and ω_{TO}) and the value of the dielectric constant at large energy values (ϵ_∞) of the bulk material:

$$\epsilon(\omega) = \epsilon_\infty \left(1 + \frac{\omega_{LO}^2 - \omega_{TO}^2}{\omega_{TO}^2 - \omega^2 + i\omega\Gamma}\right) \tag{6.1}$$

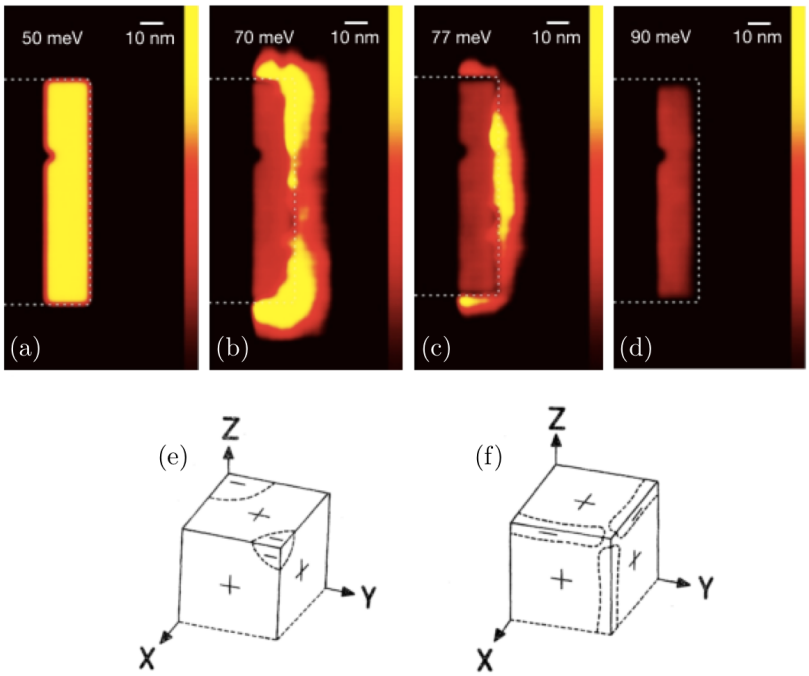

Figure 6.1: *Energy-filtered EELS maps of an MgO nano-cube corresponding to (a) the transverse optical bulk phonon mode, (b) corner-like phonon modes, (c) edge-like phonon modes and (d) the longitudinal optical bulk phonon mode. Reproduced from [24]. (e-f) Charge distributions of two phonon modes of a MgO cube calculated by Fuchs in 1975. Reproduced from [40].*

One sees in figure 6.2(a) that surface phonon (SPh) modes disperse as a function of the transferred wave-vector from ω_{TO} or ω_{LO} and converge to ω_s at large transferred wavevector. The Fuchs-Kliewer work has been extended with an impressive success [399] to the description of surface plasmons in simple systems such as slabs and cylinders [405, 406] (see figure 6.2(b). As already described in [405], a practical reason for this success is the close resemblance between the dielectric constants of systems encompassing either optical phonons or plasmons. Given similar electromagnetic boundary conditions, it is no surprise that similar physics is involved; in particular, surface waves, either SP or SPh can be regarded as surface charge densities waves. However, such a resemblance is valid in a long-wavelength limit - precisely that of the LDCM. Of course, beyond the LDCM, which will not be evoked hereafter, the microscopic origin of the surface charge density waves is rather different at the atomic scale between SPs (free electron charges) and SPhs (ions vibrations).

Stimulated by the development of the research on plasmons in nanoparticles systems, several simulation schemes basically relying on the LCDM (BEM [407, 170, 408] and DDA [409]) have been extensively used to simulate optical and EELS spectra dominated by localized SPs *confined* on nanoparticles. BEM simulations have been recently extended to the phonon range for STEM-EELS [24] using the MNPBEM [410] implementation. Now, beyond their unique simulation capabilities, LCDM derived theories have offered a deep understanding of localized SP physics. In particular, they made explicit the link between STEM-EELS and optical near-field spectroscopies as both are related to the electromagnetic local density of states (EMLDOS) [411, 10], and showed that EELS is related to the extinction cross-section for dipolar modes [119, 120].

The goal of this chapter is to show how the reasoning once made to explain SPs' confinement in nanoparticles and interpret STEM-EELS experiments can now be used to rationalize the interpretation of surface STEM-EELS vibrational experiments in nano-objects and predict new physical effects.

6.4 Definition of the confined surface phonons

In the following, we will introduce the confined surface phonon (cSPh) modes as surface phonons whose properties are mostly defined by the classical confinement that they experience in particles much smaller than the free-space equivalent wavelength. In this sense, if normal phonon modes are conceptually related to bulk plasmon modes and surface phonons to surface plasmons, cSPhs are the phononic counterpart to localized SPs.

6.4.1 Quasistatic modal decomposition

For the sake of simplicity we will neglect retardation in the following, otherwise specified. As we will show, this is justified by the relatively small sizes of phononic nanoparticles studied in the literature [23, 24].

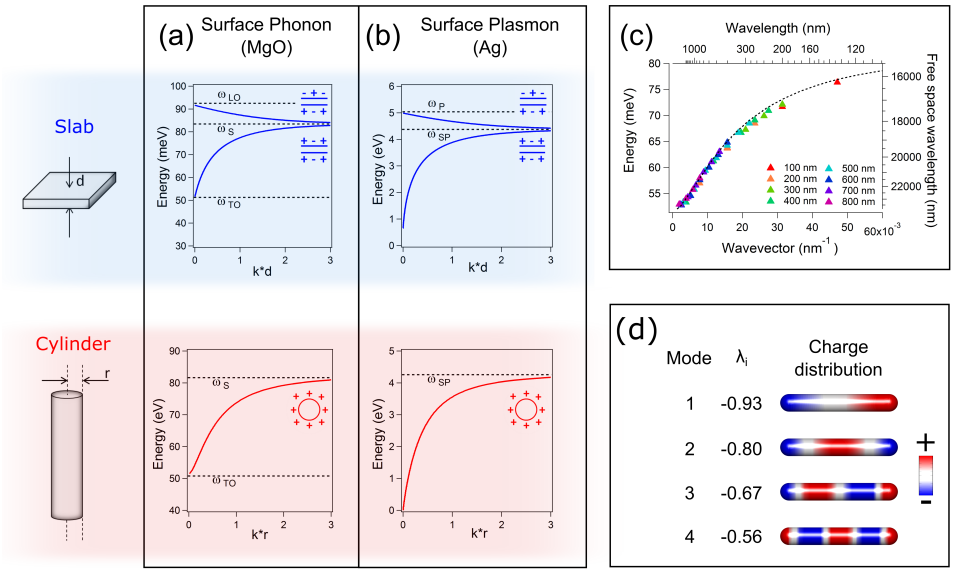

Figure 6.2: *Analogy between Fuchs-Kliewer modes and surface plasmon modes. (a) Dispersion relation of the Fuchs-Kliewer modes for a slab of thickness d (top) and a cylinder (bottom) of radius r made up of MgO. The charge symmetry of the modes is sketched in inset. For the cylinder, only the rotationally invariant modes branch is shown, as the other modes are essentially not dispersing [412]. Calculation have been performed in the quasi-static approximation. (b) Same for SP modes in silver. (c) Dispersion relation for the cSPhs of nanorods, reconstructed from a series of retarded simulation of nanorods of different lengths (the diameter is 30 nm). The dotted line is the quasi-static dispersion relation for an infinite cylinder of same diameter, showing the remarkable agreement between both approximations even for long lengths of rods. (d) Surface eigencharge distributions for the cSPh modes of a nanorod, with the given mode orders and eigenvalues λ_i.*

As we saw in chapter 5, a rigorous definition of the cSPh modes can then be given in the quasi-static approximation using a modal decomposition form, first introduced in the case of confined SPs by Ouyang and Isaacson [9, 407, 10]. Like localized surface plasmons, cSPhs are then defined as a set of eigencharges σ_i and eigenvalues λ_i, i being the mode index. In the general case, λ_i, which depends only on the geometry of the nanoparticle, has to be determined numerically, and the corresponding eigenenergies can be deduced through a simple implicit relation between λ_i and the energy dependent dielectric constant. In the case of the Drude-Lorentz model (6.1) and using equation (5.3), a general expression for the cSPh eigenergies is:

$$\boxed{\omega_i = \sqrt{\frac{\epsilon_\infty \omega_{LO}^2(\lambda_i+1) - \omega_{TO}^2(\lambda_i-1)}{\epsilon_\infty(\lambda_i+1) - (\lambda_i-1)}}} \tag{6.2}$$

cSPh energies lie between the bulk LO and TO energies, as $-1 < \lambda_i < 1$ [9]; we also directly see that the energy of two well-known FK modes for an infinitely thin slab, describing the charge-antisymmetric and -symmetric modes (see figure 6.2(a)), are retrieved for $\lambda_i = \pm 1$. In addition, other simple cases can be straightforwardly deduced. $\lambda_i = 0$ corresponds to the above-mentioned surface phonon [404] case ($\epsilon = -1$) with eigenenergy:

$$\omega_s = \sqrt{\frac{\epsilon_\infty \omega_{LO}^2 + \omega_{TO}^2}{\epsilon_\infty + 1}} \tag{6.3}$$

in a Drude-Lorentz model and $\lambda_i = -1/3$ [412] corresponds to the dipolar mode of a sphere ($\epsilon = -2$) with eigenenergies:

$$\omega_i = \sqrt{\frac{\epsilon_\infty \omega_{LO}^2 + 2\omega_{TO}^2}{\epsilon_\infty + 2}} \tag{6.4}$$

6.4.2 Pedagogical example: the nanorod

To exemplify the interest of this approach, we start with the case of nanorods that has been widely investigated in surface plasmon physics [413], and especially by EELS [414, 211]. The simplicity of the structure makes it easy to understand the intimate link between shape and modal structure, and we adapt it here to the case of a phononic material following arguments for localized SPs found in [412].

Modes in a nanorod of radius r and length L are similar to the SPh modes of the infinite rod, except that the confinement restricts the available wavevectors to multiple of $1/2L$. This is exemplified in figure 6.2(c) where the discrete modes dispersion relation, simulated for a large set of nanorods lengths, overlaps the one of an infinite rod. Such modes are the cSPh modes of the nanorod. The cSPh modes disperse between ω_{TO} and ω_s, in analogy with the corresponding dispersion for localized SPs in nanorods restricted between 0 and ω_{sp} [412]. Similarly to the corresponding localized SP modes, each mode with eigenvalue λ_i corresponds to an oscillation of the surface eigencharge, as depicted in figure 6.2(d). Despite the simulations have been performed in a retarded approximation, the nanorods energies follow quite closely the quasi-static dispersion relation (dotted line). This is a strong evidence that in the prototypical case of a nanorod, the QS approximation is much more justified for cSPhs than for LSPs for objects of same sizes. Indeed, the length (top scale in figure 6.2(c)) of a typical nanorod is much smaller than the equivalent free-space wavelength of the cSPhs (right scale in figure 6.2(c)). Another difference with SPs is the pile up of low order modes for long nano-antennas close to ω_{TO} which is obviously absent for localized surface plasmons.

	Mode 1 $\lambda_i = -0.93$ ω_1 (meV)	Mode 2 $\lambda_i = -0.8$ ω_2 (meV)	Mode 3 $\lambda_i = -0.67$ ω_3 (meV)	Mode 4 $\lambda_i = -0.56$ ω_4 (meV)	Surface $\lambda_i = 0$ ω_s (meV)
from eq. (6.2)	56.0	63.4	68.7	72.3	83.1
Simulations (figure 6.2(d))	56.8	63.6	68.6	72.0	82.9

Table 6.1: *Comparison between energies values for the nanoantenna in figure 6.2(d) calculated with equation (6.2) and as extracted from the simulated spectra in figure 6.3. Inputs for equation (6.2) are $\omega_{TO} = 50.7 meV$, $\omega_{LO} = 91.3\ meV$, $\epsilon_\infty = 3.01$ [415]. Simulations have been performed in the full retarded approximation, with the experimental dielectric constant found in [415].*

Figure 6.3(a) presents one EELS spectrum simulated for a beam impinging 10 nm away from one tip of a MgO rod of 200 nm long and 30 nm in diameter. The simulations, performed in the full retarded approximation and using an experimental dielectric constant as an input [415], reveal a series of peaks. As seen on table 6.1, a direct comparison of their energy values with that of the cSPhs' deduced from equation (6.2), which is purely quasi-static and based on the sole knowledge of the λ_i, ω_{TO}, ω_{LO} and ϵ_∞, shows an almost perfect agreement. This validates conceptually our approach, and also allows us to use a simple EELS modal decomposition for EELS simulations. Thus, the EELS probability (simplified here to the case where the beam is outside of the object of interest) reads [10]:

$$\Gamma(\boldsymbol{R}_\perp, \omega) = \frac{1}{\pi\omega^2} \sum_i \mathrm{Im}(-g_i(\omega)) |E_z^i(\boldsymbol{R}_\perp, \omega/v)|^2 \tag{6.5}$$

where $\boldsymbol{E}$ is the electrical eigenfield, v is the speed of the electron, z the direction of the electron's propagation, $\boldsymbol{R}_\perp$ the position of the beam in the plane perpendicular to z and $g_i(\omega)$ is the spectral function for mode i depending only on ϵ and λ_i [10] with imaginary part peaking at the cSPh energy ω_i. In the case where the phonon response can be characterized by a Drude-Lorentz form of the dielectric constant, the spectral function reads:

$$\mathrm{Im}(-g_i(\omega)) = \frac{\Gamma\omega}{(\omega^2-\omega_i^2)^2+\Gamma^2\omega^2}\left[\frac{2(\omega_i^2-\omega_{TO}^2)^2}{\epsilon_\infty(\omega_{LO}^2-\omega_{TO}^2)(1+\lambda_i)}\right] \tag{6.6}$$

The spectral function then takes the simple form of a lorentzian peaking at the cSPh mode energy ω_i (solution of equation (6.2), this is the energy of the ith cSPh in absence of dissipation), weighted by some energy independent prefactors. The above formulation clearly points out: (1) the fact that the EELS spectra are a superposition of cSPh spectral functions weighted spatially by the modulations of the associated electrical eigenfields, (2) the close resemblance between EELS and EMLDOS, and (3) the spectral similarities between EELS and extinction cross-section.
The above deductions can be extended analytically to the case where the object of interest is embedded in a medium. Similar developments (see SI of [120] or [416]) can be done in the retarded regime assuming a model dielectric function.

6.4.3 Analogy between localized SP and cSPh modes

From the point of view of the local continuum dielectric model, there is no functional difference between SPs and surface phonons, SP in slabs and cylinders and FK modes, and LSPs and cSPhs, as long as the details of the dielectric constant are not disclosed. In the case where the SPs are described by a Drude model and the cSPhs by a Drude-Lorentz model, the analogy between SPs and cSPhs can be simply made by replacing ω_{TO} by 0, ω_{LO} by ω_p and ϵ_∞ by 1. Then, all the expressions presented in this chapter can be compared to that for SPs, especially those found in [10]. For example, one retrieves the familiar values of $\omega_p/\sqrt{2}$ and $\omega_p/\sqrt{3}$ for the surface and dipolar surface plasmon modes.

6.5 Connection with optical quantities

6.5.1 Validity of the quasistatic approximation

In figure 6.3(a), we also compare EELS to macroscopic optical quantities such as the absorption, extinction and scattering cross-sections calculated in the retarded approximation. As in the case of EELS, the spectra do not peak at the normal modes energies ω_{LO} and ω_{TO}. Instead, they are dominated by the cSPh modes, in analogy with the well-known case of a slab spectrum dominated by the FK modes [25] or more generally for an ensemble of nanoparticles [40]. This is particularly justified from the modal decomposition of the cross-sections: the optical cross-sections are proportional to a spectral function peaking at the dipolar cSPh modes energy. Indeed, the extinction cross-section, which is equal to the absorption cross section in the QS limit, reads [119]:

$$C_{ext}(\omega) \propto \sum_{i,d} A_i\omega\,\mathrm{Im}(-g_i(\omega)) \tag{6.7}$$

where A_i is a mode dependent prefactor, and the sum runs over the dipolar d cSPh modes only. Contrary to the case of EELS, only the dipolar modes are observable (but a very slight contribution from the third order mode). The spectra obviously show a large dependence on the incoming polarization. For polarizations along the nanorod axis, the dipolar mode of the low energy branch is excited. For a polarization perpendicular to it, the dipolar modes of the other branches, almost all arising at ω_s [417], are excited, see figure 6.3(a). This points to the fact that EELS is sensitive to both bright (i. e. optically active) and dark (i.e. not optically active) cSPhs, in contrast with optical far-field techniques.

Obtaining truly dark (non-emitting/absorbing) localized SPs is difficult due to the relatively large sizes of plasmonic particles [119] with respect to the corresponding free space wavelengths. In

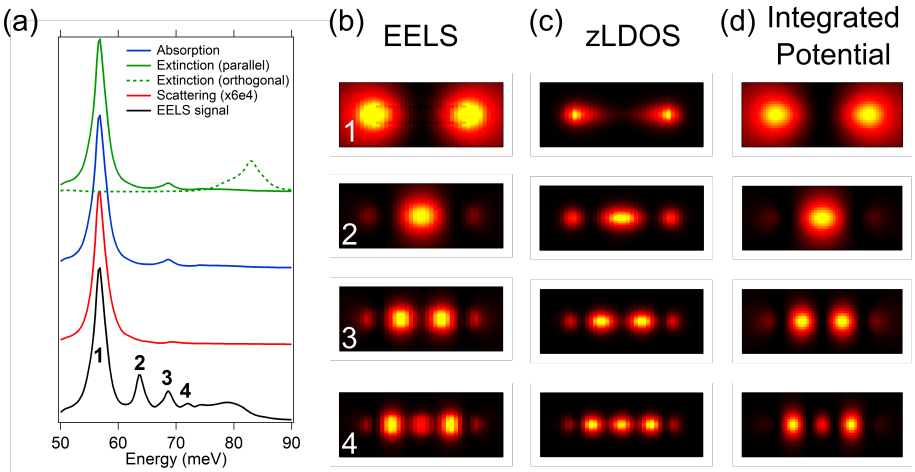

Figure 6.3: *Optical cross-sections, EELS, EMLDOS and eigenpotentials for the cSPh in a nanorod of MgO. (a) Simulated optical cross sections for an incoming beam propagating perpendicular to the nanorod axis, and EELS spectrum for an electron beam impinging 10 nm away from one tip of the nanorod. All spectra have been shifted for clarity. Optical cross-sections scales are the same for extinction and absorption, and multiplied by* 6.10^4 *for scattering. The polarization of the electrical field is parallel to the nanorod axis, except for the dotted line curve. The nanorod is 200 nm in length and 30 nm in diameter (b) EELS maps for the four first modes of the nanorod. (c) Corresponding zEMLDOS maps taken at z=10 nm from the surface of the rod. (d) Corresponding z-integrated eigenpotentials.*

contrast, for the cSPhs, where the QS approximation is justified for much larger particles sizes, almost only dipolar modes are bright. We note that the scattering cross-section is several order of magnitude smaller than the extinction one. This is basically related to the fact that, other things being equal, the ratio between scattering and extinction scales as $1/\omega^3$, where ω is the energy of interest. This makes extinction and absorption cross-sections almost identical at the low energy of the phonon regime, making EELS very close to the absorption cross-section for dipolar cSPh modes. We note that this contrasts with the case of a silver plasmonic nanorod of the same size (see figure 6.4). In this case, scattering has a major contribution in the extinction cross-section.

6.5.2 Comparison with optical experiments, EMLDOS

We can now clarify the type of selection rules when exciting cSPh optically or with electrons. To start with, in the QS approximation, only dipolar modes can be excited by a planewave, and the electrical polarization of the planewave must be aligned with the dipole direction. Away from the QS regime, similar symmetry arguments arise: even modes (mode 2 and 4 on figure 6.2(d)) cannot be excited by a planewave with electrical field in the plane containing the axis of the nanoantenna, while odd modes (1 and 3) can be excited. Tilting the beam direction with respect to the antenna axis will break the symmetry and make it possible to also detect even order modes. More generally, for optical experiments, the selection rules are completely determined by the general symmetry of the surface charge distribution with respect to the planewave direction and polarization.

The interplay between the symmetries of the incoming electron electrical field and the surface eigencharges is different. As with optics, cSPh modes are also probed by EELS, but contrary to optics, EELS is sensitive to all modes even in the QS approximation. Also, the symmetry of the surface eigencharges rather impacts the spatial distribution of the EELS signal. Indeed, EELS maps (figure 6.3(b)) closely resemble the EMLDOS projected along the electron propagation direction z (zEMLDOS, figure 6.3(c)), with the EMLDOS spatial and spectral distribution being essentially determined by the size, shape and symmetries of the object of interest. The resemblance between EELS and zEMLDOS is expected by analogy with the LSP case, where also a general analytical relation between these two quantities can be determined [411]. Much as in the case of LSPs [10], EELS as well as near-field optical techniques do not map directly the eigencharges [241]. Rather,

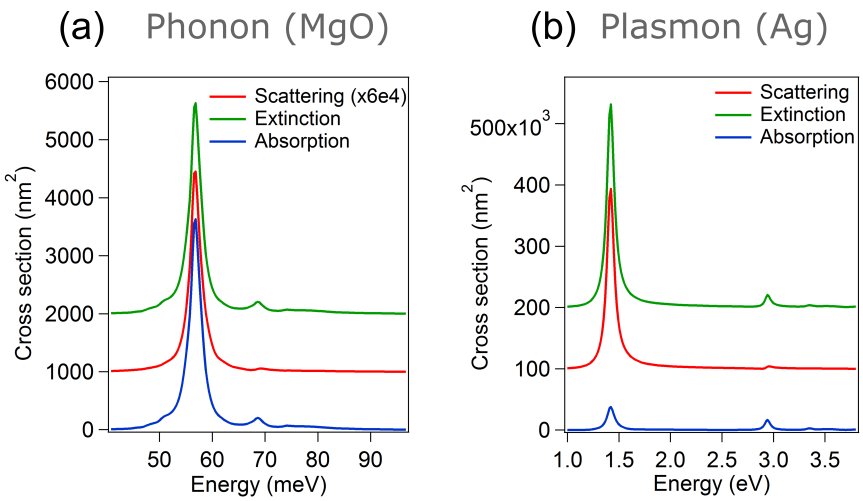

Figure 6.4: *Optical extinction, absorption and scattering cross-sections for (a) a MgO nanoantenna and (b) a silver nanoantenna. Both antennas have the same size (200 x 30 nm). Note the absolute cross-section values.*

they map the related zEMLDOS, itself related to the z-projection of the electric eigenfield in the QS limit [408, 10] as:

$$\rho_{\alpha\alpha}(\boldsymbol{r},\omega) = \frac{1}{2\pi^2\omega}\sum_i Im(-g_i(\omega))|E^i_\alpha(\boldsymbol{r})|^2 \tag{6.8}$$

where α represents the projection direction; an even more precise description of EELS on cSPhs in terms of electromagnetic quantities is given by the almost identity between EELS and the z-integrated eigenpotentials [214], see figure 6.3(d).

6.6 General properties of confined surface phonon modes

We can sum up the results exemplified on the nanorods but valid for any kind of phononic nanoobjects.

First, *surface* EELS and optical IR absorption, extinction and scattering are probing the same physical excitations, namely cSPhs. The symmetry of the cSPh surface eigencharges, which depends on the global shape and symmetry of the subtending particle, determines the coupling strength of the cSPhs with the probing electrons or photons. This is in stark contrast with IR absorption or *bulk* EELS [418, 400, 24], which are probing *normal* modes, which depend on local (atomic) symmetries, i. e. the bulk material properties. This is also a main difference between our work, which relates surface vibrational EELS to the concept of *EMLDOS*, and recent theoretical works describing the link between bulk EELS to the concept of phononic density of states (*pDOS*). Again, pDOS is dependent on the atomic structure symmetry while EMLDOS is dependent on the global (shape) symmetry of the nanoparticle. Also, for similar reasons, surface EELS is completely different to Raman spectroscopy which probes bulk properties of atomic oscillations, although following selection rules different to that of bulk IR absorption. Note that the LCDM can also be used to predict the bulk EELS experimental results through a term proportional to $-Im(1/\epsilon(\omega))$, giving essentially a peak at ω_{LO} in the Drude-Lorentz model. The intensity of the related peak may be influenced by the screening at the surface, a phenomenon handled in the LCDM theory and known as "begrenzung" effect [24]. There are however several limits explaining the need to develop dedicated theories for bulk phonons beyond the LCDM [418, 400, 24], related to the interpretation of angular resolved experiments and possible failure of the local approximation [418, 400, 24].

Second, EELS maps are close to that obtained with the near-field optical measurement which

Material	ϵ_∞	$\lambda_i = -1$ ω_{TO} (meV)	$\lambda_i = 1$ ω_{LO} (meV)	$\lambda_i = 0$ ω_s (meV)	$\lambda_i = -1/3$ ω_d (meV)	slab exp. (meV)
SiO_2	2.99 [422]	134 [422]	153 [422]	143.8	140.6	138
hBN (in-plane)	4.95 [423]	169 [423]	200 [423]	195		
hBN (out-of-plane)	4.1 [423]	187 [423]	197 [423]	195		
hBN slab ([23])						173
hBN slab (exp. [424])						187/203
hBN slab (theo. [424])						181/197

Table 6.2: *Comparison of theoretical and experimental values for $\lambda_i = -1, 1, 0, -1/3$ (charge symmetric/antisymmetric modes for infinitely thin slabs or cylinders, surface mode, dipolar spherical mode) and experimental values from [23] and [424]. In the later case, two modes (interpreted as charge symmetric and charge antisymmetric FK modes) are given.*

are related to the EMLDOS [419], and map quantities close to the cSPh electric eigenfields, and more precisely the eigenpotentials, along the electron direction integrated on the electron beam path (see an analytical proof in equation (6.5) and [214]). The typical spatial extent of the EELS signal is related to that of the EMLDOS, and almost identical to that of the integrated eigenpotentials.

Third, due to the large free space wavelength of the cSPhs compared to the typical dimensions of nano-objects, the QS approximation holds essentially true for sub-micron nanoparticles, and any nanoparticle can be described by a set of eigencharges and related λ_i that only depends on the shape of the nanoparticle.

In addition, this theory works well for understanding cSPhs, but will obviously fail to describe long-wavelength, propagating surface phonons that may arise in the particular case of very large particle or slabs. In the case of slabs or infinite cylinders, however, alternatives rigorous retarded theories exist [25]. The differences in the predictions between a quasi-static (such as presented here) and retarded formalism weakly affect lowest energy, charge-symmetric modes that are usually dominant in slabs and cylinders.

Also, a rigorous modal decomposition of all relevant EELS and optical quantities for arbitrary shaped nanoparticles (see e.g equations (6.5) and (6.7)) is possible, thus simplifying both the understanding and predictions of surface EELS experiments. Finally, the formalism presented here is not specific to the Drude-Lorentz model (except of course equations (6.2) and (6.6)). Therefore, any situation where a local dielectric constant can be deduced, either theoretically or experimentally, can be handled. For example, *ab-initio* models of the IR dielectric constant of a crystal of molecules could be computed, and re-injected in our model for interpreting quantitatively the experiments, just as recently performed by Radtke et al. [420] in the case of a planar interface to interpret results on guanine crystals [421]. With all these considerations in mind, we are in the position to synthesize observations made in the literature on surface phonons in terms of SPh modes or cSPh modes.

6.7 Review and interpretation of the experimental results found in the literature

We are now in the position to explain the apparent contradictions found in the literature.

6.7.1 Fuchs-Kliewer modes of thin material slabs

Krivanek et al. [23] reported the first observation of vibrational signatures with STEM-EELS. Among other, they reported a resonance at 173 meV on a $\approx$ 50 nm thick sheet of hexagonal boron nitride (hBN), and a resonance at 138 meV in an $\approx$ 30 nm thick SiO_2 slab. The resonance energies did not change as a function of the electron beam position, whether it was impinging in the objects or in vacuum close to them. The 173 meV resonance was attributed to the LO normal mode of

hBN, and the other compared to IR results without further assignment. Following the reasoning of this chapter, one can rationalize these results (see also table 6.2).
The 173 meV (hBN) and 138 meV (SiO_2) modes are likely to be charge-symmetric (lower branch in figure 6.2, λ_i close to -1) FK modes. Indeed, with the help of equation (6.2) (see table 6.2), one can directly deduce that their energies are between ω_{TO} and ω_s (and very close to $\omega_{TO} = 169.5$ meV in the case of hBN) but largely different from ω_{LO} (see table 6.2). For symmetry reasons, the dipole strength of the charge-antisymmetric mode vanishes with the thickness of the slab [425]. It might explain why this mode was not reported in [23].

On the other hand, as summarized in table 6.2, Batson and Lagos [424] reported the measurement of two peaks on a h-BN flake, the first at 187 meV (below ω_s) and the second at 203 meV (above ω_s). These should correspond to charge symmetric and antisymmetric modes - as confirmed by preliminary simulations in [424]- for a slightly thicker slab (as the symmetric mode energy is at higher energy and the anti-symmetric mode is still weaker but now measurable).

Recently, Govyadinov and collaborators [426] experimentally and numerically studied the influence of the h-BN flake's thickness on the phononic resonance energies and corroborate the symmetric and anti-symmetric nature of the slab modes. It is worth noting that in these cases, the energy of the modes depends on the geometry and symmetry of the nano-object, and we expect of course the observation of thickness dependent modes when more experimental works will be available in the literature.

Finally, no modes energy spatial variation has been reported on these two sorts of slabs [23, 424]. Recently, Schmidt et al. [53] showed that the plasmonic modes in thin objects with edges can be decomposed in slabs modes and edges modes independently. The slabs modes follow the infinite slabs dispersion relations, and edges follow the nanoantennas ones [371]. The modes of lowest energy branches have the same charge symmetry with respect to the slab or cylinder mid-plane, so that the slab and edge lowest energy modes share the same symmetry. Translated to surface phonons in SiO_2 slabs, it means that we should expect two different modes of same symmetry with respect to the slab mid-plane; however, both dispersion curves are very close (see e.g figure 6.2(a)), and for very thin objects both slabs and edge modes energy tend to a unique and same value (ω_{TO}), making it difficult to detect experimentally any spectral or spatial variation except an intensity decrease in vacuum.

6.7.2 Confined phonon modes of MgO nanocube

Mode	**Corner**						
Symmetry	Dipolar			Quadrupolar			Octupolar
λ_i	-0.56	-0.56	-0.53	-0.53	-0.53	-0.54	-0.52
ω (from Eq. (6.2))	72.3	72.3	73.1	73.1	73.1	72.8	73.1
ω (simulations, this paper)	72.0						
ω (simulations, Ref. [24])	72						
ω (experiments, Ref. [24])	69						

Mode	**Edge**				**Face**
λ_i	-0.44	-39	...	All summed	N/A
ω (from Eq. (6.2))	75.4	76.5	...	N/A	N/A
ω (simulations, this paper)	77.7				83.3
ω (simulations, Ref. [24])	76				83
ω (experiments, Ref. [24])	72				78

Table 6.3: *Comparison between energies values for the MgO nanocube modes calculated with equation (6.2), from retarded simulations with experimental dielectric constant found in [415], from retarded simulation in [24] and experimental results from [24]. Inputs for equation (6.2) are $\omega_{TO} = 50.7$ meV, $\omega_{LO} = 91.3$ meV, $\epsilon_\infty = 3.01$ [415]. Energies are given in meV units. Note the apparent discrepancy for the face mode values between simulations and experiments, proven in [24] to be an effect of finite spectral resolution in the experiments.*

At the opposite, Lagos et al. [24] observed outside of MgO nanocubes an EELS signal with

different energies and clear spatial modulations. They identified essentially three modes (see also figure 6.6(a)): a corner (C) one at lower energy, an edge (E) one and a face one (F) at higher energies. All the modes could be simulated without taking into account any substrate. Table 6.3 sums up Lagos' experimental and simulation results, as well as our simulations and the energies as deduced from equation (6.2).
Our simulations are in good agreement with Lagos simulations and experimental results, not a strong surprise as our calculations and Lagos' ones are performed with the same tool (MNPBEM), similar cube parametrization and the same full retarded approximation. More interestingly, we see in table 6.3 how well equation (6.2) reproduces our simulations and Lagos's ones, themselves pointed to be in very good agreement with experiments ([24]). Our theory gives however a stronger insight into the nature of the probed modes. In Lagos et al. [24], modes are denominated through their EELS spatial distribution, with no discussion on their symmetries, which are known to be complex for cubes plasmons (see section 5.4). Indeed, as shown in figure 6.5, the corner mode can be decomposed in dipolar, quadrupolar and octupolar contributions (see also table 6.3) that are degenerated in the quasistatic approximation. Because one of its components is dipolar, the corner mode is likely to be bright (i.e. theoretically measurable through an IR extinction experiment) although weakly scattering compared to a plasmonic cube of the same size. Quite interestingly, the edge mode is in fact composed of a large number of cSPhs of close λ_i, see table 6.3. The symmetry of all these constituting modes makes the edge mode a dark one. Concerning the face mode, the number of polygons required for convergence was too high to deduce a definite value or set of values for λ_i[1]. However, this highest energy mode has an energy very close to ω_s for MgO, corresponding to $\lambda_i = 0$. This is expected from LSPs analogy, as high momenta modes converge systematically to this value.

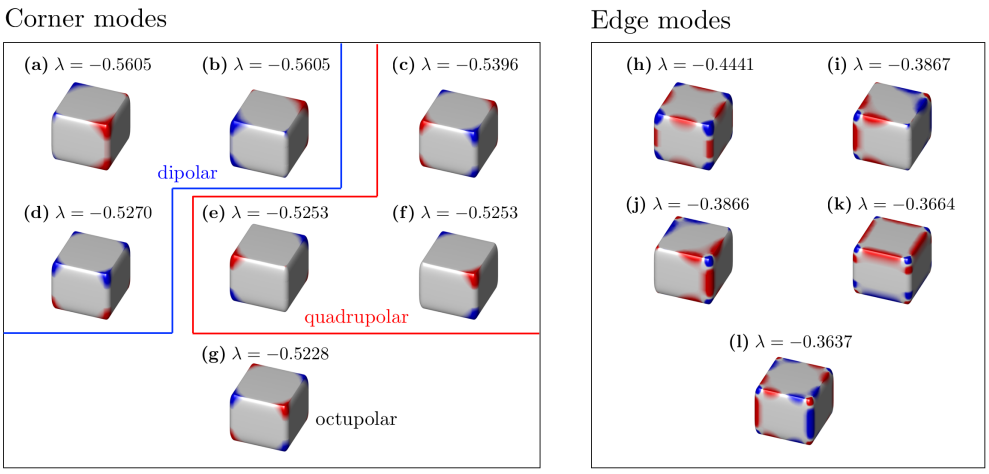

Figure 6.5: *Modes symmetry for a cube in the quasi-static approximation. Values of λ_i are given on top of the corresponding eigencharge distributions (red is minimum and blue maximum). (a-g) Corner modes. (h-l) Edge modes. Corner modes have been separated with respect to their symmetries.*

6.8 Substrate effect

We now turn to a point which has not been considered so far but may have important implications for the interpretation of the forthcoming experiments. Indeed, the effect of the substrate, known to be essential in plasmon physics, has not been discussed in the context of surface vibrational STEM-

[1] We simulated a 100 nm length cube with approximately 6000 polygons and calculated the corresponding eigencharges and geometrical eigenvalues λ_i using the `plasmonmode` solver. The radii of curvature of the cube corners in the xy plane are fixed at 3 nm. The rounding in the yz (resp. xz) direction is not precisely controlled within the `MNPBEM` toolbox [410] (when using the `tripolygon` and `edgeprofile` functions). However we estimated the radius of curvature in these planes to be much shorter than 3 nm. Because of the slight asymmetry of the mesh, the three dipole (resp. quadrupole and edge dipolar) modes are not slightly degenerated, see λ_i values on figure 6.5.

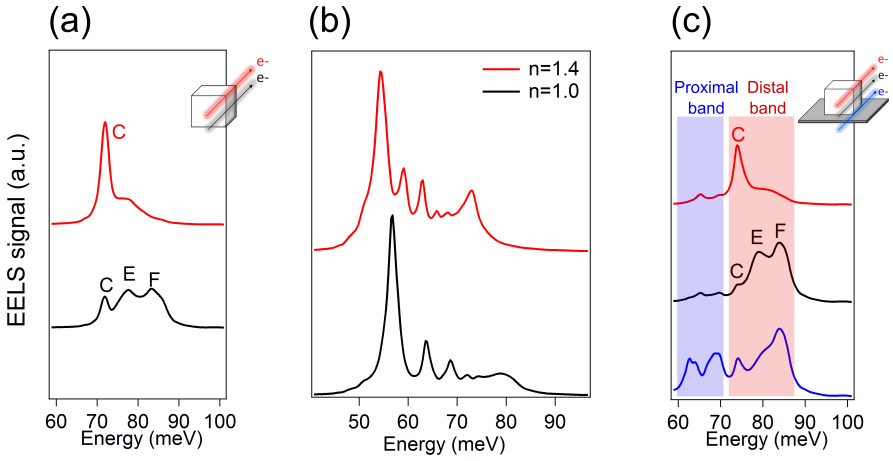

Figure 6.6: *Dielectric environment effect. (a) Simulated EELS spectra for a cube of MgO (100 nm edge long) in vacuum, exhibiting a corner (C), an edge (E) and a face (F) mode depending on the beam position. (b) Simulated EELS spectra for a nanorod (200x30 nm) in vacuum (black) and embedded into a dielectric of refractive index equals to* 1.4*. The beam is positioned at 10 nm from the tip of the nanorod in both cases. (c) Same simulations as in (a), but for a cube deposited on a substrate of refractive index n=2.3. The former C, E and F mode split into two bands. The distal band is essentially consisting in a series of C, E, F modes arising at almost the energy of the corresponding vacuum modes, while the proximal band is shifted towards the* ω_{TO} *energy. Spectra corresponding to a given trajectory are indicated by their colors.*

EELS experiments. It is well-known that localized SP energy and spatial distribution drastically depend on the close presence of other materials, like a substrate or an embedding matrix. In figure 6.6(b), we show the effect of embedding a phononic nanorod into a material of constant dielectric constant different to one. It produces an expected redshift of the excitation, yet still constrained between ω_{TO} and ω_{LO}.
The case of a nanoparticle on a substrate is more subtle. In particular, in the case of a nanocube, we saw in section 5.4 that the modes will split into proximal and distal modes. In [24], only the distal modes were reported, although both types of modes are actually predicted (see figure 6.6). We note that the distal modes energies are very close to the mode of a free space cube, explaining the good agreement between our theory, Lagos' and our simulations without substrate, and experimental results. Observation of the proximal band would however require a spectral resolution even better than actually available.

6.9 Summary and perspectives

Summary of the main results

In a pioneering work, Fuchs and Kliewer demonstrated the efficiency of the local continuum dielectric model to describe vibrational excitations in a finite system such as slabs [25] and infinite cylinders. The Fuchs-Kliewer work has been extended with an impressive success to the description of SP in simple systems such as slabs and cylinders. Indeed, given similar electromagnetic boundary conditions, it is no surprise that similar physics is involved; in particular, surface waves, either SP or SPh can be regarded as surface charge densities waves. Recently, two reports [23, 24] have demonstrated the amazing possibility to probe vibrational excitations from nanoparticles with a spatial resolution much smaller than the corresponding free-space phonon wavelength using EELS. While Lagos et al. [24] evidenced a strong spatial and spectral modulation of the EELS signal over a nanoparticle, Krivanek et al. [23] did not. In this chapter, we showed that discrepancies among different EELS experiments as well as their relation to optical near- and far-field optical experiments can be understood by introducing the concept of confined bright and dark surface phonon modes, whose density

of states is probed by EELS. Such a concise formalism is the vibrational counterpart of the broadly used formalism for localized surface plasmons, as summarized on the following table:

Plasmonics	**Phononics**
Bulk plasmons electronic DOS	Bulk phonons phononic DOS
Surface plasmon modes Localized surface plasmon EMLDOS	Fuchs-Kliewer modes Confined surface plasmon EMLDOS

It makes straightforward to predict or interpret phenomena already known for localized surface plasmons such as environment-related energy shifts or the possibility of 3D mapping of the related surface charge densities.

The theory presented here can be extended to understand more complicated situations. This is in analogy with the success of the theory presented for localized SPs [9, 407, 411, 10, 120], which has been extended to the 3D mapping of the EMLDOS [416] or of the surface eigencharges [215], the simulation of the cathodoluminescence signals [119, 120], the interaction of surface excitations with phase-shaped electron beams [241], or the coupling between localized SPs. Also, this model can be refined by developing a retarded model or a non-local approximation extension [19].

Chapter 7

Perspectives and ongoing works

At the end of each chapters, we took care of giving a summary of the important results together with the potential applications, perspectives and crucial questions to be addressed in the future. Here, instead of redundantly repeating these elements, in this short chapter, I will present a selection of the ongoing works exploring the questions raised above.

7.1 Studying the degeneracy points of the plasmon eigenproblem

In section 5.3, we saw that the plasmon eigenproblem is essentially non-Hermitian and we explored a one dimensional parameter space where the length L of one arm of a nano-dagger was tuned. It revealed an anti-crossing point which typical splitting is connected to the overlap between the two modes i.e. the skewness of the vector space.

In fact, exploring parameter spaces of higher dimension would reveal more deeply the properties of the plasmonic system. An essential feature of these vector spaces are the degeneracy points which can be of two kinds:

- The diabolic points (DP) where only the eigenvalues are degenerated (i.e. a standard Hermitian degeneracy).
- The exceptional points (EP) where both eigenvalues and eigenvectors are degenerated. Singular aspects are associated with these degeneracies: the coalescence of eigenvectors (i.e. formation of a Jordan chain), the matrix cannot be diagonalized (i.e. apparition of non-trivial out of diagonal Jordan block [427]), the metric is no more defined [331] and the system becomes extremely sensitive to any variation of the parameters [331]. The physics of exceptional points is extremely rich and has a plethora of potential applications in a wide range of systems [427, 428, 351, 429, 430, 339, 336, 330].

Matrix type	Co-dimension of DP	Co-dimension of EP
Real symmetric	2	Non-existent
Real nonsymmetric	3	1
Hermitian	3	Non-existent
Complex symmetric	4	2
Complex nonsymmetric	6	2

Figure 7.1: *Co-dimension of the EP and DP degeneracy points depending on the type of matrix. Reproduced from [334].*

Depending on the type of matrix involved, the co-dimension[1] of the EPs and DPs change. In most of the publications studying these degeneracy points, an effective complex non-Hermitian Hamiltonian is built and analytically treated (e.g. equation (1) of [336]). In our case however the kernel is real non-symmetric which prevent a direct comparison.

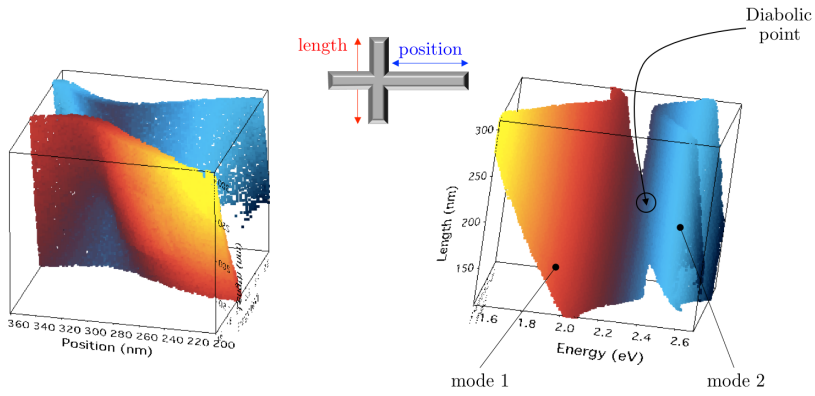

Figure 7.2: *Eigensurfaces of mode 2 and 3 of the nanodagger displaying a typical diabolic point. The two plots corresponds to the same calculation but showed from different perspectives. The colors simply reproduces the energy values in order to increase the visibility of the graph.*

Thus, we are currently exploring different parameter spaces and classifying the degeneracies. Starting from the dagger structure, we add another morphing parameter namely the position p of the arm along the main axis. Varying both L and p, we calculate the eigensurfaces associated with modes 2 and 3 of the dagger as shown on figure 7.2. We observe a typical diabolic point configuration. However, since the co-dimension is twice than in the complex case, we have no definitive conclusion on the nature of this degeneracy point and further investigation are required.

The research of an EP is even more trickier. Indeed, the LSP eigenproblem has to be solved numerically since no analytic model exists. The problem is that, at the exceptional point, all the smooth algebraic properties break down so that the numerical method will dramatically fail. We are therefore stuck in a position, where our only method to explore the phase space is doomed to failure. Nevertheless, we have some clues on how a plasmonic EP should look like.

7.1.1 Merging a sphere dimer

In 2006, Romero and collaborators [431] theoretically studied the plasmon modes of a sphere dimer as a function of the gap g. Particularly, they investigated the behavior of the plasmonic spectra when the two particles touch ($g = 0$) or even merge ($g < 0$). They observed several important features of such a merging experiment:

- When the gap between the two spheres becomes small compared to the particles' size, the geometrical eigenvalue λ of the dipole bonding mode evolves as:

$$\lambda \sim -1 + \sqrt{g} \tag{7.1}$$

  i.e. when the gap is decreased, λ approaches the value -1 following a square-root trend.

- Exactly at the contact point, a singular behavior is observed: the conductivity in the gap diverges (which could translate in the existence of arbitrarily-low-frequency modes) and the BEM cannot be applied.

- "Small changes in the region close to interparticle contact in the nearly touching and barely overlapping limits produce huge variations in the optical spectra of the dimer" i.e. the system

[1] The co-dimension of an EP in a parameter space $\mathcal{S}$ corresponds to $\mathrm{codim}(\mathrm{EP}) = \dim(\mathcal{S}) - \dim(\mathrm{EP})$

becomes extremely sensitive to perturbation close to the contact point. Authors highlight that this property could be use to design plasmon-based detectors.

- One mode disappears from the spectra when the two particle merges. This property has been demonstrated experimentally in [432].

In fact, these different features are typically what is encountered when an EP is crossed. The square-root behavior is typically displayed by an eigenvalue approaching an EP (it corresponds to a so-called square-root branch point [331]). It leads to a ultra-sensitivity of the system and possible applications in enhanced sensing have been suggested in whispering-gallery-mode micro-toroid cavity [433]. A singular behavior is usually observed at an EP, corresponding to the divergence of the metric. Moreover, the disappearance of a mode could be explained by a mode coalescence. Indeed, as noticed e.g. in [431], the first mode given by the BEM always correspond to a monopole-like mode (see mode 1 of figure 7.3) where both spheres are not neutral and carry opposite charges. This mode, which eigenvalue is -1 no matter the value of g, is always discarded because it is obviously unphysical. Nevertheless, this mode is mathematically valid and required for the algebraic consistency of the modes set. Thus, equation (7.1) basically shows that the mode 2 converges with a square-root behavior to the mode 1 and they eventually coalesce at $g = 0$. As illustrated in the inset, when the two particles are merged, both modes coalesce into the dipole mode of a dumbbell. The curves of figure 7.3 are the result of a BEM calculation and display the correct behavior.

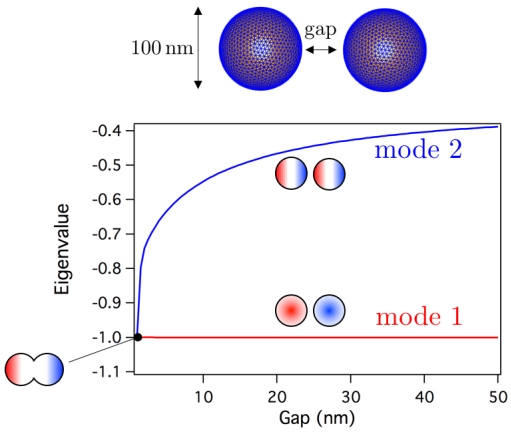

Figure 7.3: *Eigenvalues of the first and second mode of a sphere dimer (given by the BEM algorithm) as a function of the gap. The insets show a sketch of the charge distributions associated with each mode.*

Therefore, all these clues tend to show that the contact point has the characteristic of an EP where the dipole bonding mode and the unphysical "monopole mode" coalesce. Since the latter mode does not exist in practice, such a coalescence cannot be observed experimentally.

The central part in the merging experiment is the fact that the topology of the structure is not preserved: the dimer (genus 1) and the dumbbell (genus 0) are not isotopic. Intuitively, since the strong singularities involved in the BEM are treated by contour integration and residue theorem, we expect a topology change to be a signature of an EP. Although the Atiyah–Singer index theorem could give a definitive answer, we have no proof of this so far.

7.1.2 Proposed experiment

To valid our intuition, we need to build a system where the coalescence happens between two physically observable modes. To do so, let's perform the gedankenexperiment illustrated on figure 7.4. We start from a rod (as we did for the dagger) and grow two tilted arms in order to morph it to a ϕ-like structure (see insets of 7.4). We denote α the morphing parameter and only consider the mode 1 and 4. The morphing does not affect the mode 1 since it has no charge at the growing points. On the contrary, mode 4 is strongly red-shifted for the same reasons as for the cross

(see section 5.2). When the grown surfaces finally encounter and merge (when $\alpha = \alpha_2$ on the graph), the mirror charges appearing only on the arms of mode 4 cancel out. At this position, both eigenvectors become degenerated which would correspond to an exceptional point. After this point $\alpha > \alpha_2$, only one mode exists and the growth does not affect its eigenenergy anymore.

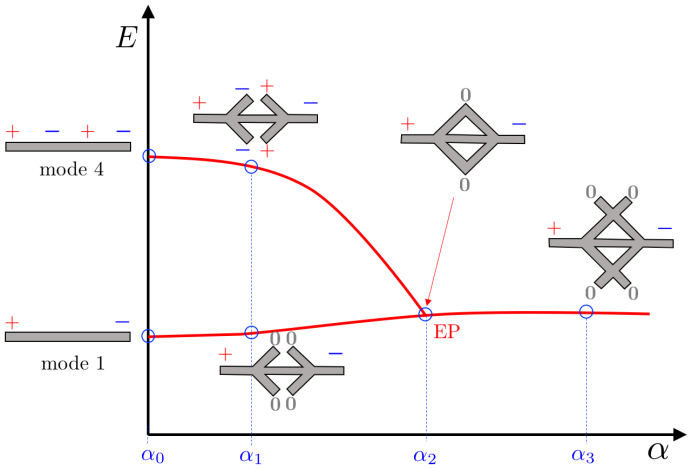

Figure 7.4: *Gedankenexperiment showing the morphing of a rod into a ϕ-like structure as a function of a morphing parameter α. The lines represent the eigenenergies of two modes which merge at an hypothetical EP. At positions marked by a blue circle, we sketched what the charge distributions should look like.*

Thus, with simple symmetry arguments, we can build an experiment where two eigenvectors must coalesce. However, let's emphasize that this is only a though experiment and numerical calculations are required to check the validity of our reasoning.

7.2 Fabrication of a tunable phase-plate on a microelectromechanical system (MEMS)

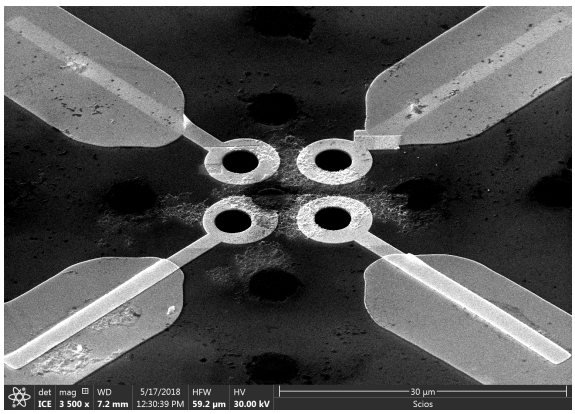

Figure 7.5: *SEM image of a set of 2×2 Einzel lenses array fabricated by e-beam lithography and focused ion beam milling.*

In chapter 4, we demonstrated that phase-shaped electron beams can be used to probe a wide range of plasmonic properties unreachable with conventional EELS e.g. phase or optical chirality. The next logical step is to test experimentally our theory. Recently, Verbeeck and collaborators demonstrated that an array of Einzel lenses [233] constitute an efficient programmable phase plate.

Following their idea, with the help of Laura Bocher[2], we produced by lithography and FIB milling a 2×2 Einzel lenses array as shown on figure 7.5 on a protoship MEMS with four electric contacts. We are now performing the first test in our Nion USTEM200 microscope. The long term project is to add an electron sorter after the sample and perform a full PSEELS experiment with an initial state preparation and post-selection step.

7.3 Realization of the plasmon coherence measurement with an electron bi-prism

We are currently performing split-beam experiments on plasmonic resonators in collaboration with Florent Houdellier of CNRS-CEMES laboratory, in order to realize the first coherence measurement of plasmons at the nanometer scale.

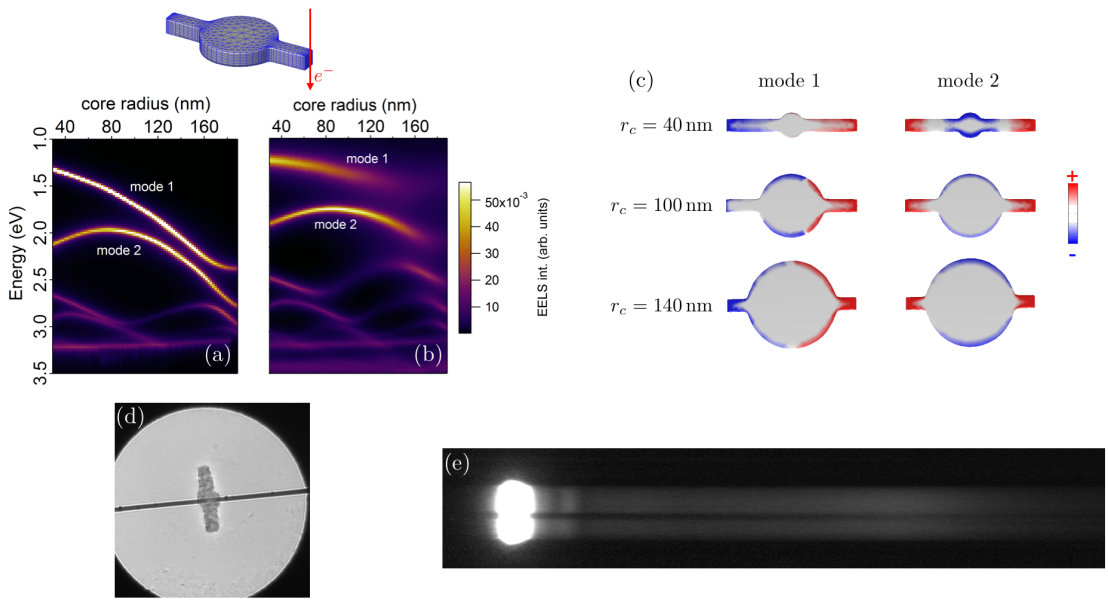

Figure 7.6: *EELS spectra of an Ag core-rod structure for different diameters of the central disk in (a) the quasistatic limit and (b) the retarded regime. (c) Charge maps (phase times modulus) of the two first modes of the structure in the retarded regime and for different diameters of the central disk. (d) TEM image of a lithographed core-rod structure with the shadow of the electron bi-prism. (e) 2D EELS spectrum taken on the core-rod resonator when the two spots of the split-beam impinge at the two tips of the rod.*

To do so, we decided to work on a silver core-rod resonator (see inset of figure 7.6)(a-b) which is basically constituted of a rod merged with a disk. The length of the rod axis is set at 400 nm while the diameter of the disk is varied from 35 nm to 190 nm. On figure 7.6(a-b) we calculated the conventional EELS spectra of the core-rod structure for different values of the disk diameter (the impact point of the electron is shown on the schematics in inset) and in the quasistatic and retarded regime. Charge maps (phase times modulus) of the two first modes of the structure in the retarded regime and for different diameters of the central disk are displayed on figure 7.6(c). Quite remarkably, the two regimes give dramatically different results. In the QS case, the growing of the core only results in an energy shift of the modes, which is expected from the geometrical LSP problem. However, in the retarded case, when the core is growing, the plasmon peaks become weaker and broader which indicates a *loss of coherence*. Thus, the core-rod structure is a remarkable example where the coherence of the plasmon modes can be tuned and therefore constitutes an good platform to test our split-beam experiment.

As shown on figure 7.6(d), we lithographed a series of core-rod resonators with different core

[2]who entirely performed the focused ion beam milling step.

diameter and systematically measured the energy loss with the two spots of the split-beam impinging at both ends of the structure. A typical 2D EELS spectrum is shown on 7.6(e) where the horizontal black stripe in the middle of the image corresponds to the shadow of the bi-prism. For now, only this preliminary test has been carried out but another experiment is planned in the near future.

Appendix A

Remarks on quantum nano-plasmonics

It is essential to highlight that, in the electron spectroscopy experiments discussed in this thesis, the quantum nature of plasmons do not intervene. The principal reason is that the decoherence time of surface plasmons (femtosecond) is much smaller than the excitation rate (typically one electron per nanosecond). In other words, what we measure in our experiments is an incoherent sum of a multitude of plasmons rather than a single quantum particle.
Nevertheless, the quantum nature of plasmons can be predominant in some situations e.g. :

- **Photon conversion experiments**. Altewischer et al. [434, 435] experimentally demonstrated that the $\gamma \rightarrow$ SPP $\rightarrow \gamma$ conversion process preserves the polarization entanglement in a pair of photons. Later, the same process has been demonstrated to also preserve energy-time entanglement [436, 437] and orbital angular-momentum entanglement [438]. In 2009, the possibility of propagating squeezed vacuum states in a gold waveguide using the same conversion process has also been demonstrated in [439]. Understanding why the dramatic losses encountered in the metal do not prevent SPPs from conserving the quantum properties of light requires a quantum treatment of the plasmon field.

- **Coupling with quantum emitters**. By coupling silver nano-wires to single photon emitters, Kolesov and collaborators experimentally demonstrated the wave-particle duality of SPPs and their bosonic nature [440]. Moreover, evidence of a strong coupling (cf section 2.2.4) between excitons and SPs have been observed experimentally [441, 80]. It corresponds to the formation of a new hybrid state called *plexciton* which theoretical description requires to take into account the quantum nature of plasmons [85, 86].

- **Time-resolved electron microscopy**. Ultrafast TEM and time-resolved pump-probe experiments in electron microscopy [154] can reach the femtosecond time-scale in which quantum nature of plasmons should be detectable.

All these works contribute to the emergence of *quantum plasmonics* [442] which is nowadays an hot field of research in nano-optics. Indeed, they open the route to amazing possible applications of plasmonics in quantum information e.g. SPP-mediated qubit-qubit entanglement [443].

The corollary of this is that a quantum theory of SPs is required. However, plasmons being severely damped excitations, a standard canonical quantization cannot be straightforwardly applied. Nevertheless, other theoretical approaches can be considered:

- **Approximate canonical quantization**. SPPs behaving essentially as light, they are less impacted by the losses in the metal than LSPs. Neglecting the radiative losses, a canonical quantization of SPP field is therefore possible using an Hopfield model [444, 445]. Quantization schemes for times t much shorter than the plasmon lifetime τ can also be considered. In this regime, plasmon damping can be neglected and therefore the field canocinally quantized [446].

- **Hydrodynamical models** which naturally take non-linearities into account [447].
- **Nonequilibrium statistical methods** such as quantum Langevin equations or Lindblad equation for the density matrix (both being equivalent [448]). Matloob used the Langevin equations to quantize the EM field in absorbing media and dieletrics. The Lindblad equation, which is basically the quantum form of the Markovian master equation, is a standard technique in optomechanics and atomic physics [449] and has been applied to plasmonics [450, 154].
- **Propagator formalism and diagrammatic expansions** [451]. These methods are heavier in terms of computation but also give more general and versatile expressions. We follow this approach in the next chapter 3 to derive a general form of the electron energy loss probability.

Appendix B

Illumination system of the STEM, spherical lens aberrations

In this appendix, we describe in details the illumination system of the STEM and the lens aberrations which can limit its performances. On figure B.1, we present a photography of a STEM Vacuum Generator (VG) model HB 501 used in this thesis together with a schematics of the illumination system of the STEM-VG in its typical alignment setup.

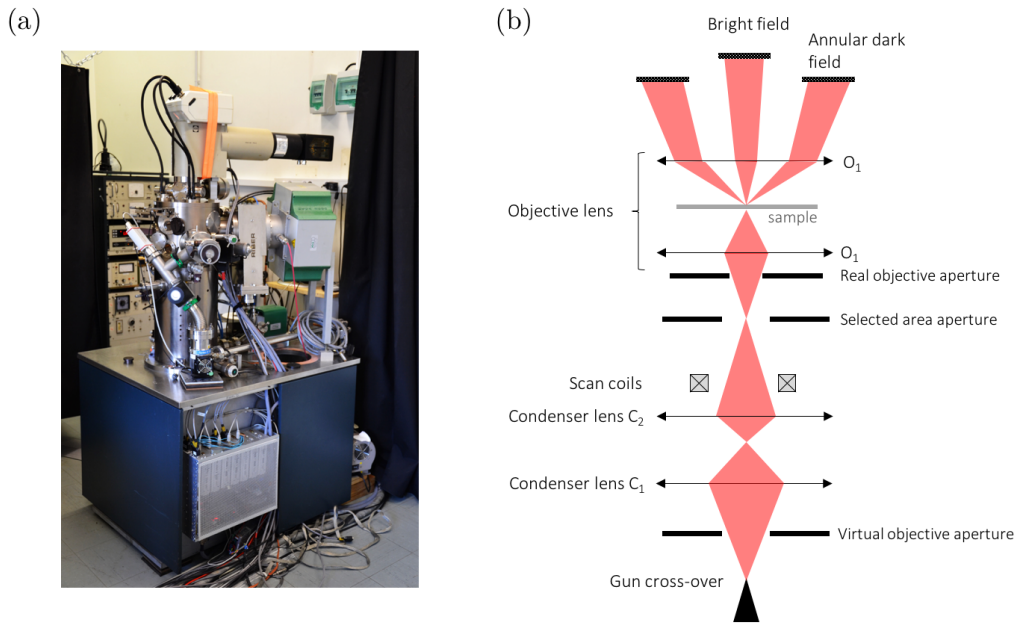

Figure B.1: *(a) Photography of a STEM VG model HB 501 used for light injection experiments in our research group. (b) Schematics of the illumination system of the STEM-VG in its typical alignment setup.*

B.0.0.1 Electron gun: electron generation

The STEM-VG is equipped with a cold field emission electron gun (cFEG). It is made of two anodes and one cathode consisting in a tungsten tip orientated along the [310] axis, see figure B.2(a-b). A potential V_e (typically 2.8-4.2 kV) is applied to the first anode (extraction anode) in order to extract electrons from the tip by tunnel effect. The electron current density is then given

by the Fowler-Nordheim:

$$j = AE^2 e^{\frac{-B\phi^{3/2}}{E}} \tag{B.1}$$

where E is the electric field at the surface of the cathode[1], ϕ is the work function of the tungsten (typically $\phi = 4.5$ eV), and A, B are two constants which can be determined exactly [452]. In our microscope, we typically have $j = 10^4$-10^5 A.cm^{-2}. Although we have an ultra-high vacuum in our gun (typically 2.10^{-11} Torr), some contamination progressively deposits on the tip which reduces the average current emission (see figure B.2(c)) and affects the quality of emission (increase of current fluctuations). Therefore, every 30 minutes or so, we proceed to a tip flashing i.e. we shortly heat the tip to high temperature (≈ 5000 K) to evaporate the contaminants.
The second anode (acceleration anode) is put at the potential V_0 (typically 60-200 kV) in order to accelerate electrons out of the gun. The combination of both anodes constitutes an electrostatic lens which leads to the formation of a crossover at the exit of the gun (see figure B.2(b)). This cross-over is the image by the lens of a fictive source of electrons which, in the STEM mode, is a virtual cross-over (i.e. the cross-over happens before the emitting tip).

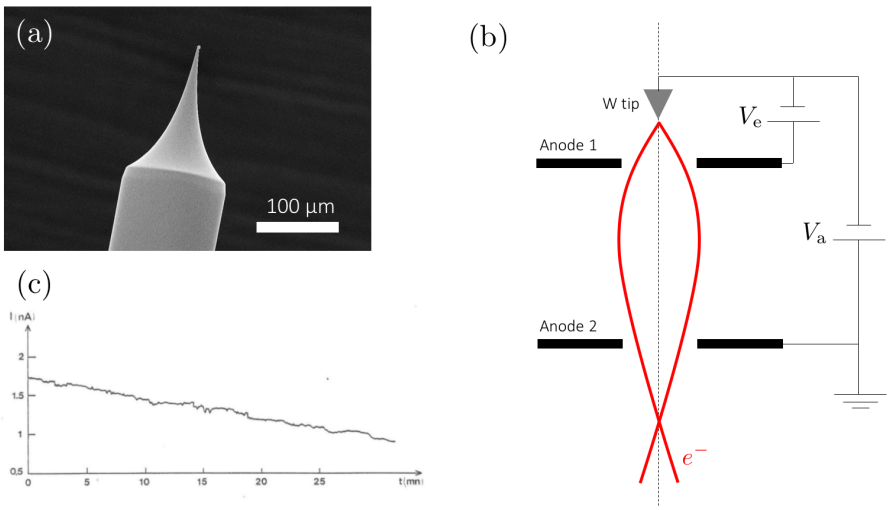

Figure B.2: *(a) Scanning Electron Microscope (SEM) image of a cFEG tungsten tip used in our STEM-VG. (b) Schematics of a cFEG electron gun. (c) Time evolution of the emission current measured in our microscope (reproduced from [453]).*

A fundamental quantity in electron microscopy in the gun brightness β (it corresponds to the radiance in optics) which corresponds to the current density per solid angle. The value of β is determined by the diameter of the source, the current density and the semi-angle of emission (i.e. the spread of transverse electron velocity). For cFEG, the brightness is typically $\beta \approx 10^9$ A.cm^{-2}.sr^{-1} [123]. Its value is limited by the aberrations (see section B.0.0.3) in the gun which tend to enlarge the spatial extension of the cross-over and increase the energy spread of the emitted electrons. Other types of guns exist (thermionic emission gun, Schottky FEG) which are based on the thermionic emission of electrons. This type of emission does not require such a good vacuum as for the cold field emission and therefore displays a more stable current over time. However, thermionic-based gun present a much weaker brightness (3 to 4 order of magnitude inferior). In addition, cFEGs display smaller energy spread (typically 0.3 eV versus 1.5 to 3 eV for Schottky FEG or thermionic gun) and a better spatial coherence. For spectroscopic applications investigated in this thesis, cFEG are therefore the most adapted guns.

[1]The electric field depends on the geometry of the tip $E = \dfrac{V_e}{KR}$ where K is a geometrical factor and R is the radius of curvature of the tip.

B.0.0.2 Condenser and objective lenses: formation of the probe

The cross-over after the gun constitutes the electron "point" source for the rest of the column and, as discussed earlier, its properties are dictated by the type of gun used and its alignment. In our STEM-VG, the size of this source is typically 40-50 Å. As depicted on figure B.1(b), the STEM-VG is equipped with three magnetic lenses including two condenser lenses (C_1 and C_2) and an objective lens. In addition, three different apertures are present: the virtual objective aperture (VOA), the selected area aperture (SAA) and the real objective aperture (ROA). The VOA is used to remove the electrons with aberrant trajectories in order to improve the spatial resolution of the probe. The SAA is used for diffraction mode (not used in this thesis) or for beam blanking in EELS experiments. Finally, the ROA fixes the convergence angle onto the sample which control the spatial resolution and the depth of focus of the microscope.

The alignment of the condenser lenses strongly depends on which type of experiment is carried out as it determines the size of the probe, the current density in the probe and the probe size (see figure 4.13 of [454]). In our illumination mode (figure B.1(b)), the two condenser lenses are excited so that the gun cross-over is conjugated at the SAA plane with a magnification close to 1. A second configuration, where only C_2 is excited, is also often employed which reduces the aberrations (therefore increasing the spatial resolution) but also reduces the probe current (approximately 6 times weaker compared to the C_1+C_2 mode). The condensers are weak magnetic lenses with long focal lengths, typically used for magnification.
The intermediate image at the SAA is then conjugated onto the sample by the objective lens. The latter is the most important part of the microscope and its properties strongly determine the performances of the machine. The aberrations of the objective lens are minimized by shortening the focal length, which imposes the gap between the two pole pieces to be the smallest as possible. However, this gap cannot be arbitrarily reduced as the sample, the objective aperture and the cathodoluminescence mirror (see next section) need to be placed between the pole pieces. The small focal length is achieved using a strong magnetic lens which, on a ray optics point of view, can be represented as a combination of condenser lens (see [454, 123] for a discussion on the different types of lenses). Finally, a coils assembly is place between C_2 and the SAA in order to scan the beam. The rocking point of the scan is chosen to coincide with the front focal plane, therefore leaving the sample illumination conditions unchanged by the scanning. We will now make further comments on lenses regarding their aberration in next section.

B.0.0.3 Spherical lens aberrations and their correction

We mentioned earlier that a limiting factor for the spatial resolution in a (S)TEM are the aberrations of the magnetic lenses. Even though we do not really bother with lens aberrations in this thesis (since we did not do high resolution microscopy), it is particularly convenient to introduce them in order to illustrate the importance of phase in electron imaging. The rest of this thesis is rather focusing on phase effects in electron spectroscopy.

It is well known from optics that lenses possess aberrations i.e. a lens systematically gives a deformed image of an object. Similarly, electron lenses also are aberrant which is one of the major difficulty for high resolution electron microscopy. A natural way to introduce and classify the aberration of lenses is to use a wave-like picture for electrons (or equivalently for light). Let's consider a plane wave Ψ_0 described in the paraxial approximation as:

$$\Psi_0(\boldsymbol{K}) = e^{ik_z z}\psi_0(\boldsymbol{k}) \tag{B.2}$$

The electrons traveling very fast (at approximately half the speed of light), the latter approximation is justified. This planewave impinges on a round lens as depicted on figure B.3; the lens then focuses the electron beam in the focal plane. If the lens is perfect, the wavefunction of the electron beam in the focal plane will be:

$$\psi(\boldsymbol{r}) = \mathscr{F}\left\{\psi_0(\boldsymbol{k})\right\} \tag{B.3}$$

On the other hand, the presence of aberrations will distort the wavefront and the resulting image

will be imperfect. One can model this effect by applying a dephasing factor which leads to:

$$\psi(\boldsymbol{r}) = \mathscr{F}\left\{\psi_0(\boldsymbol{k})e^{-i\chi(\boldsymbol{k})}\right\} \tag{B.4}$$

The term $\chi(\boldsymbol{k})$ therefore contain all the information on the so-called *spherical aberrations*. A standard procedure to quantify these aberrations is to decompose χ on a certain basis and measure the weighting coefficients. For circular lenses[2] a natural basis is formed by the Zernike polynomials $Z_{n,m}$ which are commonly used in light optics [456]:

$$\chi(k,\theta) = \sum_{n,m} c_{n,m} Z_n^m(k,\theta) \tag{B.5a}$$

$$Z_n^m(k,\theta) = R_n^m(k)\cos(m\theta) \tag{B.5b}$$

$$Z_n^{-m}(k,\theta) = R_n^m(k)\sin(m\theta) \tag{B.5c}$$

$$R_n^m(k) = \sum_{k=0}^{(n-m)/2} \frac{(-1)^k (n-k)!}{k!\left(\frac{n+m}{2}-k\right)!\left(\frac{n-m}{2}-k\right)!} k^{n-2k} \tag{B.5d}$$

where (k,θ) is the polar basis of the unit disk and $n \geq m$. From (B.5), one clearly see that n indexes the order of the polynomials and m the azimutal symmetry. The coefficients $c_{n,m}$ contain all the information on the spherical aberrations of the lens. Depending on the order of the polynomials, one can distinguish different contributions to the aberrations:

- 0th and 1st orders polynomials correspond to defocus and tilt.
- 2nd orders polynomials correspond to astigmatism.
- 3nd orders polynomials correspond to coma and threefold.
- 4nd orders polynomials correspond to e.g. spherical aberration.

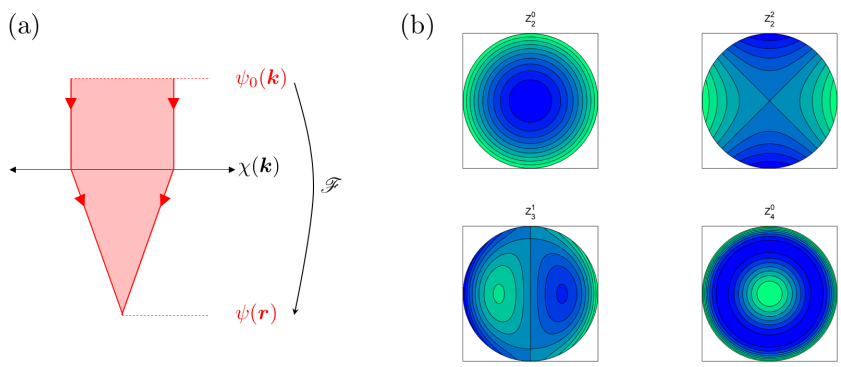

Figure B.3: *(a) Schematics of a planewave ψ_0 impinging on a lens represented by a transfer function χ and being focused on a screen. The symbol $\mathscr{F}$ denotes the Fourier transform. (b) Examples of Zernike polynomials.*

Very similar expansions exist for electron microscopy with different notation conventions [457, 458, 459, 460, 461, 462, 463, 188]. Using convention from [461, 188], the aberration function can be written for an typical electron lens (up to the third order) as:

$$\begin{aligned}\chi(\boldsymbol{k}) = \frac{C_1}{2k_0}|\boldsymbol{k}|^2 + \frac{A_1}{2k_0}|\boldsymbol{k}|^2\cos(2\theta) + \frac{B_2}{k_0^2}|\boldsymbol{k}|^3\cos(\theta) + \frac{A_2}{3k_0^2}|\boldsymbol{k}|^3\cos(3\theta) \\ + \frac{C_3}{4k_0^3}|\boldsymbol{k}|^4 + \frac{A_3}{4k_0^3}|\boldsymbol{k}|^4\cos(4\theta) + \frac{S_3}{k_0^3}|\boldsymbol{k}|^4\cos(2\theta) + \dots\end{aligned} \tag{B.6}$$

[2] If the lens is not circular, a decomposition exists but requires more involved techniques [455].

C_1 term corresponds to the defocus, A_1 to 2-fold astigmatism, B_2 to axial coma, A_2 to 3-fold astigmatism, C_3 to spherical aberration, A_3 to 4-fold astigmatism and S_3 to star aberration. Plugging the aberration phase deformation into the expressions of section 2.3.2.3, one immediately see that aberrations strongly limit the spatial resolution of electron microscopes. Nevertheless, since the pioneering work of Scherzer, aberration correctors have been developed and now equip most of modern microscopes[458, 462, 464]. In STEM, a common technique to quantify the aberrations is to measure changes in the shadow image (or electron Ronchigram [465]) of an amorphous material due to the shift of the beam [460]. Once quantified, the spherical aberrations are compensated by a series of multipole magnetic lenses (quadrupole and octopole lenses) which introduce tunable phase shifts; this ensemble of multipole elements are called C_S correctors.

A second type of aberrations called *chromatic aberrations* [454] arises from the fact that electron beam are non-monochromatic. Magnetic lenses act differently on electrons depending on their speed[3] i.e. the focal length of the lens depends on the electron energy. Therefore, if the electron beam is non-monochromatic, a point is conjugated to a chromatic-aberrant disk which size is proportional to the energy spread of the beam. Equivalent effects exist in optics due to the dispersion of light in the glass constituting the lenses. Chromatic aberrations can also be corrected by C_C correctors which consist in a combination of electrostatic and magnetic quadrupoles (contrary to the spherical aberrations correction which only requires magnetic lenses).

[3]Electrons follow helical trajectories which pitch and radius depends on their speed.

Appendix C

The Boundary Element Method and its application in plasmonics

C.1 From Maxwell equations to boundary integral equations

The first developments of BIEs to calculate the optical properties of nano-particles traced back to 1975 with the work of Fuchs on nano-cubes [40], later generalized by Ouyang and Isaacson for any kind of shapes [9]. The BEM has been introduced to nano-optics by the mutual effort of García de Abajo, Howie and Aizpurua [345, 466, 170]. In 2011, Trügler and Hohenester realized the open-source code `MNPBEM` based on these early theoretical developments. Let's first give some details on this formalism before description the numerical tool itself.

Let's consider a nano-particle of arbitrary shape S embedded in an homogeneous medium (typically air or vacuum) and subjected to an electromagnetic perturbation described by the scalar potential ϕ^{ext}. We describe this situation with the simplified scheme of two media of dielectric constants $\epsilon_1(\omega)$ and $\epsilon_2(\omega)$ separated by as sharp interface S. This is the basic assumption of the local dielectric continuum model (LDCM) already discussed in section 2.2.2.3. As shown in section 2.2.1, the scalar and vector potentials ϕ and $\boldsymbol{A}$ are solutions of the uncoupled Helmholtz equations:

$$\begin{cases} \boldsymbol{\nabla}^2\phi(\boldsymbol{r}) + k^2\epsilon(\boldsymbol{r})\phi(\boldsymbol{r}) = -4\pi\rho(\boldsymbol{r}) & \text{(C.1a)} \\ \boldsymbol{\nabla}^2\boldsymbol{A}(\boldsymbol{r}) + k^2\epsilon(\boldsymbol{r})\boldsymbol{A}(\boldsymbol{r}) = -\dfrac{4\pi}{c}\boldsymbol{j}(\boldsymbol{r}) & \text{(C.1b)} \end{cases}$$

These combined equations are completely equivalent to the Maxwell equations under the Lorenz gauge [467, 158]:

$$\boldsymbol{\nabla}.\boldsymbol{A}(\boldsymbol{r}) = ik\epsilon(\boldsymbol{r})\phi(\boldsymbol{r}) \tag{C.2}$$

C.1.1 Quasi-static approach

When the size of the nano-particle is small compared to the wavelength of light $kL \ll 1$, the optical response of the nano-particle is given by the QS limit $k \approx 0$ of the Maxwell equations. In this case and in the Lorenz gauge (C.2), the vector potential vanishes and the wave equation for the scalar potential (C.1(a)) reduces to the Poisson equation:

$$\boldsymbol{\nabla}^2\phi = -4\pi\rho \tag{C.3}$$

The corresponding Green function G_0 is then defined by:

$$G_0(\boldsymbol{r}, \boldsymbol{r}') = \frac{1}{|\boldsymbol{r} - \boldsymbol{r}'|} \tag{C.4}$$

With these notations, the total scalar potential is the sum of the induced potential and the external potential as:

$$\phi(\boldsymbol{r}) = \left(\oint_S G_0(\boldsymbol{r}, \boldsymbol{s}')\sigma(\boldsymbol{s}')d\boldsymbol{s}' \right) + \phi^{\text{ext}}(\boldsymbol{r}) \tag{C.5}$$

where $\boldsymbol{s}'$ is a vector pointing on the surface of the nano-particle as shown on figure C.1 in the case where S is a triangular shape.

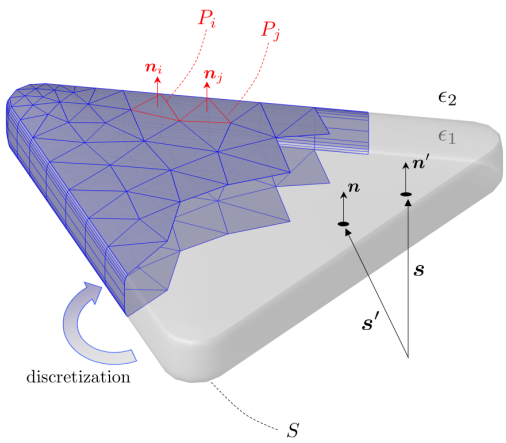

Figure C.1: *Schematics showing the different quantities involved in the BIE and BEM problems.*

As already stated in section 2.2.1, this equation have to be completed with the boundary conditions (2.3):

$$\begin{cases} \phi_1(\boldsymbol{s}, \omega) = \phi_2(\boldsymbol{s}, \omega) & \text{(C.6a)} \\ \boldsymbol{n}.(\boldsymbol{\nabla}\phi_1(\boldsymbol{s}, \omega) - \boldsymbol{\nabla}\phi_2(\boldsymbol{s}, \omega)) = 4\pi\sigma(\boldsymbol{s}, \omega) & \text{(C.6b)} \\ \epsilon_1(\omega)\boldsymbol{n}.\boldsymbol{\nabla}\phi_1(\boldsymbol{s}, \omega) = \epsilon_2(\omega)\boldsymbol{\nabla}\phi_2(\boldsymbol{s}, \omega) & \text{(C.6c)} \end{cases}$$

where ϕ_i denotes the potential in the medium i and σ the surface charge density. Due to the divergence of G_0 at $\boldsymbol{r} = \boldsymbol{r}'$, the normal derivative needs to be handled with care. More precisely, the value of the normal derivative reads:

$$\boldsymbol{n}.\boldsymbol{\nabla}\phi(\boldsymbol{s}, \omega) = \lim_{r \to s} \boldsymbol{n}.\boldsymbol{\nabla}\phi(\boldsymbol{r}, \omega) \tag{C.7}$$

$$= \lim_{r \to s} \left(\oint_S \frac{\partial G_0(\boldsymbol{r}, \boldsymbol{s}')}{\partial \boldsymbol{n}} \sigma(\boldsymbol{s}')d\boldsymbol{s}' + \frac{\partial \phi^{\text{ext}}(\boldsymbol{s}')}{\partial \boldsymbol{n}} \right) \tag{C.8}$$

where we defined $\partial/\partial\boldsymbol{n} \equiv \boldsymbol{n}.\boldsymbol{\nabla}$. From distribution theory, for $\boldsymbol{s} \neq \boldsymbol{s}'$, one can show that [345, 161]:

$$\lim_{r \to s} \frac{\partial G_0(\boldsymbol{r}, \boldsymbol{s}')}{\partial \boldsymbol{n}} = \lim_{t \to 0^+} \boldsymbol{n}.\boldsymbol{\nabla} \frac{1}{|\boldsymbol{s} \pm t\boldsymbol{n} - \boldsymbol{s}'|} = -\frac{\boldsymbol{n}.(\boldsymbol{s} - \boldsymbol{s}')}{|\boldsymbol{s} - \boldsymbol{s}'|^3} \mp 2\pi\delta(\boldsymbol{s} - \boldsymbol{s}') \tag{C.9}$$

where the $\pm$ sign is defined by the direction with which we approach the surface (positive sign when we approach from inside the particle). Plugging the latter expression in (C.8) for ϕ_1 and ϕ_2 we obtain:

$$\frac{\partial \phi_{1/2}(\boldsymbol{s}, \omega)}{\partial \boldsymbol{n}} = \mathcal{P} \oint_S F(\boldsymbol{s}, \boldsymbol{s}')\sigma(\boldsymbol{s}', \omega)d\boldsymbol{s}' \pm 2\pi\sigma(\boldsymbol{s}, \omega) + \frac{\partial \phi^{\text{ext}}(\boldsymbol{s}', \omega)}{\partial \boldsymbol{n}} \tag{C.10}$$

where $\mathcal{P}$ is the Cauchy principal value and $F(\boldsymbol{s}, \boldsymbol{s}')$ is the kernel defined, for $\boldsymbol{s} \neq \boldsymbol{s}'$, as:

$$F(\boldsymbol{s}, \boldsymbol{s}') = -\frac{\boldsymbol{n}.(\boldsymbol{s} - \boldsymbol{s}')}{|\boldsymbol{s} - \boldsymbol{s}'|^3} \tag{C.11}$$

Let's also emphasized that $\boldsymbol{n}$ denotes the normal in $\boldsymbol{s}$ and $\boldsymbol{n}'$ would denote the normal in $\boldsymbol{s}'$ as shown on figure C.1. On the other hand, combining (C.6b) and (C.6c) leads to:

$$\frac{\partial \phi_{1/2}(\boldsymbol{s},\omega)}{\partial \boldsymbol{n}} = \frac{4\pi\epsilon_{2/1}(\omega)}{\epsilon_2(\omega)-\epsilon_1(\omega)}\sigma(\boldsymbol{s},\omega) \tag{C.12}$$

Combining the latter equation together with (C.10), we obtain:

$$\boxed{\Lambda(\omega)\sigma(\boldsymbol{s},\omega) = \mathcal{P}\oint_S F(\boldsymbol{s},\boldsymbol{s}')\sigma(\boldsymbol{s}',\omega)d\boldsymbol{s}' + \frac{\partial \phi^{\text{ext}}(\boldsymbol{s}',\omega)}{\partial \boldsymbol{n}}} \tag{C.13}$$

where we defined:

$$\Lambda(\omega) = 2\pi\frac{\epsilon_2(\omega)+\epsilon_1(\omega)}{\epsilon_2(\omega)-\epsilon_1(\omega)} \tag{C.14}$$

The BIE (C.13) is the essence of the boundary element methods for nano-optics. Moreover, the cancellation of the source term leads to the Ouyang and Isaacson eigenproblem (already presented in section 2.2.2.3) which actually corresponds the definition of the classical and quasistatic LSP resonances:

$$\Lambda(\omega)\sigma(\boldsymbol{s},\omega) = \mathcal{P}\oint_S F(\boldsymbol{s},\boldsymbol{s}')\sigma(\boldsymbol{s}',\omega)d\boldsymbol{s}' \tag{C.15}$$

For an extended discussion on this aspect of the BIE, see [49, 39]. The total surface charge is then obtain through matrix inversion as:

$$\sigma = (\Lambda\mathbb{1} + F)^{-1}\left(\frac{\partial \phi^{\text{ext}}}{\partial \boldsymbol{n}}\right) \tag{C.16}$$

where $\mathbb{1}$ is the identity matrix and we used the compact matrix notation e.g. $F\sigma$ corresponds to:

$$F\sigma \equiv \oint F(\boldsymbol{s},\boldsymbol{s}')\sigma_i(\boldsymbol{s}')d\boldsymbol{s}' \tag{C.17}$$

From this charge, one can then obtain the fields and then all the observables of the simulated experiment (extinction, scattering, EELS, CL, etc).

C.1.2 Retarded approach

When $k \neq 0$, the vector potential is no more null $\boldsymbol{A} \neq 0$ and also needs to be computed. Moreover, the Green function for the Helmholtz equation now depends on the medium and the energy through:

$$G_i = \frac{e^{ik_i|\boldsymbol{r}-\boldsymbol{r}'|}}{|\boldsymbol{r}-\boldsymbol{r}'|} \tag{C.18}$$

where $i = 1, 2$ indexes the medium and $k_i = k\sqrt{\epsilon_i}$. In the retarded case, equation (C.5) has to be completed with:

$$\begin{cases} \phi(\boldsymbol{r}) = \left(\oint_S G_i(\boldsymbol{r},\boldsymbol{s}')\sigma_i(\boldsymbol{s}')d\boldsymbol{s}'\right) + \phi_i^{\text{ext}}(\boldsymbol{r}) & \text{(C.19a)} \\ \boldsymbol{A}(\boldsymbol{r}) = \left(\oint_S G_i(\boldsymbol{r},\boldsymbol{s}')\boldsymbol{h}_i(\boldsymbol{s}')d\boldsymbol{s}'\right) + \boldsymbol{A}_i^{\text{ext}}(\boldsymbol{r}) & \text{(C.19b)} \end{cases}$$

where $\boldsymbol{h}_i$ and σ_i are respectively the surface current density and the surface charge density in medium i. Thus, contrary to the quasistatic case, the current (resp. charge) takes different values inside and outside the boundary which, in a sense, makes them nonphysical. Nevertheless, as we showed in section 2.3.2.5, the far-field optical properties are controlled by the outer current and charge densities (index 2 in our notations). Like in the QS case, the latter equations need to be

completed with the boundary conditions 2.3. Using equations 2.3 and C.2 (and with some effort), we obtain (in compact notation):

$$\begin{cases} G_1\sigma_1 - G_2\sigma_2 = \phi_2^{\text{ext}} - \phi_1^{\text{ext}} & \text{(C.20a)} \\ G_1\boldsymbol{h}_1 - G_2\boldsymbol{h}_2 = \boldsymbol{A}_2^{\text{ext}} - \boldsymbol{A}_1^{\text{ext}} & \text{(C.20b)} \\ H_1\boldsymbol{h}_1 - H_2\boldsymbol{h}_2 = ik\boldsymbol{n}(G_1\epsilon_1\sigma_1 - G_2\epsilon_2\sigma_2) + \boldsymbol{\alpha} & \text{(C.20c)} \\ H_1\epsilon_1\sigma_1 - H_2\epsilon_2\sigma_2 = ik\boldsymbol{n}.(G_1\epsilon_1\boldsymbol{h}_1 - G_2\epsilon_2\boldsymbol{h}_2) + D^{\text{ext}} & \text{(C.20d)} \end{cases}$$

where we introduced:

- The normal derivatives of the Green functions H_i defined as:

$$H_{1/2}(\boldsymbol{s},\boldsymbol{s}') = \boldsymbol{n}.\boldsymbol{\nabla}G_{1/2}(\boldsymbol{s},\boldsymbol{s}') \pm 2\pi\delta(\boldsymbol{s}-\boldsymbol{s}') \tag{C.21}$$

  Using distribution theory and a reasonable approximation, one can show (see appendix A of [170] for a complete derivation) that for $\boldsymbol{s} \neq \boldsymbol{s}'$, we have:

$$\boldsymbol{n}.\boldsymbol{\nabla}G_i(\boldsymbol{s},\boldsymbol{s}') = -\frac{\boldsymbol{n}.(\boldsymbol{s}-\boldsymbol{s}')}{|\boldsymbol{s}-\boldsymbol{s}'|^3}\left(ik_i|\boldsymbol{s}-\boldsymbol{s}'|-1\right)e^{ik_i|\boldsymbol{r}-\boldsymbol{r}'|} \tag{C.22}$$

- The two quantities $\boldsymbol{\alpha}$ and D^{ext} defined as:

$$\begin{cases} \boldsymbol{\alpha} = (\boldsymbol{n}.\boldsymbol{\nabla})(\boldsymbol{A}_2^{\text{ext}} - \boldsymbol{A}_1^{\text{ext}}) + ik\boldsymbol{n}(\epsilon_1\phi_1^{\text{ext}} - \epsilon_2\phi_2^{\text{ext}}) & \text{(C.23a)} \\ D^{\text{ext}} = \boldsymbol{n}.\left(\epsilon_1(ik\boldsymbol{A}_1^{\text{ext}} - \boldsymbol{\nabla}\phi_1^{\text{ext}}) - \epsilon_2(ik\boldsymbol{A}_2^{\text{ext}} - \boldsymbol{\nabla}\phi_2^{\text{ext}})\right) & \text{(C.23b)} \end{cases}$$

The set of boundary integral equations (C.20) are the retarded counterpart (C.10) and possess eight unknowns $h_1^x, h_1^y, h_1^z, h_2^x, h_2^y, h_2^z, \sigma_1$ and σ_2. They can be resolved by matrix inversion which gives (see Appendix A.3 of [43] for a complete derivation):

$$\begin{cases} \sigma_2 = G_2^{-1}\Sigma^{-1}(D^{\text{ext}} + i\omega\boldsymbol{n}(L_1 - L_2)(\Sigma_1^{-1} - \Sigma_2^{-1})\boldsymbol{\alpha}) & \text{(C.24a)} \\ \sigma_1 = G_1^{-1}(G_2\sigma_2 + \phi_2^{\text{ext}} - \phi_1^{\text{ext}}) & \text{(C.24b)} \\ \boldsymbol{h}_2 = G_2^{-1}(\Sigma_1^{-1} - \Sigma_2^{-1})(i\omega\boldsymbol{n}(L_1 - L_2)G_2\sigma_2 + \boldsymbol{\alpha}) & \text{(C.24c)} \\ \boldsymbol{h}_1 = G_1^{-1}(G_2\boldsymbol{h}_2 + \boldsymbol{A}_2^{\text{ext}} - \boldsymbol{A}_1^{\text{ext}}) & \text{(C.24d)} \end{cases}$$

where the matrices $\Sigma_{1,2}$, $L_{1,2}$ and Σ have been introduced and defined as:

$$\begin{cases} \Sigma_{1,2} = H_{1,2}G_{1,2}^{-1} & \text{(C.25a)} \\ L_{1,2} = G_{1,2}\epsilon_{1,2}G_{1,2}^{-1} & \text{(C.25b)} \\ \Sigma = \Sigma_1 L_1 - \Sigma_2 L_2 + \omega^2\boldsymbol{n}.(L_1 - L_2)(\Sigma_1^{-1} - \Sigma_2^{-1})\boldsymbol{n}(L_1 - L_2) & \text{(C.25c)} \end{cases}$$

Of course, in the limit $k \to 0$, this formalism boils down to the QS case.

C.2 The boundary element methods and its implementation in the MNPBEM toolbox

C.2.1 Discretization procedure

The BEM consists in solving equations (C.13) or (C.20) using a discretization procedure. The MNPBEM code uses a *collocation method* in order to discretize the BIE. It consists in dividing the surface of the particle in N small polygons (usually triangles) as shown on figure C.1. We therefore move from a continuous surface to a collection of polygons $\{P_i\}_{i\in[\![1,N]\!]}$. The value of all the fields is then discrete and considered as constant over each polygon of the mesh. We therefore move from a continuous representation of the fields (e.g. $F(\boldsymbol{s},\boldsymbol{s}')$) to $N \times N$ matrices (e.g. F_{ij}). Other

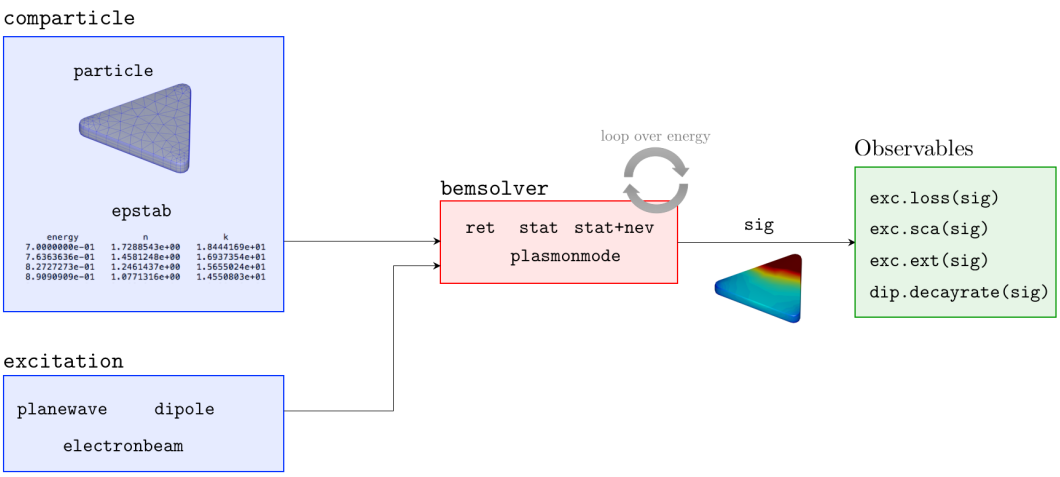

Figure C.2: *Schematics showing the simulation procedure in the* ***MNPBEM*** *toolbox. The inputs are represented in blue, the solver in red and the outputs in green.*

types of discretization procedures exist such as the Galerkine methods which use an interpolation to define the fields over the mesh.

For instance, the discrete version of (C.13) reads [162, 158]:

$$\Lambda\sigma_i = \sum_j F_{ij}\sigma_j + \left(\frac{\partial\phi^{\text{ext}}}{\partial\boldsymbol{n}}\right)_i \tag{C.26}$$

Solving this BIE and obtaining $\{\sigma_i\}_{i\in[\![1,N]\!]}$ then simply requires a $N\times N$ matrix inversion:

$$\sigma_i = \sum_j (\Lambda\mathbb{1}_{ij} + F_{ij})^{-1}\left(\frac{\partial\phi^{\text{ext}}}{\partial\boldsymbol{n}}\right)_j \tag{C.27}$$

C.2.2 The MNPBEM simulation scheme

We represented on figure C.2 the simulation scheme of the toolbox. The inputs are a dielectric constant table (`epstab` object), the ensemble of polygons (`particle`) and the excitation which can be either a planewave (`planewave` object), a dipole (`dipole` object) or an electron beam (`electronbeam` object). The particle and the dielectric table form together a so-called `comparticle` object which is the essence of the code as it enables a simpler definition of the Green functions. These inputs are sent to the solver using a matrix inversion as described earlier. Each of the resolution is obviously done at a certain energy ω as the equation presented are defined in the spectral domain. Therefore, if one wants to calculate e.g. an EELS spectrum with n points, the solver is called n times; in other words, the spectrum requires n matrix inversions to be calculated. Four different solvers exists in the toolbox:

- The `bemsolver(ret)` which computes the BIEs in the retarded case i.e. solving equations (C.20).
- The `bemsolver(stat)` which computes the BIE in the quasistatic case i.e. solving equation C.13.
- The `plasmonmode(nev=k)` which computes the k first eigenmodes i.e. solving equation C.15. More precisely, it computes the right eigenvectors σ, the left eigenvectors τ and the eigenvalues λ as described in section 2.2.2.3.

- The `bemsolver(stat,nev=k)` which computes the quasistatic response using an eigendecomposition with k vector in the basis. Contrary to the two first ones, this solver performs only one matrix inversion (to compute the eigenbasis) for all the entire set of energy points.

The result of the solver is a `sig` object which corresponds to σ in the quasistatic case or $(\sigma_1, \sigma_2, \boldsymbol{h}_1, \boldsymbol{h}_2)$ in the retarded case. This object enables us to calculate straightforwardly:

- The scattering or the extinction cross sections (for `dipole` and `planewave` excitations) respectively using the `sca(sig)` or `ext(sig)` functions.
- The electron energy loss probability (for the `electronbeam` excitation) using the `loss(sig)` function. This function is essential for this thesis and interested readers can refer to [410] for an extended discussion.
- The ELMDOS enhancement factor, thanks to equation (2.45), using the `decayrate(sig)` function.
- The cathodoluminescence emission probability by propagating the field induced by `sig` to the far-field and computing equation (2.75). The far-field is defined, *ad-hoc*, as a sphere of radius $20 \times L$ where L is the typical length of the particle. The underlying assumption is that all the photons are detected which is not true as we saw is section 2.3.2.5. In order to take into account the form of the CL collection mirror, one needs to modify the shape of the far-field. It has been partially done e.g. in [51].

C.2.3 Performances and validity domain of the method

The principal strength of the BEM and particularly the `MNPBEM` code is its efficiency. The main reason of this efficiency is that the code is based on the computation of the potentials rather than the fields which reduces the size of the matrices from $3N \times 3N$ to $N \times N$. In [158] (page 124), one can find a comparison between the computation time of a DDA, a FDTD and this BEM code on the same geometry and on the same machine. One can see that BEM, is by far, much faster than the orther methods. Our group possesses a computer cluster running under the Rocks Clusters distribution. The computer has 40 nodes with 96Gb of ram each. Our biggest calculations (typically 10000 polygons for 100-200 energy points) took approximately one week on our best computation node (CPU 2 Xeon E5-2680v2 2.8GHz, 10 cores, 64 Gb). The last version of the toolbox `MNPBEM17` released in 2017 use a combination hierarchical matrices and iterative solver to enable bigger and faster computations [375]. We have not tested the toolbox yet but performances presented in the paper are impressive.

As it is clear from the formalism shown so far, the BEM does not include non-local effects i.e. in our calculation we always assumed the relation $\epsilon(\boldsymbol{r}, \boldsymbol{r}', \omega) = \epsilon(\boldsymbol{r}, \omega)\delta(\boldsymbol{r} - \boldsymbol{r}')$ to be true. However, non-locality can have a strong influence (energy blue-shift of LSPs for example) where one of the dimension of the problem becomes smaller than typically 1 nm [468, 469, 470]. Such a situation would correspond to e.g. dimers with narrow gaps or particles with small thicknesses. In 2015, Hohenester proposed a quantum-corrected model (QCM) to the `MNPBEM` code [471] in order to take into account the non-locality arising from quantum tunneling in a dimer gap. It has been later employed to solve a long date problem on nano-cube dimers [364, 365, 472, 473]. However, we did not use any QCM in this thesis and restricted our simulations to the local domain.

Although extremely powerful and efficient, the application of BEM to simulate actual problem can lead to some difficulties that we will discuss throughout this thesis:

- In some particular situations, the meshing of surfaces can have dramatic consequences on the convergence of the simulations. The meshing procedure of the toolbox essentially relies on the `mesh2d` code [474] which is extremely efficient for two dimensional tessellation. The extension to the third dimension is done "brute force" and some subtle geometries require refinements e.g. the core-rod structure discussed in chapter 7. To overcome this difficulty, we developed an approach based on b-spline interpolation as shown on C.3. In this example,

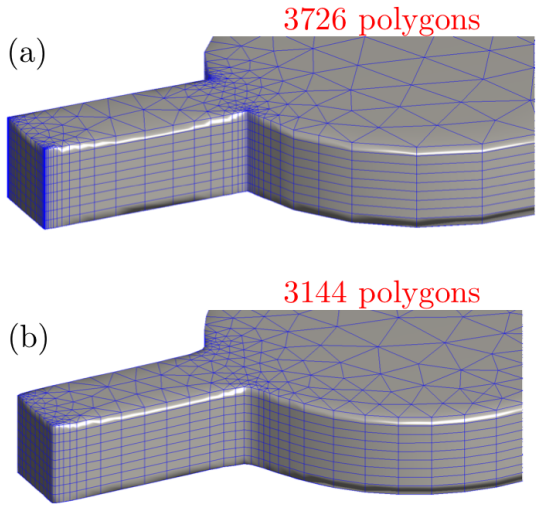

Figure C.3: *(a) Meshing of a core-rod structure realized with the* ***MNPBEM*** *standard code. (b) Meshing of the same core-rod structure realized with our b-spline approach.*

with the standard meshing of MNPBEM, the code did not converge. On the contrary, our b-spline interpolation scheme gives good results even for a coarser meshing.

- For sufficiently small nano-particles, the solver `bemsolver(stat,nev=k)` is particularly useful as: (i) it enables the interpretation of spectra in terms of plasmon modes and (ii) it dramatically speeds-up the computations. However, some pathological cases, such as the nano-cube, jeopardize this approach even for small particle sizes.

- The common denominator of all the experiments done in electron microscopy or optics is the presence of a substrate sustaining the nano-particle. In most of the cases, the substrate can, in first approximation, be neglected in the simulations. However, as shown in details in chapter 5, particular geometries (again, such as the nano-cube) are dramatically determined by the presence of this substrate. Although, the toolbox contains some layer and substrate modules [475], it still fails in efficiently computing these types of situations. An alternative route is explored in [376].

Appendix D

Additional calculations for chapter 3

D.1 Spectral representation of the electrostatic susceptibility

In this section, we derive the spectral (or Lehman) representation of the electrostatic susceptibility. First of all, we decompose χ as:

$$\chi = \chi^+ + \chi^- \tag{D.1}$$

where the two terms reads:

$$\begin{cases} \chi^+ = -\dfrac{i}{\hbar}\theta(t-t')\left\langle \mathfrak{n}(\boldsymbol{r},t)\mathfrak{n}(\boldsymbol{r}',t')\right\rangle_0 & \text{(D.2a)} \\ \chi^- = -\dfrac{i}{\hbar}\theta(t-t')\left\langle \mathfrak{n}(\boldsymbol{r}',t')\mathfrak{n}(\boldsymbol{r},t)\right\rangle_0 & \text{(D.2b)} \end{cases}$$

Defining the electron field operator $\Psi(\boldsymbol{r},t)$, we can easily re-write (D.2)(a) as:

$$\chi^+ = -\frac{i}{Z\hbar}\theta(t-t')\sum_n e^{-\beta\hbar\omega_n}\left\langle n\right| \Psi^\dagger(\boldsymbol{r},t)\Psi(\boldsymbol{r},t)\Psi^\dagger(\boldsymbol{r}',t')\Psi(\boldsymbol{r}',t')\left|n\right\rangle \tag{D.3}$$

where Z is the partition function and $\hbar\omega_n$ is the energy of the state $|n\rangle$. The unperturbed Hamiltonian H_0 being time-independent, one can write $\Psi(\boldsymbol{r},t) = e^{iH_0t/\hbar}\Psi(\boldsymbol{r})e^{-iH_0t/\hbar}$; the latter leads to:

$$\chi^+ = -\frac{i}{Z\hbar}\theta(t-t')\sum_n e^{-\beta\hbar\omega_n}\left\langle n\right| e^{i\omega_0 t}\Psi^\dagger(\boldsymbol{r})\Psi(\boldsymbol{r})e^{-iH_0t/\hbar}e^{iH_0t'/\hbar}\Psi^\dagger(\boldsymbol{r}')\Psi(\boldsymbol{r}')e^{-i\omega_0 t'}\left|n\right\rangle \tag{D.4}$$

By noting that $\mathfrak{n}(\boldsymbol{r}) = \Psi^\dagger(\boldsymbol{r})\Psi(\boldsymbol{r})$ and inserting the closure relation $\sum_{n'}|n'\rangle\langle n'| = \mathbb{1}$, the previous equation may be written:

$$\chi^+ = -\frac{i}{Z\hbar}\theta(t-t')\sum_{n,n'} e^{-\beta\hbar\omega_n}\left\langle n\right| e^{i\omega_n t}\mathfrak{n}(\boldsymbol{r})\left|n'\right\rangle e^{-i\omega_{n'}t}e^{i\omega_{n'}t'}\left\langle n'\right|\mathfrak{n}(\boldsymbol{r}')e^{-i\omega_n t'}\left|n\right\rangle \tag{D.5}$$

Consequently, in the temporal domain χ^+ reads:

$$\chi^+(\boldsymbol{r},\boldsymbol{r}',t-t') = -\frac{i}{Z\hbar}\theta(t-t')\sum_{n,n'} e^{-\beta\hbar\omega_n}e^{-i(\omega_n-\omega_{n'})(t-t')}\left\langle n\right|\mathfrak{n}(\boldsymbol{r})\left|n'\right\rangle\left\langle n'\right|\mathfrak{n}(\boldsymbol{r}')\left|n\right\rangle \tag{D.6}$$

The same development for χ^- leads to:

$$\chi^-(\boldsymbol{r},\boldsymbol{r}',t-t') = -\frac{i}{Z\hbar}\theta(t-t')\sum_{n,n'} e^{-\beta\hbar\omega_n}e^{-i(\omega_{n'}-\omega_n)(t-t')}\left\langle n\right|\mathfrak{n}(\boldsymbol{r}')\left|n'\right\rangle\left\langle n'\right|\mathfrak{n}(\boldsymbol{r})\left|n\right\rangle \tag{D.7}$$

Combining the two latter equations, expressing it in terms of $\tau = t - t'$ and inserting the Fourier transform of the Heaviside function, we get:

$$\chi(\boldsymbol{r},\boldsymbol{r}',\tau) = -\frac{i}{Z\hbar}\int_0^\infty d\tau e^{i(\omega+i\eta)\tau}\sum_{n,n'} e^{-\beta\hbar\omega_n}\Big(\langle n|\,\mathfrak{n}(\boldsymbol{r})\,|n'\rangle\,\langle n'|\,\mathfrak{n}(\boldsymbol{r}')\,|n\rangle\, e^{-i(\omega_n-\omega_{n'})\tau} + \langle n|\,\mathfrak{n}(\boldsymbol{r}')\,|n'\rangle\,\langle n'|\,\mathfrak{n}(\boldsymbol{r})\,|n\rangle\, e^{i(\omega_n-\omega_{n'})\tau}\Big) \tag{D.8}$$

Performing the integral then gives:

$$\chi(\boldsymbol{r},\boldsymbol{r}',\omega) = \frac{1}{Z\hbar}\sum_{n,n'}\left(\frac{\langle n|\,\mathfrak{n}(\boldsymbol{r})\,|n'\rangle\,\langle n'|\,\mathfrak{n}(\boldsymbol{r}')\,|n\rangle}{\omega+\omega_n-\omega_{n'}+i\eta} + \frac{\langle n|\,\mathfrak{n}(\boldsymbol{r}')\,|n'\rangle\,\langle n'|\,\mathfrak{n}(\boldsymbol{r})\,|n\rangle}{\omega-\omega_n+\omega_{n'}+i\eta}\right)e^{-\beta\hbar\omega_n} \tag{D.9}$$

Changing the summation index between the two terms of the sum, we get:

$$\chi(\boldsymbol{r},\boldsymbol{r}',\omega) = \frac{1}{Z\hbar}\sum_{n,n'}\frac{\langle n|\,\mathfrak{n}(\boldsymbol{r})\,|n'\rangle\,\langle n'|\,\mathfrak{n}(\boldsymbol{r}')\,|n\rangle}{\omega+\omega_n-\omega_{n'}+i\eta}\left(e^{-\beta\hbar\omega_n}+e^{-\beta\hbar\omega_{n'}}\right) \tag{D.10}$$

Besides, we have the following relation between distributions:

$$\frac{1}{\omega+i\eta}\xrightarrow[\eta\to 0]{}\mathcal{P}\left(\frac{1}{\omega}\right) - i\pi\delta(\omega) \tag{D.11}$$

where we recall that $\mathcal{P}$ denotes the Cauchy principal value. We can insert the latter relation in (D.10) and since $\mathfrak{n}$ has real eigenvalues, we can trivially take the imaginary part and get:

$$\mathrm{Im}\left\{\chi(\boldsymbol{r},\boldsymbol{r}',\omega)\right\} = -\frac{\pi}{Z\hbar}\sum_{n,n'}\langle n|\,\mathfrak{n}(\boldsymbol{r})\,|n'\rangle\,\langle n'|\,\mathfrak{n}(\boldsymbol{r}')\,|n\rangle\left(e^{-\beta\hbar\omega_n}+e^{-\beta\hbar\omega_{n'}}\right)\delta\left(\omega+\omega_n-\omega_{n'}\right) \tag{D.12}$$

which can be factorized as:

$$\mathrm{Im}\left\{\chi(\boldsymbol{r},\boldsymbol{r}',\omega)\right\} = -\frac{\pi}{Z\hbar}\sum_{n,n'}\langle n|\,\mathfrak{n}(\boldsymbol{r})\,|n'\rangle\,\langle n'|\,\mathfrak{n}(\boldsymbol{r}')\,|n\rangle\, e^{-\beta\hbar\omega_n}\left(1+e^{-\beta\hbar\omega}\right)\delta\left(\omega+\omega_n-\omega_{n'}\right) \tag{D.13}$$

D.2 Reciprocity theorem and symmetry properties of the Green dyadic

The reciprocity theorem corresponds to the following condition:

$$\mathscr{S}\left(G^i_j(\boldsymbol{r}',\boldsymbol{r},\omega)\right) = G^i_j(\boldsymbol{r}',\boldsymbol{r},\omega) \tag{D.14}$$

In this section, we examine the symmetry of the four tensors involved in the definition of G (3.84) by the application of $\mathscr{S}$. We first remind that (at least in the three gauges considered in 3.2.4), the vacuum photon propagators satisfy the property:

$$\mathrm{D}^{i0} = 0 \tag{D.15}$$

In other words, the temporal and the spatial components of the EM fields are not coupled in vacuum. Moreover, we recall the definition of the retarded screened interaction (3.70):

$$\mathcal{D}^\beta_\alpha(\boldsymbol{r}',\boldsymbol{r},\omega) = \int d\boldsymbol{r}_1 d\boldsymbol{r}_2\,\mathrm{D}^\beta_\mu(\boldsymbol{r}',\boldsymbol{r}_2)\,\chi^\mu_\nu(\boldsymbol{r}_2,\boldsymbol{r}_1,\omega)\,\mathrm{D}^\nu_\alpha(\boldsymbol{r}_1,\boldsymbol{r}) \tag{D.16}$$

Let's consider the first term of equation (3.84) and examine its symmetry. The relation (D.15) leads to:

$$\mathcal{D}^0_0(\boldsymbol{r},\boldsymbol{r}') = \int d\boldsymbol{r}_1 d\boldsymbol{r}_2\,\mathrm{D}^0_0(\boldsymbol{r},\boldsymbol{r}_2)\,\chi^0_0(\boldsymbol{r}_2,\boldsymbol{r}_1)\,\mathrm{D}^0_0(\boldsymbol{r}_1,\boldsymbol{r}') \tag{D.17}$$

The vacuum photon propagators can be straightforwardly reversed as $\mathrm{D}_0^0(\boldsymbol{r},\boldsymbol{r}_2) = \mathrm{D}_0^0(\boldsymbol{r}_2,\boldsymbol{r})$ and $\mathrm{D}_0^0(\boldsymbol{r}_1,\boldsymbol{r}') = D_0^0(\boldsymbol{r}',\boldsymbol{r}_1)$. From equation (3.64), the electron part can then be written:

$$\chi_0^0(\boldsymbol{r}_2,\boldsymbol{r}_1,\omega) = \frac{2}{\hbar}\sum_n \langle 0|\,\mathrm{J}^0(\boldsymbol{r}_2)\,|n\rangle\,\langle n|\,\mathrm{J}_0(\boldsymbol{r}_1)\,|0\rangle\,\Theta(\omega+\omega_n-\omega_0) \tag{D.18}$$

where $\Theta(\omega) = \frac{1}{\omega+i\eta}$. One can then see that $\chi_0^0(\boldsymbol{r}_2,\boldsymbol{r}_1) = (\chi_0^0(\boldsymbol{r}_1,\boldsymbol{r}_2))^\dagger$ because the lowering and raising of 0 indexes won't bring any sign changes. Finally, we notice that $\nabla^j\nabla'_i = \nabla'^i\nabla_j$ because the raising of i and the lowering of j will give both a minus sign. Indeed, $\nabla^j = \delta_i^j g^{ij}\nabla_j = -\nabla_j$ because $g^{jj} = -1$ by definition of the metric we have chosen. Thus, we finally have:

$$\mathscr{S}\left(\nabla'^i\nabla_j\mathcal{D}_0^0(\boldsymbol{r}',\boldsymbol{r})\right) = \nabla'^i\nabla_j\mathcal{D}_0^0(\boldsymbol{r}',\boldsymbol{r}) \tag{D.19}$$

The same arguments leads to[1]:

$$\mathscr{S}\left(\mathcal{D}_j^i(\boldsymbol{r}',\boldsymbol{r})\right) = \mathcal{D}_j^i(\boldsymbol{r}',\boldsymbol{r}) \tag{D.20}$$

We finally need to look at the last part of G i.e.:

$$M_j^i(\boldsymbol{r}',\boldsymbol{r}) \equiv \partial_j\mathcal{D}_0^i(\boldsymbol{r}',\boldsymbol{r}) + \partial'^i\mathcal{D}_j^0(\boldsymbol{r}',\boldsymbol{r}) \tag{D.21}$$

We thus calculate:

$$\begin{aligned}\mathscr{S}\left(M_j^i(\boldsymbol{r}',\boldsymbol{r})\right) &= \nabla'_i\mathcal{D}_0^j(\boldsymbol{r},\boldsymbol{r}') + \nabla^j\mathcal{D}_i^0(\boldsymbol{r},\boldsymbol{r}') &\text{(D.22)}\\ &= -\nabla'^i\mathcal{D}_0^j(\boldsymbol{r},\boldsymbol{r}') - \nabla_j\mathcal{D}_i^0(\boldsymbol{r},\boldsymbol{r}') &\text{(D.23)}\end{aligned}$$

Moreover, the first photon propagator reads:

$$\mathcal{D}_0^j(\boldsymbol{r},\boldsymbol{r}') = \int d\boldsymbol{r}_1 d\boldsymbol{r}_2 \mathrm{D}_0^0(\boldsymbol{r},\boldsymbol{r}_2)\,\chi_a^0(\boldsymbol{r}_2,\boldsymbol{r}_1)\,\mathrm{D}_a^j(\boldsymbol{r}_1,\boldsymbol{r}') \tag{D.24}$$

where we used (D.15). We can again reverse the vacuum photon propagators which are obviously symmetric. However, the susceptibility term is *antisymmetric*. Indeed, it corresponds to a charge-current correlator and lowering the time part will keep the sign unchanged, while raising the spatial part will give a minus sign. Therefore:

$$\mathcal{D}_0^j(\boldsymbol{r},\boldsymbol{r}') = -\mathcal{D}_j^0(\boldsymbol{r}',\boldsymbol{r}) \tag{D.25}$$

And similarly:

$$\mathcal{D}_i^0(\boldsymbol{r},\boldsymbol{r}') = -\mathcal{D}_0^i(\boldsymbol{r}',\boldsymbol{r}) \tag{D.26}$$

We therefore finally have:

$$\begin{aligned}\mathscr{S}\left(M_j^i(\boldsymbol{r}',\boldsymbol{r})\right) &= -\nabla'^i\mathcal{D}_j^0(\boldsymbol{r}',\boldsymbol{r}) - \nabla_j\mathcal{D}_0^i(\boldsymbol{r}',\boldsymbol{r}) &\text{(D.27)}\\ &= -M_j^i(\boldsymbol{r}',\boldsymbol{r}) &\text{(D.28)}\end{aligned}$$

The M tensor is therefore antisymmetric. To guarantee the symmetry of G, we thus have:

$$M_j^i(\boldsymbol{r}',\boldsymbol{r}) = 0 \tag{D.29}$$

Therefore, in a *reciprocal medium*, the Green dyadic reads:

$$G_j^i(\boldsymbol{r}',\boldsymbol{r},\omega) = -\frac{1}{4\pi\omega^2}\nabla'^i\nabla_j\,\mathcal{D}_0^0(\boldsymbol{r}',\boldsymbol{r},\omega) + \frac{1}{4\pi c^2}\,\mathcal{D}_j^i(\boldsymbol{r}',\boldsymbol{r},\omega) \tag{D.30}$$

where the first term is a charge-charge correlator while the second term is a current-current correlator.

[1] The only difference in this case is that the raising and lowering of indices in the electron part will give two minus signs which cancel out.

D.3 Quasi-static density matrix for plasmonic excitation

As we saw in the introductory chapter, the classical and quasi-static screened interaction associated with a plasmon field can be expanded over the set of modes:

$$\mathrm{Im}\{-W\left(\boldsymbol{x},\boldsymbol{x}\,',\omega\right)\} = \sum_m \mathrm{Im}\{-g_m\left(\omega\right)\}\ \phi_m\left(\boldsymbol{x}\right)\phi_m^*\left(\boldsymbol{x}'\right) \tag{D.31}$$

Since the convergence and collection angles are small (few milliradians), one can efficiently describe the electron wavefunctions within the *the paraxial approximation* [19]. The initial density matrix then reads:

$$\varrho_i\left(\boldsymbol{x},\boldsymbol{x}'\right) = \frac{1}{L}\psi_{i,\perp}(\boldsymbol{x}_\perp)\psi_{i,\perp}^*(\boldsymbol{x}'_\perp)e^{ip_{i,z}x_z}e^{-ip_{i,z}x'_z} \tag{D.32}$$

where L is the quantization length of the electron. Plugging the two latter equations in (3.162), we get:

$$\begin{aligned}\varrho_f\left(\boldsymbol{k}_\perp,\boldsymbol{k}'_\perp\right) = \frac{4\pi^2}{L\hbar^2v^2}\sum_m \mathrm{Im}\{-g_m\left(\omega\right)\}\ \int d\boldsymbol{x}\ d\boldsymbol{x}'\phi_m\left(\boldsymbol{x}\right)\phi_m^*\left(\boldsymbol{x}'\right)\psi_{i,\perp}(\boldsymbol{x}_\perp)\psi_{i,\perp}^*(\boldsymbol{x}'_\perp)\\ e^{-i(p_{f,z}-p_{i,z})x_z}\ e^{i(p_{f,z}-p_{i,z})x'_z}\ e^{-\boldsymbol{k}_\perp.\boldsymbol{x}}\ e^{\boldsymbol{k}'_\perp.\boldsymbol{x}'}\end{aligned} \tag{D.33}$$

Providing that $p_{f,z} - p_{i,z} \approx q$ [19], the integration over x_z and x'_z gives:

$$\begin{aligned}\varrho_f\left(\boldsymbol{k}_\perp,\boldsymbol{k}'_\perp\right) = \frac{4\pi^2}{L\hbar^2v^2}\sum_m \mathrm{Im}\{-g_m\left(\omega\right)\}\ \int d\boldsymbol{x}_\perp\ d\boldsymbol{x}'_\perp\phi_m\left(\boldsymbol{x}_\perp,q\right)\phi_m^*\left(\boldsymbol{x}'_\perp,-q\right)\\ \times\psi_{i,\perp}(\boldsymbol{x}_\perp)\psi_{i,\perp}^*(\boldsymbol{x}'_\perp)e^{-\boldsymbol{k}_\perp.\boldsymbol{x}}\ e^{\boldsymbol{k}'_\perp.\boldsymbol{x}'}\end{aligned} \tag{D.34}$$

which can be finally written as:

$$\varrho_f\left(\boldsymbol{k}_\perp,\boldsymbol{k}_\perp\,'\right) = \frac{4\pi^2}{L\hbar^2v^2}\sum_m \mathrm{Im}\{-g_m\left(\omega\right)\}\ \left[\phi_m\left(\boldsymbol{k}_\perp,q\right)*\psi_{i,\perp}(\boldsymbol{k}_\perp)\right]\left[\phi_m\left(\boldsymbol{k}\,'_\perp,-q\right)*\psi_{i,\perp}(\boldsymbol{k}\,'_\perp)\right]^* \tag{D.35}$$

This equation can be used to model phase-shaped experiment on plasmon with the density matrix formalism.

Appendix E

Optical chirality and its connection with the helicity of the electromagnetic field

It is known from the 19th century that circularly polarized light can probe the chirality of molecules e.g. circular dichroism [476] or Raman optical activity [477]. These far field effects are generally encompassed by the term *optical activity*. At first glance, these results suggest that the EM field should also be a chiral object and that a good measurement of this chirality would be the degree of circular polarization. For this reason circularly polarized light would be the EM fields of maximum chirality.

Recent works have however shown that it is, in fact, way more complicated. The pioneering work in this matter is the one of Tang and Cohen [261, 262]. They understood that the notions of chirality and polarization need to be considered separately, although chirality does depend on polarization. They phenomenologically defined the chirality as a measurement of "*the asymmetry in the rates of excitation between a small chiral molecule and its mirror image [...] in electromagnetic fields with arbitrary spatial dependence*". Such a phenomenological definition should not be puzzling. In literature, the radiative decay rate for a point dipole often serves as a *definition* of the EMLDOS. Based on the work of Lipkin [478], they proposed the following definition of the *optical chirality* $\mathscr{C}$:

$$\mathscr{C}(\boldsymbol{r},t) = \frac{1}{8\pi}\left(\boldsymbol{E}.\boldsymbol{\nabla}\times\boldsymbol{E} + \boldsymbol{B}.\boldsymbol{\nabla}\times\boldsymbol{B}\right) \tag{E.1}$$

which for monochromatic waves simplifies as:

$$\boxed{\mathscr{C}(\boldsymbol{r},\omega) = -\frac{1}{8\pi}\mathrm{Im}\left\{\boldsymbol{E}^*(\boldsymbol{r},\omega).\boldsymbol{B}(\boldsymbol{r},\omega)\right\}} \tag{E.2}$$

A major consequence of this definition is that some EM fields can display higher chirality than circularly polarized light. This phenomenon is called *super-chirality* and is now a hot field of research is nano-optics as surface plasmons appear to be a promising candidate to produce such fields [267, 268, 269]. Let's however emphasize that, quite counter-intuitively, there is no simple relation between the geometrical chirality of the plasmonic nano-particle and the optical chirality of the EM fields produced by the SPs [479]; for example Zheludev and collaborators showed that achiral (in the geometrical sense) metamaterials can produced chiral EM fields [480].

At first glance the definition (E.2) for the optical chirality seems to come out of the blue. However, it is perfectly justified and relies on a fundamental invariance of the EM field. The purpose of this appendix is to briefly justify this definition of the optical chirality. We will follow the demonstration of Cameron [481, 482] and Bliokh [483] which is based on a dual formulation of the EM Lagrangian. Let's highlight that there is no original result in this appendix and we simply give some elements of their demonstration.

E.1 Dual electromagnetism and electric-magnetic symmetry

In this appendix, we consider the EM field in absence of source $J^\nu = 0$. In this case, we see that the Maxwell equations are invariant under the so-called duality rotation:

$$\begin{cases} \boldsymbol{E} \longrightarrow \boldsymbol{E}' = \cos(\theta)\boldsymbol{E} + \sin(\theta)\boldsymbol{B} & \text{(E.3a)} \\ \boldsymbol{B} \longrightarrow \boldsymbol{B}' = \cos(\theta)\boldsymbol{B} - \sin(\theta)\boldsymbol{E} & \text{(E.3b)} \end{cases}$$

where the angle θ is a Lorentz scalar. For $\theta = \pi/2$, the duality rotation corresponds to the transformation (3.24). As emphasized by Berry [260], this rotational invariance of the Maxwell equations shows that in the source-free case, the electric and magnetic fields play equivalent roles and therefore need to be treated on the same level. However, although the Maxwell equations present this rotational invariance, the standard Lagrangian density 3.27 does not. It means that the Noether theorem fatally miss fundamental symmetries of the field when this Lagrangian is used. To fix this issue, Cameron and Barnett [481] as well as Biokh, Bekshaev and Nori [483] proposed to introduce the *electric-magnetic* Lagrangian density:

$$\mathcal{L} = -\frac{1}{8}\left(\partial_\alpha A_\beta - \partial_\beta A_\alpha\right)\left(\partial^\alpha A^\beta - \partial^\beta A^\alpha\right) - \frac{1}{8}\left(\partial_\alpha C_\beta - \partial_\beta C_\alpha\right)\left(\partial^\alpha C^\beta - \partial^\beta C^\alpha\right) \tag{E.4}$$

where C is the electric four-pseudopotential so that $\boldsymbol{\nabla} \times \boldsymbol{C} = -\boldsymbol{E}$. The trick in this formalism is to treat $F^{\mu\nu}$ and its Hodge dual ${}^\star F^{\mu\nu} \equiv G^{\mu\nu}$ as *independent* quantities. In this context the Lagrangian density (E.4) can be simply re-written as:

$$\mathcal{L} = -\frac{1}{8}\left(F^{\mu\nu}F_{\mu\nu} + G^{\mu\nu}G_{\mu\nu}\right) \tag{E.5}$$

This new Lagrangian density is clearly invariant by (E.10) and dual-symmetric. Obviously, the application of the Euler-Lagrange equations on this new Lagrangian density leads to the same laws of electromagnetism but the Maxwell equations now reads:

$$\begin{cases} \partial_\mu F^{\mu\nu} = 0 & \text{(E.6a)} \\ \partial_\mu G^{\mu\nu} = 0 & \text{(E.6b)} \end{cases}$$

One can now appreciate the symmetry of the equations in the frame of dual version of electromagnetism. Let's again highlight that this is a consequence of the absence of sources which place electric and magnetic fields on the same level.

E.2 Noether theorem, conservation law for the optical helicity

As emphasized in [481, 483], the interest of introducing this dual-symmetric Lagrangian density lies in the fact that it dramatically simplifies the application of the Noether theorem. For example, it is well known that the space-time translation invariance of the source-free Maxwell equations leads to the conservation of the stress-energy tensor $T^{\mu\nu}$:

$$\partial_\nu T^{\mu\nu} = 0 \tag{E.7}$$

where we defined:

$$T^{\mu\nu} = \frac{1}{2}\left(F^\mu_\alpha F^{\alpha\nu} + G^\mu_\alpha G^{\alpha\nu}\right) \tag{E.8}$$

The conservation law (E.7) is what is usually called the Poynting theorem [27] which, in a more usual form, reads:

$$\frac{\partial u}{\partial t} + \boldsymbol{\nabla}.\boldsymbol{S} = 0 \tag{E.9}$$

where $u = \frac{1}{8\pi}(\boldsymbol{E}^2 + \boldsymbol{E}^2)$ is the density of EM energy and $\boldsymbol{S} = \frac{c}{4\pi}(\boldsymbol{E} \times \boldsymbol{B})$ is the Poynting vector. There are several other conservation laws related to e.g. the boosts, the scale transformation or

some conformal transformations (see [483] for complete description). However, in the following, we will focus on the case of rotations which are connected to angular momentum conservation laws. To do so, let's consider an infinitesimal transformation of the potentials:

$$\begin{cases} A_\alpha \longrightarrow A'_\alpha = A_\alpha + \delta A_\alpha & \text{(E.10a)} \\ C_\alpha \longrightarrow C'_\alpha = C_\alpha + \delta C_\alpha & \text{(E.10b)} \end{cases}$$

where the transformations δA_α and δC_α respect the Euler-Lagrange equations. The resulting change $\delta\mathcal{L}$ in the Lagrangian density (E.5) is [481]:

$$\delta\mathcal{L} = \frac{\partial\mathcal{L}}{\partial(\partial_\beta A_\alpha)}\delta(\partial_\beta A_\alpha) + \frac{\partial\mathcal{L}}{\partial(\partial_\beta C_\alpha)}\delta(\partial_\beta C_\alpha) \tag{E.11a}$$

$$= \partial_\beta\left[\frac{1}{2}\left(F^{\alpha\beta}\delta A_\alpha + G^{\alpha\beta}\delta C_\alpha\right)\right] \tag{E.11b}$$

The Noether theorem then imposes $\delta\mathcal{L} = 0$. When δ is an infinitesimal rotation θ, the Noether theorem thus gives:

$$\partial_\gamma h^\gamma = 0 \tag{E.12}$$

where h^γ corresponds to:

$$h^\gamma = \frac{1}{2}\left(F^{\alpha\beta}\delta A_\alpha + G^{\alpha\beta}\delta C_\alpha\right) \tag{E.13}$$

The four-vector $h^\gamma = (h, \boldsymbol{s})$ is therefore composed of a temporal part h^0:

$$h = \frac{1}{2}\left(\boldsymbol{A}.\boldsymbol{B} - \boldsymbol{C}.\boldsymbol{E}\right) \tag{E.14}$$

corresponding to the local (optical) *helicity* of the EM field, while the spatial part reads:

$$\boldsymbol{s} = \frac{1}{2}\left(\boldsymbol{E}\times\boldsymbol{A} + \boldsymbol{B}\times\boldsymbol{C}\right) \tag{E.15}$$

corresponding to the helicity current and coinciding with the *spin density* of the EM field. The relation (E.12) is therefore the analogue for the helicity of the Poynting theorem [263] and explicitly reads:

$$\frac{1}{c}\frac{\partial h}{\partial t} + \boldsymbol{\nabla}.\boldsymbol{s} = 0 \tag{E.16}$$

One can moreover defines the total helicity contained in the field Q_h as:

$$Q_h = \iiint_{\mathbb{R}^3} h^0(\boldsymbol{r}, t)d\boldsymbol{r} \tag{E.17}$$

and one can show that the total helicity is constant in time $dQ_h/dt = 0$ in the same way as the total EM energy U is constant. This analogy is not fortuitous; in fact these quantities correspond to *Noether charges* which appear for any non-trivial symmetry. In [483], Bliokh and collaborators showed that, in the case of monochromatic field, the time average value of h, noted $\overline{h}$ is:

$$\boxed{\overline{h} = -\frac{1}{2\omega}\mathrm{Im}\left\{\boldsymbol{E}^*.\boldsymbol{B}\right\}} \tag{E.18}$$

One recognizes, up to a prefactor, the definition of the optical chirality. Thus, the optical chirality appears to be a conserved quantity of the EM field due to the invariance of the Maxwell equation by application of the dual rotation. It has therefore the same theoretical status as the energy density (which is a conserved quantity due to the invariance of the electromagnetic field with respect to the space-time translation). An extension of these developments which includes source terms can be found in [484].

Appendix F

Cathodoluminescence experiments with phase-shaped beams

In this appendix, we propose a derivation of the CL probability for a phase-shape electron in interaction with a plasmon field; these developments are based on the formalism developed in [173]. Let's highlight that this calculation only constitutes a first proposal and further checking and developments are required. As shown on schematics F.1, the CL emission is a two steps process: (1) first the electron creates a plasmon in the material and (2) this plasmon decays by emitting a photon.

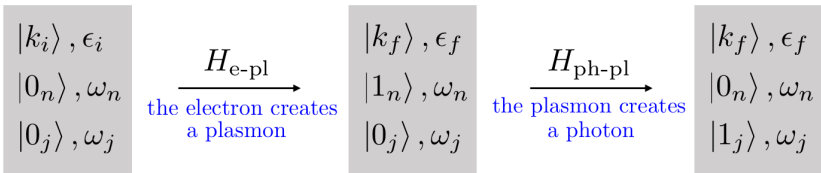

Figure F.1: *Sketch showing the two steps of the CL emission process.*

In order to model this process, we use the 2nd order Fermi golden rule which gives the probability of transiting from a state s to a state f through an intermediate state m:

$$\Gamma_{s\to f} = \frac{2\pi}{\hbar}\left|\sum_m \frac{\langle f|V_1|m\rangle\langle m|V_2|s\rangle}{E_s - E_m}\right|^2 \delta(E_f - E_s) \tag{F.1}$$

where the sum n spans over all the possible plasmon states. Thus, we can use equation (F.1) to calculate the CL probability P^{CL} (see Appendix B.2 in [173]):

$$\mathrm{P}^{\mathrm{CL}} = \frac{2\pi L}{\hbar^4 v}\sum_j \left|\sum_n \frac{\langle k_f 1_j 0_n| H_{\text{ph-pl}}|k_f 0_j 1_n\rangle\langle k_f 0_j 1_n|H_{\text{e-pl}}|k_i 0_j 0_n\rangle}{\epsilon_f - \epsilon_i - \tilde{\omega}_n}\right|^2 \delta(\epsilon_f - \epsilon_i + \omega_j) \tag{F.2}$$

where $\tilde{\omega}_n = \omega_n - i\Gamma_n/2$ includes the plasmon lifetime. Let's now make a short digression. In equation (F.2), we recognize in the terms highlighted in red the definition of the Green function for the plasmon field:

$$G(\omega) = \sum_n \frac{|1_n\rangle\langle 1_n|}{\omega - \tilde{\omega}_n} \tag{F.3}$$

which means that the CL probability could be written:

$$\mathrm{P}^{\mathrm{CL}} = \frac{2\pi L}{\hbar^4 v}\sum_j |\langle k_f 1_j 0_n| H_{\text{eff}}|k_i 0_j 0_n\rangle|^2 \delta(\epsilon_f - \epsilon_i + \omega_j) \tag{F.4}$$

where the effective Hamiltonian reads $H_{\text{eff}} = H_{\text{ph-pl}} G(\epsilon_f - \epsilon_i) H_{\text{e-pl}}$. In other terms, the CL process could be regarded as a first order process where the electron creates a photon and where the plasmon field only plays the role of an intermediate coupler, as already emphasized in [173]. The corollary is that no modal decomposition (no more than quantization) is actually required to describe such a process, although we used one to simplify the calculations.

Expression (F.2) should be related to the spectrally resolved CL probability Γ^{CL} through:

$$\Gamma^{\text{CL}} = \frac{1}{\hbar} \sum_{k_f} \text{P}^{\text{CL}} \delta(\epsilon_f - \epsilon_i + \omega) \tag{F.5}$$

Now, let's right down the electron-plasmon interaction matrix (see equation (14) of [19]):

$$\langle k_f 0_j 1_n | H_{\text{e-pl}} | k_i 0_j 0_n \rangle = \int d\boldsymbol{r} d\boldsymbol{r}' \frac{\psi_f^*(\boldsymbol{r}) \psi_i(\boldsymbol{r}) \langle 1_n | \hat{\rho} | 0_n \rangle}{|\boldsymbol{r} - \boldsymbol{r}'|} \tag{F.6}$$

where $\hat{\rho}$ is the (particle's) electronic density operator and the plasmon-photon interaction matrix is given by (see equation (8) and Appendix B.2 of [173]):

$$\langle k_f 1_j 0_n | H_{\text{ph-pl}} | k_f 0_j 1_n \rangle = i \times g_{j,n} = i \sqrt{\frac{2\pi\hbar\omega_j}{V}} d_n (\hat{x_n}.\hat{\sigma_j}) \tag{F.7}$$

where σ_j is the polarization of the photon and $\boldsymbol{d}_n = d_n \hat{x_n}$ is the dipole moment of the nth plasmon mode which can be calculated through its surface charge density:

$$\boldsymbol{d}_n = \oint_{\partial V} \sigma_n(\boldsymbol{s}) \boldsymbol{s} d\boldsymbol{s} \tag{F.8}$$

Thus, P^{CL} can be written :

$$\text{P}^{\text{CL}} = \frac{2\pi L}{\hbar^4 v} \sum_j M_j \delta(\epsilon_f - \epsilon_i + \omega_j) \tag{F.9}$$

where we have:

$$M_j = \left| \sum_n \frac{g_{j,n}}{\epsilon_f - \epsilon_i - \tilde{\omega}_n} \int d\boldsymbol{r} d\boldsymbol{r}' \frac{\psi_f^*(\boldsymbol{r}) \psi_i(\boldsymbol{r}) \langle 1_n | \hat{\rho} | 0_n \rangle}{|\boldsymbol{r} - \boldsymbol{r}'|} \right|^2 \tag{F.10}$$

Or, in an expanded way:

$$\begin{aligned} M_j = \sum_{n,m} \frac{g_{j,m} g_{j,n}^*}{(\epsilon_f - \epsilon_i - \tilde{\omega}_m)(\epsilon_f - \epsilon_i - \tilde{\omega}_n^*)} \int d\boldsymbol{r_1}\, d\boldsymbol{r_1'} \int d\boldsymbol{r_2}\, d\boldsymbol{r_2'}\, \psi_f^*(\boldsymbol{r_1}) \psi_i(\boldsymbol{r_1}) \\ \times \frac{\langle 1_m | \hat{\rho}(\boldsymbol{r_1'}) | 0 \rangle \langle 0 | \hat{\rho}(\boldsymbol{r_2'}) | 1_n \rangle}{|\boldsymbol{r_1} - \boldsymbol{r_1'}|\, |\boldsymbol{r_2} - \boldsymbol{r_2'}|} \psi_i^*(\boldsymbol{r_2}) \psi_f(\boldsymbol{r_2}) \end{aligned} \tag{F.11}$$

One can then replace $g_{j,n}$ in the previous equation and find:

$$\begin{aligned} M_j = \frac{2\pi\hbar\omega_j}{V} \sum_{n,m} \frac{d_m d_n^* (\hat{x_m}.\hat{\sigma_j})(\hat{x_n}.\hat{\sigma_j})}{(\epsilon_f - \epsilon_i - \tilde{\omega}_m)(\epsilon_f - \epsilon_i - \tilde{\omega}_n^*)} \int d\boldsymbol{r_1} d\boldsymbol{r_1'} \int d\boldsymbol{r_2} d\boldsymbol{r_2'}\, \psi_f^*(\boldsymbol{r_1}) \psi_i(\boldsymbol{r_1}) \\ \times \frac{\langle 1_m | \hat{\rho}(\boldsymbol{r_1'}) | 0 \rangle \langle 0 | \hat{\rho}(\boldsymbol{r_2'}) | 1_n \rangle}{|\boldsymbol{r_1} - \boldsymbol{r_1'}|\, |\boldsymbol{r_2} - \boldsymbol{r_2'}|} \psi_i^*(\boldsymbol{r_2}) \psi_f(\boldsymbol{r_2}) \end{aligned} \tag{F.12}$$

The sum over the photon states $\sum_j$ can be decomposed as $\sum_{\sigma_j} \sum_{k_j}$ and one can transform the sum over k_j in a sum over ω_j using $\sum_{k_j} \to V/(8\pi^3 c^3) \int d\Omega \int \omega_j^2 d\omega_j$. It leads to:

$$\mathrm{P}^{\mathrm{CL}} = \frac{L}{2\pi(\hbar c)^3 v}\sum_{\sigma_j}\sum_{m,n}\int d\Omega \int \omega_j^3 d\omega_j \frac{d_m d_n^*(\hat{x_m}.\hat{\sigma_j})(\hat{x_n}.\hat{\sigma_j})}{(\epsilon_f-\epsilon_i-\tilde{\omega}_m)(\epsilon_f-\epsilon_i-\tilde{\omega}_n^*)}\int d\boldsymbol{r_1}\, d\boldsymbol{r_1'}\int d\boldsymbol{r_2}\, d\boldsymbol{r_2'} \times\psi_f^*(\boldsymbol{r_1})\psi_i(\boldsymbol{r_1})\psi_i^*(\boldsymbol{r_2})\psi_f(\boldsymbol{r_2})\frac{\langle 1_m|\hat{\rho}(\boldsymbol{r_1'})|0\rangle\langle 0|\hat{\rho}(\boldsymbol{r_2'})|1_n\rangle}{|\boldsymbol{r_1}-\boldsymbol{r_1'}|\,|\boldsymbol{r_2}-\boldsymbol{r_2'}|}\delta(\epsilon_f-\epsilon_i+\omega_j) \tag{F.13}$$

Using the δ function, one can remove the sum over ω_j and obtain:

$$\mathrm{P}^{\mathrm{CL}} = \frac{L}{2\pi(\hbar c)^3 v}\sum_{\sigma_j}\sum_{m,n}\int d\Omega(\epsilon_f-\epsilon_i)^3\frac{d_m d_n^*(\hat{x_m}.\hat{\sigma_j})(\hat{x_n}.\hat{\sigma_j})}{(\epsilon_f-\epsilon_i-\tilde{\omega}_m)(\epsilon_f-\epsilon_i-\tilde{\omega}_n^*)} \times\int d\boldsymbol{r_1}\, d\boldsymbol{r_1'}\int d\boldsymbol{r_2}\, d\boldsymbol{r_2'}\psi_f^*(\boldsymbol{r_1})\psi_i(\boldsymbol{r_1})\psi_i^*(\boldsymbol{r_2})\psi_f(\boldsymbol{r_2})\frac{\langle 1_m|\hat{\rho}(\boldsymbol{r_1'})|0\rangle\langle 0|\hat{\rho}(\boldsymbol{r_2'})|1_n\rangle}{|\boldsymbol{r_1}-\boldsymbol{r_1'}|\,|\boldsymbol{r_2}-\boldsymbol{r_2'}|} \tag{F.14}$$

According to equation (31) in [9], one can write:

$$\langle 1_m|\hat{\rho}(\boldsymbol{r})|0\rangle = f_m(\omega)\sigma_m(\boldsymbol{r}) \tag{F.15}$$

where f_m are functions to be determined. Therefore, using equation (4) of [10], we can re-write:

$$\int d\boldsymbol{r_1'}d\boldsymbol{r_2'}\frac{\langle 1_m|\hat{\rho}(\boldsymbol{r_1'})|0\rangle\langle 0|\hat{\rho}(\boldsymbol{r_2'})|1_n\rangle}{|\boldsymbol{r_1}-\boldsymbol{r_1'}|\,|\boldsymbol{r_2}-\boldsymbol{r_2'}|} = f_m(\omega)f_n^*(\omega)\phi_m(\boldsymbol{r_1})\phi_n^*(\boldsymbol{r_2}) \tag{F.16}$$

Thus, P^{CL} can be re-written as:

$$\mathrm{P}^{\mathrm{CL}} = \frac{L}{2\pi(\hbar c)^3 v}\sum_{\sigma_j}\sum_{m,n}f_m(\omega)f_n^*(\omega)\int d\Omega(\epsilon_f-\epsilon_i)^3\frac{d_m d_n^*(\hat{x_m}.\hat{\sigma_j})(\hat{x_n}.\hat{\sigma_j})}{(\epsilon_f-\epsilon_i-\tilde{\omega}_m)(\epsilon_f-\epsilon_i-\tilde{\omega}_n^*)} \times\int d\boldsymbol{r_1}\, d\boldsymbol{r_2}\;\psi_f^*(\boldsymbol{r_1})\psi_i(\boldsymbol{r_1})\psi_i^*(\boldsymbol{r_2})\psi_f(\boldsymbol{r_2})\phi_m(\boldsymbol{r_1})\phi_n^*(\boldsymbol{r_2}) \tag{F.17}$$

Following [119] (see the corresponding supporting info, equation (16)) and assuming that the spectral responses f_n are well separated, we can neglect the cross-terms ($n \neq m$) and simply write:

$$\mathrm{P}^{\mathrm{CL}} = \frac{L}{2\pi(\hbar c)^3 v}\sum_{\sigma_j}\sum_{m}|f_m(\omega)|^2\int d\Omega(\epsilon_f-\epsilon_i)^3\frac{|\boldsymbol{d_m}|^2(\hat{x_m}.\hat{\sigma_j})^2}{|\epsilon_f-\epsilon_i-\tilde{\omega}_m|^2}\left|\int d\boldsymbol{r}\psi_f^*(\boldsymbol{r})\phi_m(\boldsymbol{r})\psi_i(\boldsymbol{r})\right|^2 \tag{F.18}$$

If we do not make this assumption, we would have another term representing the far-field interferences between the modes as done in [120] or in the introductory chapter. We thus have:

$$\Gamma^{\mathrm{CL}} = \frac{L}{2\pi\hbar^4 c^3 v}\sum_{\sigma_j}\sum_{m,k_f}|f_m(\omega)|^2\int d\Omega(\epsilon_f-\epsilon_i)^3\frac{|\boldsymbol{d_m}|^2(\hat{x_m}.\hat{\sigma_j})^2}{|\epsilon_f-\epsilon_i-\tilde{\omega}_m|^2} \times\left|\int d\boldsymbol{r}\psi_f^*(\boldsymbol{r})\phi_m(\boldsymbol{r})\psi_i(\boldsymbol{r})\right|^2\delta(\epsilon_f-\epsilon_i+\omega) \tag{F.19}$$

On the other hand, according to [19] (page 216):

$$\mathrm{Im}\{-W(\boldsymbol{r_1},\boldsymbol{r_2},\omega)\} = \sum_m\int d\boldsymbol{r_1'}d\boldsymbol{r_2'}\frac{\langle 1_m|\hat{\rho}(\boldsymbol{r_1'})|0\rangle\langle 0|\hat{\rho}(\boldsymbol{r_2'})|1_m\rangle}{|\boldsymbol{r_1}-\boldsymbol{r_1'}|\,|\boldsymbol{r_2}-\boldsymbol{r_2'}|} \tag{F.20}$$

Using equation (F.15) and the modal decomposition of W, one can write:

$$\sum_m \mathrm{Im}\{-g_m(\omega)\}\phi_m(\boldsymbol{r_1})\phi_m^*(\boldsymbol{r_2}) = \sum_m|f_m(\omega)|^2\phi_m(\boldsymbol{r_1})\phi_m^*(\boldsymbol{r_2}) \tag{F.21}$$

And, consequently:

$$\mathrm{Im}\{-g_m(\omega)\} = |f_m(\omega)|^2 \tag{F.22}$$

Using the previous equation and replacing $\epsilon_f - \epsilon_i$ by ω, we can finally write:

$$\Gamma^{\mathrm{CL}}(\omega) = \frac{L}{2\pi\hbar^4 c^3 v} \sum_{\sigma_j} \sum_m \mathrm{Im}\{-g_m(\omega)\} \frac{\omega^3}{|\omega - \tilde{\omega}_m|^2} | \left(\int d\Omega \, |\boldsymbol{d_m}|^2 (\hat{x_m}.\hat{\sigma_j})^2 \right) \\ \times \sum_{k_f} \left| \int d\boldsymbol{r} \; \psi_f^*(\boldsymbol{r}) \phi_m(\boldsymbol{r}) \psi_i(\boldsymbol{r}) \right|^2 \delta(\epsilon_f - \epsilon_i + \omega) \tag{F.23}$$

where $\tilde{\omega}_m$ is the complex plasmon resonance energy, $\boldsymbol{d}_m = d_m \hat{x}_m$ is the dipole moment of the plasmon mode m and $\hat{\sigma}_j$ is the polarization of the photon state j. This equation is based on the quasistatic approach of the electron-plasmon interaction which guarantees the separability of the screened potential but, as emphasized in [120], leads to some energy conservation issue. From (F.23), it seems that no dichroic effect is present in CL. A further investigation is however required to have a definitive conclusion.

Appendix G

Supporting information for chapter 5

G.1 De-noising procedure, adaptative median filtering

Due to noise in the experimental data and the weakness of certain plasmon peaks, the peak fitting procedure of the spectrum image can give rise to bad pixels as shown on figure G.1. An adaptative median filter has thus been used to remove these pixels without corrupting the information contained in the maps.

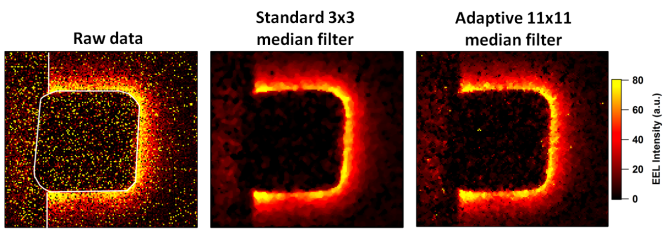

Figure G.1: *Comparison between the raw fitted map of the dipolar mode D, the map denoised with a standard median filter and the map denoised with an adaptative median filter.*

G.2 Correction of the CL system transmission

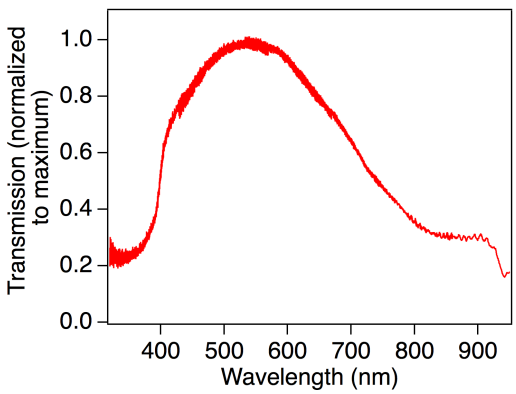

Figure G.2: *Transmission function of our CL system. The curve is normalized with respect to its maximum.*

The calibration has been performed using a commercial calibrated lamp which absolute emission spectra is provided by the manufacturer. The light is sent to the CL spectrometer and detector through the same optical fiber as used in a standard CL experiment. Comparing the measured spectrum with the one given by the manufacturer, we can deduce the transmission function of the system. The transmission function G.2 have been measured in the same conditions as for the plasmon experiment on nano-cubes (same grating, same centering of the grating). Let's however emphasized that this method completely omits to measure the transmission function of the mirror since the light is set from outside the microscope. Other methods exist employing e.g. transition radiation to also correct the mirror transmission [116].

Bibliography

[1] Harry A. Atwater and Albert Polman. Plasmonics for improved photovoltaic devices. *Nature Materials*, 9(3):205–213, 2010.

[2] Stefan A. Maier. *Plasmonics: Fundamentals and applications*. 2007.

[3] A. V. Akimov, A. Mukherjee, C. L. Yu, D. E. Chang, A. S. Zibrov, P. R. Hemmer, H. Park, and M. D. Lukin. Generation of single optical plasmons in metallic nanowires coupled to quantum dots. *Nature*, 450(7168):402–406, 2007.

[4] Joshua M Stern, Jennifer Stanfield, Wareef Kabbani, Jer-Tsong Hsieh, and Jeffrey A Cadeddu. Selective prostate cancer thermal ablation with laser activated gold nanoshells. *The Journal of urology*, 179(2):748–753, 2008.

[5] Jean Francois Masson. Surface Plasmon Resonance Clinical Biosensors for Medical Diagnostics. *ACS Sensors*, 2(1):16–30, 2017.

[6] John Pendry and David Smith. The quest for the superlens. *Scientific American*, 295:60 – 67, 2006.

[7] Mark Stockman. Spasers explained COMMENTARY. *Nature Photonics*, 2:327–329, 2008.

[8] Harry Atawater. The promise of plasmonics. *Scientific American*, 296(4):56, 2007.

[9] Feng Ouyang and Michael Isaacson. Surface plasmon excitation of objects with arbitrary shape and dielectric constant. *Philosophical Magazine Part B*, 60(4):481–492, 1989.

[10] Guillaume Boudarham and Mathieu Kociak. Modal decompositions of the local electromagnetic density of states and spatially resolved electron energy loss probability in terms of geometric modes. *Physical Review B - Condensed Matter and Materials Physics*, 85(24):1–15, 2012.

[11] Jaysen Nelayah, Mathieu Kociak, Odile Stéphan, F. Javier García de Abajo, Marcel Tencé, Luc Henrard, Dario Taverna, Isabel Pastoriza-Santos, Luis M. Liz-Marzán, and Christian Colliex. Mapping surface plasmons on a single metallic nanoparticle. *Nature Physics*, 3(5):348–353, 2007.

[12] N Yamamoto, K Araya, and F J G de Abajo. Photon emission from silver particles induced by a high-energy electron beam. *Physical Review B*, 6420(20):205419, 2001.

[13] L. H G Tizei and M. Kociak. Spatially resolved quantum nano-optics of single photons using an electron microscope. *Physical Review Letters*, 110(15):1–5, 2013.

[14] A. Howie. Electrons and photons: exploiting the connection. *Inst. Phys. Conf. Ser*, 161:311–4, 1999.

[15] F J García de Abajo and M Kociak. Electron energy-gain spectroscopy. *New Journal of Physics*, 10(7):073035, 2008.

[16] P. M. Echenique, J. Bausells, and A Rivacoba. Energy-loss probability in electron microscopy. *Physical Review B*, 35(4):1521–1524, 1987.

[17] S. L. Dudarev, L.-M. Peng, and M. J. Whelan. Space and Time and Dynamical Diffraction. *Physical Review B*, 48(18):13408–13430, 1993.

[18] Peter Schattschneider, M Nelhiebel, and B Jouffrey. Density matrix of inelastically scattered fast electrons. *Physical Review B*, 59(16):10959–10969, 1999.

[19] F. J. García de Abajo. Optical excitations in electron microscopy. *Reviews of Modern Physics*, 82(1):209–275, feb 2010.

[20] J Verbeeck, H Tian, and P Schattschneider. Production and application of electron vortex beams. *Nature*, 467(7313):301–304, 2010.

[21] Masaya Uchida and Akira Tonomura. Generation of electron beams carrying orbital angular momentum. *Nature*, 464(7289):737–739, 2010.

[22] Denis G. Baranov, Martin Wersäll, Jorge Cuadra, Tomasz J. Antosiewicz, and Timur Shegai. Novel Nanostructures and Materials for Strong Light–Matter Interactions. *ACS Photonics*, page acsphotonics.7b00674, 2017.

[23] Ondrej L. Krivanek, Tracy C. Lovejoy, Niklas Dellby, Toshihiro Aoki, R. W. Carpenter, Peter Rez, Emmanuel Soignard, Jiangtao Zhu, Philip E. Batson, Maureen J. Lagos, Ray F. Egerton, and Peter A. Crozier. Vibrational spectroscopy in the electron microscope. *Nature*, 514(7521):209–212, 2014.

[24] Maureen J. Lagos, Andreas Trügler, Ulrich Hohenester, and Philip E. Batson. Mapping vibrational surface and bulk modes in a single nanocube. *Nature*, 543(7646):529–532, 2017.

[25] R. Fuchs and K.L. Kliewer. Optical modes of vibration in an ionic crystal slab. *Physical Review*, 140(December):A2076–A2088, 1965.

[26] Lukas Novotny and Bert Hecht. *Principles of Nano-Optics*. Cambridge University Press;, cambridge edition, 2006.

[27] John David Jackson. Classical Electrodynamics Third Edition, 1999.

[28] Sami M Ali, Tarek M Habashy, and Jin Au Kong. Spectral-domain dyadic Green's function in layered chiral media. *Journal of the Optical Society of America A*, 9(3):413–423, 1992.

[29] Guillaume Boudarham. *Nanooptique avec des electrons rapides : metamateriaux, formulation modale de la EMLDOS pour des systemes plasmoniques*. PhD thesis, 2011.

[30] Henrik Bruus and Karsten Flensberg. *Many-body quantum theory in condensed matter physics*. Oxford gra edition, 2004.

[31] Ana Asenjo-Garcia. *Plasmon, light, and electron beam interactions at the nanoscale*. PhD thesis, 2014.

[32] By Christian Colliex. Taking temperature at the nanoscale. 347(6222):2015–2017, 2015.

[33] P. B. Johnson and R. W. Christy. Optical constants of the noble metals. *Physical Review B*, 6(12):4370–4379, 1972.

[34] A. J. Huber, B. Deutsch, L. Novotny, and R. Hillenbrand. Focusing of surface phonon polaritons. *Applied Physics Letters*, 92(20):92–95, 2008.

[35] Wenshan Cai, Justin S White, and Mark L Brongersma. Power-Efficient Electrooptic Plasmonic Modulators. 2009.

[36] Jiao Lin, J P Balthasar Mueller, Qian Wang, Guanghui Yuan, Nicholas Antoniou, Xiao-Cong Yuan, and Federico Capasso. Polarization-Controlled Tunable Directional Coupling of Surface Plasmon Polaritons. *Science*, 340:331–334, 2013.

[37] T V Teperik, A Archambault, F Marquier, and J J Greffet. Huygens-Fresnel principle for surface plasmons. *Optics express*, 17(20):17483–17490, 2009.

[38] Bin Zhang, Yusheng Bian, Liqiang Ren, Feng Guo, Shi Yang Tang, Zhangming Mao, Xiaomin Liu, Jinju Sun, Jianying Gong, Xiasheng Guo, and Tony Jun Huang. Hybrid dielectric-loaded nanoridge plasmonic waveguide for low-loss light transmission at the subwavelength scale. *Scientific Reports*, 7(August 2016):1–9, 2017.

[39] Isaak D. Mayergoyz, Donald R. Fredkin, and Zhenyu Zhang. Electrostatic (plasmon) resonances in nanoparticles. *Physical Review B - Condensed Matter and Materials Physics*, 72(15), 2005.

[40] R. Fuchs. Theory of the optical properties of ionic crystal cubes. *Physical Review B*, 11(4):1732–1740, 1975.

[41] Franz-Philipp Schmidt, Harald Ditlbacher, Ferdinand Hofer, Joachim R. Krenn, and Ulrich Hohenester. Morphing a plasmonic nanodisk into a nanotriangle. *Nano Letters*, 14(8):4810–4815, 2014.

[42] E D Palik. *Handbook Of Optical-Constants*, volume 1. Academic Press, 1984.

[43] Andreas Trügler. *Optical Properties of Metallic Nanoparticles*. Springer International Publishing, 2016.

[44] Ryo Ishida, Seiji Yamazoe, Kiichirou Koyasu, and Tatsuya Tsukuda. Repeated appearance and disappearance of localized surface plasmon resonance in 1.2 nm gold clusters induced by adsorption and desorption of hydrogen atoms. *Nanoscale*, 8(5):2544–2547, 2016.

[45] Mathieu L. Juan, Maurizio Righini, and Romain Quidant. Plasmon nano-optical tweezers. *Nature Photonics*, 5(6):349–356, 2011.

[46] N. Pavloff and M. S. Hansen. Effects of surface roughness on the electronic structure of metallic clusters. *Z. Phys. D - Atoms, Molecules and Clusters*, 24:57–63, 1992.

[47] Ryogo Kubo. Electronic Properties of Metallic Fine Particles. I. *Journal of the Physical Society of Japan*, 17(6):975–986, 1962.

[48] Giuseppe Toscano, Jakob Straubel, Alexander Kwiatkowski, Carsten Rockstuhl, Ferdinand Evers, Hongxing Xu, N. Asger Mortensen, and Martijn Wubs. Resonance shifts and spill-out effects in self-consistent hydrodynamic nanoplasmonics. *Nature Communications*, 6(May):1–11, 2015.

[49] D R Fredkin and I D Mayergoyz. Resonant Behavior of Dielectric Objects (Electrostatic Resonances). *Phys. Rev. Lett.*, 91(December):253902, 2003.

[50] Philip Trøst Kristensen and Stephen Hughes. Modes and Mode Volumes of Leaky Optical Cavities and Plasmonic Nanoresonators. *ACS Photonics*, 1(1):2–10, 2014.

[51] Franz Philipp Schmidt, Arthur Losquin, Ferdinand Hofer, Andreas Hohenau, Joachim R. Krenn, and Mathieu Kociak. How Dark Are Radial Breathing Modes in Plasmonic Nanodisks? *ACS Photonics*, 5(3):861–866, 2018.

[52] D. E. Gómez, Z. Q. Teo, M. Altissimo, T. J. Davis, S. Earl, and A. Roberts. The dark side of plasmonics. *Nano Letters*, 13(8):3722–3728, 2013.

[53] F P Schmidt, H Ditlbacher, U Hohenester, A Hohenau, F Hofer, and J R Krenn. Universal dispersion of surface plasmons in flat nanostructures. *Nature Communications*, 5:3604, 2014.

[54] Michel Bosman, Enyi Ye, Shu Fen Tan, Christian A Nijhuis, Joel K W Yang, Renaud Marty, Adnen Mlayah, Arnaud Arbouet, Christian Girard, and Ming-Yong Han. Surface plasmon damping quantified with an electron nanoprobe. *Scientific reports*, 3:1312, 2013.

[55] Jacob B. Khurgin. How to deal with the loss in plasmonics and metamaterials. *Nature Nanotechnology*, 10(1):2–6, 2015.

[56] Marco Bernardi, Jamal Mustafa, Jeffrey B. Neaton, and Steven G. Louie. Theory and computation of hot carriers generated by surface plasmon polaritons in noble metals. *Nature Communications*, 6:1–9, 2015.

[57] Mark L. Brongersma, Naomi J. Halas, and Peter Nordlander. Plasmon-induced hot carrier science and technology. *Nature Nanotechnology*, 10(1):25–34, 2015.

[58] Xiaohua Huang and Mostafa A. El-Sayed. Plasmonic photo-thermal therapy (PPTT). *Alexandria Journal of Medicine*, 47(1):1–9, 2011.

[59] C. K. Sun, F. Vallée, L. H. Acioli, E. P. Ippen, and J. G. Fujimoto. Femtosecond-tunable measurement of electron thermalization in gold. *Physical Review B*, 50(20):15337–15348, 1994.

[60] Martin Wolf. Femtosecond dynamics of electronic excitations at metal surfaces. *Surf. Sci.*, 377-379:343–349, 1997.

[61] Quan Sun, Kosei Ueno, Han Yu, Atsushi Kubo, Yasutaka Matsuo, and Hiroaki Misawa. Direct imaging of the near field and dynamics of surface plasmon resonance on gold nanostructures using photoemission electron microscopy. *Light: Science & Applications*, 2(12):e118, 2013.

[62] Christoph Lemke, Till Leißner, Andrey Evlyukhin, Jörn W. Radke, Alwin Klick, Jacek Fiutowski, Jakob Kjelstrup-Hansen, Horst Günter Rubahn, Boris N. Chichkov, Carsten Reinhardt, and Michael Bauer. The interplay between localized and propagating plasmonic excitations tracked in space and time. *Nano Letters*, 14(5):2431–2435, 2014.

[63] Yuya Morimoto and Peter Baum. Diffraction and microscopy with attosecond electron pulse trains. *Nature Physics*, 14(March):1–5, 2017.

[64] Katharina E. Priebe, Christopher Rathje, Sergey V. Yalunin, Thorsten Hohage, Armin Feist, Sascha Schäfer, and Claus Ropers. Attosecond electron pulse trains and quantum state reconstruction in ultrafast transmission electron microscopy. *Nature Photonics*, 11(12):793–797, 2017.

[65] F Houdellier, G M Caruso, S Weber, M Kociak, and A Arbouet. Development of a high brightness ultrafast Transmission Electron Microscope based on a laser-driven cold field emission source. *Ultramicroscopy*, 186:128–138, 2018.

[66] Xin Zhang, Hugo Lourenço-Martins, Sophie Meuret, Mathieu Kociak, Benedikt Haas, Jean-Luc Rouvière, Pierre-Henri Jouneau, Catherine Bougerol, T Auzelle, D Jalabert, Xavier Biquard, Bruno Gayral, and Bruno Daudin. InGaN nanowires with high InN molar fraction: growth, structural and optical properties. *Nanotechnology*, 27(19):195704, 2016.

[67] E U Rafailov. *The Physics and Engineering of Compact Quantum Dot-based Lasers for Biophotonics*. Wiley, 2013.

[68] Sophie Meuret, Luiz H G Tizei, Thomas Auzelle, Rudee Songmuang, Bruno Daudin, Bruno Gayral, and Mathieu Kociak. Lifetime Measurements Well below the Optical Diffraction Limit. *ACS Photonics*, 3(7):1157–1163, 2016.

[69] Luiz H G Tizei and Mathieu Kociak. *Chapter Four-Quantum Nanooptics in the Electron Microscope*, volume 199. 2017.

[70] A Wallraff, D Schuster, A Blais, L Frunzio, R Huang, J Majer, S Kumar, S Girvin, and R Schoelkopf. Strong coupling of a single photon to a superconducting qubit using circuit quantum electrodynamics. *Nature*, 431(7005):162–167, 2004.

[71] B. Darquie, M. P. A. Jones, J. Dingjan, J. Beugnon, S. Bergamini, Y. Sortais, G. Messin, A. Browaeys, and P. Grangier. Controlled Single-Photon Emission from a Single Trapped Two-Level Atom. *Science*, 309(5733):454–456, 2005.

[72] E. Togan, Y. Chu, A. S. Trifonov, L. Jiang, J. Maze, L. Childress, M. V G Dutt, A. S. Sørensen, P. R. Hemmer, A. S. Zibrov, and M. D. Lukin. Quantum entanglement between an optical photon and a solid-state spin qubit. *Nature*, 466(7307):730–734, 2010.

[73] M. Kociak and L.F. Zagonel. Cathodoluminescence in the scanning transmission electron microscope. *Ultramicroscopy*, 174(November 2016):50–69, 2017.

[74] Hugo Lourenço-Martins, Mathieu Kociak, Sophie Meuret, François Treussart, Yih Hong Lee, Xing Yi Ling, Huan-Cheng Chang, and Luiz Henrique Galvão Tizei. Probing Plasmon-NV ⁰ Coupling at the Nanometer Scale with Photons and Fast Electrons. *ACS Photonics*, page acsphotonics.7b01093, 2017.

[75] Edward Condon. A theory of intensity distribution in band systems. *Physical Review*, 28(6):1182–1201, 1926.

[76] Romain Bourrellier, Sophie Meuret, Anna Tararan, Odile Stéphan, Mathieu Kociak, Luiz H G Tizei, and Alberto Zobelli. Bright UV Single Photon Emission at Point Defects in h-BN. *Nano Letters*, 16(7):4317–4321, 2016.

[77] Pascal Anger, Palash Bharadwaj, and Lukas Novotny. Enhancement and Quenching of Single-Molecule Fluorescence. *Phys. Rev. Lett.*, 96(11):113002, mar 2006.

[78] Gary P. Wiederrecht, Gregory A. Wurtz, and Jasmina Hranisavljevic. Coherent coupling of molecular excitons to electronic polarizations of noble metal nanoparticles. *Nano Letters*, 4(11):2121–2125, 2004.

[79] Nche T. Fofang, Tae Ho Park, Oara Neumann, Nikolay A. Mirin, Peter Nordlander, and Naomi J. Halas. Plexcitonic nanoparticles: Plasmon-Exciton Coupling in Nanoshell-J- Aggregate complexes. *Nano Letters*, 8(10):3481–3487, 2008.

[80] S Inan B Alci. Ultra hybrid plasmonics : strong coupling of plexcitons with plasmon polaritons. *Opt. Lett.*, 40(14):3424–3427, 2015.

[81] R. Esteban, T. V. Teperik, and J. J. Greffet. Optical patch antennas for single photon emission using surface plasmon resonances. *Physical Review Letters*, 104(2):1–4, 2010.

[82] D. E. Chang, A. S. Sørensen, P. R. Hemmer, and M. D. Lukin. Quantum optics with surface plasmons. *Physical Review Letters*, 97(5):1–4, 2006.

[83] Darrick E. Chang, Anders S. Sørensen, Eugene A. Demler, and Mikhail D. Lukin. A single-photon transistor using nanoscale surface plasmons. *Nature Physics*, 3(11):807–812, 2007.

[84] R. Carminati, A. Cazé, D. Cao, F. Peragut, V. Krachmalnicoff, R. Pierrat, and Y. De Wilde. Electromagnetic density of states in complex plasmonic systems. *Surface Science Reports*, 70(1):1–41, 2015.

[85] A. Manjavacas, F. J García De Abajo, and P. Nordlander. Quantum plexcitonics: Strongly interacting plasmons and excitons. *Nano Letters*, 11(6):2318–2323, 2011.

[86] D. C. Marinica, H. Lourenço-Martins, J. Aizpurua, and A. G. Borisov. Plexciton quenching by resonant electron transfer from quantum emitter to metallic nanoantenna. *Nano Letters*, 13(12):5972–5978, 2013.

[87] Jakob Ebner, Andreas Trügler, and Ulrich Hohenester. Optical excitations of hybrid metal-semiconductor nanoparticles. *European Physical Journal B*, 88(1), 2015.

[88] E M Purcell, H C Torrey, and R V Pound. Resonance Absorption by Nuclear Magnetic Moments in a Solid. *Phys. Rev.*, 69(1-2):37–38, jan 1946.

[89] Karl Joulain, Jean Philippe Mulet, François Marquier, Rémi Carminati, and Jean Jacques Greffet. Surface electromagnetic waves thermally excited: Radiative heat transfer, coherence properties and Casimir forces revisited in the near field. *Surface Science Reports*, 57(3-4):59–112, 2005.

[90] G. Colas des Francs, Christian Girard, Jean Claude Weeber, C. Chicane, Thierry David, Alain Dereux, and David Peyrade. Optical analogy to electronic quantum corrals. *Physical Review Letters*, 86(21):4950–4953, 2001.

[91] C. Chicanne, T. David, R. Quidant, J. C. Weeber, Y. Lacroute, E. Bourillot, A. Dereux, G. Colas des Francs, and C. Girard. Imaging the Local Density of States of Optical Corrals. *Physical Review Letters*, 88(9):4, 2002.

[92] M. F. Crommie, C. P. Lutz, and D. M. Eigler. Confinement of Electrons to Quantum Corrals on a Metal Surface. *Science*, 262(5131):218–220, 1993.

[93] R Carminati and J J Sáenz. Scattering Theory of Bardeen's Formalism for Tunneling: New Approach to Near-Field Microscopy. *Phys. Rev. Lett.*, 84(22):5156–5159, 2000.

[94] Karl Joulain, Rémi Carminati, Jean-Philippe Mulet, and Jean-Jacques Greffet. Definition and measurement of the local density of electromagnetic states close to an interface. *Physical Review B*, 68(24):245405, 2003.

[95] G. S. Agarwal. Quantum electrodynamics in the presence of dielectrics and conductors. I. Electromagnetic-field response functions and black-body fluctuations in finite geometries. *Physical Review A*, 11(1):230–242, 1975.

[96] Ryogo Kubo. Statistical-Mechanical Theory of Irreversible Processes. I. General Theory and Simple Applications to Magnetic and Conduction Problems. *Journal of the Physical Society of Japan*, 12(6):570–586, 1957.

[97] Tim H. Taminiau, Sinan Karaveli, Niek F. Van Hulst, and Rashid Zia. Quantifying the magnetic nature of light emission. *Nature Communications*, 3:976–979, 2012.

[98] L. Aigouy, A. Cazé, P. Gredin, M. Mortier, and R. Carminati. Mapping and quantifying electric and magnetic dipole luminescence at the nanoscale. *Physical Review Letters*, 113(7):1–5, 2014.

[99] Zeinab Mohammadi, Cole P Van Vlack, Stephen Hughes, Jens Bornemann, and Reuven Gordon. Vortex electron energy loss spectroscopy for near-field mapping of magnetic plasmons. *Opt. Express*, 20(14):1351–1353, 2012.

[100] F. J. García de Abajo and M. Kociak. Probing the Photonic Local Density of States with Electron Energy Loss Spectroscopy. *Physical Review Letters*, 100(10):106804, 2008.

[101] Alain Dereux, Christian Girard, and Jean Claude Weeber. Theoretical principles of near-field optical microscopies and spectroscopies. *Journal of Chemical Physics*, 112(18):7775–7789, 2000.

[102] J. A. Porto, R. Carminati, and J. J. Greffet. Theory of electromagnetic field imaging and spectroscopy in scanning near-field optical microscopy. *Journal of Applied Physics*, 88(8):4845–4850, 2000.

[103] Emil Wolf. *Introduction to the Theory of Coherence and Polarization of Light*, volume 50. Cambridge U. Press, cambridge edition, 2007.

[104] A. Cazé, R Pierrat, and R Carminati. Spatial coherence in complex photonic and plasmonic systems. *Physical Review Letters*, 110(6):1–5, 2013.

[105] Nina Mauser and Achim Hartschuh. Tip-enhanced near-field optical microscopy. *Chemical Society Reviews*, 43(4):1248–1262, 2014.

[106] J R Krenn, A Dereux, J C Weeber, E Bourillot, Y Lacroute, J P Goudonnet, G Schider, W Gotschy, A Leitner, F R Aussenegg, and C Girard. Squeezing the optical near-field zone by plasmon coupling of metallic nanoparticles. *Physical Review Letters*, 82(12):2590–2593, 1999.

[107] B. Hecht, H. Bielefeld, L. Novotny, Y. Inouye, and D. W. Pohl. Local Excitation, Scattering, and interfacence of surface plasmons. *Physical Review Letters*, 77(c):1889, 1996.

[108] E Betzig, Eric Betzig, Robert J. Chichester, and Robert J. Chichester. Single Molecules Observed by Near-Field Scanning Optical Microscopy. *Science*, 262(5138):1422–1425, 1993.

[109] Weilun Chao, Bruce D. Harteneck, J. Alexander Liddle, Erik H. Anderson, and David T. Attwood. Soft X-ray microscopy at a spatial resolution better than 15 nm. *Nature*, 435(7046):1210–1213, 2005.

[110] E Kröger. Berechnung der Energieverluste schneller Elektronen in dünnen Schichten mit Retardierung. *Zeitschrift für Physik A Hadrons and nuclei*, 216(2):115–135, 1968.

[111] Mathieu Kociak and Odile Stéphan. Mapping plasmons at the nanometer scale in an electron microscope. *Chemical Society reviews*, 43(11):3865–83, 2014.

[112] R H Ritchie. Plasma Losses by Fast Electrons in Thin Films. *Phys. Rev.*, 106(5):874–881, 1957.

[113] P A Cherenkov. The visible glow of pure liquids under the action of γ-rays. *Dokl. Akad. Nauk SSSR*, 2:451–454, 1934.

[114] F. J. García de Abajo, A. Rivacoba, N. Zabala, and N. Yamamoto. Boundary effects in Cherenkov radiation. *Physical Review B*, 69(15):155420, 2004.

[115] A.P. Potylitsyn. Transition radiation and diffraction radiation. Similarities and differences. *Nuclear Instruments and Methods in Physics Research Section B: Beam Interactions with Materials and Atoms*, 145(1):169–179, 1998.

[116] B Brenny. *Probing light emission at the nanoscale with cathodoluminescence.* PhD thesis, 2016.

[117] M. V. Tsarev and P. Baum. Characterization of non-relativistic attosecond electron pulses by transition radiation from tilted surfaces. *New Journal of Physics*, 20(3), 2018.

[118] H Saito and N Yamamoto. Control of Light Emission by a Plasmonic Crystal Cavity. *Nano Letters*, 15(9):5764–5769, 2015.

[119] Arthur Losquin, Luiz F. Zagonel, Viktor Myroshnychenko, Benito Rodríguez-González, Marcel Tencé, Leonardo Scarabelli, Jens Förstner, Luis M. Liz-Marzán, F. Javier García De Abajo, Odile Stéphan, and Mathieu Kociak. Unveiling nanometer scale extinction and scattering phenomena through combined electron energy loss spectroscopy and cathodoluminescence measurements. *Nano Letters*, 15(2):1229–1237, 2015.

[120] Arthur Losquin and Mathieu Kociak. Link between Cathodoluminescence and Electron Energy Loss Spectroscopy and the Radiative and Full Electromagnetic Local Density of States. *ACS Photonics*, page 151021085646006, 2015.

[121] F P Schmidt, H Ditlbacher, U Hohenester, A Hohenau, F Hofer, and J R Krenn. Dark Plasmonic Breathing Modes in Silver Nanodisks. *Nano Letters*, 12(11):5780–5783, 2012.

[122] Naohiko Kawasaki, Sophie Meuret, Raphaël Weil, Hugo Lourenço-Martins, Odile Stéphan, and Mathieu Kociak. Extinction and Scattering Properties of High-Order Surface Plasmon Modes in Silver Nanoparticles Probed by Combined Spatially Resolved Electron Energy Loss Spectroscopy and Cathodoluminescence. *ACS Photonics*, 3(9):1654–1661, 2016.

[123] D B Williams and C B Carter. *Transmission Electron Microscopy: A Textbook for Materials Science*. Number vol.˜2 in Cambridge library collection. Springer, 2009.

[124] C. Jeanguillaume and C. Colliex. Spectrum-image: The next step in EELS digital acquisition and processing. *Ultramicroscopy*, 28(1-4):252–257, 1989.

[125] S J Pennycook and P D Nellist. *Scanning Transmission Electron Microscopy: Imaging and Analysis*. Springer New York, 2011.

[126] Ray F. Egerton. Electron Energy-Loss Spectroscopy in the TEM. *Reports on Progress in Physics*, 72(1):16502, 2009.

[127] S. Lazar, G. A. Botton, and H. W. Zandbergen. Enhancement of resolution in core-loss and low-loss spectroscopy in a monochromated microscope. *Ultramicroscopy*, 106(11-12 SPEC. ISS.):1091–1103, 2006.

[128] William Hadley Richardson. Bayesian-Based Iterative Method of Image Restoration. *Journal of the Optical Society of America*, 62(1):55, 1972.

[129] L. B. Lucy. An iterative technique for the rectification of observed distributions. *The Astronomical Journal*, 79(6):745, 1974.

[130] A. Gloter, A. Douiri, M. Tencé, and C. Colliex. Improving energy resolution of EELS spectra: An alternative to the monochromator solution. *Ultramicroscopy*, 96(3-4):385–400, 2003.

[131] Koji Kimoto. Practical aspects of monochromators developed for transmission electron microscopy. *Microscopy*, 63(5):337–344, 2014.

[132] G. Remond. Applications of cathodoluminescence in mineralogy. *Journal of Luminescence*, 15(2):121–155, 1977.

[133] M. Grundmann, J. Christen, N. N. Ledentsov, J. Böhrer, D. Bimberg, S. S. Ruvimov, P. Werner, U. Richter, U. Gösele, J. Heydenreich, V. M. Ustinov, A. Yu Egorov, A. E. Zhukov, P. S. Kop'Ev, and Zh I. Alferov. Ultranarrow luminescence lines from single quantum dots. *Physical Review Letters*, 74(20):4043–4046, 1995.

[134] P Das, T K Chini, and J Pond. Probing Higher Order Surface Plasmon Modes on Individual Truncated Tetrahedral Gold Nanoparticle Using Cathodoluminescence Imaging and Spectroscopy Combined with FDTD Simulations. *Journal of Physical Chemistry C*, 116(29):15610–15619, 2012.

[135] S. J. Pennycook and A. Howie. Study of single-electron excitations by electron microscopy II. Cathodoluminescence image contrast from localized energy transfers. *Philosophical Magazine A: Physics of Condensed Matter, Structure, Defects and Mechanical Properties*, 41(6):809–827, 1980.

[136] Marcel Tence and Issy Moulineaux. Adjustable Cathodoluminescence Detection System and Microscope Employing Such a System, 2013.

[137] Luiz Fernando Zagonel. Nanometer scale spectral imaging of quantum emitters in nanowires and its correlation to their atomically resolved structure. *Nano Letters*, 11(2):568–573, 2011.

[138] Zackaria Mahfoud, Arjen T Dijksman, Clémentine Javaux, Pierre Bassoul, Anne-Laure Baudrion, Jéme Plain, Benoît Dubertret, and Mathieu Kociak. Cathodoluminescence in a Scanning Transmission Electron Microscope: A Nanometer-Scale Counterpart of Photoluminescence for the Study of II-VI Quantum Dots. *The Journal of Physical Chemistry Letters*, 4(23):4090–4094, 2013.

[139] L. H.G. Tizei and M. Kociak. Spectrally and spatially resolved cathodoluminescence of nanodiamonds: Local variations of the NV0 emission properties. *Nanotechnology*, 23(17), 2012.

[140] Romain Bourrellier, Michele Amato, Luiz Henrique Galvão Tizei, Christine Giorgetti, Alexandre Gloter, Malcolm I. Heggie, Katia March, Odile Stéphan, Lucia Reining, Mathieu Kociak, and Alberto Zobelli. Nanometric Resolved Luminescence in h-BN Flakes: Excitons and Stacking Order. *ACS Photonics*, 1(9):857–862, 2014.

[141] Sounderya Nagarajan, Catherine Pioche-Durieu, Luiz H G Tizei, Chia-Yi Fang, Jean-Remi Bertrand, Eric Le Cam, Huan-Cheng Chang, Francois Treussart, and Mathieu Kociak. Simultaneous cathodoluminescence and electron microscopy cytometry of cellular vesicles labeled with fluorescent nanodiamonds. *Nanoscale*, 8:11588–11594, 2016.

[142] V Myroshnychenko, J Nelayah, G Adamo, N Geuquet, J Rodriguez-Fernandez, I Pastoriza-Santos, K F MacDonald, L Henrard, L M Liz-Marzan, N I Zheludev, M Kociak, and F J G de Abajo. Plasmon Spectroscopy and Imaging of Individual Gold Nanodecahedra: A Combined Optical Microscopy, Cathodoluminescence, and Electron Energy-Loss Spectroscopy Study. *Nano Letters*, 12(8):4172–4180, 2012.

[143] R. H. Ritchie and A. Howie. Inelastic scattering probabilities in scanning transmission electron microscopy. *Phil. Mag. A*, 58:753–767, 1988.

[144] J. M. Pitarke, V. M. Silkin, E. V. Chulkov, and P. M. Echenique. Theory of surface plasmons and surface-plasmon polaritons. *Reports on Progress in Physics*, 70(1):1–87, 2007.

[145] P. Schattschneider, S. Rubino, C. Hébert, J. Rusz, J. Kuneš, P. Novák, E. Carlino, M. Fabrizioli, G. Panaccione, and G. Rossi. Detection of magnetic circular dichroism using a transmission electron microscope. *Nature*, 441(7092):486–488, 2006.

[146] P Schattschneider. *Linear and Chiral Dichroism in the Electron Microscope*. Pan Stanford, 2012.

[147] A J Bain and A Squire. Super-Gaussian field statistics in broadband laser emission. *Optics Communications*, 18(96):157–163, 1997.

[148] R Loudon. *The Quantum Theory of Light*. Oxford University Press, 2000.

[149] H. J. Kimble, M. Dagenais, and L. Mandel. Photon antibunching in resonance fluorescence. *Physical Review Letters*, 39(11):691–695, 1977.

[150] Mark Fox. *Quantum Optics: An Introduction*. 2006.

[151] R. Hanbury Brown and R. Q. Twiss. A test of a new type of stellar interferometer on Sirius. *Nature*, 178(4541):1046–1048, 1956.

[152] A. Beveratos, S. Kühn, R. Brouri, T. Gacoin, J. P. Poizat, and P. Grangier. Room temperature stable single-photon source. *European Physical Journal D*, 18(2):191–196, 2002.

[153] Ivan Rech, Antonino Ingargiola, Roberto Spinelli, Ivan Labanca, Stefano Marangoni, Massimo Ghioni, and Sergio Cova. Optical crosstalk in single photon avalanche diode arrays: a new complete model. *Optics Express*, 16(12):8381, 2008.

[154] Sophie Meuret. *Intensity Interferometry Experiments in a Scanning Transmission Electron Microscope : Physics and Applications*. PhD thesis, 2015.

[155] S. Meuret, L. H G Tizei, T. Cazimajou, R. Bourrellier, H. C. Chang, F. Treussart, and M. Kociak. Photon bunching in cathodoluminescence. *Physical Review Letters*, 114(19):1–5, 2015.

[156] Edward M. Purcell and Carlton R. Pennypacker. Scattering and Absorption of Light by Nonspherical Dielectric Grains. *The Astrophysical Journal*, 186:705, 1973.

[157] B T Draine and P J Flatau. Discrete-Dipole Approximation For Scattering Calculations. *Journal Of The Optical Society Of America A-Optics Image Science And Vision*, 11(4):1491–1499, 1994.

[158] A Trügler. *Optical Properties of Metallic Nanoparticles: Basic Principles and Simulation*. Springer Series in Materials Science. Springer International Publishing, 2016.

[159] Allen Taflove and Susan C. Hagness. *Computational Electrodynamics: The Finite-Difference Time-Domain Method, Third Edition*. 2005.

[160] Yang Cao, Alejandro Manjavacas, Nicolas Large, and Peter Nordlander. Electron Energy-Loss Spectroscopy Calculation in Finite-Difference Time-Domain Package. *ACS Photonics*, page 150227061405005, 2015.

[161] Guillaume Boudarham. *Nanooptique avec des electrons rapides : metamateriaux, formulation modale de la EMLDOS pour des systemes plasmoniques*. PhD thesis, 2011.

[162] Ulrich Hohenester and Andreas Trügler. MNPBEM – A Matlab toolbox for the simulation of plasmonic nanoparticles. *Computer Physics Communications*, 183(2):370–381, 2012.

[163] A. Tonomura, J. Endo, T. Matsuda, T. Kawasaki, and H. Ezawa. Demonstration of single-electron buildup of an interference pattern. *American Journal of Physics*, 57(2):117–120, 1989.

[164] Y Kubo, C Gatel, E Snoeck, and F Houdellier. Optimising electron microscopy experiment through electron optics simulation. *Ultramicroscopy*, 175(December 2016):67–80, 2017.

[165] AC Williams. The Eikonal Approximation without Ambiguity in Direction. *Annals of Physics*, 32:22–32, 1980.

[166] Jonas Krehl and Axel Lubk. Rytov approximation in electron scattering. *Physical Review B*, 95(24), 2017.

[167] A Torre. *Linear Ray and Wave Optics in Phase Space: Bridging Ray and Wave Optics via the Wigner Phase-Space Picture*. Elsevier Science, 2005.

[168] D Gabor. A new microscopic principle. *Nature*, 161(4098):777–778, 1948.

[169] Richard A Beth. Direct Detection of the Angular Momentum of Light. *Phys. Rev.*, 48(5):471, sep 1935.

[170] F J de Abajo and A Howie. Retarded field calculation of electron energy loss in inhomogeneous dielectrics. *Physical Review B*, 65(11):115418, 2002.

[171] N. Zabala, A. Rivacoba, and P. M. Echenique. Energy loss of electrons travelling through cylindrical holes. *Surface Science*, 209(3):465–480, 1989.

[172] F. García de Abajo. Relativistic energy loss and induced photon emission in the interaction of a dielectric sphere with an external electron beam. *Physical Review B*, 59(4):3095–3107, 1999.

[173] A Asenjo-Garcia and F J García de Abajo. Plasmon electron energy-gain spectroscopy. *New Journal of Physics*, 15(10):103021, 2013.

[174] Ido Kaminer, Maor Mutzafi, Amir Levy, Gal Harari, Hanan Herzig Sheinfux, Scott Skirlo, Jonathan Nemirovsky, John D. Joannopoulos, Mordechai Segev, and Marin Soljacic. Quantum Čerenkov radiation: Spectral cutoffs and the role of spin and orbital angular momentum. *Physical Review X*, 6(1):1–11, 2016.

[175] Kunio Fujiwara. Relativistic Dynamical Theory of Electron Diffraction. *Journal of the Physical Society of Japan*, 16(11):2226–2238, 1961.

[176] K. Terakura, Y. H. Ohtsuky, and S. Yanagawa. Relativistic dynamical theory of electron diffraction, 1966.

[177] K Watanabe. A Relativistic n-Beam Dynamical Theory for Fast Electron Diffraction. *Acta Crystallographica Section A*, pages 379–384, 1996.

[178] A. P. Sorini, J. J. Rehr, and Z. H. Levine. Magic angle in electron energy loss spectra: Relativistic and dielectric corrections. *Physical Review B - Condensed Matter and Materials Physics*, 77(11):1–10, 2008.

[179] D. van Dyck. The path integral formalism as a new description for the diffraction of high energy electrons in crystals. *Physica Status Solidi (B)*, 72(1):321–336, 1975.

[180] D. Gratias and R. Portier. Time-like perturbation method in high-energy electron diffraction. *Acta Crystallographica Section A*, 39(4):576–584, 1983.

[181] P. Schattschneider, C. Hébert, H. Franco, and B. Jouffrey. Anisotropic relativistic cross sections for inelastic electron scattering, and the magic angle. *Physical Review B - Condensed Matter and Materials Physics*, 72(4), 2005.

[182] A Rivacoba, N Zabala, J Aizpurua, and Maxwell Garnet. Image potential in scanning transmission electron microscopy. *Progress in Surface Science*, 65(1-2):1–64, 2000.

[183] Guillaume Boudarham. *Nanooptique avec des electrons rapides : metamateriaux, formulation modale de la EMLDOS pour des systemes plasmoniques.* PhD thesis, 2011.

[184] A. Rivacoba, N Zabala, and P M Echenique. Theory of Energy Loss in Scanning Transmission Electron Microscopy of Supported Small Particles. *Physical Review Letters*, 69(1):23, 1992.

[185] H Cohen, T Maniv, R Tenne, Y Rosenfeld Hacohen, O Stephan, and C Colliex. Near-Field Electron Energy Loss Spectroscopy of Nanoparticles. *Phys. Rev. Lett.*, 80(4):782–785, 1998.

[186] a. Asenjo-Garcia and F. J. García De Abajo. Dichroism in the interaction between vortex electron beams, plasmons, and molecules. *Physical Review Letters*, 113(6):1–5, 2014.

[187] Daniel Ugarte and Caterina Ducati. Controlling Multipolar Surface Plasmon Excitation through the Azimuthal Phase Structure of Electron Vortex Beams. 205418:1–9, 2015.

[188] A. Lubk and F. Röder. Phase-space foundations of electron holography. *Physical Review A - Atomic, Molecular, and Optical Physics*, 92(3):1–13, 2015.

[189] P. Schattschneider, M. Nelhiebel, H. Souchay, and B. Jouffrey. The physical significance of the mixed dynamic form factor. *Micron*, 31(4):333–345, 2000.

[190] H. Kohl and H. Rose. Theory of Image Formation by Inelastically Scattered Electrons in the Electron Microscope. *Advances in Electronics and Electron Physics*, 65(C):173–227, 1985.

[191] J. D. Jackson. From Lorenz to Coulomb and other explicit gauge transformations. *American Journal of Physics*, 70(9):917–928, 2002.

[192] Donald B Melrose. *Quantum Plasmadynamics: Unmagnetized Plasmas*, volume 735. Springer-Verlag New York, 2008.

[193] V B Berestetskii, L D Landau, E M Lifshitz, L P Pitaevskii, and J B Sykes. *Quantum Electrodynamics.* Course of theoretical physics. Butterworth-Heinemann, 1982.

[194] R Hambach. *Theory and ab-initio calculations of collective excitations in nanostructures : towards spatially-resolved EELS.* PhD thesis, 2010.

[195] Milton Abramowitz and Irene Stegun. *Handbook of Mathematical Functions, With Formulas, Graphs, and Mathematical Tables,*. Dover Publications, Incorporated, 1964.

[196] Peter Schattschneider and Hannes Lichte. Correlation and the density-matrix approach to inelastic electron holography in solid state plasmas. *Physical Review B - Condensed Matter and Materials Physics*, 71(4):1–9, 2005.

[197] K. Joulain, R. Carminati, J.-P. Mulet, and J.-J. Greffet. Definition and measurement of the local density of electromagnetic states close to an interface. *InternationalQuantum Electronics Conference, 2004. (IQEC).*, pages 1–10, 2004.

[198] Stefan Yoshi Buhmann, David T. Butcher, and Stefan Scheel. Macroscopic quantum electrodynamics in nonlocal and nonreciprocal media. *New Journal of Physics*, 14:0–12, 2012.

[199] Léon van Hove. Quantum-mechanical perturbations giving rise to a statistical transport equation. *Physica*, 21(1-5):517–540, 1954.

[200] Léon Van Hove. Correlations in space and time and born approximation scattering in systems of interacting particles. *Physical Review*, 95(1):249–262, 1954.

[201] Peter Schattschneider, Michael Stöger-Pollach, Stefano Rubino, Matthias Sperl, Christian Hurm, Josef Zweck, and Ján Rusz. Detection of magnetic circular dichroism on the two-nanometer scale. *Physical Review B*, 78(10):104413, 2008.

[202] C. Dwyer, S. D. Findlay, and L. J. Allen. Multiple elastic scattering of core-loss electrons in atomic resolution imaging. *Physical Review B - Condensed Matter and Materials Physics*, 77(18):1–8, 2008.

[203] B. Warot-Fonrose, F. Houdellier, M. J. Hÿtch, L. Calmels, V. Serin, and E. Snoeck. Mapping inelastic intensities in diffraction patterns of magnetic samples using the energy spectrum imaging technique. *Ultramicroscopy*, 108(5):393–398, 2008.

[204] R. C. Bourret. Stochastically perturbed fields, with applications to wave propagation in random media. *Il Nuovo Cimento Series 10*, 26(1):1–31, 1962.

[205] Uriel Frisch. Propagation of waves in random media. In T Bharucha-Reid, editor, *Probabilistic Methods in Applied Mathematics*, page 75. Academic Press, New-York, academic p edition, 1968.

[206] D. Pesme, G. Laval, and R. Pellat. Approximation des phases aléatoires et de l'élargissement de résonance en turbulence faible des plasmas. *Journal de Physique*, Colloque:C3–213, 1977.

[207] L D Landau and E M Lifshitz. *Quantum Mechanics: Non-Relativistic Theory*. Butterworth-Heinemann, 3 edition, 1981.

[208] R. P. Feynman. Space-time approach to quantum electrodynamics. *Physical Review*, 76(6):769–789, 1949.

[209] A. A. Abrikosov, L. P. Gorkov, and I. E. Dzyaloshinski. Methods of Quantum Field Theory in Statistical Physics, 1975.

[210] Falk Röder and Axel Lubk. Transfer and reconstruction of the density matrix in off-axis electron holography. *Ultramicroscopy*, 146:103–116, 2014.

[211] I Alber, W Sigle, S Muller, R Neumann, O Picht, M Rauber, P A van Aken, and M E Toimil-Molares. Visualization of Multipolar Longitudinal and Transversal Surface Plasmon Modes in Nanowire Dimers. *ACS Nano*, 5(12):9845–9853, 2011.

[212] Olivia Nicoletti, Francisco de la Peña, Rowan K Leary, Daniel J Holland, Caterina Ducati, and Paul a Midgley. Three-dimensional imaging of localized surface plasmon resonances of metal nanoparticles. *Nature*, 502(7469):80–4, 2013.

[213] Edson P. Bellido, Alejandro Manjavacas, Yue Zhang, Yang Cao, Peter Nordlander, and Gianluigi A. Botton. Electron Energy-Loss Spectroscopy of Multipolar Edge and Cavity Modes in Silver Nanosquares. *ACS Photonics*, 3(3):428–433, 2016.

[214] Anton Hörl, Andreas Trügler, and Ulrich Hohenester. Tomography of Particle Plasmon Fields from Electron Energy Loss Spectroscopy. *Phys. Rev. Lett.*, 111(7):76801, 2013.

[215] S M Collins, E Ringe, M Duchamp, Z Saghi, R E Dunin-Borkowski, and P A Midgley. Eigenmode Tomography of Surface Charge Oscillations of Plasmonic Nanoparticles by Electron Energy Loss Spectroscopy. *Acs Photonics*, 2(11):1628–1635, 2015.

[216] Anton Hörl, Andreas Trügler, and Ulrich Hohenester. Full Three-Dimensonal Reconstruction of the Dyadic Green Tensor from Electron Energy Loss Spectroscopy of Plasmonic Nanoparticles. *ACS Photonics*, 2(10):1429–1435, 2015.

[217] Anton Hörl, Georg Haberfehlner, Andreas Trügler, Franz-Philipp Schmidt, Ulrich Hohenester, and Gerald Kothleitner. Tomographic imaging of the photonic environment of plasmonic nanoparticles. *Nature Communications*, 8(1):37, 2017.

[218] Anton Kuzyk, Robert Schreiber, Zhiyuan Fan, Günther Pardatscher, Eva Maria Roller, Alexander Högele, Friedrich C. Simmel, Alexander O. Govorov, and Tim Liedl. DNA-based self-assembly of chiral plasmonic nanostructures with tailored optical response. *Nature*, 483(7389):311–314, 2012.

[219] Robert Schreiber, Ngoc Luong, Zhiyuan Fan, Anton Kuzyk, Philipp C. Nickels, Tao Zhang, David M. Smith, Bernard Yurke, Wan Kuang, Alexander O. Govorov, and Tim Liedl. Chiral plasmonic DNA nanostructures with switchable circular dichroism. *Nature Communications*, 4:1–6, 2013.

[220] N. Yamamoto, X. G. Jin, A. Mano, T. Ujihara, Y. Takeda, S. Okumi, T. Nakanishi, T. Yasue, T. Koshikawa, T. Ohshima, T. Saka, and H. Horinaka. Status of the high brightness polarized electron source using transmission photocathode. *Journal of Physics: Conference Series*, 298(1), 2011.

[221] M. Kuwahara, Y. Takeda, K. Saitoh, T. Ujihara, H. Asano, T. Nakanishi, and N. Tanaka. Development of spin-polarized transmission electron microscope. *Journal of Physics: Conference Series*, 298(1), 2011.

[222] J. F. Nye and M. V. Berry. Dislocations in Wave Trains. *Proceedings of the Royal Society A: Mathematical, Physical and Engineering Sciences*, 336(1605):165–190, 1974.

[223] Mark R. Dennis, Kevin O'Holleran, and Miles J. Padgett. *Chapter 5 Singular Optics: Optical Vortices and Polarization Singularities*, volume 53. Elsevier B.V., 2009.

[224] Marat Soskin, Svetlana Boriskina, Yidong Chong, Mark R. Dennis, and Anton Desyatnikov. Singular optics and topological photonics. *Journal of Optics*, 19:010401, 2017.

[225] Konstantin Y. Bliokh, Peter Schattschneider, Jo Verbeeck, and Franco Nori. Electron vortex beams in a magnetic field: A new twist on landau levels and aharonov-bohm states. *Physical Review X*, 2(4):1–15, 2012.

[226] Ronald L Phillips and Larry C Andrews. Spot size and divergence for Laguerre Gaussian beams of any order. *Appl. Opt.*, 22(5):643–644, mar 1983.

[227] Vincenzo Grillo, Ebrahim Karimi, Gian Carlo Gazzadi, Stefano Frabboni, Mark R. Dennis, and Robert W. Boyd. Generation of nondiffracting electron bessel beams. *Physical Review X*, 4(1):1–7, 2014.

[228] M. W. Beijersbergen, L. Allen, H. E.L.O. van der Veen, and J. P. Woerdman. Astigmatic laser mode converters and transfer of orbital angular momentum. *Optics Communications*, 96(1-3):123–132, 1993.

[229] Konstantin Y. Bliokh, Mark R. Dennis, and Franco Nori. Relativistic electron vortex beams: Angular momentum and spin-orbit interaction. *Physical Review Letters*, 107(17):1–5, 2011.

[230] Giulio Guzzinati. *Exploring electron beam shaping in transmission electron microscopy.* PhD thesis, 2015.

[231] L. Clark, A. Béché, G. Guzzinati, A. Lubk, M. Mazilu, R. Van Boxem, and J. Verbeeck. Exploiting lens aberrations to create electron-vortex beams. *Physical Review Letters*, 111(6):1–5, 2013.

[232] K Y Bliokh, I P Ivanov, G Guzzinati, L Clark, R Van Boxem, A Béché, R Juchtmans, M A Alonso, P Schattschneider, F Nori, and J Verbeeck. Theory and applications of free-electron vortex states. *Physics Reports*, 690:1–70, 2017.

[233] Jo Verbeeck, Armand Béché, Knut Müller-Caspary, Giulio Guzzinati, Minh Anh Luong, and Martien Den Hertog. Demonstration of a 2 x 2 programmable phase plate for electrons. *Ultramicroscopy*, 190(December 2017):58–65, 2018.

[234] M W Beijersbergen, R P C Coerwinkel, M Kristensen, and J P Woerdman. Helical-Wave-Front Laser-Beams Produced With a Spiral Phaseplate. *Optics Communications*, 112(5-6):321–327, 1994.

[235] Roy Shiloh, Roei Remez, Peng-han Lu, Lei Jin, Yossi Lereah, Amir H Tavabi, Rafal E. Dunin-Borkowski, and Ady Arie. Spherical aberration correction in a scanning transmission electron microscope using a sculpted thin film. *Ultramicroscopy*, 189:46–53, 2018.

[236] J. Verbeeck, H. Tian, and A. Béché. A new way of producing electron vortex probes for STEM. *Ultramicroscopy*, 113:83–87, 2012.

[237] Giulio Guzzinati, Laura Clark, Armand Béché, and Jo Verbeeck. Measuring the orbital angular momentum of electron beams. *Physical Review A*, 89(2):025803, 2014.

[238] E. Mafakheri, A. H. Tavabi, P. H. Lu, R. Balboni, F. Venturi, C. Menozzi, G. C. Gazzadi, S. Frabboni, A. Sit, R. E. Dunin-Borkowski, E. Karimi, and V. Grillo. Realization of electron vortices with large orbital angular momentum using miniature holograms fabricated by electron beam lithography. *Applied Physics Letters*, 110(9), 2017.

[239] Konstantin Yu Bliokh, Yury P. Bliokh, Sergey Savel'Ev, and Franco Nori. Semiclassical dynamics of electron wave packet states with phase vortices. *Physical Review Letters*, 99(19):1–4, 2007.

[240] Armand Béché, Ruben Van Boxem, Gustaaf Van Tendeloo, and Jo Verbeeck. Magnetic monopole field exposed by electrons. *Nature Physics*, 10(1):26–29, 2013.

[241] Giulio Guzzinati, Armand Béché, Hugo Lourenço-Martins, Jérôme Martin, Mathieu Kociak, and Jo Verbeeck. Probing the symmetry of the potential of localized surface plasmon resonances with phase-shaped electron beams. *Nature Communications*, 8:14999, 2017.

[242] Noa Voloch-Bloch, Yossi Lereah, Yigal Lilach, Avraham Gover, and Ady Arie. Generation of electron Airy beams. *Nature*, 494(7437):331–335, 2013.

[243] Giulio Guzzinati, Laura Clark, Armand Béché, Roeland Juchtmans, Ruben Van Boxem, Michael Mazilu, and Jo Verbeeck. Prospects for versatile phase manipulation in the TEM: Beyond aberration correction. *Ultramicroscopy*, 151:85–93, 2015.

[244] Ioannis M Besieris and Amr M Shaarawi. A note on an accelerating finite energy Airy beam. *Optics letters*, 32(16):2447–9, 2007.

[245] J. Durnin, J. Miceli, and J. H. Eberly. Diffraction-free beams. *Physical Review Letters*, 58(15):1499–1501, 1987.

[246] J. E. Morris, T. Čižmár, H. I.C. Dalgarno, R. F. Marchington, F. J. Gunn-Moore, and K. Dholakia. Realization of curved Bessel beams: propagation around obstructions. *Journal of Optics*, 12(12), 2010.

[247] M Mousley, G Thirunavukkarasu, M Babiker, and J Yuan. Robust and adjustable C-shaped vortex beams. *New Journal of Physics*, 19(6):063008, 2017.

[248] Ulrich Hohenester and Andreas Trügler. MNPBEM – A Matlab toolbox for the simulation of plasmonic nanoparticles. *Computer Physics Communications*, 183(2):370–381, 2012.

[249] A. Asenjo-Garcia and F. J. García De Abajo. Dichroism in the interaction between vortex electron beams, plasmons, and molecules. *Physical Review Letters*, 113(6):1–5, 2014.

[250] Pabitra Das, Hugo Lourenço-Martins, Luiz Henrique Galvão Tizei, Raphaël Weil, and Mathieu Kociak. Nanocross: A Highly Tunable Plasmonic System. *The Journal of Physical Chemistry C*, 121(30):16521–16527, 2017.

[251] Lin Gu, Wilfried Sigle, Christoph T. Koch, Burcu Ögüt, Peter A. Van Aken, Nahid Talebi, Ralf Vogelgesang, Jianlin Mu, Xiaogang Wen, and Jian Mao. Resonant wedge-plasmon modes in single-crystalline gold nanoplatelets. *Physical Review B - Condensed Matter and Materials Physics*, 83(19):1–7, 2011.

[252] K. A. Nugent and D. Paganin. Matter-wave phase measurement: a noninterferometric approach. *Physical Review A - Atomic, Molecular, and Optical Physics*, 61(6):063614–063611, 2000.

[253] Martin J Bastiaans and Kurt Bernardo Wolf. Phase reconstruction from intensity measurements in linear systems. *Journal of the Optical Society of America A*, 20(6):1046–1049, 2003.

[254] J. Verbeeck, P. Schattschneider, S. Lazar, M. Stöger-Pollach, S. Löffler, A. Steiger-Thirsfeld, and G. Van Tendeloo. Atomic scale electron vortices for nanoresearch. *Applied Physics Letters*, 99(20):2014–2017, 2011.

[255] J. Barthel, J. Mayer, J. Rusz, P.-L. Ho, X. Y. Zhong, M. Lentzen, R. E. Dunin-Borkowski, K. W. Urban, H. G. Brown, S. D. Findlay, and L. J. Allen. Understanding electron magnetic circular dichroism in a transition potential approach. *Physical Review B*, 97(14):144103, 2018.

[256] M. R. Dennis and M. A. Alonso. Swings and roundabouts: Optical Poincaré spheres for polarization and Gaussian beams. *Philosophical Transactions of the Royal Society A: Mathematical, Physical and Engineering Sciences*, 375(2087), 2017.

[257] M. J. Padgett and J. Courtial. Poincaré-sphere equivalent for light beams containing orbital angular momentum. *Optics Letters*, 24(7):430, 1999.

[258] Eugeny Abramochkin, Evgeniya Razueva, and Vladimir Volostnikov. General astigmatic transform of Hermite–Laguerre–Gaussian beams. *Journal of the Optical Society of America A*, 27(11):2506, 2010.

[259] P. Schattschneider, M. Stöger-Pollach, and J. Verbeeck. Novel vortex generator and mode converter for electron beams. *Physical Review Letters*, 109(8):1–5, 2012.

[260] M V Berry. Optical currents. *J. Opt. A: Pure Appl. Opt.*, 11:094001, 2009.

[261] Yiqiao Tang and Adam E. Cohen. Optical chirality and its interaction with matter. *Physical Review Letters*, 104(16):1–4, 2010.

[262] Yiqiao Tang and Adam E. Cohen. Enhanced enantioselectivity in excitation of chiral molecules by superchiral light. *Science*, 332(6027):333–336, 2011.

[263] Konstantin Y Bliokh and Franco Nori. Characterizing optical chirality. *Physical Review A - Atomic, Molecular, and Optical Physics*, 83(2):1–3, 2011.

[264] Konstantin Y. Bliokh and Franco Nori. Transverse spin of a surface polariton. *Physical Review A - Atomic, Molecular, and Optical Physics*, 85(6):1–5, 2012.

[265] M. H. Alizadeh and Björn M. Reinhard. Enhanced Optical Chirality through Locally Excited Surface Plasmon Polaritons. *ACS Photonics*, 2(7):942–949, 2015.

[266] M.H. Alizadeh and Björn M. Reinhard. Emergence of transverse spin in optical modes of semiconductor nanowires. *Optics Express*, 24(8):8471, 2016.

[267] Martin Schäferling, Daniel Dregely, Mario Hentschel, and Harald Giessen. Tailoring enhanced optical chirality: Design principles for chiral plasmonic nanostructures. *Physical Review X*, 2(3):1–9, 2012.

[268] Martin Schäferling, Xinghui Yin, and Harald Giessen. Formation of chiral fields in a symmetric environment. *Optics Express*, 20(24):26326, 2012.

[269] Martin Schäferling, Xinghui Yin, Nader Engheta, and Harald Giessen. Helical Plasmonic Nanostructures as Prototypical Chiral Near-Field Sources. *ACS Photonics*, 1(6):530–537, 2014.

[270] Antoine Canaguier-Durand, Aurélien Cuche, Cyriaque Genet, and Thomas W. Ebbesen. Force and torque on an electric dipole by spinning light fields. *Physical Review A - Atomic, Molecular, and Optical Physics*, 88(3):88–91, 2013.

[271] Frédéric Fossard, Lorenzo Sponza, Léonard Schué, Claudio Attaccalite, François Ducastelle, Julien Barjon, and Annick Loiseau. Angle-resolved electron energy loss spectroscopy in hexagonal boron nitride. *Physical Review B*, 96(11):1–9, 2017.

[272] Vincenzo Grillo, Amir H. Tavabi, Federico Venturi, Hugo Larocque, Roberto Balboni, Gian Carlo Gazzadi, Stefano Frabboni, Peng Han Lu, Erfan Mafakheri, Frédéric Bouchard, Rafal E. Dunin-Borkowski, Robert W. Boyd, Martin P.J. Lavery, Miles J. Padgett, and Ebrahim Karimi. Measuring the orbital angular momentum spectrum of an electron beam. *Nature Communications*, 8(May):6–11, 2017.

[273] Hwi Kim, Junghyun Park, Seong Woo Cho, Seung Yeol Lee, Minsu Kang, and Byoungho Lee. Synthesis and dynamic switching of surface plasmon vortices with plasmonic vortex lens. *Nano Letters*, 10(2):529–536, 2010.

[274] Guanghao Rui, Qiwen Zhan, and Yiping Cui. Tailoring optical complex field with spiral blade plasmonic vortex lens. *Scientific Reports*, 5:1–9, 2015.

[275] Wei Cai, Ori Reinhardt, Ido Kaminer, and J. Garcia de Abajo. Efficient orbital angular momentum transfer between plasmons and free electrons. pages 1–8, 2018.

[276] V I Fabrikant. Elementary exact evaluation of infinite integrals of the product of several spherical Bessel functions, power and exponential. *Quarterly Applied Mathematics*, 71(3):573–581, 2013.

[277] M McCartney. Differential phase contrast in TEM. *Ultramicroscopy*, 65(3-4):179–186, 1996.

[278] Christoph T. Koch. A flux-preserving non-linear inline holography reconstruction algorithm for partially coherent electrons. *Ultramicroscopy*, 108(2):141–150, 2008.

[279] Hannes Lichte, Felix Börrnert, Andreas Lenk, Axel Lubk, Falk Röder, Jan Sickmann, Sebastian Sturm, Karin Vogel, and Daniel Wolf. Electron holography for fields in solids: Problems and progress. *Ultramicroscopy*, 134:126–134, 2013.

[280] Falk Röder, Axel Lubk, Daniel Wolf, and Tore Niermann. Noise estimation for off-axis electron holography. *Ultramicroscopy*, 144:32–42, 2014.

[281] C. Hébert and P. Schattschneider. A proposal for dichroic experiments in the electron microscope. *Ultramicroscopy*, 96(3-4):463–468, 2003.

[282] L. Mandel and E. Wolf. Coherence properties of optical fields. *Reviews of Modern Physics*, 37(2):231–287, 1965.

[283] Drew Morrill, Dongfang Li, and Domenico Pacifici. Measuring subwavelength spatial coherence with plasmonic interferometry. *Nature Photonics*, 10(10):681–687, 2016.

[284] Craig F Bohren and Donald R Huffman. *Absorption and scattering of light by small particles.* John Wiley & Sons, 2008.

[285] Katherine A Willets and Richard P Van Duyne. Localized surface plasmon resonance spectroscopy and sensing. *Annual Review of Physical Chemistry*, 58:267–297, 2007.

[286] Ekmel Ozbay. Plasmonics: merging photonics and electronics at nanoscale dimensions. *Science*, 311(5758):189–193, 2006.

[287] Pabitra Das, Tapas Kumar Chini, and James Pond. Probing higher order surface plasmon modes on individual truncated tetrahedral gold nanoparticle using cathodoluminescence imaging and spectroscopy combined with FDTD simulations. *J. Phys. Chem. C*, 116(29):15610–15619, 2012.

[288] Jérôme Martin, Mathieu Kociak, Zackaria Mahfoud, Julien Proust, Davy Gérard, and Jérôme Plain. High-resolution imaging and spectroscopy of multipolar plasmonic resonances in aluminum nanoantennas. *Nano Lett.*, 14(10):5517–5523, 2014.

[289] Martin Mesch, Bernd Metzger, Mario Hentschel, and Harald Giessen. Nonlinear plasmonic sensing. *Nano Lett.*, 16(5):3155–3159, 2016.

[290] M Sun. Surface-enhanced Raman scattering. *Handbook of Molecular Plasmonics*, page 321, 2013.

[291] K R Catchpole and Albert Polman. Plasmonic solar cells. *Opt. Express*, 16(26):21793–21800, 2008.

[292] P Mandal and S Sharma. Progress in plasmonic solar cell efficiency improvement: A status review. *Renewable Sustainable Energy Rev.*, 65:537–552, 2016.

[293] Simon P Hastings, Pattanawit Swanglap, Zhaoxia Qian, Ying Fang, So-Jung Park, Stephan Link, Nader Engheta, and Zahra Fakhraai. Quadrupole-enhanced Raman scattering. *ACS Nano*, 8(9):9025–9034, 2014.

[294] Achyut Maity, Arpan Maiti, Biswarup Satpati, Avinash Patsha, Sandip Dhara, and Tapas Kumar Chini. Probing localized surface plasmons of trisoctahedral gold nanocrystals for Surface Enhanced Raman Scattering. *J. Phys. Chem. C*, 120(47):27003–27012, 2016.

[295] Qingfeng Zhang, Nicolas Large, and Hui Wang. Gold nanoparticles with tipped surface structures as substrates for single-particle surface-enhanced Raman spectroscopy: concave nanocubes, nanotrisoctahedra, and nanostars. *ACS Appl. Mater. Interfaces*, 6(19):17255–17267, 2014.

[296] M Bosman, V J Keast, J L Garc\'\ia-Muñoz, A J D'Alfonso, S D Findlay, and L J Allen. Two-Dimensional Mapping of Chemical Information at Atomic Resolution. *Phys. Rev. Lett.*, 99(8):86102, 2007.

[297] O Nicoletti, M Wubs, N A Mortensen, W Sigle, P A van Aken, and P A Midgley. Surface plasmon modes of a single silver nanorod: an electron energy loss study. *Optics Express*, 19(16):15371–15379, 2011.

[298] R Gómez-Medina, N Yamamoto, M Nakano, and F J Garc\'\ia de Abajo. Mapping plasmons in nanoantennas via cathodoluminescence. *New J. Phys.*, 10(10):105009, 2008.

[299] Kohei Imura, Tetsuhiko Nagahara, and Hiromi Okamoto. Near-field two-photon-induced photoluminescence from single gold nanorods and imaging of plasmon modes. *J. Phys. Chem. B*, 109(27):13214–13220, 2005.

[300] Carsten Sönnichsen and A Paul Alivisatos. Gold nanorods as novel nonbleaching plasmon-based orientation sensors for polarized single-particle microscopy. *Nano Lett.*, 5(2):301–304, 2005.

[301] Carolina Novo, Daniel Gomez, Jorge Perez-Juste, Zhenyuan Zhang, Hristina Petrova, Maximilian Reismann, Paul Mulvaney, and Gregory V Hartland. Contributions from radiation damping and surface scattering to the linewidth of the longitudinal plasmon band of gold nanorods: a single particle study. *Phys. Chem. Chem. Phys.*, 8(30):3540–3546, 2006.

[302] Javier Aizpurua, Garnett W Bryant, Lee J Richter, F J Garc\'\ia De Abajo, Brian K Kelley, and T Mallouk. Optical properties of coupled metallic nanorods for field-enhanced spectroscopy. *Phys. Rev. B*, 71(23):235420, 2005.

[303] Mark W Knight, Lifei Liu, Yumin Wang, Lisa Brown, Shaunak Mukherjee, Nicholas S King, Henry O Everitt, Peter Nordlander, and Naomi J Halas. Aluminum plasmonic nanoantennas. *Nano Lett.*, 12(11):6000–6004, 2012.

[304] A I Denisyuk, G Adamo, K F MacDonald, J Edgar, M D Arnold, Viktor Myroshnychenko, M J Ford, F Javier de Abajo, and N I Zheludev. Transmitting hertzian optical nanoantenna with free-electron feed. *Nano Lett.*, 10(9):3250–3252, 2010.

[305] Jan Becker, Andreas Trügler, Arpad Jakab, Ulrich Hohenester, and Carsten Sönnichsen. The optimal aspect ratio of gold nanorods for plasmonic bio-sensing. *Plasmonics*, 5(2):161–167, 2010.

[306] Kat Choi Woo, Lei Shao, Huanjun Chen, Yao Liang, Jianfang Wang, and Hai-Qing Lin. Universal scaling and Fano resonance in the plasmon coupling between gold nanorods. *ACS Nano*, 5(7):5976–5986, 2011.

[307] Colleen L Nehl and Jason H Hafner. Shape-dependent plasmon resonances of gold nanoparticles. *J. Mater. Chem.*, 18(21):2415–2419, 2008.

[308] P Das and T K Chini. Substrate Induced Symmetry Breaking in Penta-twinned Gold Nanorod Probed by Free Electron Impact. *Journal of Physical Chemistry C*, 118(45):26284–26291, 2014.

[309] E J R Vesseur, R de Waele, M Kuttge, and A Polman. Direct observation of plasmonic modes in Au nanowires using high-resolution cathodoluminescence Spectroscopy. *Nano Letters*, 7(9):2843–2846, 2007.

[310] Niels Verellen, Pol Van Dorpe, Chengjun Huang, Kristof Lodewijks, Guy A E Vandenbosch, Liesbet Lagae, and Victor V Moshchalkov. Plasmon line shaping using nanocrosses for high sensitivity localized surface plasmon resonance sensing. *Nano Lett.*, 11(2):391–397, 2011.

[311] Niels Verellen, Pol Van Dorpe, Dries Vercruysse, Guy A E Vandenbosch, and Victor V Moshchalkov. Dark and bright localized surface plasmons in nanocrosses. *Opt. Express*, 19(12):11034–11051, 2011.

[312] Enyi Ye, Khin Yin Win, Hui Ru Tan, Ming Lin, Choon Peng Teng, Adnen Mlayah, and Ming-Yong Han. Plasmonic gold nanocrosses with multidirectional excitation and strong photothermal effect. *J. Am. Chem. Soc.*, 133(22):8506–8509, 2011.

[313] F J Rodr\'\iguez-Fortuño, M Mart\'\inez-Marco, B Tomás-Navarro, R Ortuño, J Mart\'\i, A Mart\'\inez, and P J Rodr\'\iguez-Cantó. Highly-sensitive chemical detection in the infrared regime using plasmonic gold nanocrosses. *Appl. Phys. Lett.*, 98(13):133118, 2011.

[314] M B Cortie, N Stokes, and A McDonagh. Plasmon resonance and electric field amplification of crossed gold nanorods. *Photonics and Nanostructures-Fundamentals and Applications*, 7(3):143–152, 2009.

[315] Hui Zhang, Hilmi Volkan Demir, and Alexander O Govorov. Plasmonic metamaterials and nanocomposites with the narrow transparency window effect in broad extinction spectra. *ACS Photonics*, 1(9):822–832, 2014.

[316] Peter B Johnson and R-W_ Christy. Optical constants of the noble metals. *Phys. Rev. B*, 6(12):4370, 1972.

[317] Andreas Trügler, Jean-Claude Tinguely, Joachim R Krenn, Andreas Hohenau, and Ulrich Hohenester. Influence of surface roughness on the optical properties of plasmonic nanoparticles. *Physical Review B*, 83(8):081412, 2011.

[318] E. Prodan, C. Radloff, N. J. Halas, and P. Nordlander. A Hybridization Model for the Plasmon Response of Complex Nanostructures. *Science*, 302(5644):419–422, 2003.

[319] P. Nordlander, C. Oubre, E. Prodan, K. Li, and M. I. Stockman. Plasmon hybridization in nanoparticle dimers. *Nano Letters*, 4(5):899–903, 2004.

[320] Sampsa Riikonen, Isabel Romero, and F. J. García De Abajo. Plasmon tunability in metallodielectric metamaterials. *Physical Review B - Condensed Matter and Materials Physics*, 71(23):4–9, 2005.

[321] Emil Prodan, Corey Radloff, Naomi J Halas, and Peter Nordlander. A hybridization model for the plasmon response of complex nanostructures. *Science*, 302(5644):419–422, 2003.

[322] Sean M. Collins, Olivia Nicoletti, David Rossouw, Tomas Ostasevicius, and Paul A. Midgley. Excitation dependent Fano-like interference effects in plasmonic silver nanorods. *Physical Review B - Condensed Matter and Materials Physics*, 90(15):1–24, 2014.

[323] P. T. Leung, S. Y. Liu, and K. Young. Completeness and orthogonality of quasinormal modes in leaky optical cavities. *Physical Review A*, 49(4):1–11, 1994.

[324] E S C Ching, P T Leung, A M van den Brink, W M Suen, S S Tong, and K Young. Quasinormal-mode expansion for waves in open systems. *Reviews of Modern Physics*, 70(4):1545–1554, 1998.

[325] P T Leung, W M Suen, C P Sun, and K Young. Waves in open systems via a biorthogonal basis. *Physical Review E*, 57(5):6101–6104, 1998.

[326] Hadiseh Alaeian and Jennifer A Dionne. Non-Hermitian nanophotonic and plasmonic waveguides. *Phys. Rev. B*, 89(7):75136–75139, 2014.

[327] Carl M Bender, Dorje C Brody, and Hugh F Jones. Complex Extension of Quantum Mechanics. *Phys. Rev. Lett.*, 89(27):L391—-4, 2002.

[328] Dorje C Brody. Biorthogonal quantum mechanics. *Journal of Physics A: Mathematical and Theoretical*, 47:035305, 2014.

[329] Carl M. Bender and Stefan Boettcher. Real spectra in non-hermitian hamiltonians having PT symmetry. *Physical Review Letters*, 80(24):5243–5246, 1998.

[330] Ramy El-Ganainy, Konstantinos G. Makris, Mercedeh Khajavikhan, Ziad H. Musslimani, Stefan Rotter, and Demetrios N. Christodoulides. Non-Hermitian physics and PT symmetry. *Nature Physics*, 14(1):11–19, 2018.

[331] W. D. Heiss. The physics of exceptional points. *Journal of Physics A: Mathematical and Theoretical*, 45(44):28, 2012.

[332] W. D. Heiss. Global and Local Aspects of Exceptional Point. *arXiv*, 311, 2002.

[333] Dieter Heiss. Mathematical physics: Circling exceptional points. *Nature Physics*, 12(9):823–824, 2016.

[334] A P Seyranian, O N Kirillov, and A A Mailybaev. Coupling of eigenvalues of complex matrices at diabolic and exceptional points. *Journal of Physics A: Mathematical and General*, 38(8):1723–1740, 2005.

[335] T Stehmann, W D Heiss, and F G Scholtz. Observation of exceptional points in electronic circuits. *Journal of Physics A: Mathematical and General*, 37(31):7813, 2004.

[336] Jörg Doppler, Alexei A Mailybaev, Julian Böhm, Ulrich Kuhl, Adrian Girschik, Florian Libisch, Thomas J. Milburn, Peter Rabl, Nimrod Moiseyev, and Stefan Rotter. Dynamically encircling exceptional points in a waveguide: asymmetric mode switching from the breakdown of adiabaticity. *Nature*, 2(2):1–13, 2016.

[337] Ashok Kodigala, Thomas Lepetit, and Boubacar Kanté. Exceptional points in three-dimensional plasmonic nanostructures. *Physical Review B - Condensed Matter and Materials Physics*, 94(20):1–5, 2016.

[338] Younghoon Shin, Hojeong Kwak, Songky Moon, Sang-Bum Lee, Juhee Yang, and Kyungwon An. Observation of an exceptional point in a two-dimensional ultrasonic cavity of concentric circular shells. *Scientific Reports*, 6(December):38826, 2016.

[339] Choloong Hahn, Youngsun Choi, Jae Woong Yoon, Seok Ho Song, Cha Hwan Oh, and Pierre Berini. Observation of exceptional points in reconfigurable non-Hermitian vector-field holographic lattices. *Nature Communications*, 7:12201, 2016.

[340] Mei C. Zheng, Demetrios N. Christodoulides, Ragnar Fleischmann, and Tsampikos Kottos. PT optical lattices and universality in beam dynamics. *Physical Review A - Atomic, Molecular, and Optical Physics*, 82(1):1–4, 2010.

[341] Hadiseh Alaeian and Jennifer A Dionne. Parity-time-symmetric plasmonic metamaterials. *Phys. Rev. A*, 89(3):33829, mar 2014.

[342] Xiaobo Yin and Xiang Zhang. Unidirectional light propagation at exceptional points. *Nature Materials*, 12(3):175–177, 2013.

[343] Bo Peng, Şahin Kaya Özdemir, Fuchuan Lei, Faraz Monifi, Mariagiovanna Gianfreda, Gui Lu Long, Shanhui Fan, Franco Nori, Carl M. Bender, and Lan Yang. Parity–time-symmetric whispering-gallery microcavities. *Nature Physics*, 10(5):394–398, 2014.

[344] Youngsun Choi, Choloong Hahn, Jae Woong Yoon, Seok Ho Song, and Pierre Berini. Extremely broadband, on-chip optical nonreciprocity enabled by mimicking nonlinear anti-adiabatic quantum jumps near exceptional points. *Nature Communications*, 8:14154, 2017.

[345] F. García de Abajo and J. Aizpurua. Numerical simulation of electron energy loss near inhomogeneous dielectrics. *Physical Review B*, 56(24):15873–15884, 1997.

[346] Fabio Bagarello, Roberto Passante, and Camillo Trapani. *Non-Hermitian Hamiltonians in Quantum Physics*, volume 184. Springer p edition, 2016.

[347] Franz-Philipp Schmidt, Harald Ditlbacher, Andreas Hohenau, Ulrich Hohenester, Ferdinand Hofer, and Joachim R. Krenn. Edge Mode Coupling within a Plasmonic Nanoparticle. *Nano Letters*, 16(8):5152–5155, 2016.

[348] C. Sauvan, J. P. Hugonin, I. S. Maksymov, and P. Lalanne. Theory of the spontaneous optical emission of nanosize photonic and plasmon resonators. *Physical Review Letters*, 110(23), 2013.

[349] Philip Trøst Kristensen, Rong Chun Ge, and Stephen Hughes. Normalization of quasinormal modes in leaky optical cavities and plasmonic resonators. *Physical Review A - Atomic, Molecular, and Optical Physics*, 92(5):1–9, 2015.

[350] Ali Mostafazadeh. Conceptual Aspects of PT-Symmetry and Pseudo-Hermiticity: A status report. *Physica Scripta*, 82:038110, 2010.

[351] Christian E. Rüter, Konstantinos G. Makris, Ramy El-Ganainy, Demetrios N. Christodoulides, Mordechai Segev, and Detlef Kip. Observation of parity–time symmetry in optics. *Nature Physics*, 6(3):192–195, 2010.

[352] R. Kretschmer and L. Szymanowski. Quasi-Hermiticity in infinite-dimensional Hilbert spaces. *Physics Letters, Section A: General, Atomic and Solid State Physics*, 325(2):112–117, 2004.

[353] C. Zener. Non-Adiabatic Crossing of Energy Levels. *Proceedings of the Royal Society A: Mathematical, Physical and Engineering Sciences*, 137(833):696–702, 1932.

[354] Lisa V. Brown, Heidar Sobhani, J. Britt Lassiter, Peter Nordlander, and Naomi J. Halas. Heterodimers: Plasmonic properties of mismatched nanoparticle pairs. *ACS Nano*, 4(2):819–832, 2010.

[355] Lukas Novotny. Strong coupling , energy splitting , and level crossings : A classical. *American Journal of Physics*, 78(July):1199–1202, 2010.

[356] A. Gloter, A. Douiri, M. Tence, and C. Colliex. Improving energy resolution of EELS spectra: an alternative to the monochromator solution. *Ultramicroscopy*, 96(3-4):385–400, 2003.

[357] D V Savin and J.-B. De Vaulx. Probing eigenfunction nonorthogonality by parametric shifts of resonance widths. *Acta Physica Polonica A*, 1074(6):3–6, 2013.

[358] Carl M Bender and Stefan Boettcher. Real Spectra in Non-Hermitian Hamiltonians Having PT-Symmetry. *Phys. Rev. Lett.*, 80(24):5243–5246, 1998.

[359] A Guo, G J Salamo, D Duchesne, R Morandotti, M Volatier-Ravat, V Aimez, G A Siviloglou, and D N Christodoulides. Observation of PT-symmetry breaking in complex optical potentials. *Physical Review Letters*, 103(9):1–4, 2009.

[360] Soo Young Lee. Decaying and growing eigenmodes in open quantum systems: Biorthogonality and the Petermann factor. *Physical Review A - Atomic, Molecular, and Optical Physics*, 80(4):1–9, 2009.

[361] K G Makris, R El-Ganainy, D N Christodoulides, and Z H Musslimani. Beam dynamics in PT symmetric optical lattices. *Physical Review Letters*, 100(10):1–4, 2008.

[362] Nadia Grillet, Delphine Manchon, Franck Bertorelle, Christophe Bonnet, Michel Broyer, Emmanuel Cottancin, Jean Lermé, Matthias Hillenkamp, and Michel Pellarin. Plasmon coupling in silver nanocube dimers: Resonance splitting induced by edge rounding. *ACS Nano*, 5(12):9450–9462, 2011.

[363] Stefano Mazzucco, Nicolas Geuquet, Ye Jian, Odile Stephan, Wim Van Roy, Pol Van Dorpe, Luc Henrard, and Mathieu Kociak. Ultra local modification of surface plasmons properties in silver nanocubes Ultra local modification of surface plasmons properties in silver nanocubes. 2012.

[364] Shu Fen Tan, Lin Wu, Joel K.W. Yang, Ping Bai, Michel Bosman, and Christian A. Nijhuis. Quantum plasmon resonances controlled by molecular tunnel junctions. *Science*, 343(6178):1496–1499, 2014.

[365] Dario Knebl, Anton Hörl, Andreas Trügler, Johannes Kern, Joachim R. Krenn, Peter Puschnig, and Ulrich Hohenester. Gap plasmonics of silver nanocube dimers. *Physical Review B - Condensed Matter and Materials Physics*, 93(8):1–5, 2016.

[366] Yijie Yang, Yih Hong Lee, In Yee Phang, Ruibin Jiang, Howard Yi Fan Sim, Jianfang Wang, and Xing Yi Ling. A Chemical Approach to Break the Planar Configuration of Ag Nanocubes into Tunable Two-Dimensional Metasurfaces. *Nano Letters*, 16(6):3872–3878, 2016.

[367] Yijie Yang, Yih Hong Lee, Chee Leng Lay, and Xing Yi Ling. Tuning Molecular-Level Polymer Conformations Enables Dynamic Control over Both the Interfacial Behaviors of Ag Nanocubes and Their Assembled Metacrystals. *Chemistry of Materials*, 29(14):6137–6144, 2017.

[368] Matthew Rycenga, Claire M Cobley, Jie Zeng, Weiyang Li, and Christine H Moran. Controlling the Synthesis and Assembly of Silver Nanostructures for Plasmonic Applications. *Chem Rev*, 111(6):3669–3712, 2012.

[369] Bart Goris, Giulio Guzzinati, Cristina Fernández-López, Jorge Pérez-Juste, Luis M. Liz-Marzán, Andreas Trügler, Ulrich Hohenester, Jo Verbeeck, Sara Bals, and Gustaaf Van Tendeloo†. Plasmon Mapping in Au@ Ag Nanocube Assemblies. *The Journal of Physical Chemistry C*, 118(28):15356–15362, 2014.

[370] Sarra Mitiche, Sylvie Marguet, Fabrice Charra, and Ludovic Douillard. Near-Field Localization of Single Au Cubes: A Group Theory Description. *Journal of Physical Chemistry C*, 121(8):4517–4523, 2017.

[371] Alfredo Campos, Arnaud Arbouet, Jérôme Martin, Davy Gérard, Julien Proust, Jérôme Plain, and Mathieu Kociak. Plasmonic Breathing and Edge Modes in Aluminum Nanotriangles. *ACS Photonics*, 4(5):1257–1263, 2017.

[372] S P Zhang, K Bao, N J Halas, H X Xu, and P Nordlander. Substrate-Induced Fano Resonances of a Plasmonic: Nanocube: A Route to Increased-Sensitivity Localized Surface Plasmon Resonance Sensors Revealed. *Nano Letters*, 11(4):1657–1663, 2011.

[373] Shunping Zhang, Kui Bao, Naomi J Halas, Hongxing Xu, and Peter Nordlander. Substrate-induced fano resonances of a plasmonic nanocube: a route to increased-sensitivity localized surface plasmon resonance sensors revealed. *Nano Letters*, 11(4):1657–1663, 2011.

[374] H.Hwang and R. A. Haddad. Adaptive median filters: Newalgorithms and results. *IEEE Trans. Image Process*, 4(4):499–502, 1995.

[375] Ulrich Hohenester. Making simulations with the MNPBEM toolbox big: Hierarchical matrices and iterative solvers. *Computer Physics Communications*, 222:209–228, 2018.

[376] Luiz Henrique Galvao, Pabitra Das, Lots Chemists, and Mathieu Kociak. h – BN monolayer as a substrate for plasmonics on metallic nanoparticles. *Submitted*.

[377] Zackaria Mahfoud. *Nanometric Spectroscopies of Plasmonic Structures and Semiconductor Nanocrystals*. PhD thesis, 2014.

[378] S Aberra Guebrou, C Symonds, E Homeyer, J C Plenet, Yu. N Gartstein, V M Agranovich, and J Bellessa. Coherent Emission from a Disordered Organic Semiconductor Induced by Strong Coupling with Surface Plasmons. *Phys. Rev. Lett.*, 108(6):66401, 2012.

[379] Y Fedutik, V V Temnov, O Schöps, U Woggon, and M V Artemyev. Exciton-plasmon-photon conversion in plasmonic nanostructures. *Physical Review Letters*, 99(13):1–4, 2007.

[380] J N Farahani, D W Pohl, H J Eisler, and B Hecht. Single quantum dot coupled to a scanning optical antenna: A tunable superemitter. *Physical Review Letters*, 95(1):1–4, 2005.

[381] Sergei Kuhn, Ulf Hakanson, Lavinia Rogobete, and Vahid Sandoghdar. Enhancement of single-molecule fluorescence using a gold nanoparticle as an optical nanoantenna. *Physical Review Letters*, 97(1):1–4, 2006.

[382] Stefan Schietinger, Michael Barth, Thomas Aichele, and Oliver Benson. Plasmon-enhanced single photon emission from a nanoassembled metal - Diamond hybrid structure at room temperature. *Nano Letters*, 9(4):1694–1698, 2009.

[383] Ryan Beams, Dallas Smith, Timothy W. Johnson, Sang Hyun Oh, Lukas Novotny, and A. Nick Vamivakas. Nanoscale fluorescence lifetime imaging of an optical antenna with a single diamond NV center. *Nano Letters*, 13(8):3807–3811, 2013.

[384] Br Fisher and Hj Eisler. Emission intensity dependence and single-exponential behavior in single colloidal quantum dot fluorescence lifetimes. *Journal of Physical Chemistry B*, 11:143–148, 2004.

[385] Jelle Storteboom, Philip Dolan, Stefania Castelletto, Xiangping Li, and Min Gu. Lifetime investigation of single nitrogen vacancy centres in nanodiamonds. *Opt. Express*, 23(9):11327–11333, 2015.

[386] Tsong-Shin Lim, Chi-Cheng Fu, Kang-Chuang Lee, Hsu-Yang Lee, Kowa Chen, Wen-Feng Cheng, Woei Wu Pai, Huan-Cheng Chang, and Wunshain Fann. Fluorescence enhancement and lifetime modification of single nanodiamonds near a nanocrystalline silver surface. *Physical Chemistry Chemical Physics*, 11(10):1508, 2009.

[387] Sebastain K H Andersen, Shailesh Kumar, and Sergey I Bozhevolnyi. Coupling of nitrogen-vacancy centers in a nanodiamond to a silver nanocube. *Opt. Mater. Express*, 6(11):3394–3406, nov 2016.

[388] M Merano, S Sonderegger, A Crottini, S Collin, P Renucci, E Pelucchi, A Malko, M H Baier, E Kapon, B Deveaud, and J.-D. Ganière. Probing carrier dynamics in nanostructures by picosecond cathodoluminescence. *Nature*, 438(7067):479–482, 2005.

[389] Sophie Meuret, Toon Coenen, Hans Zeijlemaker, Michael Latzel, Silke Christiansen, Sonia Conesa-Boj, and Albert Polman. Photon bunching reveals single-electron cathodoluminescence excitation efficiency in InGaN quantum wells. *Physical Review B*, 96(3):35308, 2017.

[390] Luiz H G Tizei and Mathieu Kociak. Chapter Four-Quantum Nanooptics in the Electron Microscope. *Advances in Imaging and Electron Physics*, 199:185–235, 2017.

[391] Julia Tisler, Gopalakrishnan Balasubramanian, Boris Naydenov, Roman Kolesov, Bernhard Grotz, Rolf Reuter, Jean-Paul Boudou, Patrick A Curmi, Mohamed Sennour, Alain Thorel, Michael Börsch, Kurt Aulenbacher, Rainer Erdmann, Philip R Hemmer, Fedor Jelezko, and Jörg Wrachtrup. Fluorescence and Spin Properties of Defects in Single Digit Nanodiamonds. *ACS Nano*, 3(7):1959–1965, 2009.

[392] Alexios Beveratos, Rosa Brouri, Thierry Gacoin, Jean-Philippe Poizat, and Philippe Grangier. Nonclassical radiation from diamond nanocrystals. *Phys. Rev. A*, 64(6):61802, nov 2001.

[393] G Liaugaudas, G Davies, K Suhling, R U A Khan, and D J F Evans. Luminescence lifetimes of neutral nitrogen-vacancy centres in synthetic diamond containing nitrogen. *Journal of Physics: Condensed Matter*, 24(43):435503, 2012.

[394] A T Collins, M F Thomaz, and M I B Jorge. Luminescence decay time of the 1.945 eV centre in type Ib diamond. *Journal of Physics C: Solid State Physics*, 16(11):2177–2181, 1983.

[395] F A Inam, T Gaebel, Carlo Bradac, L Stewart, M J Withford, J M Dawes, J R Rabeau, and M J Steel. Modification of spontaneous emission from nanodiamond colour centres on a structured surface. *New J. Phys.*, 13(7):73012, 2011.

[396] J. J. Greffet, J. P. Hugonin, M. Besbes, N. D. Lai, F. Treussart, and J. F. Roch. Diamond particles as nanoantennas for nitrogen-vacancy color centers. 2011.

[397] Xiang Meng, Shang Liu, Jerry I. Dadap, and Richard M. Osgood. Plasmonic enhancement of a silicon-vacancy center in a nanodiamond crystal. *Physical Review Materials*, 1(1):015202, 2017.

[398] Luiz H G Tizei and Mathieu Kociak. Spectrally and spatially resolved cathodoluminescence of nanodiamonds: local variations of the NV0 emission properties. *Nanotechnology*, 23:175702, 2012.

[399] Ph Lambin, L Henrard, P Thiry, C Silien, and J P Vigneron. The dielectric theory of HREELS, a short survey. *Journal of electron spectroscopy and related phenomena*, 129(2):281–292, 2003.

[400] B D Forbes and L J Allen. Modeling energy-loss spectra due to phonon excitation. *Physical Review B*, 94(1):14110, 2016.

[401] Ulrich Hohenester, Andreas Trügler, Philip E. Batson, and Maureen J. Lagos. Inelastic vibrational bulk and surface losses of swift electrons in ionic nanostructures. *Physical Review B*, 97(16):1–12, 2018.

[402] R. J. Nicholls, F. S. Hage, D. G. McCulloch, Q. M. Ramasse, K. Refson, and J. R. Yates. Theory of momentum-resolved phonon spectroscopy in the electron microscope. pages 2–7, 2018.

[403] Hugo Lourenço-Martins and Mathieu Kociak. Vibrational surface electron-energy-loss spectroscopy probes confined surface-phonon modes. *Physical Review X*, 7(4):041059, 2017.

[404] H Ibach. Optical surface phonons in zinc oxide detected by slow-electron spectroscopy. *Phys. Rev. Lett.*, 24(25):1416–1418, 1970.

[405] K L Kliewer and R Fuchs. Theory of dynamical properties of dielectric surfaces. *Adv. Chem. Phys.*, 27:355, 1974.

[406] R Ruppin. Electromagnetic Scattering from Finite Dielectric Cylinders. *Journal of Physics D-applied Physics*, 23(7):757–763, 1990.

[407] F J de Abajo and J Aizpurua. Numerical simulation of electron energy loss near inhomogeneous dielectrics. *Phys. Rev. B*, 56(24):15873–15884, 1997.

[408] Ulrich Hohenester, Harald Ditlbacher, and Joachim R. Krenn. Electron-energy-loss spectra of plasmonic nanoparticles. *Physical Review Letters*, 103(10):1–4, 2009.

[409] N Geuquet and L Henrard. EELS and optical response of a noble metal nanoparticle in the frame of a discrete dipole approximation. *Ultramicroscopy*, 110:1075, 2010.

[410] Ulrich Hohenester. Simulating electron energy loss spectroscopy with the MNPBEM toolbox. *Computer Physics Communications*, 185(3):1177–1187, 2014.

[411] F J de Abajo and M Kociak. Probing the photonic local density of states with electron energy loss spectroscopy. *Physical Review Letters*, 100(10):106804, 2008.

[412] Mathieu Kociak and Odile Stephan. Mapping plasmons at the nanometer scale in an electron microscope. *Chem. Soc. Rev.*, 43(11):3865–3883, 2014.

[413] L Novotny and N van Hulst. Antennas for light. *Nature Photonics*, 5(2):83–90, 2011.

[414] D Rossouw, M Couillard, J Vickery, E Kumacheva, and G A Botton. Multipolar Plasmonic Resonances in Silver Nanowire Antennas Imaged with a Subnanometer Electron Probe. *Nano Letters*, 11(4):1499–1504, 2011.

[415] A. M. Hofmeister, E. Keppel, and A. K. Speck. Absorption and reflection infrared spectra of MgO and other diatomic compounds. *Monthly Notices of the Royal Astronomical Society*, 345(1):16–38, 2003.

[416] Anton Hörl, Andreas Trügler, and Ulrich Hohenester. Full Three-Dimensonal Reconstruction of the Dyadic Green Tensor from Electron Energy Loss Spectroscopy of Plasmonic Nanoparticles. *ACS Photonics*, 2(10):1429–1435, 2015.

[417] R Gomez-Medina, N Yamamoto, M Nakano, and F J G Abajo. Mapping plasmons in nanoantennas via cathodoluminescence. *New Journal of Physics*, 10:105009, 2008.

[418] C Dwyer, T Aoki, P Rez, S L Y Chang, T C Lovejoy, and O L Krivanek. Electron-Beam Mapping of Vibrational Modes with Nanometer Spatial Resolution. *Physical Review Letters*, 117(25):256101, 2016.

[419] R Hillenbrand, T Taubner, and F Keilmann. Phonon-enhanced light–matter interaction at the nanometre scale. *Nature*, 418(6894):159–162, 2002.

[420] G Radtke, D Taverna, M Lazzeri, and E Balan. First-Principles Vibrational Electron Energy Loss Spectroscopy of Guanine. *Phys. Rev. Lett.*, 119(2):27402–27405, 2017.

[421] P Rez, T Aoki, K March, D Gur, O L Krivanek, N Dellby, T C Lovejoy, S G Wolf, and H Cohen. Damage-free vibrational spectroscopy of biological materials in the electron microscope. *Nature Communications*, 7:10945, 2016.

[422] M Fujii, M Wada, S Hayashi, and K Yamamoto. Infrared Absorption in Si02-Ge composite films: influences of Ge microcrystals on the longitudinal-optical phonons in SiO2. *Phys. Rev. B*, (46):15930, 1992.

[423] R Geick, C H Perry, and G Rupprecht. Normal modes in hexagonal boron nitride. *Phys. Rev.*, 1966.

[424] P E Batson and M J Lagos. Characterization of Misfit Dislocations in Si Quantum Well Structures Enabled by STEM Based Aberration Correction. *Ultramicroscopy*, page in press, 2017.

[425] O Stephan, D Taverna, M Kociak, K Suenaga, L Henrard, and C Colliex. Dielectric response of isolated carbon nanotubes investigated by spatially resolved electron energy-loss spectroscopy: From multiwalled to single-walled nanotubes. *Physical Review B*, 66(15):155422, 2002.

[426] Alexander A. Govyadinov, Andrea Konečná, Andrey Chuvilin, Saül Vélez, Irene Dolado, Alexey Y. Nikitin, Sergei Lopatin, Fèlix Casanova, Luis E. Hueso, Javier Aizpurua, and Rainer Hillenbrand. Probing low-energy hyperbolic polaritons in van der Waals crystals with an electron microscope. *Nature Communications*, 8(1), 2017.

[427] M Kammerer, F Merz, and F Jenko. Exceptional points in linear gyrokinetics. *Physics of Plasmas*, 15(5):1–7, 2008.

[428] Sang Bum Lee, Juhee Yang, Songky Moon, Soo Young Lee, Jeong Bo Shim, Sang Wook Kim, Jai Hyung Lee, and Kyungwon An. Observation of an exceptional point in a chaotic optical microcavity. *Physical Review Letters*, 103(13):1–4, 2009.

[429] M. Liertzer, Li Ge, A. Cerjan, A. D. Stone, H. E. Türeci, and S Rotter. Pump-induced exceptional points in lasers. *Physical Review Letters*, 108(17):1–5, 2012.

[430] Martin Brandstetter, Matthias Liertzer, Christoph Deutsch, P. Klang, Joachim Schöberl, Hakan E. Türeci, Gottfried Strasser, Karl Unterrainer, and Stefan Rotter. Reversing the pump dependence of a laser at an exceptional point. *Nature communications*, 5(May):4034, 2014.

[431] Isabel Romero, Javier Aizpurua, Garnett W. Bryant, and F. Javier García De Abajo. Plasmons in nearly touching metallic nanoparticles: singular response in the limit of touching dimers. *Optics Express*, 14(21):9988, 2006.

[432] Tolga Atay, Jung Hoon Song, and Arto V. Nurmikko. Strongly interacting plasmon nanoparticle pairs: From dipole-dipole interaction to conductively coupled regime. *Nano Letters*, 4(9):1627–1631, 2004.

[433] Weijian Chen, Şahin Kaya Özdemir, Guangming Zhao, Jan Wiersig, and Lan Yang. Exceptional points enhance sensing in an optical microcavity. *Nature*, 548(7666):192–195, 2017.

[434] E. Altewischer, M. P. Van Exter, and J. P. Woerdman. Plasmon-assisted transmission of entangled photons. *Nature*, 418(6895):304–306, 2002.

[435] Esteban Moreno, F J Garcia-Vidal, Daniel Erni, J Ignacio Cirac, and L Martin-Moreno. Theory of Plasmon-Assisted Transmission of Entangled Photons. *Phys. Rev. Lett.*, 92(23):236801, 2004.

[436] Sylvain Fasel, Franck Robin, Esteban Moreno, Daniel Erni, Nicolas Gisin, and Hugo Zbinden. Energy-Time Entanglement Preservation in Plasmon-Assisted Light Transmission. *Phys. Rev. Lett.*, 94(11):110501, mar 2005.

[437] Sylvain Fasel, Matthäus Halder, Nicolas Gisin, and Hugo Zbinden. Quantum superposition and entanglement of mesoscopic plasmons. *New Journal of Physics*, 8, 2006.

[438] X. F. Ren, G. P. Guo, Y. F. Huang, C. F. Li, and G. C. Guo. Plasmon-assisted transmission of high-dimensional orbital angular- Momentum entangled state. *Europhysics Letters*, 76(5):753–759, 2006.

[439] Alexander Huck, Stephan Smolka, Peter Lodahl, Anders S. Sørensen, Alexandra Boltasseva, Jiri Janousek, and Ulrik L. Andersen. Demonstration of quadrature-squeezed surface plasmons in a gold waveguide. *Physical Review Letters*, 102(24):1–4, 2009.

[440] Roman Kolesov, Bernhard Grotz, Gopalakrishnan Balasubramanian, Rainer J. Stöhr, Aurélien A L Nicolet, Philip R. Hemmer, Fedor Jelezko, and Jörg Wrachtrup. Wave-particle duality of single surface plasmon-polaritons. *Nature Physics*, 5(7):470–474, 2009.

[441] Sinan Balci. Ultrastrong plasmon-exciton coupling in metal nanoprisms with J-aggregates. *Optics letters*, 38(21):4498–501, 2013.

[442] M. S. Tame, K. R. McEnery, Ş K. Özdemir, J. Lee, S. A. Maier, and M. S. Kim. Quantum plasmonics. *Nature Physics*, 9(6):329–340, 2013.

[443] A. Gonzalez-Tudela, D. Martin-Cano, E. Moreno, L. Martin-Moreno, C. Tejedor, and F. J. Garcia-Vidal. Entanglement of two qubits mediated by one-dimensional plasmonic waveguides. *Physical Review Letters*, 106(2):1–4, 2011.

[444] J. J. Hopfield. Theory of the contribution of excitons to the complex dielectric constant of crystals. *Physical Review*, 112(5):1555–1567, 1958.

[445] Yoshiko Oi Nakamura. Quantization of Non-Radiative Surface Plasma Oscillations. *Progress of Theoretical Physics*, 70(4):908–919, 1983.

[446] David J Bergman and Mark I Stockman. Surface Plasmon Amplification by Stimulated Emission of Radiation: Quantum Generation of Coherent Surface Plasmons in Nanosystems. *Physical Review Letters*, 90(2):27402, 2003.

[447] Andreas Trügler and Ulrich Hohenester. Strong coupling between a metallic nanoparticle and a single molecule. *Physical Review B - Condensed Matter and Materials Physics*, 77(11), 2008.

[448] N. G. Kampen and I. Oppenheim. Langevin and master equation in quantum mechanics. *Journal of Statistical Physics*, 87(5-6):1325–1334, 1997.

[449] A. Asenjo-Garcia, M. Moreno-Cardoner, A. Albrecht, H. J. Kimble, and D. E. Chang. Exponential improvement in photon storage fidelities using subradiance & "selective radiance" in atomic arrays. *Physical Review X*, 7(3):1–36, 2017.

[450] Alejandro Manjavacas, Peter Nordlander, and F. Javier García De Abajo. Plasmon blockade in nanostructured graphene. *ACS Nano*, 6(2):1724–1731, 2012.

[451] V. Despoja, M. Šunjić, and L. Marušić. Propagators and spectra of surface polaritons in metallic slabs: Effects of quantum-mechanical nonlocality. *Physical Review B - Condensed Matter and Materials Physics*, 80(7), 2009.

[452] Y. L. Chiou, J. P. Gambino, and M. Mohammad. Determination of the Fowler-Nordheim tunneling parameters from the Fowler-Nordheim plot. *Solid-State Electronics*, 45(10):1787–1791, 2001.

[453] Claudie Mory. *Etude théorique et experimentale de la formation de l'image en microscopie électronique à balayage par transmission*. PhD thesis, 1985.

[454] L Reimer and H Kohl. *Transmission Electron Microscopy: Physics of Image Formation*. Springer Series in Optical Sciences. Springer New York, 2008.

[455] Virendra N. Mahajan. Orthonormal polynomials in wavefront analysis: analytical solution: errata. *Journal of the Optical Society of America A*, 29(8):1673, 2012.

[456] Robert W. Gray, Christina Dunn, Kevin P. Thompson, and Jannick P. Rolland. An analytic expression for the field dependence of Zernike polynomials in rotationally symmetric optical systems. *Optics Express*, 20(15):16436, 2012.

[457] O.L. L Krivanek. Three-fold astigmatism in high-resolution transmission electron microscopy. *Ultramicroscopy*, 55(4):419–433, 1994.

[458] O. L. Krivanek, N. Dellby, and A. R. Lupini. Towards sub-Å electron beams. *Ultramicroscopy*, 78(1-4):1–11, 1999.

[459] W. O. Saxton. A new way of measuring microscope aberrations. *Ultramicroscopy*, 81(2):41–45, 2000.

[460] A R Lupini. *Aberration Correction in STEM.* PhD thesis, 2001.

[461] L. J. Allen, M. P. Oxley, and D. Paganin. Computational Aberration Correction for an Arbitrary Linear Imaging System. *Physical Review Letters*, 87(12):3–6, 2001.

[462] H. Sawada, T. Sannomiya, F. Hosokawa, T. Nakamichi, T. Kaneyama, T. Tomita, Y. Kondo, T. Tanaka, Y. Oshima, Y. Tanishiro, and K. Takayanagi. Measurement method of aberration from Ronchigram by autocorrelation function. *Ultramicroscopy*, 108(11):1467–1475, 2008.

[463] M. Haider, P. Hartel, H. Mller, S. Uhlemann, and J. Zach. Information transfer in a TEM corrected for spherical and chromatic aberration. *Microscopy and Microanalysis*, 16(4):393–408, 2010.

[464] Fumio Hosokawa, Hidetaka Sawada, Yukihito Kondo, Kunio Takayanagi, and Kazutomo Suenaga. Development of Cs and Cc correctors for transmission electron microscopy. *Journal of Electron Microscopy*, 62(1):23–41, 2013.

[465] J. M. Cowley. Electron diffraction phenomena observed with a high resolution STEM instrument. *Journal of Electron Microscopy Technique*, 3(1):25–44, 1986.

[466] J. Aizpurua, A. Howie, and F. J. García de Abajo. Valence-electron energy loss near edges, truncated slabs, and junctions. *Physical Review B*, 60(15):11149–11162, 1999.

[467] L Lorenz. On the identity of the vibrations of light with electrical currents. *The London, Edinburgh, and Dublin Philosophical Magazine and Journal of Science*, 34(230):287–301, 1867.

[468] F. Javier García De Abajo. Nonlocal effects in the plasmons of strongly interacting nanoparticles, dimers, and waveguides. *Journal of Physical Chemistry C*, 112(46):17983–17987, 2008.

[469] Christin David and F. Javier García De Abajo. Spatial nonlocality in the optical response of metal nanoparticles. *Journal of Physical Chemistry C*, 115(40):19470–19475, 2011.

[470] Ruben Esteban, Andrei G Borisov, Peter Nordlander, and Javier Aizpurua. Bridging quantum and classical plasmonics with a quantum-corrected model. *Nature communications*, 3(May):825, 2012.

[471] Ulrich Hohenester. Quantum corrected model for plasmonic nanoparticles: A boundary element method implementation. *Physical Review B*, 91:205436, 2015.

[472] Ulrich Hohenester and Claudia Draxl. Ab initio approach for gap plasmonics. *Physical Review B*, 94(16):1–7, 2016.

[473] Dario Knebl. *Simulation of Gap Plasmonics.* PhD thesis, Graz university, 2017.

[474] D Engwirda. *Locally Optimal Delaunay-refinement and Optimisation-based Mesh Generations.* 2014.

[475] Jürgen Waxenegger, Andreas Trügler, and Ulrich Hohenester. Plasmonics simulations with the MNPBEM toolbox: Consideration of substrates and layer structures. *Computer Physics Communications*, 193:138–150, 2015.

[476] Laurence D Barron and A David Buckingham. Vibrational optical activity. *Chemical Physics Letters*, 492(4):199–213, 2010.

[477] L D Barron and A D Buckingham. Rayleigh and Raman scattering from optically active molecules. *Molecular Physics*, 20(6):1111–1119, 1971.

[478] Daniel M. Lipkin. Existence of a new conservation law in electromagnetic theory. *Journal of Mathematical Physics*, 5(5):696–700, 1964.

[479] Oriol Arteaga, Jordi Sancho-Parramon, Shane Nichols, Ben M. Maoz, Adolf Canillas, Salvador Bosch, Gil Markovich, and Bart Kahr. Relation between 2D/3D chirality and the appearance of chiroptical effects in real nanostructures. *Optics Express*, 24(3):2242, 2016.

[480] E. Plum, X. X. Liu, V. A. Fedotov, Y. Chen, D. P. Tsai, and N. I. Zheludev. Metamaterials: Optical activity without chirality. *Physical Review Letters*, 102(11):1–4, 2009.

[481] Ropert P. Cameron and Stephen M. Barnett. Electric-magnetic symmetry and Noether's theorem. *New Journal of Physics*, 14:123019, 2012.

[482] Robert P. Cameron, Stephen M. Barnett, and Alison M. Yao. Optical helicity, optical spin and related quantities in electromagnetic theory. *New Journal of Physics*, 14, 2012.

[483] Konstantin Y. Bliokh, Aleksandr Y. Bekshaev, and Franco Nori. Dual electromagnetism : helicity , spin , momentum and angular momentum. *New Journal of Physics*, 15:033026, 2013.

[484] Gerard Nienhuis. Conservation laws and symmetry transformations of the electromagnetic field with sources. *Physical Review A*, 93(2):1–9, 2016.

université PARIS-SACLAY

ÉCOLE DOCTORALE
Ondes et Matière
(EDOM)

Titre : Expériences et theorie relatives au couplage plasmonique, aux effets ondulatoires et à leur étude par spectroscopie électronique

Mots clés : Plasmonique, Spectroscopies d'électrons, Microscopie électronique

Résumé : Les plasmons de surface (SP) sont des ondes électromagnétiques se propageant à l'interface entre deux milieux, typiquement un métal et un diélectrique. Les plasmons de surface ont la capacité de confiner le champ électromagnétique dans de très petite région de l'espace, typiquement quelques nanomètres, c'est à dire bien en dessous de la limite de diffraction de la lumière. Une conséquence de ce confinement sub-longueur d'onde de la lumière est que leur observation nécessite une résolution spatiale nanométrique - ce qui exclut l'utilisation de techniques optiques standard. Néanmoins, le microscope électronique en transmission à balayage (STEM) est un outil particulièrement adapté à l'étude des plasmons de surface car il emploie des électrons rapides ayant une longueur d'onde typique comprise entre 1 et 10 picomètres. Ainsi, durant la dernière décennie, les spectroscopies électroniques appliquées à la nano-optique se sont fortement développées, parmi elle comptent : la spectroscopie de perte d'énergie électronique (EELS), la spectroscopie cathodoluminescence ou l'interférométrie de Hanbury Brown et Twiss appliquée à la CL. Dans cette thèse, j'ai exploré différents problèmes ouverts de la plasmonique et de la nano-optique dans le cadre particulier de la microscopie électronique.
Dans le chapitre 3, je présente un formalisme prenant en compte à la fois la nature quantique et relativiste des expériences d'EELS en faisant appel notamment à des éléments de théorie quantique des champs. Dans le chapitre 4, nous démontrons que la réalisation d'une expérience d'EELS avec de tels faisceaux permet de mesurer des propriétés jusqu'alors inatteignable à l'échelle du nanomètre telle que la phase des plasmons, leurs chiralité optique voire même leur longueur de cohérence. Dans le chapitre 5, je présente plusieurs résultats théoriques et expérimentaux concernant des expériences de couplage. En particulier, j'étudie le phénomène contre-intuitif d'auto-hybridation qui est une conséquence de la nature non-hermitienne du problème aux valeurs propres associé aux résonances de plasmon et établit une analogie avec les systèmes quantiques ouverts. Enfin, au chapitre 6, je discute des récentes mesures de phonon réalisées dans un STEM grâce au développement de monochromateur électroniques.

Title : Experiment and theory of plasmon coupling physics, wave effects and their study by electron spectroscopies

Keywords : Plasmonics, Electron spectroscopies, Electron microscopy

Abstract : Surface plasmons (SP) are electromagnetic waves propagating at the interface between two media typically a metal and a dielectric. SPs can confine electromagnetic fields in very short volumes (typically one to few nanometers), well below the light diffraction limit. This property has a tremendous number of applications ranging from fundamental physics (e.g. quantum optics) to applications (e.g. cancer therapy). However, the price to pay is that SPs suffer from huge ohmic losses in the metal which leads to very short lifetimes (typically few femtoseconds). Theoretically, this presence of dissipation dramatically hardens the theoretical description of SPs. Another consequence of the sub-wavelength confinement of light associated with SPs is that their observation requires a nanometric resolution - which excludes the use of standard optical techniques. Yet, the scanning transmission electron microscope (STEM) is a particularly suitable tool to study SPs as it employs fast electrons with typical wavelength from 1 to 10 picometers. Thus, the last decade has seen the tremendous development of electron-based spectroscopies applied to nano-optics such as electron energy loss spectroscopy (EELS), cathodoluminescence spectroscopy or STEM- Hanbury Brown and Twiss interferometry. In this thesis, I explore different open problems of plasmonics and nano-optics under the scope of electron microscopy and spectroscopies.
In chapter 3, I develop a formalism taking into account both the quantum and relativistic nature of EELS experiments using elements of quantum field theory. In chapter 4, I apply the latter formalism to the case of EELS measurements of SPs using electrons with shaped phase. In chapter 5, I give several theoretical and experimental results on coupling experiments involving SPs. Particularly, I demonstrate a counter-intuitive type of coupling, the so-called self- hybridization which is a consequence of the non-Hermitian nature of the LSP eigenproblem and draw analogy with open quantum system. Finally, in chapter 6, I discuss the recent result on vibrational EELS in monochromated STEM.

Université Paris-Saclay
Espace Technologique / Immeuble Discovery
Route de l'Orme aux Merisiers RD 128 / 91190 Saint-Aubin, France